Stress-Strain Behavior and Constitutive Modeling of Soils

Lade, Poul V.

Publication date:
2000

Document Version
Publisher's PDF, also known as Version of record

STRESS-STRAIN BEHAVIOR AND CONSTITUTIVE MODELING OF SOILS

by

Poul V. Lade
Department of Civil Engineering
Aalborg University
Sohngaardsholmsvej 57
DK-9000 Aalborg, Denmark

May 2000

Introduction Classical vs. Advanced Approach to Design in Geotechnical Engineering

Classical Approach to Design in Geotechnical Engineering

1. Failure or Stability Considerations

Assumed stress-strain behavior:

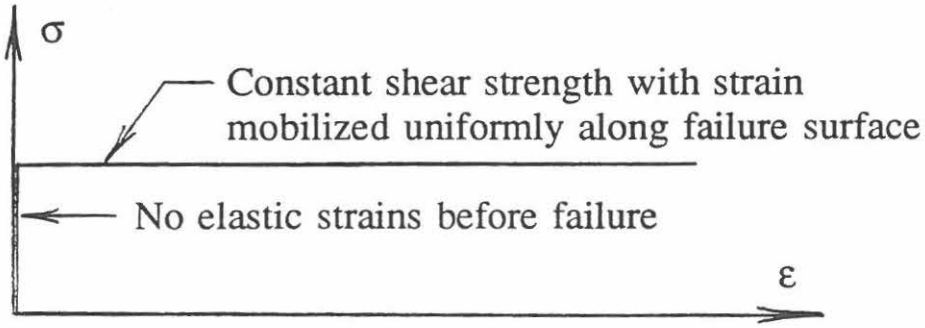

Examples:

Slope Stability

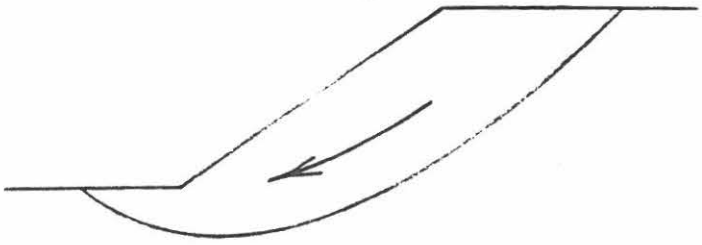

Bearing Capacity

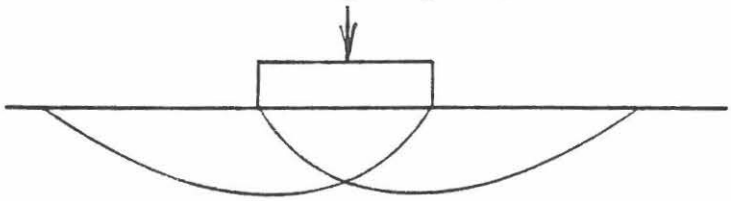

Retaining Walls

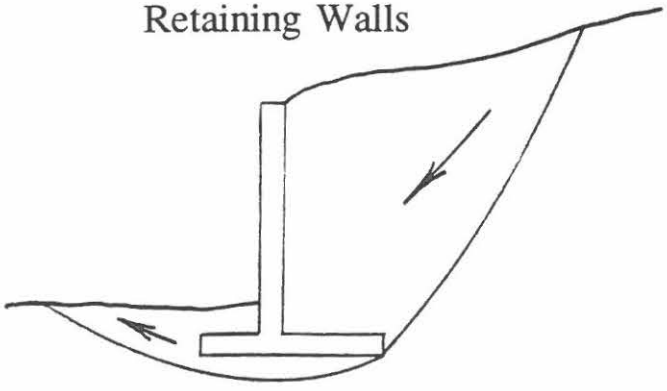

In all cases a factor of safety is produced which is then evaluated based on experience

2. Deformation Considerations

Assumed elastic behavior: Immediate deformations and/or settlements are calculated as linear elastic using closed-form solutions for elastic boundary value problems with an "elastic" modulus estimated from "a" stress-strain curve

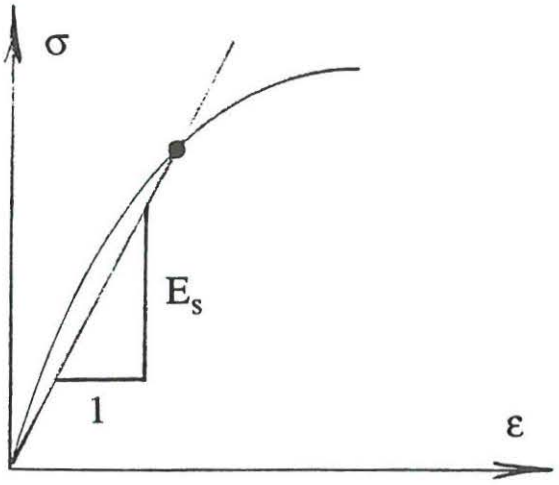

Example:

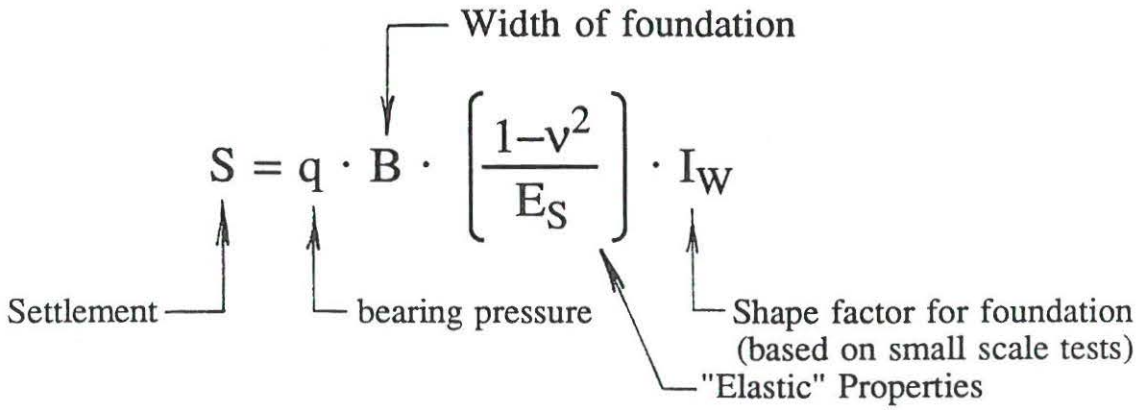

or deformation considerations are based on

a) Consolidation theory with modifications for stress distribution
b) Empirical correlations

Real Behavior of Footing

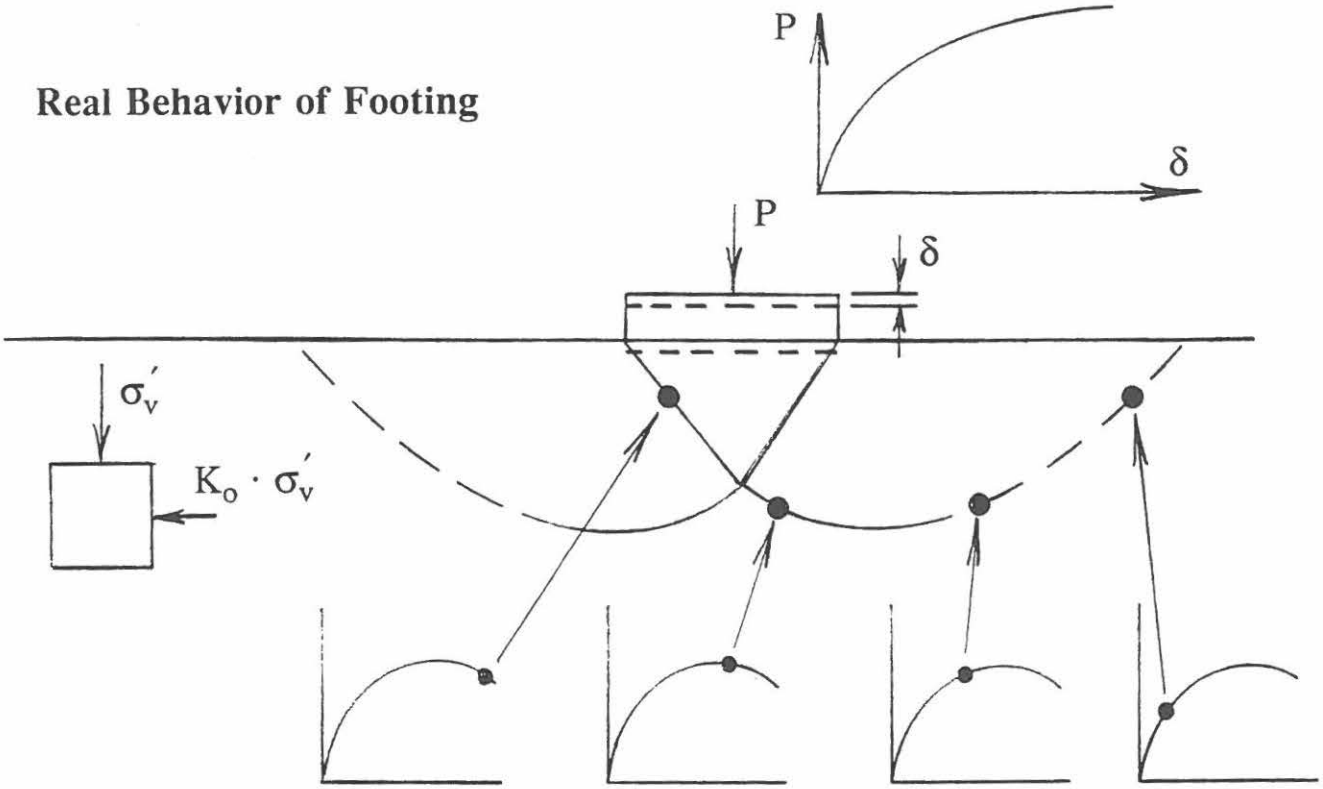

Most significant range of soil behavior:

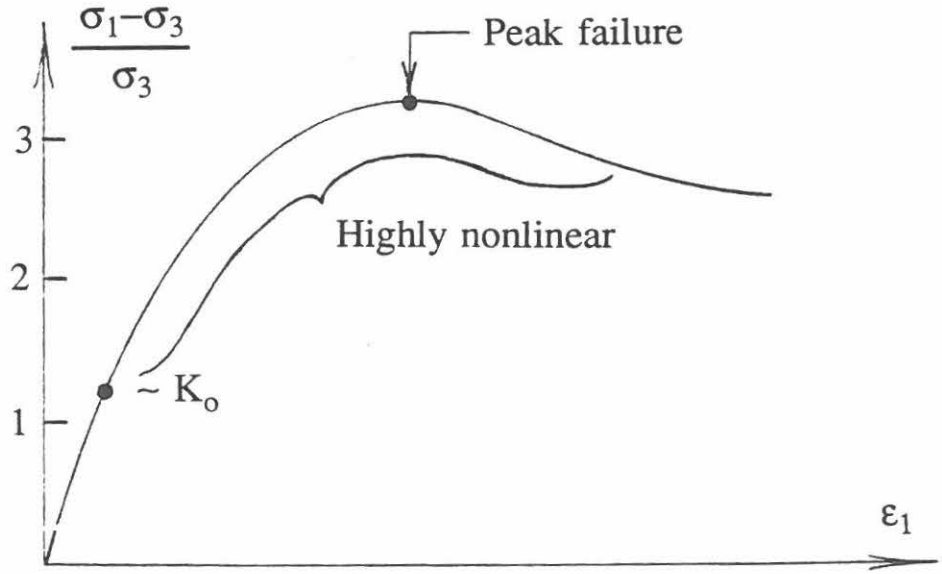

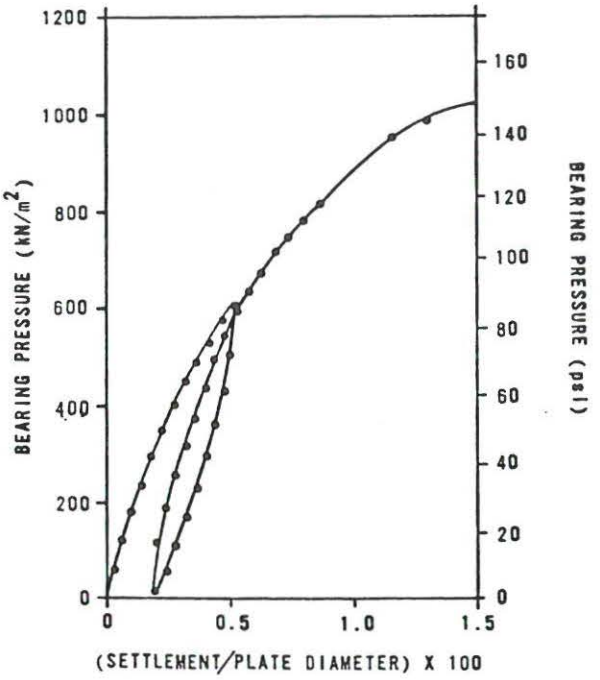

TYPICAL LOAD SETTLEMENT CURVE OBTAINED FROM PLATE BEARING TEST

Which problems can or should be solved by the finite element method?

Examples in which <u>soil–selfweight</u> plays important role:

Slopes: Cut and filled

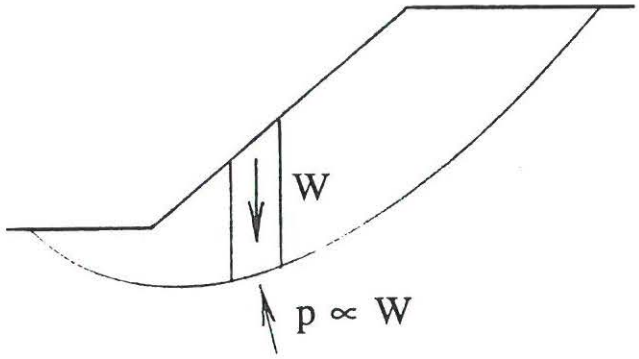

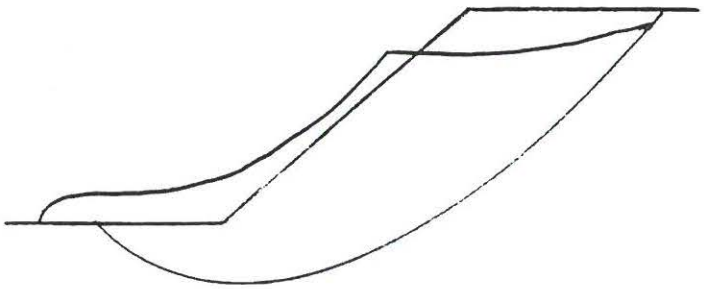

<u>Stability</u> considerations produce accurate estimate of failure, because normal stresses on failure plane are proportional to weight of soil and independent of soil behavior, but <u>Deformations</u> are not elastic

Retaining Wall:

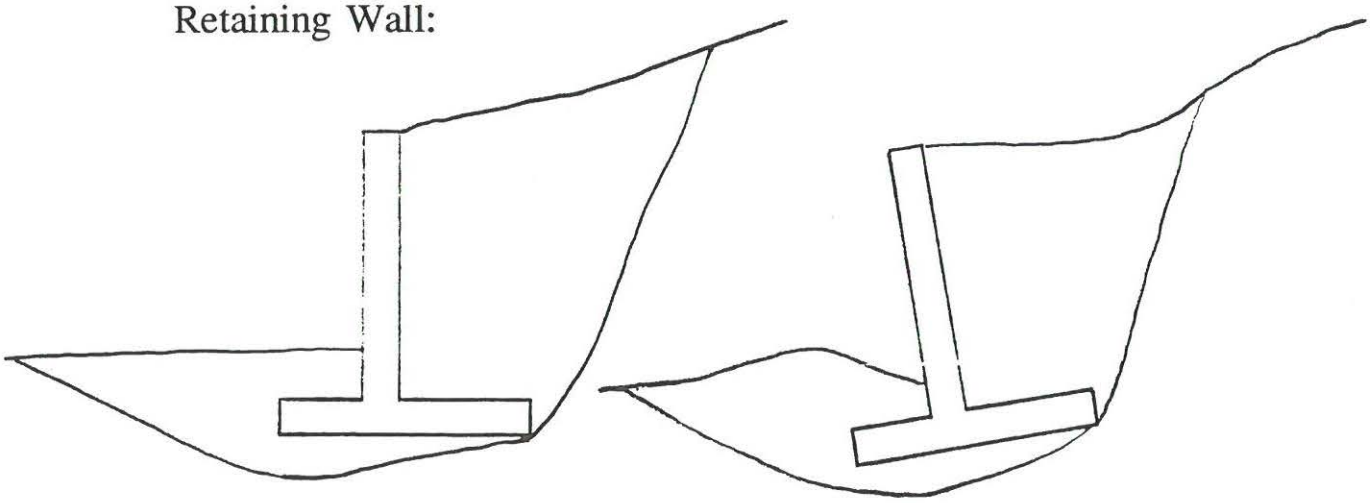

Examples in which soil behavior plays important role (1)

Excavation of Vertical Shaft or Sinking of Caisson

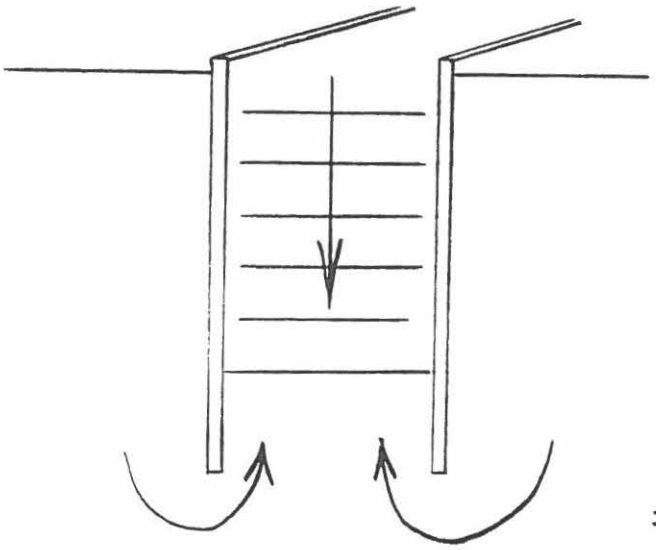

Instability

Tunnel Excavation

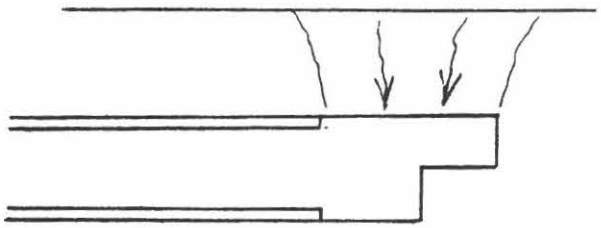

Anchor pull-out or Tie pull-out

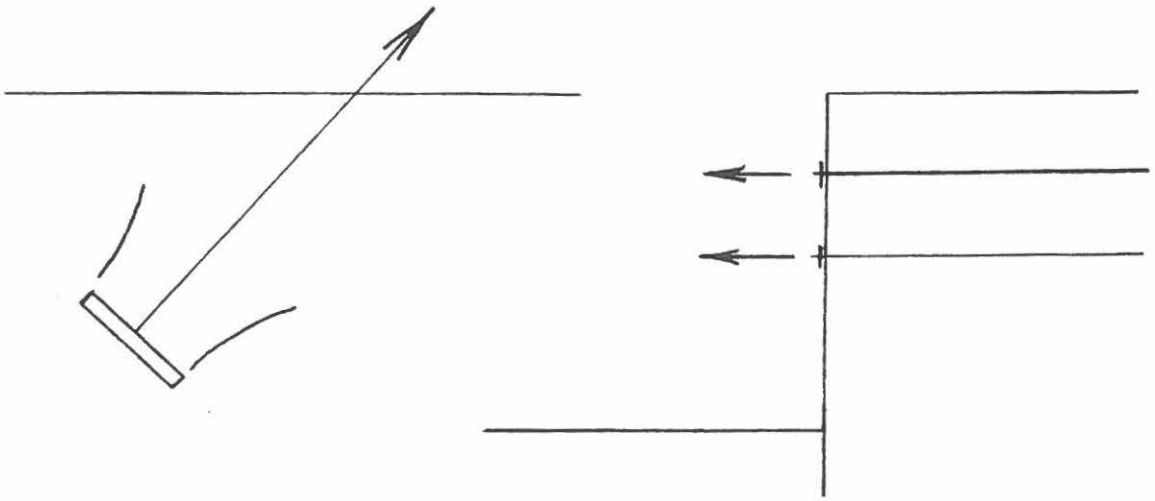

Examples in which soil behavior plays important role (2)

Filling reservoir behind earth dam

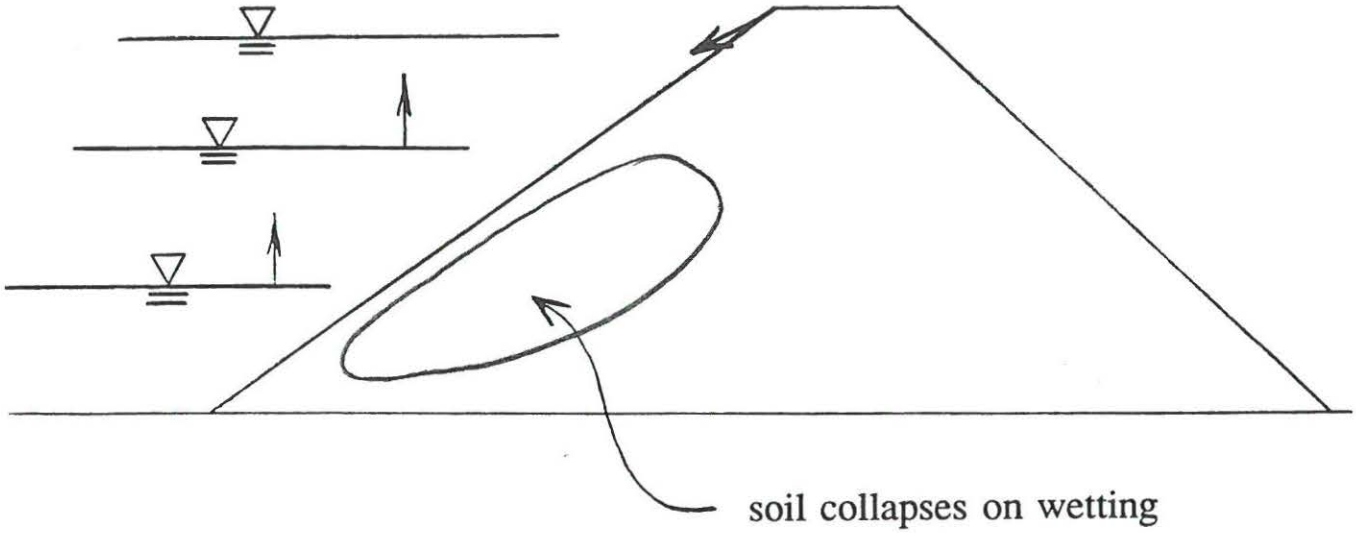

Sheet pile walls: Stress redistribution on excavation

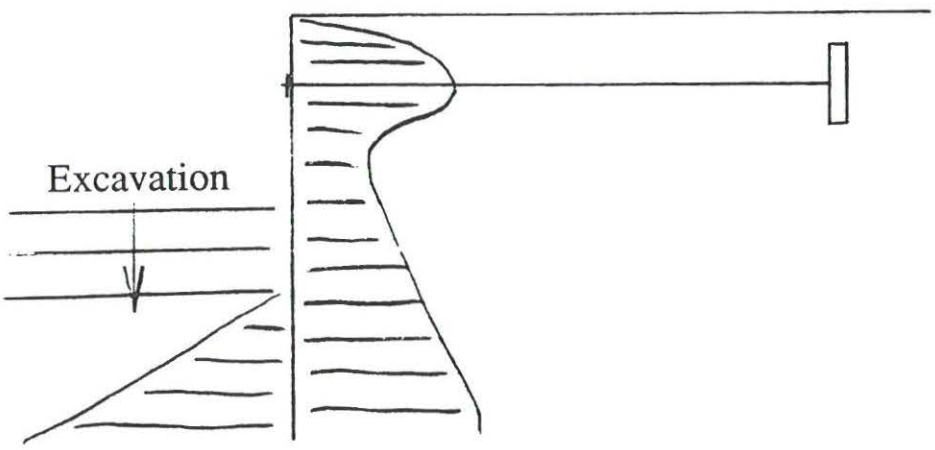

Driven Pile

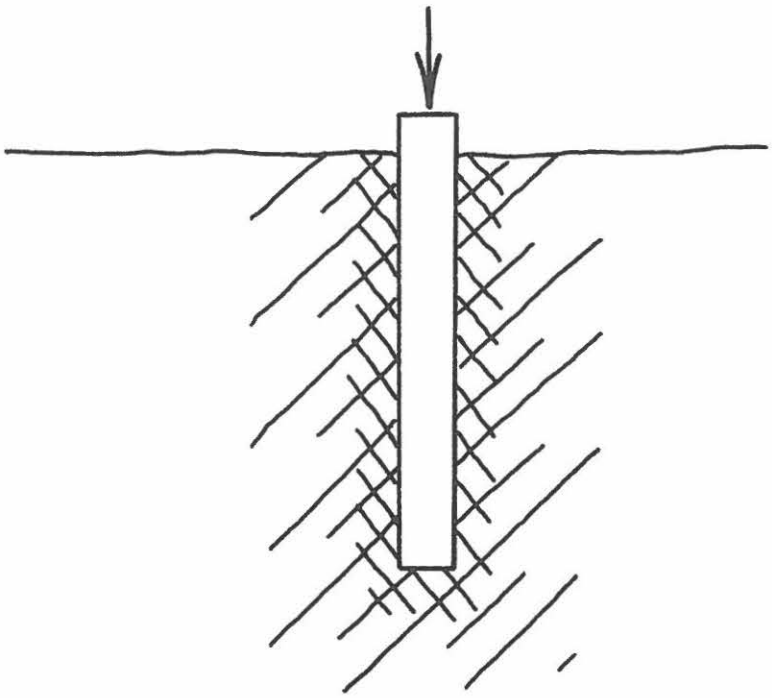

Soil exhibits volume changes during driving. How much volume change determines the normal (horizontal) stress on the pile.

Volume changes and tendency for volume changes during future loading also determines normal (horizontal) stresses on pile and therefore capacity of pile.

Anchor Pull-Out

(Tie-back, reinforced earth, other)

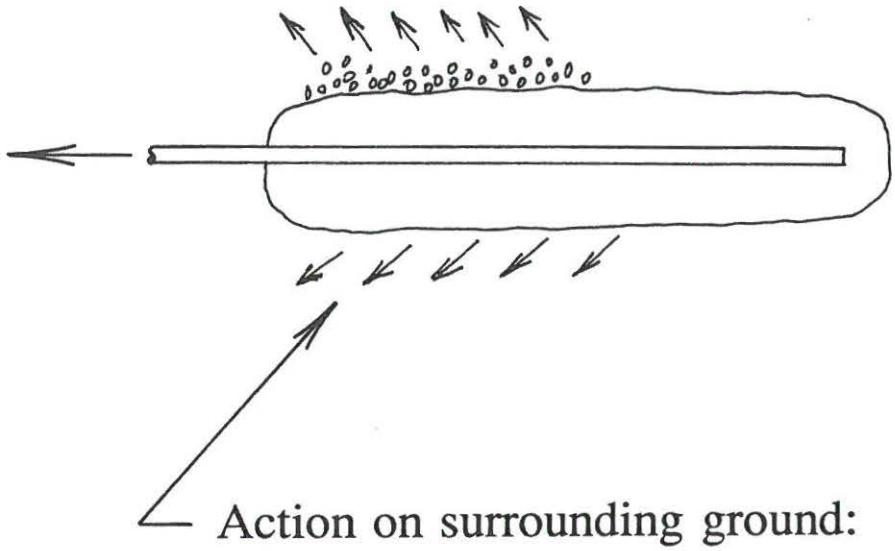

1) Volume expansion if free surface is close and normal stresses are essentially unaltered.

2) Little expansion if burried deep, but high normal stresses are generated.

TRIAXIAL SPECIMEN

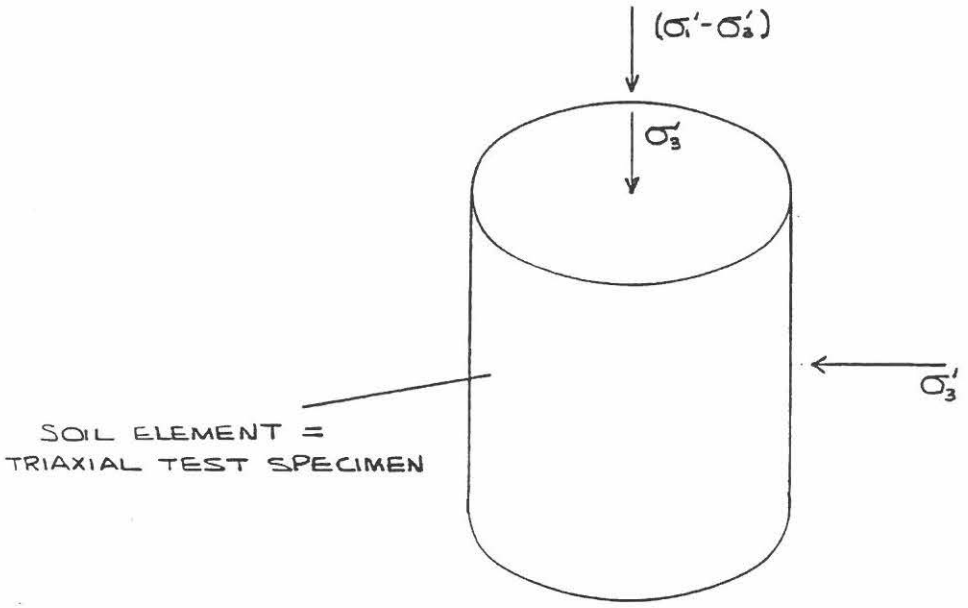

TRIAXIAL APPARATUS

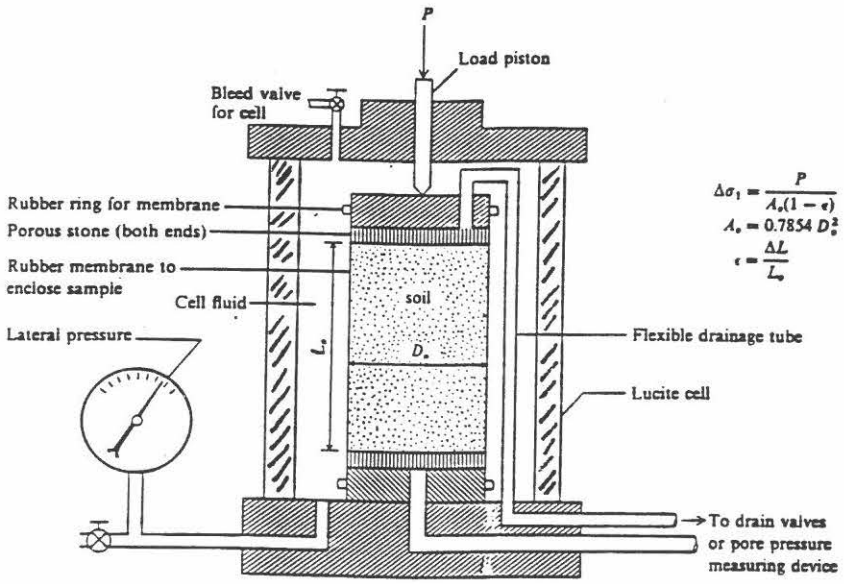

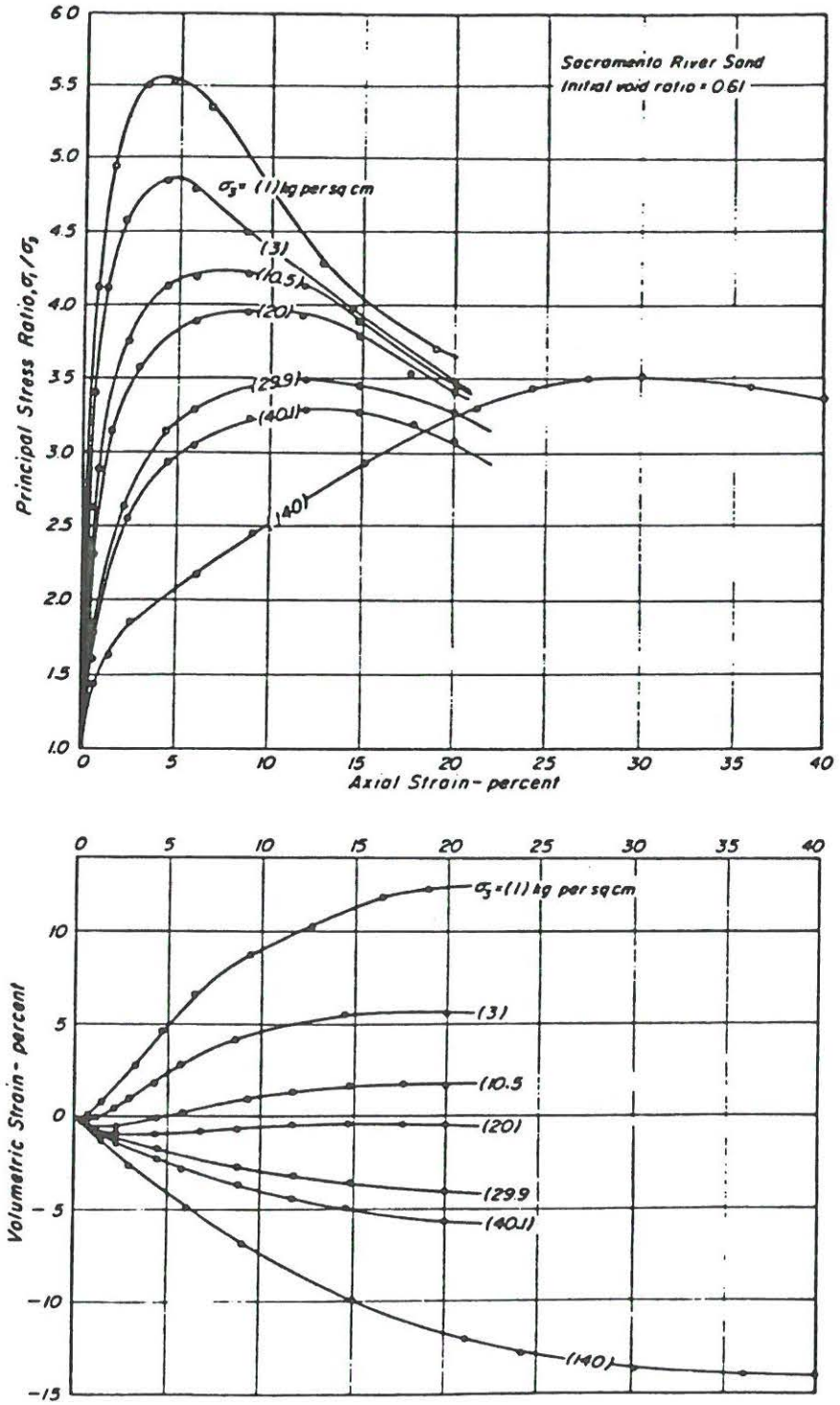

Fig. 3 - STRESS - STRAIN - VOLUME CHANGE DATA FOR DENSE SAND.

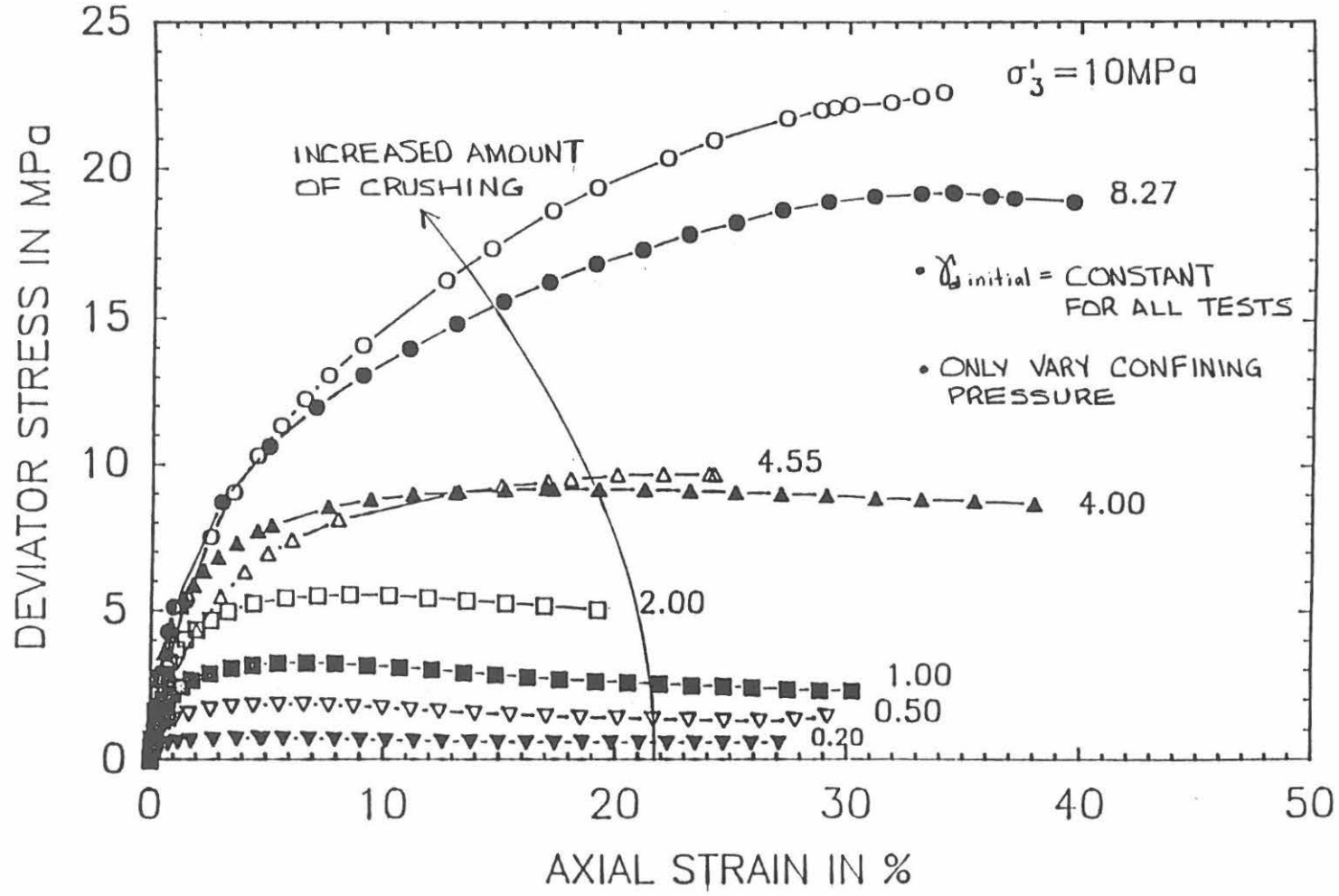

FIGURE 4.3.A Deviator stress versus axial strain for Ghiassian's [9] low pressure drained triaxial compression tests (0.2, 0.5, 1.0, 2.0, and 4.0 MPa), and for the current work (4.55, 8.27 and 10.0 MPa).

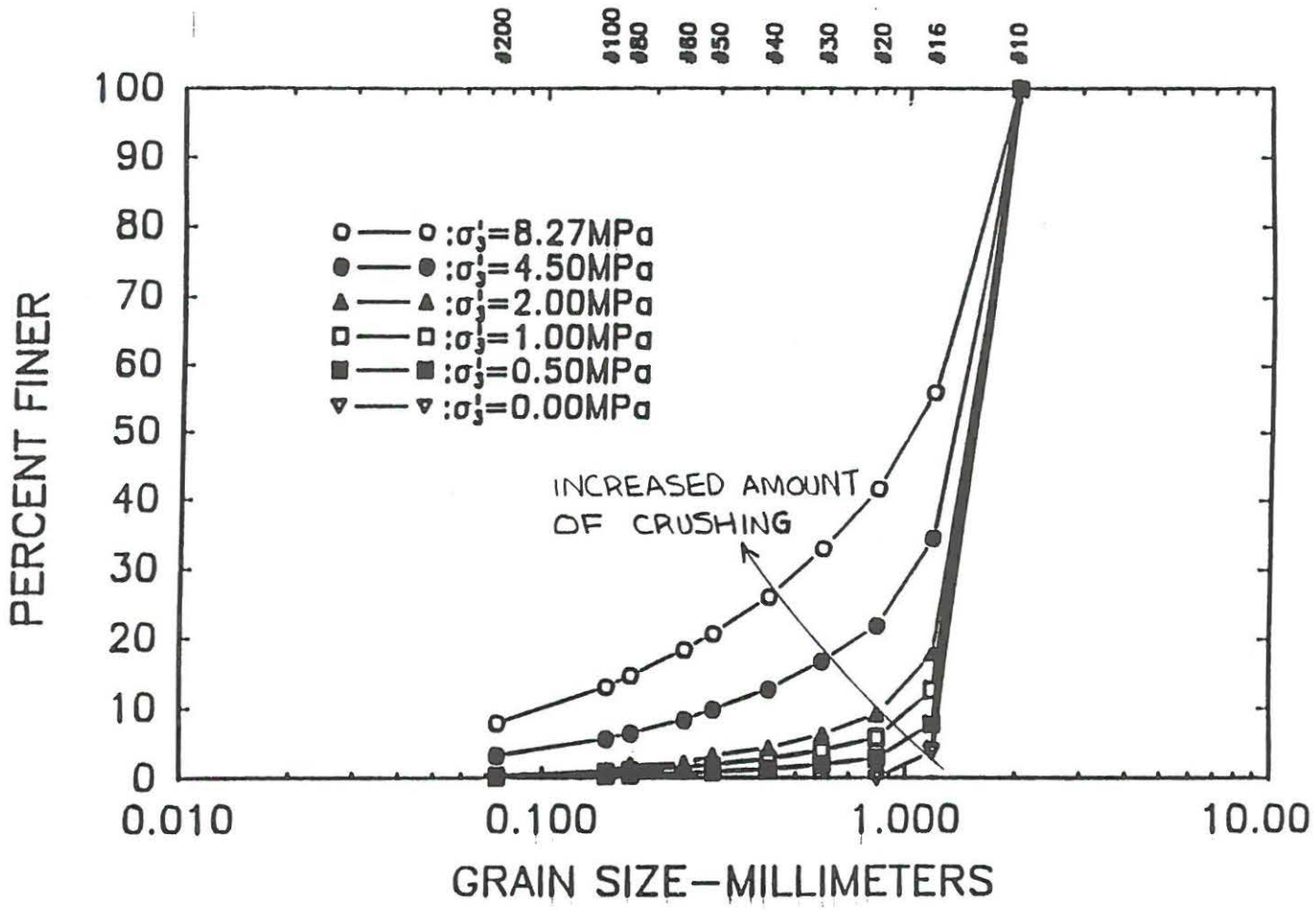

FIGURE 4.15 Sieve analysis showing the amount of particle crushing incurred in the shearing stages for consolidated-drained triaxial compression tests on Cambria sand. Effective confining pressures of 0, 0.50, 1.00, 2.00, 4.50, and 8.27 MPa. (Some results taken from Ghiassian's work [9]).

Particle crushing characterized by different factors:

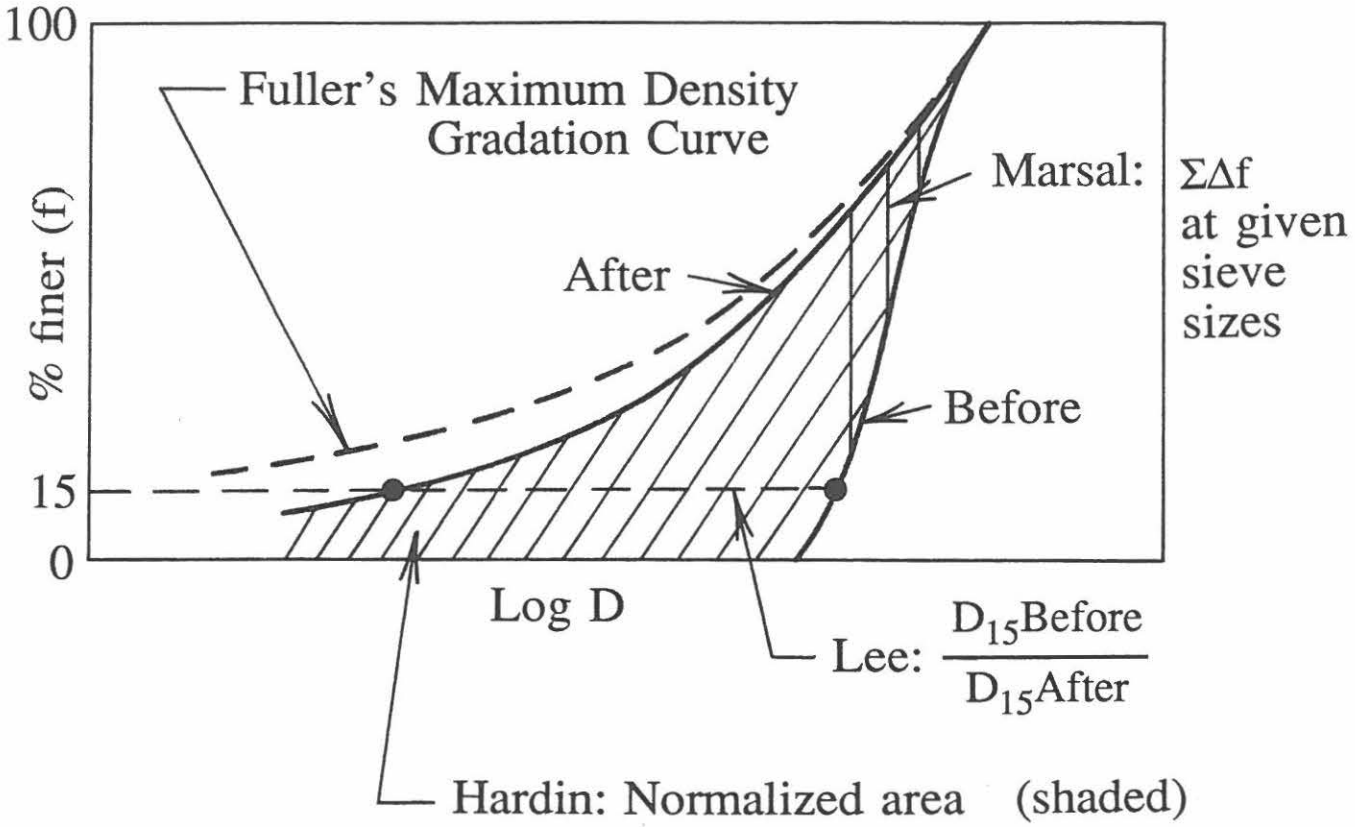

All particle breakage factors are used to characterize the change in location of grain size curve

This, in turn, determines e.g. change in permeability:

$k = f(D_{10}, D_{30}, D_{60}, e, \varepsilon_v, \text{etc.})$

Example: Construction of large earth dam:
Water loss? Pore pressure distribution?

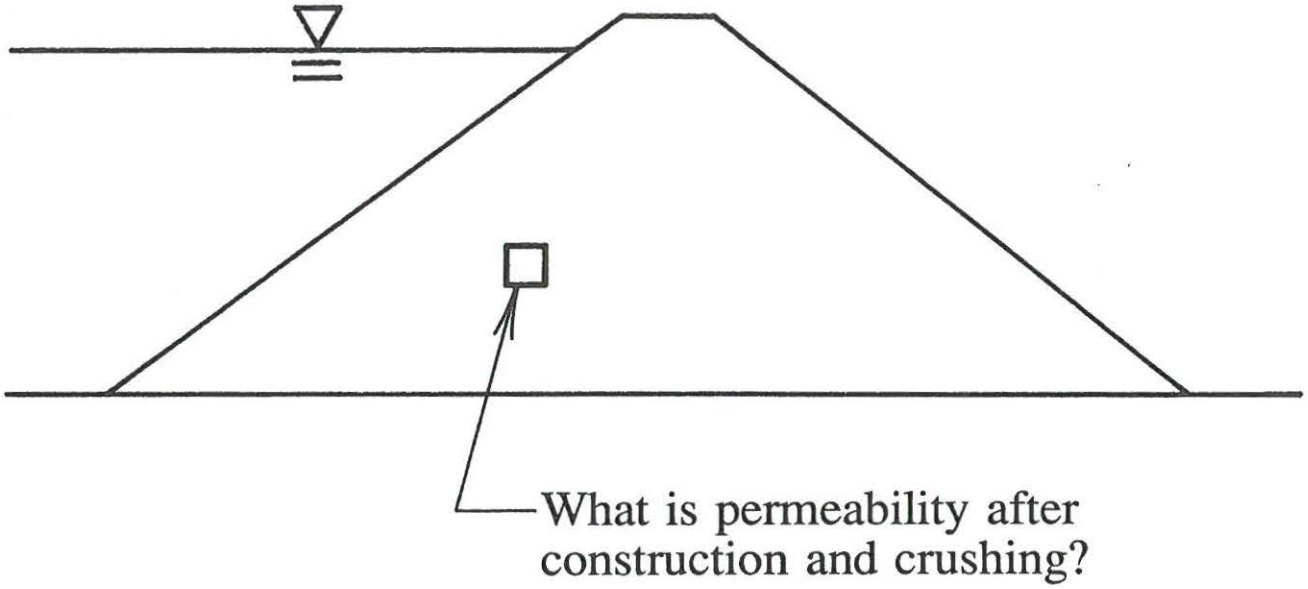

Cannot take large number of samples and determine grain size curve, etc., but .....

EARTH DAM

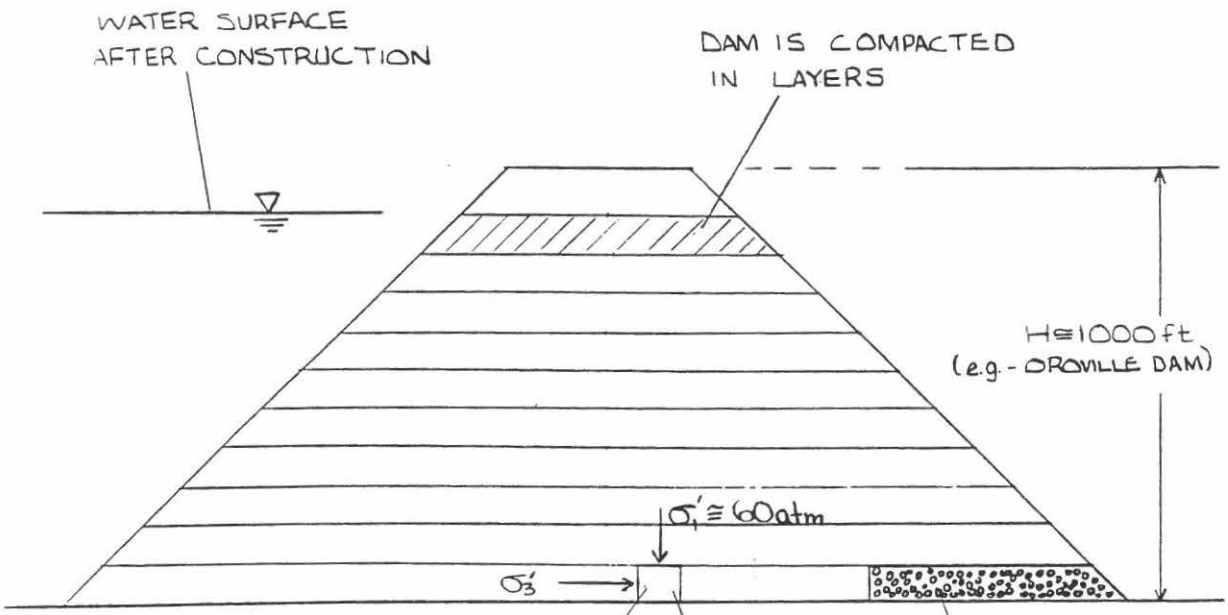

CRUSHING OF SOIL GRAINS DUE TO HIGH PRESSURE CAUSES A DECREASE IN PERMEABILITY

e.g. - HAZEN'S FORMULA

$$k\ (cm/sec) = 100\ D_{10}^{2}$$

↑ (cm)

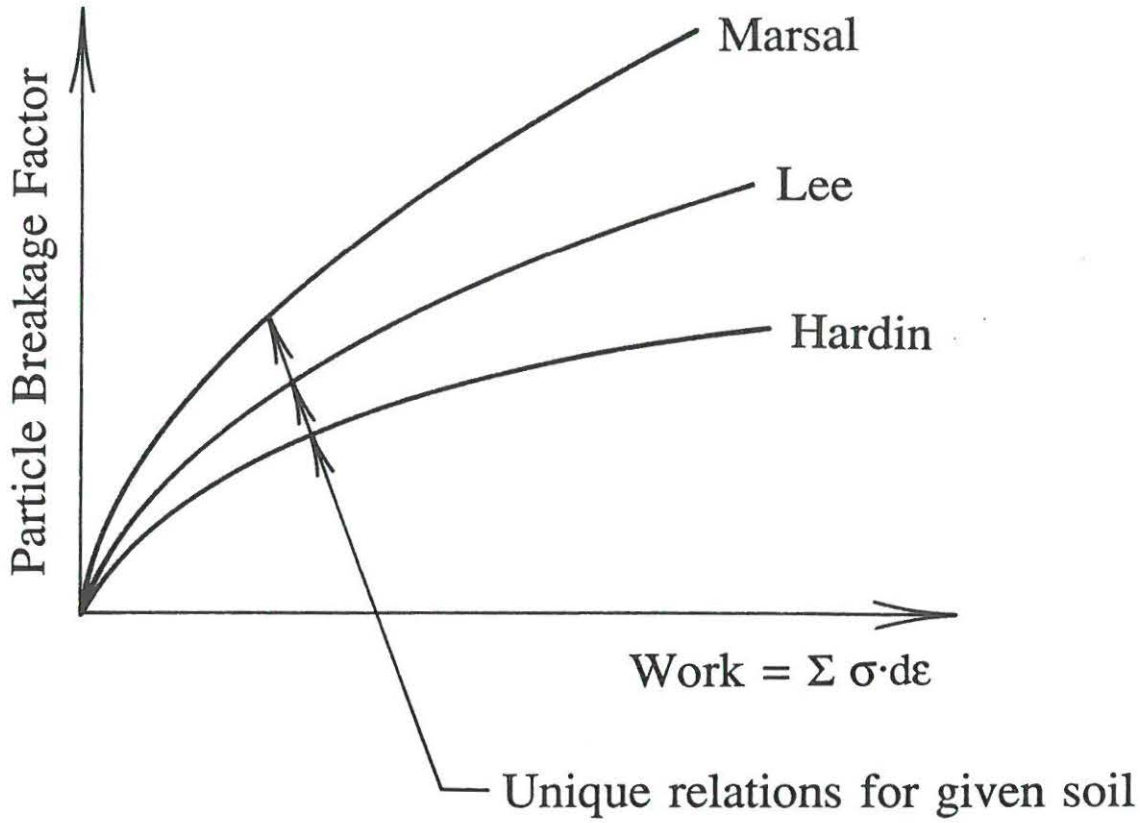

Procedure:

(a) Calculate amount of work during construction using FE program with realistic constitutive model for each soil element
(b) Determine particle breakage factors
(c) Determine grain size curves and permeabilities
(d) Calculate water loss and pore pressure distribution from finite element or finite difference programs using local values of permeability.

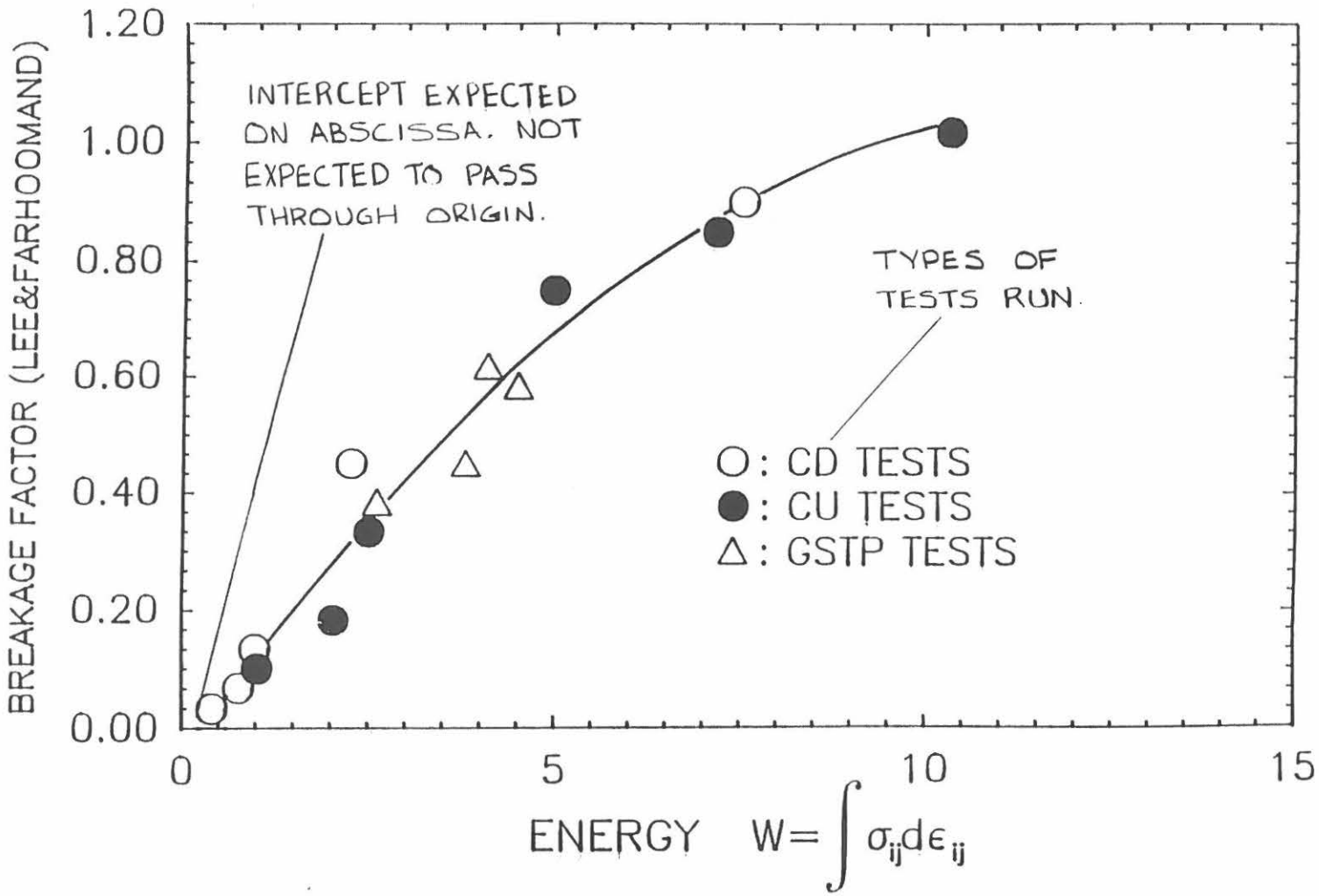

FIGURE 4.23 Lee and Farhoomand [21] breakage factor versus loading energy for various consolidated drained and undrained triaxial compression tests on Cambria sand. Test points are common to Figure 4.20.

FINITE ELEMENT GRID

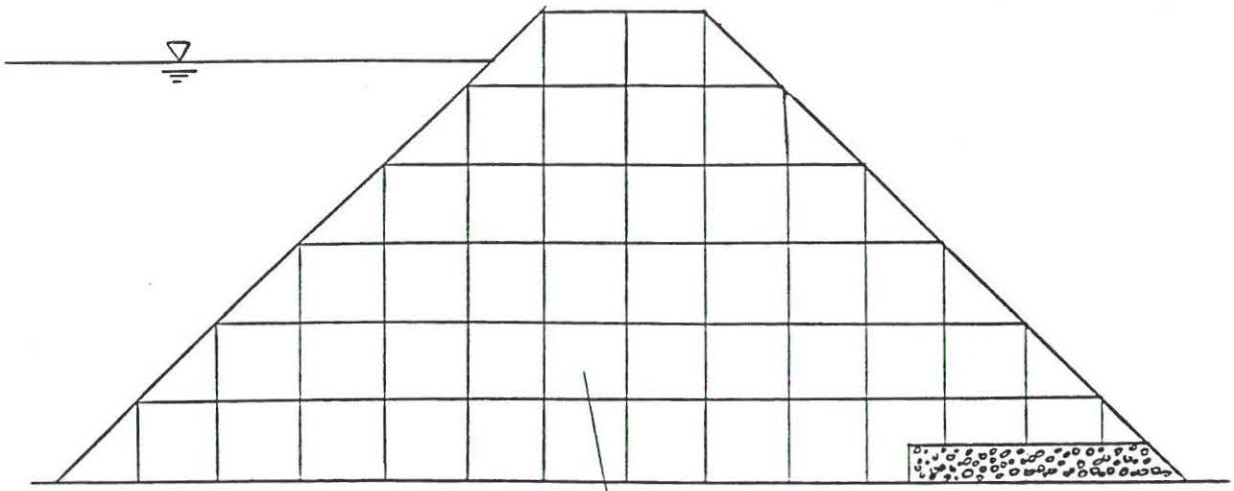

$$\text{WORK} = \int \sigma_{ij}\, d\epsilon_{ij}$$

WORK ON SOIL ELEMENT IS CORRELATED TO CRUSHING PARAMETER

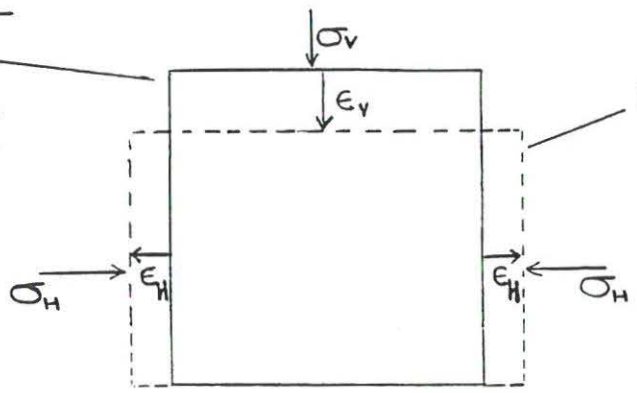

FINITE ELEMENT GRID

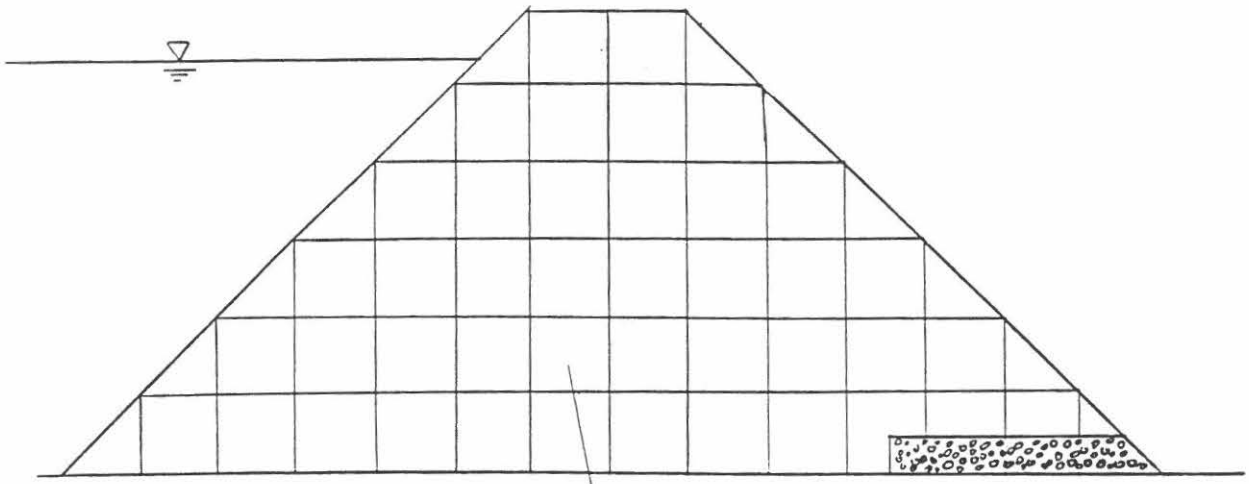

1) ASSIGN LOCAL PERMEABILITY TO EACH ELEMENT BASED ON THE ESTIMATED AMOUNT OF CRUSHING

HAZEN'S FORMULA:

$$k\,(cm/sec) = 100\,D_{10}^{2}$$

(D_{10} in cm)

2) USE FINITE ELEMEN SEEPAGE PROGRAM TO DETERMINE THE NEW PHREATIC SURFACE.

PHREATIC SURFACE PROFILE

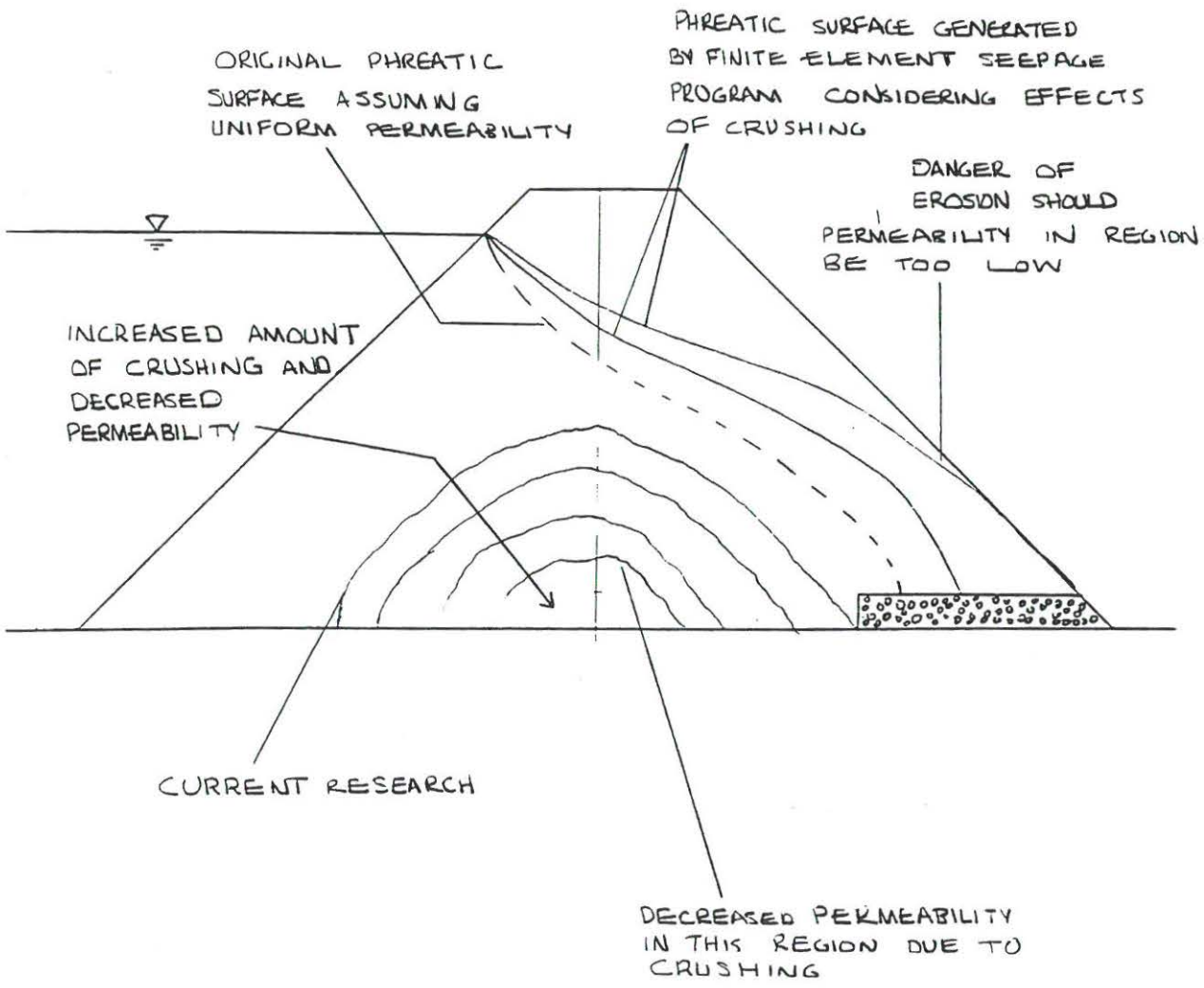

Magnitudes of **normal stresses** are key to soil behavior

Normal stresses depend on volume changes or tendency for volume changes (expansion or compression)

INTRODUCTION

Fig 1. shows a simplified diagram of the procedures generally used in geotechnical engineering. In the simple procedure simple soil parameters (e.g., c, ϕ, E, ν) are derived from laboratory and/or in-situ tests and utilized in closed from solutions for the particular boundary value problems under considerations. These procedures may be verified by prediction and comparison with model or full scale tests of elements of the prototype structure (e.g., one pile). Finally, prediction of the behavior of the prototype may be performed. The simple procedures predict simplified responses such as linear elastic settlements and failure, but prediction of the entire load-deformation relation for a prototype structure is often inaccurate, especially in the stress range where failure is a distinct possibility.

In the advanced procedure, a constitutive model is used to capture the entire stress-strain relation obtained from laboratory and/or in-situ tests. Incorporating the constitutive model in numerical methods the behavior of model or full scale tests may be predicted and serve to verify the capability of the constitutive model and the numerical method. Finally, the behavior of the prototype may be calculated with better overall accuracy.

One of the critical elements in the advanced procedure is the constitutive model. It is paramount to employ realistic constitutive models which can reproduce the important aspects of the soil stress-strain behavior under various loading conditions. To develop such models requires advanced experiments to study the soil behavior under various loading conditions and employment of mathematical tools based on sound theoretical frameworks such as e.g., elasticity and plasticity theories.

Some of the advanced experiments available today are the torsion shear, directional shear, and cubical triaxial tests. These are suitable for studying soil behavior under three-dimensional stress conditions with and without stress reversals and with and without rotation of principal stress directions. The development of pore pressures as well as strains under given stress conditions and their dependence on degradation of the soil structure during stress rotation and large stress reversals are of importance for development of future, improved constitutive models.

The constitutive models should be such that the required soil parameters can be obtained from relatively simple tests.

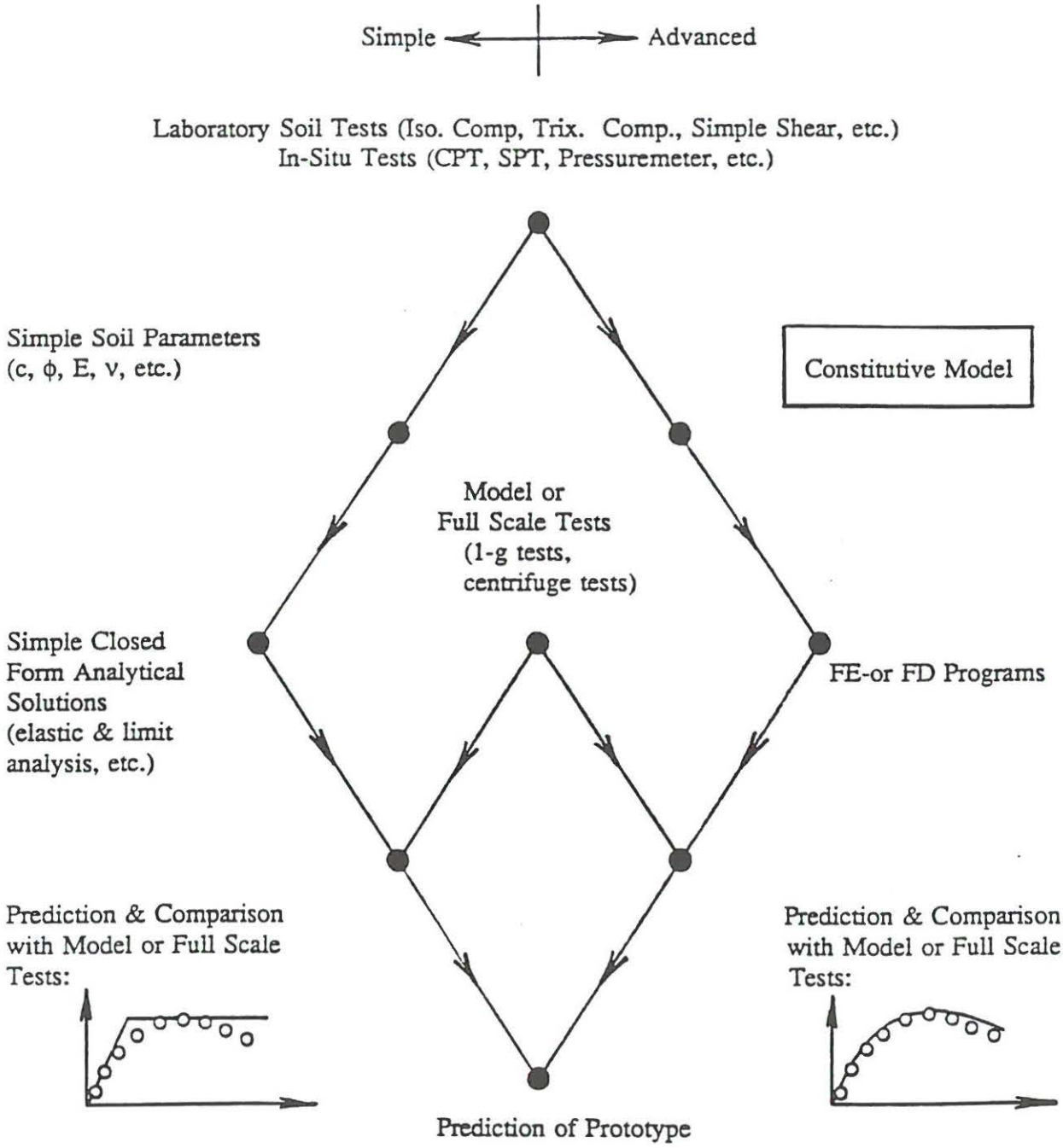

Fig. 1. Simple and Advanced Procedures of Predicting the Behavior of Prototype Structures.

Deformation and Stability of Dam

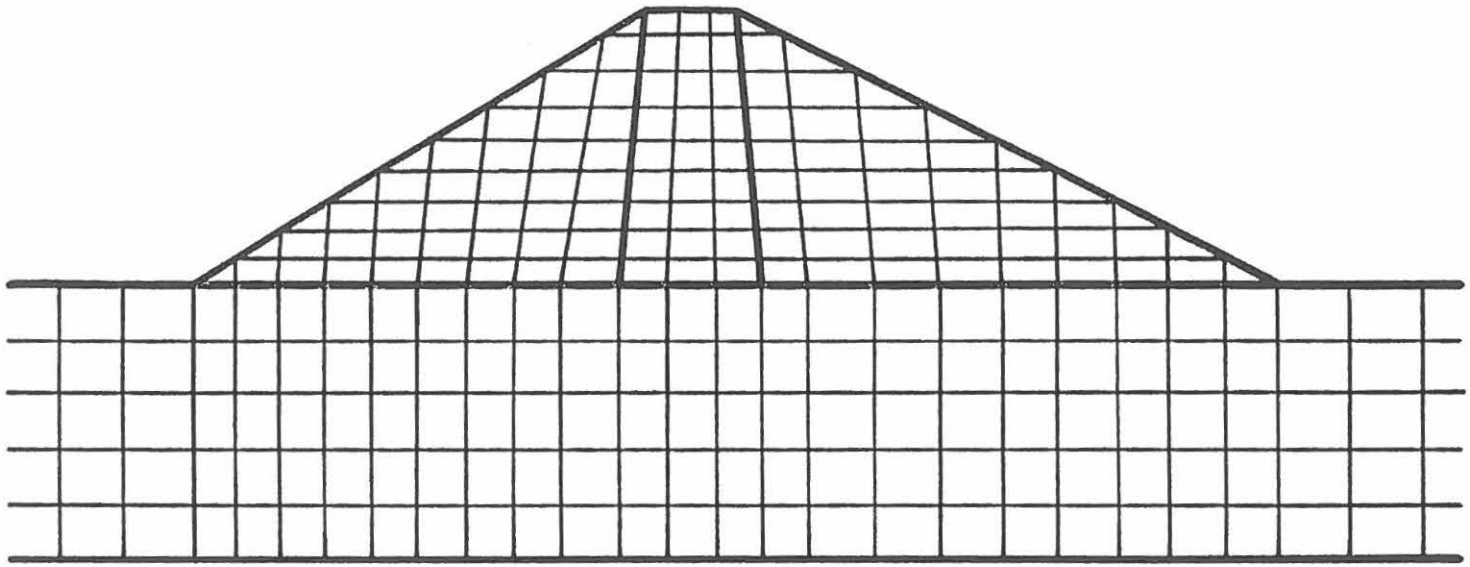

Deformation and Stability of Slope

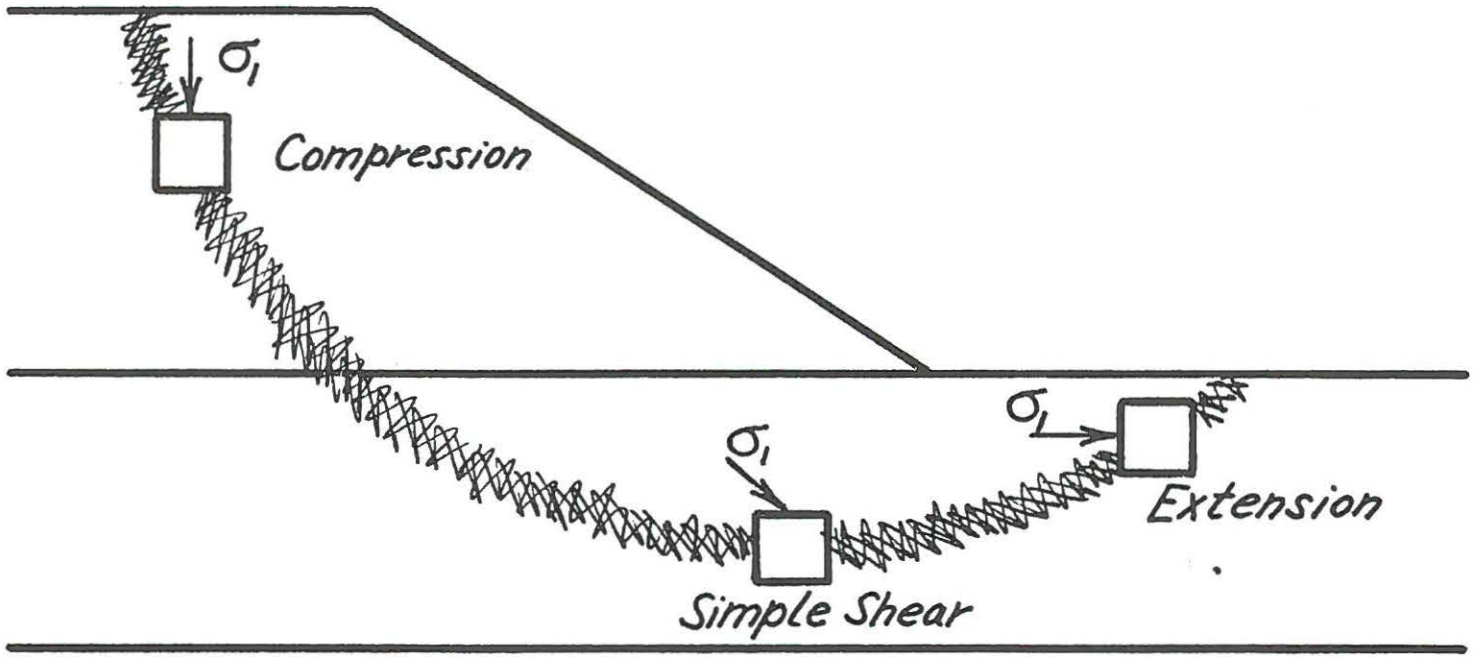

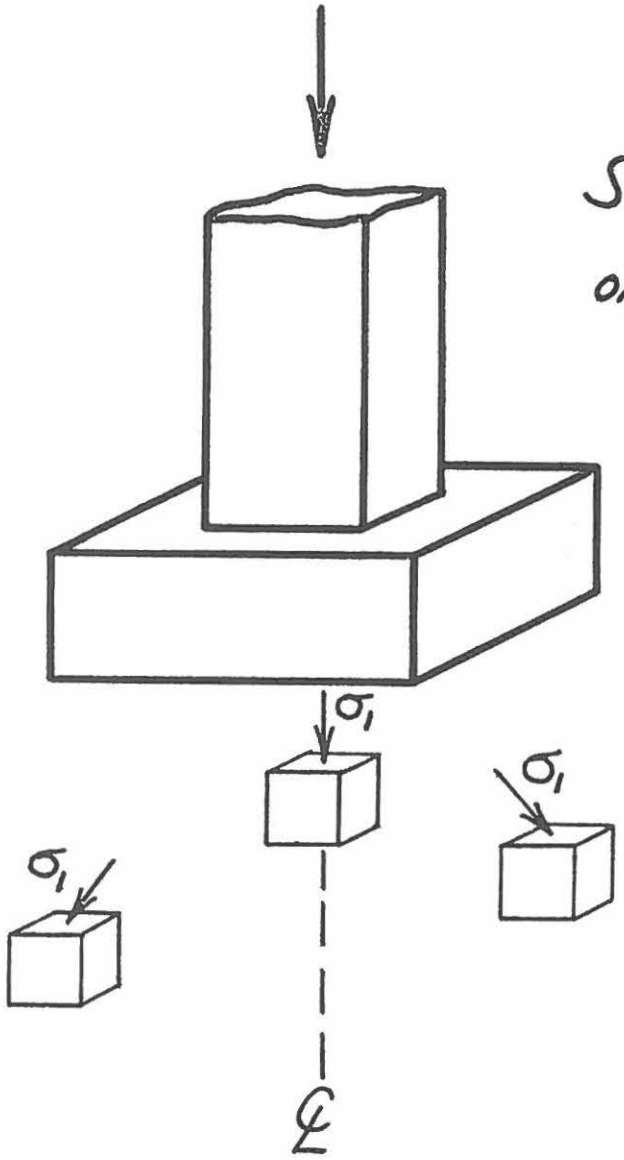

Settlement and Stability of Footing

Analysis requires knowledge about

1. Geometry of soil structure and and soil deposits

→ 2. Stress-strain behavior of soils

3. Computer programming and finite element theory

Evaluation of results

⇒ Judgment

Calculations serve only as background for the practical judgement!

(Beregninger er kun et hjaelpemiddel for det praktiske skϕn!)

Remark by Professor A. Ostenfeld in official discussion of Dr. Techn. dissertation on "Calculations of Pile Groups" by Chr. Nϕkkentved
May 10, 1924

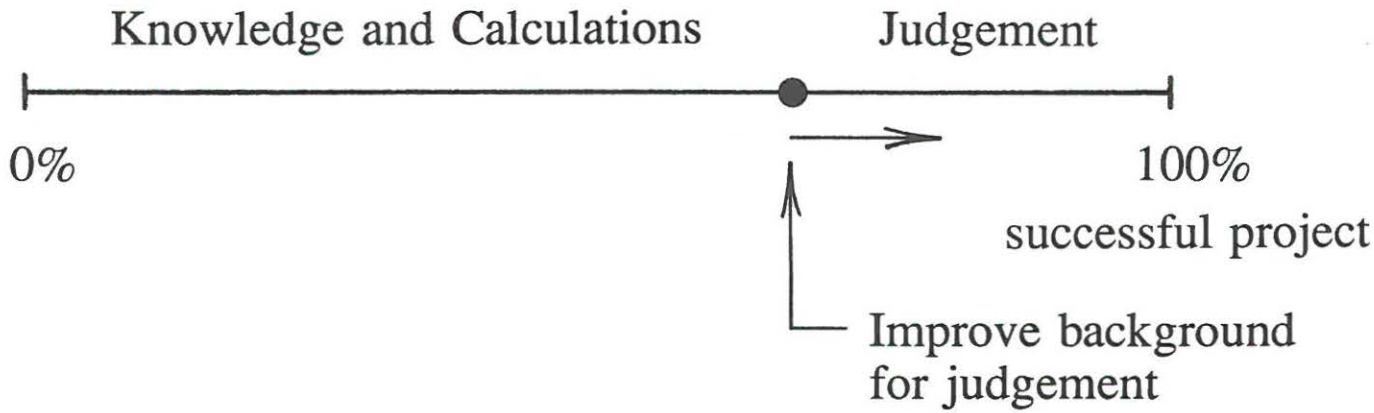

Analysis Methods are generally good to exellent
(based on assumptions)

Characterization of Material Behavior
needs improvement

Advantages of realistic stress-strain theory

1. Better *understanding* of soil stress-strain behavior

2. *Extrapolate* to conditions which cannot be produced in laboratory testing equipment

3. Use in finite element program
   $\Rightarrow$ *design* of soil structures on rational basis

4. Limited amount of testing
   $\Rightarrow$ perform *simplest* and most convenient types of *laboratory tests*

Triaxial Compression Test

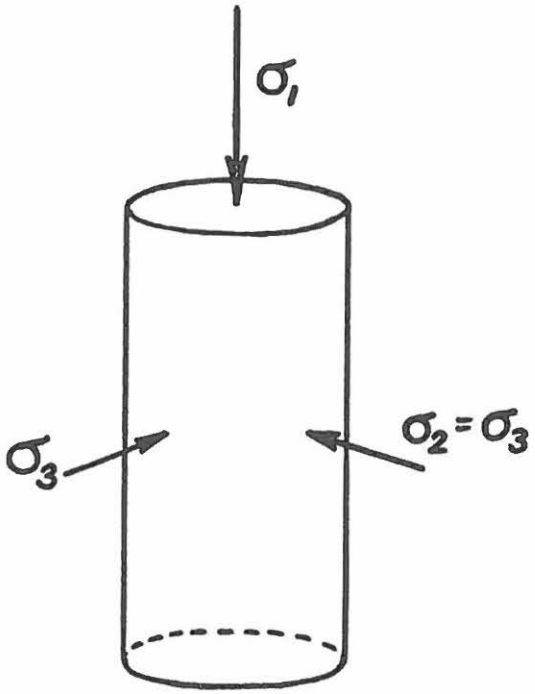

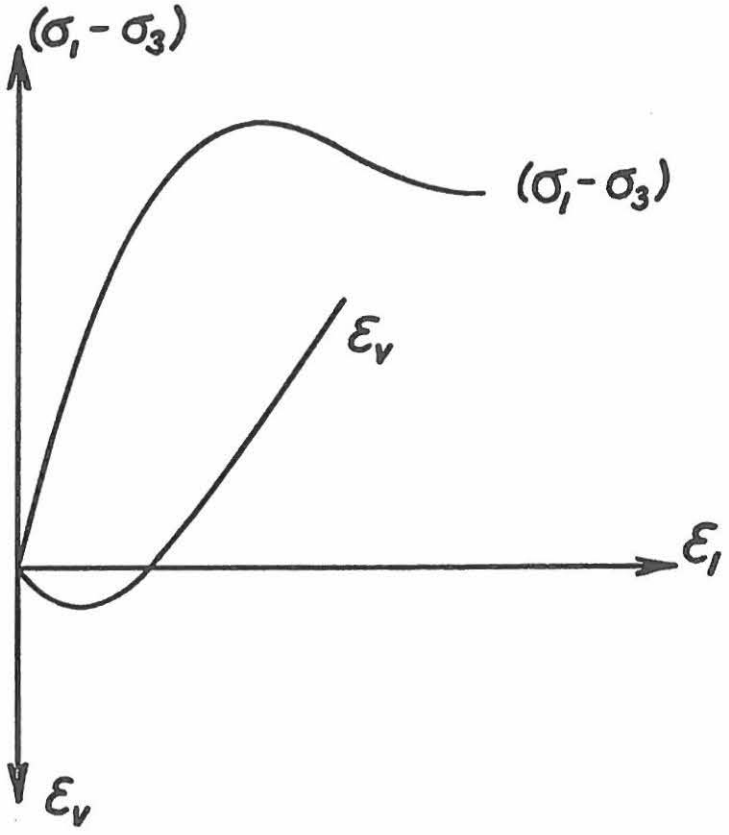

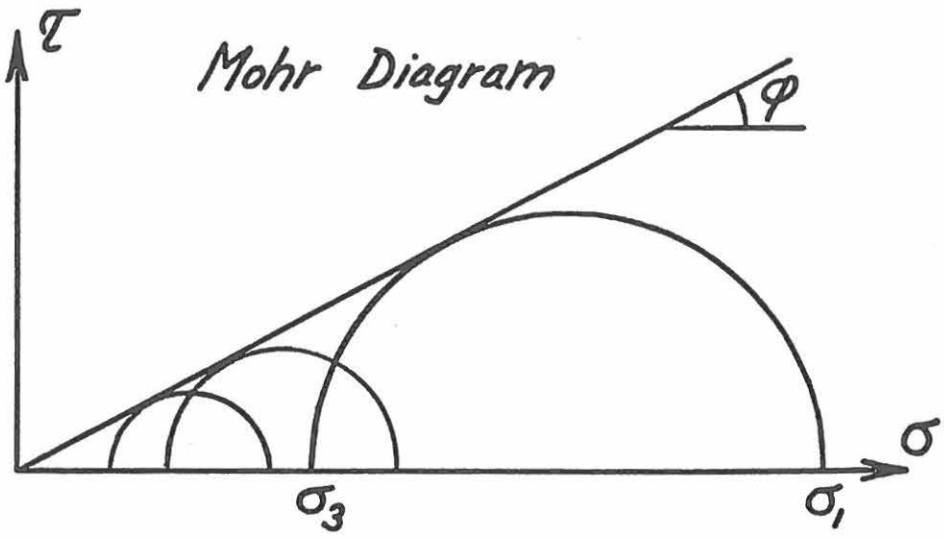

Observed Behavior of Cohesionless Soil

1. Nonlinear Stress-Strain Relation
   a) Elastic at Low Stress Levels
   transition to
   b) Plastic at High Stress Levels

2. σ_2 has Effect on Stress-Strain and Strength Behavior

3. Volume Changes of Soil:
   a) Compresses at Low Stress Levels
   b) Expands at High Stress Levels
   (Shear-Dilatancy Effect)

4. Reorientation of Principal Stress Direction
   a) ε coincides with σ or $\dot{\varepsilon}$ coincides with $\dot{\sigma}$ } at Low Stress Levels

   transition to

   b) $\dot{\varepsilon}$ coincides with σ at High Stress Levels

5. Soil Deformation is Stress-Path Dependent

6. Post-Peak Behavior:
   Strength may Decrease after Peak

Must handle **coupling effects** correctly

Hooke's law **does not:**

$$\begin{Bmatrix} \varepsilon_x \\ \varepsilon_y \\ \varepsilon_z \\ \gamma_{yz} \\ \gamma_{zx} \\ \gamma_{xy} \end{Bmatrix} = \begin{bmatrix} \frac{1}{E} & -\frac{\nu}{E} & -\frac{\nu}{E} & 0 & 0 & 0 \\ -\frac{\nu}{E} & \frac{1}{E} & -\frac{\nu}{E} & 0 & 0 & 0 \\ -\frac{\nu}{E} & -\frac{\nu}{E} & \frac{1}{E} & 0 & 0 & 0 \\ 0 & 0 & 0 & \frac{1}{G} & 0 & 0 \\ 0 & 0 & 0 & 0 & \frac{1}{G} & 0 \\ 0 & 0 & 0 & 0 & 0 & \frac{1}{G} \end{bmatrix} \begin{Bmatrix} \sigma_x \\ \sigma_y \\ \sigma_z \\ \tau_{yz} \\ \tau_{zx} \\ \tau_{xy} \end{Bmatrix}$$

? (1) — the upper-right 3×3 block of zeros

? (2) — the lower-left 3×3 block of zeros

Example (1): Increase τ => produce ε_v

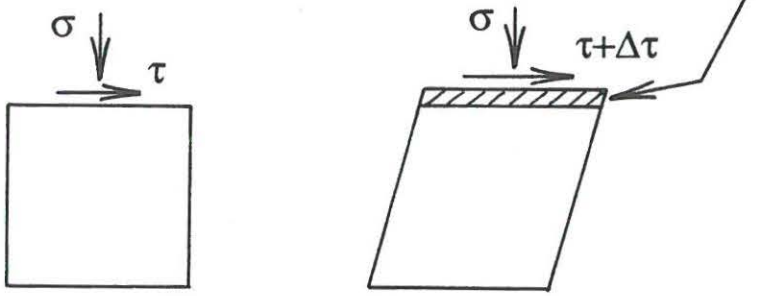

Example (2): Decrease σ => produce γ

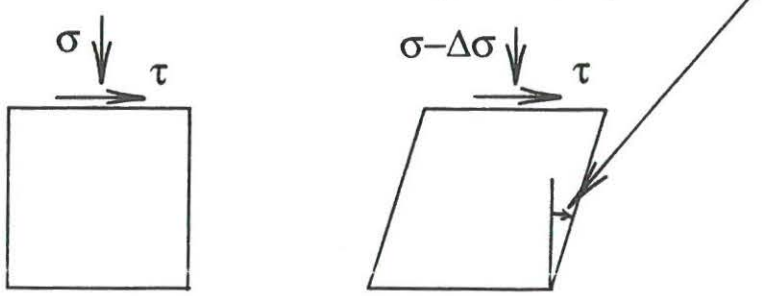

Essential Aspects of Behavior of Frictional Materials to be Incorporated in Constitutive Model

✓	Nonlinearity of Stress-Strain Behavior
✓	Irreversibility of Portion of Strains
✓	Influence of σ_3 on Stress-Strain Behavior
✓	Influence of σ_2 on Stress-Strain Behavior
✓	Influence of σ_3 on Strength
✓	Influence of σ_2 on Strength
✓	Gradual Decrease in Strength Beyond Peak Failure (Strain Softening)
✓	Shear-Dilatancy Effects over a Range of Confining Pressures (Variation in Volume Change Behavior)
✓	Pore Pressure Developments over a Range of Confining Pressures
✓	Effects of Rotation of Stress Axes
✓	Stress-Path Dependency
✓	Effects of Cohesion Due to Cementation
✓	Effects of Small Stress Reversals (including cyclic loading)
*	Hysteresis During Large Stress Reversals (including cyclic loading)

Legend:

✓ Included in constitutive model presented here

* Under current investigation

Advantages of elasto-plastic stress-strain theory

1. Theory is applicable to general 3-dimensional stress conditions

2. Stress-strain parameters can be derived entirely from results of triaxial compression tests (CD or CU) & isotropic compression test

What level of expertise is required for (a) personnel and (b) equipment, and how much testing is necessary to be able to perform the calculations?

Min. and Max. **Testing Requirements** are the same:

3 triaxial compression tests to failure (CD- or CU-)with unloading-reloading cycles

1 isotropic compression tests

Note 1: Specimens are tested with the assumption that they represent elements of the ground
-we are interested in the average soil behavior at each element location (not interested in lowest (safe) strength)

Note 2: Tests are performed by simulating as closely as possible the conditions in the ground.

This includes:

a) Range of stresses
   (due to variable, nonlinear behavior)
b) Drainage conditions
   (drained or undrained)
c) Density and soil fabric

Note 3: Measure all loads, pressures, deformations, etc. for **complete** characterization of stress-strain behavior of soil.

What level of expertise is required for calculation of soil parameters?,

and

What level of knowledge is required with regard to the capabilities of various constitutive models for soils?

Soil Behavior in Triaxial Compression

COMPRESSIBILITY

Sand, like all soils, are compressible, so the density of the sand will be higher after compression than the original placement density.

The stress-strain and strength behavior depends on the density, so consider the compressibility:

Typical data: Isotropic compression of Sacramento River Sand, No. 50 - 100 US sieves

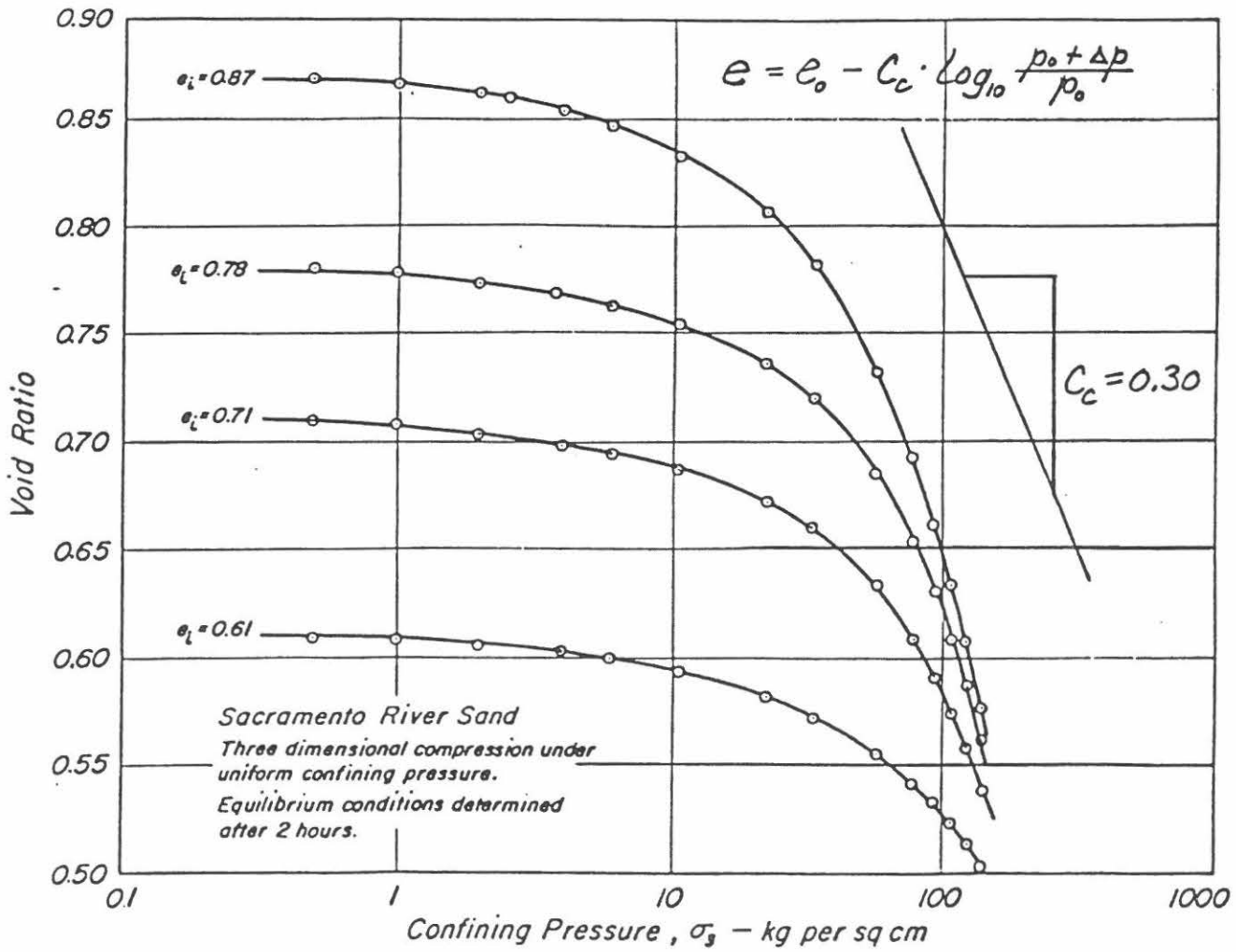

Fig. 2 - PRESSURE - VOID RATIO CURVES FOR SAND AT FOUR INITIAL DENSITIES.

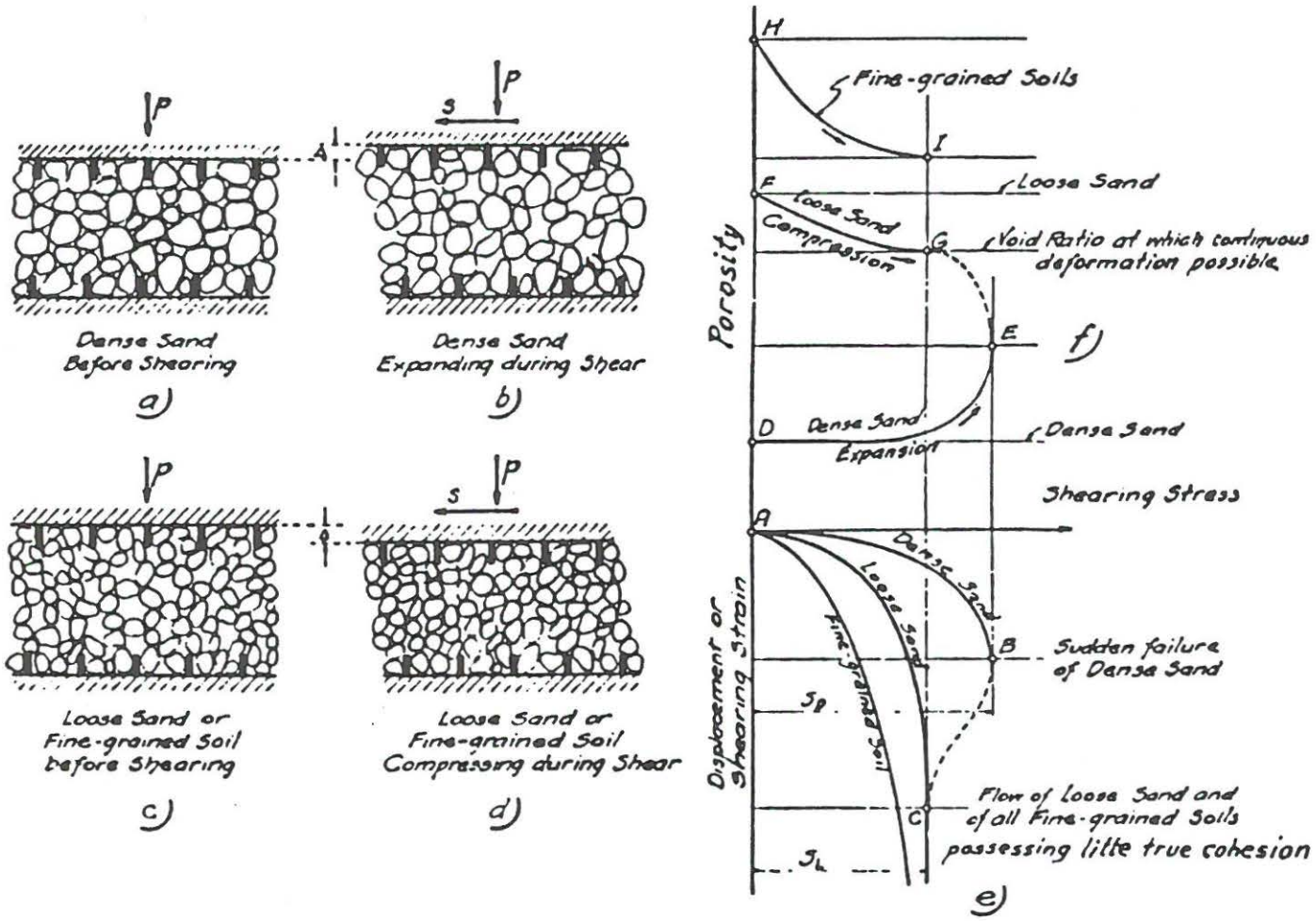

FIG. 1. — EFFECTS OF SHEARING ON THE VOLUME OF SOILS

(After Casagrande, 1936)

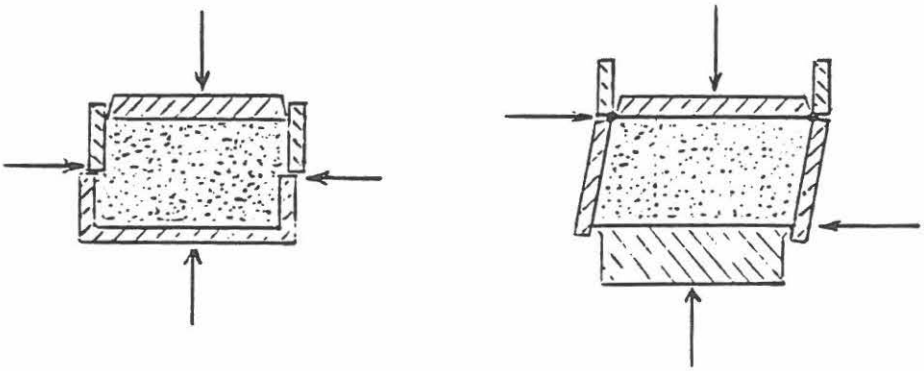

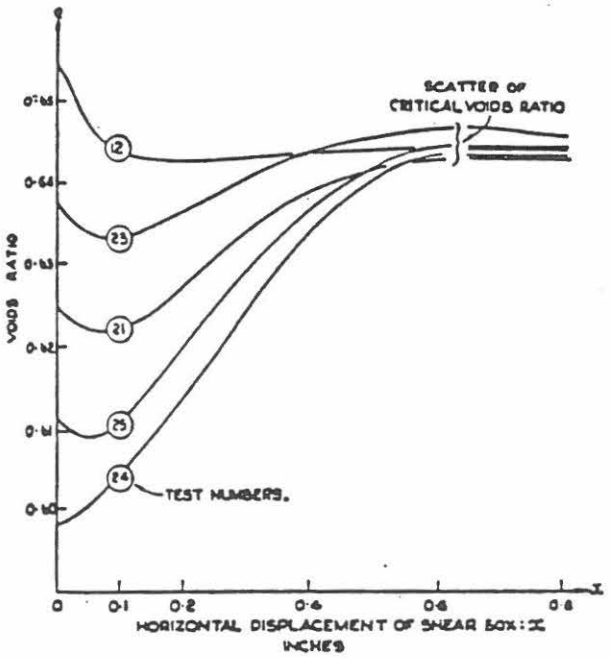

Fig. 33. Results of simple shear tests on 1-mm steel balls with normal stress—20 lb/sq. in.

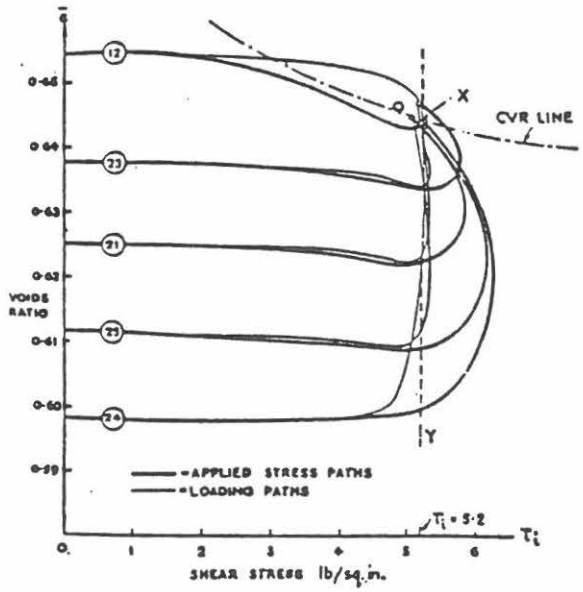

Fig. 34. Results of simple shear tests on 1-mm steel balls with normal stress —20 lb/sq. in.

(After Wroth, 1958)

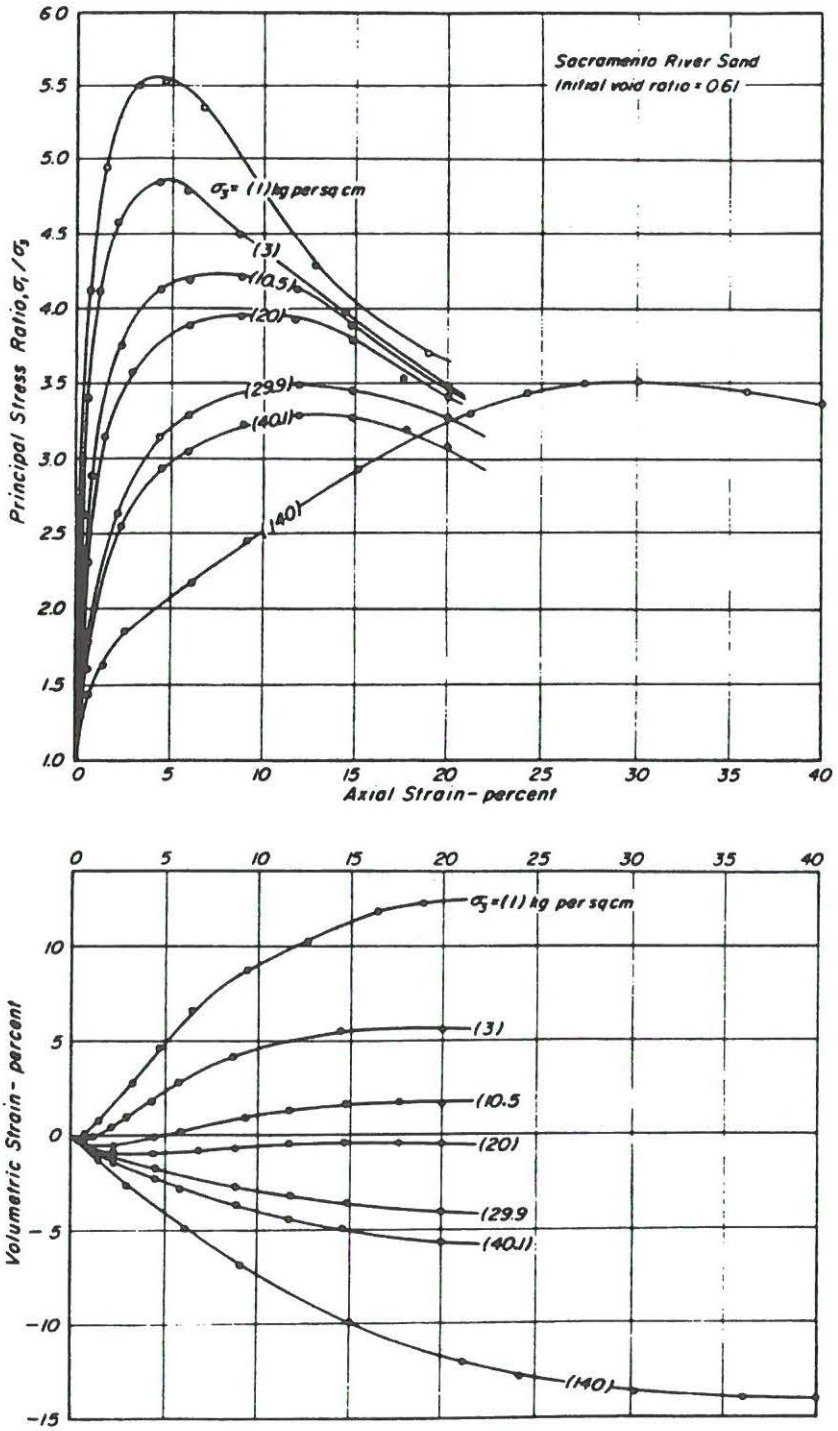

Fig. 3 - STRESS - STRAIN - VOLUME CHANGE DATA FOR DENSE SAND.

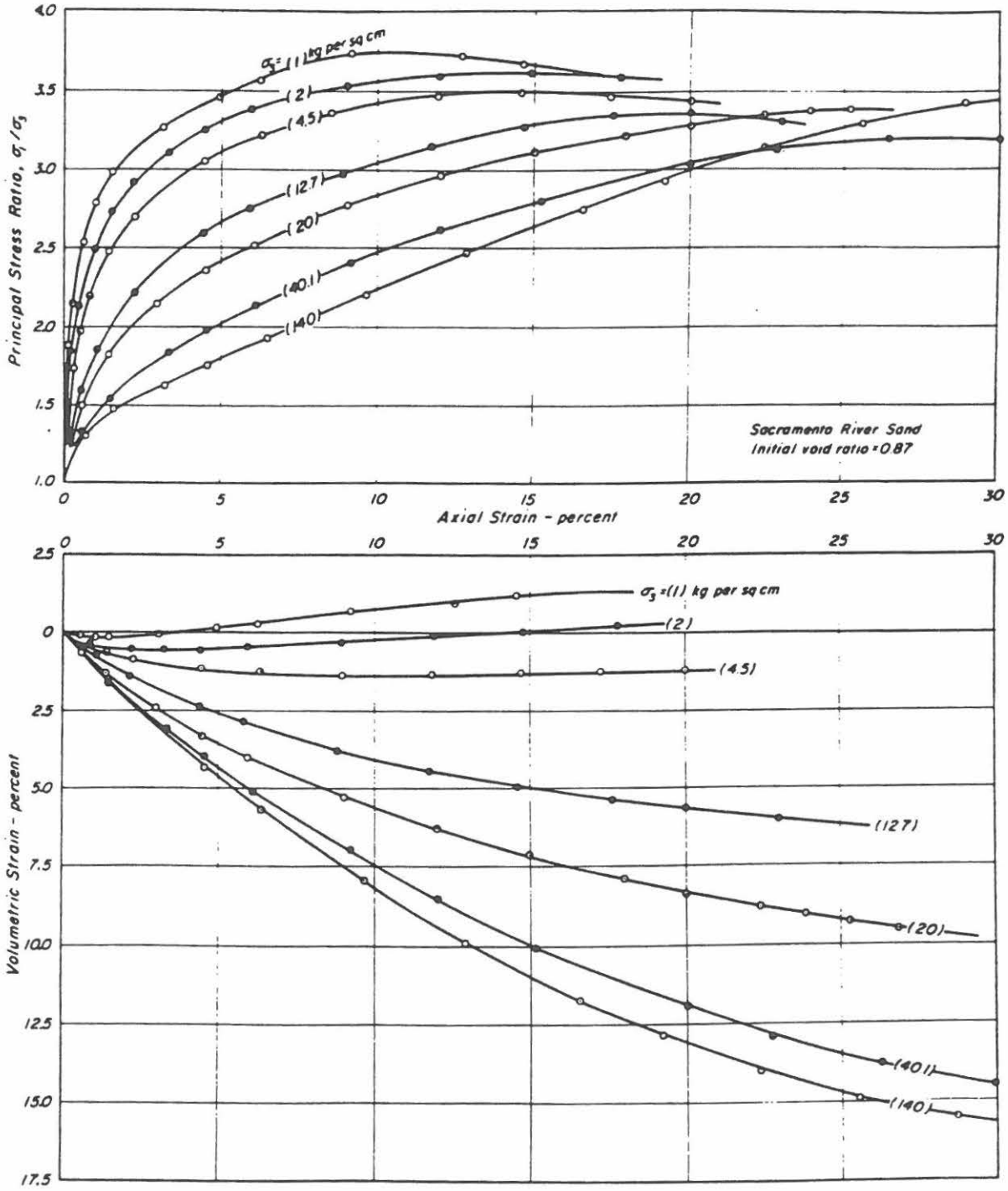

Fig. 4 - STRESS - STRAIN - VOLUME CHANGE DATA FOR LOOSE SAND.

Critical State Concepts

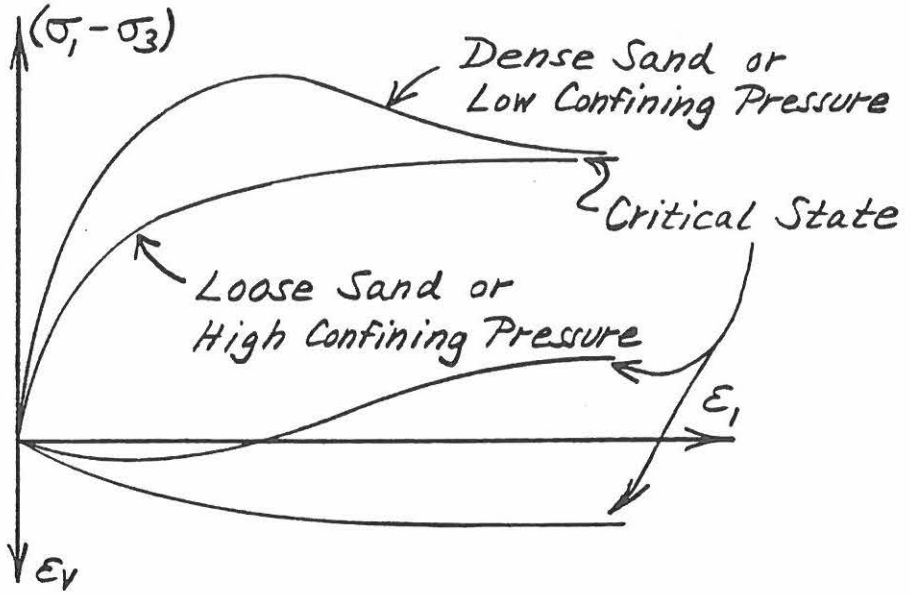

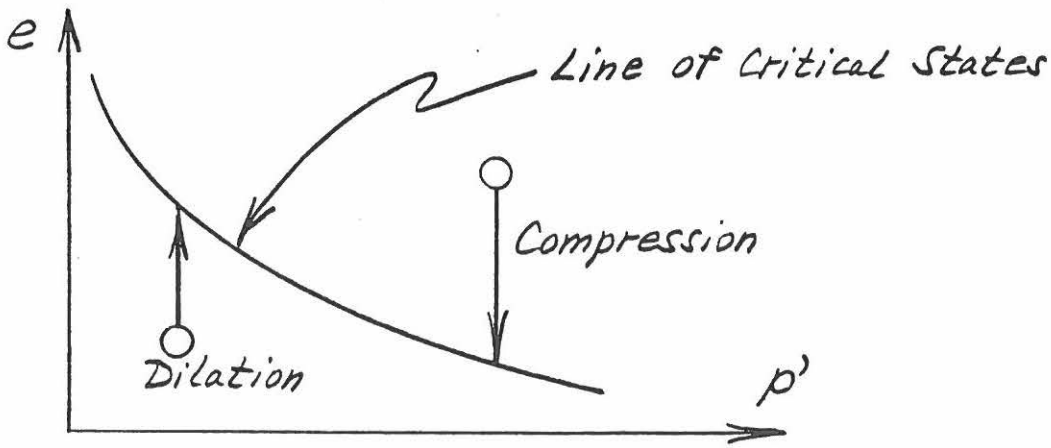

Casagrande: Critical State is defined as the State (for monotonic loading) at which further shear deformation can occur without further change of effective stresses and void ratio

$$\frac{\partial p'}{\partial \varepsilon} = 0 \qquad \frac{\partial q}{\partial \varepsilon} = 0 \qquad \text{and} \qquad \frac{\partial e}{\partial \varepsilon} = 0$$

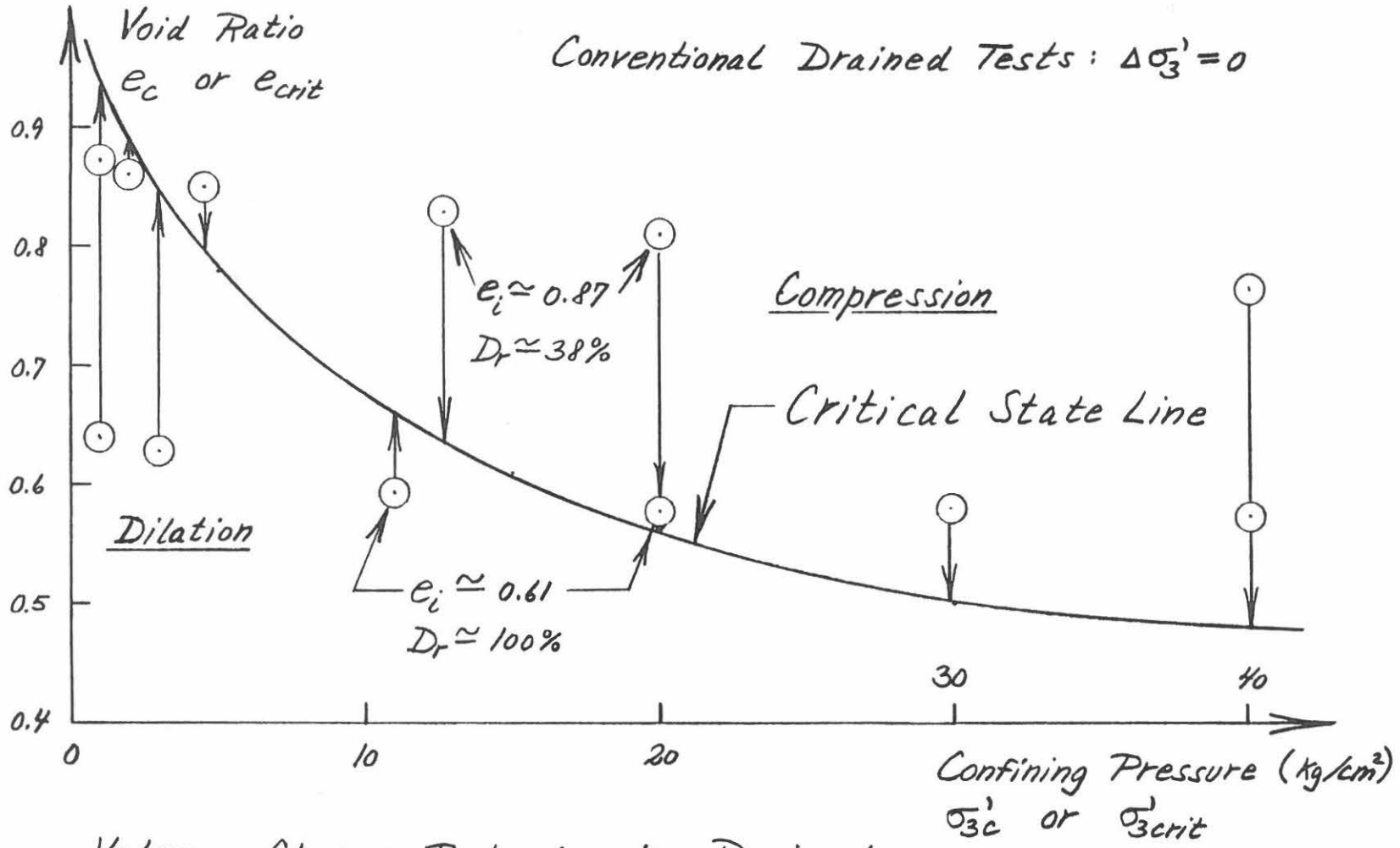

Volume Change Behavior in Drained
Triaxial Compression Tests on Sacramento River Sand

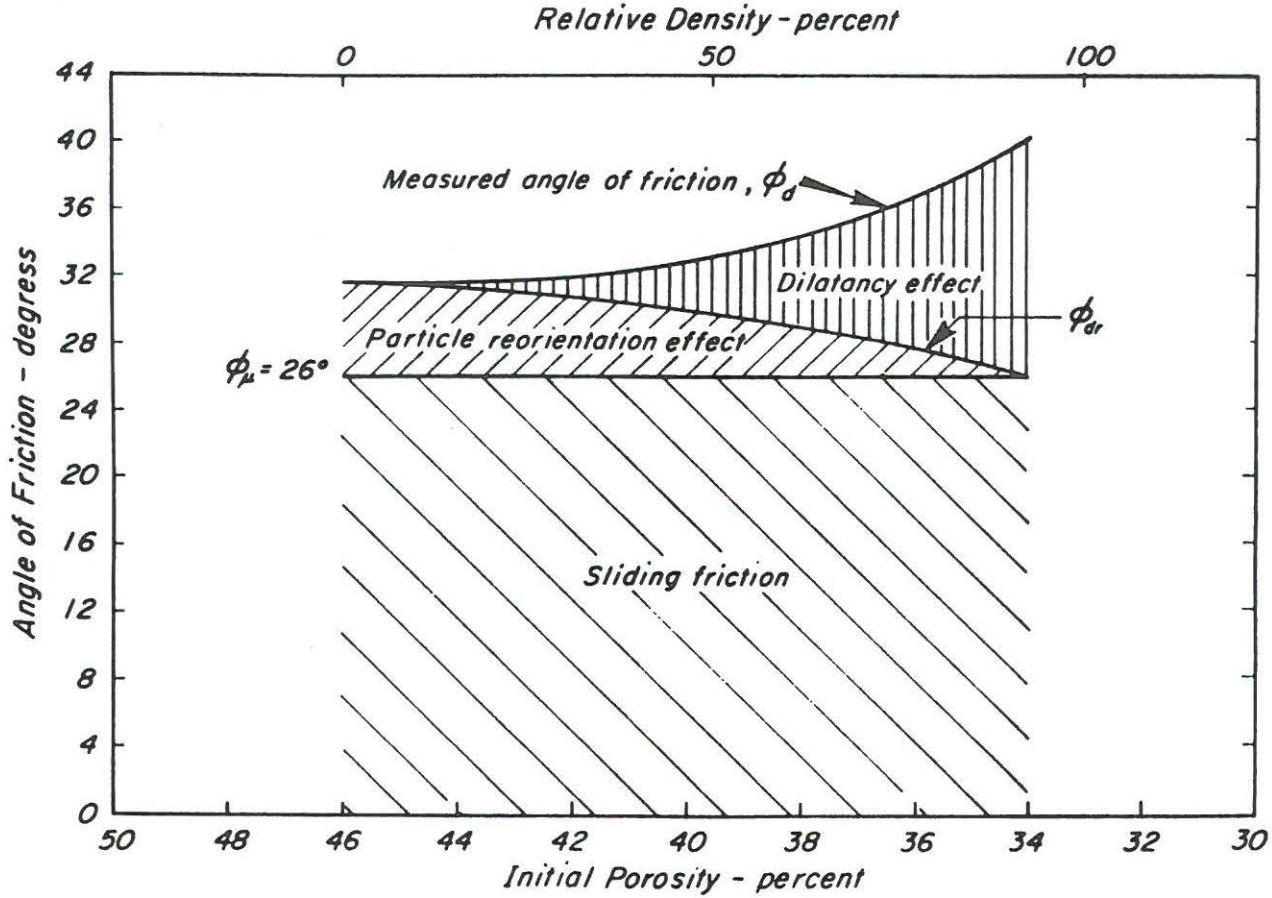

Fig. 1–COMPONENTS OF STRENGTH OF SAND DETERMINED BY P.W. ROWE.

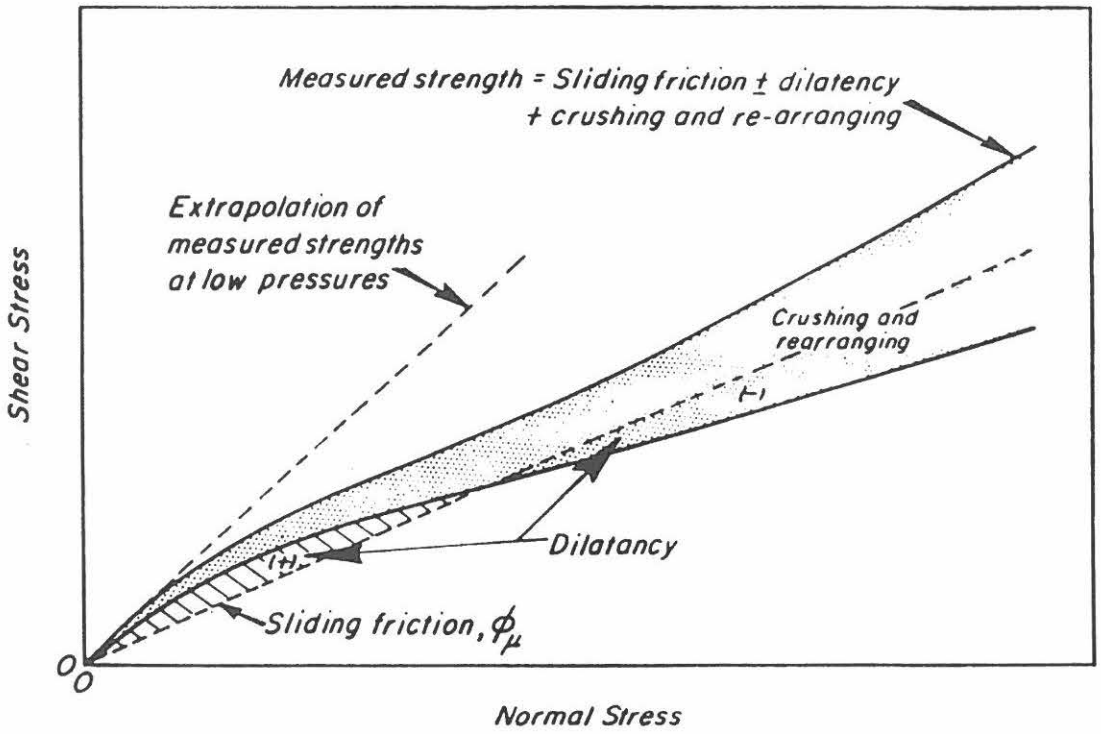

Fig. 22 - SCHEMATIC ILLUSTRATION OF CONTRIBUTION OF SLIDING FRICTION DILATANCY AND CRUSHING TO THE MEASURED MOHR ENVELOPE FOR DRAINED TESTS ON SAND

Pore Water Pressure Changes in Undrained Tests

Simple Models for Drained Tests :

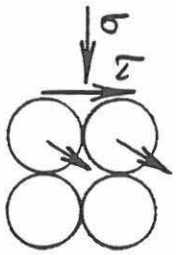

Loose and/or High σ_3'

$\Rightarrow \varepsilon_v > 0$

(Compression)

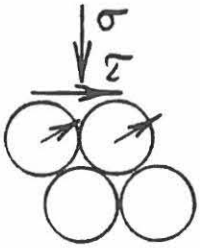

Dense and/or Low σ_3'

$\Rightarrow \varepsilon_v < 0$

(Dilation)

In Undrained Tests : $\varepsilon_v = 0$

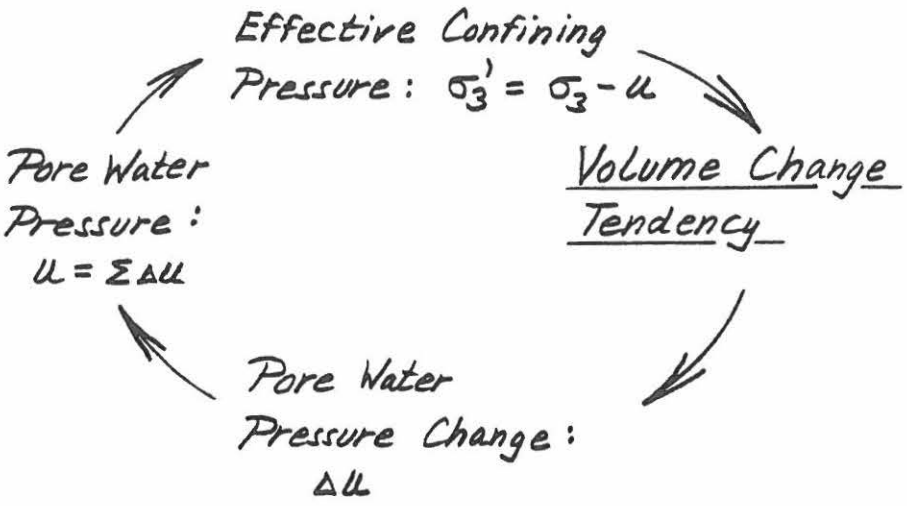

In

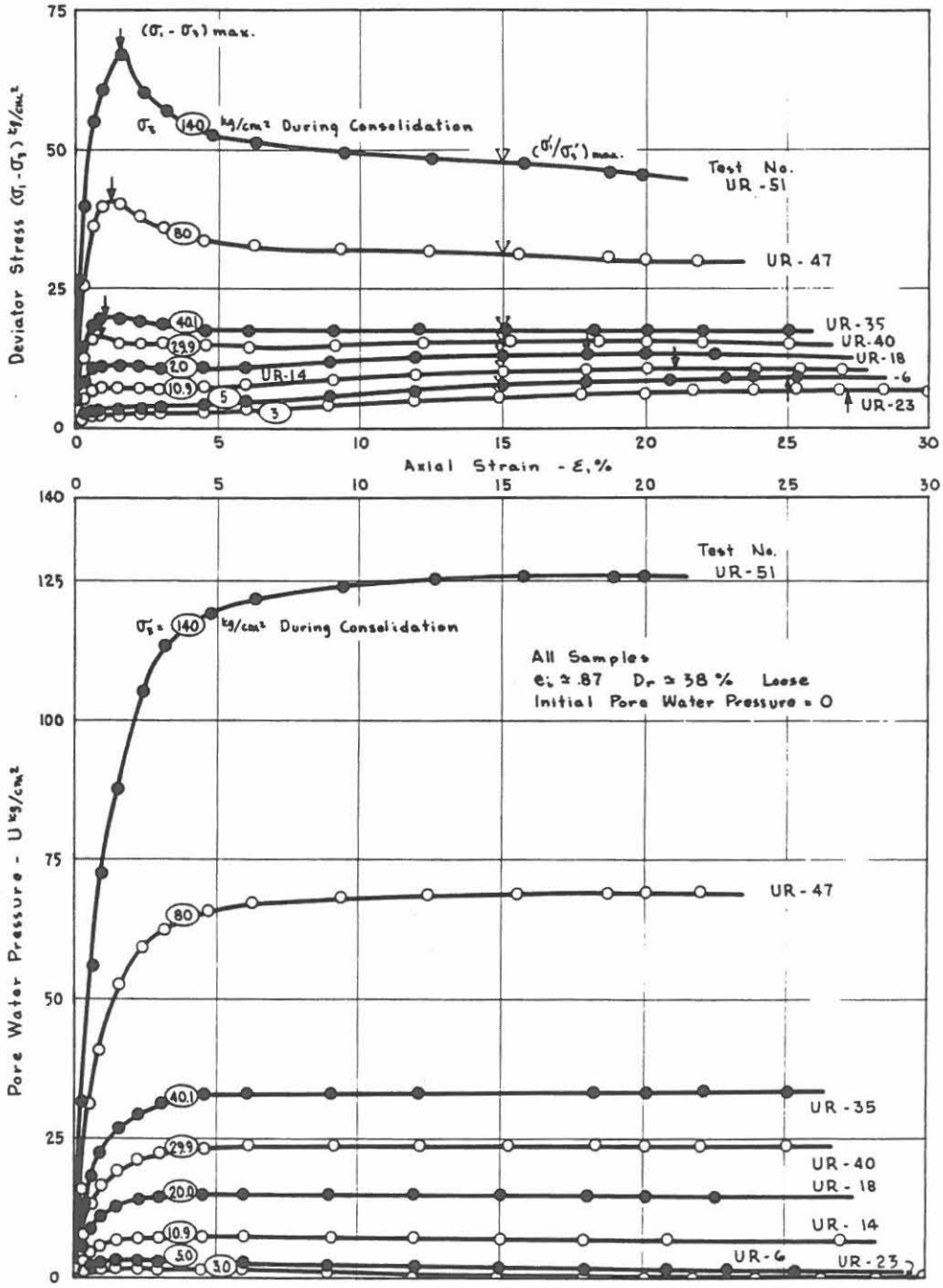

FIG. 6.3 I.C.U. TESTS ON LOOSE SACRAMENTO RIVER SAND. CONFINING PRESSURE ABOVE CRITICAL.

//

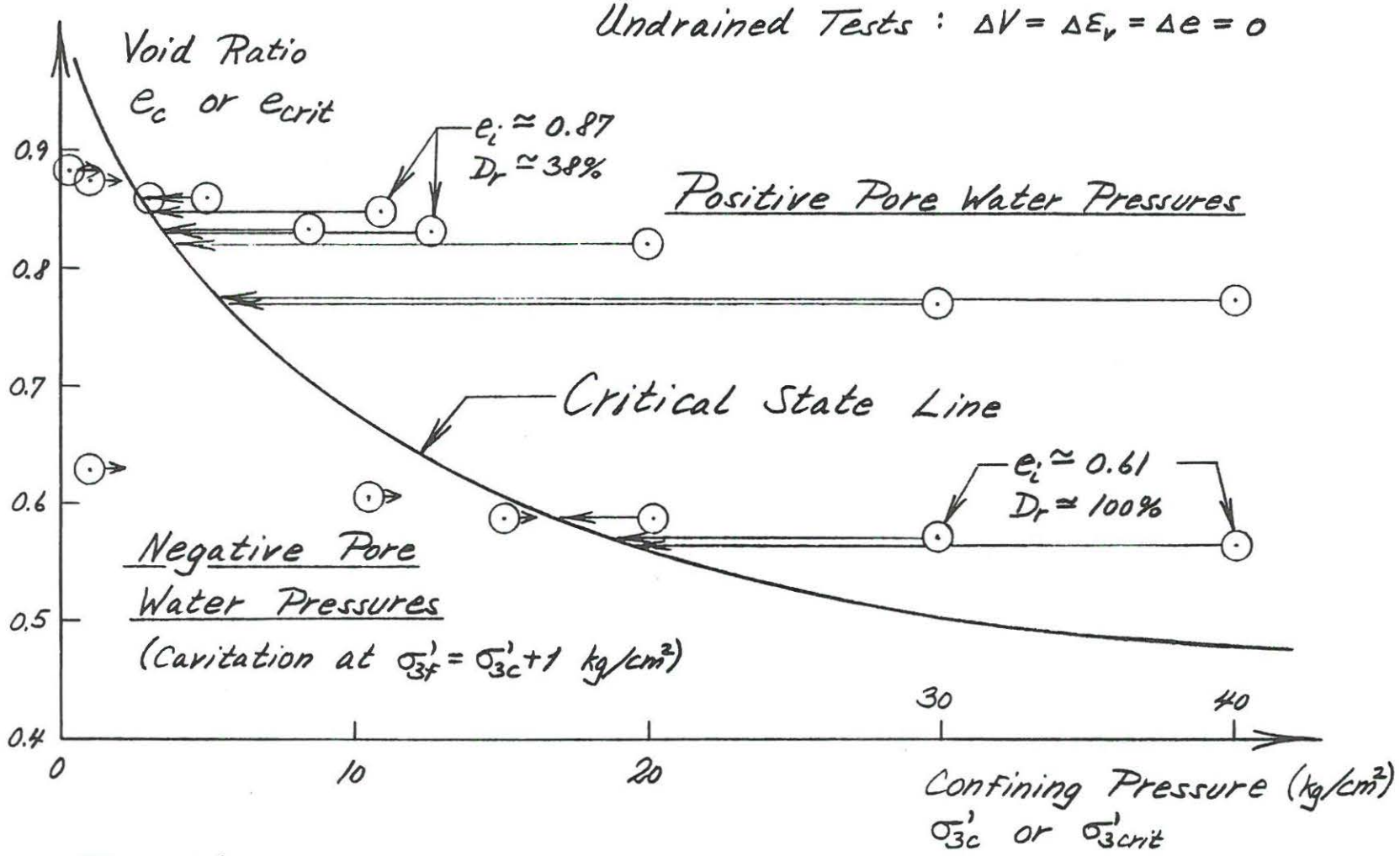

Pore Water Pressure Behavior in Undrained Triaxial Compression Tests on Sacramento River Sand

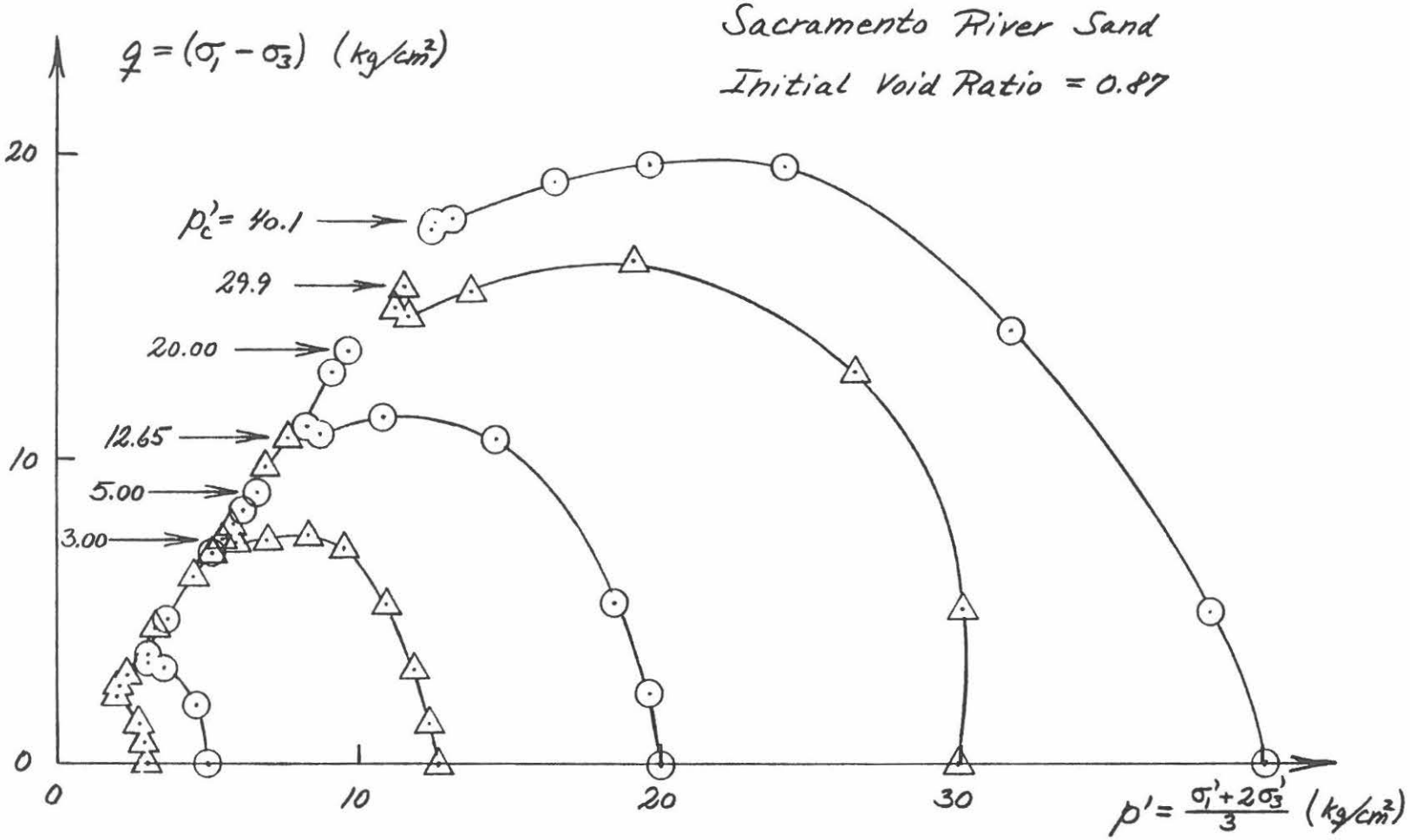

Effective Stress-Paths from Consolidated-Undrained Triaxial Compression Tests on Loose Sand.

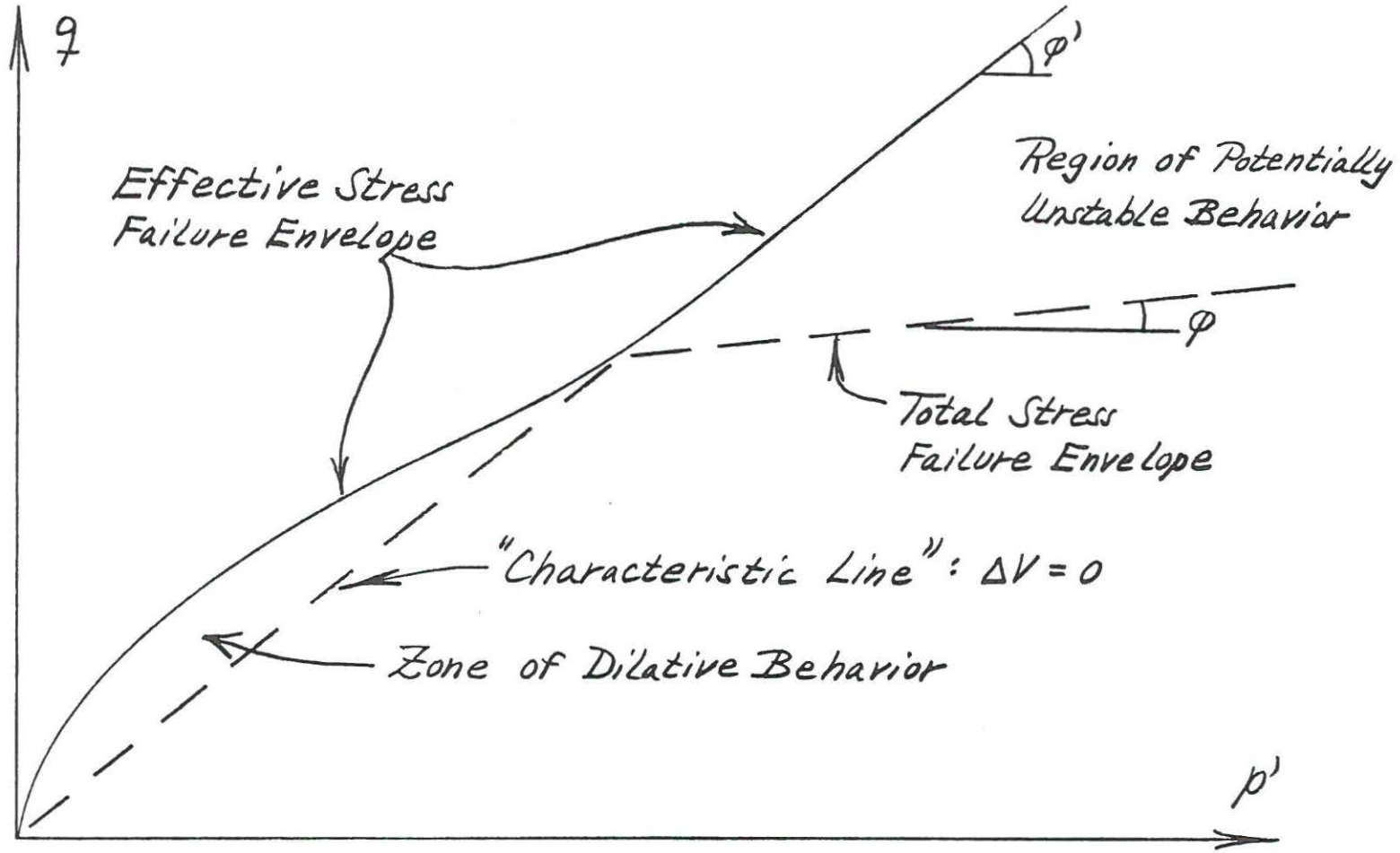
q
φ'
Effective Stress
Failure Envelope
Region of Potentially
Unstable Behavior
φ
Total Stress
Failure Envelope
"Characteristic Line": ΔV = 0
Zone of Dilative Behavior
p'

Stress Path (Anisotropic Consolidation)

The stress path or type of consolidation does not appear to have any significant influence on the subsequent soil behavior, as long as the subsequent stress path is directed outside the current yield surface. This is illustrated on the following diagrams.

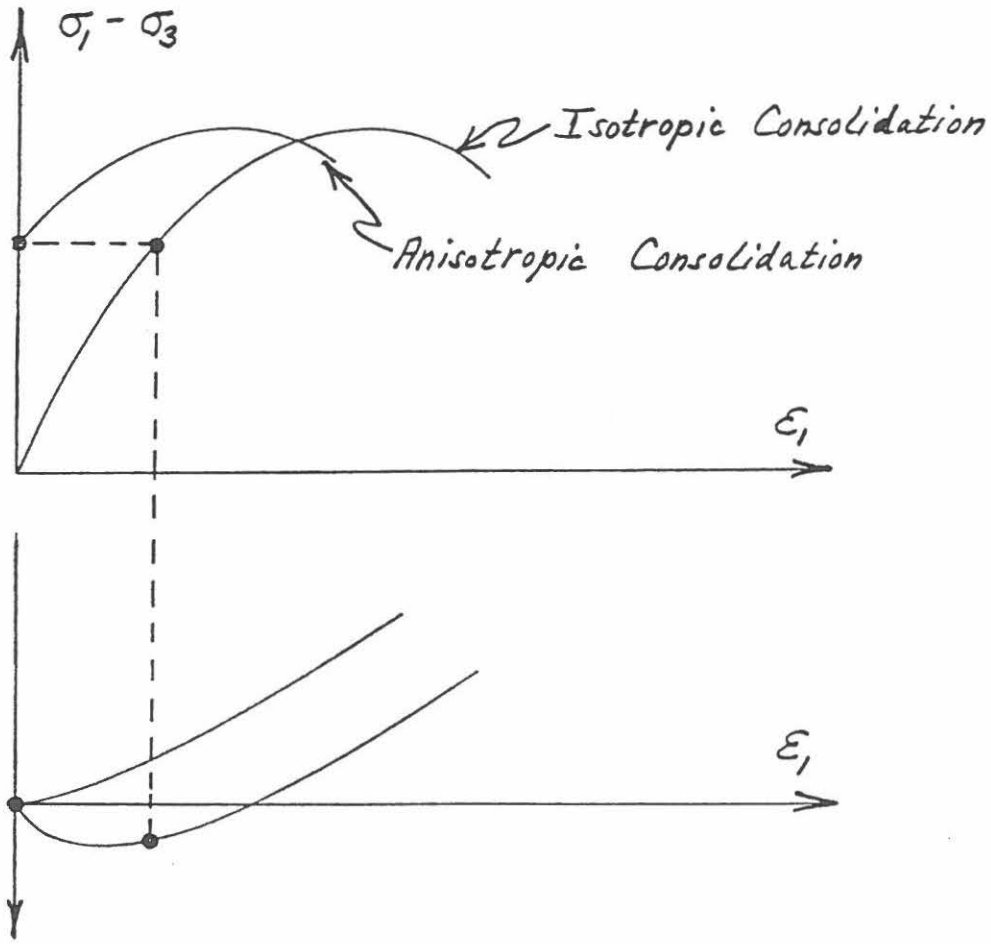

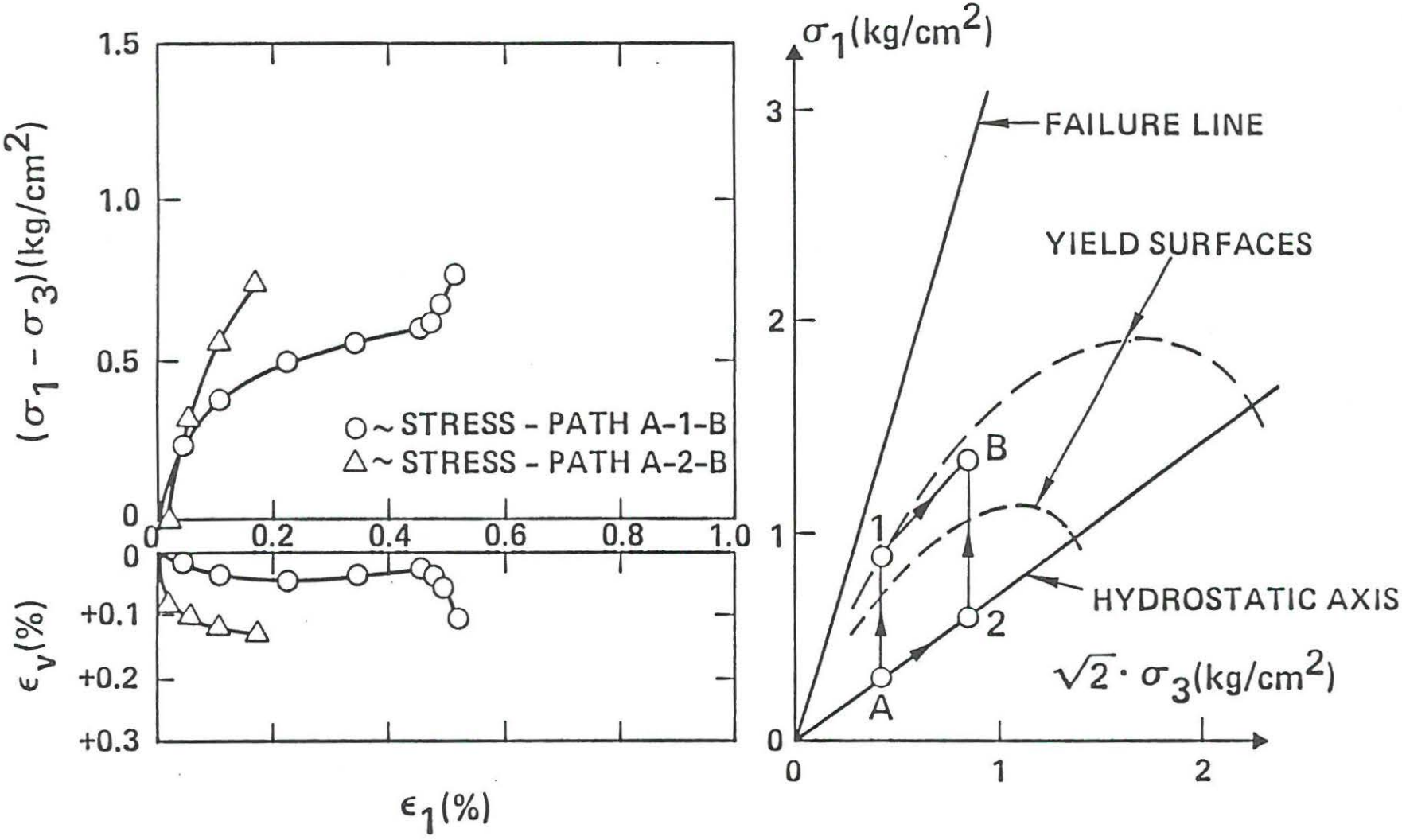

Figure 5. Comparison of Stress-Strain Behavior for two Stress-Paths, One involving Primary Loading and Unloading (A-1-B), the Other involving Proportional Loading and Primary Loading (A-2-B) for Loose Monterey No. O Sand.

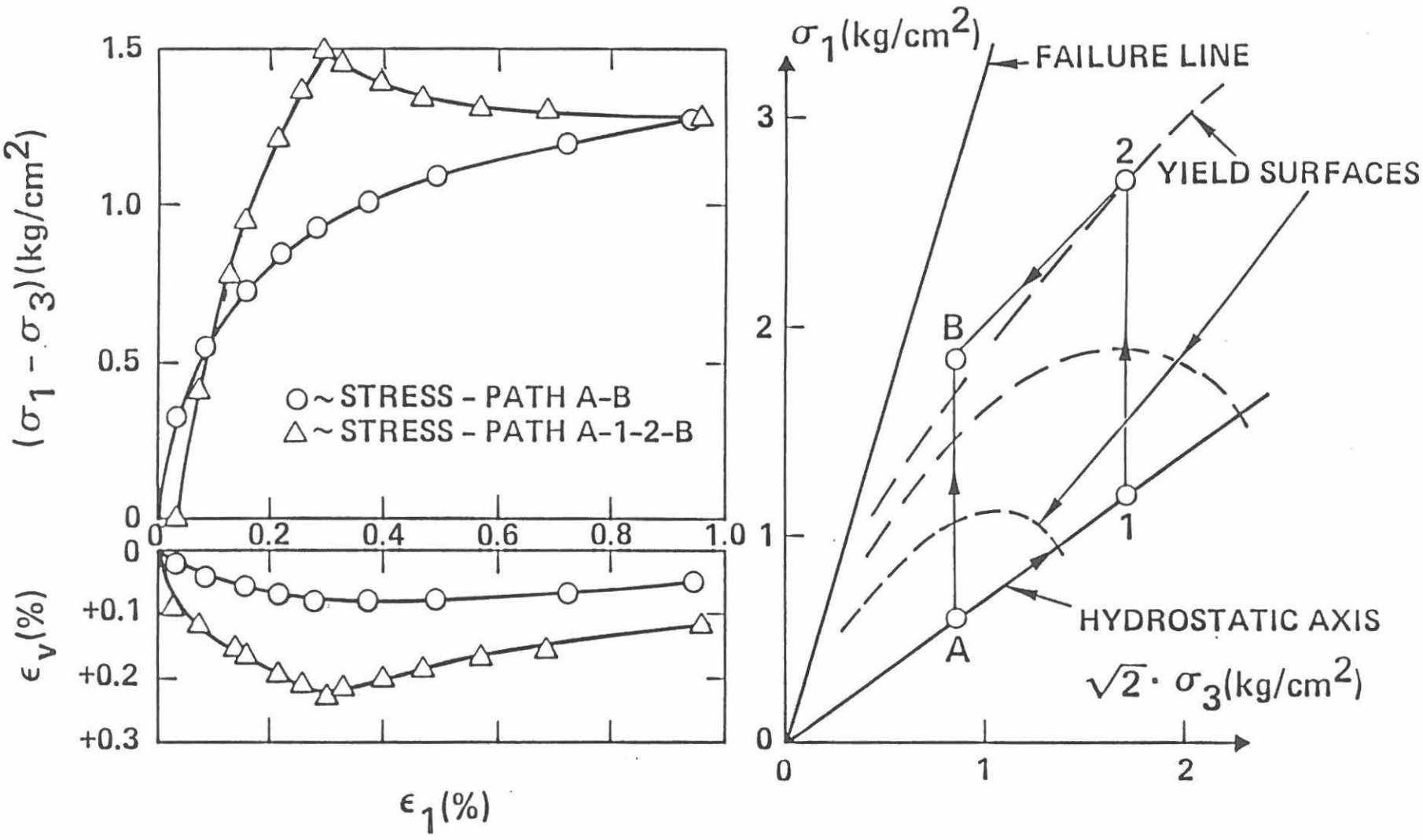

Figure 6. Comparison of Stress-Strain Behavior for two Stress-Paths, One involving Primary Loading (A-B), the Other involving Proportional Loading and Primary Loading (A-1-2-B) for Loose Monterey No. O Sand.

DIFFERENCES BETWEEN SAND AND CLAY:

1. Permeability: Clays are much less permeable than sands. Therefore, undrained conditions are often prevailing in the field problems.

2. Compressibility: In the range of stresses in conventional geotechnical problems, the compressibilities of clays are higher than those for sands.

3. Cohesion: Cohesive soils form hard lumps on drying. Effective cohesion greater than zero only exists due to cementation between grains.

4. No Cavitation: Pore water in fine capillaries does not cavitate. Suction of several hundred atmospheres can be sustained in capillary water. This enables sampling of clay.

5. Plasticity: The property of a soil that enables it to deform without cracking or crumbling.

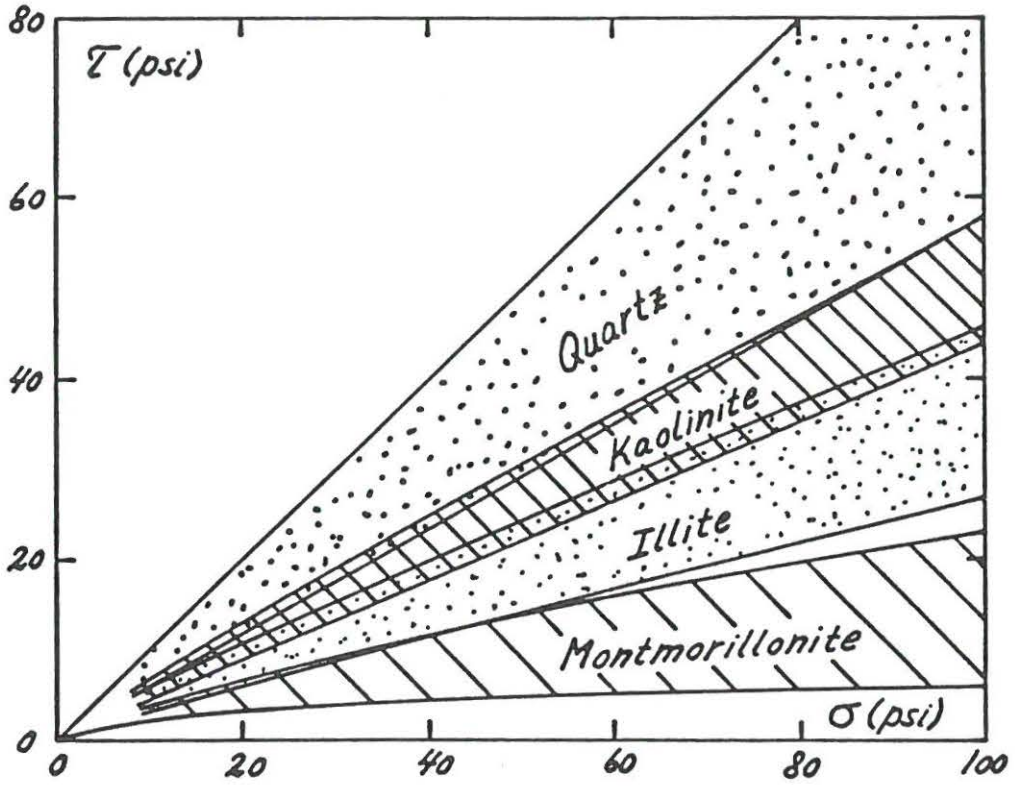

Fig. 10. Ranges in Effective Failure Envelopes For Soils Composed of Pure Clay Minerals or Quartz (Adapted from Olson, 1974).

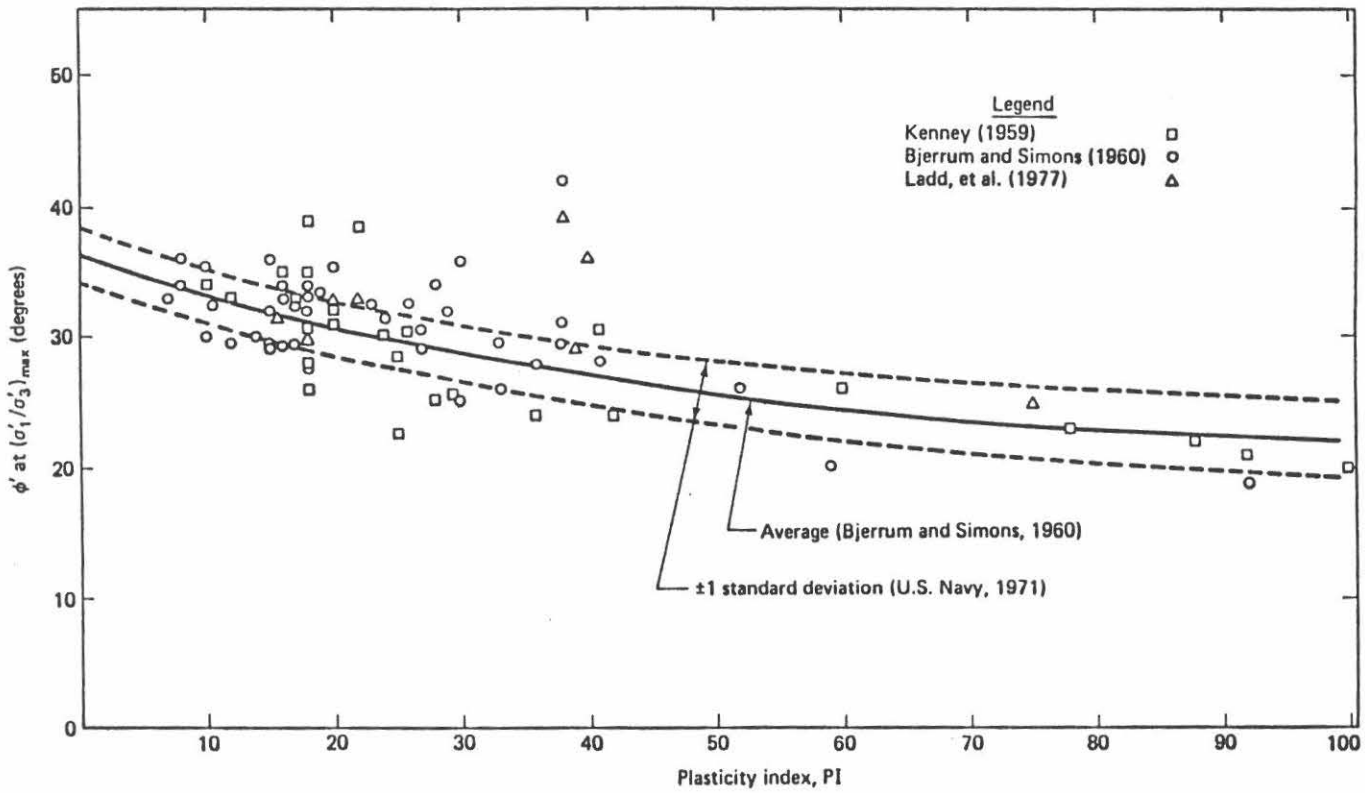

Fig. 11.27 Empirical correlation between ϕ' and PI from triaxial compression tests on normally consolidated undisturbed clays (after U.S. Navy, 1971, and Ladd, et al., 1977).

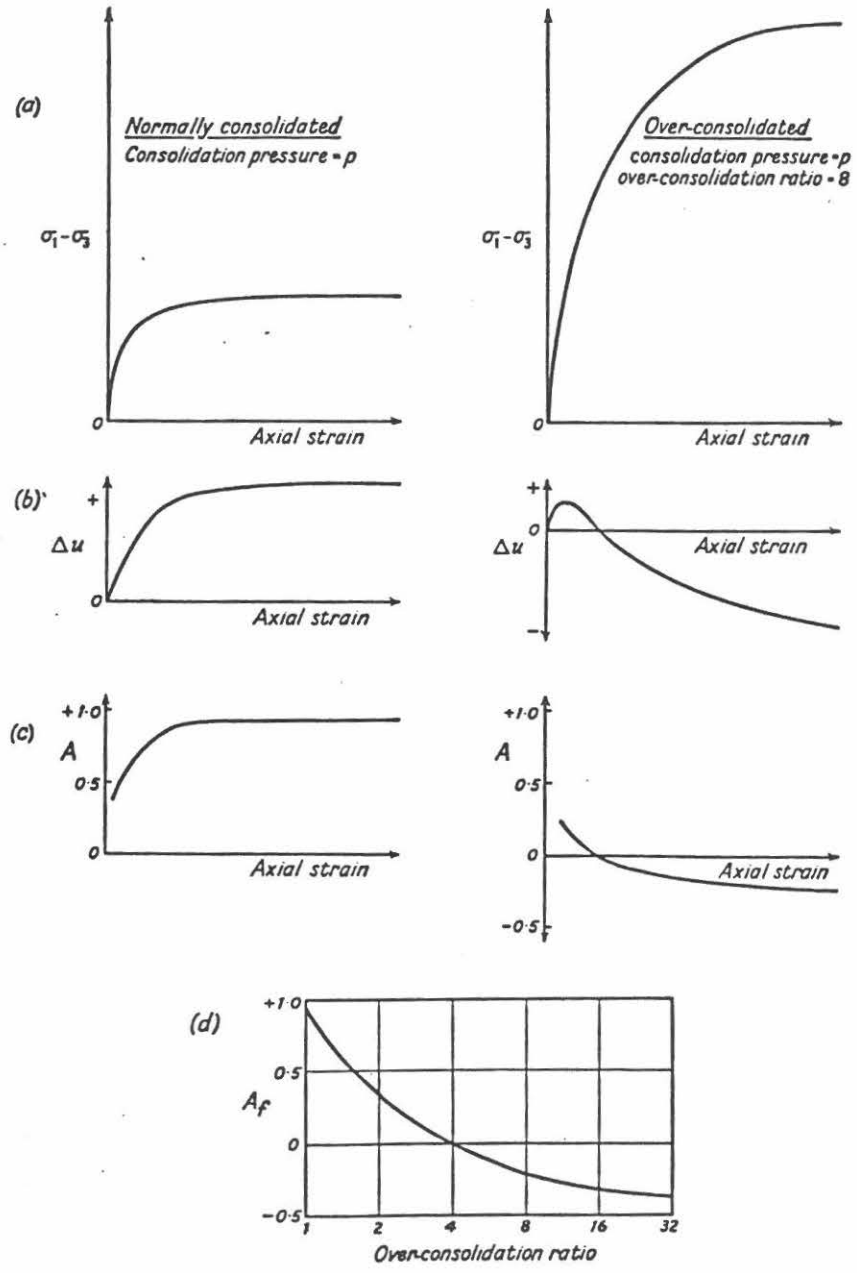

Fig. 2. The change in pore pressure during the application of the deviator stress; typical results for normally and over-consolidated clay samples

(a) deviator stress,
(b) pore pressure change, and
(c) value of parameter A, plotted against axial strain;
(d) A_f, the value of A at failure, plotted against over-consolidation ratio.

(After Bishop and Henkel, 1962)

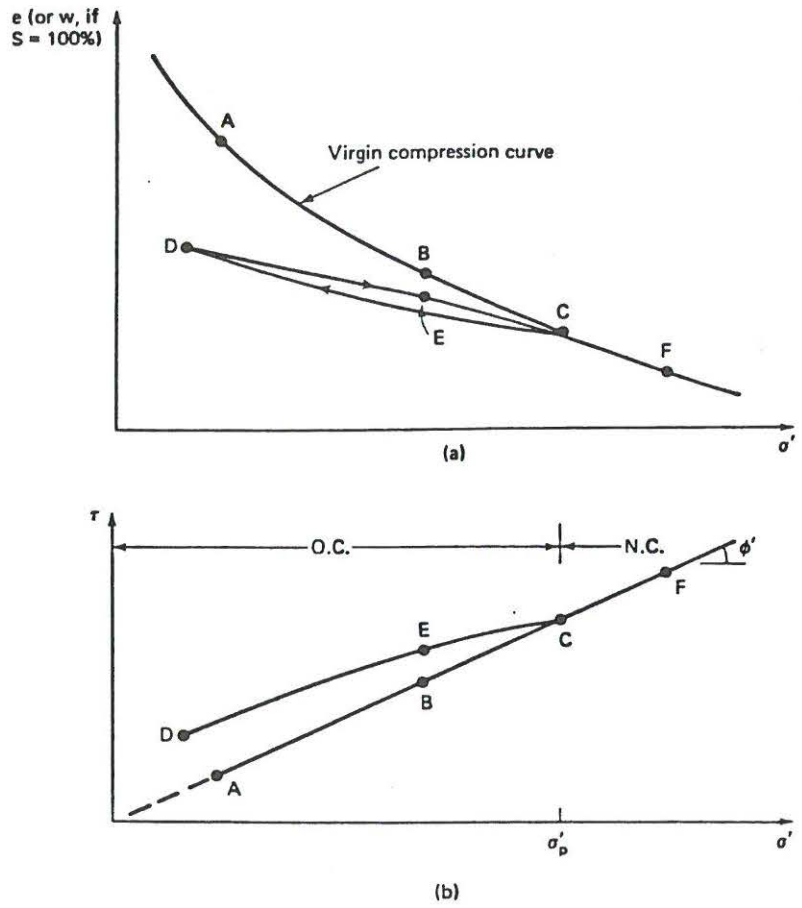

Fig. 11.26 (a) Compression curve; (b) Mohr failure envelope (DEC) for an overconsolidated clay.

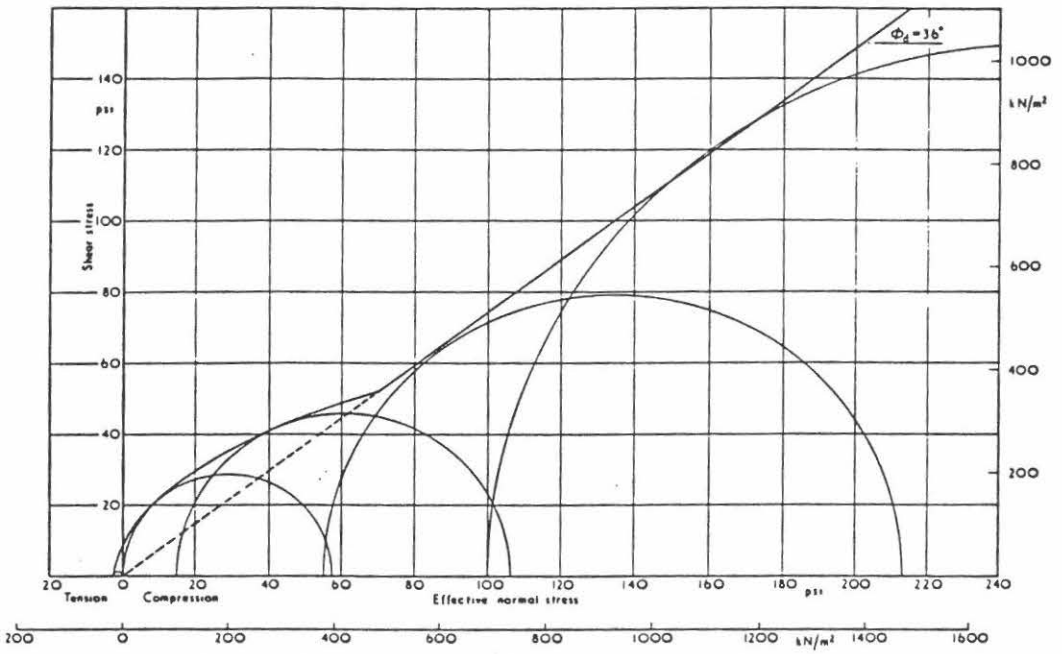

Fig. 1-27. Strength-effective normal stress relationships for undisturbed samples of Toulnustouc clay tested under drained conditions. (Data from Conlon, 1966.)

According to this:

Two factors control the strength:

1. Effective Stresses at Failure

2. Void Ratio or Water Content

   (or stress history, which in turn controls the void ratio)

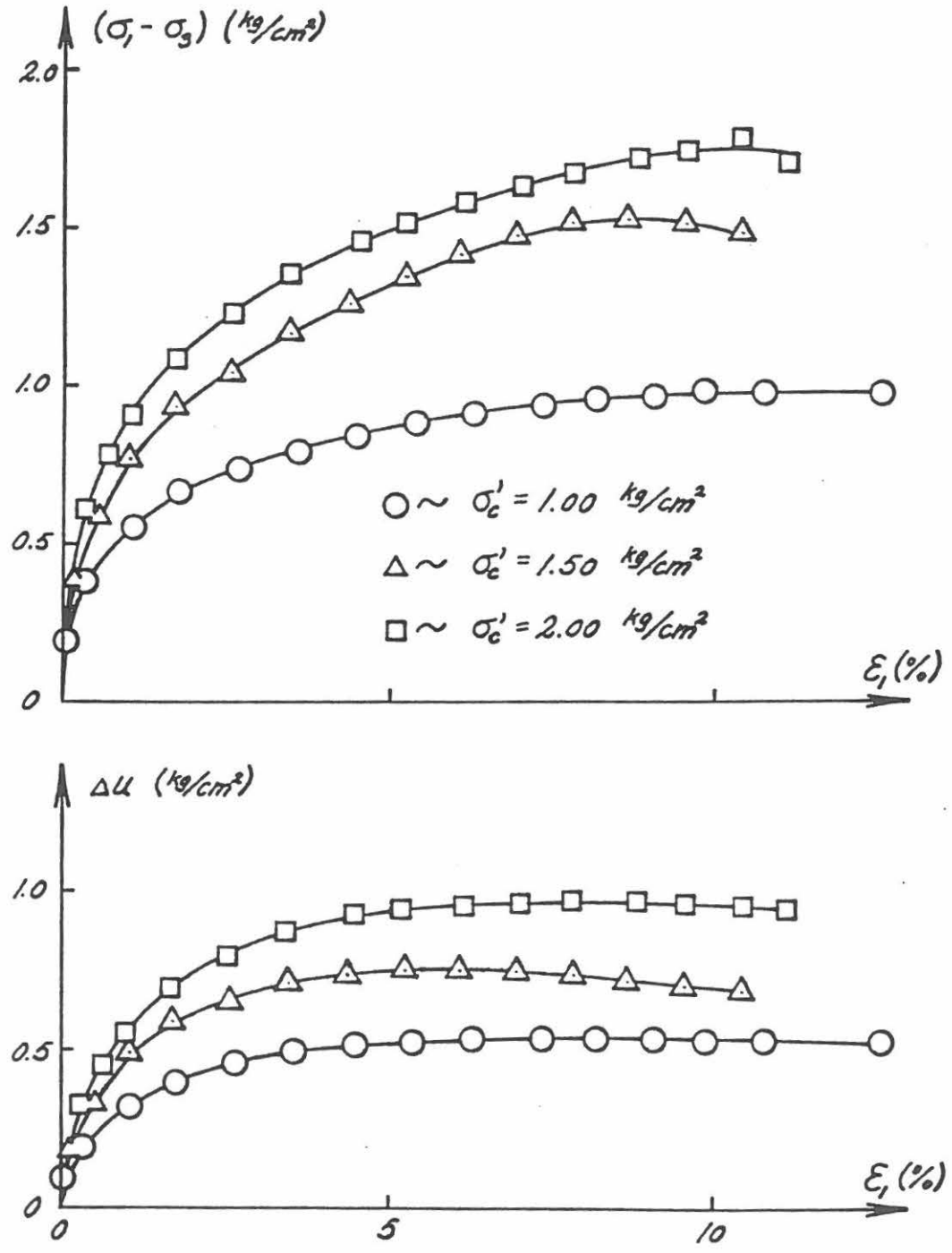

Figure 14. Variations of Deviator Stresses and Pore Pressures in Triaxial Compression Tests on Cubical Specimens of Grundite Clay Consolidated to 1.00 kg/cm^2, 1.50 kg/cm^2, and 2.00 kg/cm^2.

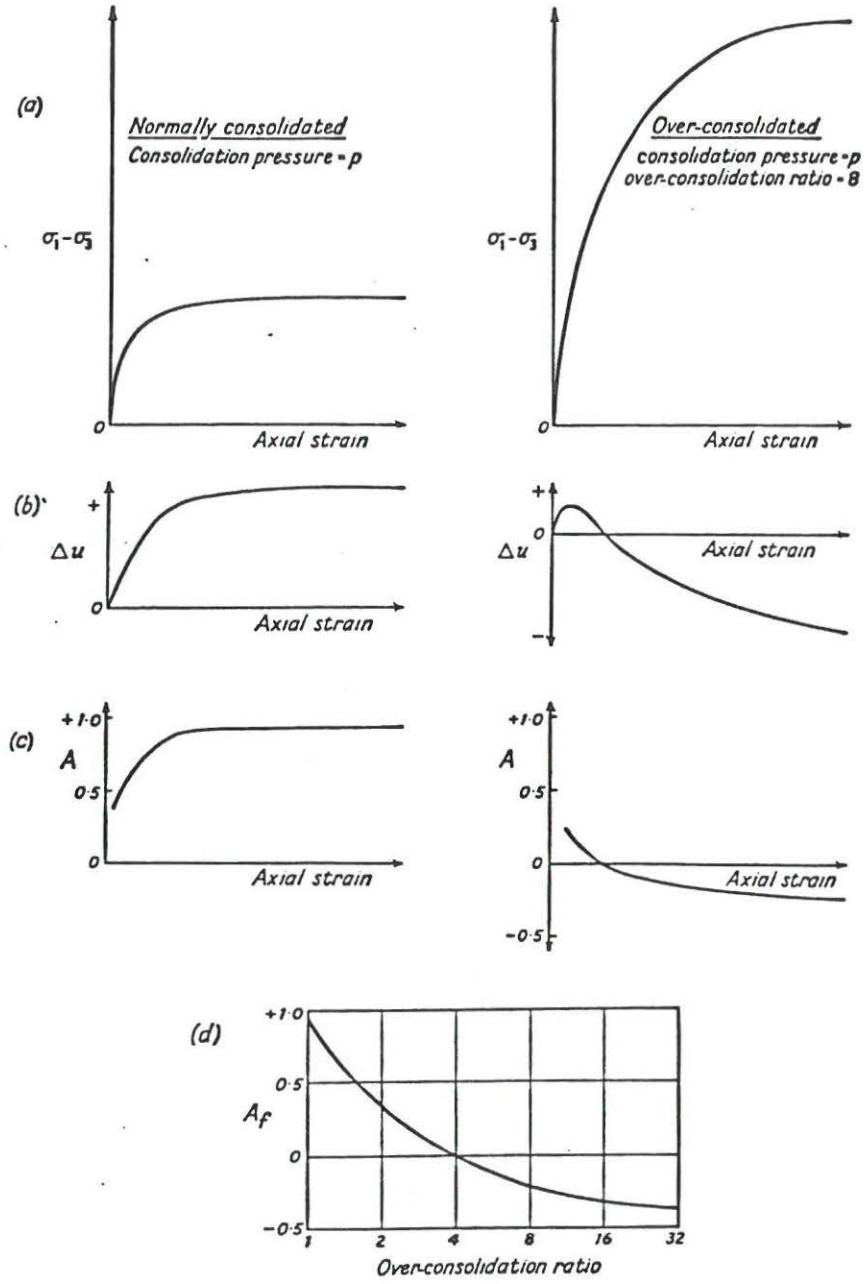

Fig. 2. The change in pore pressure during the application of the deviator stress; typical results for normally and over-consolidated clay samples

(a) deviator stress,
(b) pore pressure change, and
(c) value of parameter A, plotted against axial strain;
(d) A_f, the value of A at failure, plotted against over-consolidation ratio.

(After Bishop and Henkel. 1962)

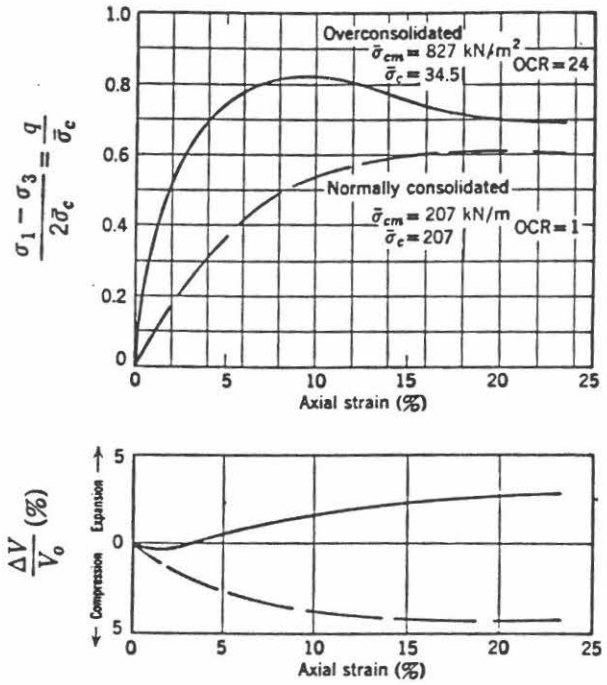

Fig. 20.10 Drained triaxial tests on Weald clay (Data from Henkel, 1956).

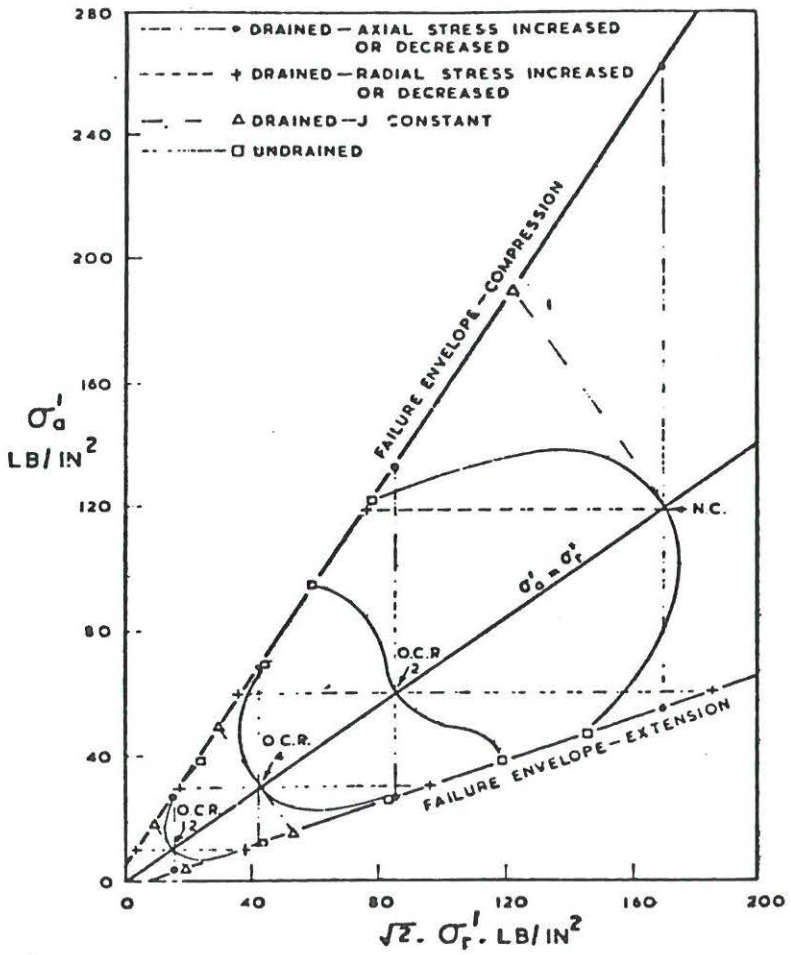

Figure 2.3: Failure Envelopes For Weald Clay. After Henkel (1960a).

Stress Invariants and Principal Stress Space

Stress Invariants

Stresses in 3 Dimensions

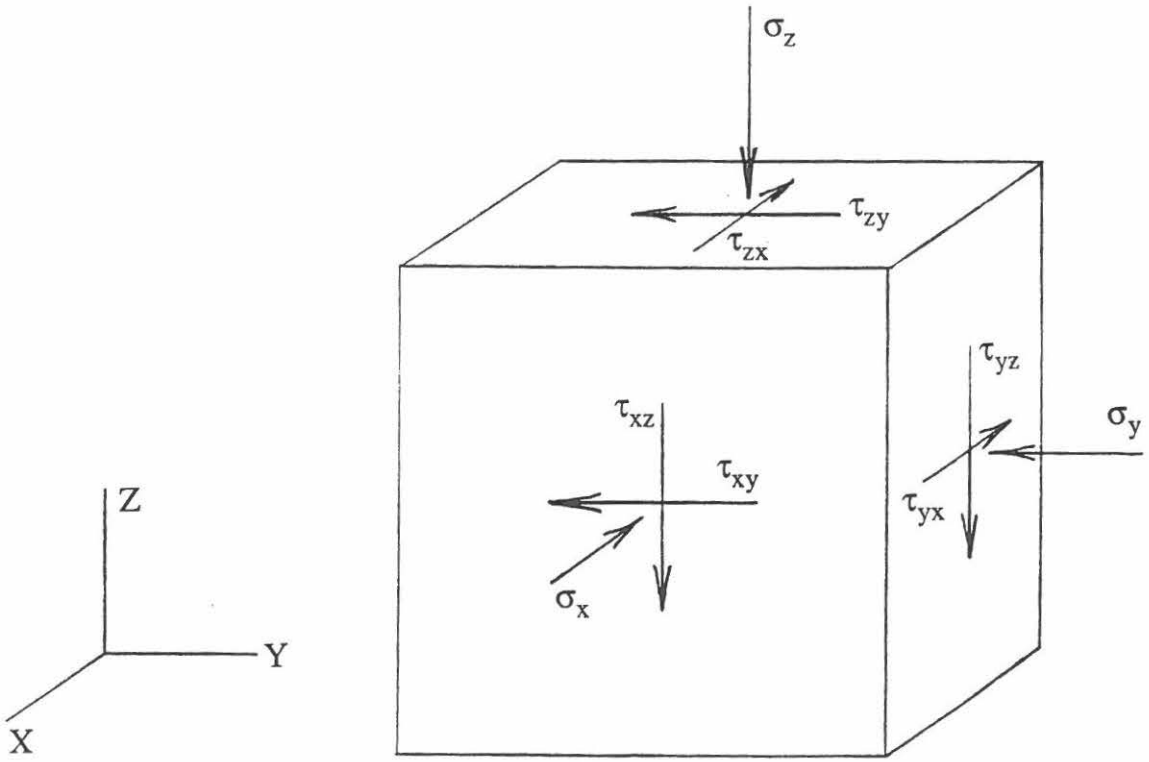

Sign rule: Normal stresses are positive when compressive

τ_{xy}: Shear stress on plane whose normal is x and direction is y

3 normal stresses and 6 shear stresses, but only 3 shear stresses are independent since $\tau_{xy} = \tau_{yx}$, etc.

Resolve stresses to get state of stress on any plane ABC:

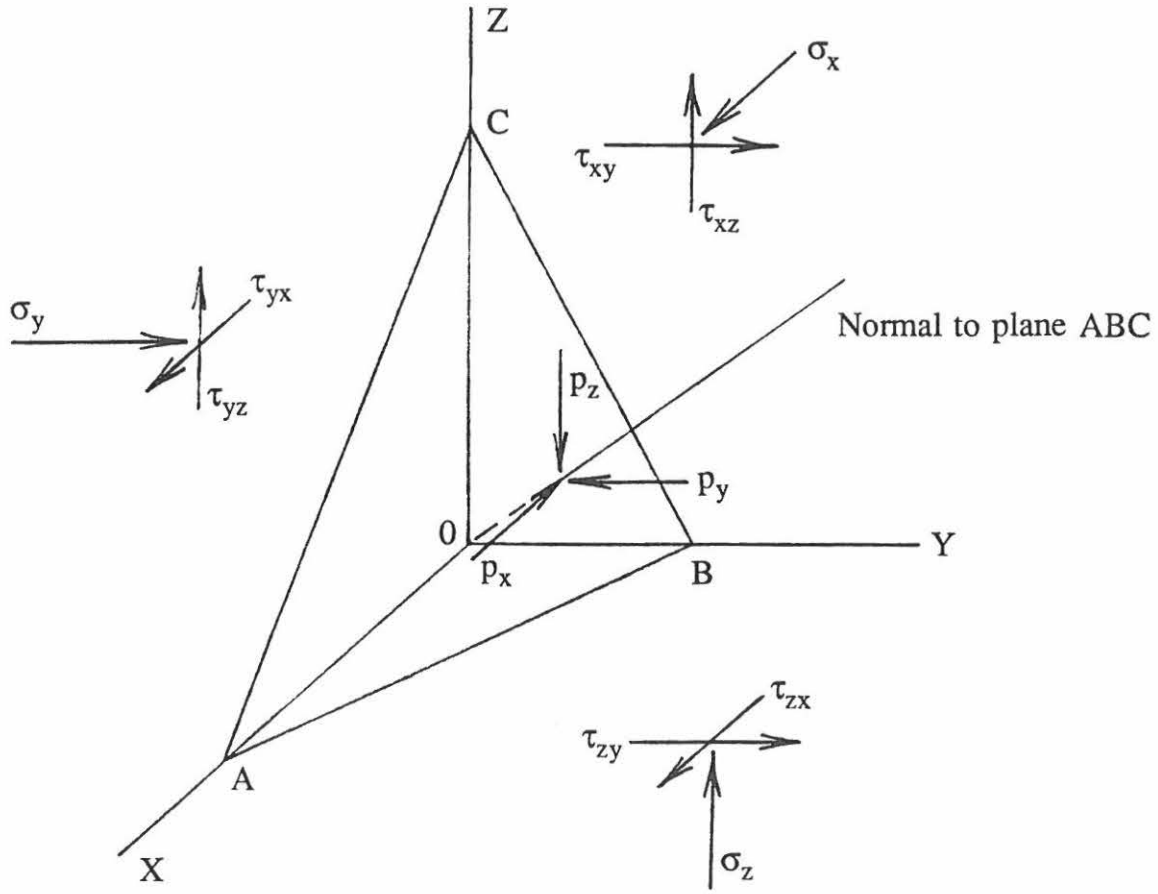

p_x, p_y, and p_z are stress components on plane ABC in directions of axes x, y, and z.

To determine the state of stress (p_x,p_y,p_z) on any plane, use force equilibrium.

=> Need areas of triangle on which stresses act to calculate forces (e.g., $F_x = \sigma_x \cdot A_{OBC}$)

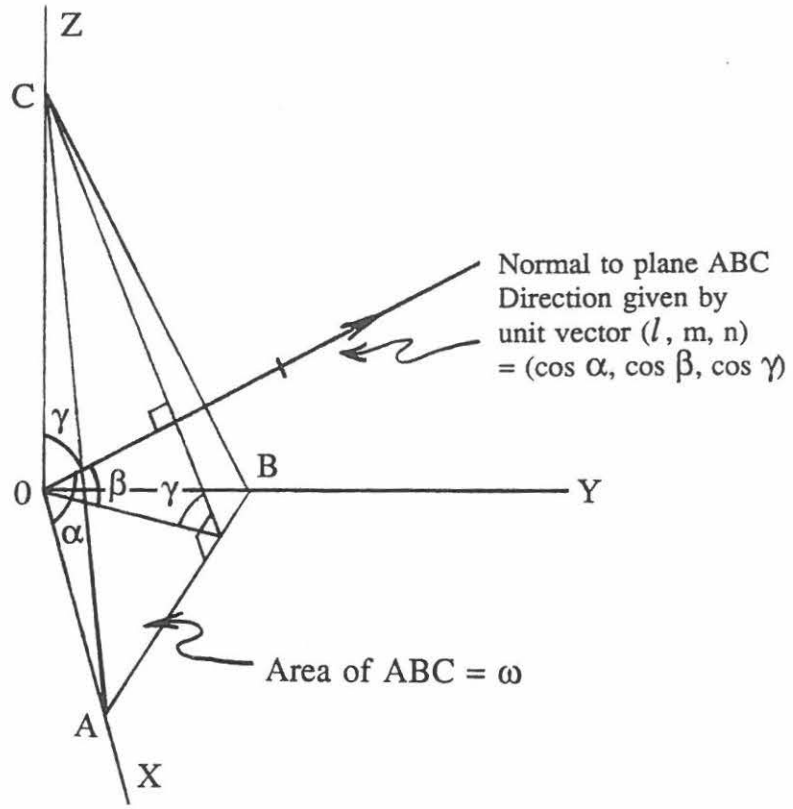

Unit vector has property:

$$l^2 + m^2 + n^2 = \cos^2 \alpha + \cos^2 \beta + \cos^2 \gamma = 1$$

=> Area of OBC = $\omega \cdot l$, and similarly
OAC = $\omega \cdot m$
OAB = $\omega \cdot n$

Equilibrium of forces in X-direction:

$$p_x \cdot \omega = \omega \cdot l \cdot \sigma_x + \omega \cdot m \cdot \tau_{yx} + \omega \cdot n \cdot \tau_{zx}$$

and similarly for the y- and z-directions:

$$p_y \cdot \omega = \omega \cdot l \cdot \tau_{xy} + \omega \cdot m \cdot \sigma_y + \omega \cdot n\, \tau_{zy}$$

$$p_z \cdot \omega = \omega \cdot l \cdot \tau_{xz} + \omega \cdot m \cdot \tau_{yz} + \omega \cdot n \cdot \sigma_z$$

and this can be written on matrix form as follows:

$$\begin{Bmatrix} p_x \\ p_y \\ p_z \end{Bmatrix} = \begin{bmatrix} \sigma_x & \tau_{yx} & \tau_{zx} \\ \tau_{xy} & \sigma_y & \tau_{zy} \\ \tau_{xz} & \tau_{yz} & \sigma_z \end{bmatrix} \begin{Bmatrix} l \\ m \\ n \end{Bmatrix}$$

Stress tensor $= \sigma_{ij}$

By rotating the normal to the plane as well as the plane ABC around 0, three locations will be encountered at which no shear stresses act on plane ABC. Such a plane is called a principal plane and the normal stress acting on this plane is a principal stress.

To determine the principal stresses, assume there is only one principal plane on which the shear stresses are zero and only a normal stress (principal stress) = σ_i exists.

Then

$$\begin{Bmatrix} p_x \\ p_y \\ p_z \end{Bmatrix} = \begin{Bmatrix} \sigma_i \cdot \cos\alpha \\ \sigma_i \cdot \cos\beta \\ \sigma_i \cdot \cos\gamma \end{Bmatrix} = \begin{Bmatrix} \sigma_i \cdot l \\ \sigma_i \cdot m \\ \sigma_i \cdot n \end{Bmatrix}$$

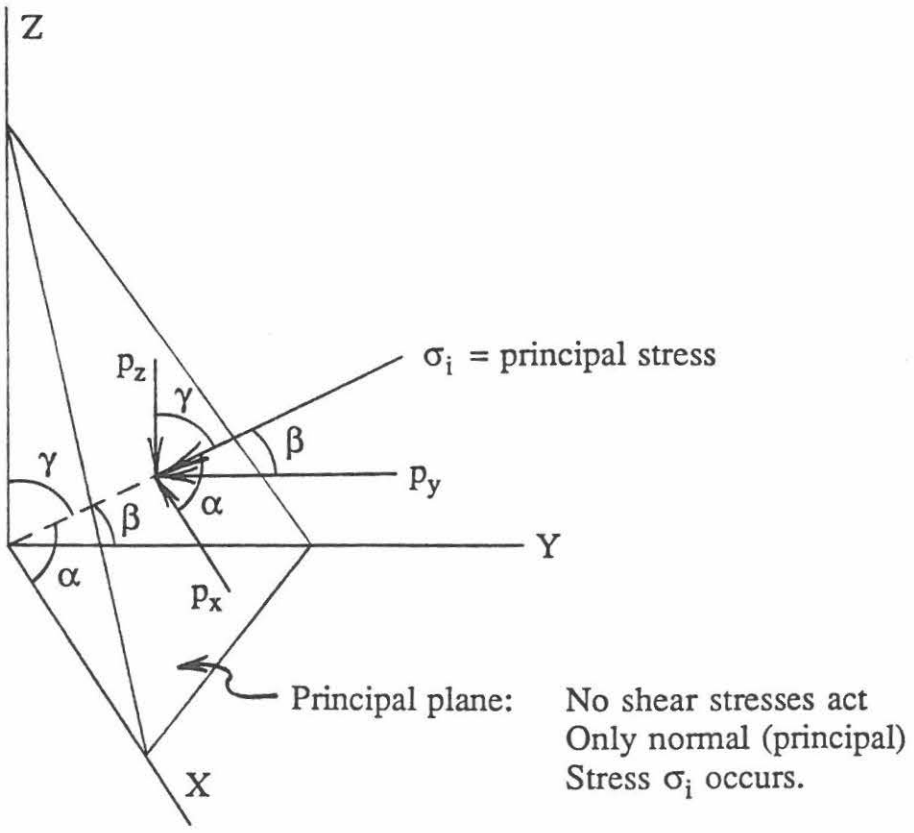

Therefore

$$\begin{bmatrix} (\sigma_x-\sigma_i) & \tau_{yx} & \tau_{zx} \\ \tau_{xy} & (\sigma_y-\sigma_i) & \tau_{zy} \\ \tau_{xz} & \tau_{yz} & (\sigma_z-\sigma_i) \end{bmatrix} \begin{Bmatrix} l \\ m \\ n \end{Bmatrix} = \begin{Bmatrix} 0 \\ 0 \\ 0 \end{Bmatrix}$$

i.e., three linear, simultaneous equations for determination of σ_i.

To obtain a nontrivial solution, the determinant of the matrix should be zero:

$$\begin{vmatrix} (\sigma_x-\sigma_i) & \tau_{yx} & \tau_{zx} \\ \tau_{xy} & (\sigma_y-\sigma_i) & \tau_{zy} \\ \tau_{xz} & \tau_{yz} & (\sigma_z-\sigma_i) \end{vmatrix} = 0$$

$$\begin{aligned} \Rightarrow\ & \sigma_i^3 - (\sigma_x + \sigma_y + \sigma_z) \cdot \sigma_i^2 \\ & + (\sigma_x \cdot \sigma_y + \sigma_y \cdot \sigma_z + \sigma_z \cdot \sigma_x - \tau_{xy} \cdot \tau_{yx} - \tau_{yz} \cdot \tau_{zy} - \tau_{zx} \cdot \tau_{xz}) \cdot \sigma_i \\ & - (\sigma_x \cdot \sigma_y \cdot \sigma_z + \tau_{xy} \cdot \tau_{yz} \cdot \tau_{zx} + \tau_{yx} \cdot \tau_{zy} \cdot \tau_{xz} \\ & \quad - \sigma_x \cdot \tau_{yz} \cdot \tau_{zy} - \sigma_y \cdot \tau_{zx} \cdot \tau_{xz} - \sigma_z \cdot \tau_{xy} \cdot \tau_{yx}) = 0 \end{aligned}$$

or (the characteristic equation):

$$\sigma_i^3 - I_1 \cdot \sigma_i^2 + I_2 \cdot \sigma_i - I_3 = 0$$

in which

$$\begin{aligned} I_1 &= \sigma_x + \sigma_y + \sigma_z \\ &= \sigma_1 + \sigma_2 + \sigma_3 \end{aligned}$$

$$* \quad I_2 = \sigma_x \cdot \sigma_y + \sigma_y \cdot \sigma_z + \sigma_z \cdot \sigma_x - \tau_{xy} \cdot \tau_{yx} - \tau_{yz} \cdot \tau_{zy} - \tau_{zx} \cdot \tau_{xz}$$
$$= \sigma_1 \cdot \sigma_2 + \sigma_2 \cdot \sigma_3 + \sigma_3 \cdot \sigma_1$$

$$I_3 = \sigma_x \cdot \sigma_y \cdot \sigma_z + \tau_{xy} \cdot \tau_{yz} \cdot \tau_{zx} + \tau_{yx} \cdot \tau_{zy} \cdot \tau_{xz}$$
$$- \sigma_x \cdot \tau_{yz} \cdot \tau_{zy} - \sigma_y \cdot \tau_{zx} \cdot \tau_{xz} - \sigma_z \cdot \tau_{xy} \cdot \tau_{yx}$$
$$= \sigma_1 \cdot \sigma_2 \cdot \sigma_3$$

The cubical equation has three real roots for a proper 3-D stress state.

For these roots (= principal stresses) to be constant and independent of the coordinate system in which the stress state is expressed, the coefficients I_1, I_2, and I_3 must themselves be constant or invariant with regard to coordinate system.

The three quantities I_1, I_2, and I_3 are called the first, the second, and the third invariants of the stress tensor.

* The sign used in the cubical equation for the coefficient to σ and the consequent sign of I_2 is the users choice, but it must be used consistently thereafter.

Stress Deviator Invariants

Decomposition of Stress Tensor

The symmetric stress tensor σ_{ij} can be decomposed into two symmetric tensors, the hydrostatic stress (or spherical stress) tensor and the deviatoric stress tensor:

$$\sigma_{ij} = \sigma_m \cdot \delta_{ij} + s_{ij}$$

or

δ_{ij} — Kronecker symbol, $\delta_{ij} = \begin{cases} 1 \text{ for } i = j \\ 0 \text{ for } i \neq j \end{cases}$

$$\begin{bmatrix} \sigma_x & \tau_{yx} & \tau_{zx} \\ \tau_{xy} & \sigma_y & \tau_{zy} \\ \tau_{xz} & \tau_{yz} & \sigma_z \end{bmatrix} = \begin{bmatrix} \sigma_m & 0 & 0 \\ 0 & \sigma_m & 0 \\ 0 & 0 & \sigma_m \end{bmatrix} + \begin{bmatrix} (\sigma_x - \sigma_m) & \tau_{yx} & \tau_{xz} \\ \tau_{xy} & (\sigma_y - \sigma_m) & \tau_{zy} \\ \tau_{xz} & \tau_{yz} & (\sigma_z - \sigma_m) \end{bmatrix}$$

The hydrostatic stress or the mean normal stress σ_m is defined as

$$\sigma_m = \frac{1}{3} \cdot (\sigma_x + \sigma_y + \sigma_z) = \frac{1}{3} \cdot I_1$$

and the deviatoric stress s_{ij} is therefore

$$s_{ij} = \sigma_{ij} - \sigma_m \cdot \delta_{ij}$$

in which the individual components are given in the deviatoric matrix above.

As for the stress tensor, invariant quantities can be determined for the deviatoric stress tensor. The characteristic equation is formed as follows:

$$s^3 - J_1 \cdot s^2 - J_2 \cdot s - J_3 = 0$$

in which the invariants of the deviatoric stress tensor have the following values:

$$J_1 = s_x + s_y + s_z = (\sigma_x - \sigma_m) + (\sigma_y - \sigma_m) + (\sigma_z - \sigma_m)$$

and with $\sigma_m = \frac{1}{3}(\sigma_x + \sigma_y + \sigma_z)$:

$$J_1 = 0$$

$$J_2 = \frac{1}{2} \cdot s_{ij} \cdot s_{ij}$$

$$= \frac{1}{6}[(\sigma_x - \sigma_y)^2 + (\sigma_y - \sigma_z)^2 + (\sigma_z - \sigma_x)^2] + \tau_{xy} \cdot \tau_{yx} + \tau_{yz} \cdot \tau_{zy} + \tau_{zx} \cdot \tau_{xz}$$

$$= \frac{1}{6}[(\sigma_1 - \sigma_2)^2 + (\sigma_2 - \sigma_3)^2 + (\sigma_3 - \sigma_1)^2]$$

$$J_3 = \frac{1}{3} \cdot s_{ij} \cdot s_{jk} \cdot s_{ki}$$

$$= (\sigma_x - \sigma_m)(\sigma_y - \sigma_m)(\sigma_z - \sigma_m) + \tau_{xy} \cdot \tau_{yz} \cdot \tau_{zx} + \tau_{yx} \cdot \tau_{zy} \cdot \tau_{xz}$$

$$- (\sigma_x - \sigma_m) \cdot \tau_{yz} \cdot \tau_{zy} - (\sigma_y - \sigma_m) \cdot \tau_{xz} \cdot \tau_{zx} - (\sigma_z - \sigma_m) \tau_{xy} \cdot \tau_{yx}$$

$$J_3 = (\sigma_1 - \sigma_m)(\sigma_2 - \sigma_m)(\sigma_3 - \sigma_m)$$

$$= \frac{1}{27}(2\sigma_1 - \sigma_2 - \sigma_3)(2\sigma_2 - \sigma_3 - \sigma_1)(2 \cdot \sigma_3 - \sigma_1 - \sigma_2)$$

The solution to the characteristic equation yields the principal stress deviators s_1, s_2, s_3.

The coefficients J_1, J_2, and J_3 are independent of the coordinate system, and they are called the first, the second, and the third stress deviator invariants, respectively.

The stress deviator invariants may be related to the stress invariants as follows:

$$J_1 = 0$$

$$J_2 = \frac{1}{3} \cdot I_1^2 - I_2$$

$$J_3 = \frac{2}{27} \cdot I_1^3 - \frac{1}{3} \cdot I_1 \cdot I_2 + I_3$$

The principal stress deviators s_1, s_2, s_3 coincide in directions with the principal stresses, and the solutions to the two characteristic equations are really equivalent, except the stress deviators are smaller than the principal stresses by the amount of σ_m.

PRINCIPAL STRESS SPACE

In order to represent a general three-dimensional state of stress it may be useful to employ the principal stress space. This space consists of a cartesian coordinate system whose axes represent the three principal stress σ_1, σ_2, and σ_3. These stresses are positive and compressive in the octant shown in figure 2.17(a). The stress condition in a soil element may be represented in the principal stress space by a point whose coordinates are given by $(\sigma_1, \sigma_2, \sigma_3,)$ as illustrated in Figure 2.17(a).

The hydrostatic axis or the space diagonal is the line in the coordinate system which forms equal angles with the axes, as shown in Figure 2.17(b). Points on this line represents hydrostatic states of stress corresponding to equal values of the principal stresses ($\sigma_1 = \sigma_2 = \sigma_3$). The angles between the hydrostatic axis and the three coordinate axes are 54.74°.

It is difficult to work with a three-dimensional stress space on a routine basis. Two planes in the principal stress space are often used for plotting test results. A triaxial plane is a plane which contains the hydrostatic axis and one of the principal stress axes. There are three triaxial planes in the principal stress space. Figure 2.18 shows the triaxial plane which contains the σ_1-axis. An octahedral plane is a

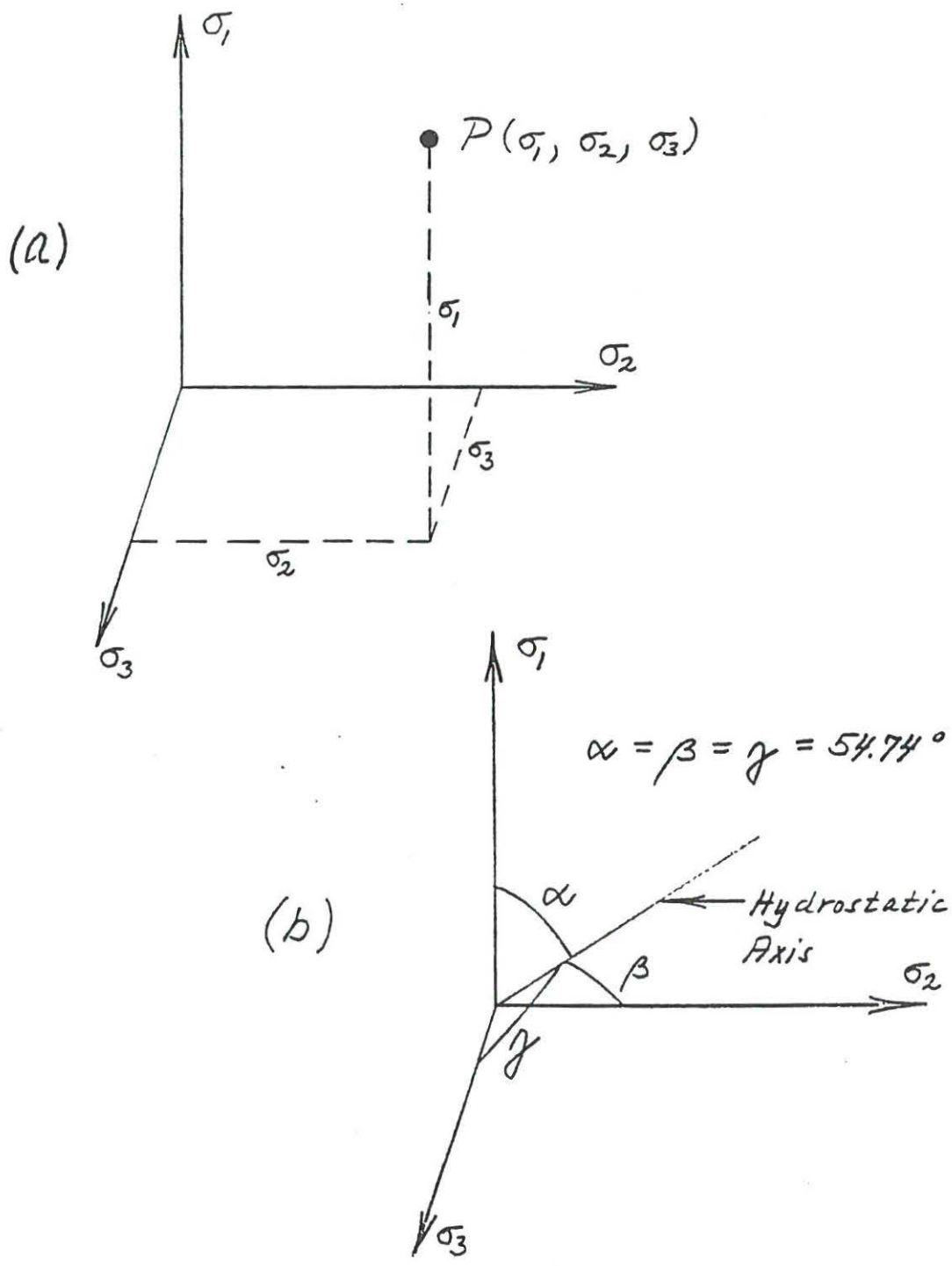

Figure 2.17 The Principal Stress Space with
(a) Location of a Stress Point, and
(b) Hydrostatic Axis

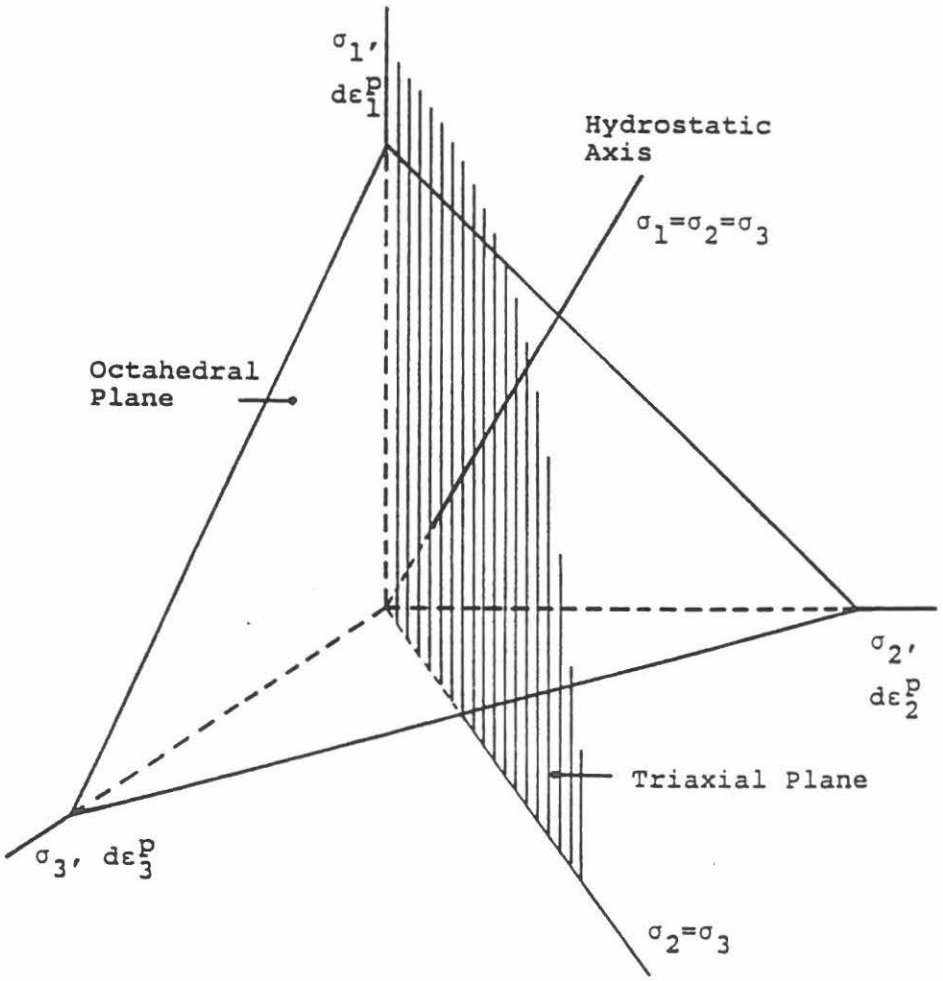

Figure 2.18 Principal Stress Space with Triaxial Plane and Octahedral Plane

plane whose normal is the hydrostatic axis. There is an infinite number of octahedral planes. Figure 2.18 shows an octahedral plane.

Octahedral Stresses

The normal and shear stresses on any octahedral plane are denoted the octahedral normal stress and the octahedral shear stress and they are given here in terms of principal stresses:

$$\sigma_{oct} = \frac{1}{3}\cdot(\sigma_1+\sigma_2+\sigma_3) \tag{2.17}$$

$$\tau_{oct} = \frac{1}{3}\cdot\sqrt{(\sigma_1-\sigma_2)^2+(\sigma_2-\sigma_3)^2+(\sigma_3-\sigma_1)^2} \tag{2.18}$$

$$= \frac{\sqrt{2}}{3}\cdot\sqrt{I_1^2-3\cdot I_2} = \sqrt{\frac{2}{3}\cdot J_2}$$

The octahedral stress components corresponding to the stress point $P(\sigma_1, \sigma_2, \sigma_3)$ can be found as illustrated in Figure 2.19. The total stress vector $\overline{OP}$ can be decomposed into the components $\overline{OQ}$ on the hydrostatic axis and $\overline{QP}$ in the octahedral plane through P. The length $|\overline{OQ}|$ can be obtained as the projection of $\overline{OP}$ on the hydrostatic axis. The scalar product of $\overline{OP}$ and the unit vector $\bar{n}$ on the hydrostatic axis gives

$$|\overline{OQ}| = \frac{1}{\sqrt{3}}\cdot\sigma_1 + \frac{1}{\sqrt{3}}\cdot\sigma_2 + \frac{1}{\sqrt{3}}\cdot\sigma_3 = \frac{\sqrt{3}}{3}\cdot(\sigma_1+\sigma_2+\sigma_3) \tag{2.19a}$$

$$|\overline{OQ}| = \sqrt{3}\cdot\sigma_{oct} \tag{2.19b}$$

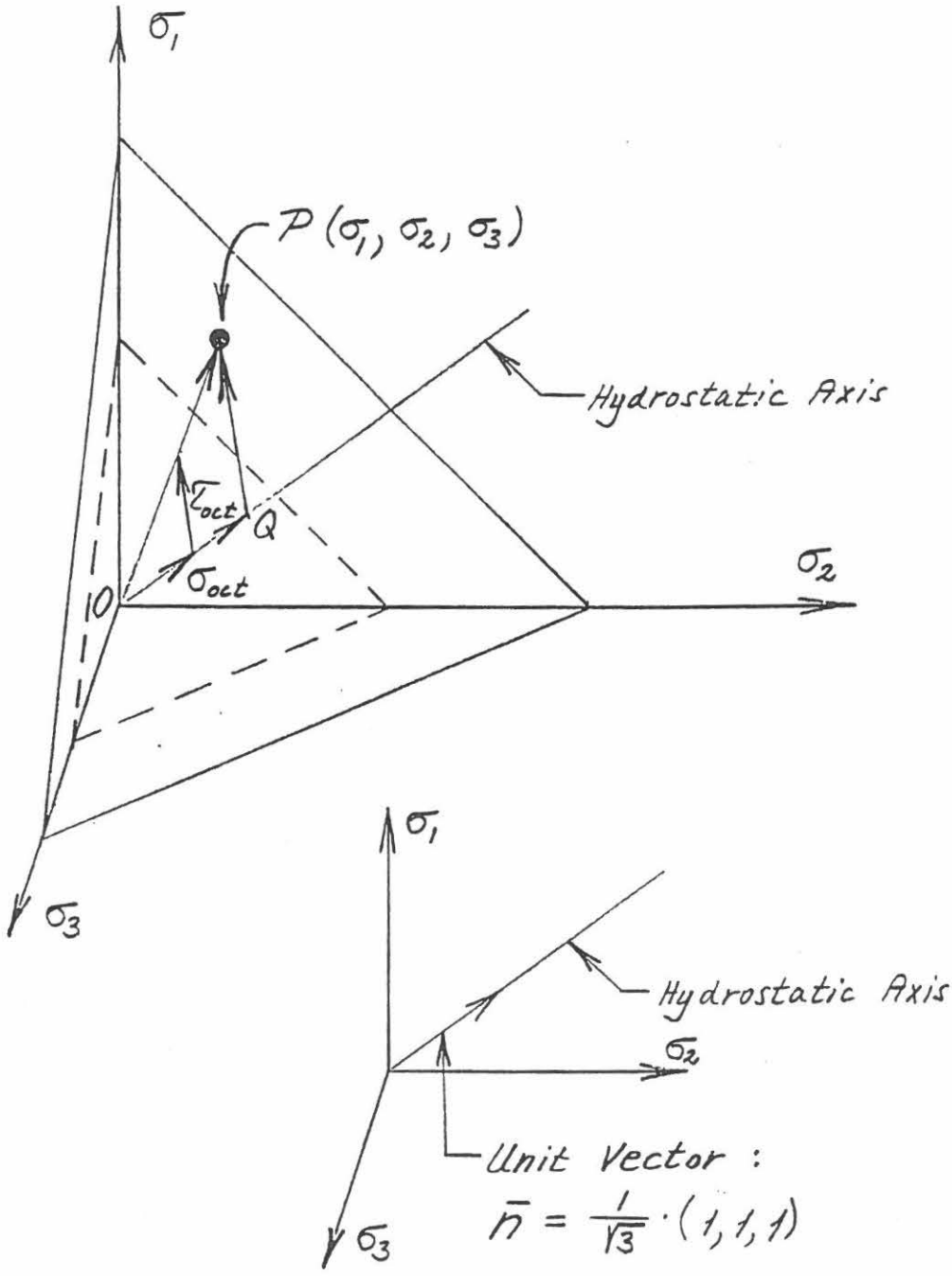

Figure 2.19 Stress Vectors, Octahedral Stresses and Octahedral Planes Used in Location of Stress Point P.

The deviatoric component $|\overline{QP}|$ of the total stress vector can be obtained as

$$|\overline{QP}| = |\overline{OP} - \overline{OQ}| \tag{2.20}$$

where

$$\overline{OP} = (\sigma_1, \sigma_2, \sigma_3) \tag{2.21}$$

and

$$\overline{OQ} = |\overline{OQ}| \cdot \bar{n} = \frac{1}{3} \cdot (\sigma_1+\sigma_2+\sigma_3)(1,1,1,) \tag{2.22}$$

Performing the calculation indicated in equation (2.20) results in

$$|\overline{QP}| = \frac{\sqrt{3}}{3} \cdot \sqrt{(\sigma_1-\sigma_2)^2+(\sigma_2-\sigma_3)^2+(\sigma_3-\sigma_1)^2} \tag{2.23a}$$

$$|\overline{QP}| = \sqrt{3} \cdot \tau_{oct} \tag{2.23b}$$

Figure 2.19 shows that the octahedral stress components, σ_{oct} and τ_{oct}, corresponding to the stress point $P(\sigma_1, \sigma_2, \sigma_3)$ are represented in the principal stress space as $\frac{1}{\sqrt{3}} \cdot |\overline{OQ}|$ and $\frac{1}{\sqrt{3}} \cdot |\overline{QP}|$, respectively. The distance from the origin to the octahedral plane which contains τ_{oct} is therefore $\frac{1}{\sqrt{3}} \cdot |\overline{OQ}|$.

//

Note that all points located on a circle in the octahedral plane have the same values of σ_{oct} and τ_{oct}, as shown in Figure 2.20.

Triaxial Plane

The triaxial plane which contains the σ_1-axis is shown in Figure 2.21. In this plane the hydrostatic axis forms an angle of $\theta = \arctan(\frac{1}{\sqrt{2}}) = 35.26°$ with the horizontal axis. Any state of stress which can be produced in a triaxial test in which the state of stress is axisymmetric can be shown in a triaxial plane. States of stress in triaxial compression plot above the hydrostatic axis, and states of stress in triaxial extension plot below the hydrostatic axis. The total and effective stress-paths for a CU-test are shown in Figure 2.21. These are the same stress-paths previously shown on the p-q diagrams in Figure 2.15.

The stress-paths shown in the triaxial plane and the Cambridge p-q diagram are very similar. In fact these two diagrams are the same within a linear transformation. Figure 2.22 shows the two diagrams superimposed with the coordinates for a stress point indicated with reference to the triaxial plane. A similar direct comparison cannot be done between the triaxial plane and the modified Mohr diagram, because the abscissa of the latter cannot be changed by a linear transformation to match the distance along the hydrostatic axis.

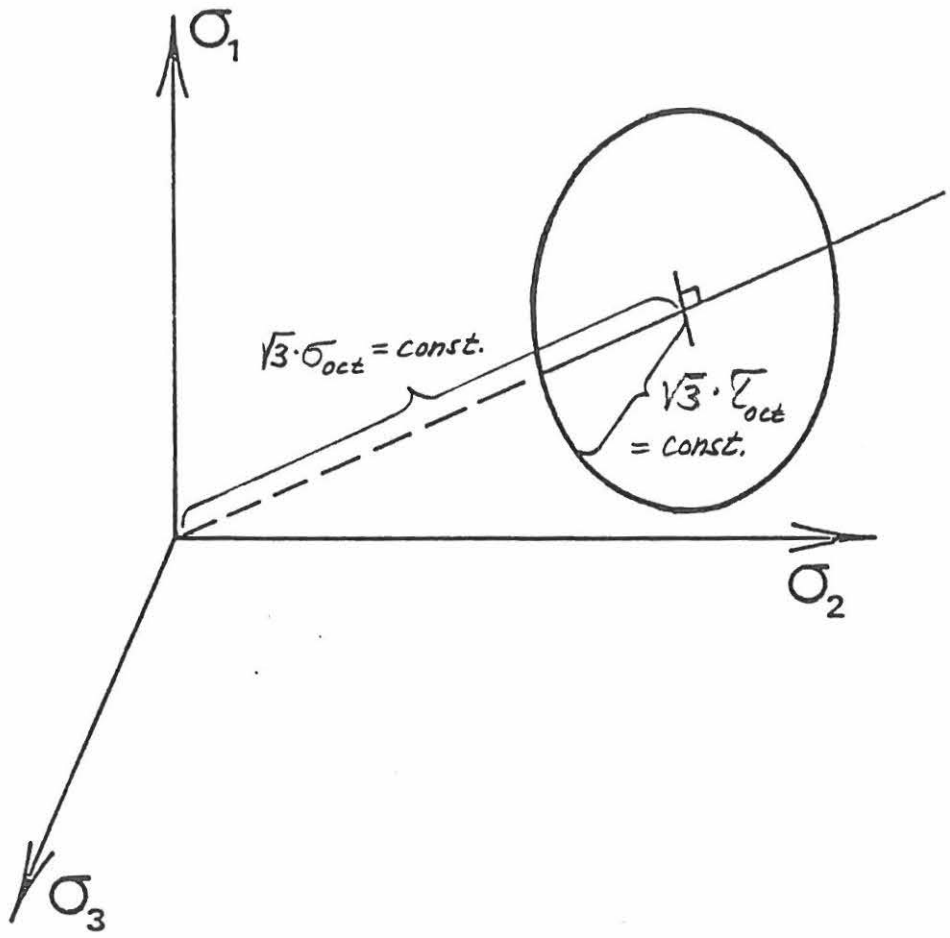

Figure 2.20 Points on a Circle in an Octahedral Plane have the Same Values of σ_{oct} and τ_{oct}

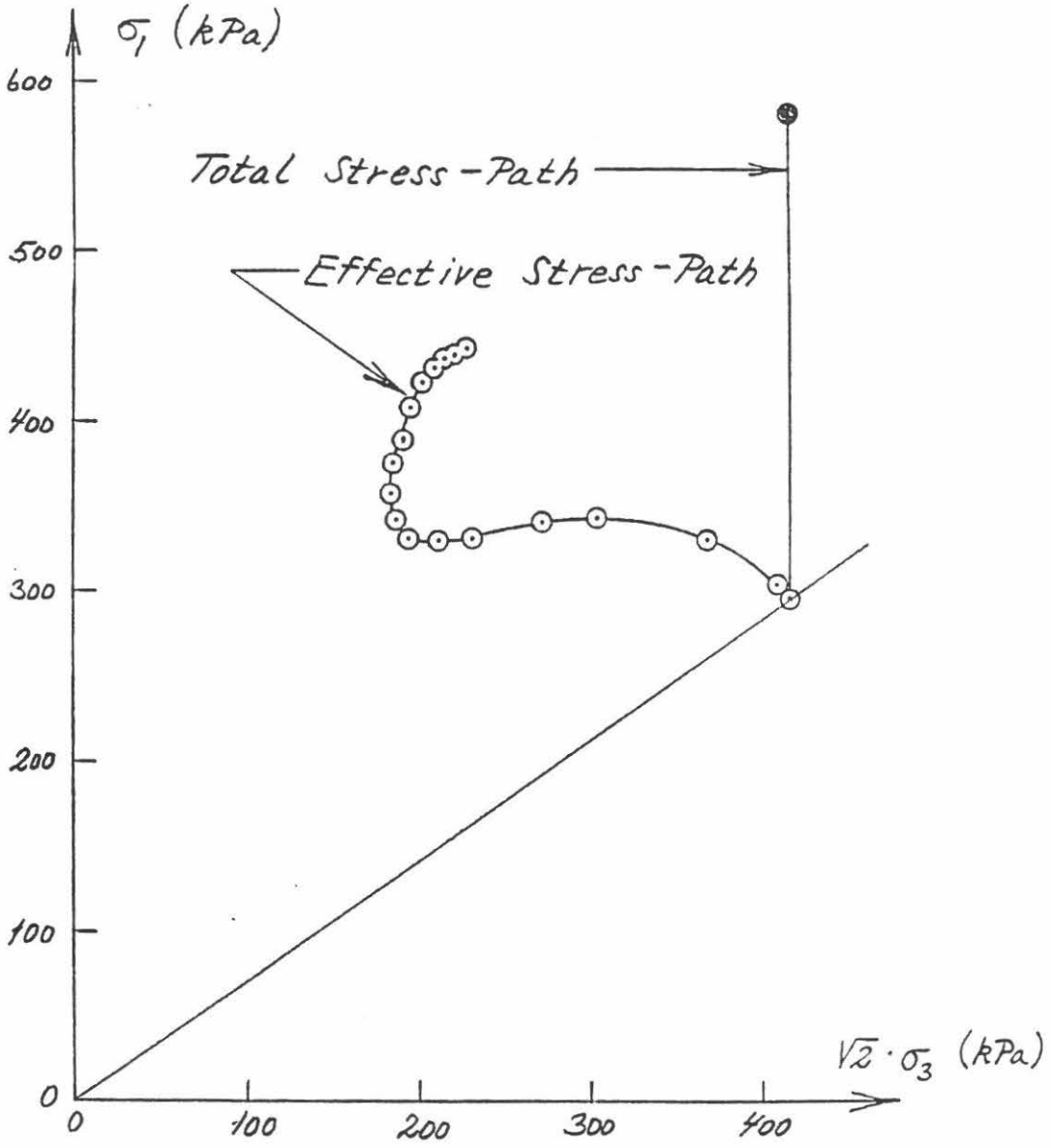

Figure 2.21 Triaxial Plane with Stress-Paths for Triaxial Test on Normally Consolidated, Remolded EPK Kaolin

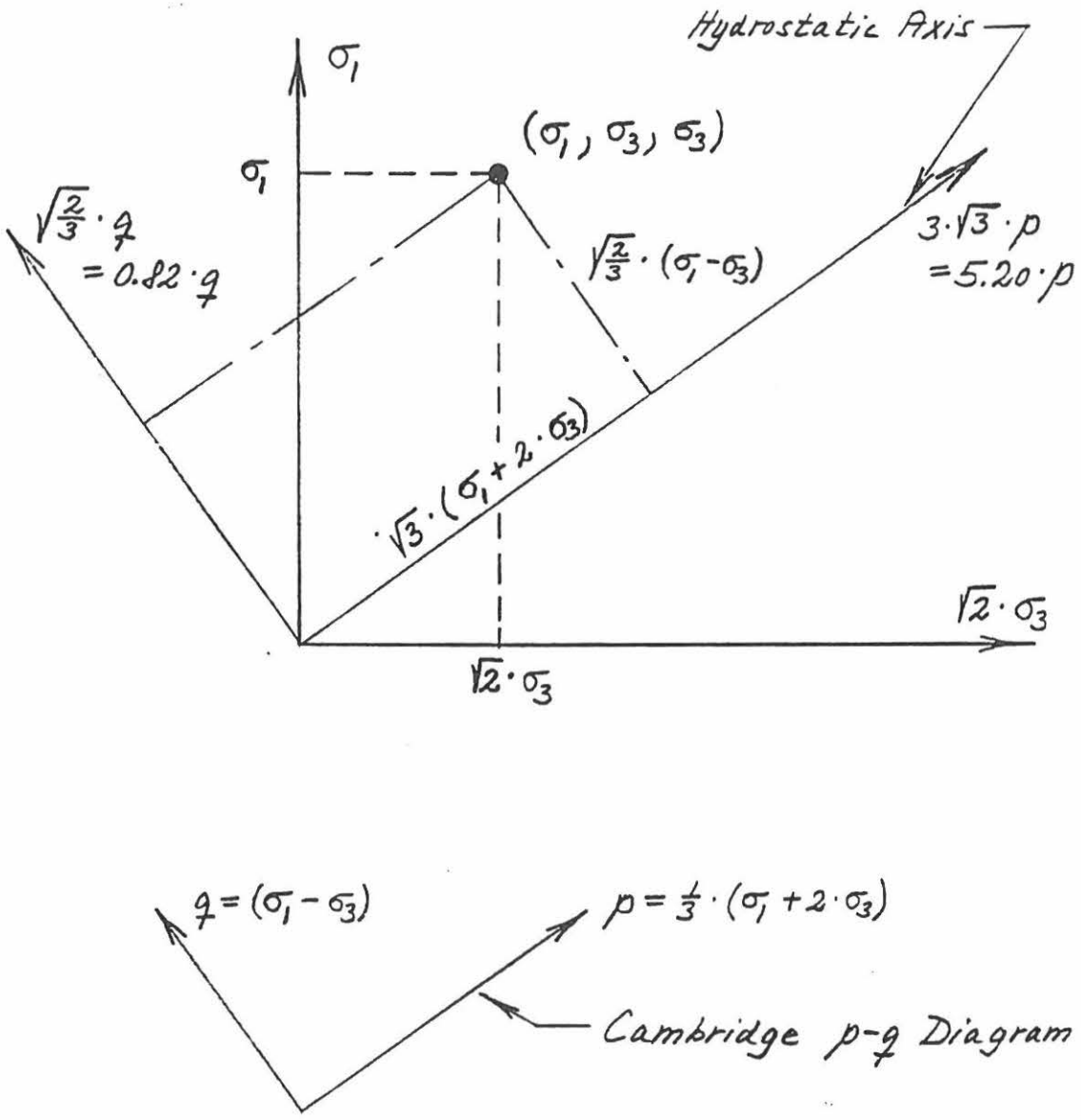

Figure 2.22 Comparison Between Triaxial Plane and Cambridge p-q Diagram.

Octahedral Plane

The other two-dimensional diagram in the principal stress space which is useful for presentation of test results is the octahedral plane. The results of tests with three unequal stresses are often shown in this diagram.

In the octahedral plane the centre point represents the hydrostatic axis as shown on figure 2.23. The three axes are 120° apart and they represent the projections of the principal stress axes on the octahedral plane. These axes are lines of symmetry such that $\sigma_1 = \sigma_2$, $\sigma_2 = \sigma_3$, and $\sigma_3 = \sigma_1$ represent the traces in the octahedral plane of the three triaxial planes.

If σ_1, σ_2, and σ_3 are taken as the major, intermediate, and minor principal stresses, only one sixth of the octant is necessary for representing any state of stress. However, any one of the three axes could be the major principal stress axis. Thus, by interchanging the subscripts (1, 2, 3) one state of stress is represented in each of the six parts of the octahedral plane. The state of stress represented by the point P is shown in each of the six parts of the plane in Figure 2.23.

Figure 2.24(a) shows the Mohr-Coulomb failure criterion in the principal stress space for a material without effective cohesion. The failure surfaces form a cone with the apex at the origin. The cross-section in an octahedral plane has the shape of an irregular hexagon with acute and obtuse angles at

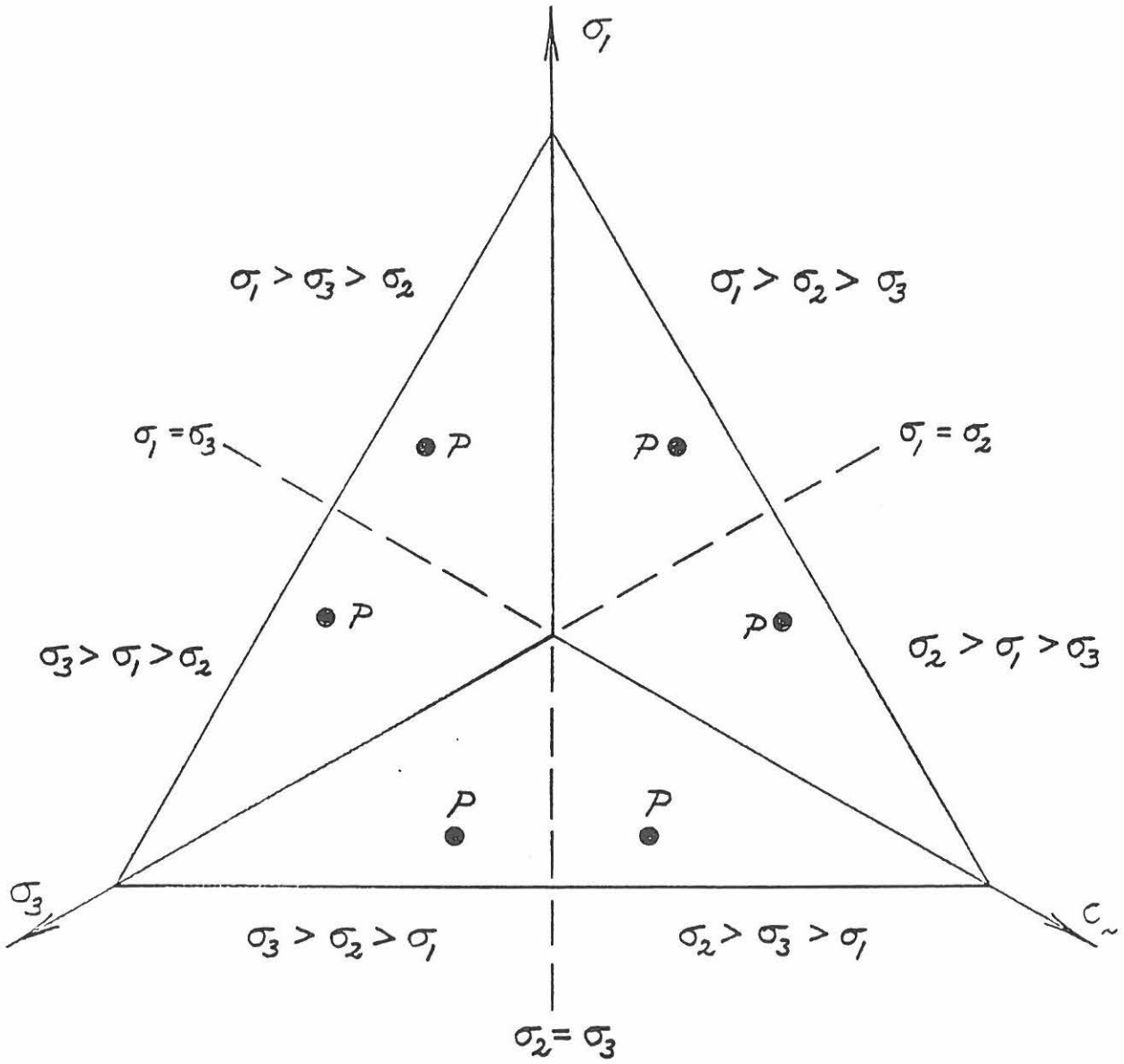

Figure 2.23 Octahedral Plane with State of Stress Represented in Each of the Six Parts

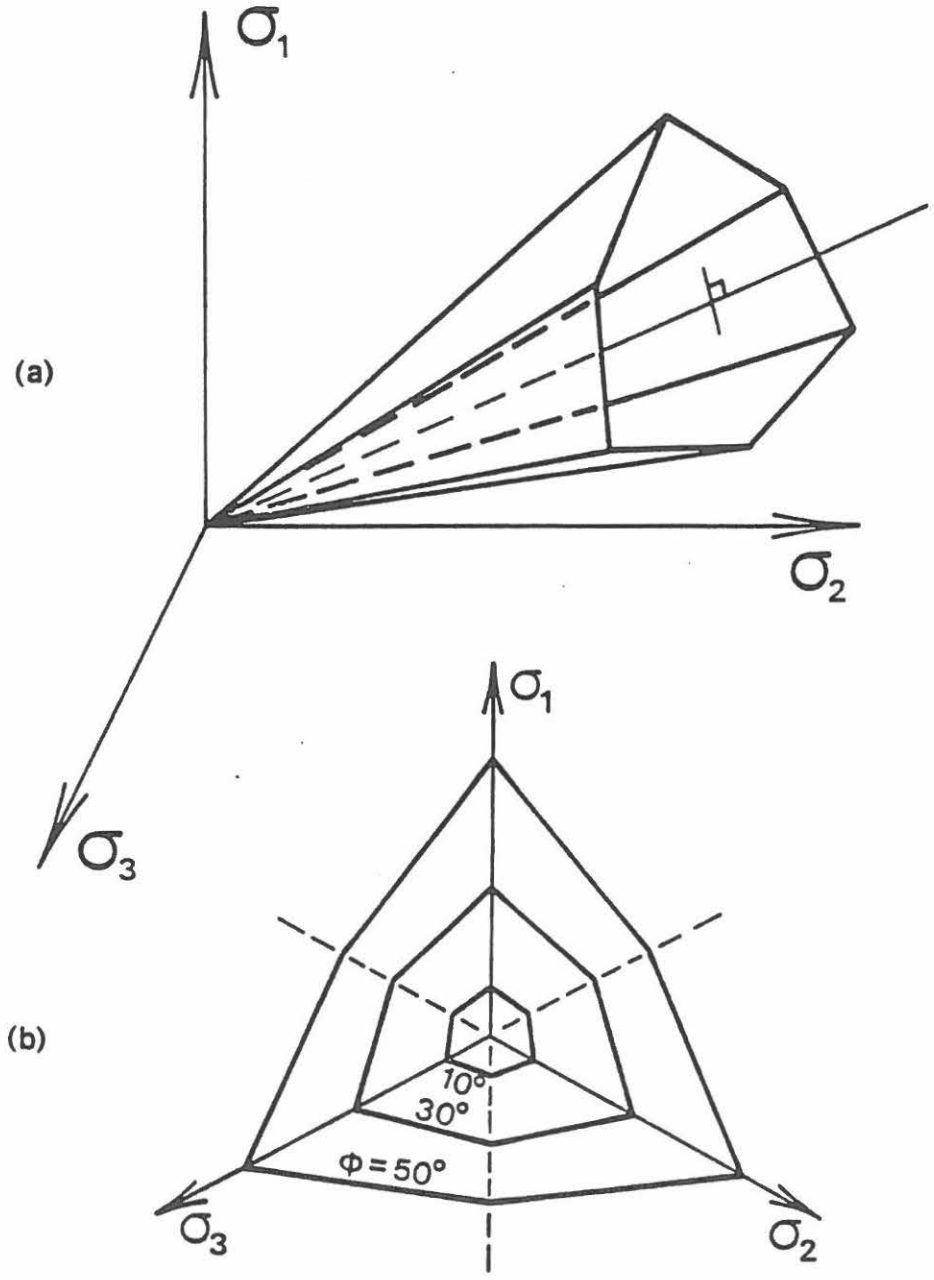

Figure 2.24 (a) Three-Dimensional Representation of Mohr-Coulomb Failure Criterion in Principal Stress Space, and
(b) Variation of Cross-Sectional Shape with Friction Angle in Octahedral Plane

the points corresponding to the states of stress in triaxial compression and extension, respectively. The cross-section changes shape as the magnitude of the friction angle changes, as indicated in Figure 2.24(b). The shape approaches an equilateral triangle for friction angles approaching 90°, and it resembles a regular hexagon at very small friction angle.

Procedure for Plotting Stress Points on an Octahedral Plane

It is often useful to study the shape of failure surfaces in the principal stress space. The cross-sectional shapes of failure surfaces are best shown on an octahedral plane. However, tests conducted with three unequal principal stresses most often do not fail at the same value of the octahedral normal stress, and the results can therefore not be plotted directly on the same octahedral plane. For soils with no cohesion and with straight failure surfaces, the principal stresses at failure can be modified according to the following expression such that all stress points fall in one octahedral plane:

$$(\sigma_1^*,\ \sigma_2^*,\ \sigma_3^*) = (\sigma_1,\ \sigma_2,\ \sigma_3) \cdot \frac{\sigma_{oct}}{\frac{1}{3}(\sigma_1+\sigma_2+\sigma_3)} \qquad (2.24)$$

where σ_1, σ_2, and σ_3 are the principal stresses measured at failure, and $\sigma_{oct}(=\frac{1}{3}(\sigma_1^* + \sigma_2^* + \sigma_3^*))$ is the octahedral normal stress corresponding to the octahedral plane on which the test

results are to be plotted. The value of σ_{oct} is of no importance to the cross-sectional shape of the failure surface for soils with no cohesion and with straight failure surfaces. Note that only the magnitudes of the principal stresses are modified, whereas the ratios between the principal stresses remain constant. Thus, the friction angle is not changed due to the modification of stresses given by equation (2.24).

The point P corresponding to the modified principal stresses σ_1^*, σ_2^*, and σ_3^* can be placed on the octahedral plane according to the following procedure. The principal stress space with the octahedral plane which contains the stress point P is shown in the upper part of Figure 2.25. The procedure for finding the distances between the projection of P on the principal stress axes in the octahedral plane and the hydrostatic axis will be demonstrated. The calculations all pertain to a triaxial plane, which is a plane containing one of the principal stress axes and the hydrostatic axis. the triaxial plane containing the σ_1-axis is shown in the lower part of Figure 2.25. The point in which the hydrostatic axis crosses the octahedral plane is designated O'. The distance between the origin and the projection of O' on the σ_1-axis is equal to $\sigma_{oct} = \frac{1}{3} \cdot (\sigma_1^* + \sigma_2^* + \sigma_3^*)$ as may be seen from the lower part of Figure 2.25. The projection of P on the triaxial plane is designated P'. The distance O'P' = a then becomes (see Figure 2.25):

$$a = (\sigma_1^* - \sigma_{oct}) \cdot \frac{1}{\cos\theta} \qquad (2.25)$$

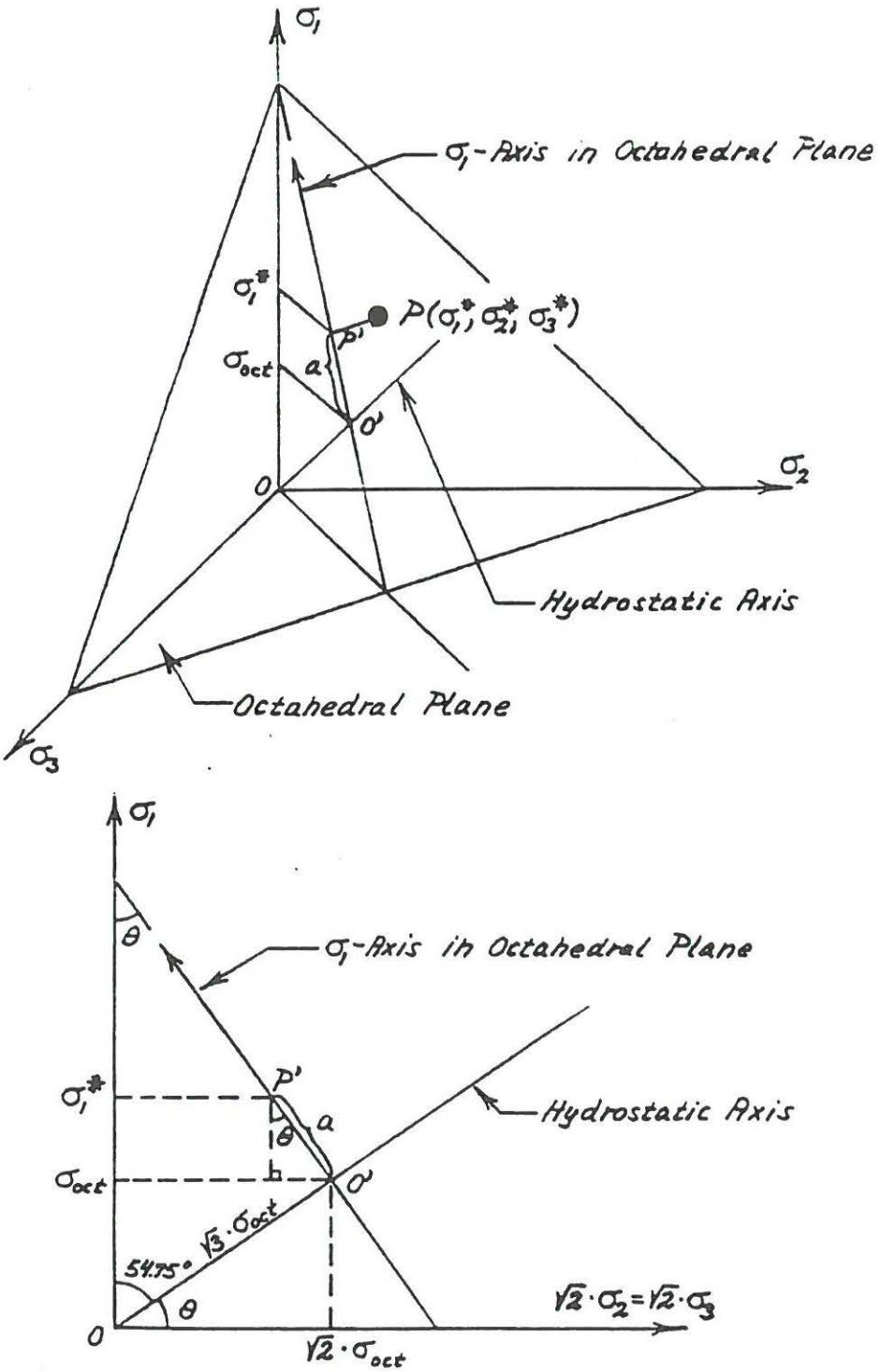

Figure 2.25 Principal Stress Space and Triaxial Plane. Determination of Distance a.

where $\cos\theta = \cos(35.26°) = \sqrt{\frac{2}{3}}$ such that

$$a = \sqrt{\frac{3}{2}} \cdot (\sigma_1^* - \sigma_{oct}) \tag{2.26}$$

Similar expressions can be obtained for the corresponding values of b and c:

$$b = \sqrt{\frac{3}{2}} \cdot (\sigma_2^* - \sigma_{oct}) \tag{2.27}$$

$$c = \sqrt{\frac{3}{2}} \cdot (\sigma_3^* - \sigma_{oct}) \tag{2.28}$$

With known values of the distances a, b and c the point P can be plotted on the octahedral plane as shown in the upper part of Figure 2.26. The lengths a, b, and c are marked out on the axes in the octahedral plane and lines perpendicular to the axes are drawn to intersection to give the position of the stress point P. It may be seen from the upper part of Figure 2.26 that it is only necessary to use two of the three values a, b, and c.

For the purpose of simplifying the positioning of the point P on the octahedral plane, the following trigonometric considerations are made so that the coordinates of P are

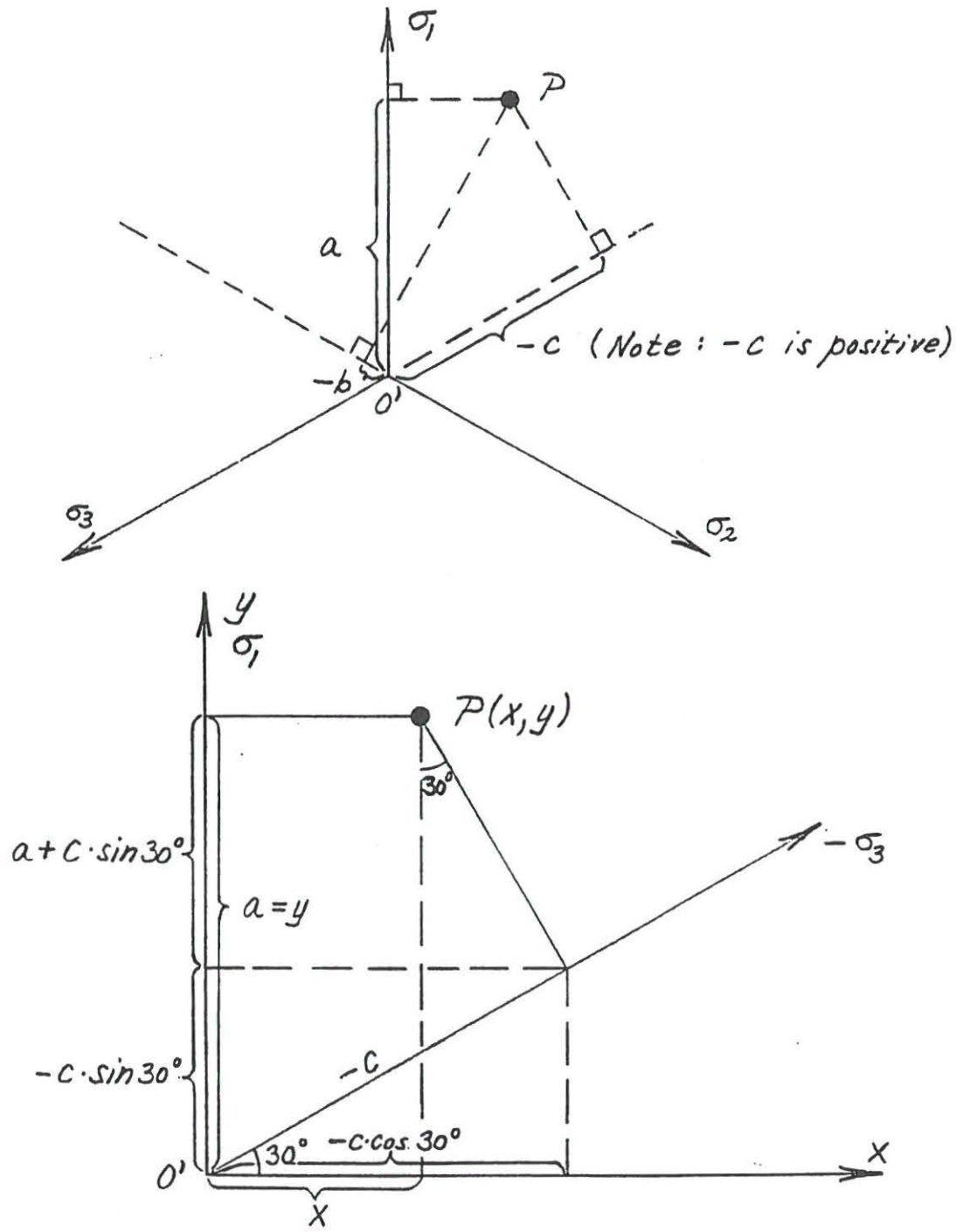

Figure 2.26 Location of Stress Point P on Octahedral Plane from a, b and c, or x and y

determined in the X-Y diagram shown in the lower part of Figure 2.26. The y-coordinate is equal to a:

$$y = \sqrt{\frac{3}{2}} \cdot (\sigma_1^* - \sigma_{oct}) \tag{2.29}$$

The x-coordinate is determined as follows (see lower part of Figure 2.26):

$$x = - c \cdot \cos 30^\circ - (a + c \cdot \sin 30^\circ) \cdot \tan 30^\circ$$

$$x = - c \cdot (\frac{\sqrt{3}}{2} + \frac{1}{2} \cdot \frac{\sqrt{3}}{3}) - a \cdot \frac{\sqrt{3}}{3} \tag{2.30}$$

$$x = \frac{\sqrt{3}}{3} (-a - 2c)$$

Substituting the values of a and c from equations (2.26) and (2.28) respectively, into equation (2.30) and reducing, the x-coordinate becomes:

$$x = \frac{\sqrt{2}}{2} (\sigma_2^* - \sigma_3^*) \tag{2.31}$$

Using equations (2.29) and (2.31), the point $P(\sigma_1, \sigma_2, \sigma_3)$ can easily be located on the octahedral plane as shown in the lower part of Figure 2.26.

Procedure for Determination of the Direction of the Projection of a Strain Increment Vector on an Octahedral Plane

A set of principal strain increments ($\dot{\varepsilon}_1$, $\dot{\varepsilon}_2$, $\dot{\varepsilon}_3$) can be considered as a vector, which can be shown in the same space as the principal stresses. Whereas the direction of the projection of the strain increment vector on the octahedral plane is of interest, the length of this vector is usually immaterial. In order to find its direction the vector is considered to have its starting point in the origin of the principal stress and strain increment space, and its end point therefore has the coordinates ($\dot{\varepsilon}_1$, $\dot{\varepsilon}_2$, $\dot{\varepsilon}_3$). The origin 0 of the three-dimensional space projects in the center 0' of the octahedral plane and the projection of the end point of the vector on this plane can be found according to the procedure for plotting a stress point on the octahedral plane. The direction of the strain increment vector is only dependent on the relative magnitudes of the strain increments. It is therefore not necessary to modify the magnitudes of the principal strain increments such that all sets of strain increments have a common mean value.

Substituting strain increments for stresses in Equations (C.6) and (C.8), the direction of the projection of the strain increment vector on the octahedral plane can be determined as a slope in the X-Y diagram in this plane (see the lower part of Figure C.2) according to:

$$\frac{dy}{dx} = \frac{y}{x} = \frac{\sqrt{\frac{3}{2}} \cdot (\dot{\varepsilon}_1 - \dot{\varepsilon}_m)}{\frac{\sqrt{2}}{2} \cdot (\dot{\varepsilon}_2 - \dot{\varepsilon}_3)} = \sqrt{3} \cdot \frac{\dot{\varepsilon}_1 - \dot{\varepsilon}_m}{\dot{\varepsilon}_2 - \dot{\varepsilon}_3} \qquad (C.9)$$

where $\dot{\varepsilon}_m$ is the mean value of the strain increments:

$$\dot{\varepsilon}_m = \frac{1}{3} \cdot (\dot{\varepsilon}_1 + \dot{\varepsilon}_2 + \dot{\varepsilon}_3) \qquad (C.10)$$

The projections of the strain increment vectors are shown originating at their respective stress points in the octahedral plane with slopes determined from Equation (C.9).

Shapes of
STRESS INVARIANTS

A.1 STRESS INVARIANTS

Usually, plasticity theories assume isotropic materials. It is therefore convenient to use stress invariants, because this ensures symmetry of the behavior of materials in stress space. Several sets of invariants are used in the literature. However, only three independent invariants are possible in each of the set.

The most common set is that emerging from the eigenvalue problem of stresses.

$$
\begin{aligned}
I_1 &= \sigma_{kk} \\
I_2 &= \frac{1}{2}\left(\sigma_{ij}\sigma_{ji} - \sigma_{kk}\sigma_{\ell\ell}\right) \\
I_3 &= \det\left|\sigma_{ij}\right| = \frac{1}{3!}\, e_{ijk}e_{\ell mn}\sigma_{i\ell}\sigma_{jm}\sigma_{kn}
\end{aligned}
\tag{A.1}
$$

In terms of the principal stresses,

$$
\begin{aligned}
I_1 &= \sigma_1 + \sigma_2 + \sigma_3 \\
I_2 &= -\sigma_2\sigma_3 - \sigma_3\sigma_1 - \sigma_1\sigma_2 \\
I_3 &= \sigma_1\sigma_2\sigma_3
\end{aligned}
\tag{A.2}
$$

The shapes of the surfaces described by these three invariants in principal stress space are shown in Fig. A.1 through A.3.

The deviatoric stress invariants are often used in addition to given in Eq. A.1.

$$J_2' = \frac{1}{2} s_{ij}s_{ji} = \frac{1}{3} I_1^2 + I_2$$
$$J_3' = \frac{1}{3} s_{ij}s_{jk}s_{ki} = \frac{2}{27} I_1^3 + \frac{1}{3} I_1 I_2 + I_3 \qquad \text{(A.3)}$$

where the deviatoric stress is

$$s_{ij} = \sigma_{ij} - \frac{1}{3} \delta_{ij}\sigma_{kk} \qquad \text{(A.4)}$$

The second invariant J_2' is related to several physical quantities, namely, deviatoric strain energy, octahedral shear stress, and mean square sum of principal shear stresses.

For computational convenience, the third invariant is often used in an alternative form (Nayak and Zienkiewicz, 1972):

$$\omega_\sigma = \frac{1}{3} \arccos \left\{ \frac{3\sqrt{3}}{2} \frac{J_3'}{(J_2')^{3/2}} \right\} \qquad \text{(A.5)}$$

where $0 \leq \omega_\sigma \leq \frac{\pi}{3}$

The angle ω_σ is the angle of the stress vector from the σ_1 axis in the octahedral plane. It is known as the Lode angle. Using I_1, J_2', and ω_σ, the principal stresses can be expressed as

$$\begin{Bmatrix} \sigma_1 \\ \sigma_2 \\ \sigma_3 \end{Bmatrix} = \frac{2}{\sqrt{3}} \sqrt{J_2'} \begin{Bmatrix} \cos \omega_\sigma \\ \cos (\omega_\sigma + 4\pi/3) \\ \cos (\omega_\sigma + 2\pi/3) \end{Bmatrix} + \begin{Bmatrix} I_1/3 \\ I_1/3 \\ I_1/3 \end{Bmatrix} \tag{A.6}$$

This set of invariants was used in calculation of the shape of various criteria reviewed in Chapter II.

In this study, all stress functions are expressed in terms of the first set of invariants. It is useful to examine the non-dimensional analogs:

$$R_2 = - \frac{I_1^2}{I_2} - 3$$

$$R_3 = \frac{I_1^3}{I_3} - 27 \tag{A.7}$$

Combined with I_1/p_a, these two modified invariants may serve as a complete set of dimensionless invariants. The modified invariants R_2 and R_3 form cones whose vertices are at the stress origin and whose centerlines coincide with the hydrostatic axis. Figs. A.4 and A.5 show that the shapes of R_2 and R_3 in the triaxial and the octahedral planes. The cross-section of R_2 is a circle while that of R_3 is a rounded triangle.

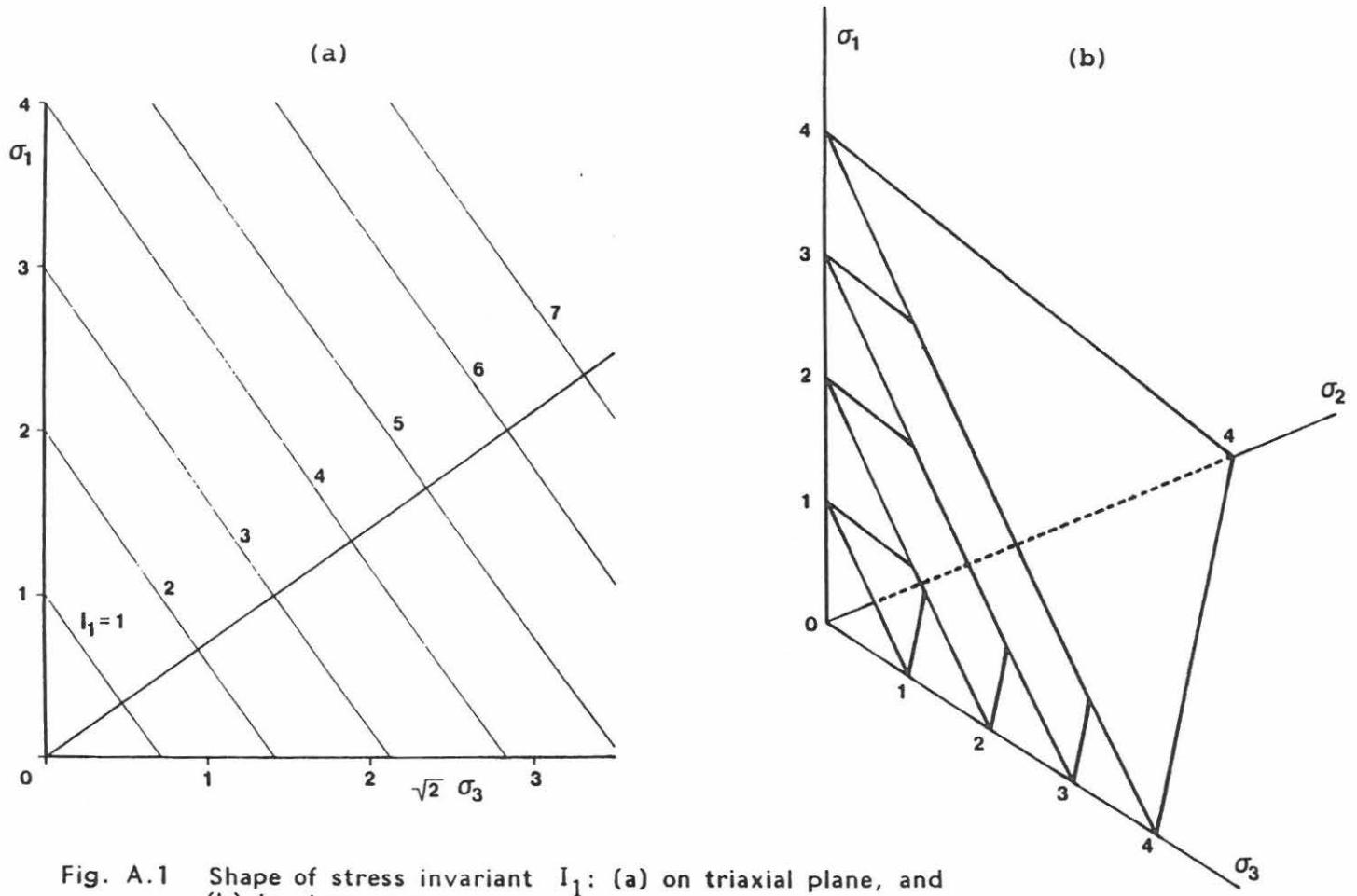

Fig. A.1 Shape of stress invariant I_1: (a) on triaxial plane, and (b) in stress space.

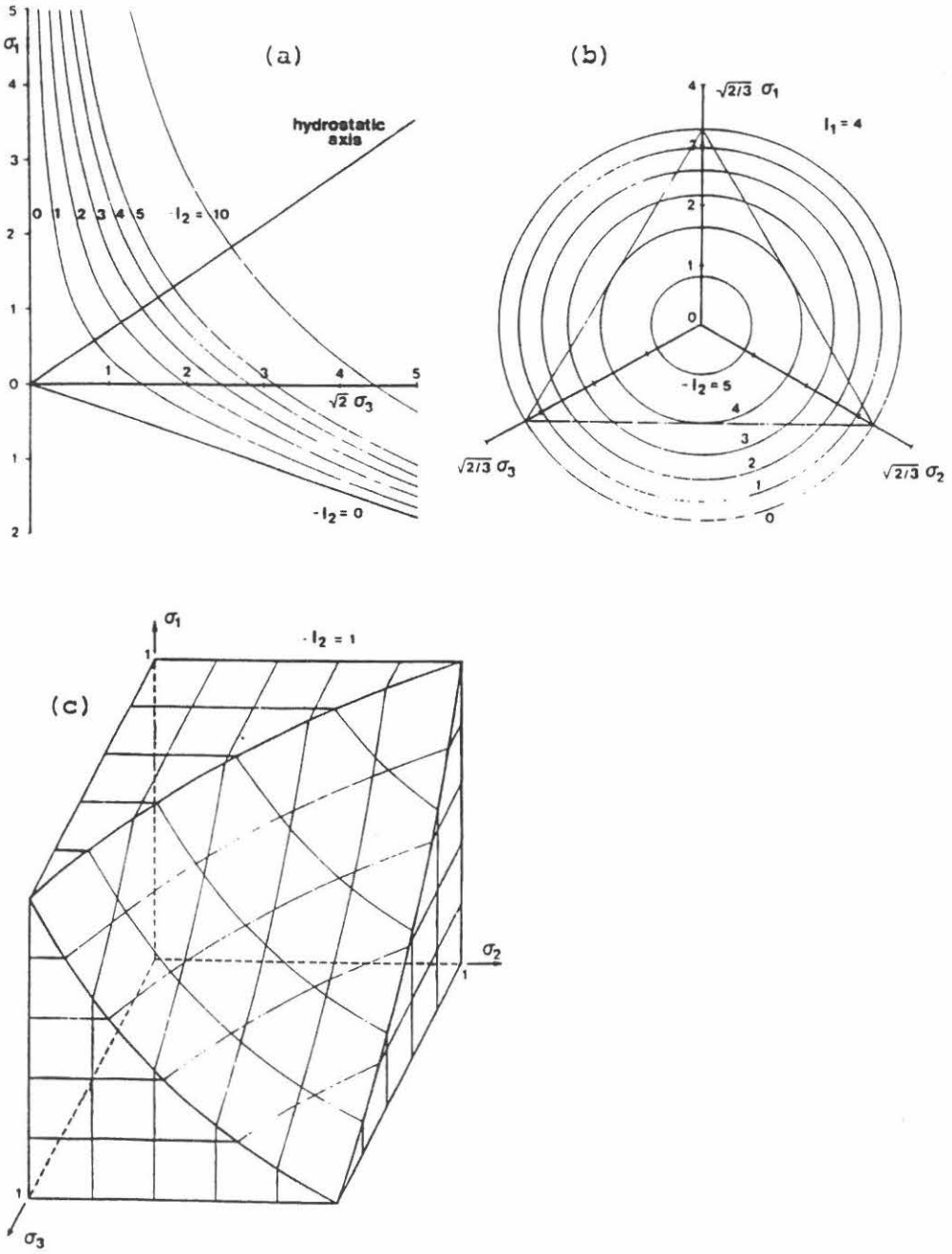

Fig. A.2 Shape of stress invariant I_2: (a) on triaxial plane, (b) on octahedral plane, and (c) in stress space.

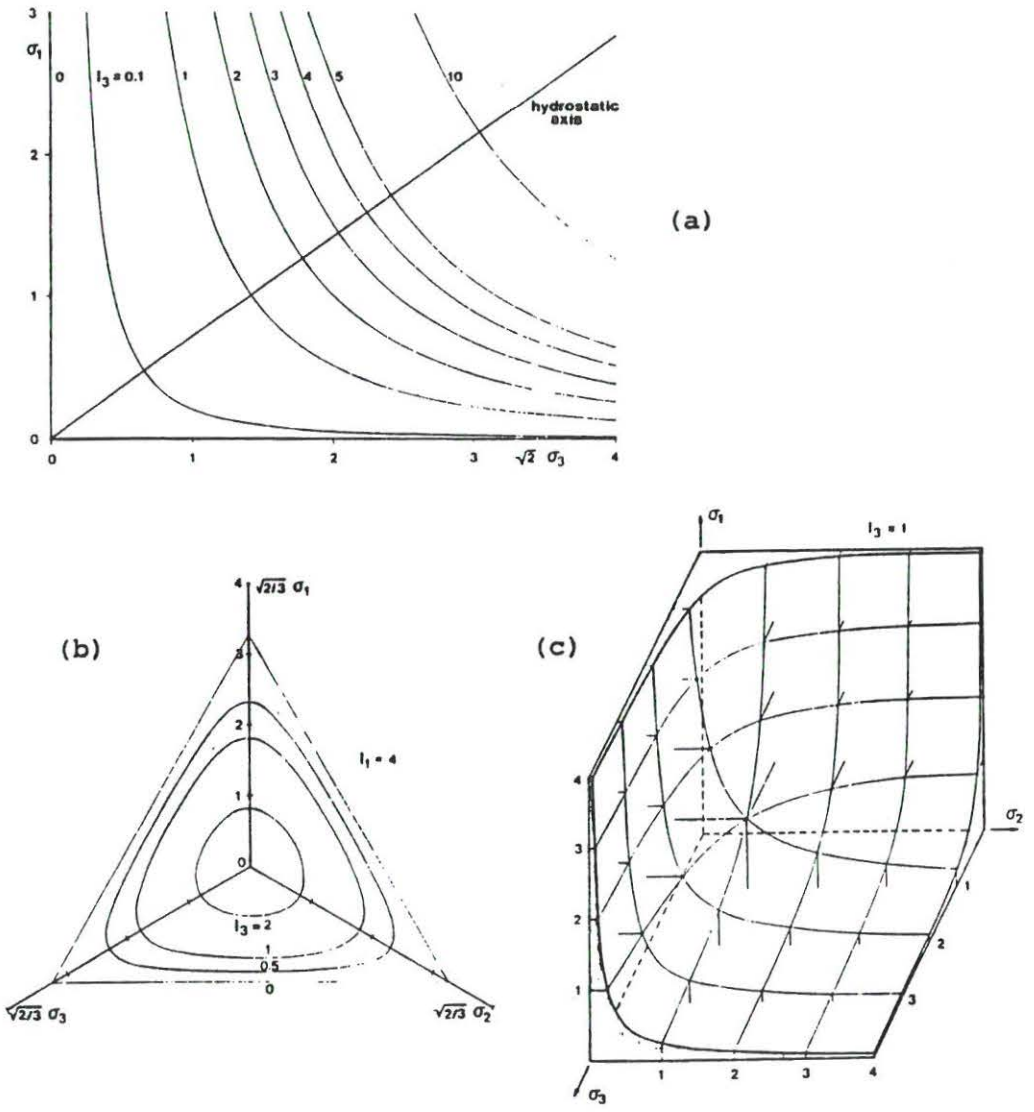

Fig. A.3 Shape of stress invariant I_3: (a) on triaxial plane, (b) on octahedral plane, and (c) in stress space.

25

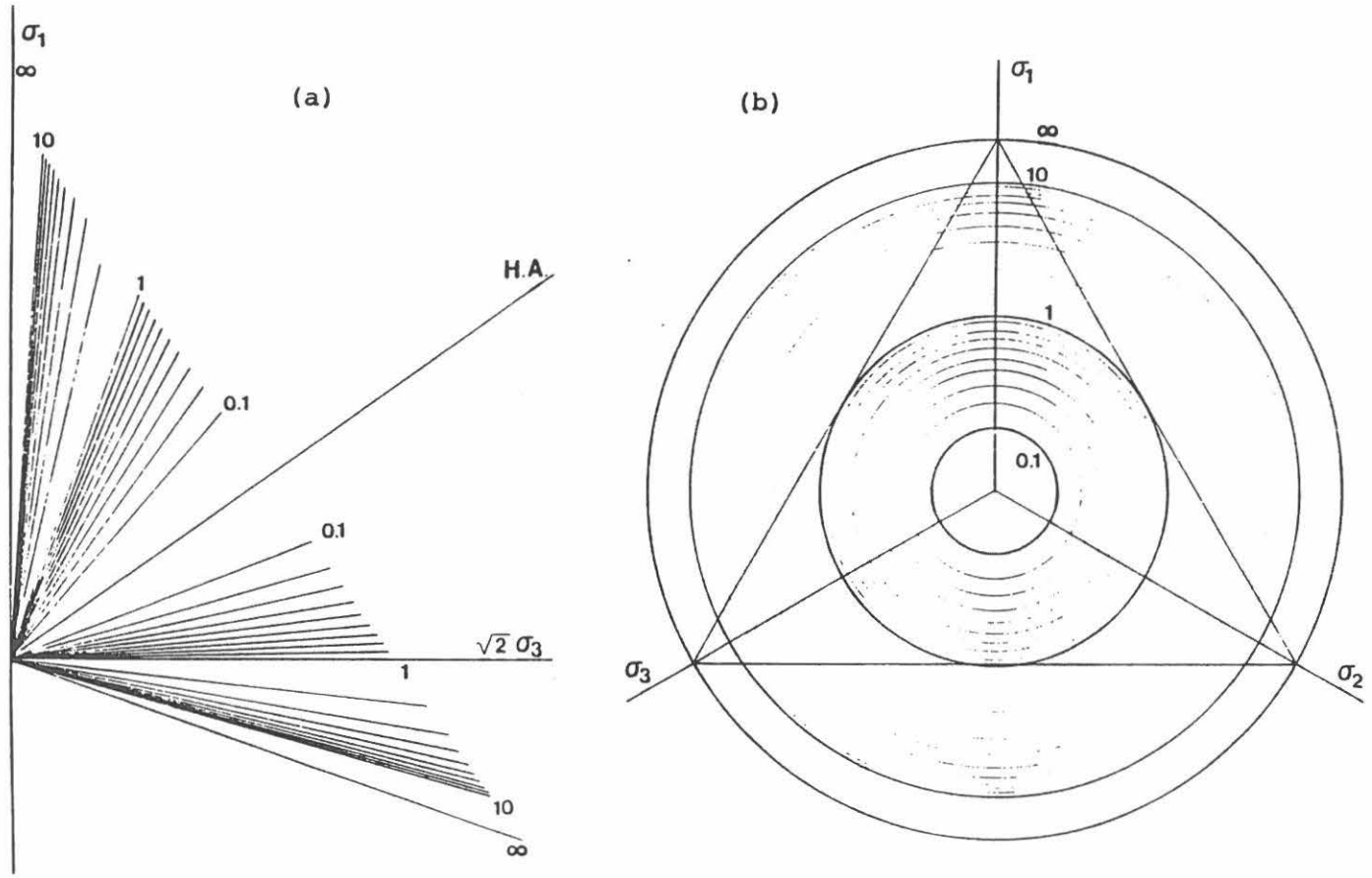

Fig. A.4 Shape of non-dimensional stress invariant R_2: (a) on triaxial plane, and (b) on octahedral plane.

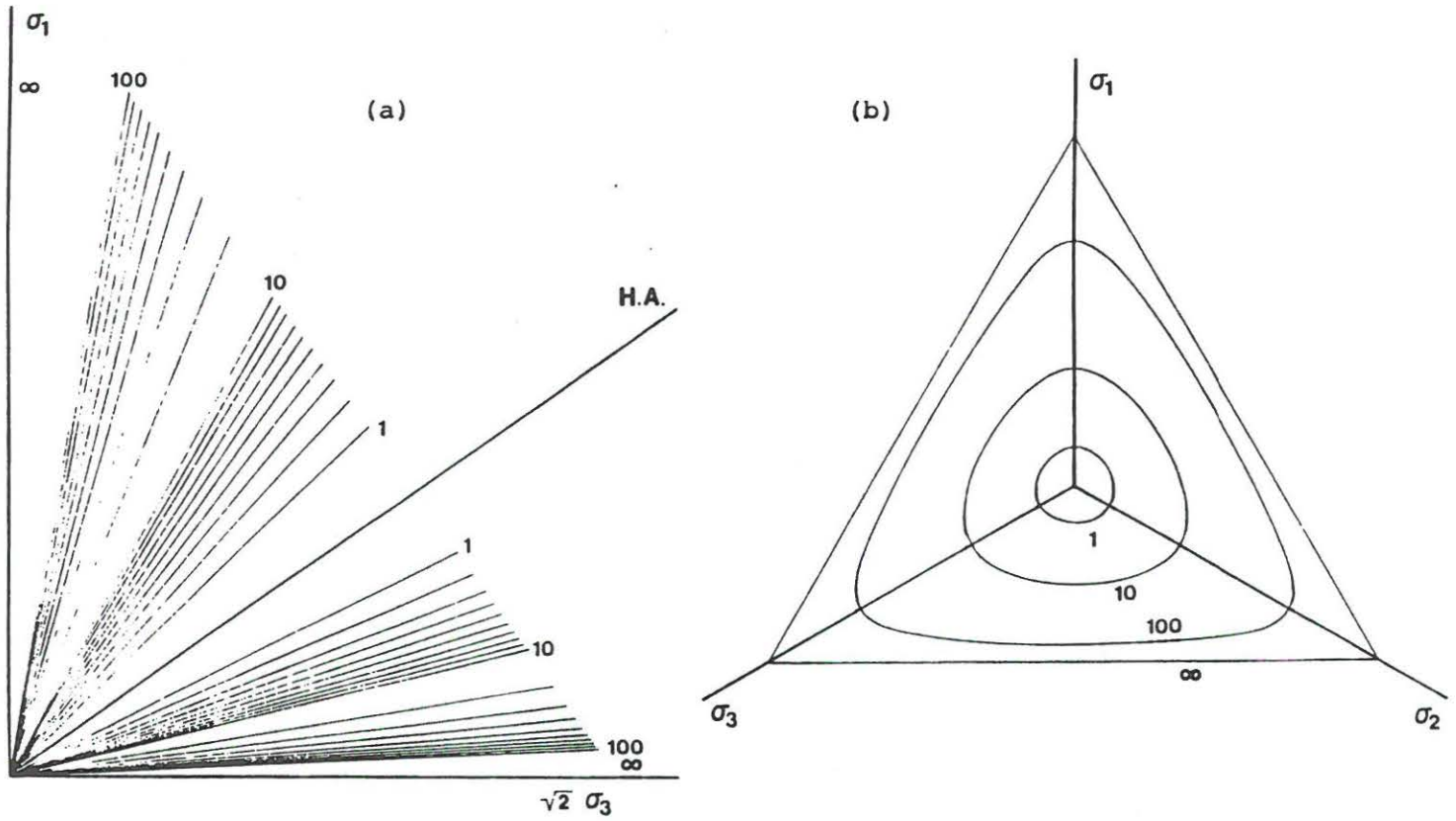

Fig. A.5 Shape of non-dimensional stress invariant R_3: (a) on triaxial plane, and (b) on octahedral plane.

3-D Soil Behavior Measured in Laboratory Experiments

10057 OCTOBER 1973 SM10

JOURNAL OF THE SOIL MECHANICS AND FOUNDATIONS DIVISION

CUBICAL TRIAXIAL TESTS ON COHESIONLESS SOIL

By Poul V. Lade,[1] A.M. ASCE and James M. Duncan,[2] M. ASCE

INTRODUCTION

Conventional triaxial compression tests only provide information regarding the soil behavior under stress conditions for which $\sigma_1 > \sigma_2 = \sigma_3$. A new type of triaxial apparatus in which three different principal stresses can be applied to a cubical soil specimen is described. This apparatus has some definite advantages over those used previously. The features of the new apparatus are described, and the results of a series of tests performed on a uniform sand at two different void ratios are examined.

The influence of the intermediate principal stress on the stress-strain and strength characteristics of cohesionless soils may be investigated to a limited extent by means of ordinary triaxial tests in which two of the principal stresses have the same value. Several investigators have carried out triaxial compression and triaxial extension tests in order to compare the behavior of soils in the two types of tests (7,8,15,28,30). Tests with three unequal principal stresses have been employed in addition to the triaxial tests. Studies incorporating results from plane strain tests, torsion tests, and thick cylinder tests have shed additional light on the behavior of cohesionless soils (4,5,10,14,17,22). An excellent review of the stress-deformation and strength characteristics of soils was presented by Scott and Ko (31).

Note.—Discussion open until March 1, 1974. To extend the closing date one month, a written request must be filed with the Editor of Technical Publications, ASCE. This paper is part of the copyrighted Journal of the Technical Publications, ASCE. This paper is part of the copyrighted Journal of the Soil Mechanics and Foundations Division, Proceedings of the American Society of Civil Engineers, Vol. 99, No. SM10, October, 1973. Manuscript was submitted for review for possible publication on March 6, 1973.

[1]Asst. Prof., Mech. and Structures Dept., School of Engrg. and Applied Sci., Univ. of California, Los Angeles, Calif.

[2]Prof. of Civ. Engrg., Univ. of California, Berkeley, Calif.

Techniques for Applying Three Different Principal Stresses

Previous studies performed to investigate the effects of σ_2 have also involved equipment in which three different principal stresses could be applied independently to a cubical specimen. The fundamental design and working principles of some of these apparatuses and the main results obtained for cohesionless soils are described in the following.

Ko and Scott (18) designed a soil test box in which a cubical specimen was contained between six membranes. Each pair of opposite membranes was interconnected and could be pressurized individually, thus providing for three different principal stresses. In order to avoid a tendency of the membranes to interfere with each other at the edges, a rigid frame separated the membranes. Tests performed on Ottawa Sand showed (20) that the friction angle increased with increasing intermediate principal stress from the condition of triaxial compression (in which $\sigma_2 = \sigma_3$) to a maximum before a slight decrease at the condition of triaxial extension (in which $\sigma_2 = \sigma_1$). This apparatus offers the advantage of easy application of normal stresses and ensures that no shear stresses are induced on the faces of the specimen. However, as the magnitudes of the strains increase, they can become nonuniform. Green (11), Arthur and Menzies (1), and Bell (3) pointed out that the rigid frame separating the membranes may cause edge restraints which result in too steep stress-strain curves and too high strengths.

An apparatus described by Bishop (6) and Green (12) employs a rectangular prismatic specimen. One horizontal stress is applied by the chamber pressure and an additional stress supplied by two vertical, stiff plates provided with a horizontal loading ram. The two vertical plates cover most of two opposite vertical faces, but are shorter than the height of the specimen, leaving space for compression of the specimen in the vertical direction, and thus avoiding interference between the vertical, stiff plates and the cap and base. Green and Bishop (13) and Green (12) performed tests on Ham River sand with σ_2 values very closely spaced in the range from σ_1 to σ_3. The friction angle was reported to increase from triaxial compression to plane strain and to remain constant from plane strain to triaxial extension. It appears from the design of this apparatus that part of the specimen can be squeezed out above and below the vertical plates, thus filling the spaces between the vertical plates and the cap and base. This may result in nonuniform straining of the specimen and may, in part, prevent the compression of the specimen, thereby resulting in too steep stress-strain curves and too high strengths. This discrepancy would be expected to be most pronounced at high values of the intermediate principal stress.

Sutherland and Mesdary (32) designed a piece of equipment similar to the apparatus described by Bishop (6). One of the horizontal stresses is applied by the chamber pressure, and the other is applied by two rubber bags filled with water. Tests performed on Lock Aline sand showed that the friction angle increased from triaxial compression to a maximum in the region of the plane strain condition and then decreased at triaxial extension to a value approximately equal to that obtained in triaxial compression. The principal disadvantages are the difficulties in evaluating the intermediate stress precisely, and the possibility of interference between the rubber bags and the cap and base.

Another cubical triaxial machine was designed by Roscoe and his co-workers

and was described by Pearce (26,27). The specimen is enclosed in a membrane and surrounded by six interconnected rigid plates, one on each face. The six rigid plates are arranged around the specimen so that they can slide over each other to produce strains along all three perpendicular axes. The apparatus can apply strains of ± 30% along any or all of the three perpendicular axes. Load cells are incorporated in some of the plates in order to measure stresses on the specimen. A large loading frame with three mutually perpendicular pairs of rams provides the compressive forces. Whereas the working principle is simple and attractive, the actual design and construction of this piece of equipment is very complicated and the expense and time for construction are considerable. Pearce noted that this true triaxial apparatus may not be useful for testing cohesionless soils due to development of excessive shear stresses along the faces of the specimen.

The four apparatuses described in the preceding represent the design principles that have been used in recent years for equipment with independent control of the three principal stresses. In addition to these, several other investigations of the behavior of cohesionless soil have been performed using equipment incorporating designs similar to those just presented (2,23,24,29,32).

Each of the apparatuses has its own advantages, but no single piece of equipment appears to incorporate accurate control of stresses and uniform strains of large magnitude with simple design features. Therefore a new cubical triaxial apparatus employing new design principles was developed for the present investigation.

Cubical Triaxial Apparatus

Stress Application.—The new cubical triaxial apparatus is shown in Fig. 1. The specimen, which is contained between a cap and base and surrounded by a membrane, has dimensions 7.6 cm × 7.6 cm × 7.6 cm. The apparatus is contained in a pressure chamber.

The three principal stresses are applied to the specimen in the following way: The minor principal stress, σ_3, which acts in one horizontal direction, is provided by the chamber pressure. A vertical load is transmitted by a rod through the top of the chamber and applied to the specimen through the cap and base. The resulting deviator stress, together with the chamber pressure, provides for a vertical principal stress different from σ_3. The second horizontal deviator stress is applied by a specially designed loading system.

Horizontal Loading System.—Fig. 2 shows this loading system, which consists of two interconnected vertical plates which sit on opposite sides of the cubical specimen. One of the plates is provided with a pressure cylinder, which supplies the horizontal load. This loading system rolls freely on two rails alongside the base, as seen in Fig. 2.

The two horizontal loading plates, which are compressible in the vertical direction, consist of horizontal laminae of alternate layers of stainless steel and balsa wood. The balsa wood has a fairly low modulus and strength in the directions perpendicular to the fibers, whereas the modulus and strength parallel to the fiber direction are relatively high. Poisson's ratio in all three directions is essentially zero. The strength in the directions perpendicular to the fibers can be further decreased by compressing the wood and allowing it to soak water, whereupon it will rebound to its original dimensions. The

balsa wood laminae were cut so that the fiber direction faces the specimen. The steel laminae are provided with rims which prevent the balsa wood laminae from being pushed back by the specimen. The thickness of the steel and balsa

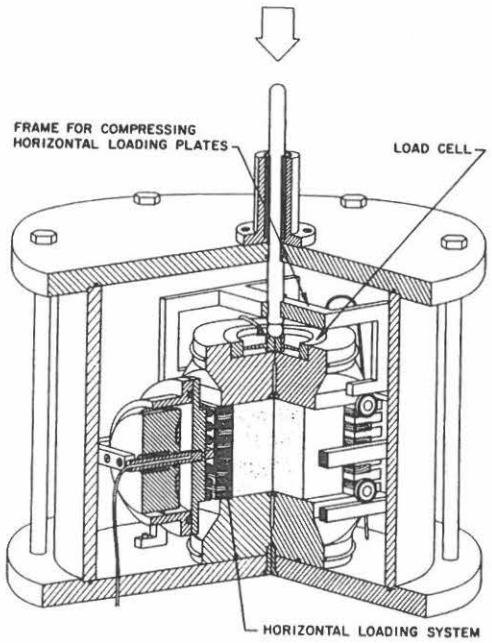

FIG. 1.—Cubical Triaxial Apparatus

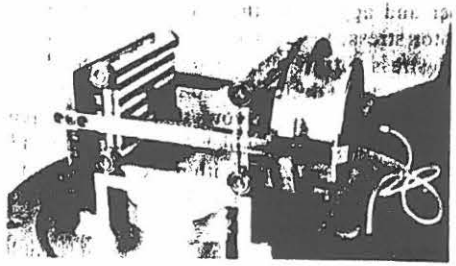

FIG. 2.—Horizontal Loading System

wood laminae are proportioned so that the plates can be compressed about 20% in the vertical direction without excessive force.

The back sides of the steel laminae are provided with rollers that can roll on a solid steel plate as seen in Fig. 2. The upper and lower steel laminae

are constructed with tongues which slip into the slots between the other steel laminae and their rollers. The tongues keep the laminae in line and prevent the plates from buckling.

The force required to compress the plates in the vertical direction is supplied from the rod which also provides the vertical load for the specimen. A frame with four legs is fastened to the rod, as seen in Fig. 1. The four legs extend around the cap and rest on the four ball bearings fastened to the upper steel laminae. The two horizontal loading plates are positioned so that there is a gap of about 1 mm between the plates and the cap and base. As the specimen is loaded vertically, the horizontal loading plates are compressed at the same rate as the specimen by the frame attached to the axial force rod, thereby avoiding any contact between the plates and the cap and base.

The vertical load applied to the specimen is measured by a load cell embedded in the cap (see Fig. 1). The force required for vertical compression of the horizontal loading plates is therefore not a part of the measured vertical load applied to the specimen.

Both the horizontal loading plates and the cap and base were provided with lubricated surfaces in order to avoid development of significant shear stresses between the loading plates and the specimen.

Specimen Saturation.—After a specimen had been built of air-dry sand and subjected to a confining pressure in the pressure chamber, it was saturated using the following procedure: Gaseous carbon dioxide (CO_2) was introduced through the bottom drainage line, thereby pushing the lighter air within the specimen up through the top drainage line. De-aired water was then introduced through the bottom drainage line and also allowed to seep slowly up through the specimen, thereby pushing most of the carbon dioxide out through the top drainage line. Since a volume of gaseous carbon dioxide can be dissolved in approximately an equal volume of de-aired water, any carbon dioxide left in the specimen below the cap would dissolve in the intruding water, which in turn would fill the voids in the specimen.

The degree of saturation was checked by measuring the pore pressure parameter, B, at the start of each test. The value of B was found to be from 0.97 to 1.00 in most cases, indicating that the specimens were practically completely saturated with water.

Measurements.—The oil pressure in the horizontal pressure cylinder was controlled and could be measured by a pressure transducer outside the triaxial cell and related to the horizontal deviator stress. The chamber pressure was also measured by a pressure transducer and the vertical load by the load cell embedded in the cap.

The linear deformations of the specimen were all measured with clip gages. These consisted of thin bands of beryllium copper on which strain gages were glued. The bands were shaped to fit around the specimen, between the horizontal loading plates, and between the cap and base. All strain gages and wires were waterproofed. In addition to the linear deformations, the volume change of the saturated specimen was measured.

The measurements of the electrical signals from the clip gages, the load cell, and the pressure transducers were recorded in digital form by a 10-channel Vidar Digital Data Acquisition System. A maximum of seven channels was used for the testing in the cubical triaxial apparatus. The response from the

seven electrical devices was measured and printed in about 10 sec.

Corrections to the measured loads and pressures were found to be negligible, but the linear and the volumetric deformations were corrected for effects of membrane penetration.

A detailed description of the design and performance of the cubical triaxial apparatus can be found elsewhere (21).

Sand Tested

All tests were performed on Monterey No. 0 Sand, which is composed of subangular to subrounded grains consisting mainly of quartz and feldspar. The characteristics of this sand are summarized as follows: Mean diameter, 0.43 mm; coefficient of uniformity, 1.53; specific gravity of grains, 2.645; maximum void ratio, 0.860; and minimum void ratio, 0.565.

Tests were performed on dense and loose specimens. The loosest deposits that could be conveniently prepared on a routine basis had a void ratio of

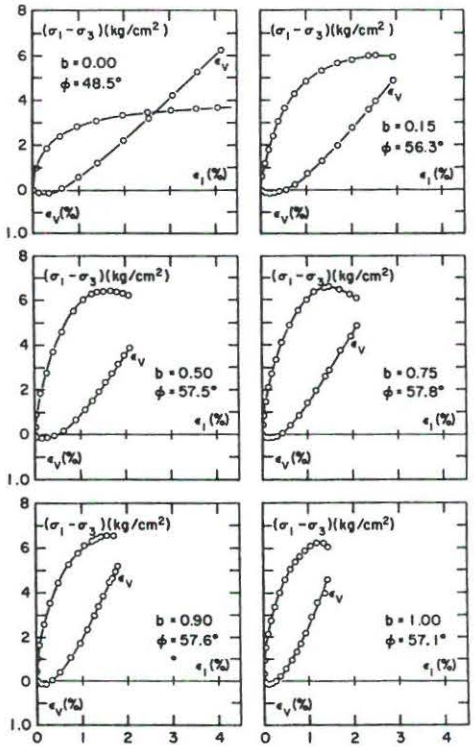

FIG. 3.—Stress-Strain and Volume Change Characteristics Obtained in Cubical Triaxial Tests on Dense Monterey No. 0 Sand (e = 0.57)—All Tests Performed with σ_3 = 58.8 kN/m²

0.78 and a corresponding relative density of D_r = 27%. The dense specimens were prepared with a void ratio of 0.57 and a relative density of D_r = 98%.

Testing Program

Drained tests were performed in the cubical triaxial apparatus at constant chamber pressures of 0.60 kg/cm² (58.8 kN/m²). A series of tests was conducted in which the horizontal and the vertical deviator stresses were increased proportionally until the specimen failed. The ratio between the deviator stresses may be denoted by the parameter, b, introduced by Habib (14) and later used by Broms and Casbarian (9) and by Bishop (5):

$$b = \frac{\sigma_2 - \sigma_3}{\sigma_1 - \sigma_3} \quad \ldots\ldots\ldots\

stress: b is zero for triaxial compression in which $\sigma_2 = \sigma_3$, and it is unity for triaxial extension in which $\sigma_2 = \sigma_1$; for intermediate values of σ_2 the value of b is between zero and unity. Each test was conducted with constant value of b throughout. The values of b used in the tests were chosen so that the failure surfaces and the stress-strain relations for both the dense and the loose sand could be determined over the full range of the intermediate principal stress. Two plane strain tests were also performed in the cubical triaxial apparatus, one on dense and one on loose sand.

Test Results

Stress-Strain Characteristics.—The stress-strain curves obtained from the cubical triaxial tests on dense and loose sand are shown in Figs. 3 and 4. It may be seen that the strength increases with increasing value of the intermediate principal stress, until the value of b reaches 0.75 to 0.90, and then decreases slightly at $b = 1.00$. The data in Figs. 3 and 4 show that for a constant value of σ_3 the initial slope of the stress-strain curve increases continually with increasing value of the intermediate principal stress for both dense and loose sand. This behavior indicates that for small stress levels the influence of σ_2 on the stress-strain curves may be accounted for, at least qualitatively, by Hooke's Law. The strain-to-failure is greatest and the strength is lowest for triaxial compression ($b = 0.00$). For loose sand the strain-to-failure decreases initially with increasing value of b and remains approximately constant for b values greater than 0.6. It may also be seen from Figs. 3 and 4 that the major deviator stress ($\sigma_1 - \sigma_3$) drops off more rapidly after the peak when the value of b is large.

Influence of Lubrication.—The lubricated surfaces on the cap and base and the horizontal loading plates consisted of rubber sheets coated with silicone grease. These lubricating sheets were in addition to the membrane which confined the specimen along its vertical faces. Whereas most tests were performed with just one lubricating sheet on each of the four loading plates, some were performed on loose sand with one sheet on the base and two on each of the three other interfaces. The stress-strain curves for these latter tests are shown with the other curves in Fig. 4 for comparison. The expected effects of added lubrication were reduction in end restraint and more uniform deformation of the specimen. Because the specimens deformed quite uniformly both with and without the added lubrication, the main effect was a reduction in end restraint, and a consequent reduction in the strengths of the specimens. However, the reduction was small, and it seems logical that further lubrication would have only a minor effect. Similarly, the results of triaxial compression tests on dense sand were affected very little by additional lubrication.

Volume Change Characteristics.—The volumetric strains measured in the cubical triaxial tests are also shown in Figs. 3 and 4. The initial rate of compression increased with increasing b value for both dense and loose sand. This characteristic is indicative of elastic behavior at low stress levels. As the stress level increased, plastic dilation began to dominate. The rate of dilation (expressed as $-\Delta\epsilon_v/\Delta\epsilon_1$) increased with increasing stress level from a negligible value at small stress levels, to such a magnitude at high stress levels as to completely dominate the elastic compression. Whereas this behavior was observed for both the dense and the loose sand, the rate of dilation at failure was much higher for the

dense than for the loose sand. The rate of dilation may be seen to increase with increasing value of b.

Relation Between Principal Strains.—The intermediate and minor principal strains, ϵ_2 and ϵ_3, are plotted versus ϵ_1 in Fig. 5 for both dense and loose sand. The upper diagrams of this figure show that the intermediate principal strains, ϵ_2, are expansive for b values smaller than those corresponding to the plane strain condition and compressive for higher b values. The minor principal strains, ϵ_3, are expansive in all cases and decrease with increasing b values as shown in the lower diagrams of Fig. 5. A given increment in b has a greater effect on the relation between the principal strains at small b values than at high b values.

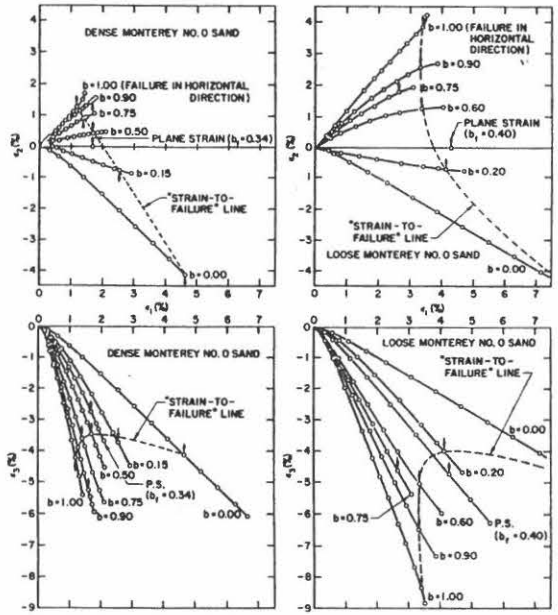

FIG. 5.—Relations Between Principal Strains Obtained in Cubical Triaxial Tests on Dense and Loose Monterey No. 0 Sand

Lines are drawn through the points corresponding to failure. The major principal strain-to-failure decreases with increasing b value for dense sand. For loose sand the major principal strain-to-failure first decreases with increasing value of b, and then remains approximately constant for b values greater than about 0.60.

Isotropy of Specimens.—For isotropic materials in triaxial compression ($\sigma_2 = \sigma_3$) the intermediate and the minor principal strains are equal ($\epsilon_2 = \epsilon_3$). Sand specimens deposited in the vertical direction deform axisymmetrically in triaxial compression and show no preference for expansion in any particular horizontal direction, because the specimens are loaded along an axis of symmetry.

In the extension tests performed in the cubical triaxial apparatus, the major principal stress, $\sigma_1 (= \sigma_2)$, was applied in the vertical direction and the intermediate principal stress, σ_2 $(= \sigma_1)$, was applied in one of the horizontal directions. The specimen was consequently loaded symmetrically around a horizontal axis, but since the specimen was deposited in the vertical direction, the principal strains, ϵ_1 and ϵ_2, would not be expected to be equal unless the sand was isotropic.

The upper diagrams of Fig. 5 show that the values of ϵ_1 for practical purposes are equal to the values of ϵ_2 for extension tests on both dense and loose sand. It was also observed that in some of the triaxial extension tests failure occurred in the horizontal direction, in others failure occurred in the vertical direction, and in others failure occurred in both directions simultaneously. The strengths measured in these tests were approximately the same. Both of these observations indicate that the sand specimens were essentially isotropic.

Strength Characteristics.—The variation of the measured friction angles with b are shown in Fig. 6 for dense and loose sand. The friction angles were calculated from

$$\sin \phi = \frac{\sigma_1 - \sigma_3}{\sigma_1 + \sigma_3} \quad \ldots \ldots \ldots

whether they failed horizontally or vertically. Interchanging the principal stress directions will therefore not have any effect on the strength of the sand. The traces of the failure surfaces in the octahedral plane are consequently symmetric around the projections of the three principal axes and intersect these at right angles.

Directions of Strain Increment Vectors

It is of interest to investigate whether the normality condition of classical plasticity theory is satisfied by these test results. According to the normality condition the plastic strain increment vector for a perfectly plastic material should be normal to the yield surface when the principal strain increments are plotted in the same space as the principal stresses [see, e.g., Hill (16) or Mendelson (25)]. If the normality condition is fulfilled, the pertinent strain

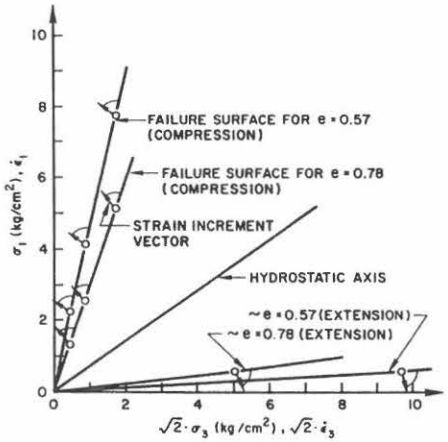

FIG. 8.—Directions of Strain Increment Vectors in Triaxial Plane for Dense and Loose Monterey No. 0 Sand (1 kg/cm² = 98.1 kN/m²)

increment vectors are perpendicular to the trace of the failure surface in a triaxial plane, and the projections of the strain increment vectors on an octahedral plane are perpendicular to the trace of the failure surface in the octahedral plane.

The magnitudes of the strain increment vectors are immaterial to the question of normality. The relative magnitudes of the principal strain increments can be obtained from the slopes of the $\epsilon_2 - \epsilon_1$ and $\epsilon_3 - \epsilon_1$ diagrams in Fig. 5, and the directions of the strain increment vectors can be plotted using these values. Only the directions of the strain increments at failure will be considered, because normality concerns only plastic strains, and by definition all strains are plastic at failure.

The triaxial plane containing the σ_1-axis is shown in Fig. 8. The traces of the experimental failure surfaces in this plane are shown for dense and loose sand, together with the directions of the strain increment vectors. Since ϵ_2

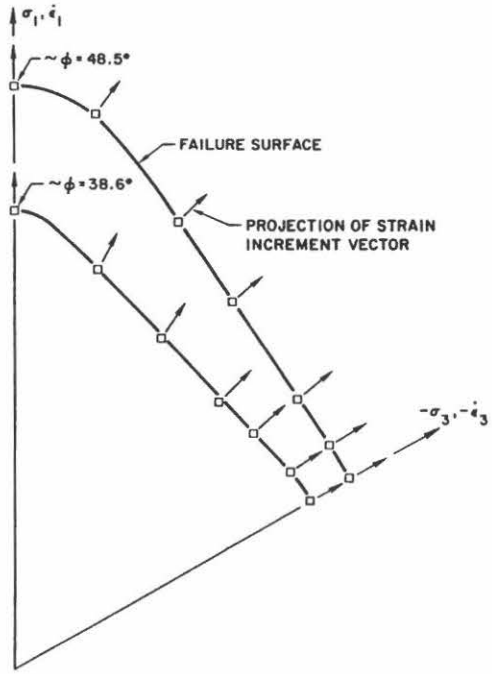

FIG. 9.—Directions of Projections of Strain Increment Vectors on Octahedral Plane for Dense and Loose Monterey No. 0 Sand

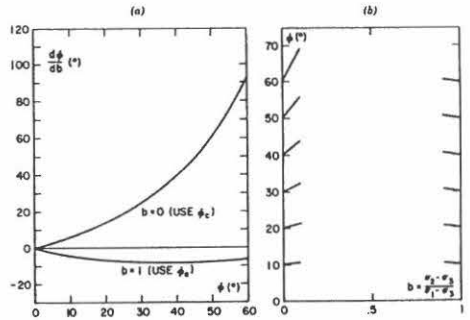

FIG. 10.—Variation of Initial (b = 0) and Final (b = 1) Slopes of Failure Surfaces in $\phi - b$ Diagram: (*a*) Variation of Numerical Values of Slopes, (*b*) $\phi - b$ Diagram Showing Initial and Final Slopes of Failure Surfaces

$= \epsilon_3$ in compression and $\epsilon_2 = \epsilon_1$ in extension, the corresponding strain increment vectors are contained in the triaxial plane. Fig. 8 shows that the directions of the strain increments form acute angles with the failure surface for sense and loose sand in both compression and extension. The normality condition is therefore not satisfied for these test results. Ko and Scott (19) also found that the normality condition was not fulfilled for their tests on Ottawa Sand, and it would appear that cohesionless soils in general do not satisfy the normality condition.

The projections of the strain increment vectors on the octahedral plane are shown in Fig. 9. Because of the symmetry about the principal stress axes, only one sixth of the plane is shown. The projections of the strain increments are very nearly perpendicular to the failure surfaces in the octahedral plane for both dense and loose sand. Only a few of the vectors at intermediate values of σ_2 deviate slightly from perpendicularity. The magnitudes of these deviations are so small that they could even be due to experimental inaccuracies.

It is clear from these results that the condition of normality is satisfied or very nearly satisfied in the octahedral plane, but not in the triaxial plane, and it is therefore not fulfilled in general for sand. The general pattern of the directions of the strain increment vectors relative to the failure surfaces is of importance in considerations regarding the applicability of plasticity theory to cohesionless soils.

Boundary Conditions for Curve Showing Variation of ϕ With b

The friction angles obtained from the cubical triaxial tests were previously shown to increase with b at $b = 0$ and to decrease slightly at $b = 1$. Using plasticity theory it is possible to prove that for isotropic cohesionless soils the end slopes of the curve showing the variation of σ with b should be as they are shown in Fig. 6. These slopes can be expressed in terms of the friction angles from triaxial compression (ϕ_c) and extension (ϕ_e) tests, respectively.

According to plasticity theory the normal strains can be expressed by equations of the following form:

$$\Delta\epsilon_{ij} = \Delta\lambda \frac{df}{d\sigma_{ij}}; \quad (i = j) \quad \ldots\ldots\ldots\ldots\ldots\ldots\ldots\ldots\ldots\ldots (3)$$

in which $\Delta\lambda$ is a proportionality factor and f represents an expression for the failure surface. Using Eq. 3 it can be shown that for isotropic materials the initial and final slopes of the failure surface in a $\phi - b$ diagram can be expressed by the following equations

$$\left(\frac{d\phi}{db}\right)_{b=0} = \frac{1}{2}(1 + \sin\phi_c)\tan\phi_c \frac{180}{\pi}; \quad \text{(in degrees)} \quad \ldots\ldots\ldots\ldots (4)$$

$$\left(\frac{d\phi}{db}\right)_{b=1} = -\frac{1}{2}(1 - \sin\phi_e)\tan\phi_e \frac{180}{\pi}; \quad \text{(in degrees)} \quad \ldots\ldots\ldots\ldots (5)$$

The derivations of Eqs. 4 and 5, which are shown in Appendix I, are based on the condition that the failure surface is smooth, as are the failure surfaces shown in Fig. 7. No specific mathematical formulation of the failure surface

was chosen for the derivations, and the expressions in Eqs. 4 and 5 are therefore generally applicable for cohesionless soils. Eqs. 4 and 5 simply express geometrical conditions, which have been observed in the principal stress space and transferred to the $\phi - b$ diagram. Note that the derivations of Eqs. 4 and 5 have not involved assumptions of normality of the strain increment vector to the failure surface in the principal stress space. It has only been assumed that the projection of the strain increment vector on an octahedral plane is perpendicular to the trace of the failure surface in the octahedral plane for the conditions of triaxial compression and triaxial extension, which is true for all isotropic materials.

The calculated variations of the slopes with ϕ are shown in Fig. 10. The left part of this figure shows the variation of the numerical values of $d\phi/db$ for $b = 0$ and $b = 1$ with the friction angles from compression and extension tests. The initial and final slopes are shown in a $\phi - b$ diagram in the right part of Fig. 10 for friction angles up to 60°. While the initial slope increases with increasing value of the friction angle in compression, the final slope is small and varies only slightly within the range of friction angles measured in extension.

The pertinent initial and final slopes are shown in Fig. 6 for comparison with the experimental failure surfaces for dense and loose sand. It appears that the boundary conditions derived from the observations in the principal stress space fit the experimental results very well. The small reductions in the friction angles close to $b = 1$, which were observed for both dense and loose sand, are supported by the boundary condition expressed in Eq. 5. The magnitudes of the increases in friction angles with increasing b value at $b = 0$ are also correctly accounted for by Eq. 4.

Conclusions

A new type of cubical triaxial apparatus was designed and constructed and a series of tests was performed to investigate the influence of the intermediate principal stress on the stress-strain and strength characteristics of Monterey No. 0 Sand. The testing program included both plane strain tests and tests conducted with constant values of $b = (\sigma_2 - \sigma_3)/(\sigma_1 - \sigma_3)$.

It was found for both dense and loose specimens that the slope of the stress-strain curve increased, the strain-to-failure decreased, and the rate of dilation increased with increasing b value. The strength of the soil as represented by the friction angle increased from triaxial compression (for which b is equal to zero) to a maximum at values of b slightly smaller than unity, and decreased slightly to triaxial extension (for which b is equal to unity). It was observed that a given increment in b had a greater effect on both the stress-strain and the strength characteristics at small b values than at high b values.

The test results showed that the directions of the strain increments at failure form acute angles with the failure surfaces for both the dense and loose sand. The results are thus not in agreement with the normality criterion from classic plasticity theory. However, it was found that the projections of the plastic strain increment vectors on the octahedral plane are perpendicular to the trace of the failure surface in that plane. Expressions were derived for the initial and final slopes of the failure surfaces in a diagram showing the variation of

ϕ with b, and the test results were shown to fit these boundary conditions well.

Appendix I.—Boundary Conditions for Failure Surface in $\phi - b$ Diagram

From the conditions, $\epsilon_2 = \epsilon_3$, in triaxial compression ($\sigma_2 = \sigma_3$) and $\epsilon_1 = \epsilon_2$ in triaxial extension ($\sigma_1 = \sigma_2$) for isotropic materials, it can be shown for cohesionless soils that the initial and the final slopes of the failure surface in a diagram showing the variation of ϕ with b can be expressed in terms of the friction angles from compression and extension tests, ϕ_c and ϕ_e.

Expressing the strains by Eq. 3 and equalizing according to the foregoing conditions results in

$$\frac{df}{d\sigma_2} = \frac{df}{d\sigma_3}; \quad \text{for} \quad b = 0 \qquad (6)$$

$$\text{and} \quad \frac{df}{d\sigma_1} = \frac{df}{d\sigma_2}; \quad \text{for} \quad b = 1 \qquad (7)$$

The strength of the cohesionless soil can for any value of $b = (\sigma_2 - \sigma_3)/(\sigma_1 - \sigma_3)$ be expressed as

$$f_1 = \sin\phi = \frac{\sigma_1 - \sigma_3}{\sigma_1 + \sigma_3} = a_0 + a_1 b + a_2 b^2 + \ldots + a_n b^n \qquad (8)$$

in which the right-hand expression represents the Taylor's series expansion of a mathematical formulation of the failure surface in a $\sin\phi - b$ diagram. Eq. 8 can be written as a failure criterion as follows

$$f = \frac{\sigma_1 - \sigma_3}{\sigma_1 + \sigma_3} - a_0 - a_1 b - a_2 b^2 - \ldots - a_n b^n = 0 \qquad (9)$$

The slope of the failure surface in a $\sin\phi - b$ diagram for any value of b is

$$\frac{df_1}{db} = a_1 + 2 a_2 b + \ldots + n a_n b^{n-1} \qquad (10)$$

The derivatives of f appearing in Eqs. 6 and 7 can be derived from Eq. 9 and reduced by Eq. 10 as follows

$$\left.\begin{aligned} \frac{df}{d\sigma_1} &= \frac{(\sigma_1 + \sigma_3)\,1 - (\sigma_1 - \sigma_3)\,1}{(\sigma_1 + \sigma_3)^2} - (a_1 + 2a_2 b + \ldots + n a_n b^{n-1})\frac{db}{d\sigma_1} \\ \frac{df}{d\sigma_1} &= \frac{2\sigma_3}{(\sigma_1 + \sigma_3)^2} + \frac{df_1}{db}\frac{(\sigma_2 - \sigma_3)}{(\sigma_1 - \sigma_3)^2} \end{aligned}\right\} \qquad (11)$$

$$\left.\begin{aligned} \frac{df}{d\sigma_2} &= -(a_1 + 2 a_2 b + \ldots + n a_n b^{n-1})\frac{db}{d\sigma_2} \\ \frac{df}{d\sigma_2} &= -\frac{df_1}{db}\frac{1}{(\sigma_2 - \sigma_3)} \end{aligned}\right\} \qquad (12)$$

$$\left.\begin{aligned} \frac{df}{d\sigma_3} &= \frac{(\sigma_1 + \sigma_3)(-1) - (\sigma_1 - \sigma_3)\,1}{(\sigma_1 + \sigma_3)^2} \\ &- (a_1 + 2 a_2 b + \ldots + n a_n b^{n-1})\frac{db}{d\sigma_3} \\ \frac{df}{d\sigma_3} &= \frac{-2\sigma_1}{(\sigma_1 + \sigma_3)^2} + \frac{df_1}{db}\frac{(\sigma_1 - \sigma_2)}{(\sigma_1 - \sigma_3)^2} \end{aligned}\right\} \qquad (13)$$

Triaxial Compression.—Substituting Eqs. 12 and 13 into Eq. 6 and reducing gives

$$\frac{df_1}{db} = \frac{\sigma_1(\sigma_1 - \sigma_3)}{(\sigma_1 + \sigma_3)^2} = \frac{\sigma_1 - \sigma_3}{\sigma_1 + \sigma_3}\frac{\sigma_1}{\sigma_1 + \sigma_3} = \sin\phi_c \frac{\sigma_1}{\sigma_1 + \sigma_3} \qquad (14)$$

The σ_1 term can be expressed as

$$\sigma_1 = \frac{1 + \sin\phi_c}{1 - \sin\phi_c}\sigma_3 \qquad (15)$$

Substituting Eq. 15 into Eq. 14 and reducing gives

$$\frac{df_1}{db} = \frac{1}{2}(1 + \sin\phi_c)\sin\phi_c \qquad (16)$$

Eq. 16 expresses the initial slope of the failure surface in a $\sin\phi - b$ diagram. In a $\phi - b$ diagram the slope can be found by expressing

$$\frac{df_1}{db} = \frac{d\sin\phi}{db} = \cos\phi\frac{d\phi}{db} \qquad (17)$$

which in connection with Eq. 16 gives

$$\left(\frac{d\phi}{db}\right)_{b=0} = \frac{1}{2}(1 + \sin\phi_c)\tan\phi_c \frac{180}{\pi}; \quad \text{(in degrees)} \qquad (18)$$

Eq. 18 expresses the initial slope, in degrees, of the failure surface in a $\phi - b$ diagram. It can be seen that it is only dependent on the friction angle obtained in triaxial compression (ϕ_c).

Triaxial Extension.—Substituting Eqs. 11 and 12 into Eq. 7 and reducing gives

$$\frac{df_1}{db} = \frac{-\sigma_3(\sigma_1 - \sigma_3)}{(\sigma_1 + \sigma_3)^2} = \frac{-\sigma_3}{(\sigma_1 + \sigma_3)}\frac{(\sigma_1 - \sigma_3)}{(\sigma_1 + \sigma_3)} = \frac{-\sigma_3}{(\sigma_1 + \sigma_3)}\sin\phi_e \qquad (19)$$

The σ_1 term can be expressed as

$$\sigma_1 = \frac{1 + \sin\phi_e}{1 - \sin\phi_e}\sigma_3 \qquad (20)$$

Substituting Eq. 20 into Eq. 19 and reducing gives

$$\frac{df_1}{db} = -\frac{1}{2}(1 - \sin\phi_e)\sin\phi_e \qquad (21)$$

Eq. 21 expresses the final slope of the failure surface in a $\sin\phi - b$ diagram. In a $\phi - b$ diagram the slope can be found from Eqs. 17 and 21:

$$\left(\frac{d\phi}{db}\right)_{b=1} = -\frac{1}{2}(1 - \sin\phi_e)\tan\phi_e \frac{180}{\pi}; \quad \text{(in degrees)} \quad \ldots\ldots\ldots\ldots \quad (22)$$

Eq. 22 expresses the final slope, in degrees, of the failure surface in a $\phi - b$ diagram. It can be seen that it is only dependent on the friction angle obtained in triaxial extension (ϕ_e).

Appendix II.—References

1. Arthur, J. R. F., and Menzies, B. K., discussion of "A New Soil Testing Apparatus" by H. -Y. Ko and R. F. Scott, *Geotechnique*, London, England, Vol. 18, No. 2, 1968, pp. 271-272.
2. Arthur, J. R. F., and Menzies, B. K., "Inherent Anisotropy in a Sand," *Geotechnique*, London, England, Vol. 22, No. 1, 1972, pp. 115-128.
3. Bell, J. M., discussion of "A New Soil Testing Apparatus" by H. -Y. Ko and R. F. Scott, *Geotechnique*, London, England, Vol. 18, No. 2, 1968, pp. 267-271.
4. Bishop, A. W., discussion of "Soil Properties and Their Measurement," *Proceedings of the 5th International Conference on Soil Mechanics and Foundation Engineering*, Paris, France, Vol. III, 1961, pp. 97-100.
5. Bishop, A. W., "The Strength of Soils as Engineering Material," 6th Rankine Lecture, *Geotechnique*, London, England, Vol. 16, No. 2, 1966, pp. 89-130.
6. Bishop, A. W., discussion of "Shear Strength of Soil Other Than Clay," *Proceedings of the Geotechnical Conference*, Oslo, Norway, Vol. II, 1967, pp. 201-204.
7. Bishop, A. W., and Eldin, A. K. G., "The Effect of Stress History on the Relation between ϕ and the Porosity of Sand," *Proceedings of the 3rd International Conference on Soil Mechanics and Foundation Engineering*, Switzerland, Vol. I, 1953, pp. 100-105.
8. Boutwell, G. P., Jr., "On the Yield Behavior of Cohesionless Material," thesis presented to Duke University, at Durham, N.C., in 1968, in partial fulfillment of the requirements for the degree of Doctor of Philosophy.
9. Broms, B. B., and Casbarian, A. O., "Effects of Rotation of the Principal Stress Axes and of the Intermediate Principal Stress on the Shear Strength," *Proceedings of the 6th International Conference on Soil Mechanics and Foundation Engineering*, Montreal, Canada, Vol. I, 1965, pp. 179-183.
10. Cornforth, D. H., "Some Experiments on the Influence of Strain Conditions on the Strength of Sand," *Geotechnique*, London, England, Vol. 14, No. 2, 1964, pp. 143-167.
11. Green, G. E., discussion of "A New Soil Testing Apparatus," by H. -Y. Ko and R. F. Scott, *Geotechnique*, London, England, Vol. 17, No. 3, 1967, p. 295.
12. Green, G. E., "Strength and Deformation of Sand Measured in an Independent Stress Control Cell," *Stress-Strain Behavior of Soils, Proceedings*, Roscoe Memorial Symposium, Cambridge University, Cambridge, England, G. T. Foulis and Co., Ltd., 1971, pp. 285-323.
13. Green, G. E., and Bishop, A. W., "A Note on the Drained Strength of Sand Under Generalized Strain Conditions," *Geotechnique*, London, England, Vol. 19, No. 1, 1969, pp. 144-149.
14. Habib, P., "Influence de la variation de la contrainte principale moyenne sur la resistance au cisaillement des sols," *Proceedings of the 3rd International Conference on Soil Mechanics and Foundation Engineering*, Switzerland, Vol. I, 1953, pp. 131-136.
15. Haythornthwaite, R. M., "Mechanics of the Triaxial Test for Soils," *Journal of the Soil Mechanics and Foundations Division*, ASCE, Vol. 86, No. SM5, Proc. Paper 2625, Oct., 1960, pp. 35-62.
16. Hill, R., *The Mathematical Theory of Plasticity*, Oxford University Press, London, England, 1950.
17. Kirkpatrick, W. M., "The Condition of Failure for Sand," *Proceedings of the 4th International Conference on Soil Mechanics and Foundation Engineering*, London, England, Vol. I, 1957, pp. 172-178.
18. Ko, H. -Y., and Scott, R. F., "A New Soil Testing Apparatus," *Geotechnique*, London, England, Vol. 17, No. 1, 1967, pp. 40-57.
19. Ko, H. -Y., and Scott, R. F., "Deformation of Sand in Shear," *Journal of the Soil Mechanics and Foundations Division*, ASCE, Vol. 93, No. SM5, Proc. Paper 5470, Sept., 1967, pp. 283-310.
20. Ko, H. -Y., and Scott, R. F., "Deformation of Sand at Failure," *Journal of the Soil Mechanics and Foundations Division*, ASCE, Vol. 94, No. SM4, Proc. Paper 6028, July, 1968, pp. 883-898.
21. Lade, P. V., "The Stress-Strain and Strength Characteristics of Cohesionless Soils," thesis presented to the University of California, at Berkeley, Calif., in 1972, in partial fulfillment of the requirements for the degree of Doctor of Philosophy.
22. Marachi, N. D., "Strength and Deformation Characteristics of Rockfill Materials," thesis presented to the University of California, at Berkeley, Calif., in 1969, in partial fulfillment of the requirements for the degree of Doctor of Philosophy.
23. Lenoe, E. M., "Deformation and Failure of Granular Media Under Three Dimensional Stresses," *Experimental Mechanics*, Feb., 1966, pp. 99-104.
24. Lomize, G. M., and Kryzhanovsky, A. L., "On the Strength of Sand," *Proceedings of the Geotechnical Conference*, Oslo, Norway, Vol. I, 1967, pp. 215-219.
25. Mendelson, A., *Plasticity: Theory and Practice*, the MacMillan Company, New York, N.Y., 1968.
26. Pearce, J. A., "A Truly Triaxial Machine for Testing Clays," Veröffentlichungen des Institutes für Bodenmechanik und Felsmechanik der Universität Fridericiana in Karlsruhe, Vol. 44, Karlsruhe, W. Germany, 1970, pp. 95-110.
27. Pearce, J. A., "A New True Triaxial Apparatus," *Stress-Strain Behaviour of Soils, Proceedings*, Roscoe Memorial Symposium, Cambridge University, Cambridge, England, G. T. Foulis and Co., Ltd., 1971, pp. 330-339.
28. Peltier, M. R., "Recherches experimentales sur la courbe intrinsique de rupture des sols pulverulents," *Proceedings of the 4th International Conference on Soil Mechanics and Foundation Engineering*, London, England, 1957, Vol. I, 1957, pp. 179-182.
29. Proctor, D. C., and Barden, L., "Correspondance on Green and Bishop: A Note on the Drained Strength of Sand Under Generalized Strain Conditions," *Geotechnique*, London, England, Vol. 19, No. 3, 1969, pp. 424-426.
30. Roscoe, K. H., Schofield, A. N., and Thurairajah, A., "An Evaluation of Test Data for Selecting a Yield Criterion for Soils," *Special Technical Publications, No. 361*, Laboratory Shear Testing of Soils, American Society for Testing and Materials, Ottawa, Canada, 1963, pp. 111-128.
31. Scott, R. F., and Ko, H. -Y., "Stress-Deformation and Strength Characteristics," *Proceedings of the 7th International Conference on Soil Mechanics and Foundation Engineering*, Mexico City, Mexico, State of the Art Volume, 1969, pp. 1-49.
32. Sutherland, H. B., and Mesdary, M. S., "The Influence of the Intermediate Principal Stress on the Strength of Sand," *Proceedings of the 7th International Conference on Soil Mechanics and Foundation Engineering*, Mexico City, Mexico, Vol. I, 1969, pp. 391-399.

Appendix III.—Notation

The following symbols are used in this paper:

$a_0, a_1, a_2, \ldots, a_n$ = constants;
B = pore pressure parameter;
$b = (\sigma_2 - \sigma_3)/(\sigma_1 - \sigma_3)$ = ratio of horizontal to vertical deviator stress;
D_r = relative density;
e = void ratio;
f = expression for failure surface;

f_1 = expression for strength of cohesionless soil;
n = exponent;
$\Delta\lambda$ = proportionality constant;
$\epsilon_1, \epsilon_2, \epsilon_3$ = principal strains;
$\dot{\epsilon}_1, \dot{\epsilon}_2, \dot{\epsilon}_3$ = principal strain increments;
$\epsilon_{ij}\ (i,j = 1,2,3)$ = strain tensor;
ϵ_v = volumetric strain;
$\sigma_1, \sigma_2, \sigma_3$ = principal stresses;
$\sigma_{ij}\ (i,j = 1,2,3)$ = stress tensor;
$\phi = \arcsin [(\sigma_1 - \sigma_3)/(\sigma_1 + \sigma_3)]$ = friction angle;
ϕ_c = friction angle obtained from triaxial compression test; and
ϕ_e = friction angle obtained from triaxial extension test.

JOURNAL OF THE GEOTECHNICAL ENGINEERING DIVISION

THREE-DIMENSIONAL BEHAVIOR OF REMOLDED CLAY

By Poul V. Lade,[1] A. M. ASCE and Horacio M. Musante[2]

INTRODUCTION

The stress-strain, pore pressure, and strength behavior obtained from undrained triaxial compression tests only pertain to stress conditions for which $\sigma_1 > \sigma_2 = \sigma_3$. Use of the Mohr-Coulomb failure criterion in connection with the strength obtained in triaxial compression implies that the intermediate principal stress does not influence the strength. However, previous experimental studies have indicated some influence of the intermediate principal stress on the behavior of soils. Only a limited number of investigations of the behavior of normally consolidated clays under three-dimensional stress conditions have been performed, and some of the available data are not consistent.

Presented herein is an experimental study of the influence of the intermediate principal stress on the stress-strain, pore pressure, and strength characteristics of normally consolidated, remolded clay under undrained conditions. Consolidated-undrained triaxial compression tests and triaxial tests with independent control of all three principal stresses on cubical specimens were performed. A complete series of tests was conducted for each of three different consolidation pressures.

REVIEW OF PREVIOUS INVESTIGATIONS

The influence of the intermediate principal stress on behavior of soils may be investigated to a limited extent by means of ordinary triaxial tests in which two of the principal stresses have the same value. Results of triaxial tests on normally consolidated clays performed by Henkel (8,9) showed that the principal

Note.—Discussion open until July 1, 1978. To extend the closing date one month, a written request must be filed with the Editor of Technical Publications, ASCE. This paper is part of the copyrighted Journal of the Geotechnical Engineering Division, Proceedings of the American Society of Civil Engineers, Vol. 104, No. GT2, February, 1978. Manuscript was submitted for review for possible publication on March 14, 1977.

[1]Asst. Prof., Mech. and Structures Dept., School of Engrg. and Applied Sci., Univ. of California, Los Angeles, Calif.

[2]Grad. Student, Mech. and Structures Dept., School of Engrg. and Applied Sci., Univ. of California, Los Angeles, Calif.

effective stress ratios at failure were approximately the same in compression (where $\sigma_1 > \sigma_2 = \sigma_3$) and extension (where $\sigma_1 = \sigma_2 > \sigma_3$) for both drained and undrained test conditions. However, the undrained strengths, $(\sigma_1 - \sigma_3)_f$, obtained in extension tests were about 14% lower than those obtained in compression tests. The lower strengths in extension were attributed to the higher pore pressures that developed in these tests.

A study performed by Wu, Loh, and Malvern (22) employed consolidated-undrained tests on hollow cylindrical specimens which permitted variation of the intermediate principal stress. Tests in conventional triaxial compression and extension were also conducted. It was found that the strength of the remolded clay agreed well with the Mohr-Coulomb failure criterion expressed in terms of Hvorslev's effective strength parameters, thus indicating that the strength was independent of the intermediate principal stress. The stress-path had reportedly no influence on the effective strength of the clay.

Pearce (16,17) and Yong and McKyes (24) presented results of undrained tests in which three independently controlled principal stresses could be applied to cubical or rectangular prismatic specimens. Both investigations, performed on saturated kaolinite, indicated that the soil behavior prior to failure was dependent on the relative magnitude of the intermediate principal stress, but the effective stress failure surface could be described adequately by the Mohr-Coulomb failure criterion.

In contrast with these findings are the results of three-dimensional undrained tests on normally consolidated clay performed by Shibata and Karube (18) and Yong and McKyes (23). Both studies showed that the relative value of the intermediate principal stress affected the deformations, the pore presures, and the strengths expressed in terms of effective stresses. The strain-to-failure in the major principal stress direction decreased and the pore pressure at failure increased with increasing relative value of the intermediate principal stress. The Mohr-Coulomb failure criterion was shown to represent a lower limit of the effective strength envelope. The actual failure surfaces shown on octahedral planes in the principal stress space were curved and circumscribed the Mohr-Coulomb failure surface such that the strengths from triaxial extension coincided with the Mohr-Coulomb failure surface.

Vaid and Campanella (20) conducted a series of consolidated-undrained triaxial compression and triaxial extension tests and plane strain tests with compression and extension type stress-paths on undisturbed Haney Clay. All test specimens were initially consolidated under a K_0-condition before they were sheared. The effective friction angles calculated from the maximum effective stress ratios in plane strain and triaxial extension were greater than those obtained from triaxial compression. The resulting failure surface is curved in the octahedral plane and is located outside the Mohr-Coulomb failure surface corresponding to the friction angle from triaxial compression.

It may be concluded that the results of these investigations are not in agreement with regard to the three-dimensional failure conditions for normally consolidated clay. Only few of these studies have been concerned with the influence of the intermediate principal stress on the stress-strain and pore pressure behavior under undrained conditions.

Because some ambiguity existed regarding the effective stress failure criterion and because only limited knowledge about the three-dimensional behavior of normally consolidated clay was available, the study of Grundite Clay presented herein was undertaken.

Clay Tested

All tests in this investigation were performed on Grundite Clay. Grim and Bradley (7) describe this clay as an illitic clay, mined in the Goose Lake area of Grundy County, Illinois. The particle size distribution indicated that the clay consisted of about equal amounts of silt and clay size particles. Atterberg limit tests gave LL = 54.8 and PL = 24.7, and the activity was 0.58. Sensitivities for Grundite Clay samples prepared in a similar manner as described herein were obtained by Houston (11) in the range from 1.04 to 2.6 with an average value of 1.75. The samples used in the present study were remolded to eliminate inherent anisotropy due to initial K_0-consolidation.

Preparation of Test Specimens

Tests were performed on tall cylindrical specimens (with heights equal to 2.3 times the diameter) without lubricated ends and on short cylindrical specimens and cubical specimens (both with heights equal to the diameters) with lubricated ends. The same procedure was used to produce and test all specimens in order that variations in test results arising from inconsistent techniques be avoided.

A batch of clay was prepared for each specimen by mixing air-dry clay powder with water to produce a clay slurry with a water content of 90%. The lean uniform slurry was consolidated in a double draining consolidometer at a vertical pressure that was 0.1 kg/cm² smaller than the final isotropic consolidation pressure to be used in the tests. After thoroughly remolding the clay, specimens with the respective shapes were trimmed, installed in the testing apparatus, and consolidated isotropically at 1.00 kg/cm², 1.50 kg/cm², and 2.00 kg/cm² corresponding to water contents of 34.4%, 31.9%, and 30.1%, respectively.

Fig. 1 shows a schematic drawing of a cubical specimen with lubricated ends, and Fig. 2 shows a photograph of a specimen of this type after it has been tested. As indicated on these figures, slotted filter papers were used on the vertical sides of the specimens to accelerate the consolidation and to help equalize the pore pressures during the shearing stage. Parts of the filter papers covered the filter stones located on the sides of the cap and base, thus providing drainage paths from the specimens to the volume change device. A pressure transducer was connected to the drainage lines immediately outside the triaxial chamber. This transducer was installed such that it could be used to measure both chamber pressure and pore-water pressure.

A nominal back pressure of 1.00 kg/cm² was applied in all tests to ensure full saturation of the specimens. The B-values measured after the consolidation stage indicated that the specimens were fully saturated.

A series of consolidated-undrained tests was performed with and without filter paper to determine the load taken by the vertically slotted Whatman No. 54 filter paper. All results presented herein have been corrected for the loads carried by the filter paper and the membrane.

Preliminary Tests

Consolidated-undrained triaxial compression tests were conducted to investigate effects of lubricated end plates, strain rate, and specimen shape on the measured behavior of Grundite Clay.

Effects of Lubricated End Plates and Strain Rate.—Lubricated end plates may be employed in triaxial tests to avoid development of significant shear stresses between the loading plates and the specimen, and to reduce nonuniformities in strains and pore pressure distributions in undrained tests. In addition, increased strain rates may be used in undrained tests with lubricated ends. Calculations to ascertain the strain rate required for pore pressure equalization are inapplicable since the stress and strain distributions are assumed to be uniform. Barden and McDermott (1) recommended a procedure for selecting strain rates for

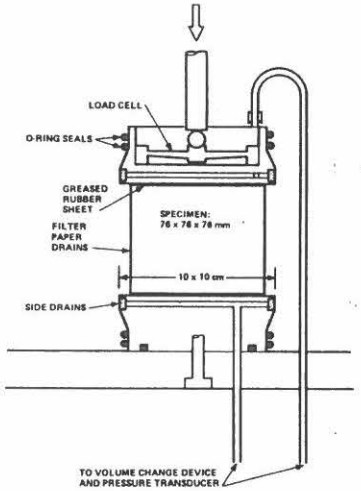

FIG. 1.—Setup of Cubical Specimen with Lubricated Ends

FIG. 2.—Cubical Specimen Tested under Three Unequal Principal Stresses

tests with lubricated ends, and following their criteria a strain rate of 0.04%/min was selected.

Tests were performed to check if the effects of lubricated ends and strain rate were similar to those previously observed (1,5,6). Cylindrical specimens with diameters of 2.8 in. (71 mm) and height-to-diameter ratios of 1.0 and 2.3 were isotropically consolidated at 1.00 kg/cm² and 1.50 kg/cm² and sheared at strain rates of 0.04%/min and 0.0025%/min. Lubricated end plates were used for the short specimens and regular ends were used for the tall specimens. The effects of lubricated ends and strain rate on the stress-strain, pore pressure, and strength characteristics observed in the tests on Grundite Clay were similar to those observed in much more elaborate investigations on other clays (1,5,6). Of prime interest in this respect is the previous observation (1) that the test

results are not significantly affected by the strain rate when lubricated ends are used. The remainder of the testing program was therefore conducted using specimens with lubricated ends and a height-to-diameter ratio of 1.0, and employing a strain rate of 0.04%/min.

Effects of Specimen Shape.—The results of the tests on short cylindrical specimens were compared with results of tests on cubical specimens with side lengths of 76 mm. These tests were conducted under identical conditions, thus only the shapes of the specimens were different. The influence of shape on the behavior of Grundite Clay was found to be negligible in all respects.

Cubical Triaxial Tests

Three series of consolidated-undrained tests were performed in a cubical triaxial apparatus similar to that described by Lade and Duncan (12). This apparatus was designed to permit application of three unequal principal stresses to a cubical specimen with side lengths of 76 mm. The specimen, shown in Figs. 1 and 2, was contained between a cap and base and a surrounding membrane. The minor principal stress, σ_3, which acted in one horizontal direction, was provided by the chamber pressure. The vertical deviator stress, together with the chamber pressure, provided for a vertical principal stress different from σ_3. The second horizontal stress was applied by the chamber pressure and a horizontal loading system, which has been described previously (12). Both the horizontal loading plates and the cap and base were provided with lubricated surfaces. The maximum linear strain that can be achieved with this apparatus is approx ±30% in any of the three principal directions. During a cubical triaxial test the vertical load, the horizontal load, the chamber pressure, and the pore-water pressure were measured in addition to the three principal deformations.

Each test in the three series was conducted with constant confining pressure σ_3 and the horizontal and vertical deviator stresses were increased proportionally until the specimen failed. Thus, the ratio between the deviator stresses, $b = (\sigma_2 - \sigma_3)/(\sigma_1 - \sigma_3)$, was maintained constant in each test. The value of b indicates the relative magnitude of the intermediate principal stress; b is zero for triaxial compression in which $\sigma_2 = \sigma_3$, and it is unity for triaxial extension in which $\sigma_2 = \sigma_1$; for intermediate values of σ_2 the value of b is between zero and unity. For each consolidation pressure the values of b used in the tests were chosen so that the failure surface, the stress-strain relations, and the pore pressure response could be determined over the full range of the intermediate principal stress.

Stress-Strain and Pore Pressure Behavior

Fig. 3 shows the stress-strain and pore pressure relations for the specimens consolidated at 1.50 kg/cm². The relationships obtained from triaxial compression tests with consolidation pressures of 1.00 kg/cm² and 2.00 kg/cm² are also shown in Fig. 3(*a*). The normalized stress differences, $(\sigma_1 - \sigma_3)/\sigma_c'$, the effective stress ratios, σ_1'/σ_3', and the normalized pore pressure changes, $\Delta u/\sigma_c'$, are plotted versus the major principal strain, ϵ_1, in these figures, and the relative magnitudes of the intermediate principal stresses are indicated by the values of b.

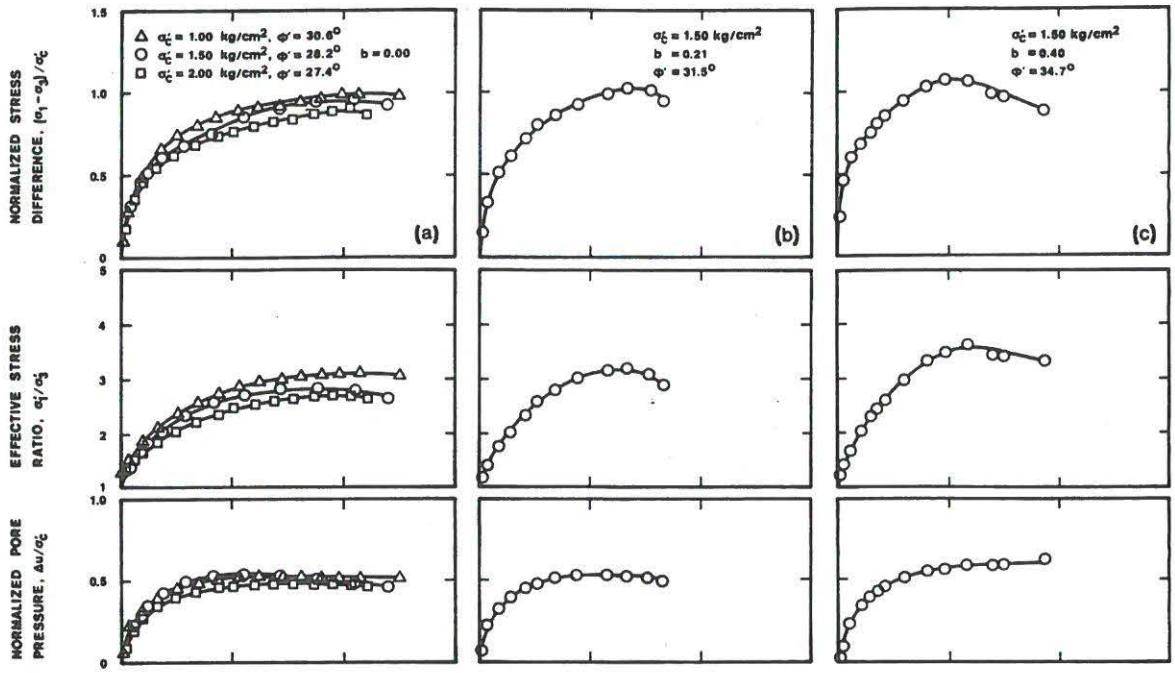

FIG. 3.—Stress-Strain and Pore Pressure Characteristics Obtained in Cubical Triaxial Tests on Grundite Clay

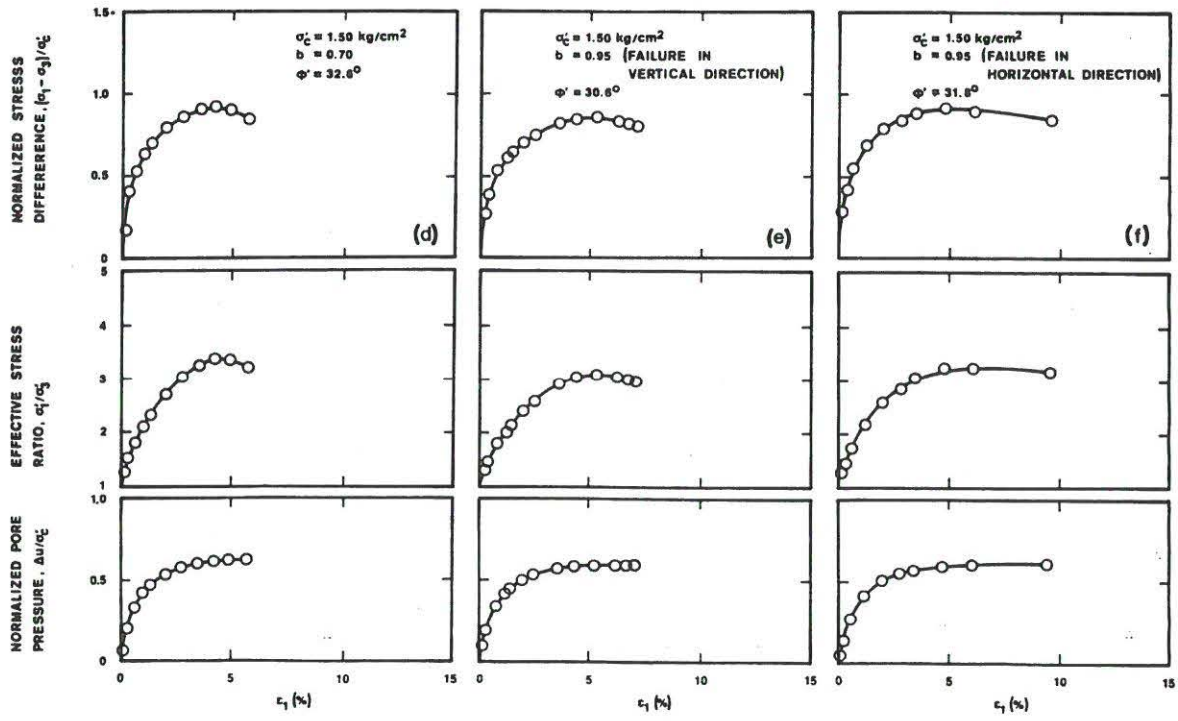

FIG. 3.—*Continued*

Considering that the stress-strain relations in Fig. 3(*a*) are normalized, it may be seen that the initial undrained modulus increases, the initial slope from the effective stress ratio diagram increases, and the effective stress ratio decreases with increasing consolidation pressure. The pore pressures shown in Fig. 3(*a*) increase to values at failure that are almost proportional to the initial consolidation pressure. Thus, the ratio of pore pressure change to consolidation pressure decreases slightly with increasing consolidation pressure. This pattern corresponds to the pattern of decreasing effective stress ratio with increasing consolidation pressure.

The results of the cubical triaxial tests shown in Fig. 3 indicate that for a constant consolidation pressure the initial slope of the stress difference—and the effective stress ratio-strain relations increase continually with increasing value of the intermediate principal stress. The strain-to-failure is greatest, the pore pressure developed at failure is lowest, the effective strength is lowest, and the undrained strength is highest for triaxial compression ($b = 0$). The strain-to-failure decreases and the pore pressure change increases initially with increasing value of b and both remain approximately constant for b-values greater

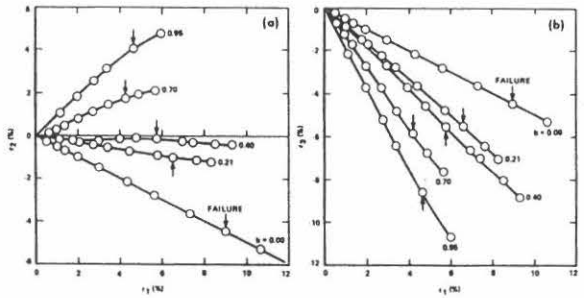

FIG. 4.—Relations Between Principal Strains Obtained in Cubical Triaxial Tests on Grundite Clay with Consolidation Pressure of 1.50 kg/cm²

than about 0.6. Note that the tests performed with initial consolidation pressures of 1.00 kg/cm² and 2.00 kg/cm² showed similar patterns of behavior as those in Fig. 3.

Relation Between Principal Strains

The intermediate and minor principal strains, ϵ_2 and ϵ_3, are plotted versus ϵ_1 in Fig. 4 for specimens consolidated at 1.50 kg/cm². Fig. 4(*a*) shows that the intermediate principal strains, ϵ_2, are expansive for b-values smaller than about 0.4 and compressive for higher values of b. The minor principal strains, ϵ_3, are expansive in all cases and decrease with increasing b-values as shown in Fig. 4(*b*). Since the tests were performed under undrained conditions, the sum of the three principal strains is always equal to zero. Fig. 4 indicates that a given increment in b has a greater effect on the relation between the principal strains at small b-values than at high b-values.

The points corresponding to failure according to the maximum effective stress

ratio are indicated on each curve in Fig. 4. The major principal strain-to-failure decreases initially with increasing b-value and remains approximately constant for b-values greater than about 0.6.

Isotropy of Specimens.—The Grundite Clay was thoroughly remolded before the final trimming and isotropic consolidation in order to avoid any anisotropy that might be caused by the initial anisotropic consolidation. The relations between the principal strains shown in Fig. 4 may be used to check the isotropic behavior of the specimens. Since the test setup is symmetric around a vertical axis, it is expected that any anisotropic behavior would be especially pronounced in triaxial extension ($b = 1$) in which the specimen is loaded symmetrically around a horizontal axis. The principal strains, ϵ_1 and ϵ_2, would not be expected to be equal in triaxial extension unless the remolded clay was isotropic. Although attempts were made to perform tests with $b = 1.00$, final calculation of the test results showed some deviation from this condition. However, extrapolation

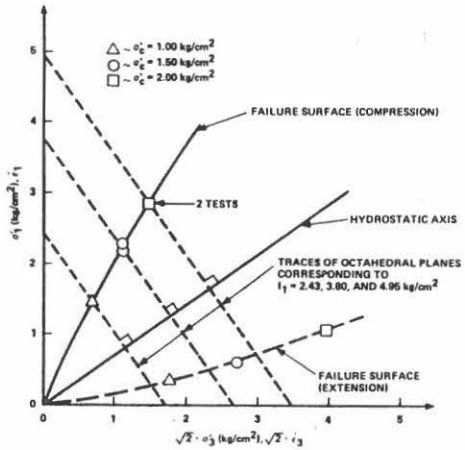

FIG. 5.—Trace of Failure Surface in Triaxial Plane for Grundite Clay

of the pattern of strains shown in Fig. 4 over the test with $b = 0.95$ to $b = 1.00$ shows that $\epsilon_2 \simeq \epsilon_1$, thus indicating isotropic behavior.

In addition, two tests were performed with $b = 0.95$, and the major deviator stress and failure occurred in the vertical direction (= direction of ϵ_1) in one test and in the horizontal direction (= direction of ϵ_1) in the other test, as shown in Figs. 3(*e*) and 3(*f*). The stress-strain curves, the pore pressure changes, and the strengths from these two tests are approximately the same, and this indicates that the specimens used for the present study were essentially isotropic.

Strength Characteristics

Several aspects of the strength of Grundite Clay are studied herein.

Strength in Terms of Effective Stresses.—Because it may be possible to model the observed stress-strain and strength behavior by plasticity theory, the strength

characteristics are examined in planes of the principal stress space.

Triaxial Plane.—The triaxial plane containing the σ_1-axis is shown in Fig. 5. The trace of the experimental failure surface corresponding to maximum effective stress ratios, $(\sigma_1'/\sigma_3')_{max}$, obtained from triaxial compression tests on Grundite clay are shown in this plane. No tests were performed in triaxial extension, i.e., with $b = 1.00$. However, the strength in extension may be determined by extrapolation over the tests performed with b-values close to unity. The dashed line in Fig. 5 represents the trace of the failure surface in extension. It may be seen that both traces of the failure surface are curved in this diagram. Curved failure envelopes have often been observed for sand as well as for clay soils (2,3,10,15). The Mohr-Coulomb failure criterion does not account for the curvature of the failure envelope.

The results of the cubical triaxial tests performed with $b > 0.0$ may be plotted in planes containing the hydrostatic axis and corresponding to constant values of b. The traces of these planes in octahedral planes are indicated in Fig. 6(*a*). The test results show that the traces of the three-dimensional failure surface in constant b-value planes are also curved.

Effect of Stress-Path on Failure.—Another important aspect of failure in soils

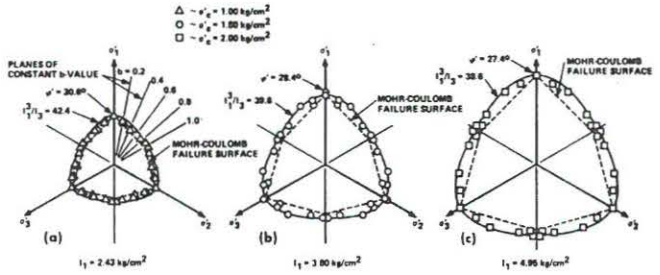

FIG. 6.—Traces of Failure Surface for Grundite Clay in Octahedral Planes

relate to the effect of stress-path on failure. It has often been observed from triaxial compression and extension tests that the failure surface corresponding to the maximum effective stress ratios for each of these tests on normally consolidated clays are, for practical purposes, independent of the stress-paths leading to failure (8,9,10,14,19,21). Thus, the failure surface can be determined uniquely from various types of shear tests performed on normally consolidated clay as long as the results are interpreted in terms of effective stresses.

Bjerrum and Simons (4) observed that the maximum deviator stress, $(\sigma_1 - \sigma_3)_{max}$, occurred almost simultaneously with the maximum effective stress ratio, $(\sigma_1'/\sigma_3')_{max}$, in isotropically consolidated, insensitive, remolded clays. This was also observed from most of the tests on remolded Grundite Clay.

Octahedral Planes.—The effective strengths from the triaxial compression tests and the tests with three unequal principal stresses on Grundite Clay are shown on the octahedral planes in Fig. 6. The location of the octahedral planes are indicated by the values of the first stress invariant, I_1, and by their traces in the triaxial plane shown in Fig. 5. The failure points shown in Fig. 6 have

been projected on the octahedral planes along the curved failure surfaces observed in planes that contain the hydrostatic axis and have constant b-values.

The specimens of remolded Grundite Clay were shown to be essentially isotropic, and it was also noticed that the strengths of the test specimens with b-values close to unity were approximately the same whether they failed horizontally or vertically. Interchanging the principal stress directions will therefore not have any effect on the strength of this isotropically consolidated clay. The traces of the failure surface in the octahedral planes are consequently symmetric around the projections of the three principal axes and intersect these at right angles.

Fig. 6 shows a comparison of the experimentally obtained effective strengths with the Mohr-Coulomb failure surfaces and with the surfaces corresponding to a failure criterion recently suggested for cohesionless soil (13). This criterion is expressed in terms of the first and the third stress invariants, I_1 and I_3:

$$\frac{I_1^3}{I_3} = \kappa_1 \quad \ldots \quad (1)$$

in which $I_1 = \sigma_1' + \sigma_2' + \sigma_3' \quad \ldots \quad (2)$

and $I_3 = \sigma_1' \sigma_2' \sigma_3' \quad \ldots \quad (3)$

and κ_1 is a constant that may be determined from results of triaxial compression tests only. The value of the ratio I_1^3/I_3 is 27 for isotropic stress conditions ($\sigma_1 = \sigma_2 = \sigma_3$), and it increases up to failure where κ_1 expresses the strength of the soil. The value of κ_1 increases with increasing friction angle in triaxial compression. In principal stress space the shape of the failure surface defined by Eq. 1 is conical, with the apex of the cone at the origin, and with cross sections of the type shown by solid lines in Fig. 6. The cross sections are symmetrical around the principal axes in the octahedral planes, and the shape is essentially circular for values of κ_1 close to 27 and it becomes increasingly triangular with increasing values of κ_1.

The irregular hexagons shown by dashed lines in Fig. 6 are described by the Mohr-Coulomb criterion corresponding to the friction angles in triaxial compression. The experimental failure points are all located outside the respective hexagons, thus indicating that the friction angles from tests with $\sigma_2 > \sigma_3$ are higher than those obtained in triaxial compression tests. Thus, the Mohr-Coulomb failure criterion underestimates the strength of remolded Grundite Clay for all but triaxial compression conditions.

The failure surfaces corresponding to Eq. 1 with values of κ_1 determined from the triaxial compression tests appear to model the failure conditions for remolded clay fairly well. Since the failure surfaces are curved as shown in Fig. 5, different values of κ_1 correspond to the cross sections in the three octahedral planes. The differences between the measured strengths and those suggested by Eq. 1 are most pronounced for the tests performed with low to intermediate values of b and with a consolidation pressure of 1.00 kg/cm². This consolidation pressure produced specimens with rather soft consistency, resulting in difficulty in handling the specimens, which probably lead to less reliable results. The results of the tests with the higher consolidation pressures are considered to be more reliable, because the specimens were stiffer and

therefore easier to handle. On the basis of these considerations it is suggested that the failure criterion in Eq. 1 with the respective values of κ_1 models the three-dimensional strength of Grundite Clay with reasonable accuracy.

Strength in Terms of Total Stresses.—Fig. 7 shows the variation of s_u/σ_c', i.e., the undrained shear strength normalized on the basis of the consolidation pressure. The results of the triaxial compression tests show that this ratio is not constant but decreases slightly with increasing consolidation pressure. This decrease may be related to the curved failure envelope shown in Fig. 5, i.e., it may be related to the decrease in effective friction angle with increasing consolidation pressure. Houston (11) found similar results for Grundite Clay. The s_u/σ_c' ratio also decreases slightly (approx 7%) from triaxial compression ($b = 0$) to triaxial extension ($b = 1$). Considering the variation in effective strength shown in Fig. 6, the slight decrease in the s_u/σ_c' ratio with increasing

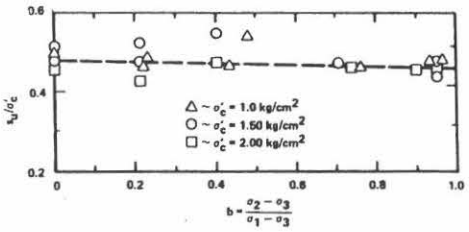

FIG. 7.—Variation of Normalized Undrained Shear Strength with Value of $b = (\sigma_2 - \sigma_3)/(\sigma_1 - \sigma_3)$

b-value is caused by the higher pore pressures which develop at higher b-values. This variation in the s_u/σ_c' ratio is similar to that presented by Henkel (8,9).

Directions of Strain Increment Vectors

It is of interest to study the directions of the plastic strain increment vectors relative to the yield or failure surface in the principal stress space, because it may be possible to model the stress-strain behavior by plasticity theory. For this purpose the principal strain increment axes are superimposed on the stress axes in the principal stress space. Only the directions of the strain increment vectors at failure will be considered. All strain increments are plastic at failure, because the changes in stress at failure are negligible, thus resulting in negligible elastic strain increments.

Triaxial Plane.—The direction of the strain increment vectors in the triaxial plane are shown initiating from the respective stress points in Fig. 8. No tests were performed in triaxial extension ($b = 1$), but the trace of the failure surface in extension is indicated with a dashed line, and the direction of strain increment vectors in triaxial extension is also indicated. Because $\epsilon_2 = \epsilon_3$ in compression and $\epsilon_2 = \epsilon_1$ in extension for an isotropic material, the corresponding strain increment vectors are contained in the triaxial plane. Because the volumetric strain is zero in undrained tests, their direction is perpendicular to the hydrostatic axis.

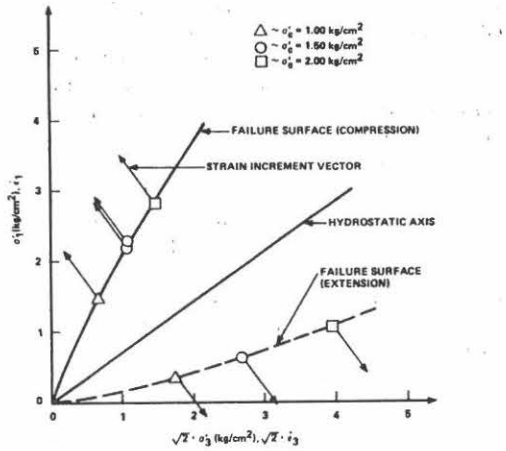

FIG. 8.—Directions of Strain Increment Vectors in Triaxial Plane for Grundite Clay

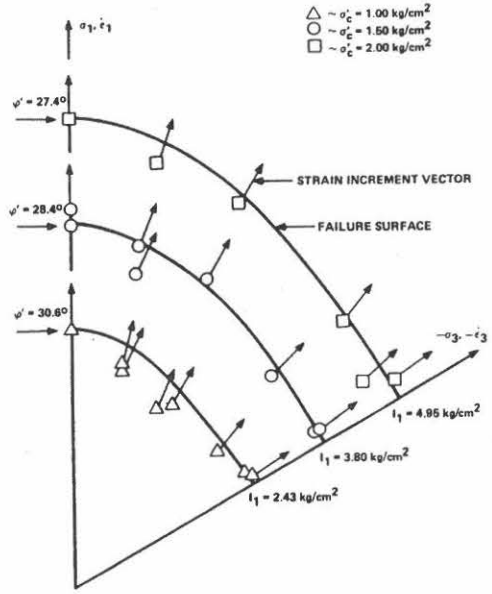

FIG. 9.—Directions of Strain Increment Vectors in Octahedral Planes for Grundite Clay

Fig. 8 shows that the directions of the strain increment vectors form acute angles with the failure surface. The normality condition of classical plasticity theory is therefore not satisfied for normally consolidated clay when its behavior is interpreted in terms of effective stresses.

Octahedral Planes.—Only one-sixth of the octahedral planes are shown in Fig. 9, because the failure surface is symmetric around the three principal axes in these planes. The directions of the strain increment vectors at failure are shown initiating from the respective stress points. These directions have been calculated from the slopes of the relations between the principal strains, shown in Fig. 4, for the tests performed with consolidation pressures of 1.50 kg/cm^2. Since the volumetric strain is zero in undrained tests, the strain increment vectors are perpendicular to the hydrostatic axis and therefore contained in the octahedral planes.

It may be seen from Fig. 9 that the strain increment vectors are nearly perpendicular to the traces of the failure surfaces in the octahedral planes. Only a few vectors at intermediate values of b deviate slightly from perpendicularity. The magnitudes of these deviations are so small that they could even be due to experimental inaccuracies.

It is clear from these results that the condition of normality is satisfied or very nearly satisfied in the octahedral plane, but not in the triaxial plane, and it is therefore not satisfied in general for normally consolidated clay when its behavior is interpreted in terms of effective stresses. The general pattern of the directions of the plastic strain increment vectors relative to the failure surface is of importance in considerations regarding the applicability of plasticity theory to normally consolidated clays.

Comparison with Behavior of Sand

The three-dimensional stress-strain and strength characteristics of Grundite Clay previously mentioned are very similar to those observed for sand. This may be verified by comparison with the behavior of Monterey No. 0 Sand and other sands as presented by Lade and Duncan (12,13). Only with respect to one aspect of this behavior do normally consolidated clays differ from sands. A sand can be deposited with different dry densities and these densities change little with confining pressure. However, the stress-strain and strength characteristics of sands vary considerably with dry density and confining pressure. In contrast, a normally consolidated clay can only exist in equilibrium at a dry density that depends on the consolidation pressure. Thus, only one failure surface is possible for a normally consolidated clay, and the stress-strain relations are correspondingly limited to one characteristic type of behavior (for a given clay) that does not vary much with consolidation pressure.

Conclusions

The influence of the intermediate principal stress on the stress-strain, pore pressure, and strength characteristics of remolded, isotropically and normally consolidated Grundite Clay has been studied using conventional triaxial compression tests and cubical triaxial tests with independent control of the three principal

stresses. The cubical triaxial tests were performed with constant values of $b = (\sigma_2 - \sigma_3)/(\sigma_1 - \sigma_3)$.

It was found that for constant consolidation pressure the initial undrained modulus and the slope of the effective stress ratio-strain curve increased with increasing b-value. The strain-to-failure decreased and the pore pressure change increased initially with increasing value of b and both remained approximately constant for b-values greater than 0.6. The effective strength of the soil can be modeled fairly well by the failure criterion $I_1^3/I_3 = \kappa_1$, in which I_1 and I_3 are the first and the third stress invariants and κ_1 is a constant that may be determined from triaxial compression tests. The undrained strength decreased slightly with increasing b-value, and this was caused by the higher pore pressures that developed at higher b-values. It was observed that a given increment in b had a greater effect on the stress-strain, pore pressure, and strength characteristics at small b-values than at high b-values.

The test results showed that the directions of the strain increments at failure form acute angles with the failure surface in the principal stress space when the data are interpreted in terms of effective stresses. The results are therefore not in agreement with the normality condition from classical plasticity theory. However, it was found that the plastic strain increment vectors in the octahedral plane are perpendicular to the trace of the failure surface in that plane.

Some aspects of the behavior of normally consolidated, remolded Grundite Clay are similar to those of sand at a given density.

Acknowledgment

Some of the laboratory tests presented here were performed by Elisha Geiger of School of Engineering and Applied Science at the University of California at Los Angeles. This study was supported by the National Science Foundation under Engineering Research Initiation Grant No. GK37445. Grateful appreciation is expressed for this support.

Appendix I.—References

1. Barden, L., and McDermott, R. J. W., "Use of Free Ends in Triaxial Testing of Clays," *Journal of the Soil Mechanics and Foundations Division,* ASCE, Vol. 91, No. SM6, Proc. Paper 4535, Nov., 1965, pp. 1–23.
2. Bishop, A. W., "The Strength of Soils as Engineering Materials," 6th Rankine Lecture, *Geotechnique,* London, England, Vol. 16, No. 2, June, 1966, pp. 91–130.
3. Bishop, A. W., "Shear Strength Parameters for Undisturbed and Remoulded Soil Specimens," *Stress-Strain Behavior of Soils, Proceedings,* Roscoe Memorial Symposium, Cambridge University, Cambridge, England, G. T. Foulis and Co., Ltd., 1971, pp. 3–58.
4. Bjerrum, L., and Simons, N. E., "Comparison of Shear Strength Characteristics of Normally Consolidated Clays," *Proceedings of the ASCE Research Conference on Shear Strength of Cohesive Soils,* Boulder, Colo., 1960, pp. 711–726.
5. Blight, G. E., "Shear Stress and Pore Pressure in Triaxial Testing," *Journal of the Soil Mechanics and Foundations Division,* ASCE, Vol. 91, No. SM6, Proc. Paper 4540, Nov., 1965, pp. 25–39.
6. Duncan, J. M., and Dunlop, P., "The Significance of Cap and Base Restraint," *Journal of the Soil Mechanics and Foundations Division,* ASCE, Vol. 94, No. SM1, Proc. Paper 5768, Jan., 1968, pp. 271–290.
7. Grim, R. E., and Bradley, R. F., "A Unique Clay from Goose Lake, Illinois Area,"

Journal of the American Ceramic Society, Vol. 22, No. 5, 1939, pp. 157–164.
8. Henkel, D. J., "The Relationship between the Strength, Pore-Water Pressure, and Volume Change Characteristics of Saturated Clays," *Geotechnique*, London, England, Vol. IX, No. 3, Sept., 1959, pp. 119–135.
9. Henkel, D. J., "The Shear Strength of Saturated Remoulded Clays," *Proceedings of the ASCE Research Conference on Shear Strength of Cohesive Soils*, Boulder, Colo., 1960, pp. 533-554.
10. Henkel, D. J., and Sowa, V. A., "The Influence of Stress History on Stress Paths in Undrained Triaxial Tests on Clay," *Special Technical Publication, No. 361*, Laboratory Shear Testing of Soils, American Society for Testing and Materials, Ottawa, Canada, 1963, pp. 280-291.
11. Houston, W. N., "Formation Mechanisms and Property Interrelationships in Sensitive Clays," thesis presented to the University of California, at Berkeley, Calif., in 1967, in partial fulfillment of the requirements for the degree of Doctor of Philosophy.
12. Lade, P. V., and Duncan, J. M., "Cubical Triaxial Tests on Cohesionless Soil," *Journal of the Soil Mechanics and Foundations Division*, ASCE, Vol. 99, No. SM10, Proc. Paper 10057, Oct., 1973, pp. 793–812.
13. Lade, P. V., and Duncan, J. M., "Elastoplastic Stress-Strain Theory for Cohesionless Soil," *Journal of the Geotechnical Engineering Division*, ASCE, Vol. 101, No. GT10, Proc. Paper 11670, Oct., 1975, pp. 1037–1053.
14. Olson, R. E., "The Shear Strength Properties of Calcium Illite," *Geotechnique*, London, England, Vol. 12, No. 1, Mar., 1962, pp. 23–43.
15. Olson, R. E., "Shearing Strength of Kaolinite, Illite, and Montmorillonite," *Journal of the Geotechnical Engineering Division*, ASCE, Vol. 100, No. GT11, Proc. Paper 10947, Nov., 1974, pp. 1215–1229.
16. Pearce, J. A., "A Truly Triaxial Machine for Testing Clays," *Veröffenlichungen des Institutes fur Bodenmechanik und Felsmechanik der Universität Fridericiana in Karlsruhe*, Vol. 44, Karlsruhe, West Germany, 1970, pp. 95–110.
17. Pearce, J. A., "A New True Triaxial Apparatus," *Stress-Strain Behavior of Soils, Proceedings*, Roscoe Memorial Symposium, Cambridge University, Cambridge, England, G. T. Foulis and Co., Ltd., 1971, pp. 330–339.
18. Shibata, T., and Karube, D., "Influence of the Variation of the Intermediate Principal Stress on the Mechanical Properties of Normally Consolidated Clays," *Proceedings of the 6th International Conference on Soil Mechanics and Foundation Engineering*, Montreal, Canada, Vol. I, 1965, pp. 359–363.
19. Simons, N. E., "The Influence of Stress Path on Triaxial Test Results," *Special Technical Publication, No. 361*, Laboratory Shear Testing of Soils, American Society for Testing and Materials, Ottawa, Canada, 1963, pp. 270–278.
20. Vaid, Y. P., and Campanella, R. G., "Triaxial and Plane Strain Behavior of Natural Clay," *Journal of the Geotechnical Engineering Division*, ASCE, Vol. 100, No. GT3, Proc. Paper 10421, Mar., 1974, pp. 207–224.
21. Whitman, R. V., Ladd, C. C., and da Cruz, P., "Discussion," *Proceedings of the ASCE Research Conference on Shear Strength of Cohesive Soils*, Boulder, Colo., 1960, pp. 1049–1056.
22. Wu, T. H., Loh, A. K., and Malvern, L. E., "Study of Failure Envelope of Soils," *Journal of the Soil Mechanics and Foundations Division*, ASCE, Vol. 89, No. SM1, Proc. Paper 3430, Feb., 1963, pp. 145–181.
23. Yong, R. N., and McKyes, E., "Yielding of Clay in a Complex Stress Field," *Proceedings of the 3rd Panamerican Conference on Soil Mechanics and Foundation Engineering*, Caracas, Venezuela, Vol. I, 1967, pp. 131–143.
24. Yong, R. N., and McKyes, E., "Yield and Failure of Clay under Triaxial Stresses," *Journal of the Soil Mechanics and Foundations Division*, ASCE, Vol. 97, No. SM1, Proc. Paper 7790, Jan., 1971, pp. 159–176.

Appendix II.—Notation

The following symbols are used in this paper:

B = pore pressure parameter;

b = ratio of deviator stresses = $(\sigma_2 - \sigma_3)/(\sigma_1 - \sigma_3)$;
I_1, I_3 = first and third stress invariants;
K_0 = coefficient of earth pressure at rest;
LL = liquid limit;
PL = plastic limit;
s_u = undrained shear strength;
Δu = change in pore water pressure;
$\epsilon_1, \epsilon_2, \epsilon_3$ = principal strains;
$\dot{\epsilon}_1, \dot{\epsilon}_2, \dot{\epsilon}_3$ = principal strain increments;
κ_1 = constant in failure criterion;
$\sigma_1, \sigma_2, \sigma_3$ = total principal stresses;
$\sigma_1', \sigma_2', \sigma_3'$ = effective principal stresses;
$\sigma_1 - \sigma_3, \sigma_2 - \sigma_3$ = deviator stresses;
σ_c' = consolidation pressure; and
ϕ' = effective friction angle = $\arcsin [(\sigma_1 - \sigma_3)/(\sigma_1' + \sigma_3')]$.

SOILS AND FOUNDATIONS Vol. 29, No. 2, 127-140, June 1989
Japanese Society of Soil Mechanics and Foundation Engineering

ELASTO-PLASTIC BEHAVIOR OF K_0-CONSOLIDATED CLAY IN TORSION SHEAR TESTS

Won Pyo Hong[i] and Poul V. Lade[ii]

ABSTRACT

A series of torsion shear tests was performed along various stress-paths on hollow cylinder specimens of K_0-consolidated clay to investigate the influence of rotation of principal stresses on the stress-strain and strength characteristics. The effects of stress-paths and reorientation of principal stresses were mainly observed in the prefailure stress-strain behavior. The experimentally obtained failure surface from torsion shear tests could practically be modeled by an isotropic failure criterion. Coupling effects between stresses and strains were observed when torsion shear and vertical normal stresses were applied. The work-space for torsion shear tests was illustrated, and the relation between stresses and strain increments was also studied in the work-space.

Key words : clay, consolidated undrained shear, failure, plasticity, shear strength, torsion, (**IGC** : D 6)

INTRODUCTION

The stress-strain behavior of natural clay deposits depends on the cross-anisotropy produced by K_0-consolidation in the field. Triaxial tests with independent control of the three principal stresses on cubical specimens have been performed to investigate the influence of principal stresses, especially the intermediate principal stress, on the behavior of clay (e. g., Lade and Musante, 1978).

Construction on or in clay deposits causes rotation of principal stress directions as well as changes in the magnitudes of stresses. The reorientation and change in magnitude of principal stresses during loading may greatly affect the stress-strain behavior of such deposits. To enhance the knowledge and understanding of soil behavior, the effects of reorientation and change in magnitude of principal stresses should be investigated. However, in triaxial tests, including cubical triaxial tests, the directions of principal stresses cannot be rotated during loading.

The purpose of the present study is to investigate the influence of rotation of prin-

[i] Associate Professor, Department of Civil Engineering, College of Engineering, Chung-Ang University, Seoul, 156-756, Korea.
[ii] Professor, Department of Civil Engineering, School of Engineering and Applied Science, University of California, Los Angeles, California 90024, USA.
Manuscript was recived for review on June 21, 1988.
Written discussions on this paper should be submitted before January 1, 1990, to the Japanese Society of Soil Mechanics and Foundation Engineering, Sugayama Bldg. 4 F, Kanda Awaji-cho 2-23, Chiyoda-ku, Tokyo 101, Japan. Upon request the closing date may be extended one month.

cipal stresses on the stress-strain, pore pressure and strength characteristics of K_0-consolidated clay. A series of undrained and drained torsion shear tests were performed along various stresspaths on hollow cylinder specimens. The stress-paths were designed to cover the full range of vertical deviator stresses from compression to extension. The relation between stresses and strain increments was also studied in the work-space.

PREVIOUS STUDIES

The effects of rotation of principal stress directions have been investigated by use of the simple shear device and the torsion shear apparatus. The behavior of soil specimens in the simple shear device has been studied extensively by Roscoe (1953), Roscoe et al. (1967), and Bjerrum and Landva (1966). However, Wright et al. (1978) showed that the uniformity of the shear stresses on the central plane of the simple shear specimen is questionable. Generally, the simple shear device has the following disadvantages : Complementary shear stresses cannot be sustained on the vertical boundaries, the stress and strain states within the specimen lack uniformity, and the evolution of the horizontal, normal stress during shear is generally unknown (Saada and Townsend, 1981).

Broms and Casbarian (1965) performed three series of consolidated-undrained torsion shear tests on hollow cylinder specimens of a remolded kaolinite clay to study the influence of stress rotation and the intermediate principal stress on the strength characteristics. Torsion shear tests have since been performed to a limited extent (Lade, 1975, 1976, 1981 ; Saada and co-workers, 1967, 1973, 1975, 1984 ; Geiger and Lade, 1979 ; Hight et al., 1983 ; Symes et al., 1984 ; Tatsuoka et al., 1986 ; Hicher and Lade, 1987).

The main advantage of the torsion shear test is that it allows inclination of the major principal stress in any desired direction while complementary shear stresses are ideally applied in the specimen. The angle between the major principal stress and vertical, Ψ, is tied to the parameter b ($=(\sigma_2-\sigma_3)/(\sigma_1-\sigma_3)$), which indicates the relative magnitude of the intermediate principal stress σ_2. The relation between b and Ψ is given by $b=\sin^2\Psi$ (Geiger and Lade, 1979). Therefore, the influence of σ_2 on the strength characteristics can be also investigated in the torsion shear apparatus.

In a torsion shear test, the hollow cylinder specimen is exposed to a plane stress state when the inside and outside pressures are equal. In order to achieve this state of plane stress, the stresses and strains should be distributed uniformly in the specimen (Saada and Townsend, 1981). The uniformity can be maximized by employment of appropriate dimensions for the specimen. Experimental and theoretical studies (Lade, 1981 ; Wright et al., 1978 ; Hight et al., 1983) have been performed to produce appropriate specimen geometries in which the non-uniformity in stresses and strains within the specimen have been minimized.

Geiger and Lade (1979) studied the behavior of cohesionless soil during large stress reversals and reorientation of principal stresses in torsion shear tests. On the basis of a limited number of torsion shear tests performed on medium-loose sand, Symes et al. (1984) showed that the initial anisotropy could be changed significantly by the loading path. An excellent review and study of the behavior of sand in torsion shear tests was presented by Tatsuoka et al. (1986).

Saada and his co-workers have performed several investigations (1967, 1973, 1975, 1984) to study the influence of anisotropy on the stress-strain behavior of clay in torsion shear tests. The influence of cyclic loading on the behavior of clay in torsion shear tests has also been studied in the past (Hicher and Lade, 1987).

TORSION SHEAR APPARATUS

Fig. 1 shows a three-dimensional drawing of a torsion shear apparatus designed and constructed to permit individual control of confining pressure, vertical deviator stress

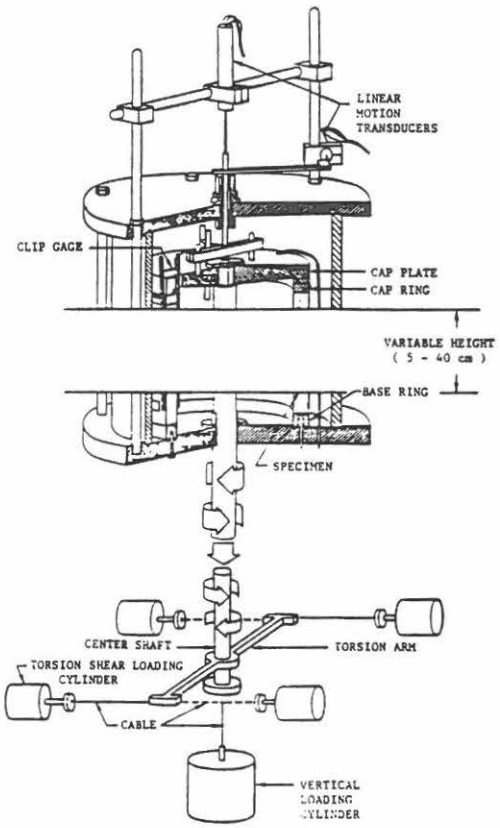

Fig. 1. Torsion shear apparatus

and shear stress to a hollow cylinder specimen. The design and operational principles of this apparatus are given by Lade (1981).

The hollow cylinder specimen employed for testing of clay has a height of 25 cm, an average diameter of 20 cm, and a wall thickness of 2 cm. Based on previous studies (Lade, 1981) these dimensions were found to be sufficient to neglect nonuniformities in stresses and strains in the specimen. The specimen is confined between cap and base rings and between inside and outside rubber membranes with thickness of 0.03 to 0.04 cm. The inside membrane was formed directly on the specimen while the outside prefabricated membrane was placed using a membrane stretcher. In order to form the inside membrane, the specimen was first sprayed with diluted rubber cement to seal it off. The inside surface was then sprayed or painted with several layers of fluid latex rubber. The fluid rubber was allowed to dry before another layer was applied. In order to transfer shear stresses from the cap and base rings to the specimen and to avoid slippage at their interfaces, full friction surfaces were provided on the rings. These consisted of a layer of sand grains glued to the rings by epoxy.

The entire setup is contained in a pressure cell, and the integrated hydraulic loading system is located below the table on which the apparatus sits. The same confining pressure is applied to the inside and outside surfaces of the specimen through the cell water that surrounds the specimen.

For the purpose of performing torsion shear tests on clay specimens, some modifications were made to the vertical loading cylinder and the torsion shear loading cylinders. An upward loading capability was added to the vertical loading cylinder. And the strokes of the torsion shear loading cylinders were increased so that larger torsional displacements can be imposed on the specimen. The maximum strains that can be achieved in this apparatus for a 25 cm tall specimen are $\varepsilon_z = \pm 25\%$ for vertical strains and $\gamma_{z\theta} = \pm 40\%$ for torsion shear strains, respectively.

The vertical load and the torque can be applied independently to the specimen through the center shaft and the cap plate, which is attached to the cap ring, as shown in Fig. 1. Both the vertical load and the torque can be either stress- or strain- controlled. The resulting deviator stress, together with the cell pressure, provides for a vertical, normal stress either larger or smaller than the confining pressure. Two sets of two interconnected pressure cylinders supply the horizontal load in either clockwise or counterclock-wise direction to the torsion arm connected to the center shaft.

During the torsion shear tests, the vertical load, the torque, the cell pressure, the vertical deformation, the change in thickness of

the wall, the outside and inside diameter changes, and the shear deformation were measured in addition to the pore pressure in undrained tests or the volumetric strain in drained tests.

CLAY TESTED

All tests were performed on Edgar Plastic Kaolinite (EPK) clay whose specific gravity was 2.62. The particle size distribution indicated that the clay consisted of 40% silt and 60% clay size particles. Atterberg limit tests produced $LL=60$ and $PL=30$. The activity was 0.5.

SPECIMEN PREPARATION

Remolded normally consolidated specimens at the K_0-stress condition were prepared from a slurry of EPK clay mixed at a water content of twice the liquid limit. The clay slurry was poured into a special consolidometer and consolidated at a vertical pressure of 2.00 kgf/cm² (196 kN/m²). The special consolidometer was built to make hollow cylindrical specimens for torsion shear tests. The consolidometer has a height of approximately 60 cm, an outer diameter of 26 cm, and an inner diameter of 16.5 cm. Two drainage plates consisting of porous plastic were placed on top and bottom of the clay slurry. In addition, long drainage strips made of porous plastic were attached along the outside wall to form a spiral from top to bottom, so it could be compressed easily as the clay slurry consolidated. After consolidation, the oversized hollow cylindrical clay sample was removed from the consolidometer and trimmed to its final dimensions in a specially designed trimming device with a rotating table and common trimming tools.

The specimen was then installed in the torsion shear apparatus and again consolidated under K_0-stress conditions by maintaining the volumetric strain equal to the vertical strain. Slotted filer paper drains were installed on the outside face of the specimen. The maximum drainage path was therefore equal to the thickness of the specimen wall (2 cm). During K_0-consolidation, a cell pressure of 4.00 kgf/cm² (392 kN/m²) and a back pressure of 2.00 kgf/cm² (196 kN/m²) were applied. The average value of K_0 for all tests was 0.55. The B-values ($=\Delta u/\Delta\sigma_{cell}$) measured after consolidation indicated that the specimens were fully staturated.

TESTING PROGRAM

Torsion Shear Tests

Fifteen undrained and two drained tests were performed on hollow cylinder specimens consolidated under K_0-stress conditions. Each test was conducted with constant confining pressure, σ_r, according to predetermined stress-paths, as shown in Fig. 2. The diagrams in this figure indicate the relations between the vertical stress difference, $(\sigma_z-\sigma_\theta)$, and the torsion shear stress, $\tau_{z\theta}$. In order to follow these stress-paths to failure and beyond, either the vertical stress difference or the torsion shear stress was applied under strain-control, and the other stress was stress-controlled. The vertical stress difference could be either increased or decreased. Strain rates of approximately 0.3 %/h for undrained tests and 0.06%/h for drained tests were employed for both vertical strain and shear strain in the strain-controlled directions. Based on a previous study of EPK clay (Kirkgard, 1981), these strain rates were found to be sufficiently slow for equalization of pore pressures in undrained tests and pore pressure dissipation in drained test.

The shear stress due to the torque produces reorientation of the principal stress directions as well as a stress state with three unequal principal stresses. If shear stresses are not applied to the specimen, the confining pressure σ_r becomes the minor principal stress σ_3 in a compression test, or the major principal stress σ_1 in an extension test. With torsional shear stresses the confining pressure becomes the intermediate principal stress σ_2.

The angle between σ_1 and vertical, Ψ, can be calculated from the following expression

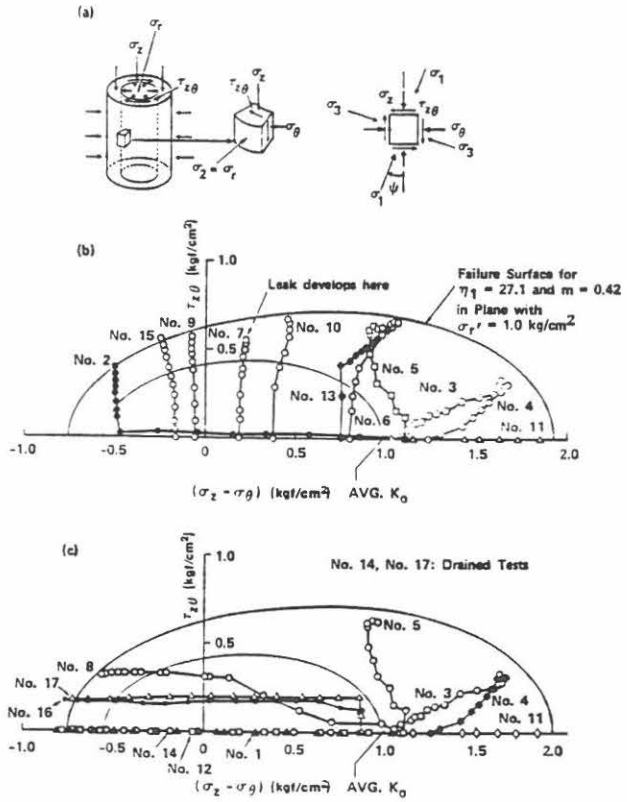

Fig. 2. (a) Stresses in hollow cylinder specimen, (b) and (c) stress-paths in torsion shear tests

$$\tan 2\Psi = \frac{2\cdot\tau_{z\theta}}{\sigma_z - \sigma_\theta} \qquad (1)$$

The value of Ψ can be varied between 0° in triaxial compression to 90° in triaxial extension. The value of b ($=\sin^2\Psi$) can be chosen between zero and unity, which covers the full range of the intermediate principal stress.

Stress-Paths

All shear tests were started after K_0-consolidation in the torsion shear apparatus. The stress-paths projected on the plane of $\sigma'_r = 1.00$ kgf/cm² (98 kN/m²) are shown in Figs. 2. Test No. 11 was performed as a triaxial compression test by increasing the vertical load under strain-control. Test Nos. 3, 4, 5, 6 and 13 were performed by increasing the torque under strain-control with only small changes of the vertical load. Test Nos. 2, 7, 9, 10 and 15 were performed by adjusting the vertical stress difference to the predetermined values under stress-control and then increasing the torque under strain-control. A leak developed in Test No. 7, and it could not be continued, as indicated in Fig. 2 (b). Test Nos. 8, 16 and 17 were performed by increasing the torsion shear stress under stress-control and then decreasing the vertical load under strain-control. Test Nos. 1, 12 and 14 were performed by decreasing the vertical load under strain-control to produce triaxial extension tests.

All except two tests were performed under undrained conditions. Test Nos. 14 and 17 were drained tests.

Triaxial Compression Tests

For comparison with the torsion shear tests, a series of triaxial compression tests with lubricated end plates were performed on cylindrical specimens with diameter=7.1 cm and height-to-diameter ratio of 1.0. The specimens were consolidated under isotropic and K_0-stress conditions and sheared at strain rates of 0.52%/h in undrained tests and 0.26%/h in drained tests.

In addition, triaxial compression tests were performed in a companion study on vertical and horizontal specimens of K_0-consolidated EPK clay. These produced stress-strain relations and undrained strengths that indicated negligible influence of orientation. The laboratory prepared clay was therefore taken to behave in an isotropic manner, although

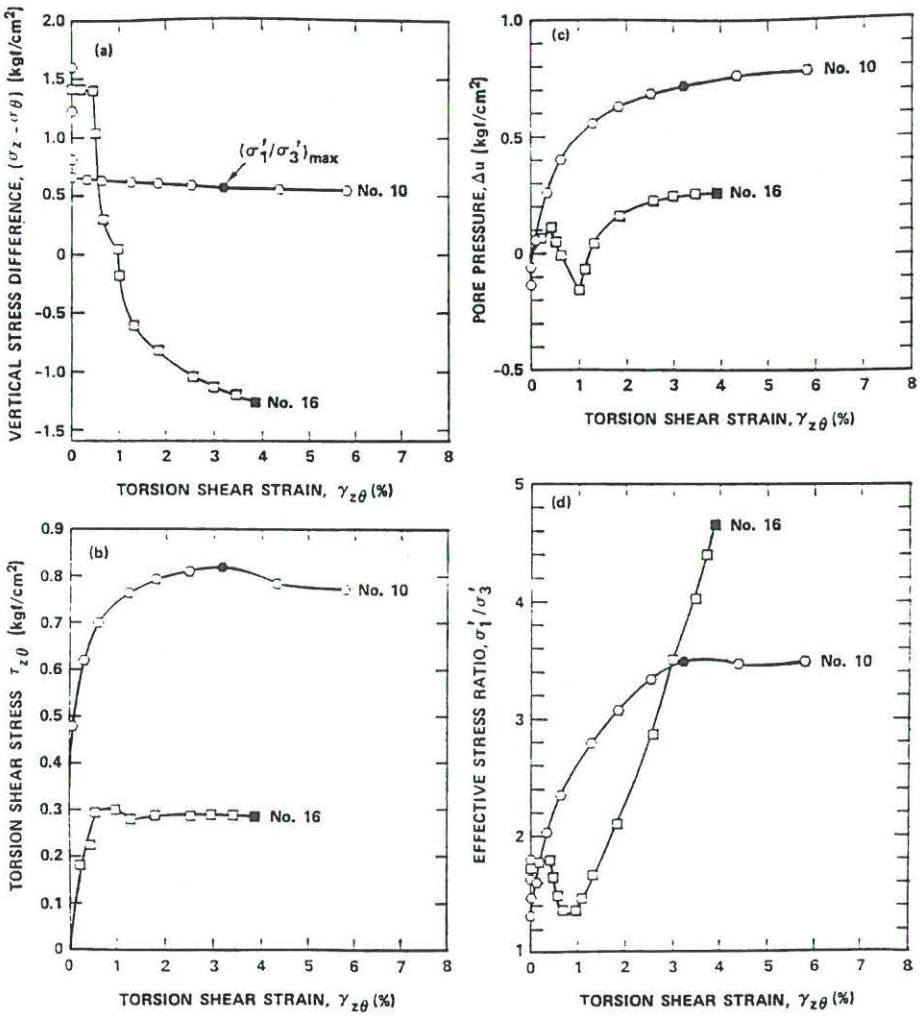

Fig. 3. (a) and (b) stress-strain, (c) excess pore pressure, and (d) effective stress ratio variations obtained in two typical torsion shear tests on Edgar Plastic Kaolinite

it had initially been K_0-consolidated. More detailed studies of the clay behavior might have indicated some anisotropic features, but these were not likely to be as pronounced as found in natural clays.

Natural clays have been produced by deposition of individual clay particles or clusters of particles, each allowed to settle and come to equilibrium with preferred orientation (most likely horizontal), and consolidated under K_0-conditions over long time periods, thus allowing the majority of creep to occur under current in-situ stresses. In comparison, the slurry of EPK clay mixed at two times the liquid limit may not have provided the individual particles with sufficient space to allow extensive alignment in a preferred direction. Further, sufficient time was allowed for the slurry to consolidate, but the amount of time allowed for creep after the end of primary consolidation was small. The EPK clay prepared for the present study therefore exhibited little anisotropy as a result of the initial K_0-consolidation. The experimental results of the torsion shear tests are consequently evaluated in view of isotropic plastic behavior.

TEST RESULTS

The results from Test Nos. 10 and 16 are shown in Fig. 3 to demonstrate the type of behavior obtained in the torsion shear tests. The vertical stress difference, $(\sigma_z-\sigma_\theta)$, the torsion shear stress, $\tau_{z\theta}$, the pore pressure, J_u, and the effective principal stress ratio, σ'_1/σ'_3, are plotted versus the torsion shear strain, $\gamma_{z\theta}$, in this figure. The stress-paths for these two tests are shown in Fig. 2.

The torsion shear stress in Test No. 10 was gradually increased causing increasing shear strain until the specimen failed, as shown in Fig. 3 (b). Strain softening developed after peak failure. In Test No. 16 the vertical stress difference was decreased while the shear strain increased until the specimen failed, as shown in Fig. 3 (a). The points corresponding to failure according to the maximum effective stress ratio are indicated on each curve. Although the specimens failed at significantly different values of torsion shear stress and vertical stress difference, there is only little difference in shear strain at failure.

Fig. 3 (c) shows that a negative pore pressure developed in Test No. 10 due to the reduction in vertical deviator stress, followed by a gradual increase caused by the applied torsion shear stress. The pore pressure in Test No. 16 increased due to the applied torque during the first part of the stress-path. The pore pressure then decreased during the initial reduction of the vertical deviator stress causing a negative pore pressure at the time of zero deviator stress. However, the pore pressure increased again as the vertical stress difference became negative.

Fig. 3 (d) shows that the effective principal stress ratio, σ'_1/σ'_3, in Test No. 10 first decreased slightly with decreasing vertical stress and then increased with increasing torque until the specimen failed. σ'_1/σ'_3 in Test No. 16 increased slightly with application of torque, then decreased with decreasing vertical load. However, σ'_1/σ'_3 again began to increase when the vertical stress difference became negative.

A set of stress-strain and pore pressure relations was obtained from each test, as exemplified by the diagrams in Fig. 3. It is the interpretation of these relations that are significant in understanding soil behavior. The experimental results are therefore presented and interpreted below in terms of several aspects of soil behavior.

STRENGTH CHARACTERISTICS

In order to study the effective strengths obtained in the torsion shear tests, the strength results have been compared internally and with those from the triaxial compression tests. Since the laboratory prepared clay exhibited little anisotropy as a result of the initial K_0-consolidation, the strength results were also compared with those predicted by an isotropic three-dimensional failure

criterion for soils. For torsion shear tests with the same inside and outside pressure, the effects of b ($=\sin^2\Psi$) and of the orientation of σ_1 (as measured by Ψ) cannot be separately examined. However, since the clay was essentially isotropic in behavior, the effect of b is described by the isotropic, three-dimensional failure criterion (Lade and Musante, 1978).

Failure Criterion

A three-dimensional failure criterion expressed in terms of stress invariants has previously been developed for soils (Lade, 1977). This isotropic failure criterion is expressed as :

$$(I_1^3/I_3-27)\cdot(I_1/p_a)^m=\eta_1 \qquad (2)$$

in which I_1 and I_3 are the first and the third invariants of the stress tensor, which for triaxial compression and torsion shear tests can be expressed as :

$$I_1=\sigma_1+\sigma_2+\sigma_3=\sigma_z+\sigma_r+\sigma_\theta \qquad (3)$$

$$I_3=\sigma_1\cdot\sigma_2\cdot\sigma_3=\sigma_z\cdot\sigma_r\cdot\sigma_\theta-\sigma_r\cdot\tau_{z\theta}\cdot\tau_{\theta z} \qquad (4)$$

and p_a is atmospheric pressure expressed in the same units as the stresses. The parameters η_1 and m are constants.

Fig. 4 shows the relation between (I_1^3/I_3-27) and (p_a/I_1) at failure in a log-log diagram. On this diagram η_1 is the intercept with $(p_a/I_1)=1$ and m is the slope of the straight line. The data from both torsion shear and triaxial compression tests on EPK clay are plotted on Fig. 4. The values of $\eta_1=27.1$ and $m=0.42$ are determined from a regression analysis for the best fitting straight line on this diagram.

Comparison of Failure Criterion and Test Data

The strength results from the torsion shear tests are presented on a diagram of torsion shear stress, $\tau_{z\theta}$, versus vertical stress difference, $(\sigma_z-\sigma_\theta)$, as shown in Fig. 5. The solid curve on this diagram represents the failure surface defined by Eq. (2). The failure surface is egg-shaped with a slightly more pointed end near the extension stress state. Whereas only one half of the surface is hown in Fig. 5, the other half is sym-

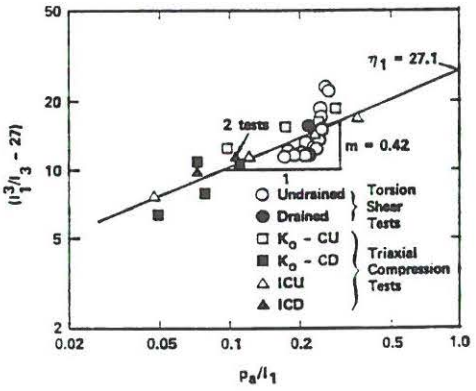

Fig. 4. Determination of material parameters η_1 and m involved in failure criterion for Edgar Plastic Kaolinite

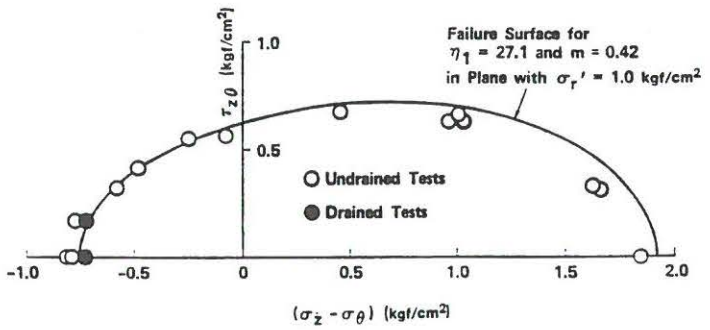

Fig. 5. Stress points at failure and failure surface for torsion shear tests on Edgar Plastic Kaolinite

metrical with that shown around the horizontal axis. Note that the failure surface is not an ellipse. An ellipse is obtained for the Mohr-Coulomb failure criterion.

The stress states at failure in the torsion shear tests did not correspond to the same value of the effective radial stress σ'_r. However, it is desirable to compare the data points on the same effective radial stress plane such that a common basis for the comparison exists. The experimental points shown in Fig. 5 have therefore been projected to a common σ'_r-plane corresponding to $\sigma'_r=1.00$ kgf/cm² (98 kN/m²). The adjusted stress states were obtained by projection of each individual stress point along a curved failure envelope. This is done mathematically using a technique involving Eq. (2) for the failure criterion.

The stresses at failure from all torsion shear tests are plotted on Fig. 5. The test results with compressive axial loads are slightly inside the failure envelope, while the test results close to $b=1.0$ were slightly outside the failure envelope. The largest difference occurred in the undrained tests close to $b=1.0$ in which the values of the effective minor principal σ'_3 were very small. Two drained tests were therefore performed to establish the failure envelope near the extension condition. The results of these two tests appear to steady the failure envelope near extension, as shown in Fig. 5. It may be seen that the failure envelope represents the failure points obtained from the torsion shear tests with reasonable accuracy. Thus, the stress conditions of K_0-consolidated clay at failure were not much affected by stress-paths and rotation of principal stress directions. The experimentally obtained failure surface from torsion shear tests can therefore be modeled with good accuracy by the isotropic failure criterion defined by Eq. (2).

As indicated on Figs. 3 and 5, the effects of stress-paths and reorientation of principal stresses were mainly observed in the pre-failure stress-strain behavior of K_0-consolidated clay, whereas sufficient changes in the clay fabric had occurred at large strains to produce failure conditions that adhered to an isotropic failure criterion.

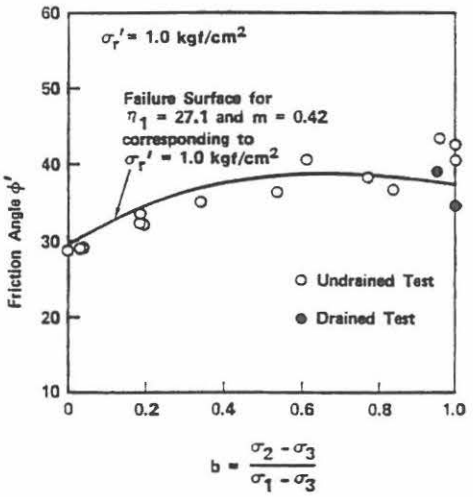

Fig. 6. Effective friction angles and failure surface shown in ϕ-b diagram for torsion shear tests on Edgar Plastic Kaolinite

Effective Friction Angle

The variation of the measured effective friction angle with the value of b is shown in Fig. 6. The friction angle ϕ' was computed from

$$\sin\phi' = \frac{\sigma'_1 - \sigma'_3}{\sigma'_1 + \sigma'_3} = \frac{2\sqrt{\tau_{z\theta}^2 + (\sigma_z - \sigma_\theta)^2/4}}{(\sigma'_z + \sigma'_\theta)} \quad (5)$$

where $\sigma'_\theta = \sigma'_{cell}$. The friction angle is affected by the b-value which in turn represents the intermediate principal stress. The friction angle was smallest for $b=0.0$ and it increased initially with increasing magnitude of the intermediate principal stress σ'_2 until b reached 0.6. The friction angle was largest at $b=1.0$ in undrained tests. However, as discussed in connection with Fig. 5, the results of the undrained tests were less reliable than those from the drained tests. The friction angles from the drained tests, corresponding to b-values near 1.0,

were smaller than those from the undrained tests. Thus, a small decrease in friction angle from $b=0.6$ to 1.0 is indicated. Cubical triaxial tests performed on clay and sand have shown the same tendency (Lade and Duncan, 1973 ; Lade and Musante, 1978 ; Ochiai and Lade, 1983 ; Tsai and Lade, 1985).

The solid line on the diagram is the failure surface described by the criterion in Eq. (2). This failure criterion appears to account fairly well for the experimental data. Therefore, any influence of the orientation of σ_1 (as measured by Ψ) appears to be negligible as expected for an isotropic material.

RELATIONS BETWEEN STRAINS

Work-Space

Fig. 7 illustrates a suitable space in which to view the results of torsion shear tests. The vertical axis represents the effective confining pressure, σ'_r, and the horizontal axis represents the vertical stress difference, $(\sigma_z-\sigma_\theta)$, and the torsion shear stress, $\tau_{z\theta}$. In this diagram the failure surface defined by Eq. (2) forms a cone with origin at $\sigma'_r=0$. The cross-section of the failure surface on a plane with $\sigma'_r=$const. resembles an egg. The egg-shaped failure surface grows from

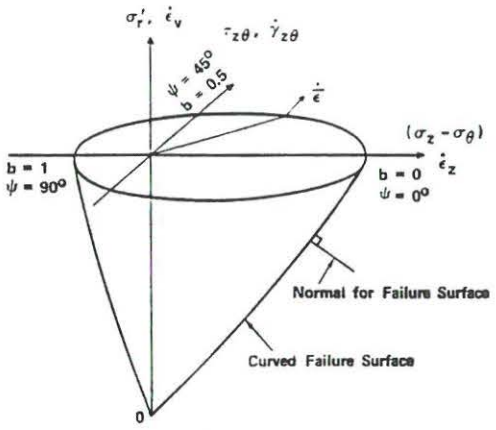

Fig. 7. Three-dimensional stress space suitable for study of data from torsion shear tests

the origin of the $(\sigma_z-\sigma_\theta)$ and $\tau_{z\theta}$-axes, as indicated in Figs. 2 and 5. Failure does not occur for stresses inside this three-dimensional, conical surface.

The increment in work done by the stresses in torsion shear tests can be expressed as follows :

$$dW=\sigma_\theta\cdot\dot{\epsilon}_\theta+\sigma_z\cdot\dot{\epsilon}_z+\sigma_r\cdot\dot{\epsilon}_r+\tau_{zr}\cdot\dot{\gamma}_{zr}+\tau_{r\theta}\cdot\dot{\gamma}_{r\theta}+\tau_{z\theta}\cdot\dot{\gamma}_{z\theta} \quad (6)$$

where $\dot{\epsilon}_\theta$, $\dot{\epsilon}_z$, and $\dot{\epsilon}_r$ are linear strain increments, and $\dot{\gamma}_{zr}$, $\dot{\gamma}_{r\theta}$, and $\dot{\gamma}_{z\theta}$ are engineering shear strain increments. The boundary conditions in a torsion shear test are such that :

$$\tau_{zr}=\tau_{r\theta}=0$$
$$\sigma_\theta=\sigma_r=\sigma_{cell}$$
$$\dot{\gamma}_{zr}=\dot{\gamma}_{r\theta}=0$$

Thus,

$$dW=\sigma_\theta\cdot\dot{\epsilon}_\theta+\sigma_z\cdot\dot{\epsilon}_z+\sigma_r\cdot\dot{\epsilon}_r+\tau_{z\theta}\cdot\dot{\gamma}_{z\theta}$$

This expression can be further specialized for the conditions in the torsion shear test :

$$dW=(\sigma_z-\sigma_\theta)\cdot\dot{\epsilon}_z+\sigma_\theta\cdot\dot{\epsilon}_z+\sigma_\theta\cdot\dot{\epsilon}_\theta+\sigma_r\cdot\dot{\epsilon}_r+\tau_{z\theta}\cdot\dot{\gamma}_{z\theta}$$
$$dW=(\sigma_z-\sigma_\theta)\cdot\dot{\epsilon}_z+\sigma_r\cdot(\dot{\epsilon}_\theta+\dot{\epsilon}_z+\dot{\epsilon}_r)+\tau_{z\theta}\cdot\dot{\gamma}_{z\theta}$$

Since the volumetric strain increment $\dot{\epsilon}_v=\dot{\epsilon}_\theta+\dot{\epsilon}_z+\dot{\epsilon}_r$,

$$dW=(\sigma_z-\sigma_\theta)\cdot\dot{\epsilon}_z+\sigma_r\cdot\dot{\epsilon}_v+\tau_{z\theta}\cdot\dot{\gamma}_{z\theta} \quad (7)$$

Therefore, to study the type of behavior observed in the space shown in Fig. 7, the strain increments, $\dot{\epsilon}_z$, $\dot{\epsilon}_v$, and $\dot{\gamma}_{z\theta}$ are superimposed on the stress axes corresponding to $(\sigma_z-\sigma_\theta)$, σ_r, and $\tau_{z\theta}$, respectively. The strain increments form a vector, $\dot{\bar{\epsilon}}$, as exemplified by that initiating at the failure surface on Fig. 7.

The results of torsion shear tests on hollow metal tubes presented by Taylor and Quinney (1931) were analyzed in view of the following equation for the increment in work :

$$dW=\sigma_z\cdot\dot{\epsilon}_z+\tau_{z\theta}\cdot\dot{\gamma}_{z\theta} \quad (8)$$

Since the metal tubes were unconfined, $\sigma_\theta=\sigma_r=0$, and for solid metals $\dot{\epsilon}_v=0$. Eq. (8) is therefore a special case of the more general expression in Eq. (7) which allows for volumetric strains in the material.

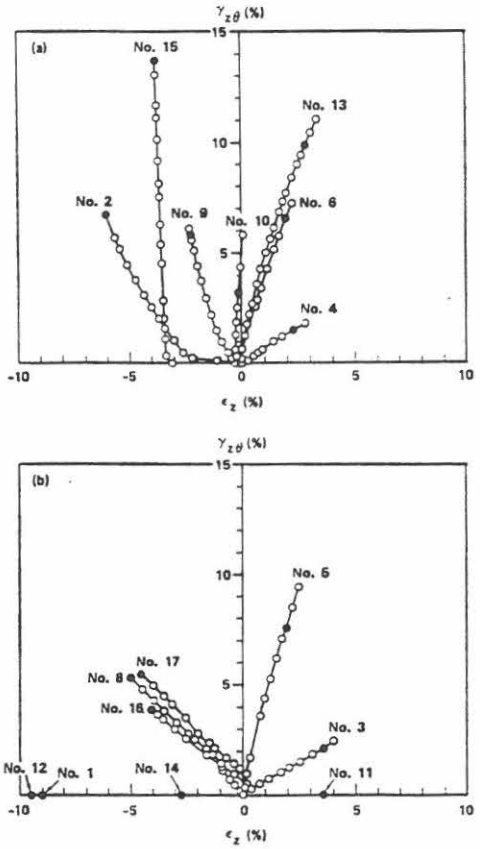

Fig. 8. Relstions between axial strains and engineering shear strains obtained in torsion shear tests on Edgar Plastic Kaolinite

Relations Between Axial and Shear Strains

The axial strains, ε_z, are plotted versus the engineering shear strains, $\gamma_{z\theta}$, in Fig. 8. The points corresponding to failure are indicated as black points on each curve in this diagram. The axial strains are compressive for tests with b-values smaller than 0.5 and expansive for larger b-values.

Note that considerable axial strains occurred in the tests in which the axial stress was held essentially constant. This coupling effect between shear stress and axial strain was observed in most cases when shear stresses were applied. Comparison of stress-paths in Fig. 2 (b) with strains in Fig. 8 (a) indicates this effect. A similar coupling effect between shear strains and axial stresses was observed in tests in which shear stress was applied and held constant and the axial stress was varied. This may be seen by comparison of stress-paths in Fig. 2 (c) with strains in Fig. 8 (b). These coupling effects between stresses and strains are typical of materials that behave plastically. They cannot be predicted by theory of elasticity.

Directions of Strain Increment Vectors

It is of interest to study the directions of plastic strain increment vectors relative to the failure surface in the work-space. If the failure surface is taken as the ultimate yield surface, it may be deduced whether associated flow is obtained for the clay. The increment

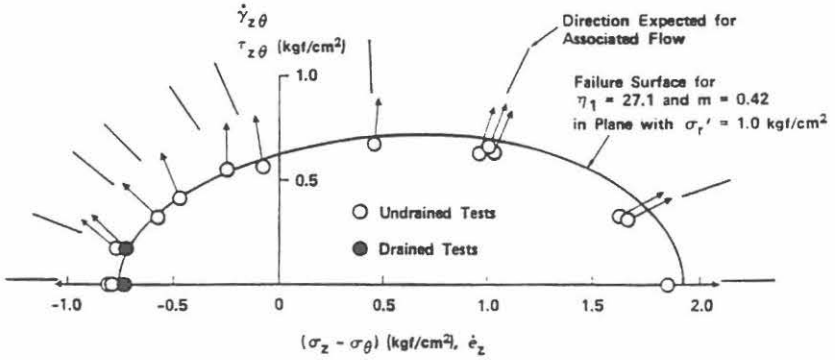

Fig. 9. Directions of strain increment vectors at failure in torsion shear tests on Edgar Plastic Kaolinite

axes of vertical strain, $\dot{\varepsilon}_z$, and torsion shear strain, $\dot{\gamma}_{z\theta}$, are therefore superimposed on the vertical stress difference, $(\sigma_z-\sigma_\theta)$, and torsion shear stress, $\tau_{z\theta}$, respecively, in the work space shown in Fig. 7. Only the directions of the strain increment vectors at failure will be considered. All strain increments are plastic at failure, because the changes in stress at failure are negligible, thus resulting in negligible elastic strain increments. The directions of the strain increment vectors are obtained from the slopes of the relations between ε_z and $\gamma_{z\theta}$ shown in Fig. 8.

The directions of strain increment vectors on the plane corresponding to $\sigma'_r=1.00$ kgf/cm^2 (98 kN/m^2) are shown in Fig. 9 together with the projected failure stress points and the failure surface defined by Eq. (2). The projected directions corresponding to associated flow are also indicated on this figure. These directions were derived mathematically as the normals to the failure surface. Note that these projected directions are not quite normal to the failure surface in Fig. 9. It may appear that the experimental directions for practical purposes coincide in direction with these normals for b-values smaller than 0.5, but coincidence is not obtained for most of the tests with larger b-values.

The experimental strain increment vectors are entirely contained in the plane in Fig. 9. This is because they correspond to undrained tests in which $\dot{\varepsilon}_r=0$. However, the directions expected for associated flow are not contained in this plane but projected onto the diagram. This is because yield surfaces for soils near failure most likely are inclined in a manner similar to the failure surface, but they cross the failure surface at a very shallow angle (Tatsuoka and Ishihara, 1974; Lade and Kim, 1989). The normal to the yield surface at failure is therefore almost perpendicular to the failure surface. Fig. 7 shows a normal to the failure surface. It is clearly not contained in the $(\sigma_z-\sigma_\theta)$-$\tau_{z\theta}$ plane. Thus, the experiments indicate that nonassociated flow most likely is necessary to model the observed behavior. A similar conclusion was reached by Lade and Musante (1977) on the basis of cubical triaxial tests performed on normally consolidated Grundite clay.

CONCLUSIONS

A series of torsion shear tests was performed on remolded K_o-consolidated Edgar Plastic Kaolinite under drained and undrained conditions to investigate the influence of reorientation of principal stress directions on the behavior of the clay. The influence of rotation of principal stresses on the stress-strain, and strength characteristics was observed as follows:

(1) The effects of stress-paths and reorientation of principal stresses were mainly observed in the prefailure stress-strain behavior.

(2) The failure surface obtained from torsion shear tests could practically be modeled by an isotropic failure criterion proposed by Lade (1977).

(3) The most accurate results of torsion shear tests close to $b=1.0$ were obtained under drained conditions.

(4) Coupling effects between shear stress and axial strain and between axial stress and shear strain were observed in most cases when shear and axial stresses were applied.

(5) The experimental strain increment vectors in the work-space were not perpendicular to the yield surface at failure. Nonassociated flow may therefore be required for models developed to capture the behavior of normally consolidated clay.

ACKNOWLEDGMENT

A portion of the study presented here was supported by the National Science Foundation, U. S. A., under Grant No. ENG-78-20239. The study was continued while the first writer was on leave at the University of California, Los Angeles, California. Support for the first writer was provided by the Korea Science and Engineering Foundation, Korea. Grateful appreciation is expressed to

both Foundations for their support of this study.

REFERENCES

1) Bjerrum, L. and Landva, A. (1966) : "Direct simple-shear tests on a Norwegian quick clay," Geotechnique, Vol. 16, No. 1, pp. 1-20.
2) Broms, B. B. and Casbarian, A. O. (1965) : "Effects of rotation of the principal stress axes and of the intermediate principal stress on shear strength," Proceedings, 6 th International Conference on Soil Mechanics and Foundation Engineering, Montreal, Canada, Vol. I, pp. 179-183.
3) Geiger, E. and Lade, P. V. (1979) : "Experimental study of the behavior of cohesionless soil during large stress reversals and reorientation of principal stresses," Report No. UCLA-ENG-7917, University of California, Los Angeles.
4) Hicher, P.-Y. and Lade, P. V. (1987) : "Rotation of principal directions in K_0-consolidated clay," Journal of Geotechnical Engineering, ASCE, Vol. 113, No. 7, pp. 774-788.
5) Hight, D. W., Gens, A. and Symes, M. J. (1983) : "The development of a new hollow cylinder apparatus for investigating the effects of principal stress rotation in soils," Geotechnique, Vol. 33, No. 4, pp. 355-383.
6) Kirkgard, M. M. (1981) : "Consolidation characteristics determined during the constant rate of strain consolidation test," M. S. Thesis, University of California, Los Angeles.
7) Lade, P. V. (1975) : "Torsion shear tests on cohesionless soil," Proceedings, 5 th Panamerican Conference on Soil Mechanics and Foundation Engineering, Buenos Aires, Argentina, Vol. I, pp. 117-127.
8) Lade, P. V. (1976) : "Interpretation of torsion shear tests on sand," Proceedings, 2 nd International Conference on Numerical Methods in Geomechanics, Blacksburg, Virginia, Vol. I, pp. 381-389.
9) Lade, P. V. (1977) : "Elasto-plastic stress-strain theory for cohesionless soil with curved yield surfaces," International Journal of Solids and Structures, Pergamon Press, Inc., New York, N. Y., Vol. 13, pp. 1019-1035.
10) Lade, P. V. (1981) : "Torsion shear apparatus for soil testing," Laboratory Shear Strength of Soil, ASTM STP 740, R. N. Yong and F. C. Townsend, Eds., American Society for Testing and Materials, pp. 145-163.
11) Lade, P. V. and Duncan, J. M (1973) : "Cubical triaxial tests on cohesionless soil," Journal of the Soil Mechanics and Foundations Division, ASCE, Vol. 99, No. SM 10, pp. 793-812.
12) Lade, P. V. and Kim, M. K. (1988) : "Single hardening constitutive model for frictional materials, II. Yield criterion and plastic work contours," Computers and Geotechnics, Vol. 6, pp. 13-29.
13) Lade, P. V. and Musante, H. M. (1977) : "Failure conditions in sand and remolded clay," Proceedings, 9 th International Conference on Soil Mechanics and Foundation Engineering, Tokyo, Japan, Vol. I, pp. 181-186.
14) Lade, P. V. and Musante, H. M. (1978) : "Three-dimensional behavior of remolded clay," Journal of the Geotechnical Engineering Division, ASCE, Vol. 104, No. GT 2, pp. 193-209.
15) Macky, T. A. and Saada, A. S. (1984) : "Dynamics of anisotropic clays under large strains," Journal of Geotechnical Engineering, ASCE, Vol. 110, No. 4, pp. 487-504.
16) Ochiai, H. and Lade, P. V. (1983) : "Three-dimensional behavior of sand with anisotropic fabric," Journal of Geotechnical Engineering, ASCE, Vol. 109, No. 10, pp. 1313-1328.
17) Roscoe, K. H. (1953) : "An apparatus for the application of simple shear to soil samples," Proceedings, 3 rd International Conference on Soil Mechanics and Foundation Engineering, Zurich, Switzerland, Vol. I, pp. 186-191.
18) Roscoe, K. H., Bassett, R. H. and Cole, E. R. L. (1967) : "Principal axes observed during simple shear of a sand," Proceedings, the Geotechnical Conference, Oslo, Norway, Vol. I, pp. 231-237.
19) Saada, A. S. and Baah, A. K. (1967) : "Deformation and failure of a cross anisotropic clay under combined stresses," Proceedings, 3 rd Panamerican Conference on Soil Mechanics and Foundation Engineering, Venezuela, Vol. I, pp. 67-88.
20) Saada, A. S. and Bianchini, G. F. (1975) : "Strength of one dimensionally consolidated clays," Journal of the Geotechnical Engineering Division, ASCE, Vol. 101, No. GT 11, pp. 1151-1164.
21) Saada, A. S. and Ou, C.-D. (1973) : "Stress-strain relations and failure of anisotropic clays," Journal of the Soil Mechanics and Foundations Division, ASCE, Vol. 99, No. SM 12, pp. 1091-1111.
22) Saada, A. S. and Townsend, F. C. (1981) : "State-of-the-art : Laboratory strength testing

of soils," Laboratory Shear Strength of Soil, ASTM STP 740, R. N. Yong and T. C. Townsend, Eds., American Society for Testing and Materials, pp. 7-77.

23) Saada, A. S. and Zamani, K. K. (1973) : "The mechanical behavior of cross-anisotropic clays," Proceedings, 7 th International Conference on Soil Mechanics and Foundation Engineering, Moscow, USSR, Vol. 1, pp. 351-359.

24) Symes, M. J. P. R., Gens, A. and Hight, D. W. (1984) : "Undrained anisotropy and principal stress rotation in saturated sand," Geotechnique, Vol. 34, No. 1, pp. 11-27.

25) Tatsuoka, F. and Ishihara, K. (1974) : "Yielding of sand in triaxial compression," Soils and Foundations, Vol. 14, No. 2, pp. 63-76.

26) Tatsuoka, F., Sonoda, S., Hara, K., Fukushima, S. and Pradhan, T. B. S. (1986) : "Failure and deformation of sand in torsional shear," Soils and Foundations, Vol. 26, No. 4, pp. 79-97.

27) Taylor, G. I. and Quinney, H. (1931) : "The plastic distortion of metals," Phil. Trans. Roy. Soc., Vol. A 230, pp. 323-362.

28) Tsai, J. I. and Lade, P. V. (1985) : "Three-dimensional behavior of remolded overconsolidated clay," Report No. UCLA-ENG-85-09, University of California, Los Angeles.

29) Wright, D. K., Gilbert, P. A. and Saada, A. S. (1978) : "Shear devices for determining dynamic soil properties," Proceedings, ASCE Specialty Conference on Earthquake Engineering and Soil Dynamics, Pasadena, California, Vol. 2, pp. 1056-1075.

Strain Increment and Stress Directions in Torsion Shear Tests

By Won Pyo Hong[1] and Poul V. Lade,[2] Members, ASCE

Abstract: The directions of the major principal strain increment, stress, and stress increment during rotation of the principal stress axes at any stress level are studied for K_0-consolidated clay using a torsion shear apparatus with individual control of the vertical normal stress, the confining pressure, and the shear stress on hollow cylinder specimens under undrained and drained conditions. The torsion shear tests are performed along predetermined stress-paths, which are chosen to cover the full range of rotation of principal stress axes from 0° to 90° relative to vertical. The test results indicate that the major principal strain increment directions coincide with the major principal stress directions at failure. The directions of major principal strain increment coincide with the directions of major principal stress increment at low stress levels and with the directions of major principal stress at higher stress levels. This indicates that the behavior of clay gradually changes from elastic to plastic as the stress level is increased. Elasto-plastic theory is therefore suitable for modeling the behavior of clay during rotation of principal stress axes.

Introduction

The behavior of soils during reorientation of principal stresses in the field should be understood for correct modeling of their stress-strain behavior. Rotation of principal stress axes can only be accomplished in the laboratory by applying a combination of normal stresses and shear stresses to the surface of a soil specimen. A torsion shear apparatus, in which there is individual control of vertical normal stress, confining pressure, and shear stress applied to a hollow cylinder specimen, was employed in this study. Rotation of principal stress axes due to construction on or in soils can be reproduced in the torsion shear apparatus by various combinations of vertical loading and torque.

One of the most important pieces of information required for modeling the stress-strain behavior of soils concerns the direction of the principal strain increment relative to the directions of principal stress and stress increment during rotation of stress axes at any stress level. For the purpose of investigating the relations among the directions of strain increment, stress, and stress increment as shearing progresses, undrained and drained torsion shear tests were performed on hollow cylinder specimens according to predetermined stress-paths. The stress-paths were chosen to cover the full range of rotation of principal stress axes from 0° to 90° with vertical. Hollow cylinder specimens were prepared by consolidating Edgar plastic kaolinlte clay under K_0-conditions before shearing, thus introducing stress states in the clay specimens similar to those found in field deposits.

[1]Assoc. Prof., Dept. of Civ. Engrg., Coll. of Engrg., Chung-Ang Univ., Seoul, 156-756, Korea.

[2]Prof., Dept. of Civ. Engrg., School of Engrg. and Appl. Sci., Univ. of Calif., Los Angeles, CA 90024.

Note. Discussion open until March 1, 1990. To extend the closing date one month, a written request must be filed with the ASCE Manager of Journals. The manuscript for this paper was submitted for review and possible publication on January 17, 1989. This paper is part of the ***Journal of Geotechnical Engineering***, Vol. 115, No. 10, October, 1989. ©ASCE, ISSN 0733-9410/89/0010-1388/$1.00 + $.15 per page. Paper No. 23934.

Previous Studies

To rotate the directions of principal stresses in soil specimens during testing, a combination of normal and shear stresses must be applied to the surface of the specimen. A review of the advantages and limitations of equipment employed for this purpose was presented by Saada and Townsend (1981).

Various forms of ring shear apparatus have been developed for measurement of residual strength of soils (Bishop et al. 1971). As the ring shear test proceeds, however, the directions of principal stresses are uncertain and the strains are not distributed uniformly in the specimen. This type of apparatus can therefore not be used for the purpose of investigating effects of reorientation of principal stresses.

Reorientation of principal stresses can be achieved in simple shear devices (Bjerrum and Landva 1966; Roscoe 1953, 1970; Roscoe et al. 1967) and in torsion shear equipment (Bojanowski 1970; Broms and Casparian 1965; Hight et al. 1983; Hong and Lade 1988; Ishibashi and Sherif 1974; Lade 1975, 1976, 1981; Lomize et al. 1969; Saada and Baah 1967; Saada and Bianchini 1975; Saada and Ou 1973). The simple shear device offers the advantage of testing soils under plane strain conditions. Roscoe and his coworkers (Roscoe 1970; Roscoe et al. 1967) have investigated the relation between the directions of strain increment and stress in sand during shear in simple shear devices. However, these apparatuses also have some disadvantages, which limit their use for more elaborate investigations (Lade 1975). The initial state of stress before shearing cannot be arbitrarily imposed. Only K_0-stress states can be imposed on the specimens before shearing. Further, the distributions of normal and shear stresses within the specimen are nonuniform (Roscoe et al. 1967; Wright et al. 1967). The evolution of the horizontal normal stress during shear is generally unknown (Saada and Townsend 1981).

Torsion shear equipment in which a hollow cylinder specimen is confined horizontally between membranes has also been employed to a limited extent during the last two decades. This equipment offers the advantage that no shear stresses are induced on the vertical surfaces of the specimen, complementary shear stresses are automatically applied to the specimen, and large and fairly uniform shear strains can be produced. Furthermore, individual control of the vertical normal stress, the confining pressure, and the shear stress makes it possible to impose various initial states of stress before the specimen is sheared (Lade 1981). However, this type of equipment also has limitations in terms of nonuniformity of stress and strain distributions, especially in specimens with inappropriate dimensions (Saada and Townsend 1981; Wright et al. 1978). In a torsion shear test, the hollow cylinder specimen should be exposed to a plane stress state (when the inside and outside pressures are equal). In order to obtain this state, the stresses and strains should be distributed uniformly in the specimen (Saada and Townsend 1981). But nonuniformities can be minimized in specimens with appropriate dimensions (Lade 1981). Thus: (1) The ratio of wall thickness and specimen diameter should be small; and (2) the height-to-diameter ratio should be high enough to avoid severe effects of end restraint, and it should be small enough to avoid buckling of the hollow cylinder specimen. With careful attention to the geometry of the specimen, the torsion shear apparatus is considered to be well suited for investigating the influence of reorientation of principal stresses. Saada and his coworkers (Saada and Baah 1967; Saada and Bianchini 1975; Saada and Ou 1973; Saada and Townsend 1981; Saada and Zamani 1973) have used the torsion shear apparatus to determine the stress-strain behavior of anisotropic clay. Recently, Hight and his coworkers (Hight et al. 1983; Symes et al. 1984) built a torsion shear apparatus and studied the effects of initial anisotropy of sand in a limited number of tests. Tatsuoka et al. (1986) have also studied failure and deformation of sand.

Torsion Shear Apparatus

Fig. 1 shows a three-dimensional drawing of a torsion shear apparatus designed and constructed to permit individual control of confining pressure, vertical deviator stress, and shear stress applied to a hollow cylinder specimen.

The hollow cylinder specimen employed here has height of 25 cm, average diameter of 20 cm, and wall thickness of 2 cm. Based on previous studies (Lade 1981) these dimensions were sufficient to neglect nonuniformities in stresses and strains in the specimens due to boundary effects. The specimen is confined between cap and base rings and inside and outside rubber membranes with thicknesses of 0.03 to 0.04 cm. The inside membrane was formed directly on the specimen, while the outside prefabricated membrane was placed using a membrane stretcher. In order to form the inside membrane, the specimen was first sprayed with diluted rubber cement to seal it off. The inside surface was then sprayed or painted with several layers of fluid latex rubber. The rubber was allowed to dry between layers. In order to transfer shear stresses from the cap and base rings to the specimen and to avoid slippage at their interfaces, full friction surfaces were provided on the rings. These consisted of a layer of sand grains glued to the rings by epoxy.

The entire setup is contained in a pressure cell, and the integrated hydraulic loading system is located below the table on which the apparatus sits. The same confining pressure is applied to the inside and outside surfaces of the specimen through the cell water that surrounds the specimen. The design and operational principles of this apparatus are given in Lade (1981).

For the purpose of performing torsion shear tests on clay specimens, some modifications were made to the vertical loading cylinder and the torsion shear loading cylinders. Upward loading capability was added to the vertical loading cylinder, and the strokes of the torsion shear loading cylinders were increased so that larger torsional displacements could be imposed on the specimen. The maximum strains that can be achieved in this apparatus for a 25-cm tall specimen are $\pm\epsilon_z = 25\%$ for vertical strains and $\gamma_{z\theta} = \pm 40\%$ for torsion shear strains.

The vertical load and the torque can be applied independently to the specimen through the center shaft and the cap plate, which is attached to the cap ring, as shown in Fig. 1. Both the vertical load and the torque can be either stress- or strain-controlled. The resulting deviator stress, with the cell pressure, provides for a vertical normal stress either larger or smaller than the confining pressure. Two sets of two interconnected pressure cylinders supply horizontal load in either a clockwise or a counterclockwise direction to the torsion arm connected to the center shaft.

During the torsion shear tests, the vertical load, the torque, the cell pressure, the vertical deformation, the thickness change of the hollow cylinder

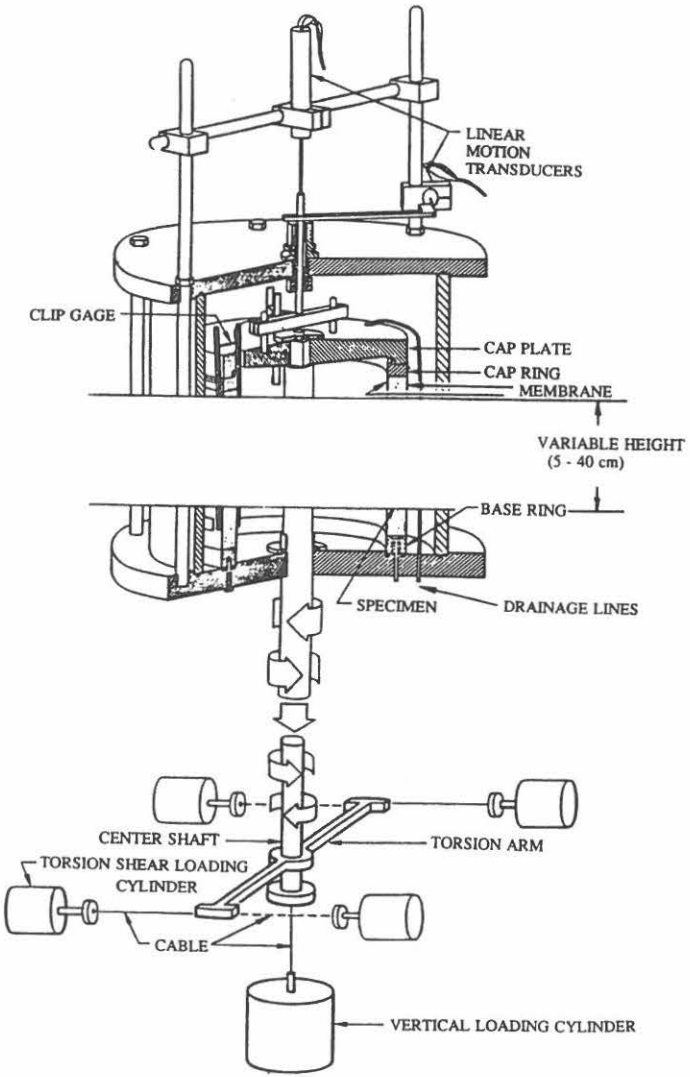

FIG. 1. Torsion Shear Apparatus

wall, and the shear deformation were measured in addition to the pore pressure in undrained tests or the volumetric strain in drained tests.

Clay Tested

All tests were performed on Edgar plastic kaolinite (EPK) clay whose specific gravity was 2.62. The particle size distribution indicated that the clay consisted of 40% silt and 60% clay-size particles. Atterberg limit tests produced $LL = 60$ and $PL = 30$. The activity was 0.5.

Specimen Preparation

Remolded specimens consolidated under K_0-stress conditions were prepared from a slurry of EPK clay mixed at a water content of twice the liquid limit. The clay slurry was poured into a special consolidometer and consolidated at an effective vertical pressure of 2.00 kg/cm^2 (196 kPa). The special consolidometer was built to make hollow cylinder specimens for torsion shear tests. The consolidometer has a height of approximately 60 cm, an outer diameter of 26 cm, and an inner diameter of 16.5 cm. Two drainage plates consisting of porous plastic were placed on the top and bottom of the clay slurry. In addition, long drainage strips made of porous plastic were attached along the outside wall to form a spiral from top to bottom, so it could be compressed easily as the clay slurry consolidated. After consolidation, the oversized hollow cylindrical clay sample was trimmed to its final dimensions in a specially designed trimming device with a rotating table and common trimming tools.

The specimen was then installed in the torsion shear apparatus and again consolidated under K_0-stress conditions by maintaining the volumetric strain equal to the vertical strain. Slotted filter paper drains were installed on the outside face of the specimen. The maximum drainage path was therefore equal to the thickness of the specimen wall (2 cm). During K_0-consolidation, a cell pressure of 4.00 kg/cm^2 (392 kPa) and a back pressure of 2.00 kg/cm^2 (196 kPa) were applied. The vertical stress difference was increased gradually to maintain $\epsilon_v = \epsilon_1$ throughout the entire K_0-consolidation. The average value of K_0 for all tests was 0.55. The pore pressure parameter B ($=\Delta u/\Delta\sigma_{cell}$) measured after the consolidation stage indicated that the specimens were fully saturated.

Testing Program

Fifteen undrained and two drained torsion shear tests were performed on hollow cylinder specimens consolidated under K_0-stress conditions. Each test was conducted with constant confining pressure, σ_r, according to predetermined stress-paths shown in Fig. 2. The diagrams in this figure indicate the relations between the vertical stress difference, $(\sigma_z - \sigma_\theta)$, and the torsion shear stress, $\tau_{z\theta}$. The stress-paths are shown on two diagrams and different symbols are used for the sole purpose of clarity. Some stress-paths appear on both diagrams for purposes of comparison. In order to follow these stress-paths to failure and beyond, either the vertical stress difference or the torsion shear stress was applied under strain-control, and the other stress was stress-controlled. The vertical stress difference could be either increased or decreased. Strain rates of approximately 0.005%/min for undrained tests and 0.001%/min for drained tests were employed for both vertical strain and shear strain in the strain-controlled directions.

All shear tests were started after K_0-consolidation in the torsion shear apparatus. The stress-paths projected on the plane of $\sigma_r' = 1.00$ kg/cm^2 are shown in Fig. 2. Projection of effective stress-paths is performed by mul-

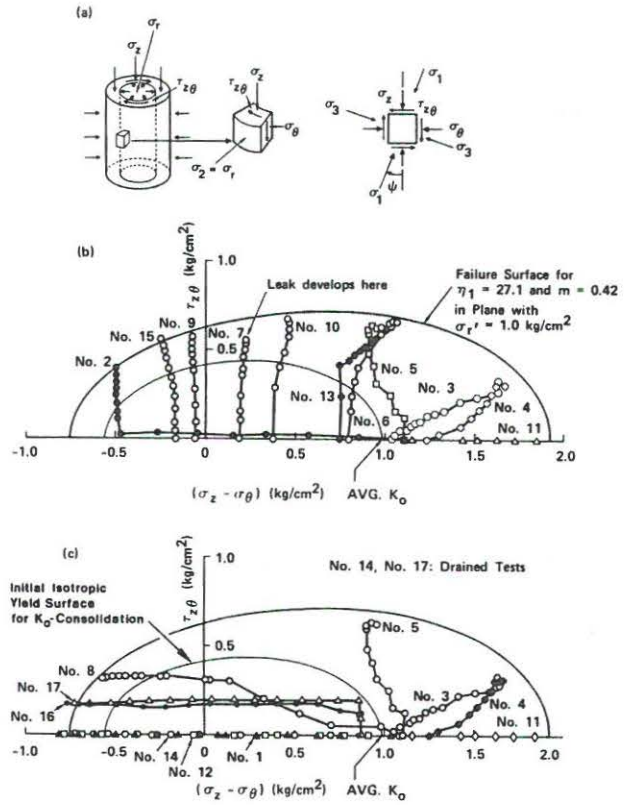

FIG. 2. (*a*) Stress in Hollow Cylinder Specimen; (*b*) and (*c*) Stress-Paths in Torsion Shear Tests in Plane with σ_r' = 1.0 kg/cm² (98 kPa)

tiplying the vertical stress difference and the applied shear stress by the ratio of σ_r' = 1.00 kg/cm² and the measured value of σ_r' (in the same stress units) at each stress point. Test 11 was performed as a triaxial compression test by increasing the vertical load under strain-control. Tests 3, 4, 5, 6, and 13 were performed by increasing the torque under strain-control with only small changes in the vertical load. Tests 2, 7, 9, 10, and 15 were performed by adjusting the vertical stress difference under stress-control to the predetermined values and then increasing the torque under strain-control. A leak developed in test 7 and it could not be continued, as indicated in Fig. 2(*b*). Tests 8, 16, and 17 were performed by increasing the torsion shear stress under stress-control and then decreasing the vertical load under strain-control. Tests 1, 12, and 14 were performed by decreasing the vertical load under strain control to produce triaxial extension tests. Tests 14 and 17 were conducted under drained conditions, whereas all other tests were performed under undrained conditions.

Relations between Strains

The shear strains, $\epsilon_{z\theta}$ ($=\gamma_{z\theta}/2$), are plotted versus the normal strain differences, $(\epsilon_z - \epsilon_\theta)/2$, in Fig. 3 for the specimens in tests 2, 3, 10, and 16, whose stress-paths are shown in Fig. 2. The points corresponding to failure according to the maximum effective stress ratio are indicated with a black solid point on each curve, and the values of $b = (\sigma_2 - \sigma_3)/(\sigma_1 - \sigma_3)$ at failure are indicated for each test in Fig. 3. The relations between the shear strains and the normal strain differences are almost linear, except at the beginning of the tests. The almost linear relations are more obvious at strains close to failure, where the behavior of the clay is plastic in nature.

Even though essentially constant vertical loads were supplied in tests 2 and 10, as shown by the stress-paths in Fig. 2, Fig. 3 indicates that normal strain differences occurred in addition to the shear strains caused by the torque. This "coupling effect" was more pronounced in test 2 than in test 10. A similar coupling effect between shear strains and axial stresses was observed in test 16, in which the axial stress was decreased while the shear stress was held constant.

Fig. 3 shows that the normal strain differences are expansive for values of $b[=(\sigma_2 - \sigma_3)/(\sigma_1 - \sigma_3)]$ larger than approximately 0.34 and compressive for smaller values of b. A given increment in b has a greater effect on the relation between the shear strains and the normal strain differences at small b-values than at high b-values.

Strain Increment and Stress Directions

The general pattern of directions of major principal strain increments at failure is of importance in considerations regarding the applicability of isotropic plasticity theory and the general framework required for modeling of

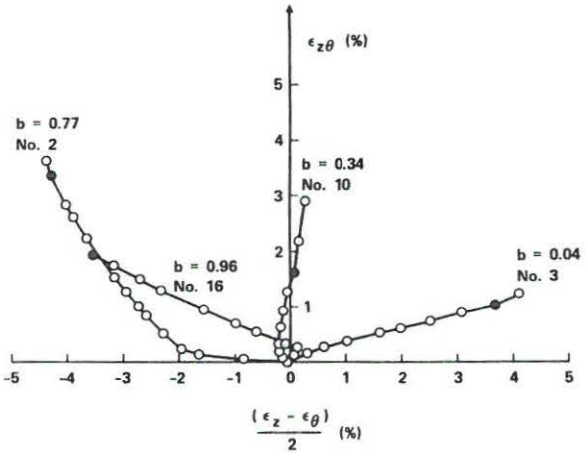

FIG. 3. Relations between Normal Strain Differences and Shear Strains in Four Torsion Shear Tests

clay with initial K_0-stress states. In order to investigate the soil behavior at failure, it is necessary to relate the directions of major principal strain increments to the directions of major principal stress in the physical space.

According to plasticity theory, the principal axes of plastic strain increments coincide in direction with the principal axes of stress during reorientation of stresses in isotropic materials, whereas the principal axes of elastic strain increments coincide in direction with the principal axes of stress increments according to isotropic elasticity theory.

Triaxial compression tests performed in a companion study on vertical and horizontal specimens of K_0-consolidated EPK clay produced stress-strain relations and undrained strengths that indicated negligible influence of orientation. The laboratory-prepared clay was therefore taken to behave in an isotropic manner, although it had initially been K_0-consolidated. More detailed studies of the clay behavior might have indicated some anisotropic features, but these were not likely to be as pronounced as those found in natural clays.

Natural clays have been produced by deposition of individual clay particles or clusters of particles, each allowed to settle and come to equilibrium with preferred orientation (most likely horizontal), and consolidation under K_0-conditions over long time periods, thus allowing the majority of creep to occur under current in situ stresses. In comparison, the slurry of EPK clay mixed at two times the liquid limit may not have provided the individual particles with sufficient space to allow extensive alignment in a preferred direction. Further, sufficient time was allowed for the slurry to consolidate, but the amount of time allowed for creep after the end of primary consolidation was small. The EPK clay prepared for the present study, therefore, exhibited little anisotropy as a result of the initial K_0-consolidation. The experimental results of the torsion shear tests are consequently evaluated in view of isotropic elastic and plastic behavior.

Mohr Circles

The directions of major principal stress, major principal stress increment, and major principal strain increment during primary loading are shown in Fig. 4, where Ψ = angle between σ_1 and vertical, X = angle between $\Delta\sigma_1$ (=maximum of increments in $\tau_{z\theta}$, σ_z, and σ_θ) and vertical, ξ = angle between $\Delta\epsilon_1$ (=maximum of increments in $\epsilon_{z\theta}$, ϵ_z, and ϵ_θ) and vertical, respectively. The relationships from Fig. 4 are as follows:

$$\tan 2\Psi = \frac{2\cdot\tau_{z\theta}}{\sigma_z - \sigma_\theta} \quad \ldots\ldots (1)$$

$$\tan 2X = \frac{2\cdot\Delta\tau_{z\theta}}{\Delta\sigma_z - \Delta\sigma_\theta} \quad \ldots\ldots (2)$$

$$\tan 2\xi = \frac{2\cdot\Delta\epsilon_{z\theta}}{\Delta\epsilon_z - \Delta\epsilon_\theta} \quad \ldots\ldots (3)$$

Therefore, isotropic elastic behavior implies that $X = \xi$, and isotropic plastic behavior requires that $\Psi = \xi$.

Directions of Major Principal Strain Increments at Failure

Fig. 5 shows a diagram of $(\sigma_z - \sigma_\theta)/2$ versus $\tau_{z\theta}$ superimposed on a diagram of $(\Delta\epsilon_z - \Delta\epsilon_\theta)/2$ versus $\Delta\epsilon_{z\theta}$. The inclinations of stress directions should

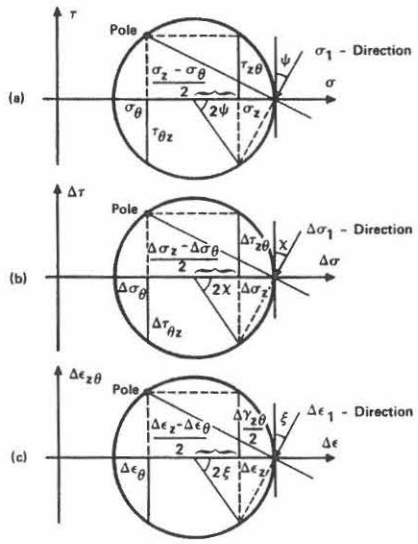

FIG. 4. Directions of Major Principal: (*a*) Stress; (*b*) Stress Increments; and (*c*) Strain Increment In Torsion Shear Tests

coincide with the inclination of strain increment directions for isotropic plastic behavior at failure, i.e.

$$\frac{2\cdot\tau_{z\theta}}{\sigma_z - \sigma_\theta} = \frac{2\cdot\epsilon_{z\theta}}{\Delta\epsilon_z - \Delta\epsilon_\theta} \quad \ldots\ldots (4)$$

where $2\cdot\tau_{z\theta}/(\sigma_z - \sigma_\theta)$ = the inclination of the stress direction; and $2\cdot\Delta\epsilon_{z\theta}/(\Delta\epsilon_z - \Delta\epsilon_\theta)$ = the inclination of the strain increment direction. In Fig. 5 the

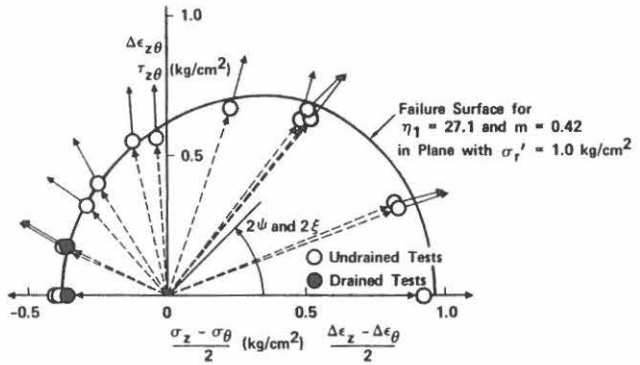

FIG. 5. Directions of Major Principal Stress and Strain Increments at Failure (Note that Double Angles are Shown)

major principal stress direction is represented by a line connecting the stress point at failure and the origin. The direction of the major principal strain increment is shown initiating from the stress point at failure. All strain increments are plastic at failure, because the changes in stress at failure are negligible, thus resulting in negligible elastic strain increments.

It should be noted that the stress states at failure in undrained tests most often do not correspond to the same value of effective confining stress, σ_r'. However, in order to indicate that failure was achieved in the tests under consideration, it may be desirable to plot the data points on the same effective confining stress plane. By projection of a given stress point along the curved failure envelope using a technique involving Lade's failure criterion (Lade 1984), it is possible to obtain the adjusted stress states. The failure stress points and the failure surface are shown in Fig. 5 on the plane corresponding to $\sigma_r' = 1.00$ kg/cm^2 (98 kPa). This failure surface is given by the following failure criterion proposed for isotropic soils (Lade 1984):

$$\eta_1 = \left(\frac{I_1^3}{I_3} - 27\right)\left(\frac{I_1}{p_a}\right)^m \quad \ldots\ldots (5)$$

in which I_1 and I_3 = the first and the third stress invariants which for the conditions in the torsion tests are defined as follows:

$$I_1 = \sigma_1 + \sigma_2 + \sigma_3 = \sigma_z + \sigma_r + \sigma_\theta \quad \ldots\ldots (6)$$

$$I_3 = \sigma_1 \cdot \sigma_2 \cdot \sigma_3 = \sigma_z \cdot \sigma_r \cdot \sigma_\theta - \sigma_r \cdot \tau_{z\theta} \cdot \tau_{\theta z} \quad \ldots\ldots (7)$$

and p_a = atmospheric pressure expressed in the same units as the stresses. The material parameters, η_1 and m, were determined to be 27.1 and 0.42, respectively, for Edgar plastic kaolinite (Hong and Lade 1989).

Only one half of the failure surface is shown in Fig. 5, because of symmetry in material behavior. The failure envelope is not a circle, but it has a unique shape that is symmetrical about the horizontal axis. It may be seen that the failure envelope represents the failure points obtained from the torsion shear tests with reasonable accuracy.

Fig. 5 shows that the major principal strain increment directions at failure for practical purposes coincide with the major principal stress directions. Only a few directions deviate slightly from each other. Because double angles are shown in Fig. 5, the deviations represent twice the deviations in physical space. The magnitudes of these deviations are so small that they could even be due to experimental inaccuracies. It appears that the effect of the initial K_0-stress state applied to the clay specimens to a large extent has been eliminated at failure, which occurred at relatively large strains in the torsion shear tests. Thus, any cross-anisotropy that might have developed in response to the initial K_0-consolidation did not affect the results at failure. Plasticity theory for isotropic materials can therefore be applied to modeling of K_0-consolidated clay at failure in torsion shear tests.

Effects of Rotation of Principal Stress Axes

A more detailed evaluation of the clay behavior in four representative tests is shown in Fig. 6. The variations of the angles between vertical and the directions of major principal stress Ψ, major principal stress increment X, and major principal strain increment ξ are plotted versus shear strain, $\gamma_{z\theta}$, for tests 2, 3, 10, and 16. The angles Ψ, X, and ξ were calculated from

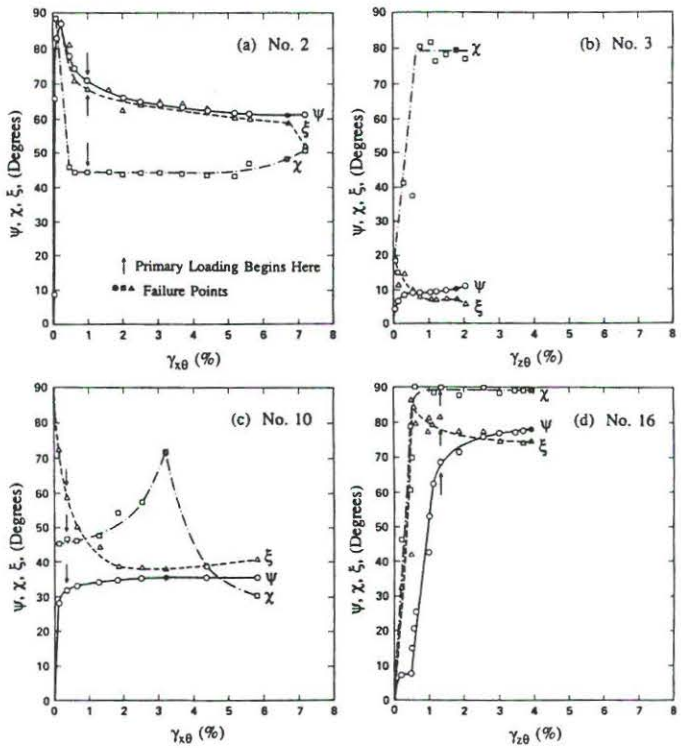

FIG. 6. Variations of Angles Ψ, X, and ξ versus Engineering Shear Strain in Four Torsion Shear Tests

Eqs. 1, 2, and 3, respectively. The arrows in the diagrams indicate the initiating points of primary loading. These points are indicated in Fig. 2, where the stress-paths cross the initial isotropic yield surface corresponding to K_0-consolidation. Thus, smaller shear strains than those shown at these points in Fig. 6 represent stress states of unloding or reloading from the K_0-stress states. The points corresponding to failure are also indicated on each curve.

Fig. 6 shows that the direction of major principal strain increment essentially coincide with the major principal stress increment direction at small shear strains or in the early stages of the tests. This indicates that the clay behaves as an isotropic elastic material at the beginning of the tests. As the stress level increased towards failure, the major principal strain increment direction approached and essentially coincided with the major principal stress direction. This is typical of isotropic plastic behavior.

Following K_0-consolidation, the stress-path in Fig. 2(b) shows that the specimen in test 2 was first unloaded vertically into the region of negative deviator stresses, then reloaded and finally primary-loaded by application of shear stresses. Fig. 6(a) shows that plastic behavior (i.e., $\Psi = \xi$) was ob-

tained slightly before the isotropic yield surface was crossed.

In test 3 [see stress-path in Fig. 2(*c*)] the specimen was primary-loaded directly from the K_0-stress state, and in this test there was essentially no elastic behavior, as indicated in Fig. 6(*b*).

Fig. 2(*b*) shows that the specimen in test 10 was first unloaded vertically, then reloaded and primary-loaded in shear. Fig. 6(*c*) indicates that a gradual transition from elastic to plastic behavior at higher stress levels was obtained in this test.

Finally, the stress-path for test 16 shown in Fig. 2(*c*) indicates that a shear stress was applied to the specimen immediately after K_0-consolidation, after which the vertical load was decreased to failure in the extension region. Most of this stress-path was located inside the isotropic yield surface, and elastic behavior is clearly indicated in Fig. 6(*d*) for the beginning of this test. A gradual transition occurred around the point where the stresses exceed the isotropic yield surface, and plastic behavior is obtained in the remaining portion of the test.

These observations from the torsion shear tests on Edgar plastic kaolinite indicate that the clay behaved as an elasto-plastic material. Thus, the applicability of isotropic elastoplastic theory for modeling the behavior of clay during rotation of the principal stress axes in torsion shear tests has been demonstrated.

Results from simple shear tests on sand reported by Roscoe and his coworkers (Roscoe 1970; Roscoe et al. 1967) showed behavior similar to that obtained in the present study on clay.

Conclusions

Undrained and drained torsion shear tests on hollow cylinder specimens of Edgar plastic kaolinite clay have been performed along various stress-paths for the purpose of investigating the relations among the directions of major prinicipal stress, stress increment, and strain increment during rotation of principal stress axes.

The clay prepared by K_0-consolidation of a slurry was found to exhibit little anisotropy. The effects of any initial cross-anisotropy caused by K_0-consolidation in the torsion shear tests were, to a large extent, eliminated at failure, which occurred at relatively large strains. The major principal strain increment directions coincided with the major principal stress directions at failure. Thus, isotropic plasticity theory may be applied for modeling the behavior of this clay at failure.

The experimental results also indicated that the directions of major principal strain increment essentially coincided with the directions of major principal stress increment at small stress levels inside the isotropic yield surface. This is typical of elastic behavior. A gradual transition from elastic to plastic behavior was observed as the stress level was increased, and the directions of major principal strain increment approached the directions of major principal stress at higher stress levels. These observations from the torsion shear tests show that the clay behaved as an elasto-plastic material. Isotropic elasto-plastic theory may therefore be suitable for modeling the behavior of K_0-consolidated EPK clay during rotation of the principal stress axes.

The study presented here provides the basic behavior of a laboratory-prepared, isotropic clay during rotation of principal stresses. The results may

therefore serve as a basis for comparison and evaluation of the behavior of natural clays that exhibit cross-anisotropic characteristics.

Acknowledgment

A portion of the study presented here was supported by the National Science Foundation under Grant No. ENG-78-20239. The study was continued while the first writer was on leave at the University of California, Los Angeles, Calif. Support for the first writer was provided by the Korea Science and Engineering Foundation, Korea. Grateful appreciation is expressed to both foundations for their support of this study.

Appendix. References

Bishop, A. W., et al. (1971). "A new ring shear apparatus and its application to the measurement of residual strength." *Geotechnique,* 21(4), 273–328.

Bjerrum, L., and Landva, A. (1966). "Direct simple-shear tests on a Norwegian quick clay." *Geotechnique,* 16(1), 1–20.

Bojanowski, W. (1970). "The study of the influence of intermediate principal stress on the strength of granular material." *Proc., 2nd Seminar on Soil Mech. and Found. Engrg.*, Lodz, Poland, 41–58.

Broms, B. B., and Casbarian, A. O. (1965). "Effects of rotation of the principal stress axes and of the intermediate principal stress on shear strength." *Proc., 6th Int. Conf. on Soil Mech. and Found. Engrg.*, Montreal, Canada, I, 179–183.

Hight, D. W., Gens, A., and Symes, M. J. (1983). "The development of a new hollow cylinder apparatus for investigating the effects of principal stress rotation in soils." *Geotechnique,* 33(4), 355–383.

Hong, W. P., and Lade, P. V. (1989). "Elasto-plastic behavior of K_0-consolidated clay in torsion shear tests." *Soils and Found.*, Tokyo, Japan, 29(2), 57–70.

Ishibashi, I., and Sherif, M. A. (1974). "Soil liquefaction by torsional simple shear device." *J. Geotech. Engrg. Div.*, ASCE, 100(8), 871–888.

Lade, P. V. (1975). "Torsion shear tests on cohesionless soil." *Proc., 5th Panamerican Conf. on Soil Mech. and Found. Engrg.*, Buenos Aires, Argentina, I, 117–127.

Lade, P. V. (1976). "Interpretation of torsion shear tests on sand." *Proc., 2nd Int. Conf. on Numerical Methods in Geomech.*, Blacksburg, Va., I, 381–389.

Lade, P. V. (1981). "Torsion shear apparatus for soil testing." *Laboratory Shear Strength of Soil,* ASTM STP 740, R. N. Yong and F. C. Townsend, eds., American Society for Testing and Materials, Philadelphia, Pa., 145–163.

Lade, P. V. (1984). "Failure criterion for frictional materials." *Mechanics of Engineering Materials,* C. S. Desai and R. H. Gallagher, eds., John Wiley and Sons, New York, N.Y., 385–402.

Lomize, G. M., et al. (1969). "Study on deformation and strength of soils under three-dimensional state of stress." *Proc., 7th Int. Conf. on Soil Mech. and Found. Engrg.*, International Society for Soil Mechanics and Foundation Engineering, I, 257–265.

Roscoe, K. H. (1953). "An apparatus for the application of simple shear to soil samples." *Proc., 3rd Int. Conf. on Soil Mechanics and Foundation Engineering,* Zurich, Switzerland, 186–191.

Roscoe, K. H. (1970). "Some results of tests in the latest model of the simple shear apparatus and new biaxial apparatus." *Veröffentlichungen des Institutes für Bodenmechanik and Felsmechanik der Universität Fridericiana,* Karlsruhe, W. Germany, Heft 44, 62–94.

Roscoe, K. H., Bassett, R. H., and Cole, E. R. I. (1967). "Principal axes observed during simple shear of a sand." *Proc., Geotech. Conf.*, Oslo, Norway, I, 231–237.

Saada, A. S., and Baah, A. K. (1967). "Deformation and failure of a cross aniso-

tropic clay under combined stresses." *Proc., 3rd Panamerican Conf. on Soil Mech. and Found. Engrg.*, Caracas, Venezuela, I, 67–88.
Saada, A. S., and Bianchini, G. F. (1975). "Strength of one-dimensionally consolidated clays." *J. Geotech. Div.*, ASCE, 101(11), 1151–1164.
Saada, A. S., and Ou, C.-D. (1973). "Stress-strain relations and failure of anisotropic clays." *J. Soil Mech. and Found. Div.*, ASCE, 99(12), 1091–1111.
Saada, A. S., and Townsend, F. C. (1981). "State-of-the-art: Laboratory strength testing of soils." *Laboratory Shear Strength of Soil*, ASTM STP 740, R. N. Yong and F. C. Townsend, eds., American Society for Testing and Materials, Philadelphia, Pa., 7–77.
Saada, A. S., and Zamani, K. K. (1973). "The mechanical behavior of cross-anisotropic clays." *Proc., 7th Int. Conf. on Soil Mech. and Found. Engrg.*, International Society for Soil Mechanics and Foundation Engineering, 1, 351–359.
Symes, M. J. P. R., Gens, A., and Hight, D. W. (1984). "Undrained anisotropy and principal stress rotation in saturated sand." *Geotechnique*, 34(1), 11–27.
Tatsuoka, F., et al. (1986). "Failure and deformation of sand in torsion shear." *Soils and Foundations*, Tokyo, Japan, 26(4), 79–97.
Wright, D. K., Gilbert, P. A., and Saada, A. S. (1978). "Shear devices for determining dynamic soil properties." *Proc., ASCE Specialty Conf. on Earthquake Engrg. and Soil Dynamics*, Pasadena, Calif., 2, 1056–1075.

Models for the Elastic Behavior of Soils

INTERNATIONAL JOURNAL FOR NUMERICAL AND ANALYTICAL METHODS IN GEOMECHANICS, VOL. 11, 521–542 (1987)

MODELLING THE ELASTIC BEHAVIOUR OF GRANULAR MATERIALS

POUL V. LADE AND RICHARD B. NELSON

Department of Civil Engineering, School of Engineering and Applied Science, University of California, Los Angeles, California 90024, U.S.A.

SUMMARY

A review of the literature indicates that the elastic behaviour of granular materials is isotropic and that Poisson's ratio is constant, whereas Young's Modulus, the bulk modulus and the shear modulus vary with the mean normal stress and the deviatoric stress. A nonlinear, isotropic model for the elastic behaviour is developed on the basis of theoretical considerations involving the principle of conservation of energy. Energy is therefore neither generated not dissipated in closed-loop stress paths or in closed-loop strain paths. The framework for the model consists of Hooke's law, in which Poisson's ratio is constant and Young's modulus is expressed as a power function involving the first invariant of the stress tensor and the second invariant of the deviatoric stress tensor. The characteristics of the model are described, and the accuracy is evaluated by comparison with experimental results from triaxial tests and three-dimensional cubical triaxial tests with a variety of stress paths. Parameter determination from unloading–reloading cycles in conventional triaxial compression tests is demonstrated, typical parameter values are given for granular materials and extension of the model to soils with effective cohesion is described.

INTRODUCTION

The time-independent stress–strain relations for soils may be characterized by elastic and plastic behaviour. Both strain components are nonlinear in nature, and the elastic strains are relatively small in the presence of plastic strains. However, the complete soil response consists of elastic strains along the initial portion of any general three-dimensional stress path involving unloading or reloading. The strains along stress paths such as proportional unloading are for practical purposes entirely elastic. Further, constitutive models must include elastic strain components in order to invert the stress–strain relations. Therefore, even though the elastic strain components may be small, they cannot be ignored.

Experimental results indicate that the elastic properties are functions of the state of the soil element, i.e. they may be expressed in terms of the soil density or void ratio and the state of stress acting on the soil. For a given void ratio, the elastic properties have been shown to vary with the mean normal stress as well as the deviatoric stress.

Presented here is an isotropic model for the elastic behaviour of soils. The model is based on a theoretical development which guarantees lack of energy generation or dissipation for any closed-loop stress path or any closed-loop strain path. Experimental data from conventional triaxial and three-dimensional cubical triaxial tests on sand are used to demonstrate the capabilities and the determination of soil parameters for the model.

0363–9061/87/050521–22$11.00

Received 15 September 1986

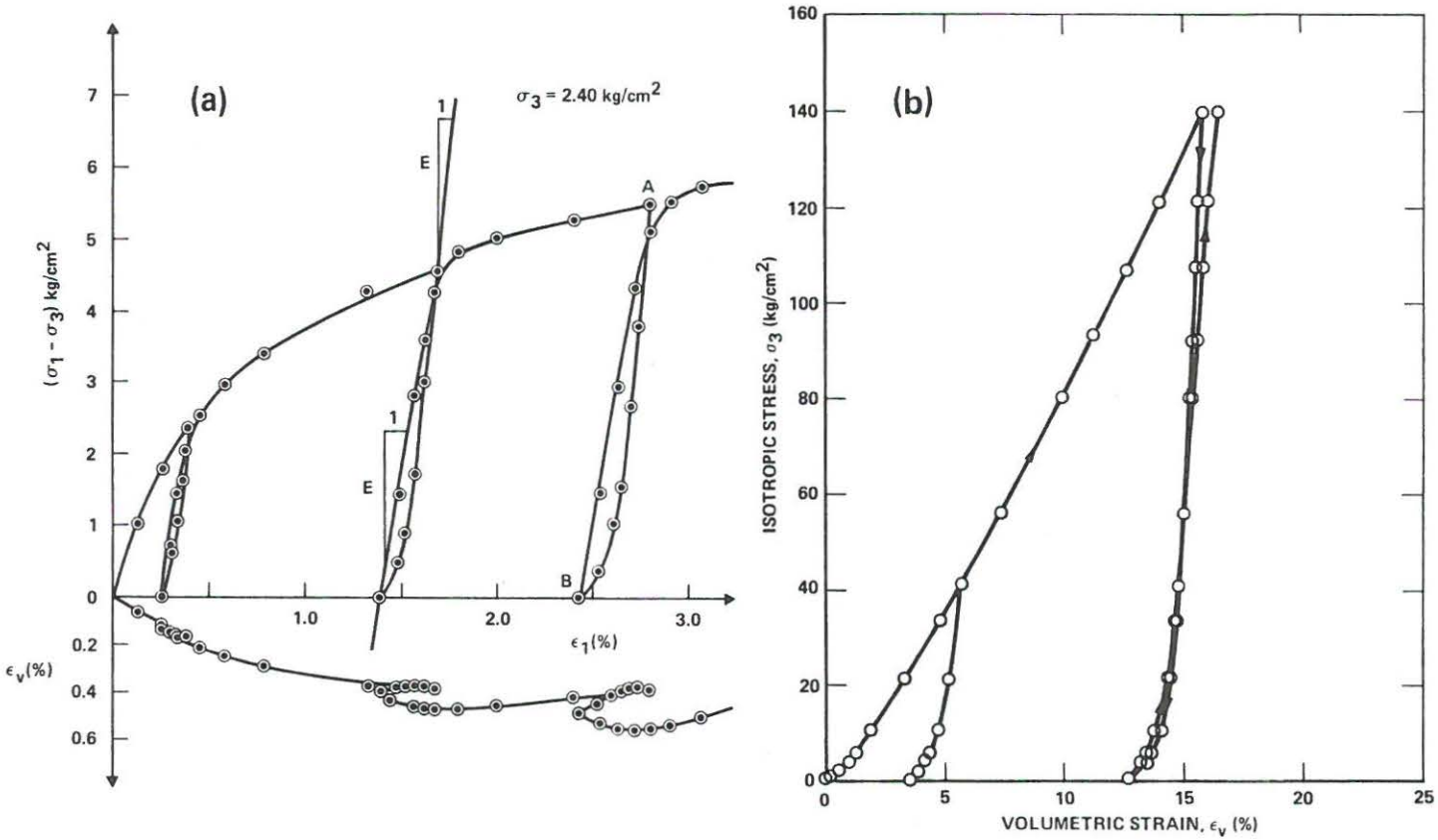

Figure 1. (a) Stress–strain and volume change behaviour of loose Santa Monica Beach Sand in triaxial compression test with several unloading–reloading cycles. (b) Isotropic compression of loose Sacramento River Sand with primary loading, unloading and reloading branches

OBSERVED BEHAVIOUR AND PREVIOUS MODELS

Basic observed behaviour

The framework for modelling the elastic behaviour of soil consists of Hooke's law, which for an isotropic material requires two independent parameters. These may be Young's modulus E and Poisson's ratio v or the bulk modulus B and the shear modulus G. The parameters B and G are related to E and v as follows:

$$B = \frac{E}{3(1-2v)} \tag{1}$$

$$G = \frac{E}{2(1+v)} \tag{2}$$

Experimental results indicate that E, B and G vary with the state of stress, whereas Poisson's ratio most often is assumed to be constant. Figure 1(a) shows the results of a conventional drained triaxial compression test on loose Santa Monica Beach Sand with three unloading–reloading cycles. The strains occurring immediately after each stress reversal are considered to be elastic. The elastic moduli indicated on the second cycle in Figure 1(a) are seen to vary with the deviatoric stress, since the effective confining pressure is maintained constant. Although the mean normal stress also varies in this test, an expression relating the elastic modulus to the mean normal stress is unable to capture the variation of Young's modulus correctly.[1]

Figure 1(b) shows the results of an isotropic compression test on loose Sacramento River Sand. The unloading–reloading branches, which for practical purposes are identical, indicate nonlinear elastic behaviour of the sand over a very large range of isotropic confining pressures.

Thus, both the mean normal stress and the deviatoric stress may influence the variations of the elastic moduli E, B and G. The most common models used to capture the variations of these three elastic moduli are briefly reviewed below.

Common models

Among the most widely studied modulus values is the initial tangent modulus, or initial slope of the stress–strain curve for triaxial compression. Both theoretical considerations and practical experiments[2–11] show that the initial tangent modulus may be expressed as a power function of the initially isotropic, effective confining pressure σ'_3:

$$E_i = K_i p_a \left(\frac{\sigma'_3}{p_a}\right)^n \tag{3}$$

in which p_a is atmospheric pressure expressed in the same units as E_i and σ'_3, K_i is a modulus number, and n is an exponent determining the rate of variation of E_i with σ'_3. Both K_i and n are dimensionless numbers. Janbu[8] presented results of a large number of tests. He found values of n from 0·35 to 0·55 for sands and silty sands with porosities of 35–50 per cent. Modulus numbers for the same sands had values from 50 to 500.

Because the initial slope of the stress–strain curve is often influenced by non-recoverable, plastic deformations, Duncan and Chang[12] proposed to use the slope of an unloading–reloading cycle from a triaxial compression test as the elastic modulus. This slope is determined between points A and B on the third cycle in Figure 1(a). Thus, K_i is replaced by K_{ur} in equation (3). Analyses of a large number of experiments[13] showed that K_{ur} was from 1 to 3 times higher than K_i, whereas n had the same value for initial loading and unloading–reloading.

The simple formulation in equation (3) has been widely used, because it appears to capture

the elastic behaviour observed in triaxial and isotropic compression, and the material parameters can be determined from the results of conventional triaxial tests. However, Zytynski *et al.*[14] pointed out that this model for the variation of Young's modulus results in violation of the principle of conservation of energy. Thus, depending on the direction of a closed stress loop, the model will generate or dissipate energy in violation of the basic premise of elastic behaviour.

The deformation characteristics of a soil may also be expressed through the bulk modulus B, which is related to the hydrostatic stress component, and the shear modulus G, which is related to the deviatoric stress component. The advantage of using B and G is that these parameters may be evaluated independently and may more readily be related to the state of stress. Modelling of B and G may then take forms similar to that in equation (3).

Hardin and Black[15] proposed an empirical expression for the shear modulus G_{max} determined from wave propagation velocities and from small amplitude cyclic simple shear tests:

$$G_{max} = 1230 OCR^k \frac{(2{\cdot}973 - e)^2}{(1 + e)} \sigma_o'^{0{\cdot}5} \tag{4}$$

in which σ_o' is the effective mean normal stress, and the exponent k applied to the over-consolidation ratio, may be related to the plasticity index of the soil. The values of G_{max} and σ_0' are expressed in psi. This expression also includes the effect of the void ratio e on the shear modulus. Many expressions with the same general form have been presented in the literature:

$$G_{max} = AF(e)\sigma_o'^n \tag{5}$$

in which A is a constant that may be related to OCR, $F(e)$ is a function describing the influence of void ratio, and the exponent n is often taken as 0·5. Hardin[16] has presented some of the specific forms of equation (5) together with typical values for the material parameters.

In addition to the formulations given above, other models for the elastic behaviour of soils have been presented in the literature (see, for example, References 17 and 18). These have gained less acceptance, in part due to the considerable number of material constants required and in part due to the requirement of results from more complicated or advanced tests. Further discussion of models for the elastic behaviour of soils have been given in References 19, 20 and 21.

Isotropy of elastic behaviour

Rowe[17] presented results of experiments on Mersey River Sand (4 void ratios), Silver Sand (4 void ratios), Fine Quartz Sand (2 void ratios), Feldspar (2 void ratios) and Glass Ballotini (3 void ratios) which all exhibited isotropic behaviour when unloaded, even when the strains during loading indicated anisotropic behaviour. Thus, sands with initial anisotropic fabric may exhibit anisotropic behaviour, but the elastic behaviour observed during unloading is for practical purposes isotropic. A similar conclusion was reached by Krizek,[22] who presented results of unconfined compression tests on sedimented specimens of kaolin clay with different degrees of inherent anisotropy. Results for sensitive clay studied by Wong and Mitchell[23] also showed nearly isotropic elastic behaviour, while the plastic stress–strain relations were anisotropic.

Poisson's ratio

The theoretical limits of Poisson's ratio are $-1 \leqslant \nu \leqslant 0{\cdot}5$. These limits are obtained on the basis that the elastic work $\frac{1}{2}\{\sigma\}^T\{\varepsilon\} \geqslant 0$ for any change in stress. Equation (1) for the bulk modulus shows that this requirement results in $\nu \leqslant 0{\cdot}5$, and equation (2) for the shear modulus provides the lower limit of $-1 \leqslant \nu$. In practice, Poisson's ratio for the elastic behaviour of soils is limited to the range from 0 to 0·5.

Experimental evidence indicates that Poisson's ratio is isotropic and practically constant for a soil at a given void ratio. The experiments on several granular materials presented by Rowe[17] showed that Poisson's ratio could be considered to be isotropic during elastic unloading.

Hardin[16] noted that accurate measurements of the elastic Poisson's ratio from wave propagation experiments was difficult, due to the insensitivity of the soil behaviour to the value of ν. However, analysis of his resonant column tests on Ottawa Sand produced constant values of ν in the range from 0·11 to 0·23. Based on a review of experimental data, Hardin[16] concluded that Poisson's ratio for soils lies somewhere between 0 and 0·2 and that any value within this range is accurate enough for most purposes.

Yokota and Konno[24] performed cyclic triaxial tests with a frequency of 0·25 Hz on reconstituted and undisturbed specimens of cohesive soils and alluvial sandy soils. Their investigation showed that Poisson's ratio was essentially constant at 0·5 for the cohesive soil, reflecting the undrained condition in these tests. The sandy soils produced values from individual tests in the range from 0·2 to 0·4. Their test results showed a tendency for slightly increasing Poisson's ratios with increasing magnitudes of shear strains, whereas the influence of confining pressure was found to be negligible.

El Hosri[25] conducted low amplitude cyclic triaxial tests on dry Hostun Sand with careful measurements of the axial and radial strains made directly on the specimens. He varied the average grain diameter, the uniformity coefficient, the void ratio, the effective confining pressure and the strain amplitude. Poisson's ratio was found to be essentially constant in each test and independent of confining pressure. Values of ν were obtained in the range from 0·18 to 0·23 for different material compositions and void ratios. El Hosri[25] also observed that Poisson's ratio was constant within cyclic strain amplitudes up to $\pm 0{\cdot}5$ per cent.

Whereas Poisson's ratio for a soil at a given void ratio appears to be constant, experimental evidence suggests that ν increases with increasing void ratio. Reanalysis of K_o-unloading branches from numerous tests performed on Ham River Sand[26] shows a consistent variation of ν from 0·20 at $e = 0{\cdot}57$ to 0·31 at $e = 0{\cdot}75$. Other experiments, including those presented below for Santa Monica Beach Sand, indicate similar results.

THEORETICAL DEVELOPMENT

The experimental evidence reviewed above indicates that the elastic behaviour of soils can be captured by an isotropic elastic model in which Poisson's ratio is constant and the elastic moduli E, B and G are functions of the mean normal stress as well as the deviatoric stress. Expressing the mean normal stress in terms of the first invariant of the stress tensor I_1 and the deviatoric stress in terms of the second invariant of the deviatoric stress tensor J'_2:

$$B = B(I_1, J'_2) \tag{6}$$

$$G = K(I_1, J'_2) \tag{7}$$

in which

$$I_1 = \sigma_1 + \sigma_2 + \sigma_3 = \sigma_x + \sigma_y + \sigma_z \tag{8}$$

and

$$J'_2 = \tfrac{1}{2}(s_x^2 + s_y^2 + s_z^2 + 2s_{yz}^2 + 2s_{zx}^2 + 2s_{xy}^2) \tag{9}$$

where the s symbols denote deviatoric stress:

$$s_x = \sigma_x - (1/3)I_1 = 1/3[(\sigma_x - \sigma_y) + (\sigma_x - \sigma_z)] \tag{10a}$$

$$s_y = \sigma_y - (1/3)I_1 = 1/3[(\sigma_y - \sigma_z) + (\sigma_y - \sigma_x)] \tag{10b}$$

$$s_z = \sigma_z - (1/3)I_1 = 1/3[(\sigma_z - \sigma_x) + (\sigma_z - \sigma_y)] \tag{10c}$$

and

$$s_{yz} = \tau_{yz};\ s_{zx} = \tau_{zx};\ s_{xy} = \tau_{xy} \tag{10d,e,f}$$

Note that

$$J'_1 = s_x + s_y + s_z = 0 \tag{11}$$

Substitution of equations (10) in equation (9) yields

$$J'_2 = \tfrac{1}{6}[(\sigma_x - \sigma_y)^2 + (\sigma_y - \sigma_z)^2 + (\sigma_z - \sigma_x)^2] + \tau_{xy}^2 + \tau_{yz}^2 + \tau_{zx}^2 \tag{12}$$

The elastic work per unit volume along stress path ACB in Figure 2 is calculated as

$$W_{ACB} = \int_{ACB} dW = \int_{ACB} \{\sigma\}^T \{d\varepsilon\} \tag{13}$$

or, as shown in Appendix I, this may be written as

$$W_{ACB} = \int_{ACB} \left(\frac{I_1 dI_1}{9B} + \frac{dJ'_2}{2G} \right) \tag{14}$$

and similarly for stress path ADB:

$$W_{ADB} = \int_{ADB} \left(\frac{I_1 dI_1}{9B} + \frac{dJ'_2}{2G} \right) \tag{15}$$

According to the principle of conservation of energy, the work must be independent of the path and $W_{ACB} = W_{ADB}$. Thus, for the cycle ACBDA:

$$W_{ACB} + W_{BDA} = \int_{ACBDA} \left(\frac{I_1 dI_1}{9B} + \frac{dJ'_2}{2G} \right) \tag{16}$$

The integral in equation (16) will be zero if it can be written in the general form

$$\oint (P dx + Q dy) = \iint_A \left(\frac{\partial Q}{\partial x} - \frac{\partial P}{\partial y} \right) dA \tag{17}$$

If $P = \partial W/\partial x$ and $Q = \partial W/\partial y$, i.e. if P and Q can be derived from a potential function, then the line integral vanishes and no net work is done on the closed stress path. Thus, for the work to

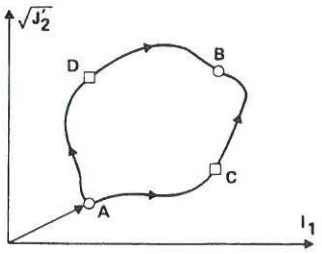

Figure 2. Stress paths from A to B shown in $I_1 - \sqrt{(J'_2)}$ diagram

be path independent, it must be possible to write the quantity dW in the form

$$dW = \frac{I_1 dI_1}{9B} + \frac{dJ'_2}{2G} = \frac{\partial W}{\partial I_1} dI_1 + \frac{\partial W}{\partial \sqrt{(J'_2)}} d\sqrt{(J'_2)} \tag{18}$$

in which I_1 and $\sqrt{(J'_2)}$ are the independent variables. Since $dJ'_2 = 2\sqrt{(J'_2)}\, d\sqrt{(J'_2)}$, equation (18) becomes

$$dW = \frac{I_1}{9B} dI_1 + \frac{\sqrt{(J'_2)}}{G} d\sqrt{(J'_2)} = \frac{\partial W}{\partial I_1} dI_1 + \frac{\partial W}{\partial \sqrt{(J'_2)}} d\sqrt{(J'_2)} \tag{19}$$

which for any $W[I_1, \sqrt{(J'_2)}]$ requires

$$\frac{\partial W}{\partial I_1} = \frac{I_1}{9B} \tag{20}$$

and

$$\frac{\partial W}{\partial \sqrt{(J'_2)}} = \frac{\sqrt{(J'_2)}}{G} \tag{21}$$

Finally, since

$$\frac{\partial^2 W}{\partial I_1 \partial \sqrt{(J'_2)}} = \frac{\partial^2 W}{\partial \sqrt{(J'_2)} \partial I_1} \tag{22}$$

the following constraints on the expressions for B and G are obtained:

$$\frac{I_1}{9B^2} \frac{\partial B}{\partial \sqrt{(J'_2)}} = \frac{\sqrt{(J'_2)}}{G^2} \frac{\partial G}{\partial I_1} \tag{23}$$

Substitution of equations (1) and (2) with $\nu =$ constant into equation (23) produces

$$\frac{1}{\sqrt{(J'_2)}} \frac{\partial E}{\partial \sqrt{(J'_2)}} = R \frac{1}{I_1} \frac{\partial E}{\partial I_1} \tag{24}$$

in which

$$R = 6 \frac{1+\nu}{1-2\nu} = \frac{9B}{G} \tag{25}$$

Equation (24) has a general solution $E = E(X)$, where

$$X = I_1^2 + R[\sqrt{(J'_2)}]^2 \tag{26}$$

It is helpful to note that, in this case,

$$dW = \frac{1}{9B} [I_1 dI_1 + R\sqrt{(J'_2)} d\sqrt{(J'_2)}] = \frac{1}{18B(X)} dX \tag{27}$$

Thus,

$$W = \int_0^X \frac{1}{18B(\bar{X})} d\bar{X} \tag{28}$$

and

$$\frac{\partial W}{\partial I_1} = \frac{\partial W}{\partial X} \frac{\partial X}{\partial I_1} = \frac{1}{18B(X)} 2I_1 = \frac{I_1}{9B} \tag{29}$$

$$\frac{\partial W}{\partial \sqrt{(J_2')}} = \frac{1}{18B} 2R\sqrt{(J_2')} = \frac{\sqrt{(J_2')}}{G} \tag{30}$$

i.e. the same expressions as in equations (20) and (21).

In terms of non-dimensional material constants and stress functions, the following power law satisfies equation (24):

$$E = Mp_a\left[\left(\frac{I_1}{p_a}\right)^2 + R\frac{J_2'}{p_a^2}\right]^{\lambda} \tag{31}$$

in which p_a is the atmospheric pressure expressed in the same units as E, I_1 and $\sqrt{(J_2')}$, and the modulus number M and the exponent λ are constant, dimensionless numbers. This functional representation can also be shown to fulfil the energy conservation argument for closed *strain* paths. This is demonstrated in Appendix II.

According to equation (31) Young's modulus is constant along rotationally symmetric ellipsoidal surfaces whose long axis coincides with the hydrostatic axis and whose centre is located at the origin of the principal stress space. The magnitude of Poisson's ratio determines the shape of the ellipsoidal surface. For $\nu = 0$, the value of $R = 6$ and the surface becomes spherical, whereas for $\nu = 0{\cdot}5$, the value of $R = \infty$ and the surface degenerates into a line coinciding with the hydrostatic axis.

Figure 3 shows cross-sections of the ellipsoidal surfaces in triaxial and octahedral planes for different values of Poisson's ratio. The cross-sections in the octahedral plane are always circular, whereas the cross-sections in the triaxial plane are shaped as ellipses whose aspect ratio depends on the value of Poisson's ratio. The locations of typical failure surfaces for cohesionless soils with friction angles from 30 to 50 degrees are shown for triaxial compression and extension. Only the portions of the ellipsoids located inside the conical failure surfaces can be reached by stress states in cohesionless soils, and only these portions are of interest for such soils.

Whereas Figure 3 shows contours along which Young's moduli are constant, the actual magnitude of E is determined by the material parameters M and λ. The results of an experimental study involving triaxial compression and three-dimensional cubical triaxial tests on sand with

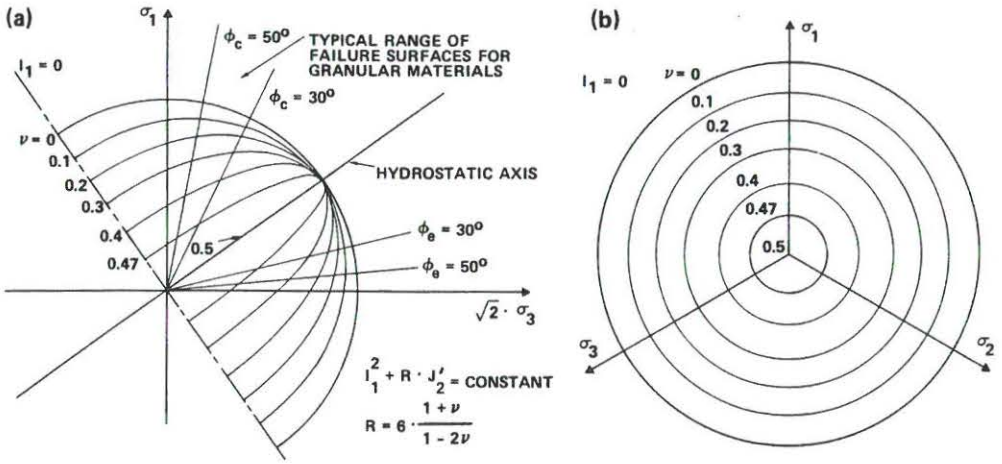

Figure 3. Contours of constant Young's modulus shown in (a) triaxial plane and (b) octahedral plane

various stress paths are used to demonstrate the determination of M and λ and to study the capability of equation (31) to capture the variation of Young's modulus.

EXPERIMENTAL STUDY

Testing program

Sand tested. All tests were performed on Santa Monica Beach Sand, which is composed of subangular to subrounded grains consisting mainly of quartz and feldspar. The characteristics of this sand are summarized as follows: mean diameter, 0·27 mm; coefficient of uniformity, 1·58; specific gravity of grains, 2·66; maximum void ratio, 0·87; and minimum void ratio, 0·58.

The tests presented here were performed on dense and loose specimens. The dense specimens had a void ratio of 0·61, corresponding to a relative density of 90 per cent, and the loose specimens had a void ratio of 0·81, corresponding to a relative density of 20 per cent. Only triaxial tests with different stress paths were performed on the dense sand. Triaxial as well as cubical triaxial tests with different stress paths were performed on the loose specimens in order to obtain relatively large strains, thus facilitating the interpretation of the results.

Specimens and measurements. The drained triaxial tests were performed on cylindrical specimens 2·8 in. (71 mm) in diameter and 7·5 in. (190 mm) high. Lubricated ends were used to minimize effects of end restraint. The initially air-dry specimens were saturated using the CO_2 method described by Lade and Duncan.[27] The vertical load, the confining pressure, the vertical deformation and the volume changes were measured during the tests. Constant or varying confining pressures in the range from 0·30 kg/cm^2 (29·4 kN/m^2) to 6·00 kg/cm^2 (588·6 kN/m^2) were employed in the triaxial tests.

The drained three-dimensional triaxial tests on loose sand were performed on cubical specimens with side lengths of 3·0 in. (76 mm). The cubical triaxial apparatus and the testing procedures used in the apparatus were described in detail by Lade.[28] A constant confining pressure of 1·20 kg/cm^2 (117·7 kN/m^2) was used in these tests, while the vertical and the horizontal deviator stresses were varied in the range from zero to 4·23 kg/cm^2 (415·0 kN/m^2) to achieve various three-dimensional stress paths.

The deformations measured in the two types of tests were corrected for sand penetration into the lubricated end plates, and the volumetric deformations were corrected for effects of membrane penetration occurring in tests with varying confining pressure.

Stress paths. Tests with simple stress paths as well as with complex stress paths were performed. Figure 4 shows the points of initiation and the directions of the stress paths involving unloading or reloading, thus resulting in primarily elastic strains. Figure 4(a) shows the stress path directions employed in the triaxial tests, and Figure 4(b) shows the stress path directions in the plane corresponding to $\sigma_3 = 1{\cdot}20$ kg/cm^2 (117·7 kN/m^2) for the cubical triaxial tests. In order to obtain an appreciation of the magnitude and composition (elastic vs. plastic) of the measured strains associated with a given stress path, each straight unloading or reloading path inside the primary yield surfaces was designed to involve relatively large stress changes.

The triaxial tests with simple stress paths were conducted with constant confining pressure. These tests included conventional triaxial compression tests with several unloading–reloading cycles at increasingly high values of stress difference, tests with compression–extension–compression cycles and tests with extension–compression–extension–compression cycles. Tests with more complex stress paths involving varying confining pressure and large unloading and reloading

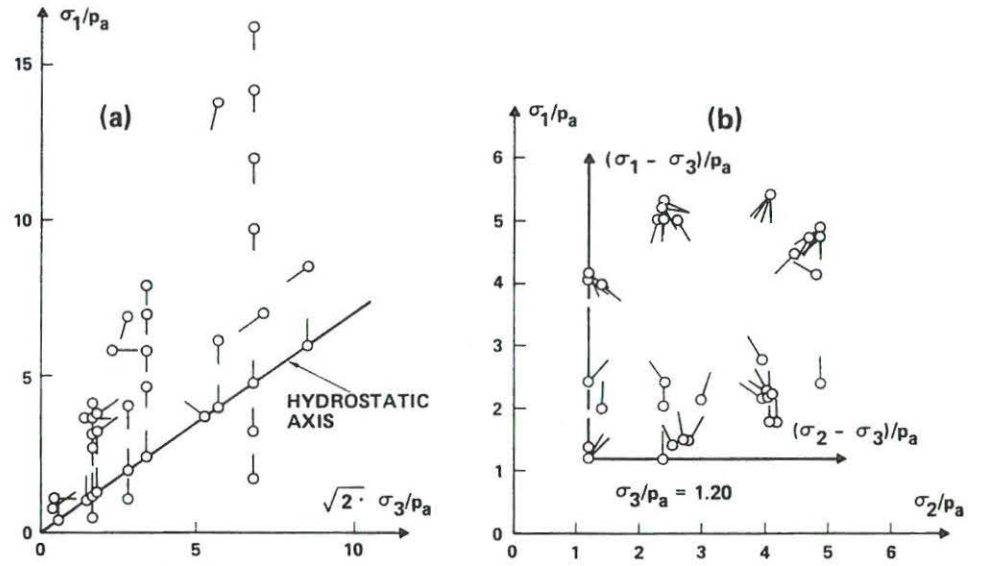

Figure 4. Points of initiation and stress path directions for tests on Santa Monica Beach Sand shown in (a) triaxial plane and (b) plane with $\sigma_3 = \text{constant}$

stress changes were also performed to study the pattern of elastic soil behaviour in relation to the current stress path and the previous stress history, if any.

The cubical triaxial tests were all performed with constant confining pressure σ_3, but the two stress differences $(\sigma_1 - \sigma_3)$ and $(\sigma_2 - \sigma_3)$ were varied to create three-dimensional stress paths from which the effects of σ_1 and σ_2 could be evaluated. These stress paths also involved large unloading and reloading stress changes to obtain reasonable amounts of strain for analysis.

Test results

The results of the tests described above form the basis for experimental verification of the theoretically developed expression for Young's modulus in equation (31). Calculation of the elastic moduli was performed using stress paths lengths of such magnitudes that at least one of the principal elastic strains was greater than $\pm$ 0·015 per cent. This was done to obtain a reasonable degree of accuracy and reliability of the moduli. Nevertheless, some scatter in the modulus values is to be expected due to the small strains encountered during unloading and reloading and due to the sensitivity of these small strains to accurate measurements and corrections. Because two of the principal stresses were changed along most of the stress paths employed in this study, the calculated elastic moduli would depend on the value of Poisson's ratio. The moduli were therefore determined in connection with regression analyses in which the constant Poisson's ratio could be varied to obtain the best overall fit. The moduli were associated with the states of stress at which unloading or reloading was initiated.

DETERMINATION OF MATERIAL PARAMETERS

Because Young's modulus is expressed in terms of stress invariants, any type of test in which all stresses and strains are measured may be used for determination of the three material parameters

M, λ and ν required to describe the elastic behaviour. In order to determine the material parameters for a given set of experimental data, a value of Poisson's ratio is estimated and the values of E are calculated from Hooke's law. In this study, a single elastic modulus was calculated for each stress path using the equation corresponding to the largest measured principal strain. The parameters M and λ in equation (31) can then be determined by plotting (E/p_a) vs. $[(I_1/p_a)^2 + R(J'_2/p_a^2)]$ in a log-log diagram, as shown in Figure 5 for dense Santa Monica Beach Sand. The intercept of the best-fitting straight line with $[(I_1/p_a)^2 + R(J'_2/p_a^2)] = 1$ is the value of M, and λ is the slope of the line.

In order to obtain the overall best-fitting parameters, regression analyses may be performed to determine the highest possible value of the coefficient of determination r^2. Figure 6 shows the effect of varying Poisson's ratio in the range from 0 to 0·5 on the values of r^2, M and λ for dense Santa Monica Beach Sand. It is interesting to note that these values are relatively insensitive to the value of Poisson's ratio in the range from $\nu = 0{\cdot}1$, $\nu = 0{\cdot}2$. The diagram shown in Figure 5 corresponds to the best-fit value of Poisson's ratio of $\nu = 0{\cdot}14$.

Poisson's ratio was also determined directly from stress paths in triaxial tests with constant confining pressures according to

$$\nu = -\frac{\dot{\varepsilon}_3}{\dot{\varepsilon}_1} = \frac{1}{2}\left(1 - \frac{\dot{\varepsilon}_v}{\dot{\varepsilon}_1}\right) \tag{32}$$

in which $(\dot{\varepsilon}_v/\dot{\varepsilon}_1)$ is the slope of the volume change curve immediately after stress reversal. Figure 7 shows values of Poisson's ratio determined from equation (32) for dense and loose Santa Monica Beach Sand plotted against I_1. The values of ν shown in Figure 7 were all determined from reloading branches initiated at the hydrostatic axis, where the best estimate of $(\dot{\varepsilon}_v/\dot{\varepsilon}_1)$ is obtained. Although there is some scatter in the test data, there are no discernible effects of the mean normal stress on Poisson's ratio. The average values, ν_{avg}, and the standard deviations, $\pm$ s, are indicated in Figure 7, and these values are also indicated in Figure 6 for dense Santa Monica Beach Sand. Figure 6 shows that the average value of $\nu_{avg} = 0{\cdot}15$, determined directly from the experimental

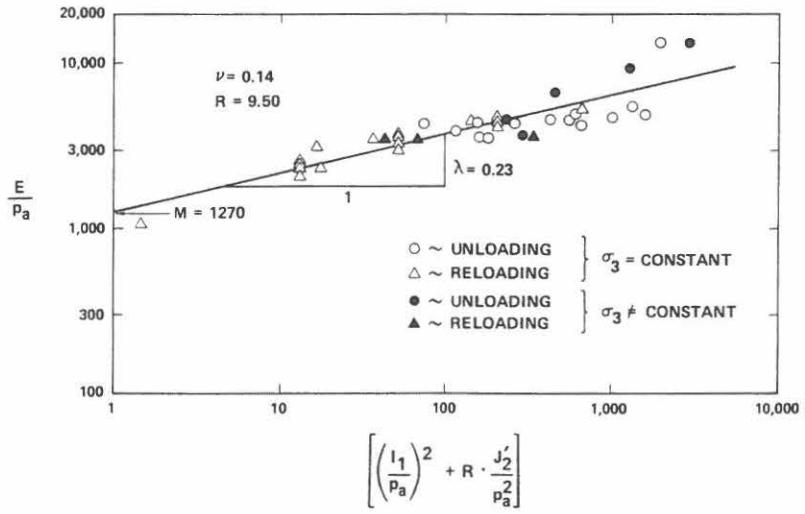

Figure 5. Variation of Young's modulus in triaxial tests for dense Santa Monica Beach Sand

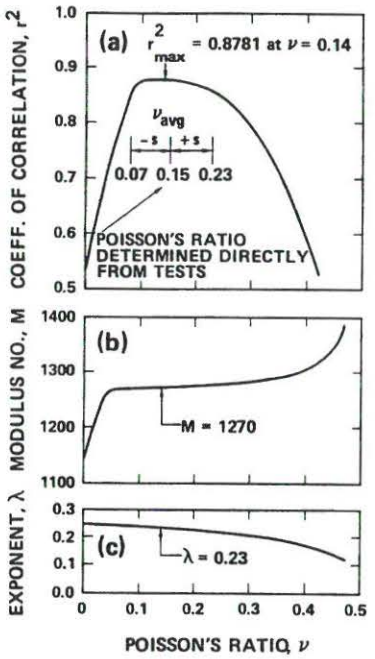

Figure 6. Variation of coefficient of correlation, modulus number and exponent with Poisson's ratio in triaxial tests on dense Santa Monica Beach Sand

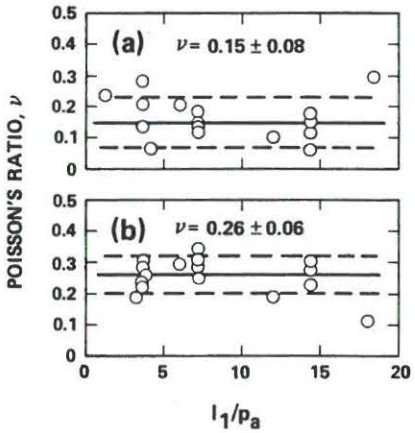

Figure 7. Poisson's ratios determined directly from results of triaxial tests on (a) dense and (b) loose Santa Monica Beach Sand

results, is located in the middle of the range in which r^2, m and λ are relatively insensitive to Poisson's ratio, and that this range is approximately indicated by the values of $\nu_{avg} \pm s$.

The results for loose Santa Monica Beach Sand are shown in Figures 8 and 9. These data include results from triaxial tests and cubical triaxial tests with various stress paths. Figure 8 shows that the results from the cubical triaxial tests fall in the range of results from the triaxial

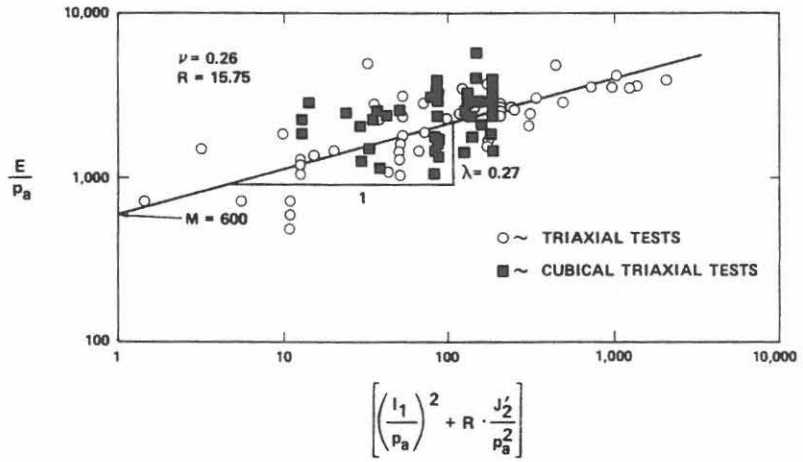

Figure 8. Variation of Young's Modulus in triaxial and cubical triaxial tests for loose Santa Monica Beach Sand

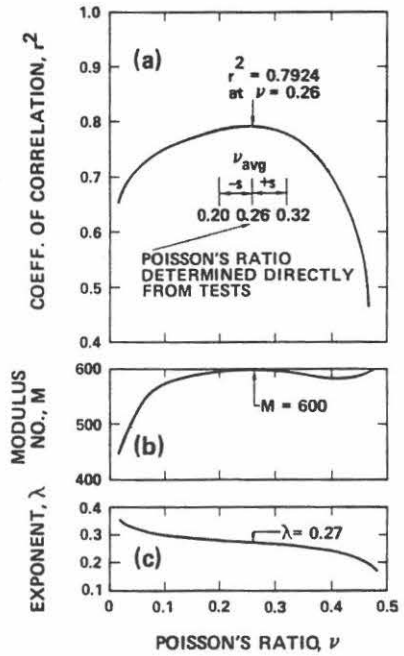

Figure 9. Variation of coefficient of correlation, modulus number and exponent with Poisson's ratio in triaxial tests on loose Santa Monica Beach Sand

tests. Thus, the values of Young's moduli determined from triaxial tests are applicable to general three-dimensional conditions. Figure 9 shows the results of regression analyses obtained by varying Poisson's ratio in the range from 0 to 0·5. The curves correspond to data from the triaxial tests. The average value and the range of Poisson's ratio determined directly from reloading branches in triaxial tests are also shown on Figure 9. Again, both ν_{avg} and $\nu_{avg} \pm s$ approximately

coincide with the best-fit value and the range in which r^2, M and λ are relatively insensitive to Poisson's ratio.

PARAMETER DETERMINATION FROM SIMPLE TESTS

Based on the results and analyses presented above, it appears that the material parameters M, λ and ν required to describe the elastic behaviour may be determined from results of conventional drained triaxial compression tests which include unloading–reloading cycles. These parameters may be determined with reasonable accuracy from such simple tests, because almost equally accurate descriptions of the elastic behaviour can be achieved over a range of Poisson's ratios.

The best estimate of Poisson's ratio is obtained from the slopes of the volume change curves associated with the reloading branches initiated at or near the hydrostatic axis. Equation (32) is then used to calculate Poisson's ratio, and it is preferable to obtain an average value from several tests. Using ν_{avg}, the value of R in equation (31) can be determined. Individual modulus values may be obtained from the slopes of the unloading and the reloading stress–strain relations obtained at constant confining pressures. These modulus values are associated with the stress states at which stress reversals are initiated. The parameters M and λ can then be determined as indicated in Figure 5 without regression analysis.

MATERIAL PARAMETER VALUES

Using the procedure based on simple tests as explained above, several sets of test data were analysed. Descriptions of soils and material parameter values are given in Table I. The average Poisson's ratios were obtained from individual data sets corresponding to reloading, as explained above, as well as from unloading at constant confining pressure and from K_o-unloading. Considerable scatter in the values of Poisson's ratio were obtained as indicated by the standard deviations. However, the average values of ν may very well be within the ranges in which M and λ are relatively insensitive to Poisson's ratio. Thus, it is possible to obtain reasonable descriptions of the elastic behaviour for the soils.

The values of the modulus number M listed in Table I vary from 440 to 1270, whereas those of the exponent λ vary in the relatively narrow range from 0·22 to 0·33. Although the data base is small, these values of M and λ may be representative of granular materials in general.

It is interesting to compare the material parameters M and λ with those to be used in equation (3) and with those implied by equation (4). According to these expressions, Young's modulus varies with the confining pressure σ'_3 and with the mean normal stress σ'_o, respectively. Because Young's modulus in equation (31) varies with both mean normal stress and deviator stress, a direct comparison of material parameter values for the three expressions can only be made at the hydrostatic axis where the stress dependency can be eliminated.

Equating Young's moduli from equations (3) and (31) produces the following expression for the modulus number K and the exponent n:

$$K = 3^{2\lambda} M \tag{33}$$

and

$$n = 2\lambda \tag{34}$$

Values of K and n calculated from these expressions are also listed in Table I. It may be seen that K varies in the range from 700 to 2300. These values compare very well with values of K_{ur} obtained from unloading–reloading branches in conventional static triaxial compression tests

Table I. Parameter values for different granular materials

	Description				Poisson's ratio	Parameters			Equation (33)	Equation (34)	Equation (35)
Soil	D_{50}(mm)	C_u	e	D_r(%)	ν_{avg}	s	M	λ	K	n	M_{hb}
Santa Monica Beach Sand	0·27	1·58	0·61	90	0·15	0·08	1270	0·23	2100	0·46	1550
			0·81	20	0·26	0·06	600	0·27	1090	0·54	1160
Monterey No. 0 Sand	0·43	1·53	0·57	98	0·17	0·14	1120	0·33	2310	0·66	1340
			0·78	27	0·17	0·05	800	0·26	1420	0·52	1150
Fine Silica Sand	0·18	2·0	0·76	30	0·27	0·08	440	0·22	710	0·44	1400
Mohawk Model Soil	3·5	6·2	0·64	73	0·25	0·13	630	0·27	1140	0·54	1470
Niagara-Type A Material	4·8	1·52	0·71	95	0·23	0·12	670	0·26	1190	0·52	1340
Niagara-Type B Material	1·2	8·6	0·52	95	0·24	0·11	570	0·29	1080	0·58	1670
Sacramento River Sand	0·21	1·5	0·87	38	0·2 (estimated)		500	0·28	930	0·56	990

and listed in Reference 13. The exponent n varies from 0·44 to 0·66. These values are also directly comparable with values obtained for granular materials and listed in Reference 13.

For comparison of parameter values for equations (4) and (31), Young's modulus is obtained from equations (2) and (4) and equated with the expression in equation (31). Equation (4) was derived for mean normal stresses and shear moduli expressed in psi. This stress unit dependency is eliminated by factoring the atmospheric pressure p_a into the equation. The exponent 0·5 in equation (4) is replaced by the general parameter n, as in equation (5). For hydrostatic stresses and normally consolidated sands ($OCR = 1$), this produces

$$M_{hb} = 2(1+\nu)1230\frac{(2{\cdot}973-e)^2}{(1+e)}\frac{1}{3^{2\lambda}}\frac{1}{\sqrt{(14{\cdot}7)}} \tag{35}$$

and the exponent n is expressed by equation (34). The values of M_{hb} for Hardin and Black's expression are calculated from Poisson's ratio ν, void ratio e and exponent λ and listed in Table I. The magnitudes of M_{hb} are one to three times higher than those of M. This is most likely, because equation (4) was derived from wave propagation velocities and from small amplitude cyclic simple shear tests. These small strain tests produce higher modulus values than static tests with larger changes in stress and strain. The average value of the exponents n listed in Table I is 0·54, with a standard deviation of $\pm 0{\cdot}06$. This compares favourably with the value of 0·5 used in Equation (4).

Whereas the material parameters evaluated at the hydrostatic axis are comparable in magnitude, the stress dependency of Young's modulus is different for the three expressions. Equation (3) indicates variation of the modulus with effective minor principal stress σ'_3, whereas experiments at constant σ'_3 show an additional dependency on stress difference. Equation (4) captures the modulus variation with effective mean normal stress σ'_o, but does not include a dependency on deviator stress. In comparison, equation (31) provides for modulus variation with effective mean normal stress as well as with deviator stress according to the pattern indicated above. Both theoretical considerations and experimental evidence support the expression for Young's modulus presented here.

MATERIALS WITH EFFECTIVE COHESION

Although only cohesionless materials were used for verification and material parameter determination, it is likely that the nonlinear elastic behaviour of materials with effective cohesion may also be modelled with good accuracy by the model presented above. In order to include the effect of cohesion, a translation of the principal stress space along the hydrostatic axis is performed.[29,30] Thus, a constant stress, ap_a, is added to the normal stresses before substitution in equations (8) and (12):

$$\bar{\sigma}_x = \sigma_x + ap_a \tag{36a}$$

$$\bar{\sigma}_y = \sigma_y + ap_a \tag{36b}$$

$$\bar{\sigma}_z = \sigma_z + ap_a \tag{36c}$$

in which 'a' is a dimensionless parameter and p_a is atmospheric pressure in the same units as σ_x, σ_y and σ_z. The value of ap_a reflects the tensile strength in materials with effective cohesion, and the parameter 'a' may be determined as indicated for concrete and other frictional materials with effective cohesion.[29,30] The translation of the co-ordinate system in connection with the elastic modulus variation is required to obtain increasing values of I_1 from the origin of the (translated) stress space. This method of accounting for the modulus variation was used

successfully in a study of frozen soil in which the effective cohesion plays an important role in the stress–strain behaviour.[31]

EVALUATION OF MODEL FOR ELASTIC BEHAVIOUR

The model developed above for the elastic behaviour of soil captures the nonlinear stress–strain relations commonly observed during unloading and reloading in triaxial compression and isotropic compression. Young's modulus varies with both mean normal stress and deviatoric stress and is therefore able to capture the elastic behaviour immediately upon unloading and upon reloading. Figure 10(a) shows a magnified diagram of the second unloading–reloading cycle for loose Santa Monica Beach Sand previously shown in Figure 1(a). The solid lines indicate the nonlinear elastic behaviour obtained from equation (31), with material parameter values as indicated in Figure 8. The slopes of the measured stress–strain relations immediately after stress reversals match quite well with those obtained from the model. The hysteresis loop is not modelled by equation (31). This loop is caused by the plastic strains occurring during unloading and reloading. The best-fit value of Poisson's ratio given in Figure 8 also matches well with the volume change curves shown in Figure 10(a). The predicted slope of the volume change curve is better defined for reloading than for unloading. This is because larger amounts of plastic strains occur during unloading which then obscure the elastic behaviour.

The isotropic compression test for loose Sacramento River Sand, previously shown in Figure 1(b), is shown in Figure 10(b), with the solid lines indicating the nonlinear behaviour obtained from the proposed model. Insufficient data was available for this sand to obtain overall best-fit values of the required material parameters. These were therefore obtained directly from the unloading–reloading branches shown in Figure 10(b). This figure serves to show the ability of the model to capture the nonlinear behaviour during isotropic unloading and reloading, for which only negligible plastic strains are usually observed.

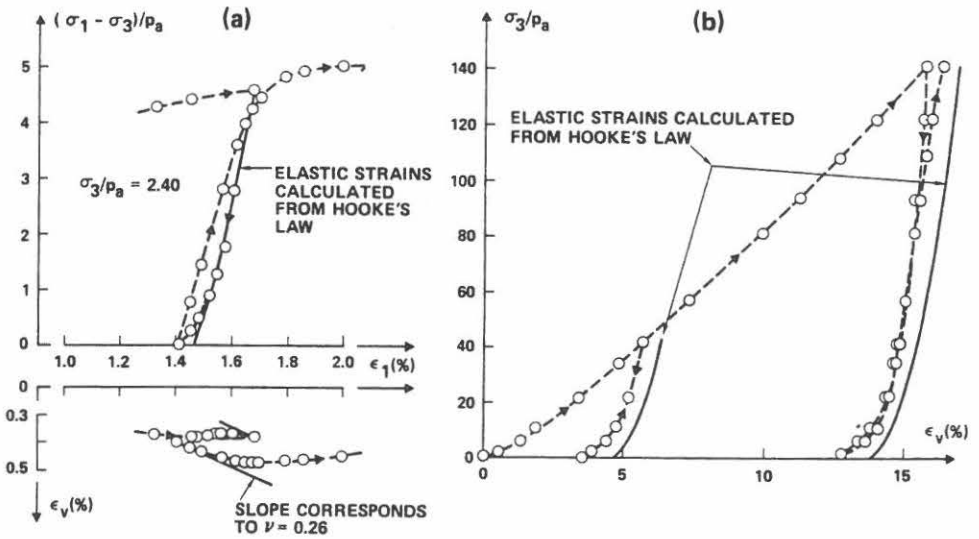

Figure 10. Characteristics of model for elastic behaviour evaluated for (a) conventional unloading–reloading cycle in triaxial compression test on loose Santa Monica Beach Sand, (b) Isotropic compression test on loose Sacramento River Sand with unloading–reloading branches

The overall fit between model and experimental results was demonstrated in Figures 5 and 8 for dense and loose Santa Monica Beach Sand. Although some scatter is present due to the small strains associated with elastic behaviour, the model appears to capture the elastic behaviour of sands with acceptable accuracy. The relative effects of the mean normal stress and the deviatoric stress are weighted by the R-value which is related to the constant value of Poisson's ratio. The model was developed on a theoretical basis, which ensures that the principle of conservation of energy is fulfilled for the nonlinear elastic behaviour of soils.

CONCLUSIONS

An isotropic model for the nonlinear elastic behaviour of granular materials has been developed. The model is based on Hooke's law in which Poisson's ratio is constant, and Young's modulus is expressed as a power function involving the first invariant of the stress tensor and the second invariant of the deviatoric stress tensor. The expression for Young's modulus is derived from theoretical considerations based on the principle of conservation of energy. Thus, energy is neither generated not dissipated along a closed-loop stress path. Experimental results from triaxial tests and cubical triaxial tests on sand with various two- and three-dimensional stress paths were used to demonstrate the ability of the model to capture the true nonlinear elastic behaviour of sands. Material parameters may be determined from unloading–reloading cycles in conventional triaxial compression tests. These parameters were shown to be applicable to general three-dimensional stress states. Although only results from tests on granular materials were employed in the present study, extension of the model to include the nonlinear elastic behaviour of materials with effective cohesion is possible, as described.

ACKNOWLEDGEMENT

The authors wish to acknowledge the valuable comments of the reviewers which led to significant improvements of the manuscript.

APPENDIX I

Equation (13) may be reduced to equation (14) as shown in the following. To distinguish between stress and strain invariants, the subscripts σ and ε are added. From equations (8) and (12):

$$dI'_{1\sigma} = d\sigma_x + d\sigma_y + d\sigma_z \tag{37}$$

and

$$dJ'_{2\sigma} = \tfrac{1}{3}[(\sigma_x - \sigma_y)(d\sigma_x - d\sigma_y) + (\sigma_y - \sigma_z)(d\sigma_y - d\sigma_z) + (\sigma_z - \sigma_x)(d\sigma_z - d\sigma_x)] + 2(\tau_{yz}d\tau_{yz} + \tau_{zx}d\tau_{zx} + \tau_{xy}d\tau_{xy}) \tag{38}$$

or

$$dJ'_{2\sigma} = s_x d\sigma_x + s_y d\sigma_y + s_z d\sigma_z + 2(\tau_{yz}d\tau_{yz} + \tau_{zx}d\tau_{zx} + \tau_{xy}d\tau_{xy}) \tag{39}$$

In the same manner as for stresses (equations (8) and (9)), the relevant strain invariants and strain deviatoric invariants are defined by the relations

$$I_{1\varepsilon} = \varepsilon_x + \varepsilon_y + \varepsilon_z \tag{40}$$

and

$$J'_{2\varepsilon} = \tfrac{1}{2}(e_x^2 + e_y^2 + e_z^2 + 2e_{yz}^2 + 2e_{zx}^2 + 2e_{xy}^2) \tag{41}$$

where the e symbols denote deviatoric strains:

$$e_x = \varepsilon_x - \tfrac{1}{3} I_{1\varepsilon} = \tfrac{1}{3}[(\varepsilon_x - \varepsilon_y) + (\varepsilon_x - \varepsilon_z)] \tag{42a}$$

$$e_y = \varepsilon_y - \tfrac{1}{3} I_{1\varepsilon} = \tfrac{1}{3}[(\varepsilon_y - \varepsilon_z) + (\varepsilon_y - \varepsilon_x)] \tag{42b}$$

$$e_z = \varepsilon_z - \tfrac{1}{3} I_{1\varepsilon} = \tfrac{1}{3}[(\varepsilon_z - \varepsilon_x) + (\varepsilon_z - \varepsilon_y)] \tag{42c}$$

and

$$e_{yz} = \varepsilon_{yz}; \quad e_{zx} = \varepsilon_{zx}; \quad e_{xy} = \varepsilon_{xy} \tag{42d,e,f}$$

Note that

$$J'_{1\varepsilon} = e_x + e_y + e_z = 0 \tag{43}$$

Substitution of equations (42) in equation (41) yields

$$J'_{2\varepsilon} = \tfrac{1}{6}[(\varepsilon_x - \varepsilon_y)^2 + (\varepsilon_y - \varepsilon_z)^2 + (\varepsilon_z - \varepsilon_x)^2] + \varepsilon_{xy}^2 + \varepsilon_{yz}^2 + \varepsilon_{zx}^2 \tag{44}$$

For an isotropic elastic material the stress–strain relations may be written in the stiffness form:

$$\sigma_x = (B + \tfrac{4}{3}G)\varepsilon_x + (B - \tfrac{2}{3}G)\varepsilon_y + (B - \tfrac{2}{3}G)\varepsilon_z \tag{45a}$$

$$\sigma_y = (B - \tfrac{2}{3}G)\varepsilon_x + (B + \tfrac{4}{3}G)\varepsilon_y + (B - \tfrac{2}{3}G)\varepsilon_z \tag{45b}$$

$$\sigma_z = (B - \tfrac{2}{3}G)\varepsilon_x + (B - \tfrac{2}{3}G)\varepsilon_y + (B + \tfrac{4}{3}G)\varepsilon_z \tag{45c}$$

$$\tau_{yz} = 2G\varepsilon_{yz} \tag{45d}$$

$$\tau_{zx} = 2G\varepsilon_{zx} \tag{45e}$$

$$\tau_{xy} = 2G\varepsilon_{xy} \tag{45f}$$

In view of the strain invariants and the deviatoric strain expressions, the stress–strain relations may also be written as

$$\sigma_x = BI_{1\varepsilon} + 2Ge_x \tag{46a}$$

$$\sigma_y = BI_{1\varepsilon} + 2Ge_y \tag{46b}$$

$$\sigma_z = BI_{1\varepsilon} + 2Ge_z \tag{46c}$$

$$\tau_{yz} = 2Ge_{yz} \tag{46d}$$

$$\tau_{zx} = 2Ge_{zx} \tag{46e}$$

$$\tau_{xy} = 2Ge_{xy} \tag{46f}$$

Summing equations (46a, b, c) produces

$$I_{1\sigma} = 3BI_{1\varepsilon} \tag{47}$$

Also, the following expression can be formed:

$$s_x = \tfrac{1}{3}[(\sigma_x - \sigma_y) + (\sigma_x - \sigma_z)] = \frac{2G}{3}[(e_x - e_y) + (e_x - e_z)] \tag{48}$$

which reduces to

$$s_x = 2Ge_x \tag{49}$$

This relationship holds for all deviatoric stress and strain components:

$$s_{ij} = 2Ge_{ij} \quad \text{with} \quad i, j = x, y, z \tag{50}$$

This means that

$$J'_{2\sigma} = 4G^2 J'_{2\varepsilon} \tag{51}$$

The increment of work dW shown in equation (13) is

$$dW = \sigma_x d\varepsilon_x + \sigma_y d\varepsilon_y + \sigma_z d\varepsilon_z + 2\tau_{yz} d\varepsilon_{yz} + 2\tau_{zx} d\varepsilon_{zx} + 2\tau_{xy} d\varepsilon_{xy} \tag{52}$$

Given the relations above, equation (52) may be written as

$$\begin{aligned} dW = {} & BI_{1\varepsilon}(d\varepsilon_x + d\varepsilon_y + d\varepsilon_z) \\ & + 2G(e_x d\varepsilon_x + e_y d\varepsilon_y + e_z d\varepsilon_z + 2e_{yz} de_{yz} + 2e_{zx} de_{zx} + 2e_{xy} de_{xy}) \end{aligned} \tag{53}$$

or

$$dW = BI_{1\varepsilon} dI_{1\varepsilon} + 2G dJ'_{2\varepsilon} \tag{54}$$

In view of equations (47) and (51) the work increment may also be written in the form

$$dW = \frac{1}{9B} I_{1\sigma} dI_{1\sigma} + \frac{1}{2G} dJ'_{2\sigma} \tag{55}$$

This is the expression given in equation (14).

APPENDIX II

Using the proposed expression for Young's modulus and constant Poisson's ratio, it may be shown that energy is conserved along a closed *strain* path. The stress invariant form in equation (26) may be written in terms of strain invariants using equation (47) and (51):

$$X = (3B)^2 I_{1\varepsilon}^2 + R4G^2[\sqrt{(J'_{2\varepsilon})}]^2 \tag{56}$$

and using the expression for R in equation (25):

$$X = (3B)^2 \left(I_{1\varepsilon}^2 + \frac{36}{R} [\sqrt{(J'_{2\varepsilon})}]^2 \right) \tag{57}$$

Assuming that the bulk modulus B is a function of X only, as presented in the text, then let

$$F(X) = \frac{X}{[3B(X)]^2} = Y \tag{58}$$

where

$$Y = I_{1\varepsilon}^2 + \frac{36}{R} [\sqrt{(J'_{2\varepsilon})}]^2 \tag{59}$$

is an invariant strain form generally similar to the invariant stress X.

Equation (58) may be inverted, at least in principle, to give

$$X = H(Y) \tag{60}$$

The work increment in equation (54) may then be written as

$$dW = BI_{1\varepsilon} dI_{1\varepsilon} + \frac{36}{R} B \sqrt{(J'_{2\varepsilon})} d\sqrt{(J'_{2\varepsilon})} \tag{61}$$

or

$$dW = B(X) \frac{dY}{2} \tag{62}$$

Thus,

$$dW = \tfrac{1}{2}B[H(Y)]dY \tag{63}$$

and

$$W = \int_0^Y \tfrac{1}{2}B[H(\bar{Y})]d\bar{Y} \tag{64}$$

Following the same argument used for the stress path, but writing the work increment dW in the form shown in equation (61), a potential function $W[I_{1\varepsilon}, \sqrt{(J'_{2\varepsilon})}]$ will exist, and the material will be conservative when exercised around closed strain paths provided that

$$\frac{\partial W}{\partial I_{1\varepsilon}} = BI_{1\varepsilon} \tag{65}$$

and

$$\frac{\partial W}{\partial \sqrt{(J'_{2\varepsilon})}} = \frac{36}{R} B\sqrt{(J'_{2\varepsilon})} \tag{66}$$

Equations (65) and (66) may be verified by differentiating equation (64).

REFERENCES

1. P. V. Lade, 'Large stress reversals in triaxial tests on sand', Proc. 4th Int. Conf. Num. Meth. Geomech., Edmonton, Canada, 1982, Vol. 1, pp. 171–182.
2. G. Wilson and J. L. E. Sutton, 'A contribution to the study of the elastic properties of sand', Proc. 2nd Int. Conf. Soil Mech. Found. Eng., Rotterdam, 1948, Vol. 1, pp. 197–202.
3. R. D. Mindlin, 'Compliance of elastic bodies in contact', *J. Appl. Mech.*, Trans. A.S.M.E., **71**, A-259–268 (1949).
4. R. D. Mindlin and H. Deresiewicz, 'Elastic spheres in contact under varying oblique forces', *J. Appl. Mech.*, Trans. A.S.M.E., **75**, A-327–344 (1953).
5. J. Duffy and R. D. Mindlin, 'Stress–strain relations and vibrations of a granular medium', *J. Appl. Mech.*, A.S.M.E., **24**(4), 585–593 (1957).
6. B. Jacobson, 'Some fundamental properties of sand', Proc. 4th Int. Conf. Soil Mech. Found. Eng., London, 1957, Vol. 1, pp. 167–171.
7. O. U. Janaradanan and A. N. Harkauli, 'Rebound characteristics of cohesionless soils', Proc. 2nd Asian Regional Conf. Soil Mech. Found. Eng., Japan, 1963, pp. 1–4.
8. N. Janbu, 'Soil compressibility as determined by odometer and triaxial tests', Proc. European Conf. Soil Mech. Found Eng., Wiesbaden, 1963, Vol. 1, pp. 19–25.
9. H. M. Makhlouf and J. J. Stewart, 'Factors influencing the modulus of elasticity of dry sand', Proc. 6th Int. Conf. Soil Mech. Found. Eng., Montreal, 1965, Vol. 1, pp. 298–302.
10. H.-Y. Ko and R. F. Scott, 'Deformation of sand in hydrostatic compression', *J. Soil Mech. Found. Div.*, A.S.C.E., **93**(SM3), 137–156 (1967).
11. H.-Y. Ko and R. F. Scott, 'Deformation of sand in shear', *J. Soil Mech. Found. Div.*, A.S.C.E., **93**(SM5), 283–310 (1967).
12. J. M. Duncan and C.-Y. Chang, 'Nonlinear analysis of stress and strain in soils', *J. Soil Mech. Found. Div.*, A.S.C.E., **96**(SM5), 1629–1653 (1970).
13. K. S. Wong and J. M. Duncan, 'Hyperbolic stress–strain parameters for nonlinear finite element analyses of stresses and movements in soil masses', *Geot. Eng. Report No. TE 74-3*, Dept. of Civ. Eng., Univ. of Calif., Berkeley (1974).
14. M. Zytynski, M. F. Randolph, R. Nova and C. P. Wroth, 'On modeling the unloading–reloading behavior of soils', *Int. j. numer. anal. methods geomech.*, **2**, 87–94 (1978).
15. B. O. Hardin and W. L. Black, Closure to 'Vibration modulus of normally consolidated clay', *J. Soil Mech. Found. Div.*, A.S.C.E., **95**(SM6), 1531–1537 (1969).
16. B. O. Hardin, 'The nature of stress–strain behavior for soils', Proc. Spec. Conf. Earthquake Eng. Soil Dyn., A.S.C.E., Pasadena, 1978, Vol. 1, pp. 3–90.
17. P. W. Rowe, 'Theoretical meaning and observed values of deformation parameters for soil', Proc. Roscoe Memorial Symp. Stress–strain Behavior of Soils, pp. 143–194 (1971).
18. M. D. Coon and R. J. Evans, 'Recoverable deformation of cohesionless soils', *J. Soil Mech. Found. Div.*, A.S.C.E., **97**(SM2), 375–391 (1971).
19. C. S. Desai and H. J. Siriwardane, *Constitutive Laws for Engineering Materials*, Prentice-Hall, Englewood Cliffs, New Jersey, 1984.

20. B. Loret, 'On the choice of elastic parameters for sand', *Int. J. Num. Anal. Methods Geomech.*, **9**, 285–292 (1985).
21. I. Nelson and M. L. Baron, 'Application of variable moduli models to soil behavior', *Int. j. solids struct.*, **7**, 399–417 (1971).
22. R. J. Krizek, 'Fabric effects on strength and deformation of kaolin clay', Proc. 9th Int. Conf. Soil Mech. Found. Eng., Tokyo, 1977, Vol. 1, pp. 169–176.
23. P. K. K. Wong and R. J. Mitchell, 'Yielding and plastic flow of sensitive cemented clay', *Geotech.*, **25**,(4), 763–782 (1975).
24. K. Yokota and M. Konno, 'Dynamic Poisson's ratio of soil', Proc. 7th World Conf. Earthquake Eng., Istanbul, 1980, Vol. 3, pp. 475–478.
25. M. S. El Hosri, 'Contribution a l'etude des proprietes mecanique des materiaux', *These d'Etat*, Univ. Paris VI, France (1984).
26. O. Daramola, 'On estimating K_o for overconsolidated granular soils', *Geotech.*, **30**(3), 310–313 (1980).
27. P. V. Lade and J. M. Duncan, 'Cubical triaxial tests on cohesionless soil', *J. Soil Mech. Found. Div.*, A.S.C.E., **99**(SM10), 793–812 (1973).
28. P. V. Lade, 'Cubical triaxial apparatus for soil testing', *Geot. Testing J.*, GTJODJ, **1**(2), 93–101 (1978).
29. P. V. Lade, 'Three-parameter failure criterion for concrete', *J. Eng. Mech. Div.*, A.S.C.E., **108**(EM5), 850–863 (1982).
30. P. V. Lade, 'Failure criterion for frictional materials', in *Mechanics of Engineering Materials* (C. S. Desai and R. H. Gallagher, Eds.), Wiley, New York, 1984, pp. 385–402.
31. P. V. Lade, H. L. Jessberger and N. Diekmann, 'Stress–Strain and volumetric behavior of frozen soil', Proc. 2nd Int. Symp. Ground Freezing, Trondheim, 1980, pp. 48–64.

Numerical Methods in Geomechanics (Innsbruck 1988), Swoboda (ed.)
 ISBN 90 6191 809 X

Model and parameters for the elastic behaviour of soils

Poul V.Lade
Department of Civil Engineering, University of California, Los Angeles, USA

ABSTRACT: A nonlinear, isotropic model for the elastic behavior of soils has been developed on the basis of theoretical considerations involving the principle of conservation of energy. Energy is therefore neither generated nor dissipated in a closed-loop stress path or strain path. The framework for the model consists of Hooke's law in which Poisson's ratio is constant and Young's modulus is expressed as a power function involving the first invariant of the stress tensor and the second invariant of the deviatoric stress tensor. The characteristics of the model are described, and the accuracy is evaluated by comparison with experimental results from triaxial tests. Parameter determination from unloading-reloading cycles in conventional triaxial compression tests is demonstrated, and parameter values are given for a variety of soils.

1 INTRODUCTION

The models employed for the elastic behavior most often assume the soil to behave as an isotropic material that obeys Hooke's law with a constant Poisson's ratio. Experimental data tend to confirm these assumptions, but the types of dependence on stress state assumed for Young's modulus, the shear modulus and the bulk modulus have shortcomings.

Presented here is an isotropic model for the nonlinear elastic behavior of soils. The model is based on a theoretical development which guaranties lack of energy generation or dissipation for any closed-loop stress path or strain path. The characteristics of the model are described, and determination of parameters from simple tests is demonstrated. Test data for fifteen different soils have been analyzed, and the parameter values are listed and evaluated.

2 COMMON ELASTIC MODELS AND THEIR SHORTCOMINGS

The two most well-known types of expressions for the elastic moduli are those given below. The first expression gives Young's modulus E as a function of the minor principal stress $\sigma_3 = \sigma_{min}$ [1,2]:

$$E = K \cdot p_a \cdot \left[\frac{\sigma_3}{p_a}\right]^n \qquad (1)$$

in which p_a is atmospheric pressure in the same units as E and σ_3. The two material parameters K and n are constant for a soil at a given void ratio. Conditions for which the minor principal stress is constant, thus producing the same value of Young's modulus, are illustrated in Figure 1. Young's modulus is constant along three perpendicular planes crossing the hydrostatic axis at the common value of minor principal stress. The expression in equation (1) has been used with constant and with variable Poisson's ratios.

For an isotropic elastic material, Young's modulus and Poisson's ratio may be replaced by the shear modulus G and the bulk modulus B in Hooke's law. These moduli have often been expressed in terms of the mean normal stress σ_0 [3,4]:

$$G \text{ and/or } B = A \cdot F(e,OCR) \cdot \sigma_0^n \qquad (2)$$

The material parameters incorporated in this class of expressions have occasionally included variations due

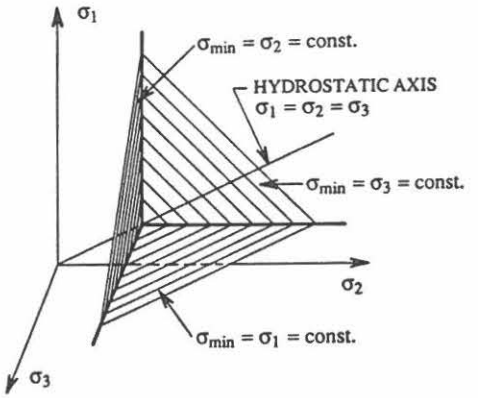

Figure 1. Three Perpendicular Planes in Which Elastic Modulus is Constant According to Equation (1).

to factors such as void ratio e and overconsolidation ratio OCR [4] as indicated in equation (2). For a soil with given e and OCR the values of A,F and n are constant. The mean normal stress and consequently the moduli given by equation (2) are constant in an octahedral plane as illustrated in Figure 2.

Theoretical reasons exist for the variation of elastic moduli with stress state [e.g. 5]. The simple formulations indicated above are empirical in nature, i.e., they have been devised on the bases of results from available, simple tests such as isotropic compression and triaxial compression. The expressions are widely used, because they appear to capture the elastic behavior observed in such tests, and because the material parameters can be determined from the results of conventional triaxial tests.

However, these models for the variation of elastic moduli result in violation of the principle of conservation of energy [6]. Thus, depending on the direction of a closed stress loop, these models will generate or dissipate energy in violation of the basic premise of elastic behavior. According to elasticity theory, a material exhibits true elastic behavior if energy is conserved at the end of a closed stress loop or strain loop.

3 TRUE ELASTIC MODEL FOR SOILS

An isotropic model for the nonlinear elastic behavior of soils was developed by Lade and Nelson [7]. This model is based on Hooke's law in which Poisson's ratio ν = constant. The expression for Young's modulus was derived from theoretical considerations based on the principle of conservation of energy. According to this derivation, Young's modulus E can be expressed in terms of a power law involving nondimensional material constants and stress functions as follows:

$$E = M \cdot p_a \cdot \left[\left(\frac{I_1}{p_a} \right)^2 + R \cdot \frac{J_2'}{p_a^2} \right]^{\lambda} \qquad (3)$$

in which

$$R = 6 \cdot \frac{1+\nu}{1-2\nu} \qquad (4)$$

I_1 is the first invariant of the stress tensor, and J_2' is the second invariant of the deviatoric stress tensor, given as follows:

$$I_1 = \sigma_x + \sigma_y + \sigma_z \qquad (5)$$

$$J_2' = \frac{1}{6} [(\sigma_x - \sigma_y)^2 + (\sigma_y - \sigma_z)^2 + (\sigma_z - \sigma_x)^2] + \tau_{xy}^2 + \tau_{yz}^2 + \tau_{zx}^2 \qquad (6)$$

The parameter p_a is atmospheric pressure expressed in the same units as E, I_1, and $\sqrt{J_2'}$, and the modulus number M and the exponent λ are constant, dimensionless numbers.

According to equation (3) Young's modulus is constant along rationally symmetric ellipsoidal surfaces whose long axis coincides with the hydrostatic axis and whose center is located at the origin of the principal stress space. The magnitude of Poisson's ratio determines the shape of the ellipsoidal surface. For $\nu = 0$ the value of R = 6 and the surface becomes spherical, whereas for $\nu = 0.5$ the value of $R = \infty$ and the surface degenerates into a line coinciding with the hydrostatic axis.

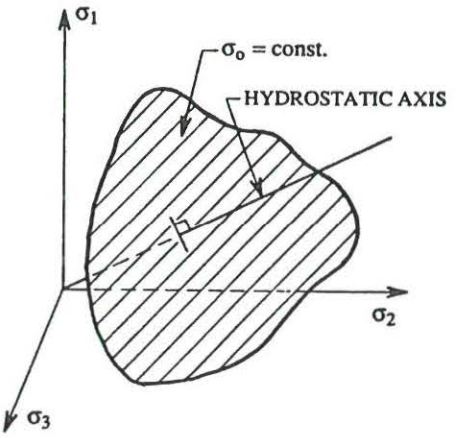

Figure 2. Octahedral Plane in Which Elastic Modulus is Constant According to Equation (2).

Figure 3 shows cross-sections of the ellipsoidal surfaces in triaxial and octahedral planes for different values of Poisson's ratio. The cross-sections in the octahedral plane are always circular, whereas the cross-sections in the triaxial plane are shaped as ellipses whose aspect ratio depends on the value of Poisson's ratio. The locations of typical failure surfaces for soils with friction angles from 30° to 50° are shown for triaxial compression and extension. Only the portions of the ellipsoids located inside the conical failure surface can be reached by stress states in soils, and only these portions are of interest.

Figure 4 shows a three-dimensional ellipsoidal surface along which Young's modulus is constant according to equation (3). Comparison of this surface with those in Figures 1 and 2 indicates that the conditions for which Young's modulus are constant are quite different for the three expressions. As shown in Figure 1, the model expressed by equation (1) produces surfaces of constant moduli which are convex with regard to the origin, whereas the truly elastic model described by equation (3) results in surfaces that are concave with regard to the origin. The model described by equation (2) produces planes of constant moduli that are neither convex nor concave with regard to the origin. None of the two previous models are contained as special cases within the truly elastic model described here.

4 DETERMINATION OF PARAMETER VALUES

The material parameters M, λ, and ν required to describe the elastic behavior of soils may be deter-

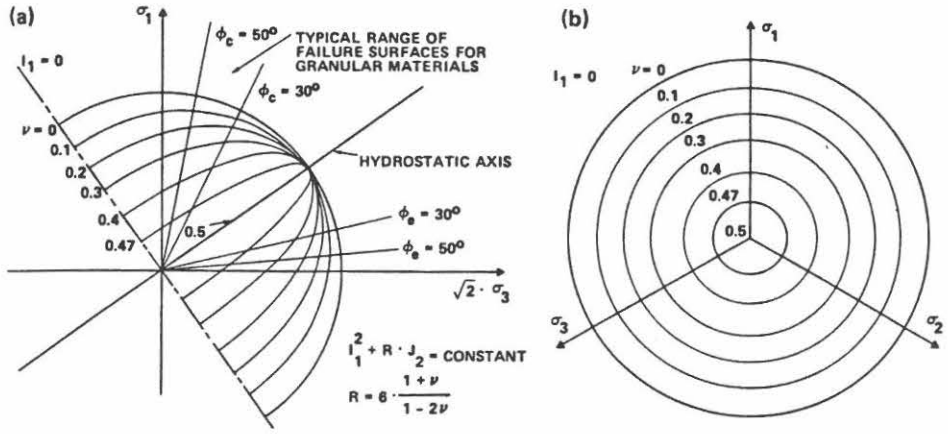

Figure 3. Contours of Constant Young's Modulus Shown in (a) Triaxial Plane and in (b) Octahedral Plane.

mined from conventional drained triaxial compression tests which include unloading-reloading cycles.

4.1 Possion's ratio

The best estimate of Poisson's ratio is obtained from the slope of the volume change curve associated with reloading initiated at or near the hydrostatic axis according to .

$$\nu = -\frac{\dot{\varepsilon}_3}{\dot{\varepsilon}_1} = \frac{1}{2} \cdot \left[1 - \frac{\dot{\varepsilon}_v}{\dot{\varepsilon}_1}\right] \qquad (7)$$

in which $(\dot{\varepsilon}_v/\dot{\varepsilon}_1)$ is the slope of the volume change curve immediately after stress reversal, as indicated in the lower part of Figure 5.

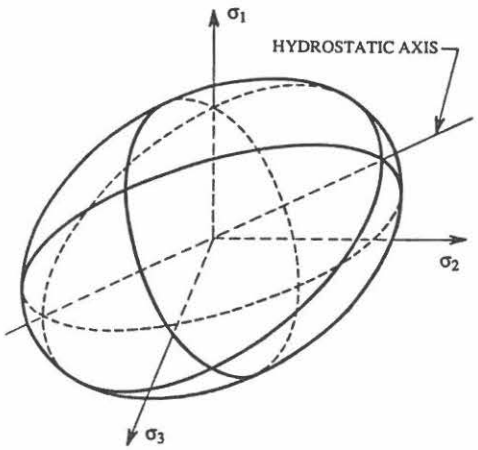

Figure 4. Ellipsoidal Surface Along Which Young's Modulus is Constant According to Equation (3).

It is preferable to obtain an average value of Poisson's ratio from several tests. Figure 6 shows values determined from equation (7) for medium dense Sacramento River Sand plotted against I_1/p_a. Although there is some scatter in the data, there is no discernible

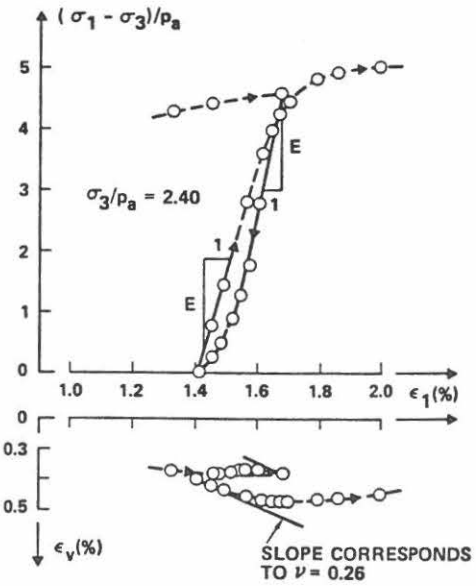

Figure 5. Young's Moduli and Slopes of Volume Change Curve for Determination of Poisson's Ratio from Unloading-Reloading Cycle in Conventional Triaxial Compression Test on Loose Santa Monica Beach Sand.

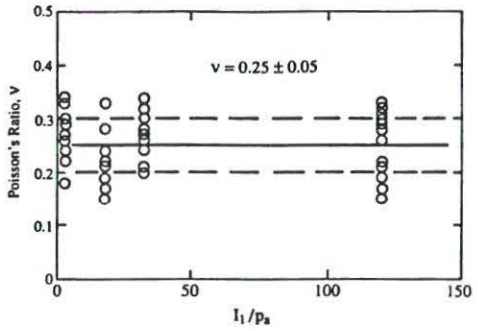

Figure 6. Possion's Ratios Determined from Results of Triaxial Tests on Medium Dense Sacramento River Sand (e_i = 0.71, D_r = 78%)

effect of mean normal stress on Poisson's ratio. Similar results have also been obtained for several other soils [e.g. 7,8]. The average value and the standard deviation for Poisson's ratio are indicated on Figure 6.

4.2 Young's modulus

Using the average value of Poisson's ratio, the value of R can be determined from equation (4). Individual modulus values may be obtained from the slopes of the unloading and the reloading stress-strain relations as shown in the upper part of Figure 5. These modulus values are associated with the stress states at which stress reversals are initiated. The parameters M and λ in equation (3) are then determined by plotting (E/p_a) versus $[(I_1/p_a)^2 + R\cdot(J_2'/p_a^2)]$ in a log-log diagram as shown in Figure 7 for medium dense Sacramento River Sand. The intercept of the best fitting straight line with $[(I_1/p_a)^2 + R\cdot(J_2'/p_a^2)] = 1$ is the value of M, and λ is the slope of the line.

It is interesting to note that the reloading moduli obtained at the hydrostatic axis where $J_2' = 0$ essentially define the straight line in Figure 7. The positions of the unloading moduli are suitably adjusted through J_2' and R so as to fall on the same line. For this particular case, the points corresponding to isotropic compression are located slightly below the other points. However, this is usually not the case. Thus, once ν and R have been determined, any type of test may, in principle, be used to obtain the parameter M and λ.

5 ELASTIC PARAMETER VALUES

Seventeen sets of data from fifteen different soils have been analyzed to study the range of parameter values obtained. Descriptions of soils and material parameter values are given in Table 1. The average Poisson's ratios were obtained from reloading, as explained above, as well as from unloading at constant confining pressure and from K_0-unloading. Considerable scatter in the values of Poisson's ratio were obtained as indicated by the standard deviations. However, it was

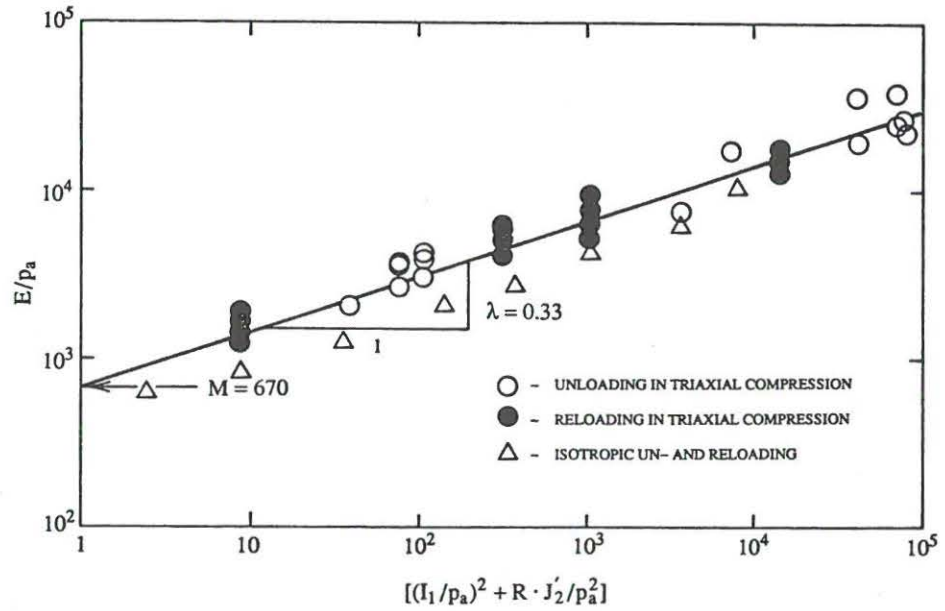

Figure 7. Determination of Parameters for Young's Modulus for Medium Dense Sacramento River Sand (e_i = 0.71, D_r = 78%)

Table 1. Description and Elastic Parameter Values for 15 Different Soils

Soil (Reference*)	Description				Poisson's Ratio		Young's Modulus		
	D_{50}(mm)	C_u	e	D_r (%)	ν_{avg}	s	M	λ	Coeff. of Correlation r
Santa Monica Beach Sand	0.27	1.58	0.61	90	0.15	0.08	1270	0.23	0.878
(Lade and Nelson [7])			0.81	20	0.26	0.06	600	0.27	0.792
Montery No. 0 Sand	0.43	1.53	0.57	98	0.17	0.14	1120	0.33	0.849
Lade and Duncan [9])			0.78	27	0.17	0.05	800	0.26	0.659
Fine Silica Sand	0.18	2.0	0.76	30	0.27	0.08	440	0.22	0.673
Mohawk Model Soil	3.5	6.2	0.64	73	0.25	0.13	630	0.27	0.782
Niagara-Type A Material	4.8	1.52	0.71	95	0.23	0.12	670	0.26	0.872
Niagara-Type B Material	1.2	8.6	0.52	95	0.24	0.11	570	0.29	0.788
Dense Silica Sand (Duncan and Chang [2])	0.25	1.8	0.50	100	0.16	-	750	0.21	0.960
Ottawa Sand (Yong and Ko, [10])	0.42	1.3	0.51	87	0.13	0.04	800	0.18	0.429
Dense Sand (Goldscheider [11])	0.42	1.8	0.56	100	0.14	-	280	0.38	0.970
Hostun Sand (Saada [12])	0.34	1.7	0.62	98	0.22	0.04	400	0.32	0.914
Reid Bedford Sand (Saada [12])	0.24	1.7	0.68	51	0.11	-	550	0.33	0.859
Intact Clayey Sand	0.20	200	0.51	65	0.25	0.03	400	0.36	0.963
Remolded Clayey Sand	0.20	200	0.51	65	0.25	0.03	390	0.36	0.987
Compacted Silt	0.013	U.S. Class. ML	0.42	RC = 95% Mod. Proctor	0.27	0.06	340	0.20	0.762
Sacramento River Sand (Lee [13])	0.21	1.5	0.71	78	0.25	0.05	670	0.33	0.975

* Those without reference are from the author's files.

shown in [7] that the average values of ν may well be within ranges in which M and λ are relatively insensitive to Poisson's ratio. Table 1 shows that Poisson's ratio varies from 0.11 to 0.27 with an average value for all soils (mostly granular) of 0.21.

The modulus number M varies from 280 to 1270, whereas the exponent λ varies from 0.18 to 0.38. The coefficient of correlation r is also listed in Table 1 to indicate the quality of fit with the model for each data set. In view of the number of data sets that have been evaluated, the magnitudes and ranges of M, λ, and ν listed in Table 1 are considered to be representative for granular materials.

6 CONCLUSION

An isotropic model for the nonlinear elastic behavior of soils has been presented. The model is based on Hooke's law in which Poisson's ratio is constant, and Yong's modulus is expressed in terms of stress invariants. The expression for Young's modulus has been derived from theoretical considerations based on the principle of conservation of energy. Material parameters may be determined from unloading-reloading cycles in conventional triaxial compression tests. Parameters were determined and studied for fifteen different soils.

REFERENCES

[1] N. Janbu, Soil Compressibility as Determined by Odometer and Triaxial Tests, Proc. Europ. Conf. Soil Mech. Found. Eng., Wiesbaden, 1, 19-25 (1963)

[2] J.M. Duncan and C.-Y. Chang, Nonlinear Analysis of Stress and Strain in Soils, J. Soil Mech. Found. Div., 96, 1629-1653 (1970)

[3] B.O. Hardin and W.L. Black, Closure to Vibration Modulus of Normally Consolidated Clay, J. Soil Mech. Found. Div., 95, 1531-1537 (1969)

[4] B.O. Hardin, The Nature of Stress-Strain Behavior of Soils, Proc. Spec. Conf. Earthquake Eng. Soil Dyn., Pasadena, 1, 3-90 (1978)

[5] R.D. Mindlin, Compliance of Elastic Bodies in Contact, J. Appl. Mech., 71, A-259-268 (1949)

[6] M. Zytynski, M.F. Randolph, R. Nova and C.P. Wroth, On Modeling the Unloading-Reloading Behavior of Soils, Int. J. Anal. Methods Geomech., 2, 87-94 (1978)

[7] P.V. Lade and R.B. Nelson, Modeling the Elastic Behavior of Granular Materials, Int. J. Anal. Methods Geomech., 11 (1987)

[8] P.W. Rowe, Theoretical Meaning and Observed Values of Deformation Parameters for Soil, Proc. Roscoe Memorial Symp. Stress-Strain Behavior of Soils, 143-194 (1971)

[9] P.V. Lade and J.M. Duncan, Cubical Triaxial Tests on Cohesionless Soils, J. Soil Mech. Found. Div., 99, 793-812 (1973)

[10] R.N. Yong and H.-Y. Ko, Pre-Workshop Package, Proc. Workshop Limit Equilibrium, Plasticity and Generalized Stress-Strain in Geotechnical Engineering, Montreal (1980)

[11] M. Goldscheider, True Triaxial Tests on Dense Sand, Constitutive Relations for Soils, Grenoble (1982), Balkema, Rotterdam, 11-54 (1984)

[12] A.S. Saada, Information Package, Proc. Int. Workshop on Constitutive Equations for Granular Non-Cohesive Soils, Cleveland (1987)

[13] K.L. Lee, Triaxial Compressive Strength of Saturated Sand Under Seismic Loading Conditions, Ph.D.-thesis, Univ. of California, Berkeley (1965)

Work-Hardening Plasticity Theory for Soils

General Framework
⟹ Failure Criteria
Associated vs. Nonassociated Flow

Mechanics of Engineering Materials
Edited by C. S. Desai and R. H. Gallagher

Chapter 20

Failure Criterion for Frictional Materials

P. V. Lade

20.1 INTRODUCTION

Failure of engineering structures, whether simple or complex, usually involves three-dimensional stress conditions in the materials. Detailed analyses of such structures therefore require knowledge of the stress–strain behaviour and the states of stress which constitute failure. However, the use of inadequate material models, especially for frictional materials, is often one of the limiting factors in the analyses procedures. In addition, the behaviour and the stress distributions are likely to be different in intact and in fractured materials. To determine the stress conditions which govern fracture of intact materials, a general three-dimensional failure criterion is required. Such a criterion is also one of the important parts of a constitutive law for frictional materials.

Frictional materials are characterized by increasing shear strengths with increasing normal stresses. Many experimental investigations have been performed, especially in recent years, to study the failure conditions for frictional materials such as sands, clays, cemented soils, concrete, mortar, rock, etc. These laboratory investigations have been characterized by utilization of increasingly improved equipment, in which the boundary conditions are well known, thus leading to reliable results of good quality. Along with these studies, formulations of failure criteria have been proposed. Some of these are aimed at practical design applications, whereas other more complex expressions have been developed for use in advanced computer codes. Most of the failure criteria proposed for three-dimensional stress states involve relatively complex expressions for which more than three material parameters are required.

These criteria have been developed to capture the experimentally determined shape of the failure surfaces as observed in the principal stress space. Several studies have shown that the failure surfaces in the principal stress space are shaped as pointed bullets with cross-sections in octahedral planes which are triangular, monotonically curved surfaces with smoothly rounded corners.

In addition to the characteristic cross-sectional shape in the octahedral plane, the three-dimensional failure surfaces for frictional materials have three inde-

pendent characteristics: (1) the opening angle of the failure surface, often described by the friction angle, (2) the curvature of the failure surface in planes containing the hydrostatic axis, i.e. curved meridians, and (3) the tensile strength (which is zero for materials without effective cohesion). At least three independent parameters are necessary for description of the three separate and distinct characteristics of the failure surface for frictional materials.

A general, three-dimensional failure criterion expressed in terms of stress invariants has been developed for frictional materials. It involves three independent material parameters, each relating to one of the three characteristics mentioned above. These parameters may be determined from any type of strength tests, including the simplest possible such as uniaxial compression and triaxial compression or biaxial tests.

The procedure for determination of the three material parameters is demonstrated and comparisons between failure criterion and experimental results are presented for different frictional materials. The values of the three parameters are summarized for the various materials, and their magnitudes are compared and discussed in light of the materials to which they belong.

20.2 FRICTIONAL MATERIALS WITHOUT EFFECTIVE COHESION

Many frictional materials such as gravels, sands, silts, clays, rockfill, mine tailings, coal, feed grain, etc. do not have effective cohesion. According to Mitchell [1] 'tests over large ranges of effective stress show that the actual effective stress failure envelope is curved,' and 'that cohesion is either zero or very small, even for heavily over-consolidated clays. Thus, a significant true cohesion, if defined as strength present at zero effective stress, does not exist in the absence of chemical bonding (cementation)'. Several studies of materials without effective cohesion under two- and three-dimensional stress conditions show that these materials have many characteristics in common.

20.2.1 Evaluation of classical failure criteria

Several existing constitutive models employ the Extended Tresca criterion or the Extended von Mises (or Drucker–Prager) criterion to describe the failure condition for frictional materials. The shapes of the corresponding failure surfaces in the principal stress space are conical and they have cross-sections of a regular hexagon (Tresca) or a circle (von Mises) with their centre lines coinciding with the hydrostatic axis. According to both these criteria the material has the same strength in compression and extension for a given magnitude of mean normal stress.

In an evaluation of possible failure criteria for sands, Bishop [2] pointed out that the two failure criteria described above are in principle unable to represent

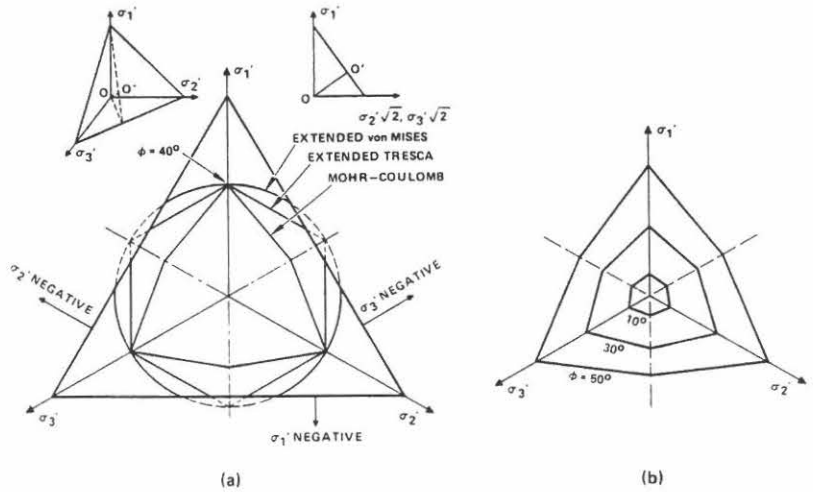

Figure 20.1 (a) Representation of classical failure criteria in principal stress space, showing boundaries of positive stress space (after Bishop [2]). (b) Cross-sections of the Mohr–Coulomb failure criterion shown for three different friction angles

the behaviour of cohesionless materials. Figure 20.1(a) indicates that the failure surfaces may extend outside the part of the principal stress space where all stresses are compressive and positive. The friction angle in triaxial compression for which both these failure surfaces are tangential to the coordinate planes is 36.9°. For higher friction angles the states of stress near triaxial extension are located in the parts of the stress space where one of the principal stresses is negative, and this is clearly unreasonable for materials without effective cohesion. Even for friction angles in triaxial compression smaller than 36.9°, the two criteria fail to model correctly the experimentally observed variation of the three-dimensional strengths of frictional materials.

The Mohr–Coulomb failure surface is also conical, and its cross-section is an irregular hexagon as indicated in Figure 20.1(a). This failure surface exhibits some of the characteristics necessary for correct modelling of failure of frictional materials. Thus, for materials without effective cohesion all principal stresses remain positive, even for very high friction angles. The shape of the cross-section of the Mohr–Coulomb failure surface resembles a regular hexagon for very small friction angles and it approaches an equilateral triangle for friction angles approaching 90°. The variation in shape for more conventional friction angles, as shown in Figure 20.1(b), is supported by experimental evidence.

The intermediate principal stress does not appear in the Mohr–Coulomb failure criterion, the failure surfaces are pointed in octahedral planes as indicated in Figure 20.1(b), and their traces in planes containing the hydrostatic axis are

straight lines. However, experimental evidence clearly shows that the intermediate principal stress has an important influence on the strength of frictional materials. Furthermore, traces of experimental failure surfaces in octahedral planes are smooth throughout their lengths, and they intersect the projections of the principal stress axes at right angles. Experimental results also indicate that the failure surfaces are curved in planes containing the hydrostatic axis. The Mohr–Coulomb criterion does not model these significant aspects of failure in frictional materials.

20.2.2 Three-dimensional failure criterion

The three-dimensional failure criterion for frictional materials without effective cohesion presented here was previously developed for soils with curved failure envelopes [3]. This criterion is expressed in terms of the first and third stress invariants of the stress tensor as follows:

$$(I_1^3/I_3 - 27)\cdot(I_1/p_a)^m = \eta_1 \tag{20.1}$$

where

$$I_1 = \sigma_1 + \sigma_2 + \sigma_3 = \sigma_x + \sigma_y + \sigma_z \tag{20.2}$$

$$\begin{aligned} I_3 &= \sigma_1\cdot\sigma_2\cdot\sigma_3 \\ &= \sigma_x\cdot\sigma_y\cdot\sigma_z + \tau_{xy}\cdot\tau_{yz}\cdot\tau_{zx} + \tau_{yx}\cdot\tau_{zy}\cdot\tau_{xz} \\ &\quad -(\sigma_x\cdot\tau_{yz}\cdot\tau_{zy} + \sigma_y\cdot\tau_{zx}\cdot\tau_{xz} + \sigma_z\cdot\tau_{xy}\cdot\tau_{yx}) \end{aligned} \tag{20.3}$$

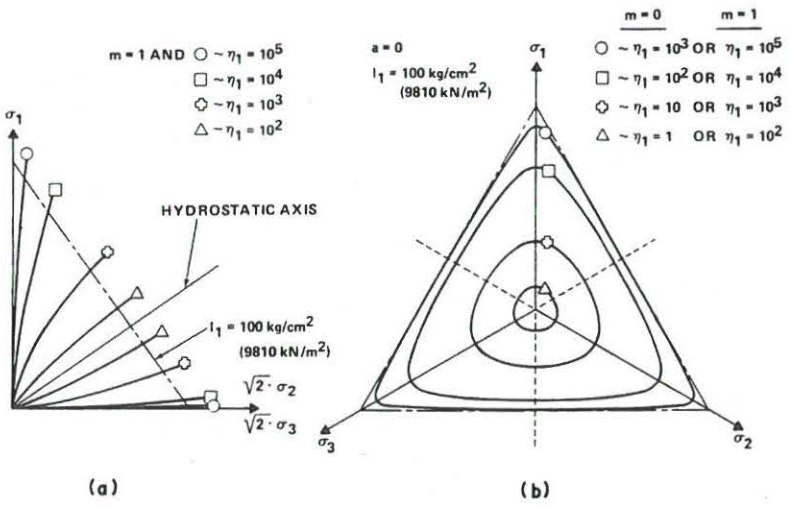

Figure 20.2 Characteristics of failure surfaces shown in principal stress space. Traces of failure surfaces shown in (a) triaxial plane, and in (b) octahedral plane

and p_a is atmospheric pressure expressed in the same units as the stresses. The value of I_1^3/I_3 is 27 at the hydrostatic axis where $\sigma_1 = \sigma_2 = \sigma_3$. The parameters η_1 and m in equation (20.1) can be determined by plotting $(I_1^3/I_3 - 27)$ versus (p_a/I_1) at failure in a log–log diagram and locate the best fitting straight line. The intercept of this line with $(p_a/I_1) = 1$ is the value of η_1 and m is the slope of the line.

In principal stress space the failure surface defined by equation (20.1) is shaped like an asymmetric bullet with the pointed apex at the origin of the stress axes as shown in Figure 20.2(a). The apex angle increases with the value of η_1. The failure surface is concave towards the hydrostatic axis, and its curvature increases with the value of m. For $m = 0$ the failure surface is straight. Figure 20.2(b) shows typical cross-sections in the octahedral plane ($I_1 = \text{const.}$) for $m = 0$ and $\eta_1 = 1$, 10, 10^2, and 10^3. As the value of η_1 increases, the cross-sectional shape changes from circular to triangular with smoothly rounded edges in a fashion that conforms to experimental evidence. The shape of these cross-sections does not change with the value of I_1 when $m = 0$. For $m > 0$ the cross-sectional shape of the failure surface changes from triangular to become more circular with increasing value of I_1. Similar changes in cross-sectional shape are observed from experimental studies on frictional materials. The cross-sections in Figure 20.2(b) also correspond to $m = 1$ and $\eta_1 = 10^2$, 10^3, 10^4, and 10^5.

20.2.3 Comparison of failure criterion and test data

The failure criterion described above has been shown to model the experimentally determined three-dimensional strengths of sand and clay with good

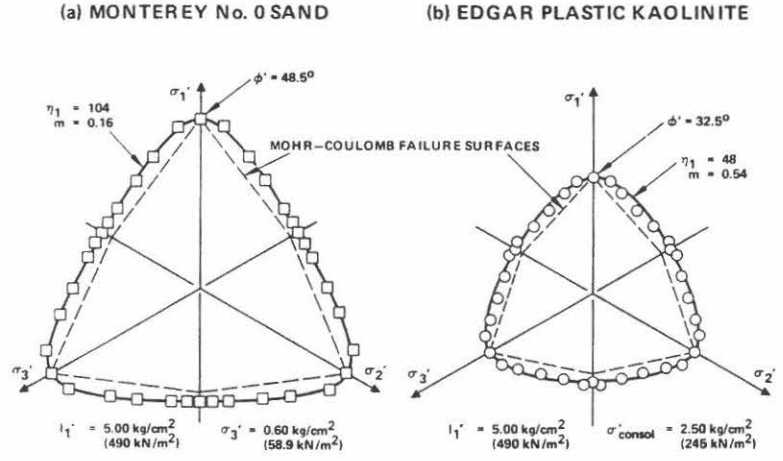

Figure 20.3 Comparison of failure criterion in octahedral planes with results of cubical triaxial tests on (a) dense Monterey No. 0 sand, and (b) normally consolidated, remoulded Edgar plastic kaolinite

accuracy in the range of stresses where the failure envelopes are concave towards the hydrostatic axis [3 to 5].

Figure 20.3 shows examples of comparisons between failure criterion and test data in terms of effective stresses for dense Monterey No. 0 sand and normally consolidated, remoulded Edgar plastic kaolinite. The values of η_1 and m suitable for description of failure in the two soils are given in Figure 20.3. The data points were projected on the common octahedral planes along curved meridians in order to provide a correct comparison between failure criterion and experimental data. It may be seen that the failure criterion models the experimentally obtained three-dimensional failure surfaces with good accuracy for both sand and clay.

20.3 FRICTIONAL MATERIALS WITH EFFECTIVE COHESION

Examples of frictional materials with effective cohesion include cemented soils (artificial and natural), frozen soils, ice, concrete, mortar, rocks, ceramics, graphite, plaster of Paris, and hydrostone. These materials exhibit tensile strengths and their shear strengths increase with increasing normal stresses.

20.3.1 General three-dimensional failure criterion for frictional materials

Because frictional materials with effective cohesion have many characteristics in common with those without effective cohesion, it has been proposed [6] that

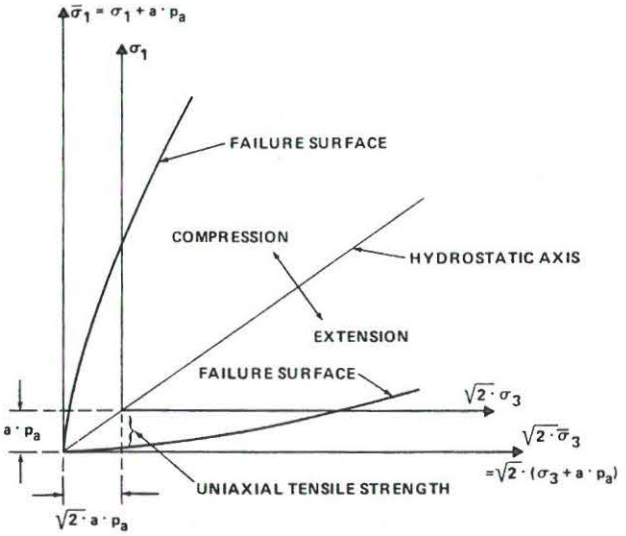

Figure 20.4 Translation of principal stress space along hydrostatic axis to include effect of tensile strength in failure criterion

their strengths can be expressed by a criterion similar to that in equation (20.1). In order to include the cohesion and the tensile strength in the failure criterion, a translation of the principal stress space along the hydrostatic axis is performed as illustrated in Figure 20.4. Thus, a constant stress $a \cdot p_a$ is added to the normal stresses before substitution in equation (20.1):

$$\bar{\sigma}_x = \sigma_x + a \cdot p_a \tag{20.4a}$$

$$\bar{\sigma}_y = \sigma_y + a \cdot p_a \tag{20.4b}$$

$$\bar{\sigma}_z = \sigma_z + a \cdot p_a \tag{20.4c}$$

where 'a' is a dimensionless parameter and p_a is atmospheric pressure in the same units as σ_x, σ_y, and σ_z. The value of $a \cdot p_a$ reflects the effect of the tensile strength of the material. Although the three material parameters describe separate characteristics of the failure surface, they do interact in calculation of, for example, the uniaxial compressive strength of the material. Thus, an infinite number of combinations of 'a', η_1, and m could result in the same value of the uniaxial compressive strength.

20.3.2 Determination of material parameters

In order to determine the values of the three material parameters for a given set of experimental data, the value of 'a' is estimated and $a \cdot p_a$ is added to the normal stresses before substitution in equation (20.1). The procedure for finding η_1 and m as described above is then followed. To facilitate the estimate of 'a', advantage may be taken of the fact that $a \cdot p_a$ must be slightly greater than the uniaxial tensile strength as indicated on Figure 20.4. If tensile tests are not part of a regular testing programme, a sufficiently accurate value of the uniaxial tensile strength may be obtained from the following approximation formula.

20.3.2.1 *Uniaxial tensile strength*

The uniaxial tensile strength, σ_t, has often been expressed as a fraction of the uniaxial compressive strength, σ_c. For example, Mitchell [7] indicates that σ_t (actually given as the flexural strength which may be higher than the true value of

Table 20.1 Values of parameters T and t for various types of frictional materials

Material	T	t	Reference
Cemented soils	−0.37	0.88	Mitchell [7]
Concrete and mortar	−0.61	0.67	Wastiels [9]
Igneous rocks	−0.53	0.70	This chapter
Metamorphic rocks	−0.00082	1.6	This chapter
Sedimentary rocks	−0.22	0.75	This chapter
Ceramics	−1.0	0.73	This chapter

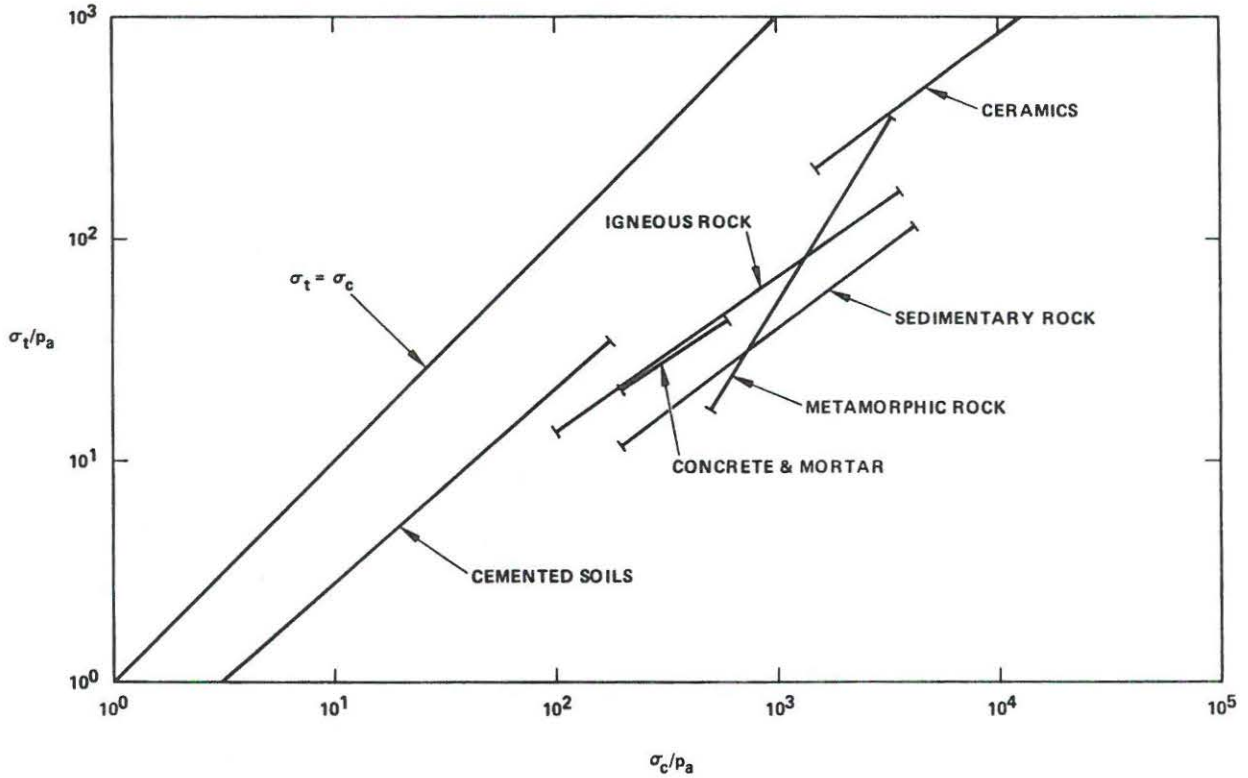

Figure 20.5 Relations between uniaxial tensile strengths and uniaxial compressive strengths for various types of frictional materials

σ_t) for cemented soils is about $\frac{1}{5}$ to $\frac{1}{3}$ of σ_c, whereas data compiled by Hannant [8] show that σ_t for concrete varies between 5 per cent and 13 per cent of σ_c. However, the values of σ_t and σ_c may be related through a power function of the following type [7, 9]:

$$\sigma_t = T \cdot p_a \cdot \left(\frac{\sigma_c}{p_a}\right)^t \tag{20.5}$$

where T and t are dimensionless numbers, and p_a is atmospheric pressure in the same units as those of σ_t and σ_c.

Values of T and t have been determined for several frictional materials and listed in Table 20.1. These values represent the best fit between experimental data and the simple expression in equation (20.5). Scatter in the test data was present for all materials, and the values of T and t given in Table 20.1 may not suitable for individual cases. The data base for ceramics was taken from only a few sources, whereas more extensive data bases were used for the other materials in Table 20.1.

Figure 20.5 shows a comparison of the relations between uniaxial tensile and uniaxial compressive strengths for the materials listed on Table 20.1. The straight lines shown on the log–log diagram span over the ranges of uniaxial compressive strengths indicated by available data. Both relatively weak and very strong frictional materials are represented in Figure 20.5. Note that the lines tend to cluster in an oblong area which slopes away from the line representing equal uniaxial tensile and uniaxial compressive strengths. Thus, the weak materials have relatively higher uniaxial tensile strengths than the strong materials.

20.3.2.2 *Regression analyses*

Because the failure criterion is expressed in terms of stress invariants, any type of test in which all stresses are measured may be used for determination of the three material parameters. However, it is advantageous to require only the simplest possible types of tests such as, for example, uniaxial compression and triaxial compression or biaxial tests for this determination, and then check whether these simple tests are sufficient for adequate characterization of the failure condition for the particular material under investigation. This may be done using various sets of data available in the literature which include both simple and more complex three-dimensional tests.

In order to obtain the overall best fitting parameters, regression analyses may be performed to determine the highest possible value of the coefficient of determination r^2. Figure 20.6 shows an example of the effect of varying the parameter 'a' on the values of r^2, η_1, and m for the tests on Mix A concrete performed by Mills and Zimmerman [10]. Only the results of the uniaxial compression and the triaxial compression tests in addition to the estimated value of the uniaxial tensile strength (from equation (20.5)) were used to

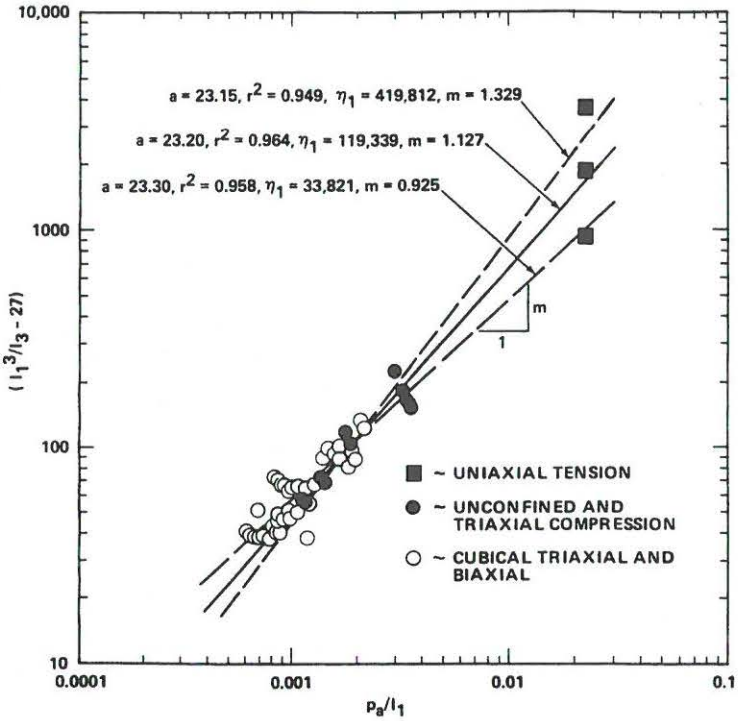

Figure 20.6 Determination of material parameters involved in failure criterion for Mix A concrete tested by Mills and Zimmerman [10]

determine the three material parameters. The uniaxial tensile strength was estimated to be $-23.1\,\text{kg/cm}^2$ ($-2266\,\text{kN/m}^2$) for Mix A concrete and the best fit value of 'a' = 23.2 resulted in $\eta_1 = 119{,}339$ and $m = 1.127$.

Except the three points corresponding to the uniaxial tensile strength on Figure 20.6, the points corresponding to the other tests do not translate enough on the diagram to show their separate locations. The points corresponding to the uniaxial tensile strength tend to influence the location of the best fit straight line. However, each of the three lines would describe the failure surface in the region of compressive stresses with reasonable accuracy. Thus, it is an advantage to incorporate the uniaxial tensile strength, even though it may be an estimate, in determination of the material parameters in order to stabilize the failure criterion in the region close to the origin and to describe the tensile strength for the material with reasonable accuracy.

The results of the cubical triaxial tests on Mix A concrete are shown on Figure 20.6 for comparison. It may be seen that some scatter of the data around

the solid line does exist, but the material parameters selected on the basis of the simple tests appear to represent the data quite well.

20.3.3 Comparison of failure criterion and test data

In order to evaluate the capabilities of the three-dimensional failure criterion, comparisons have been made between experimental data and failure surfaces calculated from equations (20.1) and (20.4). Data were plotted on the biaxial plane, and data points were projected on the octahedral plane for all available data sets. Those data sets containing results of triaxial compression and extension tests were also shown on the triaxial plane. Examples of these comparisons are given below for concrete and rock.

Comparison of test data (points) and failure surface (solid line) is shown on the normalized biaxial plane in Figure 20.7(a) for the tests performed on concrete with $\sigma_c = 590\,\text{kg/cm}^2$ ($57\,880\,\text{kN/m}^2$) by Kupfer *et al.* [11]. All data, except those corresponding to tension–tension, were used to determine the material parameters. The failure critertion is seen to represent the test data with reasonable accuracy. In order to study the failure surface relative to the data in the tension–tension area, the data are shown on the enlarged diagram in Figure 20.7(b). It may be seen that the failure surface is smoothly rounded at the corner and that it corresponds very well with the data in this region.

A major investigation was performed by Mills and Zimmerman [10]. The results of their tests on Mix A concrete, which contained tests in triaxial, biaxial,

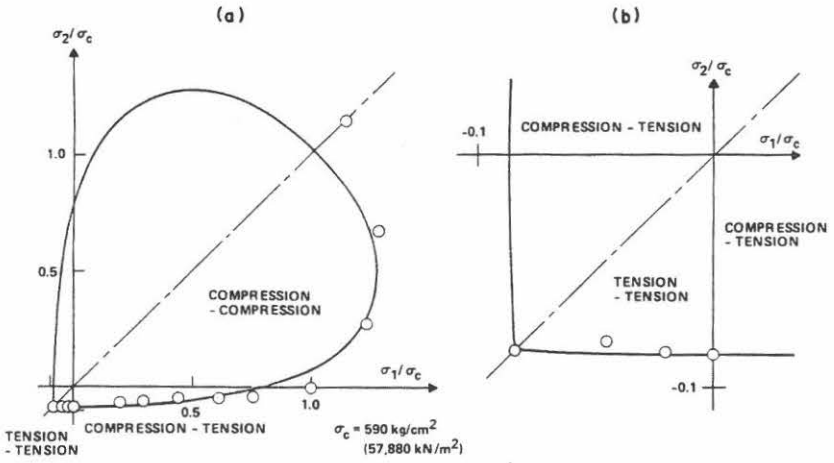

Figure 20.7 Comparison of failure criterion with results of biaxial tests performed by Kupfer, Hilsdorf, and Rusch [11] in (a) biaxial plane, and (b) enlarged tension–tension region

and octahedral planes, provided a good, coherent set of data. This set of data was used for illustration of material parameter determination in Figure 20.6. Comparisons between failure criterion and test data for Mix A concrete are shown in Figure 20.8. The material parameters for this concrete were determined on the basis of data from uniaxial compression and triaxial compression tests, and an estimated value of the uniaxial tensile strength. Thus, the good agreement shown in Figure 20.8(a) between the results of the triaxial compression tests and the failure critertion could be expected. However, the strengths obtained in triaxial extension are also well represented by the failure criterion. The data obtained in the compression–compression region of the biaxial plane are shown in Figure 20.8 (b). Although there is some scatter in the test results, the failure criterion is seen to represent the data quite well. Note that the pointed corner in the tension–tension area is actually smoothly rounded as shown in Figure 20.7(b).

Figure 20.8(a) also shows that the failure surface in extension cuts across the $\sigma_1 = 0$ plane at a very shallow angle. Therefore, any small deviation between test data and failure surface at this intersection in the triaxial plane will appear as a large deviation in the biaxial plane. Comparison of the data points for Mix A concrete indicated by arrows in Figures 20.8(a) and 20.8(b) shows that these appear to deviate somewhat from the failure surface in the biaxial plane (Figure 20.8(b)), whereas the same points in the triaxial plane are very close to the proposed failure surface. Any little amount of restraint in the testing apparatus would result in too large strength in biaxial extension, and this would show up very clearly in the biaxial plane. However, an evaluation in the triaxial plane would likely show that the test data are not that far from the actual failure surface. The natural scatter in test data could easily account for deviations of the magnitude indicated in Figure 20.8(b).

The data from cubical triaxial tests on Mix A concrete obtained by Mills and Zimmerman [10] are projected on the octahedral plane corresponding to $I_1 = 150\,\text{kg/cm}^2$ ($14\,715\,\text{kN/m}^2$) in Figure 20.8(c). Values of the minor principal stress, σ_3, of 0, $29.5\,\text{kg/cm}^2$ ($2894\,\text{kN/m}^2$), $59.11\,\text{kg/cm}^2$ ($5798\,\text{kN/m}^2$), and $88.6\,\text{kg/cm}^2$ ($8692\,\text{kN/m}^2$) were used in these tests. The points in Figure 20.8(c) corresponding to these values of σ_3 are shown separately on the octahedral plane for comparison with the failure surface. The projected data points were transferred to the common octahedral plane along the curved meridians using a technique involving the diagram in Figure 20.6. Note again that only data from uniaxial compression, triaxial compression, and uniaxial tension were used for determination of material parameters. The data from these tests are at the top of the diagrams in Figure 20.8(c). The experimental points on the octahedral plane describe a failure surface which is triangular with monotonically curved surface and smoothly rounded edges, as does the failure criterion.

A study of the three-dimensional strength of sandstone performed by Akai and Mori [12] involved uniaxial compression, triaxial compression, biaxial

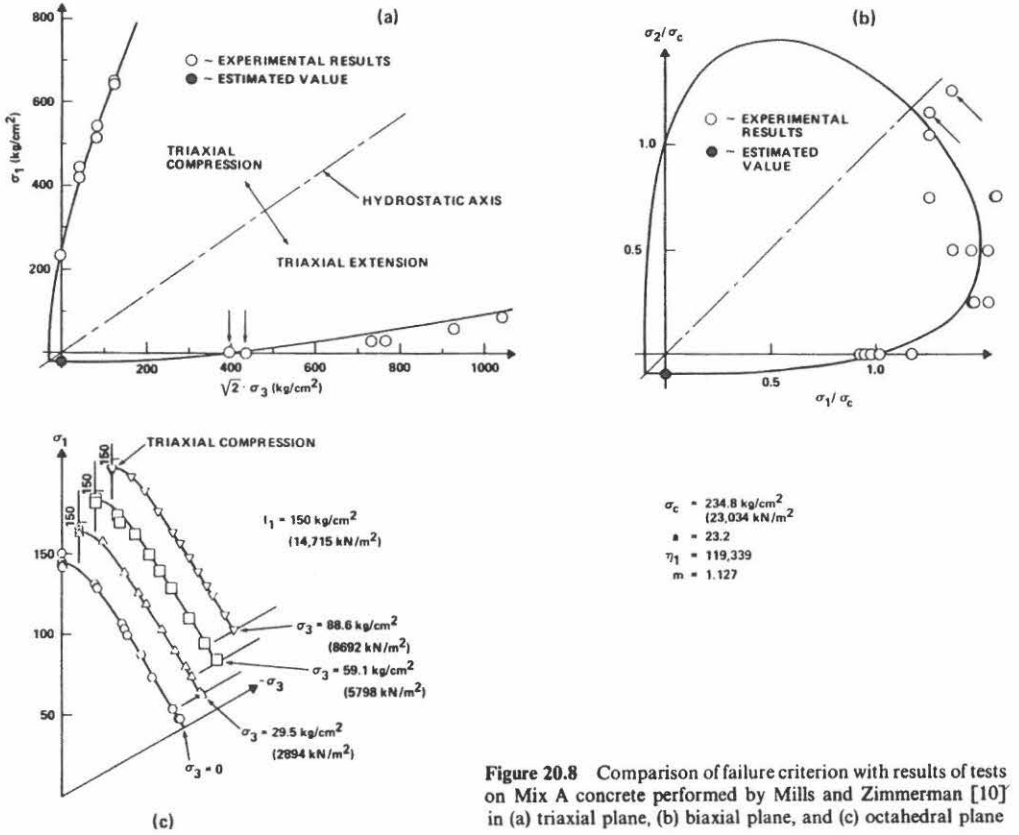

Figure 20.8 Comparison of failure criterion with results of tests on Mix A concrete performed by Mills and Zimmerman [10] in (a) triaxial plane, (b) biaxial plane, and (c) octahedral plane

compression, and cubical triaxial tests. Comparisons between failure criterion and test data for the sandstone are shown in Figure 20.9. The material parameters listed on Figure 20.9 for this rock were determined from the results of the uniaxial compression, triaxial compression, and biaxial compression tests. The value of the uniaxial tensile strength was not measured, but an estimate based on equation (20.5) with values of T and t for sedimentary rock from Table 20.1 gave $\sigma_t = -44.6$ kg/cm^2. This value was not used for material parameter determination in this case. The value of $a \cdot p_a = 37.4$ kg/cm^2 resulted in a better overall fit when the estimated value of σ_t was not employed for determination

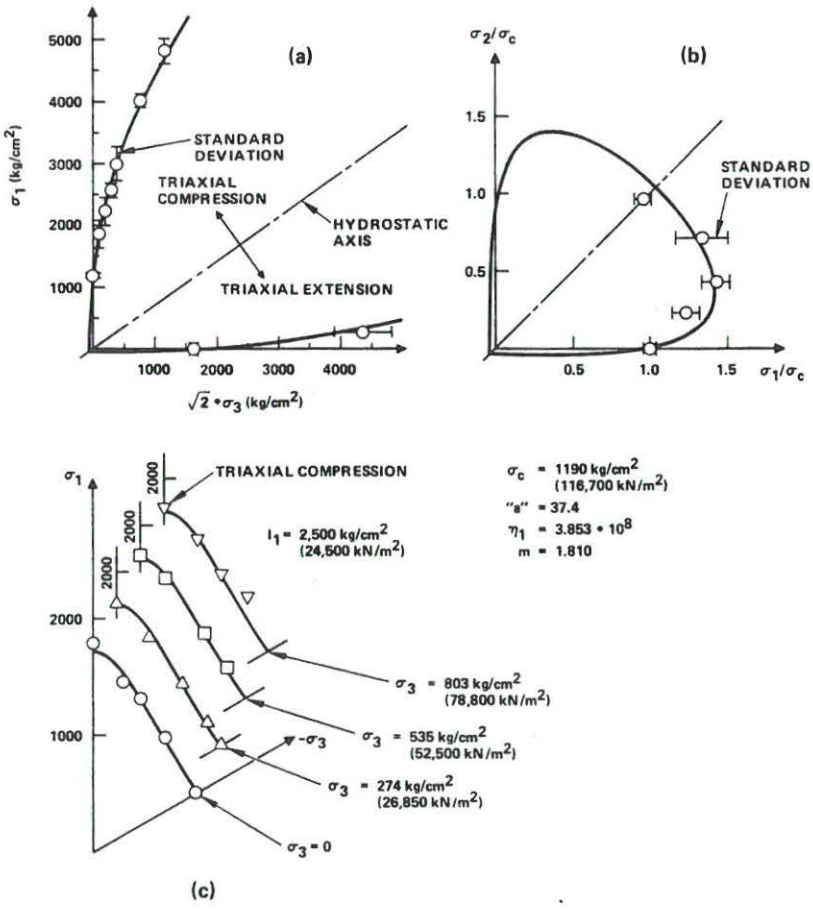

Figure 20.9 Comparison of failure criterion with results of tests on sandstone performed by Akai and Mori [12] in (a) triaxial plane, (b) biaxial plane, and (c) octahedral plane

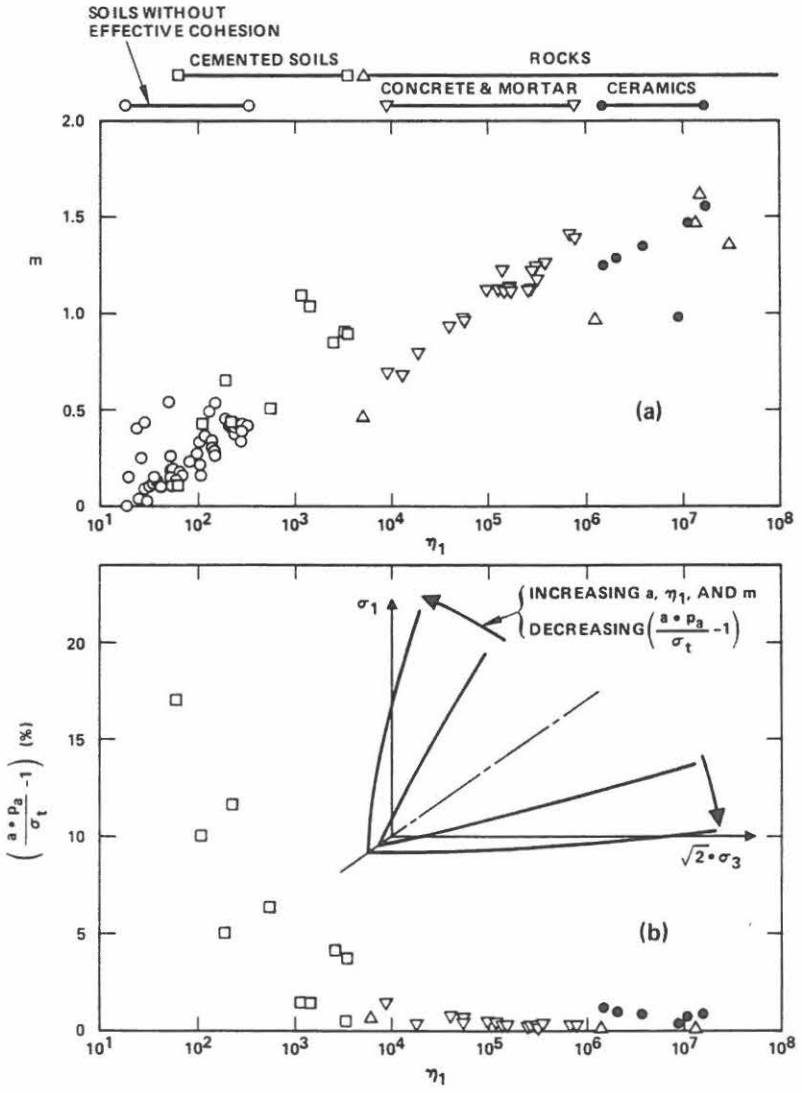

Figure 20.10 (a) Variation and ranges of the parameters η_1 and m for various frictional materials. (b) Magnitudes of the parameter 'a' relative to the uniaxial tensile strength σ_t plotted against η_1 for frictional materials with effective cohesion

of parameters. If σ_t were included, $a \cdot p_a$ would become 44.7 kg/cm^2, but these two values of $a \cdot p_a$ are easily within the scatter of the data employed to obtain T and t.

The comparison between failure criterion and test data for sandstone shown in Figure 20.9 indicates similar results as discussed in connection with Figure 20.8 for Mix A concrete. The strength of the sandstone is about five times higher than that of Mix A concrete as measured by the uniaxial compressive strengths. The values of the parameters a, m, and especially η_1 are therefore higher for the sandstone than for the concrete. The shape of the failure surface in the biaxial plane is somewhat different for the two materials, and this is correctly modelled by the failure criterion given by equations (20.1) and (20.4). The standard deviations of the major principal stresses, σ_1, as listed by Akai and Mori [12], are shown on Figures 20.9(a) and (b). The overall fit between failure surface and experimental data in Figure 20.9 is considered to be quite good and generally within the scatter of the test results.

Because emphasis was placed on obtaining the best overall fit between data and failure criterion, equal weights were placed on all test results used for parameter determination. It may therefore occur that the proposed failure criterion does not fit perfectly with the results of any one particular test. For example, the failure surface in Figure 20.7(a) does not go through the point corresponding to the uniaxial compressive strength. If it is desirable to obtain good correlation between the failure criterion and the uniaxial compressive strength, it may be necessary to apply heavier weights to this strength than to the results from other tests used for parameter determination.

20.4 PARAMETER VALUES FOR VARIOUS FRICTIONAL MATERIALS

Because the characteristic features of the three-dimensional failure surfaces have been observed for many different types of frictional materials, such as those described above, it is reasonable to believe that they exist for other frictional materials which have not yet been tested under general three-dimensional stress conditions. Therefore, the values of the three material parameters have also been determined for other frictional materials for which results of simple tests are available in the literature.

Figure 20.10(a) shows a diagram in which values of m are plotted against values of η_1 for several types of frictional materials with and without effective cohesion. The ranges of η_1 which have been obtained for these different materials are indicated by the bars in the upper part of Figure 20.10(a). It is likely that these ranges will be expanded when additional data sets for each type of material are analysed. Thus, the transition from cemented soils to rock is most likely smooth with no clear distinction between the two materials. Only a few sources of data for ceramics have been consulted for this study, and the range of the parameters for

ceramics is probably larger than indicated in Figure 20.10. However, it is clear that the increased frictional strength indicated by η_1 is accompanied by an increased curvature of the failure surface as expressed by the value of m.

The parameter 'a' used for frictional materials with effective cohesion must be higher than the uniaxial tensile strength, σ_t. Values of σ_t are related to the uniaxial compressive strength, σ_c, in Figure 20.5. Thus, if uniaxial tension tests are not part of the testing programme, an approximate value of σ_t may be obtained from Figure 20.5 or from equation (20.5). Because many engineering materials are exposed to both compressive and tensile stresses in the same structure, it was proposed to include a reasonable value of the uniaxial tensile strength in the parameter determination in order to obtain an overall representative failure criterion for the material under investigation. The values of the parameter 'a' obtained in this study have been related to σ_t through the term $(a \cdot p_a - \sigma_t)/\sigma_t$ (in per cent) which expresses the percentage by which 'a' is greater than σ_t. This percentage is plotted versus η_1 in Figure 20.10(b). The high values (up to 17 per cent) of this percentage were obtained for cemented soils for which the parameter η_1 is relatively small. Values below 2 per cent were obtained for all other frictional materials with effective cohesion. In fact, a gradual decrease in percentage is obtained with increasing value of η_1.

The insert in Figure, 20.10(b) indicates the general trend for the three parameters 'a', η_1, and m. All three parameters have been found to increase with increasing strength of the frictional material.

Some materials, such as compacted, partly saturated soils, may exhibit an apparent cohesion. These materials have not been included in the present study. However, the failure conditions for such materials may be modelled by the failure criterion in equations (20.1) and (20.4) using total stressed for parameter determination and subsequent application in analysis procedures.

20.5 CONCLUSION

Failure surfaces for frictional materials with and without effective cohesion have several characteristics in common, and these are all captured by a general three-dimensional failure criterion formulated in terms of the first and the third stress invariants of the stress tensor. This failure criterion involves only three independent material parameters. Although these parameters interact with one another, each parameter corresponds to one of three failure characteristics of the frictional materials. The material parameters may be determined from simple tests such as uniaxial compression and triaxial compression or biaxial tests. For the purpose of including reasonable values of tensile strengths in the failure criterion (for frictional materials with effective cohesion), it may be necessary to include the uniaxial tensile strength in the parameter determination. A simple expression for evaluation of the uniaxial tensile strength on the basis of the uniaxial compressive strength is given. Representative sets of data for soils,

concrete, and rock, for which results of three-dimensional tests were available, have been analysed, and comparisons between the failure criterion and the experimental data are made in triaxial, biaxial, and octahedral planes. Typical values of the three material parameters for various types of frictional materials have been determined, and their magnitudes are compared and discussed in light of the materials to which they belong. The ability of the general three-dimensional failure criterion to capture the characteristics of failure in frictional materials appears to be quite good with accuracies generally within the natural scatter of the test data.

ACKNOWLEDGEMENTS

Messrs E. Geiger and J. Tsai performed the tests on Edger Plastic Kaolinite, and Mr M. Kim compiled the data relating to failure of rock. Their assistance is gratefully acknowledged. Financial support for the work relating to soils has been provided under several grants from the National Science Foundation.

REFERENCES

1. J. K. Mitchell, *Fundamentals of Soils Behavior*, John Wiley & Sons, Inc., New York, NY, 1976.
2. A. W. Bishop, 'The strength of soils as engineering materials', 6th Rankine Lecture, *Geotechnique*, **16**, 2, 91–130 (1966).
3. P. V. Lade, 'Elasto-plastic stress–strain theory for cohesionless soil with curved yield surfaces', *International Journal of Solids and Structures*, **13**, 1019–1035, Pergamon Press, Inc., New York, NY, 1977.
4. P. V. Lade, 'Prediction of undrained behavior of sand', *Journal of the Geotechnical Engineering Division, ASCE*, **104**, No. GT6, Proc. Paper 13834, 721–735 (1978).
5. P. V. Lade and H. M. Musante, 'Three-dimensional behavior of remolded clay', *Journal of the Geotechnical Engineering Division, ASCE*, **104**, No. GT2, Proc. Paper 13551, 193–209 (1978).
6. P. V. Lade, 'Three-parameter failure criterion for concrete', *Journal of the Engineering Mechanics Division, ASCE*, **108**, No. EM5, Proc. Paper 17383, October 1982.
7. J. K. Mitchell, 'The properties of cement-stabilized soils', *Proc., Workshop on Materials and Methods for Low Cost Road*, pp. 365–404, Rail and Reclamation Works, Leura, Australia, September 1976.
8. D. J. Hannant, 'Nomograms for the failure of plain concrete subjected to short-term multiaxial stresses', *The Structural Engineer*, **52**, 5, 151–165 (1974).
9. J. Wastiels, 'Behaviour of concrete under multiaxial stresses—a review', *Cement and Concrete Research*, Vol. 9, pp. 35–44, Pergamon Press, 1979.
10. L. L. Mills and R. M. Zimmerman, 'Compressive strength of plain concrete under multiaxial loading conditions', *American Concrete Institute Journal*, **67**, 802–807 (1970).
11. H. Kupfer, H. K. Hilsdorf, and H. Rusch, 'Behavior of concrete under biaxial stresses', *American Concrete Institute Journal*, **66**, 656–666 (1969).
12. K. Akai and H. Mori, 'Ein Versuch über Bruchmechanismus von Sandstein under mehrachsigem Spannungszustand', *Proc. of the Second Congress of the International Society of Rock Mechanics*, Vol. II, Paper No. 3–30, Belgrade, Yugoslavia, 1970.

Work-Hardening Plasticity Theory for Soils

General Framework
Failure Criteria
⟹ Associated vs. Nonassociated Flow

Nonassociated Flow and Stability of Granular Materials

By Poul V. Lade,[1] Richard B. Nelson,[2] Members, ASCE, and Y. Marvin Ito[3]

Abstract: Materials exhibiting nonassociated flow should, according to Drucker's stability postulate, become unstable when exposed to certain stress paths inside the failure surface. Results of a series of triaxial tests designed to expose the type of behavior displayed by granular materials are presented and discussed. The sand dilates during shear, it exhibits nonassociated flow, and when exposed to stress paths in the region of potential instability, none is observed. The reliability of the test results, the possible influence of viscous effects on the stability, and the effect of release of elastic energy are studied and discussed in detail. Thus, Drucker's stability postulate is not applicable to granular materials. The type of volume-change behavior displayed by the material is of great importance in the question of stability of granular materials.

Introduction

The occurrence of nonassociated plastic flow in frictional materials such as sand, clay, concrete, and rock has raised questions regarding the uniqueness and stability of such materials. The stability postulate formulated by Drucker (3–5) for time-independent materials provides a sufficient condition for stability and ensures uniqueness in dynamic as well as static problems. Drucker's postulate is satisfied provided that associated flow is employed in construction of constitutive models involving convex, plastic yield surfaces. Whereas this postulate provides a sufficient condition for stability, it has been suggested that it is not a necessary condition (13,15).

Considerations of stability have mainly been explored on a theoretical level. Experiments to study whether or not frictional materials are, in fact, unstable under certain loading conditions have not been performed. A series of tests is presented on granular materials designed to expose the type of behavior that is characteristic of frictional materials. The problem of instability and the factors that control the occurrence of unstable behavior are discussed in light of experimental results. It is shown that Drucker's stability postulate is not applicable to frictional materials in general and that the volume-change behavior (dilatancy) plays an important role in the stability of such materials.

Drucker's Stability Postulate

The condition for stability formulated by Drucker (3–5) involves two components expressed in terms of plastic work increments:

[1]Prof., Dept. of Civ. Engrg., Univ. of California, Los Angeles, CA 90024.
[2]Prof., Dept. of Civ. Engrg., Univ. of California, Los Angeles, CA 90024.
[3]Adjunct Prof., Dept. of Civ. Engrg., School of Engrg. and Applied Sci., Univ. of California, Los Angeles, CA 90024; Mgr., Engrg. Mech. Group, California Res. and Tech., Inc., Chatsworth, CA 91311.

Note.—Discussion open until February 1, 1988. To extend the closing date one month, a written request must be filed with the ASCE Manager of Journals. The manuscript for this paper was submitted for review and possible publication on August 4, 1986. This paper is part of the *Journal of Engineering Mechanics*, Vol. 113, No. 9, September, 1987. ©ASCE, ISSN 0733-9399/87/0009-1302/$01.00. Paper No. 21769.

$$dW_p - dW_p^* = (\sigma_{ij} - \sigma_{ij}^*)\,\dot{\epsilon}_{ij}^p \geq 0 \quad \ldots\ldots (1a)$$

$$d^2W = \dot{\sigma}_{ij}\dot{\epsilon}_{ij}^p \geq 0 \quad \ldots\ldots (1b)$$

where σ_{ij} = a stress state located on the yield surface; σ_{ij}^* = a stress state located inside the yield surface; and $\dot{\sigma}_{ij}$ = a stress increment initiated at σ_{ij} on the yield surface, causing the plastic strain increment, $\dot{\epsilon}_{ij}^p$. Eq. 1*a*, which is often referred to as stability in the large, requires the yield surface to be convex. Eq. 1*b* is referred to as stability in the small, and it is fulfilled, in general, if the plastic strain increment vector is perpendicular to the yield surface. This implies that the plastic potential surface coincides with the yield surface, so that the plastic strain increments produced upon yielding are perpendicular to the yield surface. Thus, Drucker's stability postulate requires constitutive laws to incorporate a so-called associated flow rule in order to guarantee that stable behavior is obtained.

It is Eq. 1*b* that will be used to define stable or unstable behavior. If this inequality is fulfilled for any $\dot{\sigma}_{ij}$, then the material will be unconditionally stable. Otherwise, according to Drucker's postulate the material is conditionally stable, with the second increment d^2W positive for some $\dot{\sigma}_{ij}$ but negative for others, or completely unstable with d^2W negative for all $\dot{\sigma}_{ij}$. Complete instability, with d^2W negative, is obtained for all materials after the failure surface has been reached, whether the material exhibits associated or nonassociated flow.

The instability of interest here occurs before the failure surface has been reached. All nonassociated flow models exhibit a region where d^2W is negative. However, it is by no means clear that the materials which are being modeled are physically unstable in this region. It is the purpose of this experimental investigation to determine the physical behavior of a real soil in this region of negative d^2W.

Occurrence of Nonassociated Flow

In relation to a previous study of stress-path–dependent behavior of cohesionless soil (10), the uniqueness of stress-strain behavior for materials exhibiting nonassociated flow was discussed. Several triaxial tests were performed on Monterey number 0 sand with stress paths involving primary loading with decreasing stress difference ($\sigma_1 - \sigma_3$) and decreasing confining pressure, σ_3. The results of these tests were compared with results of conventional triaxial compression tests in which the confining pressure was held constant. If stresses and strain increments are plotted on the same diagram, as in Fig. 1(*b*), the direction of the plastic strain-increment vector is uniquely determined from the state of stress and is independent of the stress path leading to this state of stress. All strains are calculated as engineering strains, i.e., they refer to the original dimensions of the specimens. Since the prefailure strains of interest in this study are less than 6%, any effects of second-order terms or large strains are negligible. The failure surface indicated in Fig. 1(*b*) corresponds to peak failure conditions from drained tests in which maximum stress difference and maximum effective stress ratio occur simultaneously. The prefailure stress path with decreasing stresses shown in Fig. 1(*b*) is so steep as to form an obtuse angle (θ = 110°) with the direction of the strain-increment vector. Nevertheless, the two plastic strain-increment vectors are parallel. This has also been demonstrated by Poorooshasb, et al. (16).

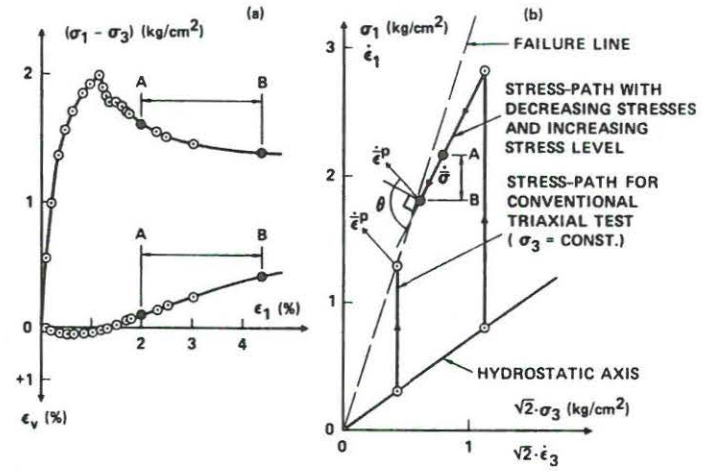

FIG. 1.—(*a*) Stress-Strain Behavior; (*b*) Stress Path with Decreasing Stresses Indicating Nonassociated Flow for Triaxial Test on Loose Monterey Number 0 Sand (e = 0.78; D_r = 27%) (1.0 kg/cm² = 98 kN/m²)

The fact that plastic yielding is occurring along the stress path with decreasing stresses is seen from the stress-strain curve in Fig. 1(*a*). Section AB on the stress path is labeled similarly on the stress-strain curve, which indicates large plastic strains between A and B. Since the yield surface is being pushed out, it must be steeper than the stress-path direction AB. If it were less steep, so as, e.g., to be perpendicular to the plastic strain-increment vector thereby indicating associated flow, then point B would be inside point A, corresponding to unloading from A to B. This would contradict the large plastic strains shown in Fig. 1(*a*). Consequently, the yield surface must be steeper than stress path AB and nonassociated flow is therefore clearly obtained.

Since the stress-increment vector and the strain-increment vector form an obtuse angle for the stress path considered, the scalar product of these two vectors (Eq. 1*b*) is negative. According to Drucker's stability postulate, the sand should exhibit unstable behavior along this stress path. However, the tests in Ref. 10 were all performed under strain control. This method of testing does not allow instabilities (i.e., gross collapse) of the material to be exposed. To force exposure of such instabilities, it is necessary to perform the tests under load or stress control.

It is important to recognize that the sand stress-strain curve in Fig. 1(*a*) corresponds to work hardening rather than softening. Although the stresses along stress path AB are decreasing, failure has not been reached, and softening of the material is therefore not occurring. The decreasing stresses along stress path AB are deliberately followed and not imposed

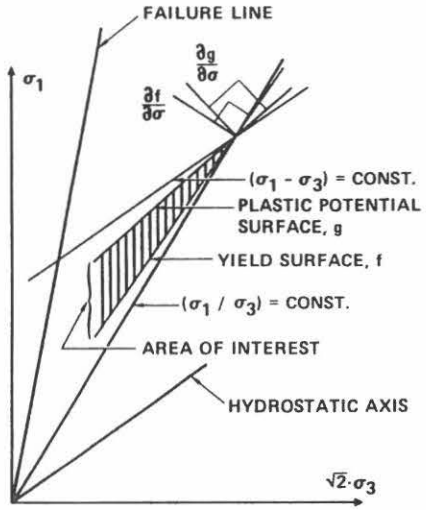

FIG. 2.—Wedge-Shaped Region of Stress Paths with Decreasing Stresses in which Granular Material with Nonassociated Flow May Be Unstable during Hardening Inside Failure Surface

by the material, whereas decreasing stresses are dictated by a softening material, because its strength has been exceeded and it is behaving in an unstable fashion.

Fig. 2 shows a schematic illustration of the region in which Eq. 1*b* is not fulfilled for a material with nonassociated flow. The region is shaped as a wedge between the current yield surface f and the plastic potential surface g corresponding to the current stress point. This wedge-shaped region is located within a larger region bounded by lines corresponding to (σ_1/σ_3) = const and $(\sigma_1 - \sigma_3)$ = const, as indicated in Fig. 2. All stresses, including the stress difference $(\sigma_1 - \sigma_3)$, are decreasing within the wedge between f and g, whereas the stress ratio (σ_1/σ_3) is increasing in this region. By performing triaxial tests with stress paths located in this region, it should be possible to obtain experimental evidence regarding the stability of materials with nonassociated flow.

Experimental Setup

In order to study experimentally the potential instabilities in soil behavior that might occur for the stress paths in the prefailure region described earlier, it is necessary to perform triaxial tests under stress control rather than strain control. This allows the triaxial specimen to exhibit any unstable behavior that may occur for the stress paths of interest.

Fig. 3 shows the experimental setup used to apply both horizontal and vertical stresses to a triaxial specimen under stress control. The minor principal stress, σ_3, was applied as a confining pressure in the triaxial

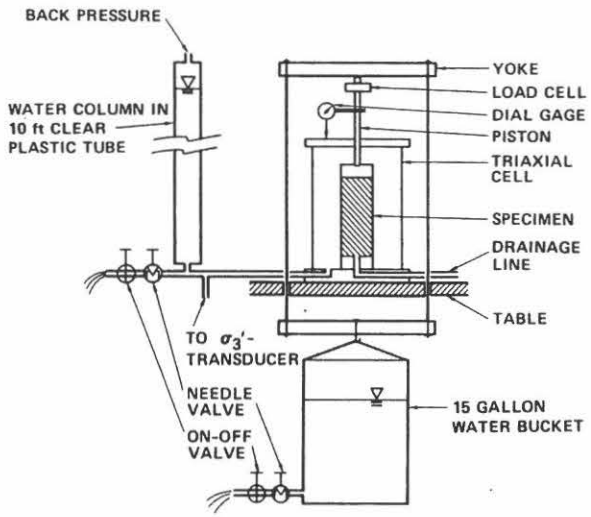

FIG. 3.—Experimental Setup for Stress Control of Triaxial Test

cell. This pressure was supplied by a column of water contained in a 10-ft tall clear platic tube. The water could be metered out through the needle valve at the bottom of the column, thus decreasing the minor principal stress on the specimen at a desired rate.

The vertical stress difference $(\sigma_1 - \sigma_3)$ was applied to the specimen by the piston protruding from the top plate of the triaxial cell. The vertical load was supplied by a bucket of water hanging in a yoke below the table supporting the triaxial cell. By filling the 15 gal bucket with water at any desired rate, it was possible to increase the stress difference $(\sigma_1 - \sigma_3)$ and to fail the specimen under load control with increasing vertical stress. However, all tests performed for the present study were conducted under load control with decreasing vertical stresses. This was accomplished by metering water out through a needle valve located near the bottom of the bucket. Thus, after having first loaded the specimen by filling water into the bucket, the water was let out through the needle valve at a desired rate. The actual vertical load applied to the specimen was measured with a load cell attached to the piston as seen in Fig. 3. The vertical stress rates employed during loading of the specimens averaged 0.025 kg/cm^2/min (2.5 kN/m^2/min) for increasing stresses and 0.001 kg/cm^2/min (0.1 kN/m^2/min) for decreasing stresses.

This simple experimental setup, in which the specimen was loaded under stress control, would allow any unstable behavior of the granular material to reveal itself by an inability to support the bucket of water. Thus, unstable soil behavior was expected to result in a dramatic drop of the water bucket to the laboratory floor, leaving no doubt about the nature of the soil behavior along certain stress paths of the types discussed earlier.

Sand Tested

To avoid experimental problems due to excessive effects of membrane penetration caused by changing confining pressures (11,14), the tests were performed on a fine sand. Membrane penetration into the pores of granular soils is small to negligible when the average diameter of the soil grains is smaller than 0.1–0.2 mm (6).

Fine silica sand composed of angular particles consisting mainly of quartz were used in the study. The characteristics of this sand are summarized as follows: (1) Mean diameter, 0.18 mm; (2) coefficient of uniformity, 2.0; (3) specific gravity of grains, 2.66; (4) maximum void ratio, 0.85; and (5) minimum void ratio, 0.55.

Tests were performed on dense specimens with void ratio of 0.58, corresponding to a relative density of 90%.

Specimen Preparation and Testing Procedures

All triaxial tests in the experimental program were performed on cylindrical specimens with diameter = 2.80 in. (7.1 cm). Some tests were performed on specimens with height = 2.80 in. (7.1 cm), corresponding to a height-to-diameter ratio of $H/D = 1.0$. Other tests were conducted on specimens with height = 7.4 in. (18.8 cm) corresponding to $H/D = 2.65$. The tall specimens were employed in most of the tests to allow any instabilities, e.g., development of shear planes or bands, to occur freely and uninterrupted by the end plates. In addition, lubricated end plates were used in all tests to avoid development of significant shear stresses at the cap and base.

The specimens were prepared by dry pluviation of sand and saturated using the CO_2-method (9). In addition, a nominal back pressure of 30 psi (207 kN/m^2) was applied to the specimens to ensure a high degree of saturation. B-values of 0.97 or better were measured in most tests.

The vertical load, the confining pressure, the vertical deformation, and the volume changes were measured during each test. Corrections were applied to the measured vertical load for uplift forces on the piston, piston friction, the load taken by the rubber membrane, and for the buoyed weight of the cap and the buoyed weight of the upper half of the specimen. The measured confining pressure was corrected for the additional hoop tension produced in the rubber membrane due to the volume change of the sand specimen. Corrections to linear as well as volumetric strains were found to be negligible.

Conventional Drained Triaxial Compression Tests

Four conventional, consolidated-drained, triaxial compression tests were performed to establish the stress-strain behavior and the strength of the fine silica sand. Three of the four triaxial tests were performed on specimens with $H/D = 1.0$ and with effective confining pressures of 0.075, 0.150, and 0.300 kg/cm^2 (7.4, 14.7, and 29.4 kN/m^2), corresponding to water column heights of 30, 59, and 118 in. (75, 150, and 300 cm). The fourth test was performed on a specimen with $H/D = 2.65$ and with an effective confining pressure of 0.250 kg/cm^2 (24.5 kN/m^2), corresponding to 100 in. (250 cm) of water. The four tests were all performed under strain control. Following failure, each specimen was unloaded to enable determination of the elastic behavior of the sand.

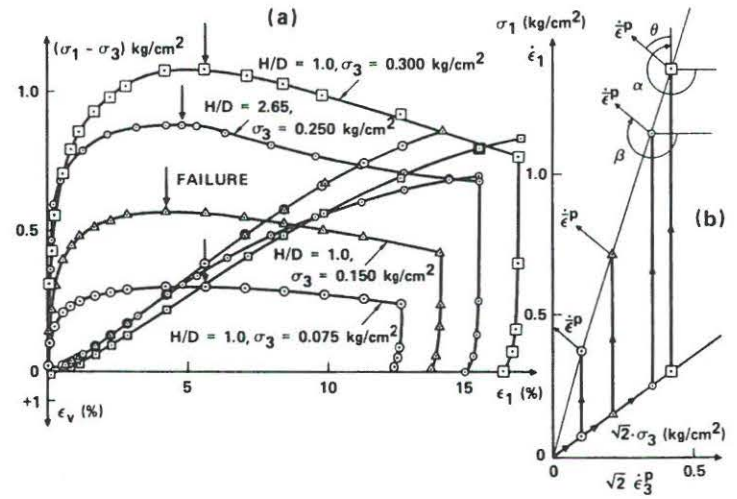

FIG. 4.—(*a*) Stress-Strain and Volume-Change Behavior; (*b*) Stress Path and Plastic Strain-Increment Vector Directions Observed in Conventional Triaxial Compression Tests on Fine Silica Sand (1.0 kg/cm^2 = 98 kN/m^2)

Stress differences and volumetric strains are plotted versus vertical strains for the four tests in Fig. 4(*a*). It may be seen that the differences in stress-strain and volumetric behavior between the short and the tall specimens are small. The initial modulus is a little higher for the tall specimen than for the short specimens, but the strain-to-peak failure is in the range of 4–6% for all specimens. The decreases in strength following peak failure also appear to form a consistent pattern. The friction angles from the four tests are listed in Table 1.

To compare these friction angles in a meaningful way, they have been adjusted to correspond to a void ratio of $e = 0.580$ and a relative density of 90.0%. The relationship $e \cdot \tan \phi = \text{const}$ is suitable for adjustment of friction angles when small differences in void ratio are present between

TABLE 1.—Results of Conventional Triaxial Compression Tests on Fine Silica Sand (1.0 kg/cm^2 = 98 kN/m^2)

Test number (1)	H/D (2)	e (3)	σ_3 (kg/cm^2) (4)	ϕ' (measured) (degrees) (5)	ϕ' (adjusted e = 0.580) (degrees) (6)	α (σ) (degrees) (7)	β ($\dot{\epsilon}$) (degrees) (8)	θ (degrees) (9)
CD-30	1.0	0.579	0.075	41.7	41.7	270.0	218.8	51.2
CD-59	1.0	0.579	0.150	40.8	40.8	270.0	218.7	51.3
CD-100	2.65	0.580	0.250	39.6	39.6	270.0	219.9	50.1
CD-118	1.0	0.585	0.300	39.9	40.1	270.0	220.1	49.9

the specimens (1). The friction angles for the short specimens show a pattern of decreasing values with increasing confining pressure as is usually found for soils (8). The tall specimen produced a friction angle that is slightly lower than those from the short specimens. Those differences have also been observed before from similar tests on tall and short specimens (7).

Fig. 4(*a*) also shows that the volume changes observed in the four tests form a consistent pattern with only slightly decreasing rates of dilation with increasing confining pressures. The corresponding strain-increment vector directions are superimposed on the triaxial plane shown in Fig. 4(*b*). These vector directions are directly related to the rates of dilation. The vectors are shown initiating from the failure points at the ends of the stress paths for the four triaxial compression tests.

From the diagram in Fig. 4(*b*), it appears that the strain-increment vectors are parallel. To obtain a more sensitive measure of their relative directions, the angles β measured clockwise from the σ_3-axis to the positive directions of the vectors, were calculated from the original test data according to the following expression:

$$\tan(\beta - 180°) = \frac{\sqrt{2}}{1 - \frac{\dot{\epsilon}_v}{\dot{\epsilon}_1}} \quad \ldots\ldots (2)$$

The values of β (Table 1) increase slightly with increasing confining pressure, thus reflecting the pattern of dilation rates shown in Fig. 4(*a*). The β-values vary consistently from 218.7°–220.1°, i.e., over a very narrow range of 1.40° with an average value of 219.4°.

The directions of the stress-increment vectors resulting in the aforementioned strain-increment vectors are vertical on Fig. 4(*b*). The corresponding α-values are therefore 270.0°, as listed in Table 1.

The angles θ between the stress-increment and strain-increment directions are all smaller than 90°. The scalar product given in Eq. 1*b* is therefore positive, corresponding to stable behavior in theory as well as experimentally.

Stress-Path Tests with Decreasing Stresses

A total of seven tests were performed with stress paths in the sector defined by the yield surface and the plastic potential surface. Six of these were conducted on tall specimens with $H/D = 2.65$, and one was performed on a short specimen with $H/D = 1.0$.

All tests were initiated at a confining pressure of 0.300 kg/cm^2 (29.4 kN/m^2). The specimens were first loaded vertically by filling the 15 gal bucket with water at a moderately slow, constant rate. As listed in Table 2, in five of the seven tests the specimens were loaded to a vertical stress difference of 0.98 kg/cm^2 (96 kN/m^2), whereas stress differences of 0.86 kg/cm^2 and 0.72 kg/cm^2 (84 and 71 kN/m^2) were used in the other two tests. The proximity of these stress states to the failure line may be expressed in terms of the stress level S defined as the ratio of the current to the maximum stress difference at a given confining pressure. Thus, the failure stress state corresponds to a stress level of $S = 1.00$. The three

TABLE 2.—Results of Stress Path Tests with Decreasing Stresses on Fine Silica Sand (1.0 kg/cm^2 = 98 kN/m^2)

Test number (1)	H/D (2)	e (3)	$(\sigma_1 - \sigma_3)_{max}$ (kg/cm^2) (4)	S at $(\sigma_1 - \sigma_3)_{max}$ (5)	σ_{3F} (kg/cm^2) (6)	ϕ' (measured) (degrees) (7)	ϕ' (adjusted $e = 0.580$) (degrees) (8)	α ($\dot{\sigma}$) (degrees) (9)	β ($\dot{\epsilon}$) (degrees) (10)	θ (degrees) (11)
SP2	2.65	0.591	0.97	0.97	0.281	38.4	38.9	116.2	220.9	104.7
SP3	1.0	0.568	0.99	0.93	0.254	40.0	39.4	112.2	218.2	106.0
SP4	2.65	0.582	0.98	0.95	0.275	39.1	39.2	117.5	219.2	101.7
SP5	2.65	0.582	0.98	0.92	0.253	40.0	40.1	112.8	219.0	106.2
SP6	2.65	0.580	0.98	0.94	0.254	39.7	39.7	116.8	219.4	102.6
SP7	2.65	0.580	0.86	0.86	0.209	39.6	39.6	109.5	219.0	109.5
SP8	2.65	0.580	0.72	0.75	0.173	40.0	40.0	115.2	218.6	103.4

stress differences reached in the seven tests correspond to stress levels of 0.94, 0.86, and 0.75, respectively.

Following the initial loading, the specimens were exposed to stress paths in which all stresses, as well as the vertical stress difference, were reduced in such ratios that the specimens were observed to compress vertically. Too severe a reduction of the vertical stress difference would result in unloading and therefore vertical extension of the specimens. Thus, the stress paths imposed on the specimens were of the type that would potentially lead to unstable behavior of the sand.

Fig. 5 shows the stress-strain and volume change curves, as well as the stress path for test number SP7. These results clearly illustrate the essence of the study presented here. Fig. 5(*a*) indicates that the vertical stress difference was first increased to 0.86 kg/cm^2 (84 kN/m^2), while the confining pressure was held constant at 0.300 kg/cm^2 (29.4 kN/m^2). From the corresponding stress level of 0.86, the specimen was further loaded under load control along a stress path, which potentially could lead to unstable behavior of the sand. Fig. 5(*b*) shows that this second branch of the stress path is curved, although the flow rates from the two reservoirs were held constant. The curvature is caused by the accelerated increase in cross-sectional area of the specimen as failure is approached and subsequently crossed.

It is clear from the stress-strain curve that failure cannot be distinguished from observation of the vertical stress difference alone. However, the effective stress ratio will reach a maximum along the stress path indicated in Fig. 5(*b*). This maximum occurs at the point on the stress path that, when connected with the origin, forms the greatest slope of any point on the stress path. This criterion of failure is often used for granular materials and for soils without effective cohesion. Thus, for such materials and for frictional materials in general (soils, rock, concrete), it is important to consider the magnitude of all stresses when conditions of failure are to be described.

The portion of the stress path of interest in the present study is that from point B to point C. All stresses, as well as the vertical stress difference, are decreasing along this second branch. The strain increments produced along this branch correspond to dilation of the sand. Superimposed on the triaxial plane in Fig. 5(*b*) are the strain-increment vectors at points B and C. These strain-increment vectors, which are almost par-

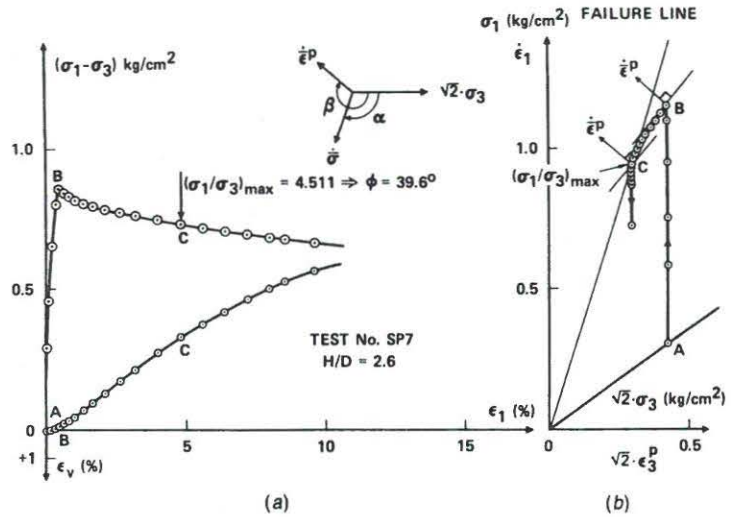

FIG. 5.—(*a*) Stress-Strain and Volume-Change Curves; (*b*) Stress Path and Plastic Strain-Increment Vectors for Test Number SP7 on Fine Silica Sand (1.0 kg/cm² = 98 kN/m²)

allel, are by definition perpendicular to the respective plastic potential surfaces indicated at these two points.

It is clear that each increment of stress along the entire length of branch BC forms obtuse angles, θ, with the corresponding strain-increment directions. Thus, the scalar product of the two vectors expressed in Eq. 1*b* is negative, and the behavior of the granular material should be unstable according to the inequality. However, each of the seven tests exhibited stable behavior before the maximum stress ratio had been reached. In fact, the specimens deformed uniformly, i.e., there was no visible evidence of bulging or shear-band formation until well beyond failure as measured by the maximum stress ratio.

The essential results of the seven tests are summarized in Table 2. Detailed results are given in Ref. 12. As for the conventional tests, the friction angles have been adjusted to correspond to a void ratio of e = 0.580. The seven specimens failed within a narrow range of confining pressures, and the adjusted friction angles are therefore directly comparable. The average value of the friction angles is 39.6° with a standard deviation of 0.46°. Thus, the strengths obtained from the seven stress-path tests are exactly the same as those obtained from conventional triaxial compression tests (ϕ' = 39.6° for test number CD-100 with H/D = 2.65). This shows that the sand specimens remained perfectly stable, and they reached the same failure surface as obtained from conventional tests. In none of the tests did shear planes or bands develop until well beyond failure, and there was consequently no difference in terms of stability and strength between the short specimens, in which shear-plane propagation may be inhibited, and tall specimens, in which shear planes are free to develop and propagate when they occur (see Ref. 7).

The directions of the strain-increment vectors are indicated by the angles β measured clockwise from the σ_3-axis to the positive directions of these vectors. The β-values are calculated from Eq. 2 and listed in Table 2. Since all specimens failed within a narrow range of confining pressures, there should not and there does not appear to be any systematic variation of the β-values in the seven tests. The average β-value is 219.2° and the standard deviation is 0.85°. Thus, the strain-increment directions obtained from the stress-path tests are the same as those obtained from the conventional tests in which the average β-value is 219.4°. The fact that the directions of the strain-increment vectors are independent of the stress path has been observed before (10,16). These important characteristics of the material behavior make it possible to express and determine the relative magnitudes of the plastic strain increments from a potential function.

The directions of the stress-increment vectors are calculated from the stresses leading up to failure. The directions are expressed in terms of the angles α, measured clockwise from the σ_3-axis to the positive directions of the stress-increment vectors. The values of α are determined from the following expression:

$$\tan(\alpha - 90°) = \frac{\sqrt{2}\,\dot{\sigma}_3}{\dot{\sigma}_1} \quad \ldots\ldots (3)$$

and listed in Table 2. It may be seen that a range of α-values from 109.5°–117.5° are covered in the experiments.

The angles θ between the positive directions of the strain-increment and stress-increment directions are calculated as the difference between β and α and listed in Table 2. The values of θ range from 101.7°–109.5°, i.e., from 11.7°–19.5° greater than 90°, which corresponds to perpendicularity of the two vectors. Thus, the plastic flow of the granular material is clearly of the nonassociated type. More importantly in the present context, the seven stress paths all involve conditions for which the scalar products of the strain-increment and stress-increment vectors are negative. Therefore the material behavior should be unstable. However, each specimen behaved in a stable manner, and they all reached strengths of the same magnitudes as those obtained from conventional triaxial compression tests.

Analysis

The occurrence of nonassociated flow and the consequent problem of stability of materials that exhibit nonassociated flow behavior have been the subject of much discussion. For example, the reliability of the experimental data that provided the evidence for nonassociated flow has at times been questioned. In a similar fashion, assuming and accepting the possibility that instabilities may occur, the potential problem has been circumvented by inclusion of rate effects, e.g., viscous flow or creep, to disguise the unstable behavior and to temporarily maintain stability of the material. Release of stored elastic energy to counter dissipation of

plastic work along stress paths with decreasing stresses has also been proposed. Each of these points will be considered in detail below.

Reliability of Test Data.—Because experimental data are at times subject to justified criticism and because such data may be unreliable, the occurrence of nonassociated flow occasionally has been considered to be the result of imprecise performance and measurements in tests that otherwise would exhibit associated flow.

Applied loads and pressures can be measured with good accuracy in experiments such as triaxial compression tests. The most obvious inaccuracies in these tests arise from nonuniform strains exhibited by, e.g., bulging of the specimen. This mode of deformation is due to end restraint caused by development of shear stresses between the end plates and the specimen. To avoid this problem, lubrication consisting of one or more thin rubber sheets coated with silicone grease may be used on the cap and base. By adjusting the number of rubber sheets and the amount of silicone grease, the specimen can be made to deform as a right cylinder, thereby producing uniform strains.

Lubricated ends were used in the tests performed for this study. The shape of the specimen was carefully monitored during each test to detect any signs of bulging or other nonuniform deformation patterns. The specimens in all tests deformed as perfect right cylinders until well beyond failure (maximum stress ratio). The experimental results presented here are therefore considered to be reliable and to correctly reflect the true behavior of the soil.

In spite of the care with which the present experimental program was executed, it was of interest to investigate the degree to which nonuniform strain distributions could disguise the type of behavior (associated or nonassociated flow) exhibited by the soil. For this purpose, the specimen has been assumed to deform nonuniformly and to develop from a right cylinder into the shape of a barrel. It is therefore obvious that the lateral strain, ϵ_3, is nonuniformly distributed along the vertical axis of the specimen. In the analysis, it is assumed that the contour of the barrel is shaped as a parabola with no expansion at the ends. Two simple options are available for the distribution of the vertical strain, ϵ_1: (1) Parabolic distribution with zero strains at the ends and maximum strain in the middle; and (2) uniform strain distribution. Both these assumed strain distributions are extreme on either side of the real strain distribution in a specimen with full friction on the end plates.

The results of the analyses are given in Table 3 in terms of the ratio $\dot{\epsilon}_1/(\sqrt{2}\,\dot{\epsilon}_3)$, which is equivalent to the negative value of the right-hand side of Eq. 2. The values of $\dot{\epsilon}_1$ and $\dot{\epsilon}_v$ in Table 3 are those usually calculated by assuming the specimen to deform as a right cylinder with uniform strains. The strain-increment ratio is calculated for the ends and the middle of the specimen for various combinations of uniform and parabolic strain distributions. The expression for the strain-increment ratio for uniform strain distributions (Col. 2) is that employed in Eq. 2.

For parabolic distributions of both ϵ_1 and ϵ_3 with no strains at the ends, the ratio of the strain increments in the middle (Col. 3) becomes the same as that obtained for uniform strain distributions. Thus, the type of behavior exhibited by the soil is easily recognizable, even from grossly noncylindrical specimens with most of the deformation occurring in the

TABLE 3.—Values of $\dot{\epsilon}_1/(\sqrt{2}\dot{\epsilon}_3)$ for Different Assumed Strain Distributions in Triaxial Specimen

Strain conditions (1)	Uniform ϵ_1, uniform ϵ_3 (2)	Parabolic ϵ_1, parabolic ϵ_3, no strains at ends (3)	Uniform ϵ_1, parabolic ϵ_3, $\epsilon_3 = 0$ at ends (4)
At ends	$-2/(1 - \dot{\epsilon}_v/\dot{\epsilon}_1)$	$0/0 = ?\ (-\infty)$	$-\infty$
In middle	$-2/(1 - \dot{\epsilon}_v/\dot{\epsilon}_1)$	$-2/(1 - \dot{\epsilon}_v/\dot{\epsilon}_1)$	$-2/3 \cdot \sqrt{2}/(1 - \dot{\epsilon}_v/\dot{\epsilon}_1)$

middle. Although fixity in terms of ϵ_3, i.e., $\epsilon_3 = 0$, can occur at the ends, at least mathematically, the value of $\epsilon_1 = 0$ would correspond to an infinite modulus. Allowing for a modulus of finite value, the ratio of $\dot{\epsilon}_1/(\sqrt{2}\,\dot{\epsilon}_3) = -\infty$ is reasonable for full fixity at the ends of the specimen. Alternatively, the specimen might be unloading at the ends (due to reducing stresses along the stress path under consideration), in which case the soil behavior is elastic and not of interest in the present context.

If, on the other hand, the vertical strain distribution is assumed to be uniform, the results listed in Col. 4 of Table 3 are obtained. In this case, the ratio of the strain increments in the middle is multiplied by a factor of 2/3, i.e., the strain-increment vector is apparently moving towards perpendicularity to the stress path. Additional considerations are necessary to investigate whether the results of the triaxial tests now indicate associated flow, and this in turn might be the reason for the stable behavior of the granular material.

Since the ϵ_3-distribution is assumed to be parabolic, the cross-sectional area in the middle of the specimen is larger than that obtained from a perfect cylindrical specimen with the same measured vertical deformation and volume change. The cross-sectional area at the middle of the barrel-shaped specimen may be expressed as

$$A_{\text{barrel}} = A_{\text{cylinder}} \cdot \left[1 + \frac{1}{2} \cdot (\epsilon_1 - \epsilon_v)\right] \quad \ldots\ldots\ldots\

TABLE 4.—Directions of Stress Increment and Strain Increment for Assumed Parabolic Lateral Strain Distribution and Assumed Uniform Vertical Strain Distribution in Triaxial Specimens

Test number (1)	H/D (2)	α ($\dot{\sigma}$) (degrees) (3)	β ($\dot{\epsilon}$) (degrees) (4)	θ (degrees) (5)
SP2	2.65	110.8	210.0	99.2
SP3	1.0	105.4	207.7	102.3
SP4	2.65	109.2	208.6	99.4
SP5	2.65	105.8	208.4	102.6
SP6	2.65	112.1	208.7	96.6
SP7	2.65	103.9	208.3	104.4
SP8	2.65	109.8	208.0	98.2

was perpendicularity obtained. In fact, the angles θ remained in all cases greater than 90°, and the soil therefore exhibited nonassociated flow behavior. Thus, even an unlikely combination of parabolic ϵ_3-distribution and uniform ϵ_1-distribution is insufficient to disguise the real soil behavior. The true ϵ_1-distribution in a specimen with full-end restraint is most likely in between the assumed uniform and parabolic distributions, and the true θ-values for these boundary conditions are therefore higher than those listed in Table 4.

Rate/Time Effects.—The occurrence of viscous flow or creep may maintain the stability, at least temporarily, of otherwise unstable materials. This effect often manifests itself through increasing strength with increasing loading rate. Thus, the material appears to remain stable at high magnitudes of shear stresses when these are applied at a fast rate. Examples of this behavior can be found for soils, ice, rock, concrete, etc. (see Ref. 2).

In a similar fashion, it is possible that the granular material tested for this study remained stable because the load was changed at a reasonable finite rate. To check if effects of viscious behavior were artificially maintaining stability of the sand specimens, the testing procedures for two of the seven specimens included establishment of creep curves at several stress levels. One representative set of creep curves is shown in Fig. 6 for test number SP5. The first four creep curves were established during loading of the specimen at the constant confining pressure of 0.300 kg/cm^2 (29.4 kN/m^2). This was done by simply stopping the vertical loading of the specimen and observing the deformation with time. Very little but increasing amounts of creep occur with increasing stress level. The following two creep curves were determined along the stress path involving decreasing stresses. These curves were measured after having stopped the changes in both vertical and lateral stresses. Because the stress levels were closer to the failure stress ratio (i.e., 0.96 and 0.99), greater amounts of creep strains occurred. However, in both cases the creep rates decreased to very small values after 60 min. The specimen was perfectly stable, even after the majority of viscous effects had gone away. Thus, it is clear that viscous effects cannot account for the stability of the sand.

The last creep curve was measured after the maximum (failure) stress ratio had been obtained. The stress level for this curve was initially 0.98,

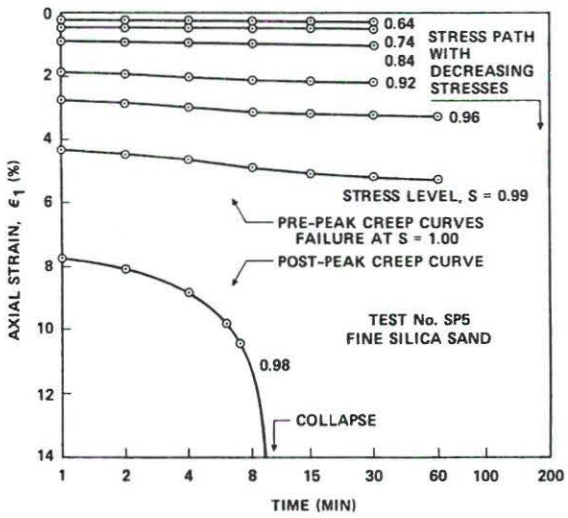

FIG. 6.—Creep Curves Obtained at Several Stress Levels in Test Number SP5 on Fine Silica Sand

i.e., the stresses had only decreased a small amount after failure due to increasing cross-sectional specimen area. Nevertheless, the specimen was clearly unstable after failure, and it moved to complete collapse with no further change in vertical load or confining pressure. The reason that instability was not observed immediately upon failure, i.e., immediately after $S = 1.00$ had been reached, was that viscous effects maintained stability over a short period of time, allowing further increase in cross-sectional area to occur before it was realized that failure had been passed and that collapse was in progress.

It can be seen that the sand specimen maintains stability before failure independent of any viscous effects exhibited by the material. However, immediately following failure, according to the maximum stress-ratio criterion, the instability of the sand is clearly evident. The deformation to complete collapse of the specimen begins slowly and then accelerates to a constant terminal velocity, after which the specimen deforms at a constant rate. Thus, the specimen did not exhibit catastrophic failure, as, e.g., in a liquefaction failure of loose sand.

Release of Stored Elastic Energy.—In order to account for the stability of granular materials during stress paths with decreasing stresses, it may be possible that elastic energy is released to counter the dissipation of plastic energy. Stability should then be maintained as long as

$$\dot{\sigma}_{ij} \cdot \dot{\epsilon}_{ij} = \dot{\sigma}_{ij} \cdot (\dot{\epsilon}^e_{ij} + \dot{\epsilon}^p_{ij}) = \dot{\sigma}_{ij} \cdot \dot{\epsilon}^e_{ij} + \dot{\sigma}_{ij} \cdot \dot{\epsilon}^p_{ij} \geq 0 \quad \ldots\ldots\ldots\ldots\ldots\ldots\ldots\ldots (5)$$

in which case the sign of the elastic energy increment is the opposite of the sign of the plastic energy increment along stress paths with decreas-

ing stresses. Thus, stability should be maintained along potentially unstable stress paths as long as

$$\dot{\sigma}_{ij}\,\dot{\epsilon}^{e}_{ij} \geq |\,\dot{\sigma}_{ij}\,\dot{\epsilon}^{p}_{ij}| \quad \ldots\ldots (6)$$

in which both sides of the unequal sign have positive values. By forming the ratio of elastic to plastic energy increments and expanding the terms, the following inequality is produced:

$$\frac{\frac{1}{E}\cdot[\dot{\sigma}_1^2 - 4\dot{\sigma}_1\dot{\sigma}_3 + 2(1-\nu)\dot{\sigma}_3^2]}{|\dot{\sigma}_1\dot{\epsilon}_1^p + 2\dot{\sigma}_3\dot{\epsilon}_3^p|} \geq 1 \quad \ldots\ldots (7)$$

The test most likely to fulfill this condition for stability is that whose value of θ in Table 2 is nearest to 90°. Test number SP4 involves the lowest value of $\theta = 101.7°$. The left-hand side of Eq. 7 is therefore calculated for this test, using an elastic modulus of $E = 400$ kg/cm^2 (39,240 kN/m^2) (determined from the unloading branches in Fig. 4) and a Poisson's ratio of 0.25 (determined from the initial portion of the volume change curve during reloading). The value of the ratio of energy increments is determined to be 0.031, i.e., much less than unity. The other six tests would have even smaller values of the ratio of energy increments occurring on the left-hand side of Eq. 7. Therefore, the release of stored elastic energy accounts for a maximum of 3.1% of the plastic energy increment in the seven stress-path tests with decreasing stresses, and this mechanism cannot account for the stability of the granular material.

The tests described earlier all exhibited stable behavior until the failure surface was reached. These tests were performed on dense sand at low confining pressures, at which the material exhibits the type of behavior that is very characteristic of frictional materials. Notably, the granular material dilated under the conditions under which it was tested. On the other hand, granular materials that tend to compress may become unstable and liquefy during shear. The type of volume-change behavior exhibited by the material is of overriding significance in the question of stability. This has been discussed in further detail by the writers (12).

Summary

The stability postulate formulated by Drucker provides a sufficient condition for stability and requires that materials obey an associated plastic flow rule. Frictional materials exhibit nonassociated plastic flow, and the stability of such materials has often been questioned. To provide experimental evidence regarding the stability of granular materials, a series of triaxial tests was performed on specimens of dense sand exposed to stress paths with decreasing stresses and increasing stress levels. These tests were performed under stress control so that any instability in the material could freely develop. The results of the tests showed that the granular material dilated during shear, it followed a nonassociated flow rule, and stability was obtained in all cases until the failure surface was reached. Thus, stable behavior was observed in a region in which Drucker's stability postulate was violated. The reliability of the test results, the possible influence of viscous effects on the stability of the material, and the effect of release of elastic energy were investigated experimentally and discussed in detail. None of these effects could account for the stability of the material.

The occurrence of stable behavior found in this study is related to the dilation exhibited by the granular material. The type of volume-change behavior exhibited by the material is of great significance in the question of stability of granular materials.

Appendix.—References

1. Caquot, A., and Kerisel, J., *Traité de Mecanique des Sols*, 4th ed., Gauthier-Villars, Paris, France, 1966.
2. Casagrande, A., and Wilson, S. D., "Effects of Rate of Loading on the Strength of Clays and Shales at Constant Water Content," *Geotechnique*, Vol. 2, 1951, pp. 251–264.
3. Drucker, D. C., "A More Fundamental Approach to Stress-Strain Relations," *Proceedings, 1st U.S. National Congress on Applied Mechanics*, 1951, pp. 487–491.
4. Drucker, D. C., "On Uniqueness in the Theory of Plasticity," *Quarterly Applied Mathematics*, 1956, Vol. 14, pp. 35–42.
5. Drucker, D. C., "A Definition of Stable Inelastic Material," *Journal Applied Mathematics*, Vol. 26, 1959, pp. 101–106.
6. Frydman, S., Zeitlen, J. G., and Alpan, I., "The Membrane Effect in Triaxial Testing of Granular Soils," *Journal of Testing and Evaluation*, Vol. 1, No. 1, Jan., 1973, pp. 37–41.
7. Lade, P. V., "Localization Effects in Triaxial Tests on Sand," *Proceedings, Symposium on Deformation and Failure of Granular Materials*, International Union of Theoretical and Applied Mechanics, P. A. Vermeer and H. J. Luger, Eds., Delft, Holland, Aug., 1982, pp. 461–471.
8. Lade, P. V., "Failure Criterion for Frictional Materials," Chapter 20, *Mechanics of Engineering Materials*, C. S. Desai and R. H. Gallagher, Eds., John Wiley and Sons, Ltd., New York, N.Y., 1984, pp. 385–402.
9. Lade, P. V., and Duncan, J. M., "Cubical Triaxial Tests on Cohesionless Soil," *Journal of the Soil Mechanics and Foundations Division*, ASCE, Vol. 99, No. 10, Oct., 1973, pp. 793–812.
10. Lade, P. V., and Duncan, J. M., "Stress-Path Dependent Behavior of Cohesionless Soil," *Journal of the Geotechnical Engineering Division*, ASCE, Vol. 102, No. 1, Jan., 1976, pp. 51–68.
11. Lade, P. V., and Hernandez, S. B., "Membrane Penetration Effects in Undrained Tests," *Journal of the Geotechnical Engineering Division*, ASCE, Vol. 103, No. 2, Feb., 1977, pp. 109–125.
12. Lade, P. V., Nelson, R. B., and Ito, Y. M., "Experimental Study of Nonassociated Flow and Stability of Granular Materials," California Research and Technology, Inc., Chatsworth, Calif., Sep., 1985.
13. Mandel, J., "Conditions de Stabilite et Postulat de Drucker," *Proceedings, International Union of Theoretical and Applied Mechanics Symposium on Rheology and Soil Mechanics*, Grenoble, France, 1964, pp. 58–67.
14. Martin, G. R., Finn, W. D. L., and Seed, H. B., "Effects of System Compliance on Liquefaction Tests," *Journal of the Geotechnical Engineering Division*, ASCE, Vol. 104, No. 4, Apr., 1978, pp. 463–479.
15. Mroz, Z., "Nonassociated Flow Laws in Plasticity," *Journal de Mecanique*, Vol. 2, No. 1, 1963, pp. 21–42.
16. Poorooshasb, H. B., Holubec, I., and Sherbourne, A. N., "Yielding and Flow of Sand in Triaxial Compression: Part I," *Canadian Geotechnical Journal*, Vol. III, No. 4, Nov., 1966, pp. 179–190.

Instability of Granular Materials with Nonassociated Flow

By Poul V. Lade,[1] Member, ASCE, Richard B. Nelson,[2] Member, ASCE, and Y. Marvin Ito[3]

Abstract: Materials exhibiting nonassociated flow should, according to Drucker's stability postulate, become unstable when exposed to certain stress-paths inside the failure surface. Results of a series of triaxial tests designed to expose the type of behavior displayed by granular materials are presented and discussed. The sand tends to compress during shear, it exhibits nonassociated flow, and instability is observed along stress-paths in the region of potential instability. In a previous study of similar type in which dilation developed during shear and the sand exhibited nonassociated flow, when the specimens were exposed to stress-paths in the region of potential instability, none was observed. The type of volume change behavior displayed by the material is of great importance in the question of stability of granular materials. Stability conditions for materials with nonassociated flow are presented.

Introduction

Frictional materials such as sand, clay, concrete, and rock exhibit nonassociated plastic flow, and consequently questions have been raised regarding uniqueness and stability of such materials. Drucker's stability postulate for time-independent materials (Drucker 1951, 1956, 1959) provides a sufficient condition for stability and ensures uniqueness in dynamic as well as static problems. Drucker's postulate is satisfied provided that associated flow is employed in construction of constitutive models involving convex, plastic yield surfaces. Although Drucker's postulate provides a sufficient condition for stability, theoretical considerations have suggested that it is not a necessary condition (Mandel 1964, Mroz 1963).

Experiments to support this conclusion have been presented by the authors (Lade et al. 1987). In a series of tests designed to expose the type of behavior that is characteristic of granular materials, the sand exhibited nonassociated flow, and stability was obtained at the same time Drucker's postulate was being violated. The occurrence of stable behavior inside the failure surface (i.e., before failure had been reached) was found to be associated with the dilation or volumetric expansion exhibited by granular materials.

In the present paper a sand very similar to that investigated in Lade et al. (1987) is again investigated, but in a loading region where shear induced volumetric compression occurs, rather than dilation as in Lade et al. (1987). Again, stress-paths are explored along which Drucker's stability postulate is

[1]Prof., Dept. of Civ. Engrg., School of Engrg. and Appl. Sci., Univ. of California, Los Angeles, CA 90024.

[2]Prof., Dept. of Civ. Engrg., School of Engrg. and Appl. Sci., Univ. of California, Los Angeles, CA 90024.

[3]Adj. Prof., Dept. of Civ. Engrg., School of Engrg. and Appl. Sci., Univ. of California, Los Angeles, CA 90024; Engrg. Mech. Grp., Calif. Res. and Tech., Inc., Chatsworth, CA 91311.

Note. Discussion open until May 1, 1989. To extend the closing date one month, a written request must be filed with the ASCE Manager of Journals. The manuscript for this paper was submitted for review and possible publication on June 26, 1987. This paper is part of the ***Journal of Engineering Mechanics***, Vol. 114, No. 12, December, 1988. ©ASCE, ISSN 0733-9399/88/0012-2173/$1.00 + $.15 per page. Paper No. 23046.

violated. The experimental apparatus is a load controlled device so that any instabilities will develop freely. It will be shown that, for the load paths considered herein, instabilities develop.

The problem of instability and the factors which control the occurrence of unstable behavior of granular materials are discussed in view of experimental results in the present paper. Based on the evidence presented here and in the previous publication (Lade et al. 1987), conditions for stability are formulated for granular materials. These conditions take the form of additions to Drucker's stability postulate.

Drucker's Stability Postulate

The stability condition formulated by Drucker (1951, 1956, 1959) involves two components expressed in terms of plastic work increments:

$$dW_p - dW_p^* = (\sigma_{ij} - \sigma_{ij}^*)\dot{\epsilon}_{ij}^p \geq 0 \quad \ldots\ldots (1a)$$

$$d^2W_p = \dot{\sigma}_{ij}\dot{\epsilon}_{ij}^p \geq 0 \quad \ldots\ldots (1b)$$

where σ_{ij} = a stress state located on the yield surface; σ_{ij}^* = a state located inside the yield surface; and $\dot{\sigma}_{ij}$ = a stress increment initiated at σ_{ij} on the yield surface causing the plastic strain increment $\dot{\epsilon}_{ij}^p$. Inequality 1(a), which is often referred to as stability in the large, requires the yield surface to be convex. Inequality 1(b) is referred to as stability in the small, and it is fulfilled in general if the plastic strain increment vector is perpendicular to the yield surface. This implies that the plastic potential surface coincides with the yield surface such that the plastic strain increments produced upon yielding are perpendicular to the yield surface. Thus, Drucker's stability postulate requires constitutive laws which incorporate an associated flow rule in order to guarantee that stable behavior is obtained.

It is the second Inequality 1(b) which defines stable or unstable behavior. If this inequality is fulfilled for any $\dot{\sigma}_{ij}$, then the material will be unconditionally stable. Otherwise, according to Drucker's postulate the material will be unconditionally stable, with the second increment d^2W_p positive for some $\dot{\sigma}_{ij}$ but negative for others, or it may be unstable with d^2W_p negative for all $\dot{\sigma}_{ij}$.

The instability of interest here occurs before the failure surface has been reached. Complete instability with d^2W_p negative, is obtained for all materials after the failure surface has been reached, whether the material exhibits associated or nonassociated flow. Inside the failure surface, but in a state of inelastic behavior (yield), all nonassociated flow mathematical models exhibit a region where d^2W_p is negative and, hence, where the material is unstable. However, it is by no means clear that the real materials which are being modeled are physically unstable in this region. It is the purpose of the experimental investigation to determine the physical behavior and the factors that influence the behavior of a real sand in this region of negative d^2W_p.

Nonassociated Flow and Possible Consequences

A typical pattern of yield surfaces for an isotropic granular material is shown on the triaxial plane in Fig. 1. In three dimensions these yield surfaces are shaped as asymmetric tear drops. For an isotropic material the yield

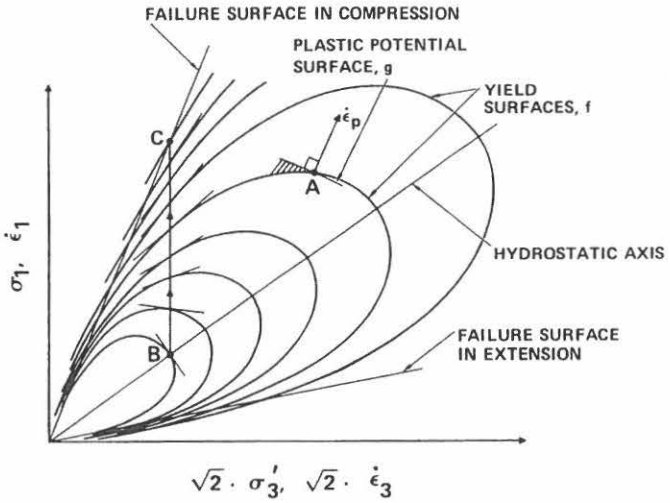

FIG. 1. Pattern of Yield Surfaces for Isotropic Granular Materials. Stress-Path for Conventional Triaxial Compression Test (BC)

surfaces intersect the hydrostatic axis in a perpendicular manner, they bend smoothly backwards towards the origin, and cross the failure surface at sharp angles as indicated in Fig. 1.

Plastic potential surfaces have similar shapes as yield surfaces, but for nonassociated flow the two families of surfaces cross each other. Experimental evidence for frictional materials indicates that the plastic potential surfaces have flatter rounded ends and the apex of the surface is not at the origin, but rather located at a point on the negative pressure axis. A typical plastic potential surface is shown at point A in Fig. 1.

The shaded wedge between the yield surface and the plastic potential surface defines a region in which Inequality 1(b) is not fulfilled for a material with nonassociated flow. Since a stress increment vector from point A located inside the wedge and the plastic strain increment vector form an obtuse angle, the scalar product of these two vectors [see Inequality 1(b)] is negative. According to Drucker's stability postulate, the sand may exhibit unstable behavior if a stress increment lies in the shaded region. However, as will be seen, the sand is perfectly stable at stress points where the normal to the yield surface points in the outward direction of the hydrostatic axis. For this condition the deviator stress can be safely increased to produce further plastic shear strains (work-hardening). In other words, the sand can sustain higher loads and behave in an inelastic manner without undergoing any instability or collapse.

Potential instability occurs in regions where the yield surface opens up in the outward direction of the hydrostatic axis. This allows plastic strains (loading) to occur while the stresses are decreasing. Here loading occurs inside the failure surface and instability may develop in the form of inability to sustain the current deviator stresses.

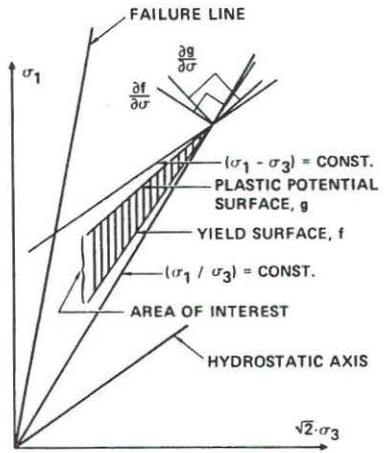

FIG. 2. Wedge-Shaped Region of Stress-Paths with Decreasing Stresses in which Granular Material with Nonassociated Flow may be Unstable during Hardening Inside Failure Surface

Fig. 1 shows the stress-path for a conventional triaxial compression test performed at constant confining pressure. As the specimen is loaded from B to C the inclination of the yield surface changes. At low deviator stresses near point B, the yield surface is inclined towards the outwards direction of the hydrostatic axis. As loading proceeds, the inclination of the yield surface changes gradually and becomes inclined towards the origin as failure is approached at point C. It is in this region of high deviator stresses where the yield surface is inclined towards the origin that instability may occur.

Fig. 2 shows a schematic illustration of the region in which Inequality 1(b) is not fulfilled for a material with nonassociated flow. The region is shaped as a wedge between the current yield surface f and the plastic potential surface g corresponding to the current stress point. This wedge shaped region is located within a larger region bounded by lines corresponding to (σ_1/σ_3) = const. and $(\sigma_1 - \sigma_3)$ = const. as indicated on Fig. 2. All stresses, including the stress difference $(\sigma_1 - \sigma_3)$, are decreasing within the wedge between f and g, but the stress ratio (σ_1/σ_3) is increasing in this region. By performing triaxial tests with stress-paths located in this region, experimental evidence regarding the stability of materials with nonassociated flow can be obtained.

It is important to recognize that the material behavior obtained for stress-paths within the shaded wedge in Fig. 2 corresponds to work-hardening with positive plastic work, $dW_p > 0$, and outward motion of the yield surface. Although the stresses in any direction within the wedge are decreasing, failure has not been reached and softening of the material is therefore not occurring. The decreasing stresses along a stress-path within the wedge may be deliberately followed and not imposed by the material. Such a stress-path is not possible in a softening material, because its strength has been exceeded, and it is behaving in an unstable fashion.

Region of Stability

In a previous study (Lade et al. 1987) performed to provide experimental evidence regarding the stability/instability of granular materials, a number of triaxial tests were performed on specimens of dense sand exposed to stress-paths with decreasing stresses and increasing stress ratios. The tests were performed under stress control so that any instability in the material could freely develop. The results of the tests showed that the granular material dilated during shear, following a nonassociated flow rule, and stability was obtained in all cases until the failure surface was reached. Thus, stable behavior was observed in a region in which Drucker's stability postulate was violated. The reliability of the test results, the possible influence of viscous effects on the stability of the material, and the effect of release of elastic energy were investigated experimentally, and discussed in detail. None of these effects could account for the stability of the material.

The occurrence of stable behavior found in the previous study is related to the dilation exhibited by the granular material. The triaxial tests were performed on dense sand at low confining pressures at which the material exhibited the type of behavior which is very characteristic of frictional materials, namely dilation under the test conditions. The tests showed that granular materials appear to be stable in the region of stresses where dilation occurs. This region is located near the failure surface at low to medium confining pressures for materials at a given void ratio. For higher confining pressures the same material undergoes volumetric compression during shear. The unique relation between void ratio and confining pressure for which a granular material dilates or compresses at failure is described by the concept of critical state as defined by Seed and Lee (1967) and by Lee and Seed (1967).

Region of Potential Instability

According to the critical state concept a granular material at a given void ratio will compress during shear at sufficiently high confining pressures. If the question of stability is related to the type of volume change (dilation or compression) occurring in the material, then it should be possible to induce instability inside the failure surface by conducting tests at high confining pressures with stress-paths within the shaded wedge shown in Fig. 2. Under these conditions the specimens will tend to compress during shear.

Undrained triaxial compression tests performed at high confining pressures on saturated granular materials exhibit effective stress-paths whose directions inside the failure surface may fulfill the requirements presented above. Fig. 3 shows the effective stress-paths for four undrained triaxial compression tests on loose Sacramento River Sand performed by Lee (1965). The specimens were initially consolidated isotropically at the effective consolidation pressures, σ'_{3c}, indicated on the figure. The volumetric strain in undrained tests on saturated specimens is zero, but the tendency for compression at high confining pressures results in increasing pore pressures which in turn force the effective stress-path into the desired direction. In the triaxial plane shown in Fig. 3, the stress difference $(\sigma_1 - \sigma_3)$ is proportional to the perpendicular distance from the hydrostatic axis. For the tests at high confining pressures the maximum stress differences occur well within the failure sur-

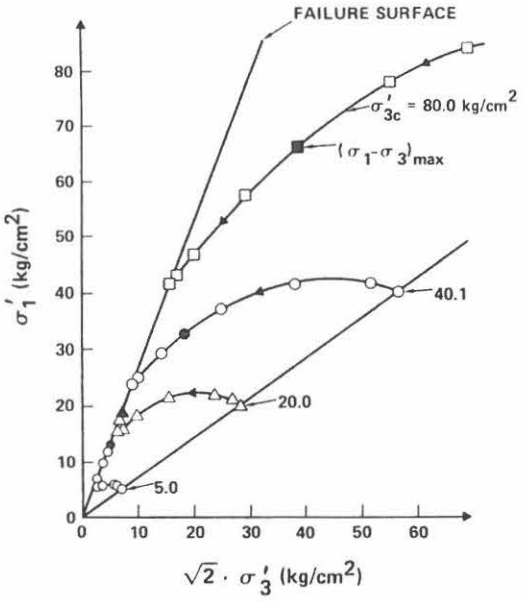

FIG. 3. Effective Stress-Paths for Undrained Triaxial Compression Tests at Four Different Confining Pressures on Loose Sacramento River Sand Shown in Triaxial Plane (1.0 kg/cm^2 = 98 kN/m^2)

face. Thus, true failure does not occur at the maximum stress difference. The region of potential instability is located at and above the solid points indicating the maximum stress differences. This region will be discussed further.

The stress-strain and pore pressure relations for the four undrained tests are shown in Fig. 4. The stress-strain curve for the test at 5.0 kg/cm^2 (490 kN/m^2) exhibits continuously increasing stress difference, although a tendency for leveling off occurs early in the test. The corresponding pore pressure curve shows first increasing and then decreasing pore pressures. This reflects a tendency for compression followed by a tendency for dilation as the failure surface is approached. Since the load carrying ability is continuously increasing until failure at large strains, the specimen appears to be stable.

The test performed at a confining pressure of 20.0 kg/cm^2 exhibits a temporary decline in the load carrying capacity between 1.0 and 4.0% axial strain. This may reflect a temporary instability which is then overcome as further straining occurs. The pore pressure curve exhibits similar behavior as that described above, reflecting the tendencies for compression followed by dilation. The tendency for dilation almost coincides with the recovery and increasing stress difference applied to the specimen.

The two tests with the highest confining pressures of 40.1 and 80.0 kg/cm^2 (3,930 and 7,850 kN/m^2) both show similar behavior. The stress dif-

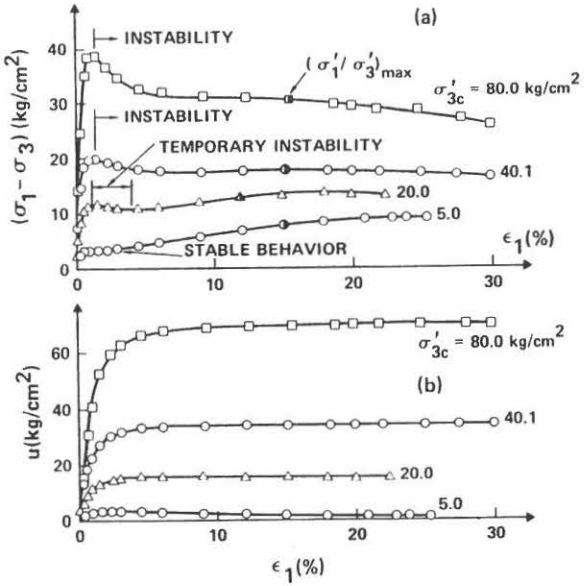

FIG. 4. Undrained Triaxial Compression Tests on Loose Sacramento River Sand (1.0 kg/cm^2 = 98 kN/m^2): (*a*) Stress-Strain Relations; (*b*) Pore Pressure Relations

ference increases to a peak at relatively small axial strains and then decreases at larger strains. The pore pressures increase steadily before reaching essentially constant values at large strains. This reflects tendencies for compression with negligible or no tendency for dilation towards the end of the test. Thus, by increasing the confining pressure to sufficiently high values, the tendency for dilation observed at lower confining pressures can be suppressed.

The effective stress ratios, often taken to indicate failure in soils, occur at axial strains of 12 to 15% in all tests. Thus, the peak stress difference in the tests at high confining pressures are reached much earlier than the stress states corresponding to failure, i.e., the maximum stress difference may not indicate true failure of the granular material. The decline in load carrying capacity may indicate that instability can occur inside the failure surface. However, the tests whose results are shown in Figs. 3 and 4 were all performed under strain control. This method of testing does not allow instabilities of the material to be exposed. To demonstrate instabilities, it is necessary to perform the test under load or stress control.

Nonassociated Flow in Undrained Tests

To study the region of potential instability in stress space and to investigate the occurrence of nonassociated flow in undrained tests, the effective stress-paths are further analyzed below. There are basically three different types of effective stress-paths in undrained tests. These are shown, one at a

time, in Fig. 5. Strain increments are superimposed on the stress diagrams to allow analyses of strain increment vector directions and to derive the directions of the plastic potential surfaces g. These surfaces are by definition perpendicular to the plastic strain increment vector directions.

For undrained tests the total volumetric strain is zero corresponding to the total strain increment vector being perpendicular to the hydrostatic axis everywhere along the effective stress-path. This is shown in Fig. 5(*a*). This figure also shows that volumetric compression is characterized by a strain increment vector pointing away from the origin, whereas volumetric dilation corresponds to a strain increment vector inclined towards the origin of the stress space.

The stress-strain curves in Fig. 4 show that plastic strains are produced everywhere along the undrained stress-paths. The yield surface must therefore be pushed out, and this requires it to be inclined relative to the effective stress-paths as indicated at each point in Fig. 5.

The direction of the elastic portion of the total strain increment vector in the triaxial plane depends on the value of Poisson's ratio, ν, and the ratio of the stress increments, $K = \dot{\sigma}_1/\dot{\sigma}_3$. The following relations may be deduced from Hooke's law: For $\dot{\sigma}_3 \neq 0$:

$$\frac{\dot{\epsilon}_1}{\sqrt{2}\cdot\dot{\epsilon}_3} = \frac{(K - 2\nu)}{\sqrt{2}\cdot[1 - \nu\cdot(1 + K)]} \quad \ldots\ldots (2)$$

and for $\dot{\sigma}_3 = 0$:

$$\frac{\dot{\epsilon}_1}{\sqrt{2}\cdot\dot{\epsilon}_3} = -\frac{1}{\sqrt{2}\cdot\nu} \quad \ldots\ldots (3)$$

These relations give the slopes of the elastic strain increment vectors on the triaxial plane. Since granular materials have $0 \leq \nu \leq 0.5$, these two limits will be used to bracket the directions of the elastic strain increment vectors.

For $\dot{\sigma}_3 \neq 0$ and $\nu = 0$, Eq. 2 produces

$$\frac{\dot{\epsilon}_1}{\sqrt{2}\cdot\dot{\epsilon}_3} = \frac{K}{\sqrt{2}} = \frac{\dot{\sigma}_1}{\sqrt{2}\cdot\dot{\sigma}_3} \quad \ldots\ldots (4)$$

i.e., the elastic strain increment vector is parallel to the stress increment vector or the stress path on the triaxial plane.

For $\dot{\sigma}_3 = 0$ and $\nu = 0$, Eq. 3 gives

$$\frac{\dot{\epsilon}_1}{\sqrt{2}\cdot\dot{\epsilon}_3} = -\infty \quad \ldots\ldots (5)$$

i.e., the elastic $\dot{\epsilon}$-vector is again parallel to the $\dot{\sigma}$-vector, both being vertical on the triaxial plane.

For $\nu = 0.5$ both Eqs. 2 and 3 lead to

$$\frac{\dot{\epsilon}_1}{\sqrt{2}\cdot\dot{\epsilon}_3} = -\sqrt{2} \quad \ldots\ldots (6)$$

i.e., the elastic strain increment vector is perpendicular to the hydrostatic axis corresponding to no elastic volume change.

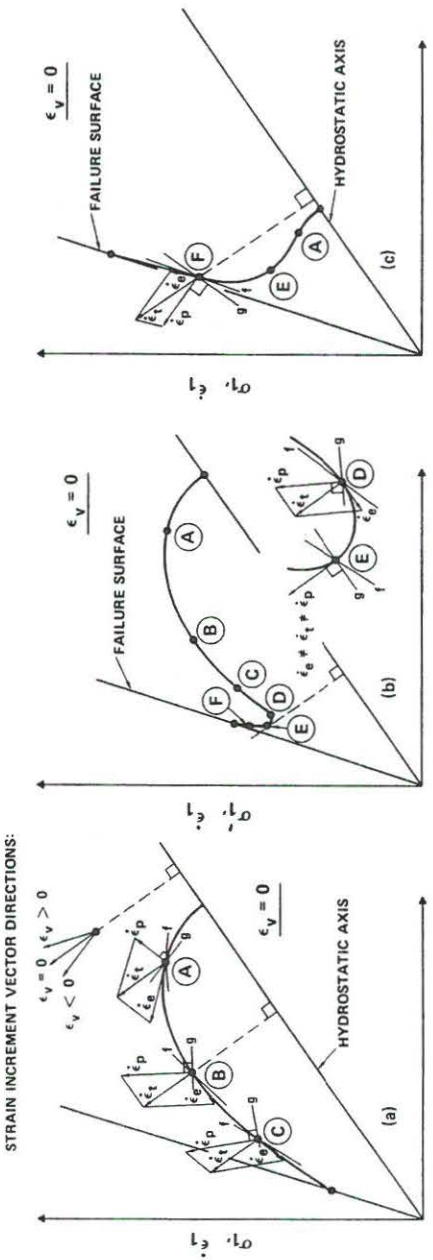

FIG. 5. Evaluation of Relative Inclinations of Yield (f) and Plastic Potential (g) Surfaces Along Undrained Effective Stress-Paths: (*a*) Type 1; (*b*) Type 2; and (*c*) Type 3

For values of Poisson's ratio between zero and 0.5 the elastic strain increment vector will be between the two extreme positions discussed. With no loss of generality, it will be assumed in the following that the elastic strain increment vector is parallel to the stress increment vector or the stress path on the triaxial plane, i.e., corresponding to $\nu = 0$. This simplifies the diagrams in Fig. 5, but does not limit the arguments presented below.

Three points of interest are indicated along the undrained effective stress-path of Type 1 in Fig. 5(*a*). The elastic portion of the total strain increment vector is pointed in the current direction of the effective stress-path. The length and direction of the plastic strain increment vector is obtained by vectorial subtraction of the elastic from the total strain increment vector. It is clear that only the directions of the elastic and the total strain increment vectors are known, and that the derived direction of the plastic strain increment vector depends on the assumed relative magnitudes of the elastic and total strain increments. However, as will be seen, it can be shown that nonassociated flow prevails at points B and C independent of the assumed magnitudes of strains.

At point A the length of the elastic vector is chosen so as to show that nonassociated flow could occur. In fact, in the absence of actual experimental determination of the elastic and plastic strain magnitudes, it is not possible to argue whether the plastic flow is associated or nonassociated, i.e., whether the yield and plastic potential surfaces are identical or not. However, this is of no importance to the study of instability presented here. Whether associated flow (which guarantees stability) or nonassociated flow is observed at point A, stability is obtained everywhere along the effective stress-path from the hydrostatic axis up to point B. Along this portion of the stress-path the load can be maintained constant or increased without any observable instability.

Nonassociated flow is clearly obtained at points B and C. For the limiting case where the elastic strain increments become negligible the plastic strain increment vectors become perpendicular to the hydrostatic axis. Since the yield surfaces must be inclined relative to the effective stress-paths as shown, nonassociated flow is clearly demonstrated to occur at points B and C.

Similar arguments can be made for point D on stress-path Type 2 in Fig. 5(*b*). Point D corresponds to a minimum stress difference along this portion of the effective stress-path. The load carrying capacity increases from point D to failure. At point E the effective stress-path is perpendicular to the hydrostatic axis. The elastic strain increment vector is therefore parallel with the total strain increment vector, and so is the plastic strain increment vector. The plastic potential surface is consequently parallel with the hydrostatic axis. Since the yield surface becomes steeper with increasing stress level, it cannot coincide with the plastic potential surface at point E, and nonassociated flow is demonstrated.

At point F on stress-path Type 3 in Fig. 5(*c*) the relative directions of the elastic and plastic strain increment vectors have been reversed (reversal occurs at point E). Point F is located in the region of plastic dilation. Large plastic strains occur in this region (see stress-strain curve corresponding to $\sigma'_{3c} = 5.0$ kg/cm^2 in Fig. 4), and the elastic strains are therefore relatively small. For the limiting case where the elastic strain increments reduce to zero, the plastic strain increment vector becomes perpendicular to the hydrostatic axis and the plastic potential surface becomes parallel with the hydrostatic axis. The yield surface is relatively steep, close to failure, as indicated on Fig. 1, and nonassociated flow is therefore obtained. In this region of dilation stability has been demonstrated as discussed.

It is the undrained test with effective stress-path of Type 1 that will be used as a tool to study stability/instability in the following. In this test the effective stress-path from point B to failure (point C being a typical point) is located in the shaded wedge region shown in Fig. 2. The decline in load carrying capacity may indicate that instability can occur inside the failure surface. Stress-controlled tests are required to study this possibility.

Experimental Program and Procedures

Sand Tested

Sacramento River Sand from the same batch previously tested by Lee (1965) was used in the experimental program. This sand is composed of subangular to subrounded particles consisting mostly of feldspar and quartz. The characteristics of this sand are summarized as follows: Mean diameter, 0.21 mm; coefficient of uniformity, 1.5; specific gravity of grains, 2.68; maximum void ratio, 1.03; and minimum void ratio, 0.61.

Effects of membrane penetration on the developed pore pressures are small to negligible in undrained tests when the average diameter of the soil grains is smaller than 0.1–0.2 mm (Frydman et al. 1973; Lade and Hernandez 1977; Martin et al. 1978). Tests were performed on loose specimens with void ratios around 0.84 corresponding to relative densities of 45%.

Specimen Preparation

All triaxial tests were performed on cylindrical specimens with diameter = 1.40 in. (3.56 cm) and height = 3.25 in. (8.26 cm) corresponding to $H/D = 2.32$. Filter stones were employed at each end of the specimens. This setup is similar to that used by Lee (1965).

The loose specimens were prepared by dry deposition of sand through a funnel with essentially zero drop height. The CO_2-method (Lade and Duncan 1973) was employed for saturation, and a nominal back pressure of 30 psi (207 kN/m^2) was applied to the specimens to insure a high degree of saturation. The B-values averaged 0.98 for all tests.

Testing Procedures

All specimens were first isotropically consolidated to 29.9 kg/cm^2 (2,930 kN/m^2). The vertical load was applied by a pneumatic cylinder, thus obtaining stress-controlled loading due to the high compressibility of air.

The vertical load, the confining pressure, the vertical deformation, and the volume change or the pore pressure were measured during each test. Vertical stress differences were calculated using current cross-sectional areas, and all strains were calculated as engineering strains. Corrections were applied to the measured vertical load for uplift forces on the piston. All other corrections to loads, pressures, linear deformations and volumetric strains were found to be negligible.

Effective Stress-Path Tests with Decreasing Stresses

Following application of the isotropic consolidation pressure, the specimens were loaded vertically under drained conditions by increasing the air

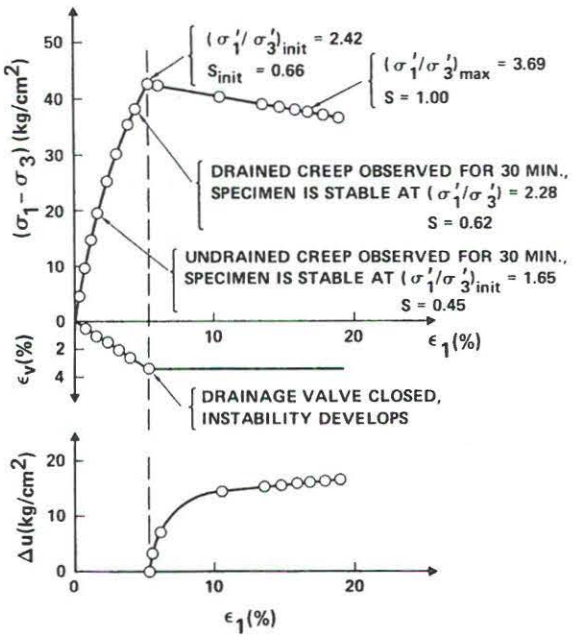

FIG. 6. Stress-Strain, Volume Change, and Pore Pressure Relations in Stress-Controlled Triaxial Compression Test on Loose Sacramento River Sand (1.0 kg/cm² = 98 kN/m²)

pressure in the pneumatic cylinder. Vertical stress differences of $(\sigma_1-\sigma_3)$ = 38.09, 42.72, 47.64, and 51.39 kg/cm² (3,737; 4,191; 4,673; and 5,041 kN/m²) were applied to the specimens. These correspond to effective stress ratios of (σ_1'/σ_3') = 2.28, 2.42, 2.59, and 2.72, whereas the maximum effective stress ratio at failure was $(\sigma_1'/\sigma_3')_{max}$ = 3.69, obtained from the strain-controlled tests discussed in the foregoing as well as from the stress controlled tests presented here. The proximity of these stress states to the failure line may be expressed in terms of the stress level S defined as the ratio of the current to the maximum stress difference at a given confining pressure. Thus, the failure stress state corresponds to a stress level of S = 1.00. The four stress differences reached in the tests correspond to stress levels of 0.62, 0.66, 0.70, and 0.74.

After the desired stress difference was obtained under drained conditions, the drainage valve was closed while the vertical load was maintained constant. The undrained condition imposed on the specimen caused the pore pressure to increase, thus forcing the effective stress-path into the shaded wedge shown in Fig. 2. Unstable behavior of the sand was observed in each test performed for this study.

Fig. 6 shows the results of the test performed with S_{init} = 0.66. These results are typical for all tests. The initial portions of the stress-strain and volume change relations correspond to drained loading. Note that the vol-

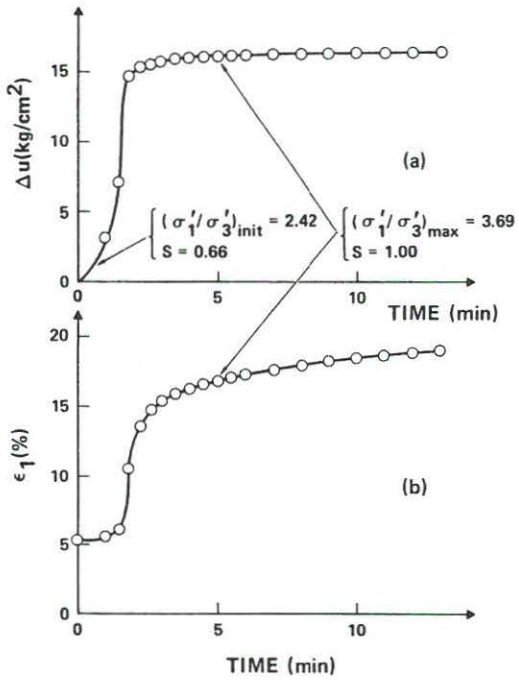

FIG. 7. Relations: (*a*) Pore Pressure; and (*b*) Axial Strain versus Time for Unstable Portion of Stress-Controlled Triaxial Compression Test on Loose Sacramento River Sand (1.0 kg/cm² = 98 kN/m²)

umetric strain is compressive until the drainage valve is closed at a vertical strain of ϵ_1 = 5.3%. Following closure of the drainage valve the specimen becomes unstable and compresses without any additional vertical load. The effective confining pressure decreases due to increasing pore pressure, and the stress difference decreases due to increasing cross-sectional area of the specimen. However, the decreasing stress difference cannot be sustained by the specimen.

Fig. 7 shows the pore pressure development and the axial strain development versus time after closure of the drainage valve. The pore pressure development slightly precedes the development of axial strain. Although the pore pressure starts increasing immediately upon closure of the drainage valve, the axial strain development initially occurs at a lower rate. The axial strains along this stress-path are very small, because the stresses push the yield surface out very little. If a drained stress-path was followed barely inside the undrained effective stress-path, then the stress state would move inside the yield surface and elastic axial expansion would be recorded due to decreasing stresses. It is therefore understandable why very small compressive strains are recorded along the undrained effective stress-path. This type of behavior was observed in all tests.

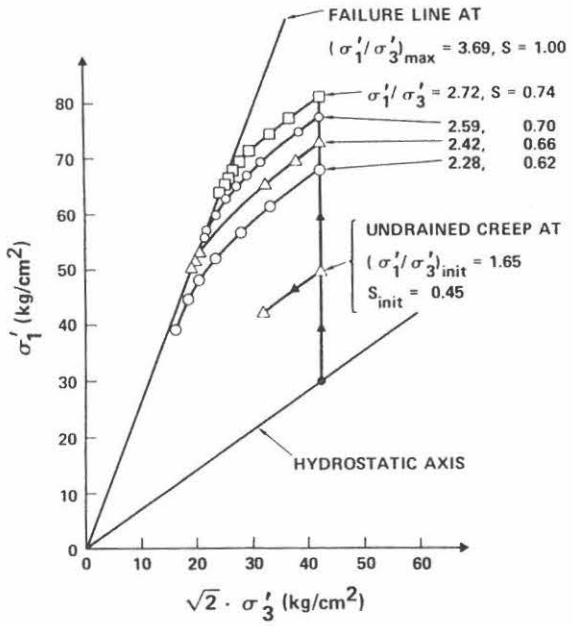

FIG. 8. Effective Stress-Paths for Stress-Controlled Triaxial Compression Tests on Loose Sacramento River Sand (1.0 kg/cm² = 98 kN/m²)

The effective stress-paths for the stress-controlled triaxial compression tests are shown in Fig. 8. The specimens were first loaded at constant confining pressure until the desired vertical loads were reached, corresponding to preselected stress levels. These stress levels were all well below that required to cause failure at the constant confining pressure. Thus, the specimens were perfectly stable at each of these stress levels before the drainage valve was closed. Following closure of the drainage valve, the effective stress-paths were forced into the shaded wedge in Fig. 2 due to the increasing pore pressures. Within this wedge the specimens became unstable and the effective stresses moved to failure with no further change in external load. Due to increasing cross-sectional areas of the specimens, the calculated stress differences, $(\sigma_1 - \sigma_3)$, decreased along these stress-paths. It should be emphasized that the undrained test is only used as a tool to produce effective stress-paths in the shaded wedge within which nonassociated flow has been shown to occur.

Discussion

In the study presented here instability was taken to be the inability to sustain or carry a given load, which includes the ability to sustain small perturbations in the loads. However, the possibility that instability might manifest itself as localization of plastic deformation and development of shear

bands or in any other way was not overlooked. The specimens were therefore inspected after the tests (they were enclosed in a steel-walled triaxial apparatus and could not be observed during the tests) at which time they had sustained 15% to 30% axial strain. The instabilities were induced at axial strains of 2.8% to 5.3%. Thus, substantial amounts of strain had occurred after the instabilities were induced. Nevertheless, the specimens had bulged only slightly and there were no visible shear planes. In fact, a uniform distribution of horizontal wrinkles in the membrane was observed after each test, thus revealing a fairly uniform pattern of internal strains in the specimens. Instability did not appear to be associated with localization of plastic deformations and consequent shear banding of the type discussed by Lade (1982), Hettler and Vardoulakis (1984), and Peters et al. (1988). This is consistent with previous observations that shear planes are not observed in soils that compress (Lade 1982).

The yield surfaces at each of the stress points at which the drainage valve was closed and instability developed must have been inclined such as to open up in the outward direction of the hydrostatic axis. This is the only inclination which would allow plastic strains and instability to occur while the stresses were decreasing. If, on the other hand, the yield surface is inclined such as to close in the outward direction of the hydrostatic axis (as at point A in Fig. 1), then stable behavior should be observed. To test this hypothesis, the drainage valve was closed at an effective stress ratio of $(\sigma_1'/\sigma_3') = 1.65$ corresponding to S = 0.45 in the test whose results are shown in Fig. 6. While the external loads were maintained constant, the pore pressure increased some due to a tendency for undrained volumetric creep as indicated in Fig. 8. The axial strains observed over a 30-min period are plotted versus time in Fig. 9. Very little axial strain (0.3%) occurred over this period. This strain was caused by creep in the elastic region within the teardrop shaped yield surface (see Fig. 1). Thus, stability is obtained in the region where the yield surface is closing towards the outward direction of the hydrostatic axis.

To test whether rate/time effects such as viscous flow or creep could cause the instability discussed above, the test whose results are shown in Fig. 6 was stopped at a stress ratio of $(\sigma_1'/\sigma_3') = 2.28$ coresponding to S = 0.62. This is precisely the same stress state at which one of the other tests was forced to exhibit instability by closing the drainage valve. In the current test the drainage valve was maintained open, and drained creep was observed for a period of 30 min. The axial creep strains are shown in Fig. 9. It is seen that creep could not be responsible for the large strains observed in the tests discussed above. The axial strain-time relation for the test in which instability was induced is also shown in Fig. 9 for comparison. It is clear that instability causes large strains to occur within relatively short time. The tendency for volumetric creep, however small it may be, causes the pore pressure to increase under undrained conditions, providing the small perturbation which renders the material unstable. However, the large strains discussed here could not be caused by creep or viscous flow, but are the effects of nonassociated flow combined with stress-paths within the shaded wedge in Fig. 2 where plastic volumetric compression occurs.

It should be emphasized that instability is not synonymous with failure. Thus, a failure surface does not go through each of the points at which instability was produced. In fact, these points are well within the failure

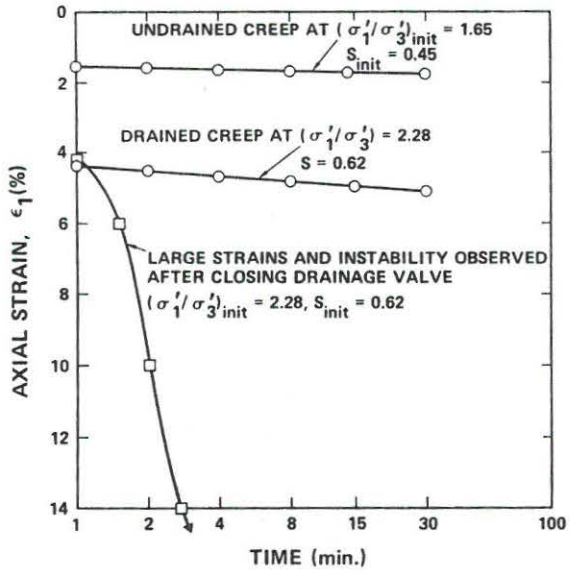

FIG. 9. Axial Strain-Time Relations in Semi-Log Diagram for Undrained Creep, Drained Creep, and Instability Observed in Stress-Controlled Triaxial Compression Tests on Loose Sacramento River Sand

surface as obtained from drained tests. Obviously, each of the specimens could have been loaded to higher stress differences as long as the stress-paths were outside the wedge between the yield and the plastic potential surfaces. Therefore, a failure condition expressed in terms of the maximum stress differences obtained from, e.g., undrained tests initiated at the hydrostatic axis (see Fig. 3) would clearly underestimate the true effective strength of the soil.

Material models which employ associated plastic flow rules must assume the failure surface to go through the point at which instability is produced. This is because stability is guaranteed according to Drucker's stability condition until the failure surface is reached, at which instability ensues. But then stable loading to higher stress differences, which is clearly possible, could not be predicted by such models. Further, since instability as well as stability can be obtained at any point in the region above the line roughly defined by the maximum stress differences in Fig. 3, it is not possible to define any one consistent failure surface to be used in a model which incorporates associated flow.

Stability Conditions for Granular Materials

Based on the arguments and the experimental evidence presented here and in Lade et al. (1987), it is possible to state the conditions for which granular materials exhibit stable behavior. These conditions take the form of additions to Drucker's stability condition [Inequality 1(*b*)], which by itself is sufficient to guarantee stability. However, this is not a necessary condition for stability

of granular or frictional materials, i.e., stability may be obtained even when Inequality 1(*b*) is violated. Thus, the tests presented here, together with the work in Lade et al. (1987) indicate that stable material behavior exists when

$$\dot{\sigma}_{ij} \cdot \dot{\epsilon}_{ij}^{p} < 0 \quad \ldots\ldots (7)$$

and

$$\frac{\partial f}{\partial \sigma_{ij}} \cdot \delta_{ij} > 0 \quad \ldots\ldots (8)$$

where δ_{ij} = a vector on the hydrostatic axis. Inequality 8 expresses that the yield surface closes in the outward direction of the hydrostatic axis, i.e., stability is obtained along the "front portion" of the teardrop shaped yield surface.

Further, stability is also obtained when Inequality 7 holds and both

$$\frac{\partial g}{\partial \sigma_{ij}} \cdot \delta_{ij} \leq 0 \quad \ldots\ldots (9)$$

and

$$\frac{\partial f}{\partial W_p} \geq 0 \quad \ldots\ldots (10)$$

Inequality 9 holds when the material exhibits plastic dilation or a tendency for plastic dilation in undrained tests in which the total volumetric strain is zero. Since instability is observed beyond failure, where both Inequalities 7 and 9 are satisfied, it is necessary to add Inequality 10, which expresses that loading and therefore plastic yielding occurs *inside* the failure surface. Thus, stability is obtained for stress-paths within the shaded wedge (see Fig. 2) as long as the plastic volumetric strain show dilation or a tendency for dilation. Experiments to support this stability condition were presented in Lade et al. (1987).

Conditions for Instability of Granular Materials

The conditions for stability stated above may be reversed to produce requirements for instability of granular materials. These may be important and sometimas easier to employ than the stability conditions. Specifically, instability will occur when Inequality 7 is fulfilled together with

$$\frac{\partial f}{\partial W_p} < 0 \quad \ldots\ldots (11)$$

which expresses the fact that softening occurs *beyond* failure. This condition for instability is implied in Drucker's stability condition (Inequality 1*b*).

Instability is also obtained *inside* the failure surface when Inequality 7 is combined with

$$\frac{\partial g}{\partial \sigma_{ij}} \cdot \delta_{ij} > 0 \quad \ldots\ldots (12)$$

and

$$\frac{\partial f}{\partial \sigma_{ij}} \cdot \delta_{ij} < 0 \quad \text{(13)}$$

Inequality 12 holds when the material exhibits plastic volumetric compression or a tendency for plastic compression under undrained conditions where the total volumetric strain is zero. Inequality 13 stipulates that the yield surface must open up in the outwards direction of the hydrostatic axis. Thus, instability is obtained for stress-paths within the shaded wedge (see Fig. 2) when the plastic volumetric strains are compressive or show a tendency for compression under undrained conditions. Again, these results are based on experimental evidence supporting these conditions for instability.

It should be noted that the elastic strains will maintain stability slightly beyond the conditions for instability stated. For example, stability is recovered along the undrained effective stress-path from point D to point E in Fig. 5(*b*) due to elastic expansion. The conditions for instability stated above are fulfilled from D to E, but stability is obtained, because the plastic compression goes to zero at point E and the elastic expansion produces stable behavior beginning at point D. Similar stable behavior is obtained immediately before point B in Fig. 5(*a*) due to elastic expansion. The conditions for instability are fulfilled a little before point B is reached, where the yield surface is parallel with the hydrostatic axis. However, as the elastic strains become negligible, the stated conditions for instability prevail.

Finally, plastic work, W_p, is used as the hardening parameter to indicate loading or hardening in Inequality 10 and softening in Inequality 11. Any other measure of hardening, consistent with the findings presented above, may be used in lieu of plastic work to indicate loading inside the failure surface and softening beyond failure.

Conclusion

The stability condition formulated by Drucker provides a sufficient condition for stability and is satisfied for materials that obey an associated plastic flow rule. Frictional materials exhibit nonassociated plastic flow, and the stability of such materials has often been questioned. To provide experimental evidence regarding the stability of granular materials, two series of triaxial tests were performed under stress control so that any instability in the material could freely develop.

In one series of tests previously reported (Lade et al. 1987), specimens of dense sand were exposed to stress-paths with decreasing effective stresses and increasing stress levels. The results showed that the granular material dilated during shear, it followed a nonassociated flow rule, and stability was obtained in all cases until the failure surface was reached. Thus, stable behavior was observed in a region in which Drucker's stability postulate was violated.

In the second series of tests reported here, specimens of loose sand were also exposed to stress-paths with decreasing effective stresses and increasing stress levels. The results of these tests showed that the granular material tended to compress during shear, it followed a nonassociated flow rule, and instability was obtained in all cases *inside* the failure surface. The possible influence of viscous effects on the instability of the material, and the effect

of elastic energy release were investigated experimentally and discussed in detail. None of these effects could account for the instability of the material.

The occurrence of stable and unstable behavior found in these two studies is related to the volume change characteristics of the material. Stable behavior is found when the material dilates, and unstable behavior may occur when the material compresses during shear.

Stability conditions for granular materials exhibiting nonassociated flow are formulated on the basis of the experimental results obtained in the two studies. These conditions take the form of augmentations to Drucker's stability postulate. Conditions for instability of granular materials are also presented. Both types of conditions are expressed in terms of the orientations of the plastic potential surface and the yield surface.

Appendix I. References

Drucker, D. C. (1951). "A more fundamental approach to stress-strain relations." *Proc., First U.S. Nat. Congress Appl. Mech.*, 487–491.

Drucker, D. C. (1956). "On uniqueness in the theory of plasticity." *Quarterly Appl. Math.*, 14, 35–42.

Drucker, D. C. (1959). "A definition of stable inelastic material," *J. Appl. Mech.*, 26, 101–106.

Frydman, S., Zeitlen, J. G., and Alpan, I. (1973). "The membrane effect in triaxial testing of granular soils." *J. Testing and Evaluation*, ASTM, Philadelphia, Pennsylvania, 1(1), 37–41.

Hettler, A., and Vardoulakis, I. (1984). "Behaviour of dry sand tested in a large triaxial apparatus." *Geotechnique*, 34(2), 183–197.

Lade, P. V. (1982). "Localization effects in triaxial tests on sand." *Proc., Symp. on Deformation and Failure of Granular Materials*, International Union of Theoretical and Applied Mechanics, P.A. Vermeer and H. J. Luger, eds., Delft, Holland, Aug., 461–471.

Lade, P. V., and Duncan, J. M. (1973). "Cubical triaxial tests on cohesionless soil." *J. Soil Mech. and Found. Div.*, ASCE, 99(SM10), 793–812.

Lade, P. V., and Hernandez, S. B. (1977). "Membrane penetration effects in undrained tests." *J. Geotech. Engrg. Div.*, ASCE, 103(GT2), 109–125.

Lade, P. V., Nelson, R. B., and Ito, Y. M. (1987). "Nonassociated flow and stability of granular materials." *J. Engrg. Mech.*, ASCE, 113(9), Sept. 1302–1318.

Lee, K. L. (1965). "Triaxial compressive strength of saturated sand under seismic loading conditions." Thesis presented to the University of California, at Berkeley, California, in partial fulfillment of the requirements for the degree of Doctor of Philosophy.

Lee, K. L., and Seed, H. B. (1967). "Drained strength characteristics of sands." *J. Soil Mech. and Found. Div.*, ASCE, 93(SM6), 117–141.

Mandel, J. (1964). "Conditions de stabilite et postulat de Drucker." *Proc. Int. Union of Theoretical and Appl. Mech., Symp. on Rheology and Soil Mechanics*, Grenoble, France, 58–67.

Martin, G. R., Finn, W. D. L., and Seed, H. B. (1978). "Effects of system compliance on liquefaction tests." *J. Geotech. Engrg. Div.*, ASCE, 104(GT4), April, 463–479.

Mroz, Z. (1963). "Nonassociated flow laws in plasticity." *J. de Mechanique*, 2(1), 21–42.

Peters, J. F., Lade, P. V., and Bro, A. (1988). "Shear band formation in triaxial and plane strain tests." *Advanced Triaxial Testing of Soil and Rock*, ASTM XXX, R. T. Donaghe, R. C. Chaney and M. L. Silver, eds., Amer. Soc. Test. Mat.

Seed, H. B., and Lee, K. L. (1967). "Undrained strength characteristics of cohesionless soils." *J. Soil Mech. and Found. Div.*, ASCE, 93(SM6), 333–360.

Static Instability and Liquefaction of Loose Fine Sandy Slopes

By Poul V. Lade,[1] Member, ASCE

Abstract: Soils that exhibit nonassociated flow may, according to stability postulates by Drucker and by Hill, become unstable when exposed to certain stress paths inside the failure surface. Series of conventional triaxial tests on fully saturated and on partly saturated specimens were performed under drained and undrained conditions to study the regions of stable and unstable behavior. For specimens that compress and have degrees of saturation higher than critical, undrained conditions lead to effective stress paths directed within the region of potential instability, and instability was observed provided the yield surface opens up in the outward direction of the hydrostatic axis. Thus, instability occurs inside the failure surface. Instability is not synonymous with failure, although both may lead to catastrophic events. The location of the instability line is discussed. Examples of a shallow submarine slope and a nearly fully saturated steeper slope representing a tailings dam, which both should remain stable according to conventional stability analyses, are presented to show that they could become unstable due to small disturbances and proceed to fail catastrophically.

Introduction

Two criteria for failure in soils are commonly employed in interpretation of results of triaxial tests: (1) Failure occurs when the stress difference reaches a limiting value, $(\sigma_1 - \sigma_3)_{max}$; and (2) failure occurs when the effective principal stress ratio reaches a limiting value, $(\sigma_1'/\sigma_3')_{max}$. The two conditions are reached simultaneously in drained tests. The confusion as to the definition of failure arises in interpretation of undrained tests on loose sands and sensitive clays in which the pore pressures increase monotonically during shear. For these types of soils, the maximum stress difference is reached before the maximum effective stress ratio. The choice of failure criterion varies with the purpose for which the strength is to be used. Typically, $(\sigma_1 - \sigma_3)_{max}$ is employed in total stress analyses and $(\sigma_1'/\sigma_3')_{max}$ is used in effective stress analyses. These issues have been discussed at length by e.g., Bjerrum and Simons (1960), Seed et al. (1960), and Whitman (1960).

The condition of maximum stress difference does not correspond to a true failure condition, but rather to a condition of minimum stress difference at which instability may develop inside the true failure surface. This condition was studied in detail by Kramer and Seed (1988). Stress states can be reached above the minimum stress difference condition described by $(\sigma_1 - \sigma_3)_{max}$, and instability can be induced anywhere between the $(\sigma_1 - \sigma_3)_{max}$ condition and the true failure surface described by $(\sigma_1'/\sigma_3')_{max}$. Thus, instability is not synonymous with failure, although both may lead to catastrophic events.

The location of the line separating potentially unstable stress states from stable stress states, herein called the instability line, is discussed. Examples

[1]Prof., Dept. of Civ. Engrg., School of Engrg. and Appl. Sci., Univ. of California, Los Angeles, CA 90024-1593.

Note. Discussion open until May 1, 1992. To extend the closing date one month, a written request must be filed with the ASCE Manager of Journals. The manuscript for this paper was submitted for review and possible publication on February 27, 1991. This paper is part of the ***Journal of Geotechnical Engineering***, Vol. 118, No. 1, January, 1992. ©ASCE, ISSN 0733-9410/92/0001-0051/$1.00 + $.15 per page. Paper No. 1454.

are presented to illustrate the use of the instability line in analyses of a shallow submarine slope and a nearly fully saturated steeper slope representing a tailings dam or a spoil heap. Such slopes can and do become unstable due to small disturbances, although conventional stability analyses indicate that they should remain stable.

Stability Postulates

Experimental evidence from tests on several types of soils have clearly indicated that the use of conventional associated flow rules results in prediction of too large volumetric expansion. To characterize the volume change correctly, it is necessary to employ a nonassociated flow rule. The plastic potential surfaces do not therefore coincide with the yield surfaces, but the two families of surfaces cross each other.

The application of nonassociated plastic flow rules for soils have resulted in questions regarding uniqueness and stability of such materials. The stability postulates for time-independent materials due to Drucker (1951, 1956, 1959), Bishop and Hill (1951), and Hill (1958) provide sufficient conditions for stability and ensure uniqueness in dynamic, as well as static, problems. Drucker's postulate is satisfied provided that associated plastic flow is employed in construction of constitutive models involving convex, plastic yield surfaces. Hill's stability condition is expressed in terms of total strain increments (elastic and plastic), and it extends the condition for stability a little beyond that of Drucker. Although these conditions are sufficient to guarantee stability, theoretical considerations have suggested that they are not necessary conditions (Mroz 1963; Mandel 1964).

The stability postulate formulated by Drucker is suitable for solid metals that exhibit associated flow. According to this postulate, stability requires that the second increment of plastic work is positive or zero:

$$\dot{\sigma}_{ij} \cdot \dot{\varepsilon}^p_{ij} \geq 0 \quad \ldots\ldots\ldots\

Fig. 2 shows a schematic illustration of the region in which (1) is not fulfilled for a material with nonassociated flow. The region is shaped as a wedge between the current yield surface f and the plastic potential surface g corresponding to the current stress point. This wedge-shaped region is located within a larger region bounded by lines corresponding to $(\sigma_1'/\sigma_3') =$ constant and $(\sigma_1 - \sigma_3) =$ constant as indicated on Fig. 2. All stresses, including the stress difference $(\sigma_1 - \sigma_3)$, are decreasing within the wedge between f and g, but the stress ratio (σ_1'/σ_3') is increasing in this region. By performing triaxial tests with stress paths located in this region, experimental evidence regarding the instability of materials with nonassociated flow can be obtained.

It is important to recognize that the material behavior obtained for stress paths within the shaded wedge in Fig. 2 corresponds to work-hardening with positive plastic work, $dW_p > 0$, and outward motion of the yield surface. Although the stresses in any direction within the wedge are decreasing, failure has not been reached and softening of the material is therefore not occurring.

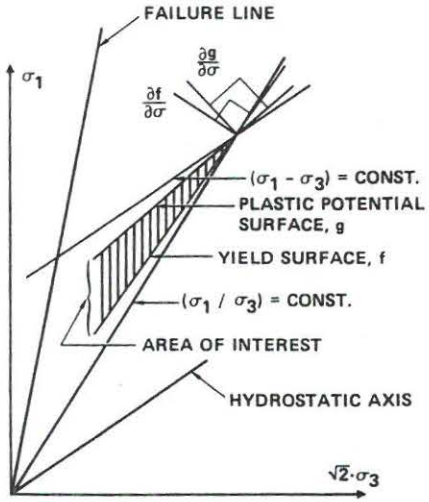

FIG. 2. Wedge-Shaped Region of Stress Paths with Decreasing Stresses in which Soils with Nonassociated Flow may be Unstable during Hardening Inside Failure Surface

NONASSOCIATED FLOW IN GRANULAR SOILS

Drained Conditions

To demonstrate that nonassociated plastic flow is obtained for granular materials, the results of a drained triaxial test on fine silica sand are shown in Fig. 3. This test was performed with a stress path inside the failure surface involving primary loading (hardening) with decreasing stress difference $(\sigma_1 - \sigma_3)$ and decreasing confining pressure σ_3. If stresses and strain increments are plotted on the same diagram, as in Fig. 3(b), the direction of the plastic

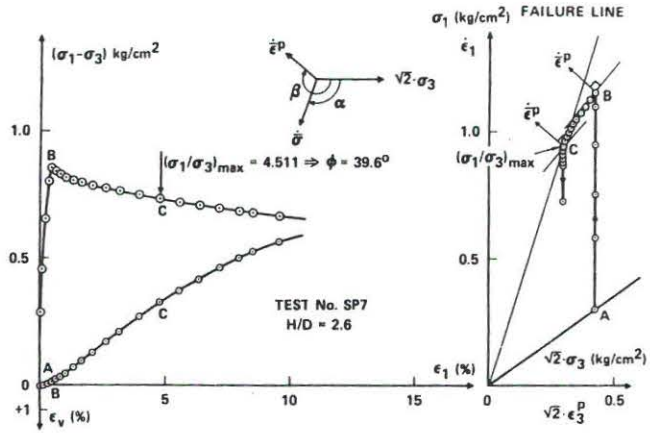

FIG. 3. (*a*) Stress-Strain and Volume Change Curves; and (*b*) Stress Path and Plastic Strain Increment Vectors for Test on Fine Silica Sand

strain increment vector is uniquely determined from the state of stress, and it is independent of the stress path leading to this state of stress, as shown by Poorooshasb et al. (1966) and Lade and Duncan (1976). The stress path with decreasing stresses, shown in Fig. 3(b), is so steep as to form an obtuse angle $(\beta - \alpha = 110°)$ with the direction of the plastic strain increment vector. Thus, the inequality in (1) is violated.

The fact that plastic yielding is occurring along the stress path with decreasing stresses is seen from the stress-strain curve in Fig. 3(a). Section BC on the stress path is labeled similarly on the stress-strain curve, which indicates large plastic strains between B and C. Since the yield surface is being pushed out, it must be steeper than the stress path direction BC. If it were less steep, so as, for example, to be perpendicular to the plastic strain increment vector, thereby indicating associated flow, then point C would be inside the yield surface, passing through point B, corresponding to unloading from B to C. This would contradict the large plastic strains shown in Fig. 3(a). Consequently, the yield surface must be steeper than stress path BC, and nonassociated plastic flow is therefore clearly indicated.

Undrained Conditions

To study the region of potential instability in stress space, and to investigate the occurrence of nonassociated flow under undrained conditions, a typical effective stress path observed in an undrained test performed with high confining pressure is shown in Fig. 4. Strain increments are superimposed on the stress diagram to allow analyses of strain increment vector directions and to derive the directions of the plastic potential surfaces g. These surfaces are, by definition, perpendicular to the plastic strain increment vector directions.

For undrained tests, the total volumetric strain is zero corresponding to the total strain increment vector being perpendicular to the hydrostatic axis everywhere along the effective stress path. This is shown in Fig. 4. This figure also shows that volumetric compression is characterized by a strain

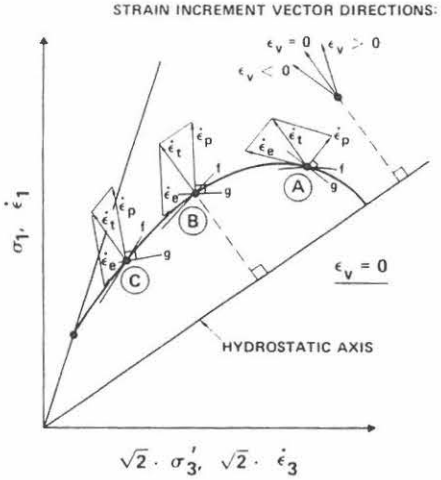

FIG. 4. Evaluation of Relative Inclinations of Yield (*f*) and Plastic Potential (*g*) Surfaces along Undrained Effective Stress Path

increment vector pointing away from the origin, whereas volumetric dilation corresponds to a strain increment vector inclined towards the origin of the stress space.

The stress-strain relation corresponding to the effective stress path in Fig. 4 shows that plastic strains are produced everywhere along the undrained stress path. The yield surface must therefore be pushed out, and this requires it to be inclined relative to the effective stress path as indicated in Fig. 4.

The direction of the elastic portion of the total strain increment vector in the triaxial plane depends on the value of Poisson's ratio, ν. For $\nu = 0$ the elastic strain increment vector is parallel to the stress increment vector, which is tangential to the stress path on the triaxial plane shown in Fig. 4. For $\nu = 0.5$, the elastic strain increment vector is perpendicular to the hydrostatic axis corresponding to no elastic volume change. For values of Poisson's ratio between 0 and 0.5, the elastic strain increment vector will be between the two extreme positions. With no loss of generality, it will be assumed in the following that the elastic strain increment vector is parallel to the stress increment vector, i.e., corresponding to $\nu = 0$.

Three points of interest are indicated along the undrained effective stress path in Fig. 4. The elastic portion of the total strain increment vector is pointed in the current direction of the effective stress path. The length and direction of the plastic strain increment vector is obtained by vectorial subtraction of the elastic from the total strain increment vector. It is clear that only the directions of the elastic and the total strain increment vectors are known, and that the derived direction of the plastic strain increment vector depends on the assumed relative magnitudes of the elastic and total strain increments. However, as will be seen, it can be shown that nonassociated flow prevails at points B and C, independent of the assumed magnitudes of strains.

At point A, the length of the elastic vector is chosen so as to show that

nonassociated flow could occur. In fact, in the absence of actual experimental determination of the elastic and plastic strain magnitudes, it is not possible to argue whether the plastic flow is associated or nonassociated, i.e., whether the yield and plastic potential surfaces are identical or not. However, this is of no importance to the study of instability presented here. Whether associated flow (which guarantees stability) or nonassociated flow is observed at point A, stability is obtained everywhere along the effective stress path from the hydrostatic axis up to point B. Along this portion of the stress path, the load can be maintained constant or increased without any observable instability.

Nonassociated flow is clearly obtained at points B and C. For the limiting case where the elastic strain increments become negligible, the plastic strain increment vectors become perpendicular to the hydrostatic axis. Since the yield surfaces must be inclined relative to the effective stress paths as shown, nonassociated flow is clearly demonstrated to occur at points B and C.

Note that the plastic strain increment vectors in Fig. 4 indicate that plastic volumetric compression occurs while the total volumetric strain is zero.

Behavior under Drained Conditions

Several series of triaxial compression tests were performed to study stability and instability in granular materials. The details of these experiments are given by Lade et al. (1987, 1988), and by Lade and Pradel (1990).

In order to expose the potential instabilities in soil behavior that might occur for the stress paths in the prefailure region described earlier (see Fig. 2), it is necessary to perform triaxial tests under stress control. A series of drained tests similar to that shown in Fig. 3 was therefore performed under stress control (Lade et al. 1987). In fact, the test shown in Fig. 3 is one of these tests. Seven experiments were performed. They all exhibited plastic dilation, and they all clearly showed nonassociated flow. When the sand specimens were exposed to stress paths in the region of potential instability ($\dot{\sigma}_{ij} \cdot \dot{\epsilon}_{ij}^p < 0$), none was observed. The tall cylindrical specimens with lubricated ends deformed as perfect right cylinders with no developing shear bands, no bulging or shearing in a nonuniform manner, nor any other signs of instability. Little, but negligible, creep was present in the sand specimens. Thus, stable behavior was observed in the region in which Drucker's stability postulate was violated.

In order to investigate whether the type of volume change (dilation or compression) was important for stability of granular soils, a second series of tests was performed on sand that compressed during shear (Lade and Pradel 1990). Drained tests with stress paths within the shaded wedge shown in Fig. 2 were performed on loose sand that exhibited compression during shear. Although Drucker's stability condition was violated inside the failure surface, none of the specimens showed any signs of instability.

The results of these two series of triaxial compression tests demonstrated that drained conditions produce stable behavior irrespective of: (1) The sign of the second increment of work; (2) the sign of the volumetric strain (dilation or compression); and (3) the sign and direction of the increments in stress components. Thus, under fully controlled conditions such as those prevailing for drained conditions, unstable runaway situations cannot occur. These results, therefore, clearly show that Drucker's stability postulate is not a necessary condition for stability.

Behavior under Undrained Conditions

Fully Saturated Soil

On the other hand, fully saturated soils that tend to compress during shear may become unstable inside the failure surface, and this may lead to liquefaction. A series of stress-controlled tests was performed on granular soil that tended to compress during shear (Lade et al. 1988). The specimens were exposed to stress paths within the shaded wedge shown in Fig. 2. Fig. 5 shows the actual stress paths followed in these tests, and Fig. 6 shows the observed stress strain, volume change, and pore pressure development in one of the tests. In each test, the saturated specimen was first loaded under drained conditions to a preselected stress level S (expressed as the ratio of the current to the maximum stress difference at a given confining pressure). The drainage valve was then closed and instability developed in each specimen due to increasing pore pressures, i.e., the specimens could not sustain the applied load. The tendency for volumetric creep, however small, caused the pore pressure to increase under undrained conditions, providing the small perturbation that rendered the material unstable. However, the large strains observed along the unstable stress paths could not be caused by creep or viscous flow as shown by Lade et al. (1988). The effective stress paths shown in Fig. 5 were within the shaded wedge in Fig. 2, the specimens exhibited nonassociated flow and plastic volumetric compression (although

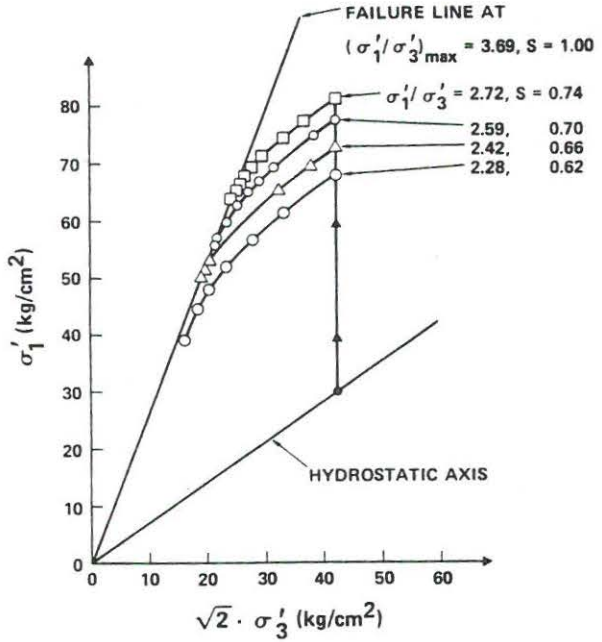

FIG. 5. Effective Stress Paths for Stress-Controlled Triaxial Compression Tests on Loose Sacramento River Sand

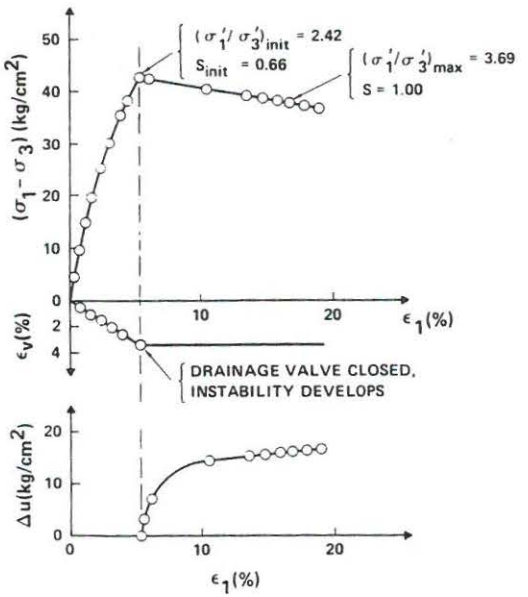

FIG. 6. Stress-Strain, Volume Change, and Pore Pressure Relations in Stress-Controlled Triaxial Compression Test on Loose Sacramento River Sand

the total volumetric strain was zero), and instability was obtained in all cases in the hardening regime inside the failure surface.

In the studies presented here, instability was taken to be the inability to sustain or carry a given load, which includes the ability to sustain small perturbations in the loads. However, the possibility that instability might manifest itself as localization of plastic deformation and development of shear planes or in any other way was not overlooked. The specimens were therefore inspected after the tests (they were enclosed in a steel-walled triaxial apparatus and could not be observed during the tests), at which time they had sustained 15–30% axial strain. The instabilities were induced at axial strain of 2.8–5.3%. Thus, substantial amounts of strain had occurred after the instabilities were induced. Nevertheless, the specimens had bulged only slightly and there were no visible shear planes. In fact, a uniform distribution of horizontal wrinkles in the membrane was observed after each test, thus revealing a fairly uniform pattern of internal strains in the specimens. Instability did not appear to be associated with localization of plastic deformations and consequent shear banding of the type discussed by Lade (1982) and Peters et al. (1988). This is consistent with previous observations that shear planes are not observed in soils that compress (Lade 1982).

Partly Saturated Soil

Stress paths with only one particular direction are obtained from undrained tests on fully saturated soils at each particular stress state, as shown in Fig. 5. In order to study the soil behavior for other stress path directions

under undrained conditions, a series of tests, similar to those described previously, was performed on specimens with decreasing degrees of saturation (Lade and Pradel 1990). By purposely introducing a controlled amount of compressible air into the specimens, the undrained effective stress paths could be pointed in different directions within the shaded wedge in Fig. 2. The specimens in both tests, in which the effective stress paths were inside the shaded wedge, exhibited unstable behavior. The stress path in a third test was above the shaded wedge because the amount of air introduced in the specimen was greater than critical. In this test the specimen was perfectly stable.

It is clear from these experiments that a change in drainage conditions for a fully or nearly fully saturated soil can activate unstable behavior. This may occur due to static or dynamic disturbances such as experienced in static flow failures of tailings dams or in liquefaction of granular materials during earthquakes.

Conditions for Instability of Soils

Based on the arguments and the experimental evidence presented here and by Lade et al. (1987, 1988) and Lade and Pradel (1990), it is possible to state the conditions for which soils with nonassociated flow exhibit unstable behavior. Instability will occur when

$$\dot{\sigma}_{ij} \cdot \dot{\varepsilon}^{t}_{ij} < 0 \quad \ldots\ldots (3)$$

and

$$\frac{\partial f}{\partial W_p} < 0 \quad \ldots\ldots (4)$$

which expresses the fact that softening occurs beyond failure. This condition for instability is implied in both Drucker's and Hill's stability conditions.

Instability is also obtained inside the failure surface when (3) is combined with

$$\frac{\partial g}{\partial \sigma_{ij}} \cdot \delta_{ij} > 0 \quad \ldots\ldots (5)$$

in which δ_{ij} = a vector on the hydrostatic axis, and

$$\frac{\partial f}{\partial \sigma_{ij}} \cdot \delta_{ij} < 0 \quad \ldots\ldots (6)$$

Eq. (5) holds when the material exhibits plastic volumetric compression or a tendency for plastic compression under undrained conditions where the total volumetric strain is zero. Eq. (6) stipulates that the yield surface must open up in the outward direction of the hydrostatic axis. Thus, instability is obtained for stress paths within the shaded wedge (see Fig. 2) when the plastic volumetric strains are compressive or show a tendency for compression under undrained conditions. These results are based on experimental evidence supporting these conditions for instability.

Based on the experimental observations, the conditions for which granular soils exhibit stable and unstable behavior can be summarized as shown in Table 1. The conditions leading to unstable behavior of granular materials have been identified from experimental evidence. The role of the degree

TABLE 1. Experimental Observations of Conditions for Stability and Instability Inside Failure Surface

Soil volumetric behavior, drainage (1)	Dilation		Compression		
	Drained (2)	Undrained (3)	Drained (4)	Undrained (5)	
$d^2W > 0$	Stability[a]	Stability[a]	Stability[a]	Stability[a]	
$d^2W < 0$	Stability[b]	N.A.[c]	Stability[d]	Degree of saturation	—
$d^2W < 0$	Stability[b]	N.A.[c]	Stability[d]	$S_r = 100\%$	Instability[e]
$d^2W < 0$	Stability[b]	N.A.[c]	Stability[d]	$S_r \geq (Sr)_{crit}$	Instability[d]
$d^2W < 0$	Stability[b]	N.A.[c]	Stability[d]	$S_r < (Sr)_{crit}$	Stability[d]

[a]Stability is guaranteed according to Drucker (1951), Bishop and Hill (1951), and Hill (1958)
[b]Shown by Lade et al. (1987)
[c]This combination cannot be achieved inside the failure surface
[d]Shown by Lade and Pradel (1990)
[e]Shown by Lade et al. (1988)

of saturation in conditions for instability and its relations to other material properties has been explored further in an analytical investigation presented by Pradel and Lade (1990).

Instability and Failure of Soils

Instability and failure are two different behavior aspects of soils that exhibit nonassociated flow. Although both may lead to catastrophic events, they are not synonymous. Thus, a failure surface does not go through each of the points at which instability was produced. In fact, these points are well within the failure surface as obtained from drained tests. Obviously, each of the specimens could have been loaded to higher stress differences, as long as the stress paths were outside the wedge between the yield and the plastic potential surfaces. Therefore, a failure condition expressed in terms of the maximum stress differences obtained from, e.g., undrained tests initiated at the hydrostatic axis (see Fig. 4), would clearly underestimate the true effective strength of the soil.

Material models that employ associated plastic flow rules must assume the failure surface to go through the point at which instability is produced. This is because stability is guaranteed according to Drucker's and Hill's stability conditions until the failure surface is reached, at which instability ensues. But then stable loading to higher stress differences, which is clearly possible, could not be predicted by such models. Further, since instability as well as stability can be obtained at any point in the region above the line defined by the maximum stress differences in Fig. 4, it is not possible to define any one consistent failure surface to be used in a model that incorporates associated flow.

Location of Instability Line

It is the fact that loading of a compressible soil (resulting in large plastic strains) can occur under decreasing stresses that leads to unstable behavior

under undrained conditions. Loose, fine sands and silts have relatively low permeabilities, and small disturbances in load or even small amounts of volumetric creep may produce undrained conditions in such soils, and instability of the soil mass follows. As long as the soil remains drained, it will remain stable in the region of potential instability.

When the condition of instability is reached, the soil may not be able to sustain the current stress state. This stress state corresponds to the top of the current yield surface as shown schematically on the p'-q diagram in Fig. 7. Following this top point, the soil can deform plastically under decreasing stresses. The top of the undrained effective stress path, corresponding to $(\sigma_1 - \sigma_3)_{max}$, occurs slightly after, but very close to, the top of the yield surface. The difference is due to the additional stability provided by the elastic strains, as expressed in Eq. (2). Therefore, the line connecting the tops of a series of effective stress paths from undrained tests on loose soil provides the lower limit of the region of potential instability. Experiments show that this line is straight, and it goes through the ultimate state point. For very loose sands, the ultimate state strength is very low, and for practical purposes, the line goes through the origin of the stress space. The lower limit of the region of potential instability is labeled the instability line in Fig. 7. The upper limit of this region is defined by the failure line.

In the p'-q diagram in Fig. 8, the location of the instability line is compared with locations of the effective stress failure line, the total stress failure line,

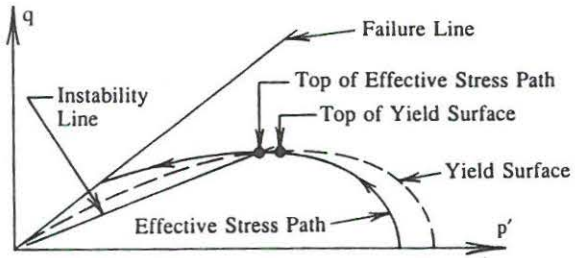

FIG. 7. Location of Instability Line for Loose Sand

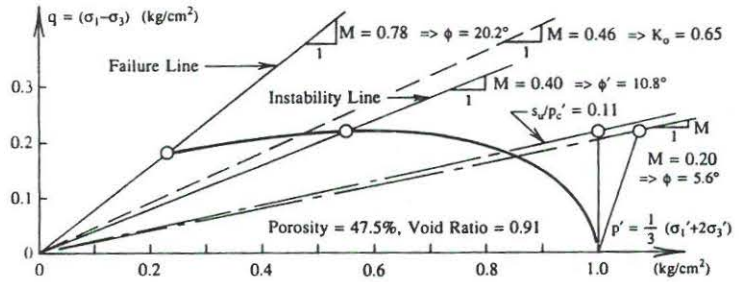

FIG. 8. Effective Stress Path for ICU-Test on Very Loose, Fine Valgrinda Sand [Deduced from Bjerrum et al. (1961)]

and the line corresponding to the normalized undrained shear strength s_u/p_c'. The effective stress path from an isotropically consolidated-undrained triaxial compression test on very loose, fine Valgrinda sand deduced from results presented by Bjerrum et al. (1961) forms the background for this comparison. The effective stress failure line for this loose sand corresponds to an effective friction angle of $\phi' = 20.2°$. The region between this line and the instability line, which corresponds to $\phi' = 10.8°$, bounds the stress states for which static instability may occur.

The total stress failure line indicates a total stress friction angle of $\phi = 5.6°$, whereas the s_u/p_c' line is located slightly higher. These two lines do not correspond to the effective stress states at the condition of instability because they do not imply anything about the pore pressures that develop during undrained shear. Rather, they represent means of characterizing the undrained shear strength as related to the effective consolidation pressure, which may be obtained from static analysis. They are used in total stress analyses in which the pore pressures that develop under undrained shear are unknown. They are not useful for analyses of static instability, which require considerations in terms of effective stresses as shown below.

As the density of the sand increases, the instability line moves up and away from the origin of the p'-q diagram, and it crosses the failure line at a point corresponding to the steady state or critical state value of p'. According to Poorooshasb (1989), these two states are, in fact, the same, and they are more appropriately referred to as the ultimate state. The instability line may then be described by a straight line in terms of c_i' and ϕ_i'. Sladen et al. (1985) have summarized data for seven loose sands to give variations of ultimate state values of p' with void ratio, effective stress friction angles, ϕ', for the failure surface, and friction angles, ϕ_i', to describe the slope of the instability line. For the seven fine sands in loose conditions, the average value of $\phi' = 30°$, and the average $\phi_i' = 17°$. Based on typical p'-value at the ultimate state condition and a ϕ_i'-value of 17°, a typical instability line for loose sand may correspond to $c_i' = 0.20$ kg/cm² (410 psf = 20 kPa). These values are used in the following analysis of a nearly fully saturated loose fine sandy slope as found in a tailings dam or a spoil heap.

Instability of Submarine Slope

Andresen and Bjerrum (1967) and Bjerrum (1971) reviewed a series of large submarine slope failures that occurred in loose, fine sand and silt deposits in the fjords mainly within a small area in the middle of Norway. These slides took place in deposits with gentle slopes of 3–15°. Bjerrum (1971) reports that "these slides have been surrounded by considerable mystery as they frequently occur in slopes which, according to conventional stability analysis, should be stable beyond any doubt."

Such slides may be initiated by very small disturbances or small amounts of volumetric creep resulting in static instability. This is made possible by the fact that the states of stress on some planes in the soil mass are within the region of potential instability. Using the data shown in Fig. 8 for very loose, find Valgrinda sand (from a site south of Trondheim, Norway), an analysis of the state of stress in a submarine slope with an inclination $\alpha = 7°$ is shown in Fig. 9. Since these slopes are typically stretching over large areas, an infinite slope-stability analysis may provide the appropriate conventional procedure. According to such an analysis, the factor of safety would be

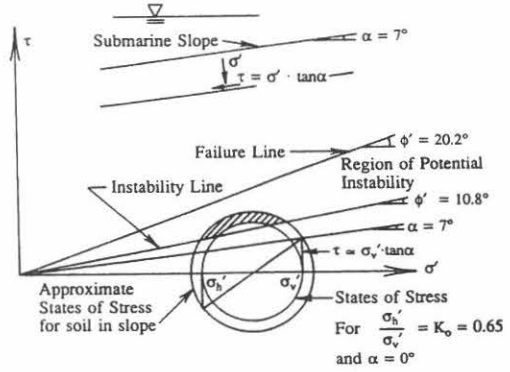

FIG. 9. Analysis of Gently Inclined Submarine Slope. States of Stress on Some Planes are in Region of Potential Instability

$$F = \frac{\tan \phi'}{\tan \alpha} = \frac{\tan 20.2°}{\tan 7°} = 3.00 \quad \ldots\ldots\ldots\ldots\ldots\ldots\ldots\ldots\ldots\ldots (7)$$

Even if the friction angle corresponding to the instability line is used, F becomes

$$F = \frac{\tan \phi'}{\tan \alpha} = \frac{\tan 10.8°}{\tan 7°} = 1.55 \quad \ldots\ldots\ldots\ldots\ldots\ldots\ldots\ldots\ldots\ldots (8)$$

This indicates that the slope should be stable beyond any doubt as stated by Bjerrum (1971). However, this analysis is only concerned with the stresses along the sliding surface, which is assumed to be parallel with the sloping ground surface. The horizontal stresses acting in the soil deposit have been ignored in the conventional analysis.

The state of stress under level ground is obtained from the value of K_0, which for very loose Valgrinda sand is in the order of 0.65. Thus, $\sigma'_h = 0.65 \cdot \sigma'_v$. The corresponding Mohr circle is shown in Fig. 9. For a gently sloping ground surface, the normal stresses on vertical and horizontal planes may be approximated by those obtained from the K_0 stress state. The shear stresses acting on these planes may be obtained from $\tau = \sigma' \cdot \tan \alpha$. The corresponding states of stress are represented by the larger Mohr circle in Fig. 9. Whereas this circle may represent an approximation to the real states of stress, these are likely to be between the two Mohr circles shown in Fig. 9. This diagram also shows that the states of stress on some planes are located in the region of potential instability (shaded areas), but they are not close to the failure line corresponding to $\phi' = 20.2°$. Therefore, as long as the soil remains drained, it is stable. But a small disturbance will cause the fine sand and silt deposit, which has relatively low permeability, to become undrained and subsequently render the slope unstable under what amounts to essentially static conditions.

It is interesting to note that even the K_0 stress state obtained under level ground ($\alpha = 0°$) on some planes reaches up into the region of potential instability. Thus, the soil under a level ground surface may become unstable due to small disturbances.

Bjerrum (1971) noted that the initial submarine slides tended to occur at low tide. It is difficult to imagine that very large amounts of water would drain out of the fjord bottom (due to the very low compressibility of water), thus causing a disturbance of the submarine slope, but the change in tide may have provided the small disturbances (possibly in the form of drag on the fjord bottom) that caused the gentle slopes to become unstable. All other requirements for instability were already fulfilled.

Instability of Tailings Slope

An example slope is analyzed to demonstrate that a tailings slope or a spoil heap consisting of loose granular materials with permeabilities near those of fine sands and silts may become unstable under essentially static loading conditions. Such slopes are often not engineered, but simply created by dumping material in a loose state.

Slope Definition

The slope shown in Fig. 10 has an inclination of horizontal: vertical = 2:1 (inclination angle = 26.6°); a height of $H = 150$ ft (45.7 m); and effective strength parameters of $c' = 0$ and $\phi' = 30°$. The soil in the slope is assumed to have a void ratio of 0.89 and a dry density of 87.5 lb/cu ft (13.75 kN/m^3). It is also assumed to be nearly saturated, say due to rain water infiltration, with a degree of saturation of 97%, and the total density is therefore $\gamma_t = 116.0$ lb/cu ft (18.22 kN/m^3). Only vertical water flow inside the slope is assumed, and the pore water pressure is therefore dissipated as the water infiltrates the slope.

Conventional Slope Stability

Conventional slope-stability methods indicate that the most critical failure surface for a cohesionless slope is parallel to the slope surface. Thus, an infinite slope-stability analysis of a slope with vertical seepage produces

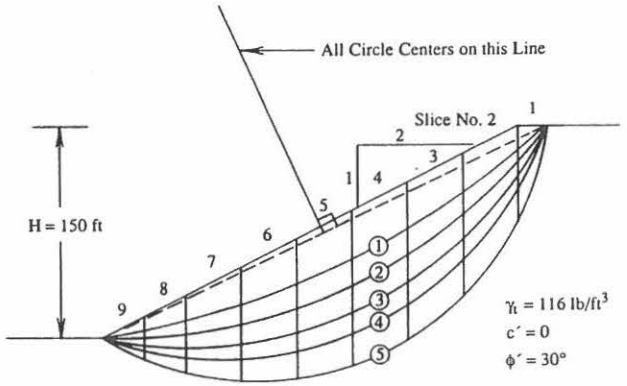

FIG. 10. Example Slope with Circular Slip Surfaces for Analyses of Static State of Stress

$$F = \frac{\tan \phi'}{\tan \alpha} = \frac{\tan 30°}{\tan 26.6°} = 1.15 \quad \ldots\ldots\ldots\ldots\ldots\ldots\ldots\ldots\ldots\ldots (9)$$

indicating that the slope should be stable.

Stress State in Slope

To determine whether the slope can become unstable, it is necessary to compare the states of stress in the slope with those required to produce unstable behavior. The simple stress analysis indicated for the shallow submarine slope cannot be employed for the steeper slope, because its states of stress are far removed from the K_0 state. A correct stress analysis could be performed by the finite element method incorporating a realistic constitutive model to describe the stress-strain behavior of the soil. Whereas such an approach would be desirable, it is not simple in comparison with conventional slope-stability analyses methods. Although not ideal, the latter may be employed to evaluate the state of stress to an approximate degree. This approach has been used to determine the consolidation stress state in slopes [e.g., Lowe and Karafiath (1960)].

Spencer's slope-stability method (Spencer 1967; Wright 1969; Pyke 1984) was employed to determine the approximate effective stress state along five circular slip surfaces as seen in Fig. 10. Since none of these circles are critical, they all produce factors of safety above unity, and the stress states can be calculated along each slip surface. Because the calculation procedure requires the factor of safety to be constant along a given circle, the computed stress states are located on a straight line given by

$$\tau = \frac{c' + \sigma' \cdot \tan \phi'}{F} = c'_d + \sigma' \cdot \tan \phi_d \quad \ldots\ldots\ldots\ldots\ldots\ldots (10)$$

For a cohesionless slope $c' = c'_d = 0$, and the straight line goes through the origin of the τ-σ' diagram. Fig. 11 indicates the stress states obtained from the five circles shown in Fig. 10. Some of the stress states reach up into the region of potential instability, the lower limit of which is described by $c'_i = 0.20$ kg/cm^2 and $\phi'_i = 17°$. Thus, the slope is potentially unstable according to the concepts presented here.

To obtain the region within the slope in which the stresses reach values

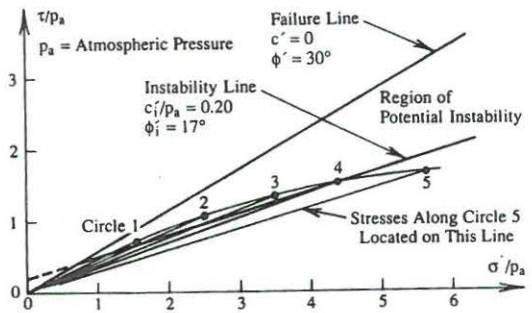

FIG. 11. Stress States along Circular Slip Surfaces Reach into Region of Potential Instability

that are in the area of potential instability in Fig. 11, the stress states (calculated at the middle of each slice) have been plotted in Fig. 12(*a*). This diagram shows values of $(\tau - c'_i)/\sigma'$ versus the horizontal distance from the toe. The stress states for which

$$\frac{\tau - c'_i}{\sigma'} \geq \tan \phi_i \quad \ldots\ldots\ldots\ldots\ldots\ldots\ldots\ldots\ldots\ldots\ldots\ldots\ldots\ldots (11)$$

are within the region of potential instability. The range of stresses for which this inequality is fulfilled is then transferred to the respective circles in Fig. 12(*b*), and a region of potential instability may be identified within the slope.

To study the reliability of this method for determination of the stress state in a slope, another set of five circles were employed. These circles had a fixed center (namely that of circle 3 in the first series of analyses) and variable radius. The corresponding region of potential instability is indicated by a dashed line in Fig. 12(*b*). The two regions are not exactly the same. Thus, this method of obtaining the stress states in the slope is not entirely satisfactory but may suffice for an approximate determination of the susceptibility of a given slope to static instability and liquefaction.

Finite element analyses of slopes (Wright et al. 1973; Pyke 1984) indicate that the ratio of shear stress to normal stress near the middle section of the slip surface may be obtained with reasonable accuracy from conventional equilibrium slope-stability methods. Near the upper end of the slip surface, this ratio tends to be higher, and near the lower end it tends to be lower than obtained from the slope-stability methods. Thus, the real region of potential instability reaches higher up towards the crest of the slope than indicated in Fig. 12(*b*), and it may not reach as far down towards the toe as shown in Fig. 12(*b*).

Effect of Slope Height

Using geometrically similar toe circles, such as those shown in Fig. 10, the influence of slope height on the extent of the potentially unstable region was studied. Fig. 13 shows that the relative magnitude of the potentially unstable region increases with slope height, whereas slopes with heights smaller than approximately 90 ft do not have stresses reaching up into the critical stress region shown in Fig. 11. For slopes higher than 90 ft, a region is present in which instability may be induced under essentially static loading conditions, e.g., due to increasing stresses caused by the weight of additional rain water. Once a local zone of instability has been created, the resulting pore pressure build-up will propagate and enlarge the unstable region in the slope. Thus, a progressively larger volume of unstable soil will be engaged, and the slope will fail by static liquefaction.

Note that instability is not produced along a particular slip surface, but rather, in a volume of soil within the slope, and classical slope stability methods cannot be used to produce a factor of safety. A slope with a large region of potentially unstable soil is perfectly stable as long as the soil remains drained. But the moment the soil becomes undrained, it becomes unstable, and the volume of unstable material will spread beyond the calculated boundaries indicated in Fig. 13.

Other Slopes

The regions of potential instability indicated on Fig. 13 are specific to the slope inclination and soil parameters assumed for this study. However, these values are not unlike those found in actual tailings dams and spoil heaps.

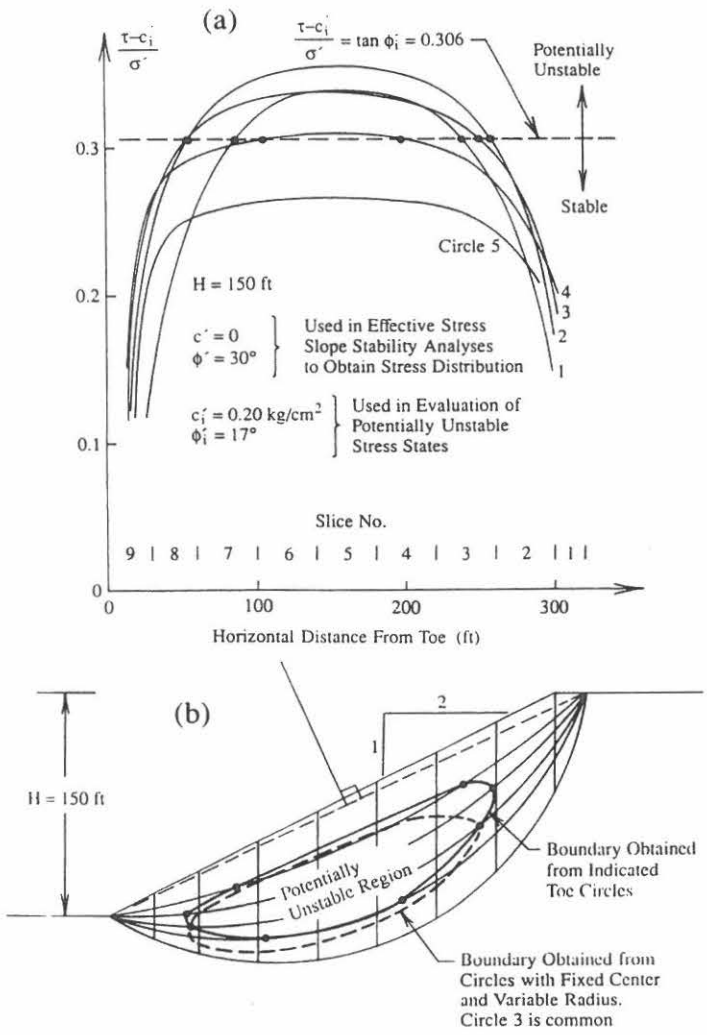

FIG. 12. (*a*) Detailed Analysis of Stress State Relative to Instability Line; and (*b*) Determination of Region of Potential Instability in Slope

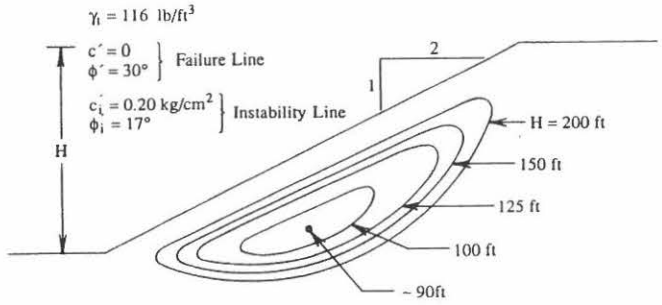

FIG. 13. Effect of Slope Height on Extent of Region of Potential Instability

An analysis of potential instability of a slope may take the form suggested herein: (1) Determine the failure line and the instability line for the given soil and soil density, both lines in terms of effective strength parameters, using consolidated undrained triaxial compression tests with pore pressure measurements; (2) establish the approximate states of stress in the slope from effective stress analyses using a conventional slope-stability procedure and several slip surfaces; (3) compare the stresses with those required for potential instability; and (4) determine the region in the slope (if any) that may become unstable.

Conclusions

Soils exhibit nonassociated flow and they may therefore become unstable inside the effective stress failure surface. Experiments have shown that soils are stable as long as they remain under drained conditions. Instability may be obtained under undrained conditions in the region where the yield surface opens up in the outward direction of the hydrostatic axis. Initiation of instability also requires that the soil tends to compress during undrained shear. Thus, loading (i.e., hardening inside the failure surface resulting in large plastic strains) can occur under decreasing stresses, and this leads to unstable behavior under undrained conditions. The location of the lower boundary for instability, herein called the instability line, is identified. Together with the effective stress failure line it defines the region of potential instability. The instability of a gently inclined submarine slope and a steeper slope representing a tailings dam or a spoil heap are analyzed. Conventional stability analyses indicate both slopes to be stable. The analysis procedures presented here clearly show the potential for instability, as actually observed in many submarine deposits of loose, fine sands and silts, and in tailings dams or spoil heaps of granular materials with properties of similar character.

Acknowledgment

The study of slope instability was supported by the Air Force Office of Scientific Research under Grant Number 910117. Grateful appreciation is expressed for this support.

APPENDIX. REFERENCES

Andresen, A., and Bjerrum, L. (1967). "Slides in subagueous slopes in loose sand and silt." *Norwegian Geotechnical Institute Publication 81*, Norwegian Geotechnical Institute, Oslo, Norway.

Bishop, J. F. W., and Hill, R. (1951). "A theory of the plastic distortion of a polycrystalline aggregate under combined stresses." *Philosophical Magazine*, 42(327), 414–427.

Bjerrum, L. (1971). "Subagueous slope failures in norwegian fjords." *Norwegian Geotechnical Institute Publication 88*, Norwegian Geotechnical Institute, Oslo, Norway.

Bjerrum, L., Kringstad, S., and Kummeneje, O. (1961). "The shear strength of a fine sand." *Norwegian Geotechnical Institute Publication 45*, Norwegian Geotechnical Institute, Oslo, Norway.

Bjerrum, L., and Simons, N. E. (1960). "Comparison of shear strength characteristics of normally consolidated clays." *Proc. ASCE Res. Conf.*, ASCE, New York, N.Y., 711–726.

Drucker, D. C. (1951). "A more fundamental approach to stress-strain relations." *Proc. First U.S. Nat. Cong. Appl. Mech.*, 487–491.

Drucker, D. C. (1956). "On uniqueness in the theory of plasticity." *Quart. Appl. Math.*, 14, 35–42.

Drucker, D. C. (1959). "A definition of stable inelastic material." *J. Appl. Mech.*, 26, 101–106.

Hill, R. (1958). "A general theory of uniqueness and stability in elasto-plastic solids." *J. Mech. Physics Sol.*, 6, 236–249.

Kramer, S. L., and Seed, H. B. (1988). "Initiation of soil liquefaction under static loading conditions." *J. Geotech. Engrg.*, ASCE 114(4), 412–430.

Lade, P. V. (1982). "Localization effects in triaxial tests on sand." *Proc. IUTAM Symp. Deformation and Failure of Granular Materials*, International Union of Theoretical and Applied Mechanics, 461–471.

Lade, P. V., Duncan, J. M. (1976). "Stress-path dependent behavior of cohesionless soil." *J. Geotech. Engrg. Div.*, ASCE 102(1), 51–68.

Lade, P. V., Nelson, R. B., and Ito, Y. M. (1987). "Nonassociated flow and stability of granular materials." *J. Engrg. Mech.*, ASCE, 113(9), 1302–1318.

Lade, P. V., Nelson, R. B., and Ito, Y. M. (1988). "Instability of granular materials with nonassociated flow." *J. Engrg. Mech.*, ASCE, 114(12), 2173–2191.

Lade, P. V., and Pradel, D. (1990). "Instability and plastic flow of soils. I: Experimental observations." *J. Engrg. Mech.*, ASCE, 116(11), 2532–2550.

Lowe, J., III, and Karafiath, L. (1960). "Effect of anisotropic consolidation on the undrained shear strength of compacted clays." *Proc. ASCE Res. Conf.*, ASCE, New York, N.Y., 837–858.

Mandel, J. (1964). "Conditions de stabilite et postulat de Drucker." *Proc. IUTAM Symp. Rheology and Soil Mech.*, 58–68 (in French).

Mroz, Z. (1963). "Non-associated flow laws in plasticity." *J. de Mechanique*, 2(1), 21–42.

Peters, J. F., Lade, P. V., and Bro, A. (1988). "Shear band formation in triaxial and plane strain tests." *Advanced Triaxial Testing of Soil and Rock, ASTM STP 977*, American Society for Testing and Materials, 604–627.

Poorooshasb, H. B. (1989). "Description of flow of sand using state parameters." *Comput. Geotech.*, 8(3), 195–218.

Poorooshasb, H. B., Holubec, I., Sherbourne, A. N. (1966). "Yielding and flow of sand in triaxial compression: Part I." *Can. Geotech. J.*, 3(4), 179–190.

Pradel, D., and Lade, P. V. (1990). "Instability and plastic flow of soils. II: Analytical investigation." *J. Engrg. Mech.*, ASCE, 116(11), 2551–2566.

Pyke, R. (1984). *User's manual for TSLOPE/TSTAB, computer programs for limit equilibrium slope stability analyses*. TAGA Engineering Systems and Software, Lafayette, Calif.

Seed, H. B., Mitchell, J. K., and Chan, C. K. (1960). "The strength of compacted cohesive soils." *Proc. ASCE Res. Conf.*, ASCE, New York, N.Y., 877–964.

Sladen, J. A., D'Hollander, R. D., and Krahn, J. (1985). "The liquefaction of sands, a collapse surface approach." *Can. Geotech. J.*, 22(4), 564–578.

Spencer, E. (1967). "A method of analysis of the stability of embankments assuming parallel inter-slice forces." *Geotechnique*, 17(1), 11–26.

Whitman, R. V. (1960). "Some considerations and data regarding the shear strength of clays." *Proc. ASCE Res. Conf.*, ASCE, New York, N.Y., 581–614.

Wright, S. G. (1969). "A study of slope stability and the undrained shear strength of clay shales," thesis presented to the Univ. of California, Berkeley, at Berkeley, Calif., in partial fulfillment of the requirements for the degree of doctor of philosophy.

Wright, S. G., Kulhawy, F. H., and Duncan, J. M. (1973). "Accuracy of equilibrium slope stability analysis." *J. Soil Mech. Found. Div.*, ASCE, 99(10), 783–791.

Double Hardening Model and Its Capabilities

Int. J. Solids Structures, 1977, Vol. 13, pp. 1019–1035. Pergamon Press. Printed in Great Britain

ELASTO-PLASTIC STRESS-STRAIN THEORY FOR COHESIONLESS SOIL WITH CURVED YIELD SURFACES

POUL V. LADE

Mechanics and Structures Department, School of Engineering and Applied Science, University of California, Los Angeles, CA 90024, U.S.A.

(*Received* 2 *August* 1976; *revised* 27 *January* 1977)

Abstract—An elasto-plastic stress-strain theory for cohesionless soil with curved yield surfaces is developed on the basis of soil behavior observed in laboratory tests. This theory is applicable to general three-dimensional stress conditions, but the parameters required to characterize the soil behavior can be derived entirely from results of isotropic compression and conventional drained triaxial compression tests. The theory is shown to predict soil behavior under various loading conditions with good accuracy. Of special interest is its capability of predicting soil behavior under drained as well as undrained conditions over a range of confining pressures where the behavior changes from that typical of dense sand to that typical of loose sand. Work-hardening as well as work-softening is incorporated in the theory.

1. INTRODUCTION

The elasto-plastic stress-strain theory previously developed for cohesionless soils[1, 2] reflects many of the characteristics of sand behavior observed in laboratory tests. Results of cubical triaxial tests on cohesionless soil[1, 3] and concepts from elasticity and plasticity were employed in formulating the theory, which incorporates a yield criterion, a non-associated flow rule, and an empirical work-hardening law.

This stress-strain theory is applicable to general three-dimensional conditions, but the values of the nine soil parameters required to characterize the soil behavior can be derived entirely from the results of conventional triaxial compression tests. Several essential aspects of the behavior of cohesionless soil observed in experimental investigations are modeled by the theory: nonlinearity, the influence of σ_2, stress-path dependency, shear-dilatancy effects, and coincidence of strain increment and stress increment axes at low stress levels with transition to coincidence of strain increment and stress axes at high stress levels. Results of cubical triaxial tests, torsion shear tests, and tests performed using various stress-paths were analyzed using this theory, and it was found that the stress-strain and strength characteristics observed in these tests were predicted with reasonable accuracy[1, 2, 4].

Involved in this theory are some simplifying assumptions, which result in limitations in its capabilities in some respects. Thus, only elastic strains are predicted for proportional loading[4], whereas laboratory tests show that proportional loading with increasing stresses causes some plastic deformation. Experiments show that failure envelopes for sands most often are curved in the Mohr diagram, whereas they are assumed to be straight in the previous theory. The gradual change in behavior characteristics with increasing confining pressure from those typical of dense sand to those typical of loose sand is not accounted for in the previously developed theory.

Incorporation of additional aspects of the real behavior of cohesionless soils in the stress-strain theory requires further development. The modified theory presented herein is based on the behavior observed in isotropic compression and triaxial compression tests on three different cohesionless soils, each tested at two different densities. All aspects of soil behavior included in the previous theory are retained, and the previous theory is merely a special case (i.e. for straight failure envelopes) which is contained within the framework of the new theory.

The accuracy of the theory presented here is evaluated by comparing predicted and measured strains for a number of laboratory test conditions. Thus, it is demonstrated that the theory can accurately predict soil behavior in triaxial tests over a range of confining pressures in which the maximum stress ratio decreases (curved failure envelope) and the volume change behavior becomes compressive with increasing confining pressure. The post-peak behavior is also correctly modeled in the range of confining pressures used in the tests. The predicted and

the measured behavior for proportional loading is compared, and "at rest" loading conditions can be calculated with good accuracy. Finally, pore pressures in undrained tests are predicted, and since stress-path dependency can be handled by the theory[4], most aspects of undrained behavior can be accounted for by the new theory.

2. BASIC BEHAVIOR OF COHESIONLESS SOILS

The development of the new theory is based on a consistent pattern of behavior observed from tests on three different cohesionless soils: Sacramento River Sand[5], Crushed Napa Basalt[6], and Painted Rock Material[7]. Each of the soils were tested at two different relative densities. These three soils had quite different characteristics in terms of composition, grain shape, grain size, and maximum and minimum void ratios. The diagrams used to illustrate the developments presented here refer to loose Sacramento River Sand (initial void ratio = 0.87, relative density = 38%).

2.1 *Types of strain*

For the purpose of modeling the stress-strain behavior of soils by an elasto-plastic theory, the total strain increments, $\{d\epsilon_{ij}\}$, are divided into an elastic component, $\{d\epsilon_{ij}^{e}\}$, a plastic collapse component, $\{d\epsilon_{ij}^{c}\}$, and a plastic expansive component, $\{d\epsilon_{ij}^{p}\}$, such that

$$\{d\epsilon_{ij}\} = \{d\epsilon_{ij}^{e}\} + \{d\epsilon_{ij}^{c}\} + \{d\epsilon_{ij}^{p}\}. \tag{1}$$

These strain components are calculated separately, the elastic strains by Hooke's law, the plastic collapse strains by a plastic stress-strain theory involving a cap-type yield surface, and the plastic expansive strains by a stress-strain theory which involves a conical yield surface with apex at the origin of the stress space.

Figure 1 illustrates schematically the parts of the total strain which for the present purpose are considered to be elastic, plastic collapse, and plastic expansive components of strain in a triaxial compression test. Typical observed variations of stress difference $(\sigma_1 - \sigma_3)$, and volumetric strain, ϵ_v, with axial strain, ϵ_1, are shown in this figure for a test performed with

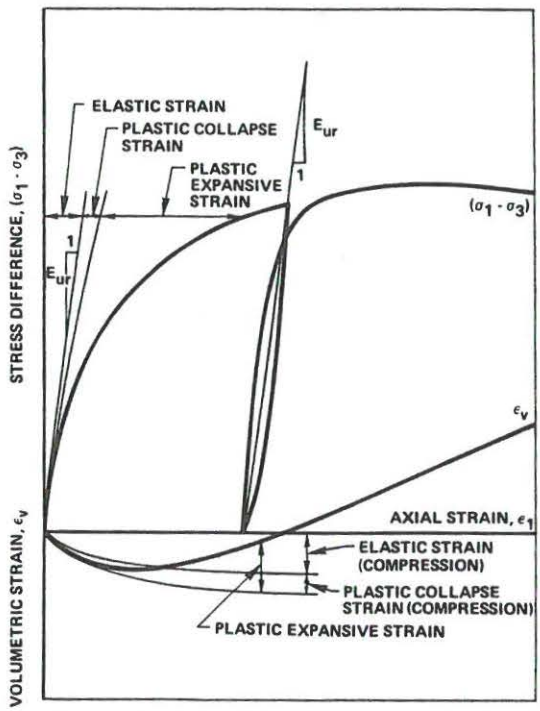

Fig. 1. Schematic illustration of elastic, plastic collapse and plastic expansive strain components in drained triaxial compression test.

constant value of the confining pressure, σ_3. Both elastic (recoverable) and plastic (irrecoverable) deformations occur from the beginning of loading of a cohesionless soil, the stress-strain relationship is nonlinear, and a decrease in strength follows peak failure. The volumetric strain is initially compressive and this behavior may be followed by expansion (as shown in Fig. 1) or by continued compression. The plastic strains are initially smaller than the elastic strains, but at higher values of stress difference the plastic strains dominate the elastic strains. The nature of the elastic, plastic collapse, and plastic expansive strain components and the methods of calculation for these components are discussed in the following.

3. ELASTIC STRAINS

The elastic strain increments, which are recoverable upon unloading, are calculated from Hooke's law, using the unloading-reloading modulus defined as[8]:

$$E_{ur} = K_{ur} \cdot p_a \cdot \left(\frac{\sigma_3}{p_a}\right)^n \tag{2}$$

The dimensionless, constant value of the modulus number K_{ur} and the exponent n are determined from triaxial compression tests performed with various values of the confining pressure, σ_3. In equation (2) p_a is atmospheric pressure expressed in the same units as E_{ur} and σ_3.

The value of Poisson's ratio has often been found to be close to 0.2 for the elastic parts of unloading-reloading stress-paths[8–10]. This value is therefore used in the following calculations.

4. PLASTIC COLLAPSE STRAINS

Part of the strains occurring during isotropic compression are irrecoverable, i.e. they are plastic in nature. Thus, a partial collapse of the grain structure resulting in a volumetric compression is caused by increasing isotropic stresses. This is illustrated in Fig. 2 for loose

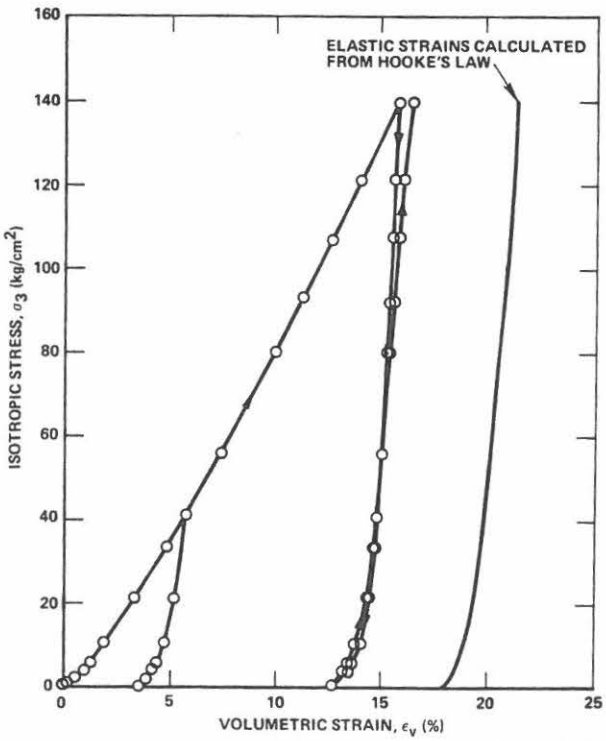

Fig. 2. Isotropic compression of loose Sacramento River Sand with primary loading, unloading and reloading branches.

Sacramento River Sand. The elastic strains which are recoverable upon unloading can be calculated with good accuracy from Hooke's law as shown in this figure. The collapse strains can therefore be separated from the total strains observed in these tests by subtracting the elastic strains.

It is reasonable to believe that plastic collapse strains are produced by any increase in mean normal stress, and that within this mode of behavior, plastic shear strains will be associated with shear stresses acting on the soil. However, it is difficult to separate the collapse strains from the plastic expansive strains for a general stress increment (not along the hydrostatic axis), because both types of strain occur simultaneously for such a stress increment. It is therefore necessary to find the magnitudes of the collapse strains from isotropic compression, the only loading condition which does not produce plastic expansive strains.

4.1 *Yield criterion.*

In order to model the described behavior, a yield criterion which forms a cap on the open end of the conical yield surface is used. Figure 3(a) shows the position of the yield cap. Cap-type yield criteria have been proposed in order to account for the plastic collapse strains occurring during isotropic compression[11–14]. Very often such cap yield surfaces have been continued smoothly into a conically shaped surface in such a way that the normality condition from theory of perfect plasticity[15, 16] could be employed over the entire surface[11, 12]. Two yield surfaces, a cone and a cap, have been used more recently[13, 14].

In the present development a collapse yield criterion which forms a sphere with center in the origin of the principal stress space is used in connection with the conical yield surface. The equation for the yield cap can be written in terms of the first and the second stress invariants, I_1 and I_2, as follows:

$$f_c = I_1^2 + 2 \cdot I_2 \tag{3}$$

As the value of f_c increases beyond its current value, the soil work-hardens and collapse strains are produced. It should be noted that yielding according to equation (3) does not result in eventual failure. Failure is controlled entirely by the conical yield surface.

4.2 *Plastic potential and flow rule*

Isotropic compression of an isotropic soil results in equal linear strains in the three principal directions. Thus, for this condition the strain increment vector should be pointed in the direction outward from the origin and coincide with the hydrostatic axis, as shown in Fig. 3(a). For this condition to be fulfilled the plastic potential function, g_c, must be identical to the yield criterion, f_c. The flow rule is then derived from:

$$\Delta\epsilon_{ij}^c = \Delta\lambda_c \cdot \frac{\partial f_c}{\partial \sigma_{ij}} \tag{4}$$

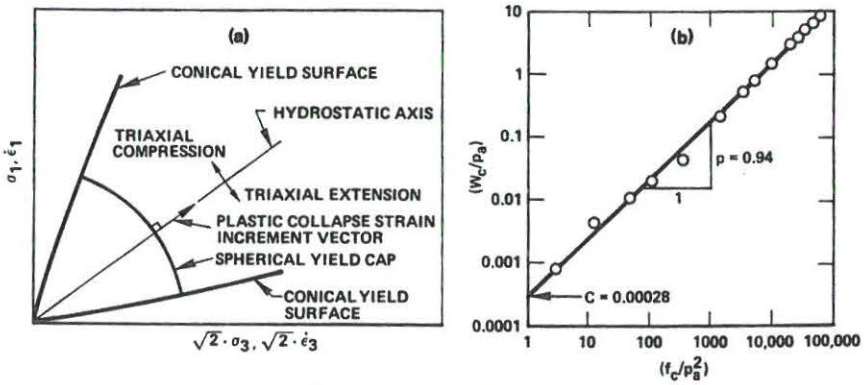

Fig. 3. (a) Location of yield cap relative to conical yield surface shown in triaxial plane, (b) relation between plastic collapse work, W_c, and the value of f_c for loose Sacramento River Sand.

where $\Delta\lambda_c$ is a proportionality constant. The derivatives of f_c with respect to the normal stresses become:

$$\frac{\partial f_c}{\partial \sigma_x} = 2 \cdot \sigma_x \tag{5a}$$

and similar expressions are obtained for the other normal stresses by interchanging the indices on the stresses. The derivatives of f_c with respect to the shear stresses become:

$$\frac{\partial f_c}{\partial \tau_{yz}} = 2 \cdot \tau_{yz} \tag{5b}$$

and similar expressions are obtained for the other shear stresses by interchanging the indices on the stresses.

4.3 *Work-hardening law*

The collapse stress-strain relationship involves one parameter, $\Delta\lambda_c$, which determines the absolute magnitude of the strain increment. The value of $\Delta\lambda_c$ can be determined from the work-hardening law.

The magnitudes of the strain increments can be calculated using an experimentally determined relation between the total plastic work required to produce collapse strains, W_c, and the degree of hardening expressed by f_c (from eqn 3):

$$W_c = F_c(f_c) \tag{6}$$

where F_c is a monotonically increasing, positive function. It is assumed that the relation expressed in eqn (6) is unique, and this implies that the work-hardening relationship is independent of the stress-path.

The relationship expressed in eqn (6) can be determined empirically from an isotropic compression test. The plastic work is calculated from

$$W_c = \int \{\sigma_{ij}\}^T \{d\epsilon_{ij}^c\} \tag{7}$$

which for isotropic compression reduces to

$$W_c = \int \sigma_3 \cdot d\epsilon_v{}^c \tag{8}$$

where $\sigma_3 \cdot d\epsilon_v{}^c$ is the plastic work done per unit volume during the volumetric strain increment $d\epsilon_v{}^c$.

The value of f_c reduces for isotropic compression to

$$f_c = 3 \cdot \sigma_3{}^2. \tag{9}$$

The diagram in Fig. 3(b) shows the relationship between W_c and f_c plotted on log-log scales for loose Sacremento River Sand. This relationship can be described with good accuracy as a straight line for which the following expression is used

$$W_c = C \cdot p_a \cdot \left(\frac{f_c}{p_a{}^2}\right)^p. \tag{10}$$

The dimensionless, constant value of the collapse modulus C is determined at $f_c/p_a{}^2 = 1$ and the collapse exponent p is the slope of the straight line as indicated in Fig. 3(b). In eqn (10) p_a is atmospheric pressure expressed in the same units as W_c and $\sqrt{f_c}$.

Noting that the yield criterion in eqn (3) is a homogeneous function of degree 2 and following

the development outlined in [17], the proportionality constant $\Delta\lambda_c$ in eqn (4) can be written as:

$$\Delta\lambda_c = \frac{dW_c}{2 \cdot f_c} \tag{11}$$

where dW_c is the increment in plastic collapse work over the increment $df_c(\geq 0)$. The value of dW_c may be determined from the derivative of W_c (given in eqn 10) with regard to (f_c/p_a^2):

$$dW_c = C \cdot p \cdot p_a \cdot \left(\frac{p_a^2}{f_c}\right)^{1-p} \cdot d(f_c/p_a^2). \tag{12}$$

The plastic collapse stress-strain relations are then determined from eqns (4), (5), (11) and (12).

5. PLASTIC EXPANSIVE STRAINS

The component of strain which has been referred to as plastic and expansive is shown in Fig. 1. Experimental evidence suggests, however, that some compression occurs due to shear stresses at small stress levels before the plastic strains become expansive at higher stress levels [18, 19]. Although compression is included, the component of strain dealt with in this section will be referred to as plastic expansive strain.

5.1 *Failure criterion–failure surface*

The failure surface is curved for most cohesionless soils, i.e. the friction angle decreases with increasing magnitude of the mean normal stress. In order to include this curvature in the failure criterion, data from triaxial compression tests on many different cohesionless soils were studied. A suitable relationship between the stresses at failure was developed in terms of the first and the third stress invariants, I_1 and I_3:

$$f_p = (I_1^3/I_3 - 27) \cdot (I_1/p_a)^m \tag{13a}$$

$$f_p = \eta_1 \text{ at failure} . \tag{13b}$$

The values of η_1 and m in eqn (13) can be determined by plotting $(I_1^3/I_3–27)$ vs (p_a/I_1) at failure in a log–log diagram, as shown in Fig. 4 for loose Sacramento River Sand. On this diagram η_1 is the intercept with $(p_a/I_1) = 1$ and m is the slope of the straight line.

In principal stress space the failure surface defined by eqn (13) is shaped like an asymmetric bullet with the pointed apex at the origin of the stress space as shown in Fig. 5(a). The apex angle increases with the value of η_1, and the curvature of the failure surface increases with the value of m. For $m = 0$ the failure surface is straight and the expression in eqn (13) becomes identical to that used in the previous theory [1, 2]. Figure 5(b) shows typical cross-sections for given values of I_1^3/I_3 and for constant value of I_1. These cross-sections are exactly the same as for the previous

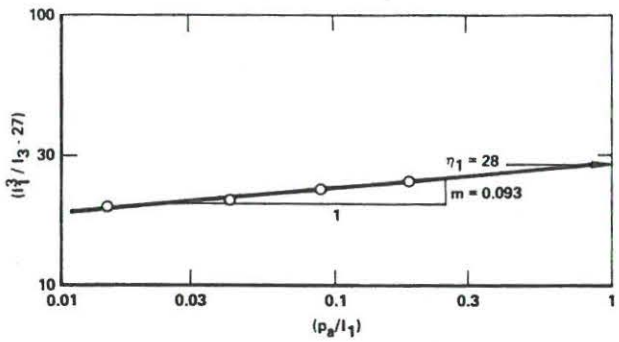

Fig. 4. Determination of the values of η_1 and m involved in failure criterion for loose Sacramento River Sand.

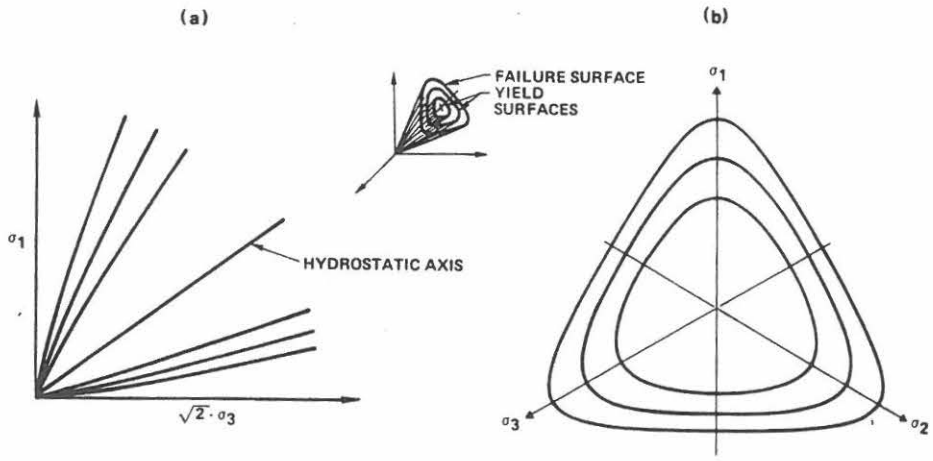

Fig. 5. Characteristics of proposed failure and yield surfaces shown in principal stress space. (a) Traces of failure and yield surfaces in triaxial plane. (b) Traces of failure and yield surfaces in octahedral plane.

theory, and it has been shown that they model the experimentally determined three-dimensional strengths of sands with good accuracy[1, 2].

The failure surface given in eqn (13) is always concave towards the hydrostatic axis. However, the real failure surfaces for cohesionless soils open up and become conical at very high values of the mean normal stress[5]. The failure criterion is therefore only valid in the range of mean normal stresses where the failure surface is concave towards the hydrostatic axis. This range of mean normal stresses is dependent on the integrity of the soil grains, and only when crushing becomes an important factor in the soil behavior does the real failure surface deviate from that expressed in eqn (13). However, for most soils the stresses necessary to produce appreciable crushing are of a magnitude to be found, e.g. at the bottom of very tall earth dams.

5.2 *Yield surface-yield criterion*

The yield surface, which defines the boundary between states of stress where both elastic and plastic deformations occur and those where only elastic deformations occur, is assumed to have the same general shape as the failure surface and to be expressible by eqn (13a). During continued loading the yield surface expands symmetrically around the hydrostatic axis as the value of f_p increases, such as shown in the insert in Fig. 5. The ultimate position of the yield surface for which $f_p = \eta_1$ is the failure surface for the sand. During unloading and neutral loading, the yield surface remains in the same position corresponding to the highest value of f_p previously applied to the sand. Thus, the soil is assumed to harden isotropically.

5.3 *Plastic potential and flow rule*

It is often assumed in plasticity theory that the plastic potential and the yield criterion are identical. This assumption was employed for the behavior of the plastic collapse strains. However, it has been found that this assumption is not accurate for the plastic expansive strain component[3, 4, 20, 21]. The plastic potential function incorporated in the theory described herein is expressed in a form similar to the failure criterion:

$$g_p = I_1^3 - \left(27 + \eta_2 \cdot \left(\frac{p_a}{I_1}\right)^m\right) \cdot I_3 \tag{14}$$

where η_2 is a constant for given values of f_p and σ_3. The plastic potential function describes a series of surfaces which are normal to the plastic strain increment directions. The selection of the function in eqn (14) was based on observations made during this and previous studies[1–4] of the directions of plastic strain increments determined from experiments.

The plastic potential surfaces given by eqn (14) are shaped like asymmetric bullets with

their pointed apices at the origin of the stress space. Their traces in octahedral planes are the same as those for the yield surfaces (Fig. 5b). Their traces in triaxial planes resemble those of the yield surface (Fig. 5a), but their apex angles are greater, they are more curved, they cut the yield surfaces, and they become asymptotic to the hydrostatic axis at a greater rate than the yield surfaces.

The relation between stress and strain is derived according to the following expression:

$$\Delta\epsilon_{ij}^{p} = \Delta\lambda_p \cdot \frac{\partial g_p}{\partial \sigma_{ij}} \tag{15}$$

which expresses that the strain increments are proportional to the derivatives of the plastic potential. The derivatives of g_p with respect to the normal stresses become:

$$\frac{\partial g_p}{\partial \sigma_x} = 3 \cdot I_1^2 - \left(27 + \eta_2 \cdot \left(\frac{p_a}{I_1}\right)^m\right) \cdot \left(\sigma_y \cdot \sigma_z - \tau_{yz}^2\right) + \frac{I_3}{I_1} \cdot m \cdot \eta_2 \cdot \left(\frac{p_a}{I_1}\right)^m$$

and similar expressions are obtained for the other normal stresses by interchanging the indices on the stresses. The derivatives of g_p with respect to the shear stresses become:

$$\frac{\partial g_p}{\partial \tau_{yz}} = \left(27 + \eta_2 \cdot \left(\frac{p_a}{I_1}\right)^m\right) \cdot (\sigma_x \cdot \tau_{yz} - \tau_{xy} \cdot \tau_{zx}) \tag{16b}$$

and similar expressions are obtained for the other shear stresses by interchanging the indices on the stresses.

A significant feature of the stress-strain relations is that they model the coupling between shear stresses and normal strains (eqns 15 and 16a) and between normal stresses and shear strains (eqns 15 and 16b). These coupling effects are consistent with observed soil behavior.

Two parameters are involved in the stress-strain relationship: $\Delta\lambda_p$ and η_2. The value of $\Delta\lambda_p$ determines the magnitude of the plastic strain increment, and the value of η_2 determines the directions of the strain increments in planes perpendicular to the octahedral plane.

The value of η_2 may be determined from the directions of the plastic strain increments in the triaxial plane, as shown for the similar strain increment directions in connection with the previous theory[1, 2]. η_2 can be determined by expressing:

$$\nu^p = -\frac{\Delta\epsilon_3^p}{\Delta\epsilon_1^p} \tag{17}$$

Substituting expressions for $\Delta\epsilon_1^p$ and $\Delta\epsilon_3^p$ from eqns (15) and (16a) into eqn (17) and solving for η_2 gives:

$$\eta_2 = \frac{3 \cdot (1 + \nu^p) \cdot I_1^2 - 27 \cdot \sigma_3 \cdot (\sigma_1 + \nu^p \cdot \sigma_3)}{\left(\frac{p_a}{I_1}\right)^m \cdot \left[\sigma_3 \cdot (\sigma_1 + \nu^p \cdot \sigma_3) - \frac{m \cdot (1 + \nu^p) \cdot I_1^2}{f_p \cdot (p_a/I_1)^m + 27}\right]}. \tag{18}$$

It is assumed that the values of η_2 calculated from the triaxial compression tests at any stress level are the correct values to use for prediction of the relative magnitudes of the strain increments at the same stress levels in tests with any combination of the three principal stresses. This assumption was shown to result in good agreement between observed behavior and the predictions of the previous theory[1, 2].

Values of η_2 were calculated from eqn (18) and plotted as a function of f_p given by eqn (13a). In order to determine the ratio $\nu^p = -\Delta\epsilon_3^p/\Delta\epsilon_1^p$ from the triaxial compression tests, the plastic expansive strain increments were calculated by subtracting the elastic and the plastic collapse strains from the total strains according to eqn (1). The variation of η_2 with f_p and σ_3 is shown in Fig. 6(a) for loose Sacramento River Sand. It may be seen from this figure that η_2 is very nearly linearly related to f_p for constant values of σ_3. The slopes of the straight lines are the same, but the intercept of the lines with the η_2-axis vary with σ_3. The variation of η_2 can be

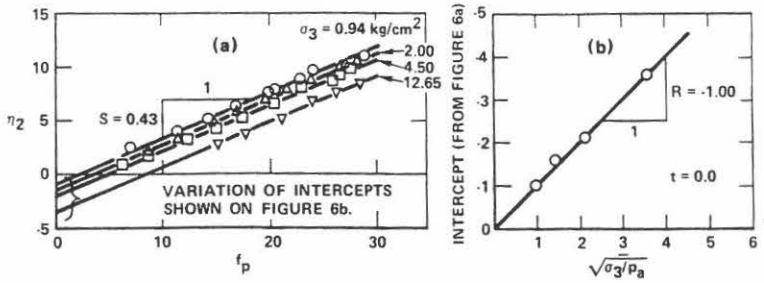

Fig. 6. (a) Variation of η_2 with f_c and σ_3. (b) Variation of intercepts with σ_3 for loose Sacramento River Sand.

modeled by a simple expression of the following type:

$$\eta_2 = S \cdot f_p + R \cdot \sqrt{\frac{\sigma_3}{p_a}} + t \tag{19}$$

where S is the slope of the straight lines, and the last two terms model the variation of the intercept. R and t are constants to be determined as shown on the diagram in Fig. 6(b).

Considerations of the strain increment ratios suggest that the value of η_2 should be zero for isotropic stress conditions where the value of f_p is also zero. However, the plastic strains which occur for very small values of f_p are negligible, and the fact that the straight lines, which model the variations of η_2, do not go through the origin is therefore not of practical importance.

Negative values of η_2 correspond to plastic volumetric strains which are compressive, whereas positive values of η_2 correspond to plastic expansive strains. Figure 6(a) shows that loose Sacremento River Sand compresses slightly at small stress levels before expansive strains are produced at high stress levels. The diagram indicates that the initial compression is most pronounced for high confining pressures, which is in accordance with observed soil behavior.

The experimental data show that the values of η_2 are smaller than f_p, thus indicating that the plastic potential surface and the yield surface do not coincide. If η_2 was equal to f_p at all stress levels, the plastic potential function in eqn (14) would be identical to the yield function in eqn (13a) and the normality criterion would apply to the soil. However, Fig. 6(a) indicates that the chosen yield criterion cannot substitute as the plastic potential function for cohesionless soil.

5.4 *Work-hardening and -softening law*

The magnitudes of the strain increments caused by a given stress increment can be calculated using an experimentally determined relation between plastic work and stress level. An isotropic work-hardening and -softening law is employed, and this implies that the yield surface expands or contracts uniformly and that the degree of hardening or softening is independent of stress-path. Thus, according to the isotropic hardening hypothesis, there exists a unique relationship between the total plastic work W_p and the degree of hardening or softening expressed by the value of f_p (given by eqn 13a):

$$W_p = F_p(f_p) \tag{20}$$

where F_p is a monotonically increasing or decreasing, positive function.

The relationship expressed in eqn (20) can be determined empirically by calculating the plastic work and plotting its variation with f_p. The plastic work at each stage of the triaxial compression tests was calculated from

$$W_p = \int \{\sigma_{ij}\}^T \{d\epsilon_{ij}^p\} \tag{21}$$

in which $\{\sigma_{ij}\}^T\{d\epsilon_{ij}^p\}$ is the plastic work done per unit volume during the strain increment $\{d\epsilon_{ij}^p\}$. The diagram in Fig. 7 shows the variation of the total plastic work with the value of f_p and the

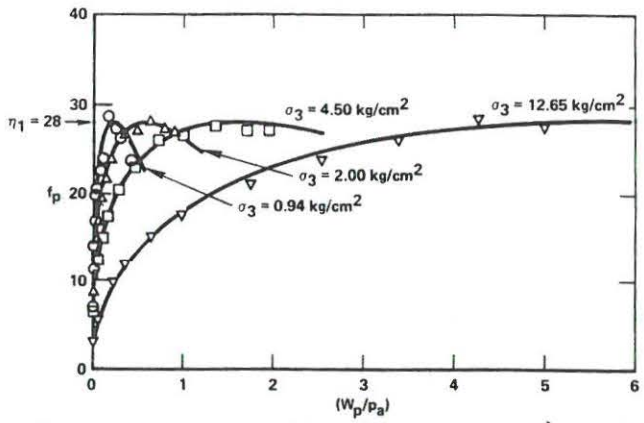

Fig. 7. Variation of total plastic work with f_p and σ_3 for loose Sacramento River Sand.

confining pressure σ_3. The fact that very small or negligible plastic strains are produced at small stress levels (as shown schematically in Fig. 1) is reflected in the work-hardening relationships which have vertical tangents at the origin. Increasing increments of plastic strains are produced with increasing stress levels. Figure 7 also demonstrates a significant influence of the confining pressure on the amount of plastic work necessary to produce plastic strains at high stress levels. The peaks of the relationships all occur at $f_p = \eta_1$, but the amount of plastic work required to reach the peaks increases with increasing confining pressure. The decreases in the values of f_p with further work input also follow a consistent pattern which depends on σ_3, as shown in Figure 7. This post-peak behavior is referred to as work-softening or strain softening.

In order to be able to handle both work-hardening and work-softening, it is necessary to consider the function F_p in eqn (20) first as monotonically increasing and then as monotonically decreasing. Therefore, the value of W_p at the peak stress level (i.e. at peak failure) is used to distinguish between the parts of the relation between W_p and f_p where F_p is increasing and the parts where F_p is decreasing.

The plastic potential function for the plastic expansive strains (eqn 14) is not a homogeneous function. However, proceeding as in [17], the operations indicated in the expression $\sigma_{ij} \cdot (\partial g_p/\partial \sigma_{ij})$ result in

$$\sigma_{ij} \cdot \frac{\partial g_p}{\partial \sigma_{ij}} = 3 \cdot g_p + m \cdot \eta_2 \cdot \left(\frac{p_a}{I_1}\right)^m \cdot I_3. \tag{22}$$

The value of the proportionality constant $\Delta\lambda_p$ in eqn (15) can therefore be written as

$$\Delta\lambda_p = \frac{dW_p}{3 \cdot g_p + m \cdot \eta_2 \cdot \left(\frac{p_a}{I_1}\right)^m \cdot I_3} \tag{23}$$

where g_p is the plastic potential function and dW_p is the increment in plastic work due to an increase in the stress level df_p.

The increment of plastic work per volume, dW_p, can be determined from the relations between W_p and f_p shown in Fig. 7. These rlations can be approximated by exponential functions for which the following expression is used:

$$f_p = a \cdot e^{-b \cdot W_p} \cdot \left(\frac{W_p}{p_a}\right)^{1/q}, \quad q > 0 \tag{24}$$

where the parameters a, b and q are constants for a given value of the confining pressure σ_3.

The expression in eqn (24) models several aspects of the work-hardening and work-softening behavior shown in Fig. 7: (1) The initial tangent is vertical, and the expression

therefore models the soil behavior at the origin, as discussed above; (2) the value of f_p increases with W_p until a peak value is reached; and (3) f_p decreases with further increase in W_p in a way similar to that exhibited by the soil behavior. The only limitiation of the exponential expression in eqn (24) is that the value of f_p decreases asymptotically to zero for very large values of W_p. Thus, it implies that the residual strength of the soil is zero. However, eqn (24) models the soil behavior very accurately within strain magnitudes of interest, and only for very large strains does it deviate from the observed soil behavior.

The values of q, a and b in eqn (24) can be determined for a given value of the confining pressure according to the following expressions:

$$q = \frac{\log\left(\frac{W_{ppeak}}{W_{p60}}\right) - \left(1 - \frac{W_{p60}}{W_{ppeak}}\right) \cdot \log e}{\log\left(\frac{\eta_1}{f_{p60}}\right)} \tag{25}$$

where (W_{p60}, f_{p60}) and (W_{ppeak}, η_1) are two sets of corresponding values on a curve in Fig. 7 and e is the base for natural logarithms. Any two points on a curve could in principle be used for determination of q, but the best overall curvefit is obtained when the peak point of the curve and the point corresponding to 60% of η_1 on the work-hardening part of the curve are used.

$$a = \eta_1 \cdot \left(\frac{e \cdot p_a}{W_{ppeak}}\right)^{1/q} \tag{26}$$

and

$$b = \frac{1}{q \cdot W_{ppeak}} \tag{27}$$

where q is determined from eqn (25), e is the base for natural logarithms and W_{ppeak} is the value of W_p at the peak point.

The variation of W_{ppeak} with the confining pressure σ_3 is shown on the diagram in Fig. 8(a), and this variation can be approximated by a straight line in the log–log diagram, such that

$$W_{ppeak} = P \cdot p_a \cdot \left(\frac{\sigma_3}{p_a}\right)^l \tag{28}$$

where P and l are constants to be determined as shown on Fig. 8(a) and p_a is atmospheric pressure expressed in the same units as W_{ppeak} and σ_3.

The variation of q with confining pressure σ_3 is shown on the diagram in Fig. 8(b), and this variation can best be modeled by a simple expression as follows:

$$q = \alpha + \beta \cdot \frac{\sigma_3}{p_a} \tag{29}$$

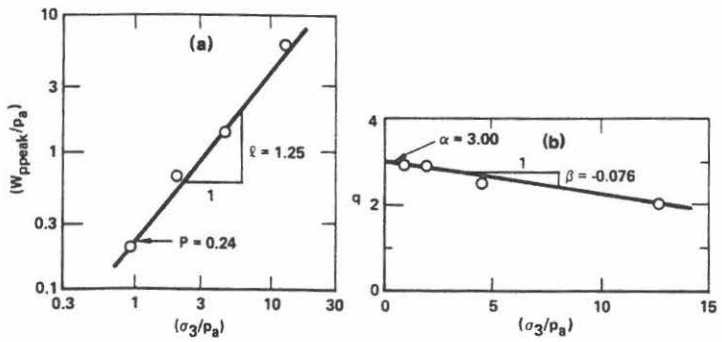

Fig. 8. (a) Variation of W_{ppeak} with confining pressure σ_3 and (b) variation of q with confining pressure σ_3 for loose Sacramento River Sand.

where α and β are, respectively, the intercept and the slope of the straight line shown on Fig. 8(b).

The solid lines on Fig. 7 have been drawn on the basis of the relationship in eqn (24) and the values of a, b, and q determined from eqns (26)–(29). It may be seen that the expression in eqn (24) models all aspects of the observed soil behavior with good accuracy for all values of the confining pressure σ_3.

Based on the expression in eqn (24) the increment in plastic work can be expressed as follows:

$$dW_p = \frac{df_p}{f_p} \cdot \frac{1}{\left(\frac{1}{q \cdot W_p} - b\right)} \tag{30}$$

where q is given by eqn (29), b is given by eqns (27) and (28), f_p is the current value of the stress level, and df_p is the difference in f_p between two successive stress states.

It should be noted that it is important to distinguish between the work-hardening and the work-softening parts of the $W_p - f_p$ relationship, because two values of W_p corresponds to the same value of f_p. This is best done by comparing the current value of W_p with W_{ppeak} calculated from eqn (28). Thus, for $W_p < W_{ppeak}$ the soil is work-hardening and for $W_p > W_{ppeak}$ the soil is work-softening. For $W_p = W_{ppeak}$ the value of dW_p in eqn (30) is infinite. For all other conditions the value of dW_p is positive and definite. The calculations presented in Section 7 were made on the basis of total stresses rather than stress increments, and the condition $W_p = W_{ppeak}$ could therefore easily be avoided with no loss in accuracy.

6. SUMMARY OF STRESS-STRAIN PARAMETERS

The values of the parameters included in the elasto-plastic stress-strain theory presented above can be evaluated using only the results of isotropic compression and conventional drained triaxial compression tests. The values of the parameters were determined from the results of tests on Sacramento River Sand, Crushed Napa Basalt, and Painted Rock Material, each tested at two different relative densities. The parameters are listed in Table 1. It should be noted that none of these parameters have dimensions. All dimensions are controlled, where appropriate, by the dimension of the atmospheric pressure, p_a, as e.g. in eqn (28). The parameters in Table 1 may be used to calculate strains in the respective soils for any combination of stresses and changes in stress during primary loading, neutral loading, unloading, and reloading.

Table 1. Summary of soil parameters for Sacramento River Sand, crushed Napa basalt, and painted rock material

Parameter \ Soil	Sacramento River Sand		Crushed Napa Basalt		Painted Rock Material		Strain Component
Relative Density, D_r(%)	100	38	100	70	100	70	
Void Ratio, e	0.61	0.87	0.53	0.66	0.40	0.48	
Modulus No., K_{ur}	1680	960	1520	900	1580	730	Elastic
Exponent, n	0.57	0.57	0.34	0.38	0.49	0.66	
Poisson's Ratio, ν	0.20	0.20	0.20	0.20	0.20	0.20	
Collapse Modulus, C	0.00023	0.00028	0.00075	0.00120	0.00100	0.00140	Plastic
Collapse Exponent, p	0.86	0.94	0.74	0.775	0.63	0.644	Collapse
Yield Const., η_1	80	28	280	130	101	67	
Yield Exponent, m	0.23	0.093	0.423	0.30	0.21	0.16	
Pl. Potent. Const., R	-2.95	-1.00	-5.90	-3.03	-2.34	-2.21	
Pl. Potent. Const., S	0.44	0.43	0.41	0.40	0.44	0.44	Plastic
Pl. Potent. Const., t	8.45	0.00	0.00	0.00	2.80	3.10	Expansive
Work-Hard. Const., α	3.00	3.00	2.22	2.35	3.45	3.28	
Work-Hard. Const., β	0.060	-0.076	-0.023	-0.046	-0.033	-0.029	
Work-Hard. Const., P	0.12	0.24	0.50	0.35	0.12	0.080	
Work-Hard. Exponent, ℓ	1.16	1.25	1.09	1.23	1.38	1.61	

7. PREDICTION OF SOIL BEHAVIOR FOR VARIOUS LOADING CONDITIONS

To test the abilities of the elasto-plastic stress-strain theory developed in the previous sections, predictions of this theory are compared to measured soil behavior for a variety of loading conditions. In addition to results of drained triaxial compression tests, experimental data are available for proportional loading and undrained compression on Sacramento River Sand and for "at rest" loading conditions on Crushed Napa Basalt and Painted Rock Material. These types of loading conditions are of special interest because they were either predicted with only moderate accuracy or they were not compared to the predictions of the previous theory. Appropriate computer programs were developed to perform the necessary calculations involved in using the theory for prediction of the various loading conditions. Only the soil parameters listed in Table 1 are used for all predictions.

7.1 *Drained triaxial compression tests*

The relation between stress difference, volumetric strain, and axial strain for drained triaxial compression tests were determined by specifying discrete stress points for such tests and calculating the strain increments from the theory. The comparison between measured and calculated stress-strain and volume change behavior for loose and dense Sacramento River Sand is shown in Fig. 9. The points in these figures represent the measured soil behavior and the solid lines represent the calculations from the theory.

Most aspects of the soil behavior are calculated with good accuracy using the stress-strain theory. Notably, the decrease in maximum stress ratio, σ_1/σ_3, with increasing confining pressure is well accounted for, and the gradual variation of the volumetric strain behavior, from being expansive at small confining pressures to being compressive at high confining pressures, is also modeled correctly by the theory. The predicted post-peak stress-strain curves are in good agreement with those measured within the range of strains considered.

7.2 *Proportional loading*

Proportional loading is defined as a loading condition where the ratio between the principal stresses is held constant while the stress magnitudes are increased or decreased. Tests with proportional loading and decreasing stresses result in only elastic strains [4, 22, 23]. Proportional loading with increasing stresses results in both elastic and plastic strains, and the measured

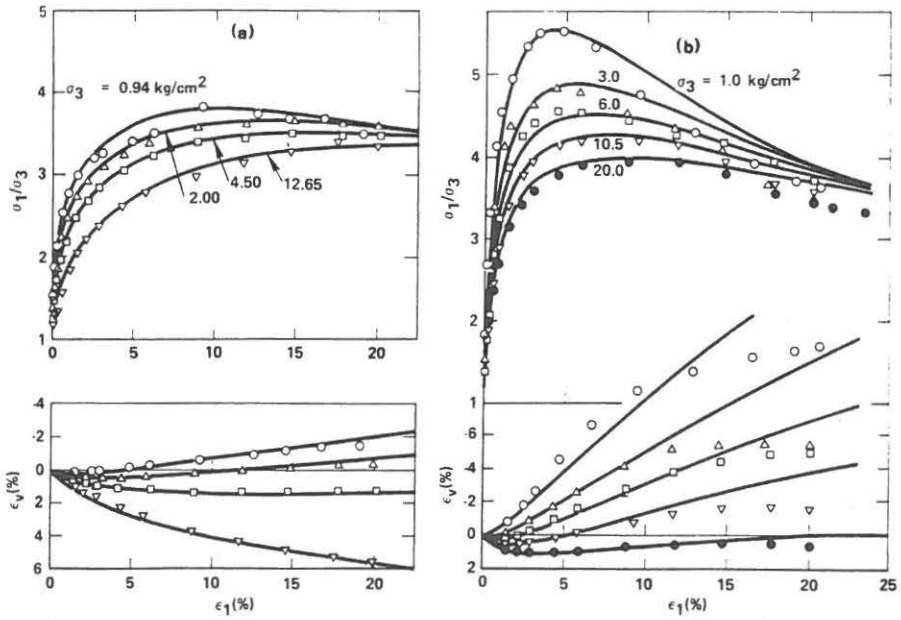

Fig. 9. Comparison between measured and predicted stress-strain and volume change behavior for (a) loose and (b) dense Sacramento River Sand in drained triaxial compression tests.

axial and volumetric strains generally become larger with increasing stress ratio [4, 9, 22, 23].

Curved yield surfaces are used for the plastic expansive strains, and both yield surfaces, the cone and the cap, are therefore pushed out when the stresses are increased proportionally. Thus, both elastic and plastic strains will occur for proportional loading with increasing stresses. Only elastic strains are predicted by the theory for conditions of constant stress ratio and decreasing stresses, which is in accordance with observed soil behavior [4].

Prediction of stress-strain relations for proportional loading were performed by specifying discrete stress points and calculating the strain increments from the theory. Figure 10 shows observed and predicted strains for proportional loading conditions with increasing stresses on loose and dense Sacramento River Sand. Stress ratios of 1.00, 1.77, 2.20 and 2.80 were used in the tests. Figure 10(a) shows that the axial strains for the loose sand are calculated to be somewhat higher (solid lines) than those measured (points). However, the volumetric strains are fairly accurately predicted for all values of the stress ratio. Figure 10(b) shows that both axial and volumetric strains for the dense sand are predicted with good accuracy for all stress ratios. The volumetric compression of the dense sand is quite similar in magnitude for all stress ratios used, whereas the loose sand shows increasing volumetric compression with increasing stress ratio. This difference in behavior is predicted by the theory.

7.3 *"At rest" loading conditions*

Tests performed on specimens under conditions of zero lateral strain are referred to as "at rest" tests or K_o-tests, where K_o is the coefficient of earth pressure at rest which may be defined as [24]:

$$K_o = \left(\frac{\Delta\sigma_3}{\Delta\sigma_1}\right)_{\epsilon_h=0} \tag{31}$$

where $\Delta\sigma_3$ and $\Delta\sigma_1$ are the increments in the principal stresses such that no lateral strain occurs. For the case of increasing stresses both plastic and elastic strains are produced, whereas mainly elastic strains occur in the specimen for the case of decreasing stresses [24]. For increasing stresses the plastic and the elastic strains cancel each other out such that the total lateral strain is zero:

$$\Delta\epsilon_h^e + \Delta\epsilon_h^c + \Delta\epsilon_h^p = 0 \tag{32}$$

where $\Delta\epsilon_h^e$, $\Delta\epsilon_h^c$, and $\Delta\epsilon_h^p$ refer to lateral increments in elastic, plastic collapse, and plastic expansive strains.

The soil behavior during K_o-tests was calculated by specifying the vertical stresses and using a simple iteration procedure to find the horizontal stresses that would result in lateral strains fulfilling eqn (32) within specified narrow limits. The results of a K_o-test on dense Crushed Napa Basalt (relative density = 100%) are shown on Fig. 11. The predicted behavior

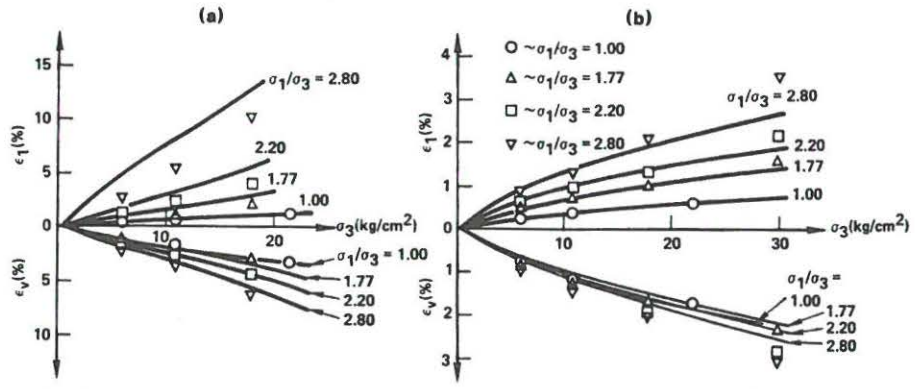

Fig. 10. Comparison of measured and predicted strains for proportional loading with increasing stresses on (a) loose and (b) dense Sacramento River Sand.

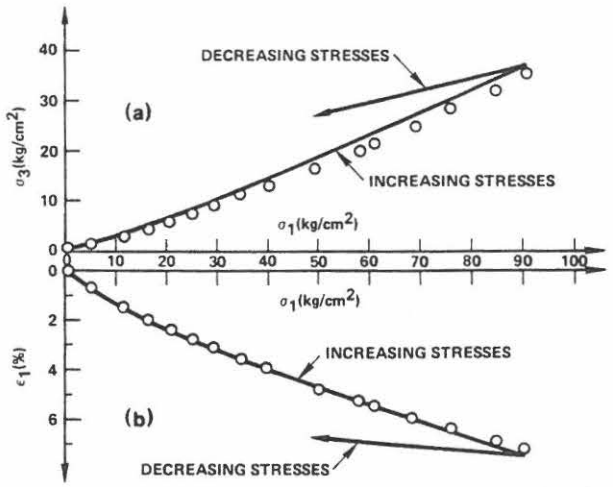

Fig. 11. Comparison of measured and predicted (a) stresses and (b) stress-strain relationship in K_o-test on dense crushed Napa basalt.

(solid lines) is seen to correspond very well to the measured behavior (points) for increasing stresses. The value of K_o calculated from eqn (3) is not constant as is often assumed. K_o increases with increasing stresses, and this aspect of the soil behavior is accurately predicted by the theory. No test results were available for decreasing stresses, but tests by others [25–27] indicate that they follow a pattern shown by the lines denoted "Decreasing Stresses." The states of stress and the axial strains indicated by these lines are actually the ones predicted by the theory. The value of K_o for decreasing stresses may be calculated from elasticity theory and corresponds to $K_o = \nu/(1-\nu)$, where $\nu = 0.2$ is Poisson's ratio.

7.4 *Undrained triaxial compression tests*

The prediction of pore pressures and soil behavior in undrained tests on saturated specimens is based on the condition that no volume change occurs in the soil for any load increment:

$$\Delta\epsilon_v^e + \Delta\epsilon_v^c + \Delta\epsilon_v^p = 0 \tag{33}$$

where $\Delta\epsilon_v^e$, $\Delta\epsilon_v^c$ and $\Delta\epsilon_v^p$ are the volumetric strain components corresponding to the three types of strain occurring in the soil. The calculation of pore pressures was performed by specifying the chamber pressure and discrete values of effective stress ratio, σ_1'/σ_3', or stress difference, $(\sigma_1 - \sigma_3)$. The effective confining pressure producing volumetric strains which would satisfy eqn (33) within specified limits was found by iteration. The pore pressure was then calculated as the difference between the chamber pressure and the required effective confining pressure. It should be noted that calculation of pore pressures and soil behavior using the restraint in eqn (33) is based on the fact that a balance can be found between the compressive volumetric strains, $\Delta\epsilon_v^e$ and $\Delta\epsilon_v^c$, and the expansive volumetric strains, $\Delta\epsilon_v^p$, such that their sum is zero at each stress level.

The results of isotropically consolidated undrained triaxial compression tests were available for loose and dense Sacramento River Sand [28], and these results were used for comparison with the predictions of the theory. Two examples which illustrate the capabilities of the theory are shown in Fig. 12. The test on loose sand was performed with an initial effective confining pressure of 12.65 kg/cm^2. Figure 12(a) shows that the variation of both the effective stress ratio, σ_1'/σ_3', and the pore pressure, u, with axial strain is correctly predicted. The initial effective confining pressure for the test on dense sand was 10.50 kg/cm^2 as shown in Fig. 12(b). After the initial increase, the pore pressure decreased to -0.9 kg/cm^2 at which cavitation of the pore water was observed. After cavitation was initiated, the specimen expanded as in a conventional drained test. The fact that cavitation occurred at -0.9 kg/cm^2 was included in the calculations.

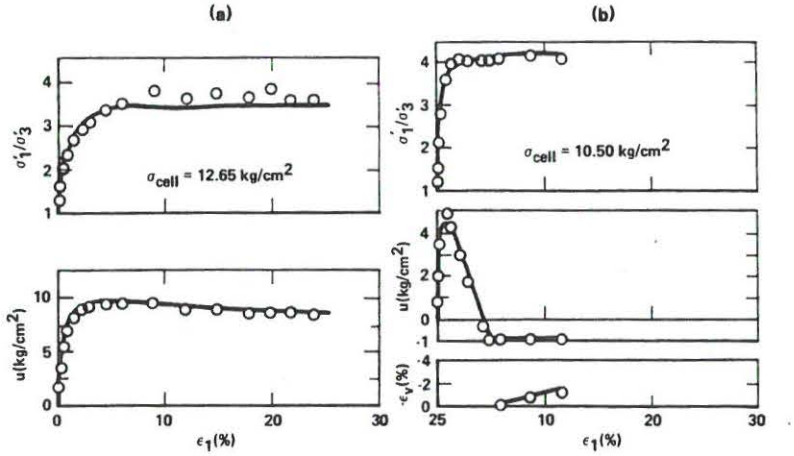

Fig. 12. Comparison of measured and predicted stress-strain, pore pressure, and volume change behavior for undrained tests on (a) loose and (b) dense Sacramento River Sand.

The observed stress-strain, pore pressure, and volume change behavior in the undrained test on dense sand is also predicted accurately by the theory presented herein.

8. SUMMARY AND CONCLUSIONS

An elasto-plastic stress-strain theory for cohesionless soil with curved yield surfaces has been developed on the basis of the soil behavior observed in isotropic compression and triaxial compression tests performed on three different cohesionless soils, each tested at two different relative densities. This development constitutes an expansion of a previously presented stress-strain model such that additional aspects of soil behavior could be incorporated in the theoretical framework. The yield criterion, the plastic potential, and the work-hardening law included in the constitutive law presented here have all been modified relative to those used in the previous theory. In addition, work-softening is included in the new theory, and the irrecoverable strains which occur during isotropic compression are modeled by a separate plasticity theory which involves a cap-type yield surface.

The accuracy of the modified theory has been evaluated by comparing predicted and measured strains for several types of laboratory tests performed on loose and dense sand. Thus, it is demonstrated that the modified theory can accurately predict soil behavior in triaxial tests over a range of confining pressures in which the maximum stress ratio decreases (curved failure envelope) and the volumetric strain behavior gradually changes from expansive to compressive with increasing confining pressure. The post-peak behavior is also correctly modeled in the range of confining pressures employed in the tests. The predicted behavior for proportional loading with increasing stresses is compared with the measured behavior for one of the cohesionless soils in loose and dense states, and stresses as well as strains occurring under K_o-conditions can be calculated with good accuracy. Finally, the stress-strain and pore pressure behavior observed in undrained tests on both loose and dense sand are accurately predicted.

None of the aspects of soil behavior included in the previous theory have been sacrificed in the elasto-plastic theory presented here. The previous theory is merely a special case included in the modified theory, i.e. for straight failure envelopes the modified theory without the cap is similar to the previous theory. Therefore, the modified theory is applicable to general three-dimensional stress conditions, but the fourteen soil parameters required to characterize the soil behavior can be derived entirely from the results of isotropic compression and conventional drained triaxial compression tests.

Acknowledgements—The original test data for Sacramento River Sand were kindly provided by K. L. Lee of the University of California, Los Angeles. The research presented here was supported by the National Science Foundation under Engineering Research Initiation Grant No. GK 37445.

REFERENCES

1. P. V. Lade, The stress-strain and strength characteristics of cohesionless soils. Ph.D. Dissertation, University of California, Berkeley (1972).
2. P. V. Lade and J. M. Duncan, Elastoplastic stress-strain theory for cohesionless soil. *ASCE: J. Geotech. Eng. Div.* **101**, 1037 (1975).
3. P. V. Lade and J. M. Duncan, Cubical triaxial tests on cohesionless soil. *ASCE: J. Geotech. Eng. Div.* **99**, 793 (1973).
4. P. V. Lade and J. M. Duncan, Stress-path dependent behavior of cohesionless soil. *ASCE: J. Geotech. Eng. Div.* **102**, 51 (1976).
5. K. L. Lee and H. B. Seed, Drained strength characteristics of sands. *ASCE: J. Soil Mech. Found. Div.* **93**, 17 (1967).
6. M. M. Al-Hussaini, Drained plane strain and triaxial compression tests on crushed Napa basalt, USAE WES, Miss., Report S-71-2, No. 2, June 1971.
7. M. M. Al-Hussaini, Plane strain and triaxial compression tests on Painted Rock Dam material, USAE WES, Miss., Report S-71-2, No. 3, September 1972.
8. J. M. Duncan and C.-Y. Chang, Nonlinear analysis of stress and strain in soils. *ASCE: J. Soil Mech. Found. Div.* **96**, 1629 (1970).
9. I. Holubec, Elastic behavior of cohesionless soil. *ASCE: J. Soil Mech. Found Div.* **94**, 1215 (1968).
10. C. R. Calladine, Overconsolidated clay: A microstructural view. *Proc. Symp. Role of Plasticity in Soil Mechanics* (Edited by A. C. Palmer). p. 144. Cambridge University (1973).
11. D. C. Drucker, R. E. Gibson and D. J. Henkel, Soil mechanics and work-hardening theories of plasticity. *ASCE Trans.* **122**, 338 (1957).
12. K. H. Roscoe and J. B. Burland, On the generalized stress-strain behavior of "wet" clay. *Engineering Plasticity* (Edited by J. Heyman and F. A. Leckie). p. 535. Cambridge University (1968).
13. F. L. DiMaggio and I. S. Sandler, Material model for granular soils. *ASCE: J. Eng. Mech. Div.* **97**, 935 (1971).
14. J.-H. Prevost and K. Höeg, Effective stress-strain-strength model for soils. *ASCE: J. Geotech. Eng. Div.* **101**, 259 (1975).
15. D. C. Drucker, Some implications of work hardening and ideal plasticity. *Quart. Appl. Math.* **7**, 411 (1950).
16. D. C. Drucker, A more fundamental approach to stress-strain relations. *ASME: 1st Nat. Cong. Appl. Mech.*, p. 487 (1951).
17. R. Hill, *The Mathematical Theory of Plasticity*. Oxford University Press (1950).
18. M. L. Silver and H. B. Seed, Volume changes in sands during cyclic loading. *ASCE: J. Soil Mech. Found. Div.* **97**, 1171 (1971).
19. T. L. Youd, Compaction of sands by repeated shear straining. *ASCE: J. Soil Mech. found. Div.* **98**, 709 (1972).
20. H. B. Poorooshasb, I. Holubec and A. N. Sherbourne, Yielding and flow of sand in triaxial compression: Part I. *Can. Geotech. J.* **3**, 179 (1966).
21. H.-Y. Ko and R. F. Scott, Deformation of sand in shear. *ASCE: J. Soil Mech. Found. Div.* **93**, 283 (1967).
22. M. A. El-Sohby, Deformation of sands under constant stress ratios. *Proc. 7th Int. Conf. Soil Mech. Found. Eng.*, Mexico City, Vol. I, 111 (1969).
23. P. W. Rowe, Theoretical meaning and observed values of deformation parameters for soil. *Proc. Stress-Strain Behavior of Soils* (Edited by R. H. G. Parry). p. 143. Cambridge University (1971).
24. K. Z. Andrawes and M. A. El-Sohby, Factors affecting coefficient of earth pressure K_0. *ASCE: J. Soil Mech. Found. Div.* **99**, 527 (1973).
25. A. W. Bishop and D. J. Henkel, *The Measurement of Soil Properties in the Triaxial Test*, 2nd Edn. St. Martin's Press (1962).
26. A. J. Hendron, The behavior of sand in one-dimensional compression. Ph.D. Dissertation, University of Illinois, Urbana (1963).
27. E. W. Brooker and H. O. Ireland, Earth pressures at rest related to stress history. *Can. Geotech. J.* **2**, 1 (1965).
28. H. B. Seed and K. L. Lee, Undrained strength characteristics of cohesionless soils. *ASCE: J. Soil Mech. found. Div.* **93**, 333 (1967).

JOURNAL OF THE GEOTECHNICAL ENGINEERING DIVISION

PREDICTION OF UNDRAINED BEHAVIOR OF SAND

By Poul V. Lade,[1] A. M. ASCE

INTRODUCTION

Prediction of soil and pore pressure behavior under undrained loading conditions is often important for analyses of movements and failure of soil masses and soil-structure interaction problems. Detailed analyses of deformation and pore pressure distribution for problems involving simple as well as complex boundaries may be performed using the finite element method. This method of analysis requires a constitutive model for the soil behavior that accurately accounts for various aspects of stress-strain and strength characteristics as may be observed in laboratory tests.

An elasto-plastic stress-strain theory for cohesionless soil with curved yield surfaces has been presented previously (13). The principles involved in this theory and its ability to model various aspects of observed soil behavior are briefly described. It is demonstrated herein that this theory is applicable to prediction of soil and pore pressure behavior in undrained tests on loose and dense sand over a range of confining pressures. Based on the behavior observed in drained and undrained tests on cohesionless soil as well as the analysis of such tests, the condition of failure and its importance for prediction of undrained behavior is examined.

STRESS-STRAIN THEORY

The details regarding development and determination of appropriate soil parameters for the stress-strain theory employed here have been presented by the writer (13). The basic principles of the theory are outlined herein.

For the purpose of modeling the stress-strain behavior of soils by an elasto-plastic theory, the total strain increments, $d\epsilon_{ij}$, are divided into an elastic

Note.—Discussion open until November 1, 1978. To extend the closing date one month, a written request must be filed with the Editor of Technical Publications, ASCE. This paper is part of the copyrighted Journal of the Geotechnical Engineering Division, Proceedings of the American Society of Civil Engineers, Vol. 104, No. GT6, June, 1978. Manuscript was submitted for review for possible publication on October 21, 1978.

[1]Asst. Prof. of Engrg. and Applied Sci., Univ. of California, Los Angeles, Calif.

component, $d\epsilon_{ij}^{e}$, a plastic collapse component, $d\epsilon_{ij}^{c}$, and a plastic expansive component, $d\epsilon_{ij}^{p}$, such that

$$d\epsilon_{ij} = (d\epsilon_{ij}^{e}) + (d\epsilon_{ij}^{c}) + (d\epsilon_{ij}^{p}) \quad \ldots \ldots \ldots

The plastic expansive strains are calculated from a nonassociated flow rule, whereas the plastic collapse strains are calculated from an associated flow rule. The result of a change in stress is shown in the triaxial plane in Fig. 3. The plastic strain increment vectors are superimposed on the stress space in this diagram. Both plastic collapse and plastic expansive strains are caused by the change in stress from point A to point B, because both yield surfaces are pushed out: The magnitudes of the strain increments are indicated by the lengths of the vectors, and the total plastic strain increment is calculated according to Eq. 1 as the vector sum of the two components. The elastic strain components are further added (not shown in Fig. 3) to obtain the total strain increment for the stress change from A to B.

The elasto-plastic stress-strain theory employed here represents an expansion of a previously presented stress-strain model (12,14). None of the aspects of soil behavior included in the previous theory has been sacrificed in the new stress-strain theory. Therefore, the theory is applicable to general three-dimensional stress conditions, but the 14 soil parameters required to characterize the soil behavior can be derived entirely from the results of isotropic compression and conventional drained triaxial compression tests. The accuracy of the theory has been evaluated by comparing predicted and measured strains for several types of laboratory tests performed on cohesionless soils. Thus, it has been demonstrated that the following important aspects of observed stress-strain and strength behavior are modeled by the theory: (1) Nonlinearity; (2) effects of σ_2 and σ_3 including curved yield and failure surfaces; (3) decrease in strength after peak has been reached (strain softening); (4) stress-path dependency including proportional loading and K_0-loading; (5) shear-dilatancy effect and its variation over a range of confining pressures; and (6) coincidence of strain increment and stress increment axes at low stress levels with transition to coincidence of strain increment and stress axes at high stress levels (12,13,14,15).

Previous Approaches to Pore Pressure Prediction

Several different approaches have been employed for prediction of pore pressures in soils under undrained conditions. The simplest and most often used method was suggested by Skempton (27), who introduced the concept of pore pressure parameters. For a saturated soil the change in pore pressure, Δu, is expressed as

$$\Delta u = \Delta\sigma_3 + \bar{A}\,(\Delta\sigma_1 - \Delta\sigma_3) \quad \ldots\ldots\ldots\

and dense Sacramento River sand (initial void ratios = 0.87 and 0.61, relative densities = 38% and 100%, respectively). The necessary soil parameters were derived from the isotropic compression and drained triaxial compression tests, and the values of these parameters are given by the writer (13). The results of the undrained triaxial compression tests are used for comparison with the predictions of the elasto-plastic stress-strain theory.

The measured and predicted pore pressure and stress-strain behavior for loose Sacramento River sand is shown in Fig. 4 for tests with initial consolidation pressures of 1.00 kg/cm^2, 3.00 kg/cm^2, 5.00 kg/cm^2, 8.44 kg/cm^2, 12.65 kg/cm^2, and 20.00 kg/cm^2 (98 kN/m^2, 290 kN/m^2, 490 kN/m^2, 828 kN/m^2, 1,241 kN/m^2, and 2,000 kN/m^2). Similar diagrams are shown in Fig. 5 for undrained tests on dense Sacramento River sand with initial effective confining

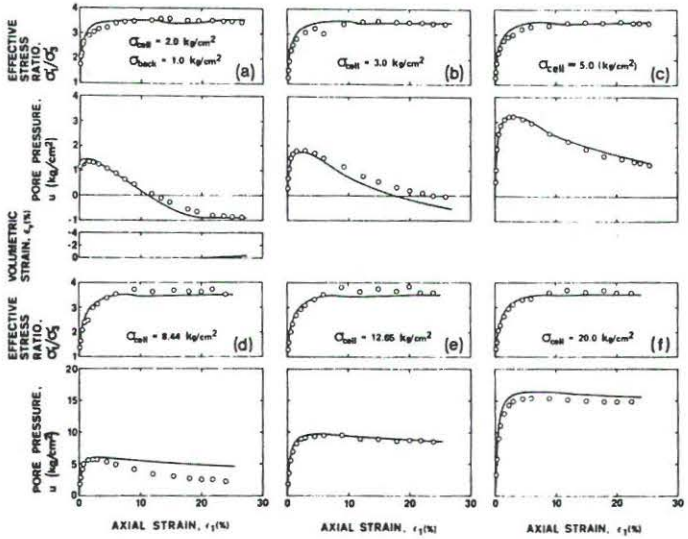

FIG. 4.—Measured and Predicted Stress-Strain and Pore Pressure Relations for Loose Sacramento River Sand (1 kg/cm^2 = 98.1 kN/m^2)

pressures of 1.0 kg/cm^2, 10.50 kg/cm^2, 15.10 kg/cm^2, 20.20 kg/cm^2, 29.90 kg/cm^2, and 40.10 kg/cm^2 (98 kN/m^2, 1,030 kN/m^2, 1,480 kN/m^2, 1,981 kN/m^2, 2,932 kN/m^2, and 3,932 kN/m^2). The points on these figures represent the measured solid behavior and the solid lines represent the predictions from the theory.

Back pressures were not used except in the test on loose Sacramento River sand shown in Fig. 4(*a*). This was taken into account in the calculations using the elasto-plastic stress-strain theory. It was observed that the pore water cavitated at about −0.9 kg/cm^2 (−88 kN/m^2) in tests performed with low initial effective confining pressures (17). After cavitation was initiated, the specimens expanded as in conventional drained tests. The fact that cavitation occurred at −0.9 kg/cm^2 (−88 kN/m^2) was included in the computer program used for the predictions.

A term accounting for the flexibility of the pore pressure measuring system was also included in the calculations. The effect of this flexibility was negligible for most of the tests, and it had only minor effects in tests with large changes in pore pressure.

Fig. 4 shows that the stress-strain and pore pressure predictions compare favorably with the behavior measured in the undrained tests on loose Sacramento River sand. Fig. 4(*a*) indicates that cavitation of the pore water is predicted towards the end in the test with low initial effective confining pressure. However, the resulting rate of expansion is very low, and expansion was not observed

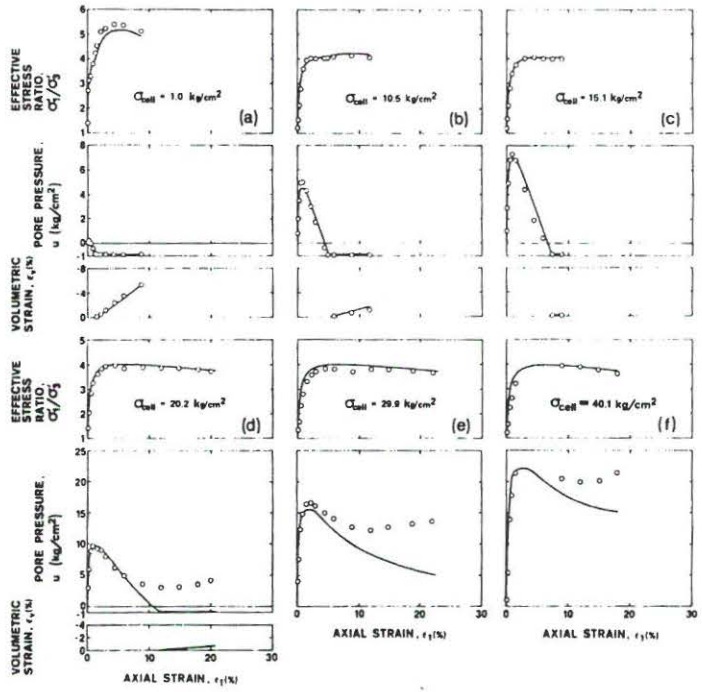

FIG. 5.—Measured and Predicted Stress-Strain and Pore Pressure Relations for Dense Sacramento River Sand

in the test although the magnitude of the final pore-water pressure was the same as that predicted. Fig. 4(*d*) shows that the predicted decrease in pore pressure following its peak value does not agree with the observed behavior. However, because the pore pressure behavior predicted from the theory forms a consistent pattern within the tests shown in Fig. 4, and because the other test results are predicted with good accuracy, it is reasonable to believe that the solid line in Fig. 4(*d*) reflects the correct variation in pore pressure.

The results of the undrained tests on dense Sacramento River sand are also predicted with good accuracy as shown in Fig. 5. Cavitation of the pore water

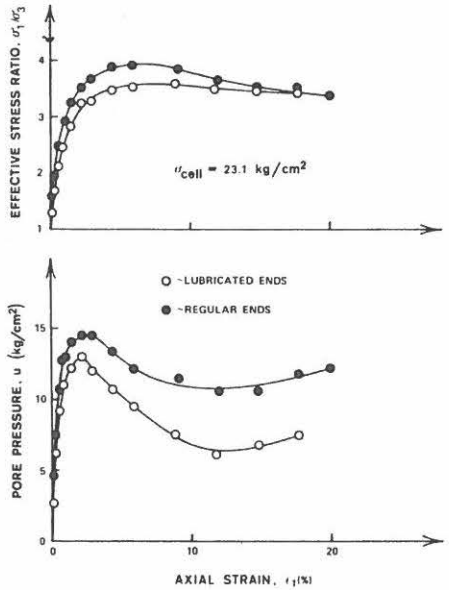

FIG. 6.—Undrained Triaxial Compression Tests with Regular and Lubricated Ends on Medium Dense Sacramento River Sand

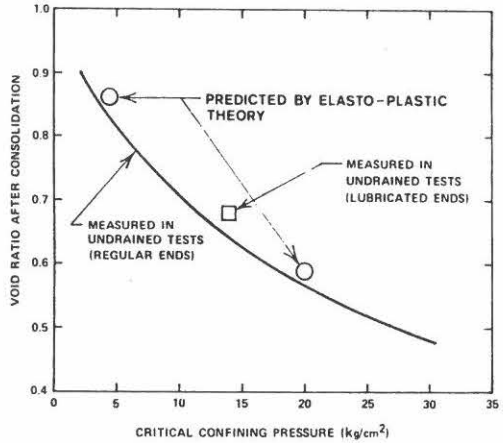

FIG. 7.—Comparison of Relationships between Void Ratio after Consolidation and Critical Confining Pressure

occurred in the tests with low initial effective confining pressures and the consequent expansion of the specimens is correctly predicted by the elasto-plastic theory. The predicted pore pressures for the tests performed with high initial effective confining pressures deviate from the measured pore pressures at large axial strains. This is most likely an effect of nonuniform strains that tend to develop in tests on dense specimens with regular ends on which friction can develop. Thus, it was observed (17) that the dense specimens would develop a shear plane resulting in grossly nonuniform strain patterns and a decreasing tendency for dilation at medium to large axial strains (the loose specimens bulged and shear planes were not observed). The corresponding decrease in pore pressure is smaller than that observed in tests with more uniform strains. This may be seen from Fig. 6 which shows a comparison of undrained triaxial compression tests performed with regular ends and with lubricated ends on medium dense Sacramento River sand (initial void ratio = 0.71, relative density = 78%). The test with lubricated ends and relatively uniform strains produced pore pressures lower than those measured in the test with regular ends and nonuniform strains. Thus, it is considered that the predicted pore-water pressures shown in Fig. 5 represent the real behavior better than those measured in the tests.

Critical Confining Pressure

The critical confining pressure has been defined (18) as the confining pressure at which the total volume change in a drained test is zero at failure for a sand at given void ratio. This void ratio is by definition the critical void ratio. The unique relationship between critical confining pressure and critical void ratio may be determined from drained as well as undrained tests (25).

On the basis of the predicted soil behavior the critical confining pressure can be determined for each of the two void ratios used in the tests on Sacramento River sand. Fig. 7 shows a comparison between the critical confining pressure-critical void ratio relation determined from the undrained tests (solid line) and the two points determined from the predictions of the elasto-plastic theory. The third point shown in Fig. 7 was obtained from measurements on specimens with lubricated ends. The strains produced in these specimens were more uniform than those occurring in specimens with regular ends, and the pore pressures associated with fairly uniform strains are believed to represent the behavior better than those from tests with nonuniform strains. A perfectly reasonable curve could be drawn through the three points shown in Fig. 7, thus indicating that the two predicted points are in good agreement with results measured in tests with relatively uniform strains. This lends support to the ability of the elasto-plastic theory to predict pore pressures at large strains with good accuracy.

Effective Stress-Paths

Some of the predicted and measured test results are compared on the $p' - q$ diagram in Figs. 8 and 9 for loose and dense Sacramento River sand. In this type of diagram the pore pressure is measured by the horizontal distance from a line at 45° to the stress point as indicated on the inserted diagrams in both figures. The $p' - q$ diagram is very sensitive to differences between

predicted and measured pore pressures, especially at small strains. The diagrams in Figs. 8 and 9 show that some differences between measured and predicted behavior are present, but the stress paths predicted for the undrained tests generally compare favorably with those observed. The differences may be due to scatter in the test results as is indicated by the two effective stress paths shown in Fig. 9 for the tests on dense sand with high initial confining pressures. Results of undrained tests on Ham River sand presented by Bishop (4) show effective stress paths very similar to those predicted and shown in Fig. 8 for

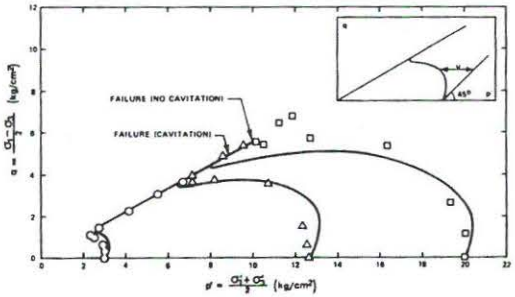

FIG. 8.—Comparison of Measured and Predicted Effective Stress-Paths on $p' - q$ Diagram for Loose Sacramento River Sand

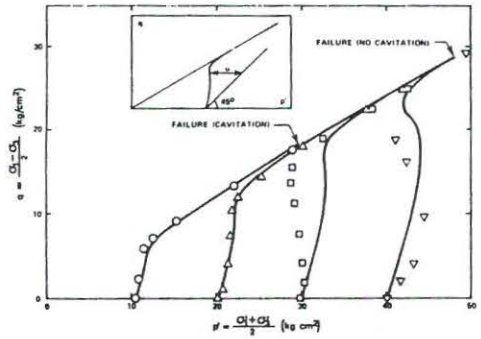

FIG. 9.—Comparison of Measured and Predicted Effective Stress-Paths on $p' - q$ Diagram for Dense Sacramento River Sand

loose Sacramento River sand. According to Bishop's results and as argued by Seed and Lee (25) failure occurs within a fairly narrow range of deviator stresses for undrained tests in which the pore water does not cavitate. This behavior is predicted by the elasto-plastic theory for the Sacramento River sand as shown in Figs. 8 and 9. It should be noted that the predicted stress paths reflect the observed fact that the sand increasingly behaves as a loose sand as the initial effective confining pressure increases. This pattern in soil behavior is independent of the initial density as shown by Seed and Lee (25).

Failure Criteria for Soils

The failure criteria generally adopted for interpretation of test results and for use in stability analyses are the maximum deviator stress, $(\sigma_1 - \sigma_3)_{max}$, and the maximum principal effective stress ratio, $(\sigma_1'/\sigma_3')_{max}$ (see, e.g., Ref. 6). The two criteria coincide for drained loading conditions.

Two types of effective stress-paths encountered in undrained tests on soils are shown on the $p' - q$ diagram in Fig. 10. In the Type II stress path the maximum deviator stress is reached before the maximum effective stress ratio,

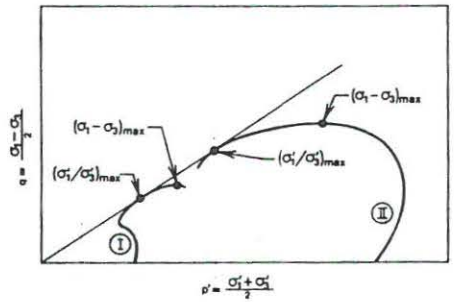

FIG. 10.—Schematic Illustration of Two Types of Effective Stress-Paths Encountered in Undrained Tests

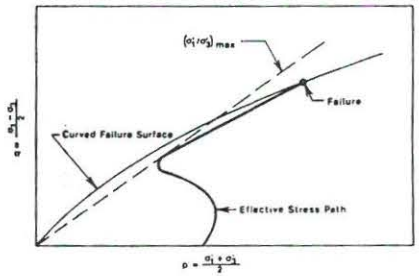

FIG. 11.—Schematic Illustration of Occurrence of Failure in Undrained Test on Soil with Curved Failure Surface

whereas the opposite is the case for the Type I stress path. Using these two failure criteria often results in different values of the effective friction angle. An extreme stress path of Type II was illustrated by Bishop (4) based on data obtained by Castro (7) for a saturated loose sand. From these data an effective friction angle of 16.1° was calculated on the basis of $(\sigma_1 - \sigma_3)_{max}$, whereas the effective friction angle was 30° according to $(\sigma_1'/\sigma_3')_{max}$. Thus, the condition of failure is not consistently defined from these criteria. In addition, the strain-to-failure according to these two criteria can be substantially different.

Failure may be defined consistently as the limiting states of stress forming

TABLE 1.—Values of η_1 and m Determined from Published Test Data for Cohesionless Soils

Soil (1)	e (2)	D_r, as a percentage (3)	η_1 (4)	m (5)	Reference (6)
Sacramento River Sand	0.61	100	80	0.23	Lee and Seed (18)
	0.71	78	53	0.188	Lee (17)
	0.78	60	34	0.110	
	0.87	38	28	0.093	
Crushed Napa Basalt	0.53	100	280	0.423	Al-Hussaini (1)
	0.66	70	130	0.30	
Painted Rock Material	0.40	100	101	0.21	Al-Hussaini (2)
	0.48	70	67	0.16	
Ottawa Sand, No. 20–30	0.49	100	130	0.335	Lee and Seed (18)
Antioch Sand, Saturated	0.75	100	110	0.361	Lee, et al. (19)
Oven Dry	0.75	100	250	0.424	
Chattahoochee River Sand	0.70	82	40	0.10	Vesic and Clough (28)
	1.00	20	18	0.00	
Ham River Sand			35	0.149	Bishop, et al. (5)
Coal Waste Embankment Material, γ = 85 pcf			28	0.435	Holubec (11)
Monterey No. 20 Sand	0.55	93	95	0.272	Marachi, et al. (20)
	0.65	60	53	0.191	
	0.75	27	31	0.105	
Pyramid Dam Material, in inches					Marachi, et al. (20)
D_{max} = 6	0.45		203	0.408	
D_{max} = 2	0.45		215	0.385	
D_{max} = 0.47	0.45		310	0.419	
Crushed Basalt Material, in inches					Marachi, et al. (20)
D_{max} = 6	0.43		234	0.411	
D_{max} = 2	0.43		220	0.372	
D_{max} = 0.47	0.43		275	0.386	
Oroville Dam Material, in inches					Marachi, et al. (20)
D_{max} = 6	0.22		149	0.280	
D_{max} = 2	0.22		149	0.257	
D_{max} = 0.47	0.22		285	0.335	
Oroville Dam Material, in inches					Becker, et al. (3)
D_{max} = 2	0.41		53	0.105	
Venato Sandstone Material, in inches					Becker, et al. (3)
D_{max} = 6	0.45		51	0.152	
D_{max} = 2	0.45		65	0.168	
D_{max} = 0.47	0.45		60	0.144	
D_{max} = 0.47	0.72		29	0.029	
Monterey No. 0 Sand	0.57	98	104	0.16	Lade (12)
	0.78	27	36	0.12	

a surface in stress space that separates stress conditions that can be reached from stress conditions that cannot be reached for a given soil. If this definition is adopted, the failure surface is curved for most soils. A curved failure surface is included in the elasto-plastic theory used here and it may be expressed by Eq. 2. Failure occurs according to this theory at the points indicated on Figs. 8 and 9. At these points do the values of f_p reach η_1 (see Eq. 2), whereas f_p is smaller than η_1 for any previous point on the stress-paths, i.e., the stress paths do not follow the failure surfaces, but approach them gradually until the indicated failure points are reached. Since the failure surfaces are curved and the stress paths lead away from the origin, the maximum effective stress ratio can occur before failure. This cannot be seen from Figs. 8 and 9, but it is shown with exaggerated curvatures in Fig. 11. This behavior is most pronounced for soils whose failure surfaces are highly curved.

Note that stress paths of Type II can also be predicted by the elasto-plastic stress-strain theory. According to this theory, neither of the two previously adopted criteria for failure necessarily corresponds to failure in the sense that the states of stress are located on the limiting failure surface. However, both stress states given by these criteria are included and can be predicted by the elasto-plastic theory.

Curved Failure Surfaces

Published test data for different cohesionless soils have been analyzed with respect to the shapes of their failure envelopes. The test data could in all cases be described with good accuracy by the criterion given in Eq. 2. The values of η_1 and m determined from the published data are listed in Table 1 together with void ratios and relative densities. From the cases where comparative data are available it may be seen that both the apex angle and the curvature, measured by η_1 and m, respectively, increase with increasing density of the soil. Only the results of tests on loose Chattahoochee River sand indicate a straight failure surface corresponding to $m = 0$. All other test data in this table show curved failure envelopes and the maximum value of $m = 0.435$. The test data available for soils with different maximum particle sizes D_{max}, parallel gradation curves, and similar grain shapes do not appear to indicate any trend regarding apex angle or curvature.

Recent data from cubical triaxial tests on normally consolidated, remolded clay (16) and tests on clay by others (9,21) indicate that the failure surfaces for clays are also curved.

Summary and Conclusions

A recently developed elasto-plastic stress-strain theory for cohesionless soil with curved yield surfaces is used for prediction of soil and pore pressure behavior in undrained triaxial compression tests on saturated sand specimens. The basic principles of the theory and its ability to model various aspects of observed soil behavior are briefly reviewed. Prediction of pore pressures is performed using the condition that no volume change occurs in undrained shear tests for any increment in load. The soil stress-strain relations are calculated from the effective stress paths deduced from the applied deviator stress, the

cell pressure, and the predicted pore pressure. Influence of back pressure and of cavitation of pore water resulting in expansion of the sand can be calculated from the theory.

Predictions of stress-strain relations, pore pressure variation, expansion after cavitation, and effective stress paths compare favorably with experimental results for loose and dense Sacramento River sand. The theory correctly predicts the observed fact that sand with a given density increasingly behaves as loose sand as the initial effective confining pressure increases. This pattern in soil behavior is independent of the initial density, and it is demonstrated that the theory reflects this pattern for both loose and dense sand. The critical confining pressures for both the loose and the dense sand specimens are calculated and shown to be in agreement with results measured in tests with relatively uniform strains.

Analyses of test results and predictions indicate the importance of employing curved failure surfaces when realistic predictions of undrained behavior of cohesionless soils are desired. It is shown that most soils exhibit curved failure surfaces, and the curvature increases with increasing density for a given soil.

Acknowledgment

The original test data for Sacramento River sand were kindly provided by K. L. Lee of the University of California, Los Angeles. The research presented here was supported by the National Science Foundation under Engineering Research Initiation Grant No. GK 37445.

Appendix.—References

1. Al-Hussaini, M. M., "Drained Plane Strain and Triaxial Compression Tests on Crushed Napa Basalt," *Technical Report S-71-2*, No. 2, U.S. Army Engineers Waterways Experiment Station, Vicksburg, Miss., June, 1971.
2. Al-Hussaini, M. M., "Plane Strain and Triaxial Compression Tests on Painted Rock Dam Material," *Technical Report S-71-2*, No. 3, U.S. Army Engineers Waterways Experiment Station, Vicksburg, Miss., Sept., 1972.
3. Becker, E., Chan, C. K., and Seed, H. B., "Strength and Deformation Characteristics of Rockfill Materials in Plane Strain and Triaxial Compression Tests," *Report No. TE 72-3*, Department of Civil Engineering, University of California, Berkeley, Calif., Oct., 1972.
4. Bishop, A. W., "Shear Strength Parameters for Undisturbed and Remoulded Soil Specimens," *Stress-Strain Behavior of Soils, Proceedings*, Roscoe Memorial Symposium, G. T. Foulis and Co., Ltd., 1971, pp. 143–194.
5. Bishop, A. W., Webb, D. L., and Skinner, A. E., "Triaxial Tests on Soil at Elevated Cell Pressure," *Proceedings of the 6th International Conference on Soil Mechanics and Foundation Engineering*, Vol. I, 1965, pp. 170–174
6. Bjerrum, L., and Simons, N. E., "Comparison of Shear Strength Characteristics of Normally Consolidated Clays," *Proceedings*, ASCE Research Conference on Shear Strength of Cohesive Soils, Boulder, Colo., 1960, pp. 711–726.
7. Castro, G., "Liquefaction of Sands," thesis presented to Harvard University, at Cambridge, Mass., in 1969, in partial fulfillment of the requirements for the degree of Doctor of Philosophy.
8. Henkel, D. J., "The Shear Strength of Saturated Remoulded Clays," *Proceedings*, ASCE Research Conference on Shear Strength of Cohesive Soils, Boulder, Colo., 1960, pp. 533–554.
9. Henkel, D. J., and Sowa, V. A., "The Influence of Stress History on Stress Paths in Undrained Triaxial Tests on Clay," *Special Technical Publication, No. 361*, Laboratory Shear Testing of Soils, American Society for Testing and Materials, Ottawa, Canada, 1963, pp. 280–291.

10. Henkel, D. J., and Wade, N. H., "Plane Strain Tests on a Saturated Remolded Clay," *Journal of the Soil Mechanics and Foundations Division*, ASCE, Vol. 92, No. SM6, Proc. Paper 4970, Nov., 1966, pp. 67–80.
11. Holubec, I., "Geotechnical Aspects of Coal Waste Embankments," *27th Canadian Geotechnical Conference*, Edmonton, Alberta, Canada, Nov., 1974.
12. Lade, P. V., "The Stress-Strain and Strength Characteristics of Cohesionless Soils," thesis presented to the University of California, at Berkeley, Calif., in 1972, in partial fulfillment of the requirements for the degree of Doctor of Philosophy.
13. Lade, P. V., "Elasto-Plastic Stress-Strain Theory for Cohesionless Soil with Curved Yield Surfaces," *International Journal of Solids and Structures*, Pergamon Press, Inc., New York, N.Y., Vol. 13, Nov., 1977, pp. 1019–1035.
14. Lade, P. V., and Duncan, J. M., "Elastoplastic Stress-Strain Theory for Cohesionless Soil," *Journal of the Geotechnical Engineering Division*, ASCE, Vol. 101, No. GT10, Proc. Paper 11670, Oct., 1975, pp. 1037-1053.
15. Lade, P. V., and Duncan, J. M., "Stress-Path Dependent Behavior of Cohesionless Soil," *Journal of the Geotechnical Engineering Division*, ASCE, Vol. 102, No. GT1, Proc. Paper 11841, Jan., 1976, pp. 51–68.
16. Lade, P. V., and Musante, H. M., "Failure Conditions in Sand and Remolded Clay," *Proceedings of the 9th International Conference on Soil Mechanics and Foundation Engineering*, Tokyo, Japan, Vol. I, 1977, pp. 181–186.
17. Lee, K. L., "Triaxial Compressive Strength of Saturated Sand under Seismic Loading Conditions," thesis presented to the University of California, at Berkeley, Calif., in 1965, in partial fulfillment of the requirements for the degree of Doctor of Philosophy.
18. Lee, K. L., and Seed, H. B., "Drained Strength Characteristics of Sands," *Journal of the Soil Mechanics and Foundations Division*, ASCE, Vol. 93, No. SM6, Proc. Paper 5561, Nov., 1967, pp. 117–141.
19. Lee, K. L., Seed, H. B., and Dunlop, P., "Effects of Moisture on the Strength of a Clean Sand," *Journal of the Soil Mechanics and Foundations Division*, ASCE, Vol. 93, No. SM6, Proc. Paper 5551, Nov., 1967, pp. 17–40.
20. Marachi, N. D., et al., "Strength and Deformation Characteristics of Rockfill Materials," *Report No. TE-69-5*, Department of Civil Engineering, University of California, Berkeley, Calif., Sept., 1969.
21. Olson, R. E., "Shearing Strength of Kaolinite, Illite, and Montmorillonite," *Journal of the Geotechnical Engineering Division*, ASCE, Vol. 100, No. GT11, Proc. Paper 10947, Nov., 1974, pp. 1215–1229.
22. Roscoe, K. H., and Burland, J. B., "On the Generalized Stress-Strain Behavior of 'Wet' Clay," *Engineering Plasticity*, J. Heyman and F. A. Leckie, eds., Cambridge University Press, Cambridge, England, 1968, pp. 535–609.
23. Roscoe, K. H., Schofield, A. N., and Thurairajah, A., "Yielding of Clays in States Wetter than Critical," *Geotechnique*, London, England, Vol. 13, No. 3, Sept., 1963, pp. 211–240.
24. Roscoe, K. H., Schofield, A. N., and Wroth, C. P., "On the Yielding of Soils," *Geotechnique*, London, England, Vol. 8, No. 1, Mar., 1958, pp. 22–52.
25. Seed, H. B., and Lee, K. L., "Undrained Strength Characteristics of Cohesionless Soils," *Journal of the Soil Mechanics and Foundations Division*, ASCE, Vol. 93, No. SM6, Proc. Paper 5618, Nov., 1967, pp. 333–360.
26. Shibata, T., and Karube, D., "Influence of the Variation of the Intermediate Principal Stress on the Mechanical Properties of Normally Consolidated Clays," *Proceedings of the 6th International Conference on Soil Mechanics and Foundation Engineering*, Vol. I, 1965, pp. 359–363.
27. Skempton, A. W., "The Pore Pressure Coefficients A and B," *Geotechnique*, London, England, Vol. 4, No. 4, Dec., 1954, pp. 143–147.
28. Vesic, A. S., and Clough, G. W., "Behavior of Granular Materials under High Stresses," *Journal of the Soil Mechanics and Foundations Division*, ASCE, Vol. 94, No. SM3, Proc. Paper 5954, May, 1968, pp. 661–688.

Third International Conference on Numerical Methods in Geomechanics / Aachen / 2-6 April 1979

Stress-strain theory for normally consolidated clay

POUL V. LADE
University of California, Los Angeles, Calif., USA

1 INTRODUCTION

The behavior of normally consolidated, remolded cohesive soil observed in laboratory tests is very similar to that of cohesionless soil when the test results are interpreted in terms of effective stresses. Thus, the effective cohesion is zero for both soil types, they exhibit increasing moduli and decreasing effective friction angles (curved failure surfaces (1,2,5,12, 15)) with increasing confining pressure, the three-dimentional variation in strengths can be expressed by the same failure criterion (12), and the moduli increase and the strains-to-failure decrease with increasing value of $b = (\sigma_2-\sigma_3)/(\sigma_1-\sigma_3)$ (10,13). In addition, test data for both normally consolidated clay and sand indicate that the directions of the strain increment vectors at failure form acute angles with the failure surfaces in the principal stress space whereas the projections of these vectors on the octahedral plane are perpendicular to the traces of the failure surfaces in that plane (10,12,13). Two aspects of the behavior are different for normally consolidated clay and sand: [1] The compressibility of normally consolidated clay follows a pattern different from that of sand; and [2] only one failure surface is possible for normally consolidated clay (12), whereas a sand can have many different failure surfaces, mainly depending on its initial density. Time related properties such as creep and permeability may also be different for clay and sand, but these properties are not included in the present considerations.

Previous stress-strain theories developed for clay (4,16,17,18,19,20,22) have not taken into account all of the aspects of observed soil behavior described above. The extended Von Mises failure criterion is employed in some of these theories (16,17, 18,19,20) whereas the Mohr-Coulomb criterion is used in others (4,22). Experimental evidence from cubical triaxial tests on clay does not support the use of these criteria for clay (12,13). In addition, some of the models (4,17) are developed in terms of total stresses whereas effective stresses control the strains in soils.

Because of the similarities in behavior of normally consolidated, remolded clay and sand, it can be expected that the same basic framework for stress-strain models applies to these two soil types. An elasto-plastic stress-strain theory developed in terms of effective stresses for cohesionless soil with curved yield surfaces (8) was shown to be applicable to prediction of pore pressures in undrained triaxial compression tests (9). It is shown herein that this theory, with one minor modification relating to the compressibility pattern, is also applicable to normally consolidated, remolded clay. The main components of the elasto-plastic theory are recapitulated (see (8) regarding details of the development), the modification and the derivation of soil parameters are explained in detail, and the ability of this model to predict soil and pore pressure behavior for normally consolidated, remolded clay under three-dimensional undrained loading conditions and for K_o-consolidation is demonstrated.

2 RECAPITULATION OF ELASTO-PLASTIC THEORY

In the elasto-plastic stress-strain theory for cohesionless soil with curved yield surfaces the total strain is considered to consist of three components: Elastic, plastic collapse, and plastic expansive strains. The equations used for calcula-

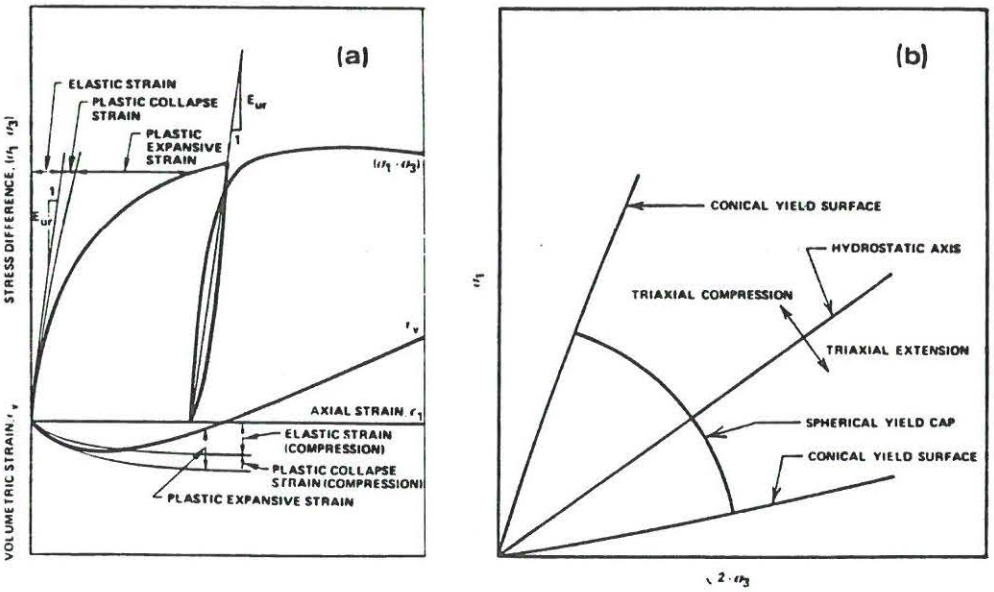

Figure 1. Schematic Illustrations of (a) Elastic, Plastic Collapse, and Plastic Expansive Strain Components in Drained Triaxial Compression Test, and (b) Conical and Spherical Cap Yield Surfaces in Triaxial Plane.

tion of these strains are given below without proof or discussion. Fig. 1a illustrates schematically the parts of the total strain which are considered to be elastic, plastic collapse, and plastic expansive components in a drained triaxial compression test on sand. The yield surfaces for the two plastic strain components are indicated on the triaxial plane in Fig. 1b. Schematic diagrams illustrating the derivation of the necessary soil parameters from the results of isotropic compression and conventional triaxial compression tests are shown in Figs. 2 and 3.

2.1 Elastic Strains

The elastic strain increments, which are recoverable upon unloading, are calculated from Hooke's law using the unloading-reloading modulus defined as (4,6):

$$E_{ur} = K_{ur} \cdot p_a \cdot \left(\frac{\sigma_3}{p_a}\right)^n \qquad (1)$$

The dimensionless, constant values of the modulus number K_{ur} and the exponent n are determined from triaxial compression tests performed with various values of the confining pressure σ_3. In Eq. 1 p_a is atmospheric pressure expressed in the same units as E_{ur} and σ_3. Fig. 2a illustrates the determination of the constants K_{ur} and n. A value of Poisson's ratio of 0.2 was used for calculation of the elastic strains in sand.

2.2 Plastic Collapse Strains

The plastic collapse strains are calculated from a simple plastic stress-strain theory which incorporates (1) a cap-type spherical yield surface with center at the origin of the principal stress space, (2) an associated flow rule, and (3) a work-hardening relationship which can be determined from an isotropic compression test. The yield criterion, f_c, and the plastic potential function, g_c, have the form:

$$f_c = g_c = I_1^2 + 2 \cdot I_2 \qquad (2)$$

where I_1 and I_2 are the first and the second stress invariants:

$$I_1 = \sigma_1 + \sigma_2 + \sigma_3 = \sigma_x + \sigma_y + \sigma_z \qquad (3)$$

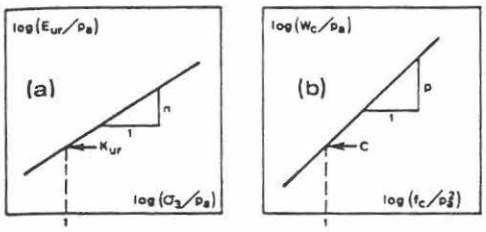

Figure 2. Determination of Soil Parameters for Elastic and Plastic Collapse Stress-Strain Relationships.

$$I_2 = -(\sigma_1\cdot\sigma_2+\sigma_2\cdot\sigma_3+\sigma_3\cdot\sigma_1) = \tau_{xy}\cdot\tau_{yx} + \tau_{yz}\cdot\tau_{zy} + \tau_{zx}\cdot\tau_{xz} - (\sigma_x\cdot\sigma_y + \sigma_y\cdot\sigma_z + \sigma_z\cdot\sigma_x) \quad (4)$$

Performing all the necessary derivations, the final form of the plastic collapse stress-strain relationships become:

$$\begin{Bmatrix} \Delta\varepsilon^c_x \\ \Delta\varepsilon^c_y \\ \Delta\varepsilon^c_z \\ \Delta\varepsilon^c_{yz} \\ \Delta\varepsilon^c_{zx} \\ \Delta\varepsilon^c_{xy} \end{Bmatrix} = \frac{dW_c}{f_c} \cdot \begin{Bmatrix} \sigma_x \\ \sigma_y \\ \sigma_z \\ \tau_{yz} \\ \tau_{zx} \\ \tau_{xy} \end{Bmatrix} \quad (5a\text{-}f)$$

where dW_c is an increment in work per unit volume for a given value of f_c and a given increment of the yield function, df_c. The plastic collapse work is calculated from

$$W_c = \int \sigma_{ij} \cdot d\varepsilon^c_{ij} \quad (6)$$

which for an isotropic compression test reduces to

$$W_c = \int \sigma_3 \cdot d\varepsilon^c_v \quad (7)$$

W_c is plotted as a function of f_c which for isotropic compression can be calculated from:

$$f_c = 3 \cdot \sigma_3^2 \quad (8)$$

Fig. 2b shows a schematic diagram of the relationship between W_c and f_c plotted in dimensionless form on log-log scales for cohesionless soil. This relationship can be modeled by the following expression:

$$W_c = C \cdot p_a \cdot \left(\frac{f_c}{p_a^2}\right)^p \quad (9)$$

where the collapse modulus C and the collapse exponent p are determined as shown in Fig. 2b. On this diagram C is the intercept with $(f_c/p_a^2) = 1$ and p is the slope of the straight line. The increment in plastic collapse work is then determined from:

$$dW_c = C\cdot p\cdot p_a \cdot \left(\frac{p_a^2}{f_c}\right)^{1-p} \cdot d(f_c/p_a^2) \quad (10)$$

and used in connection with Eqs. 5a-f for calculation of plastic collapse strains.

2.3 Plastic Expansive Strains

The curved yield surfaces which best describe the behavior of cohesionless soils is expressed in terms of the first and the third stress invariants:

$$f_p = (I_1^3/I_3 - 27) \cdot (I_1/p_a)^m \quad (11a)$$

$$f_p = \eta_1 \text{ at failure} \quad (11b)$$

where I_1 is given by Eq. 3 and I_3 is given by

$$I_3 = \sigma_1\cdot\sigma_2\cdot\sigma_3 = \sigma_x\cdot\sigma_y\cdot\sigma_z+\tau_{xy}\cdot\tau_{yz}\cdot\tau_{zx}+\tau_{yx}\cdot\tau_{zy}\cdot\tau_{xz} - (\sigma_x\cdot\tau_{yz}\cdot\tau_{zy}+\sigma_y\cdot\tau_{zx}\cdot\tau_{xz}+\sigma_z\cdot\tau_{xy}\cdot\tau_{yx}) \quad (12)$$

The values of η_1 and m in Eq. 11 can be determined by plotting $(I_1^3/I_3 - 27)$ versus (p_a/I_1) at failure in a log-log diagram as shown schematically in Fig. 3a. On this diagram η_1 is the intercept with $(p_a/I_1)=1$ and m is the slope of the straight line.

The non-associated flow rule employed for the plastic expansive strains is characterized by a plastic potential function, g_p, of a form similar to the yield criterion:

$$g_p = I_1^3 - \left(27 + \eta_2 \cdot \left(\frac{p_a}{I_1}\right)^m\right) \cdot I_3 \quad (13)$$

where η_2 is constant for given values of f_p and σ_3. The values of η_2 can be determined from the results of triaxial com-

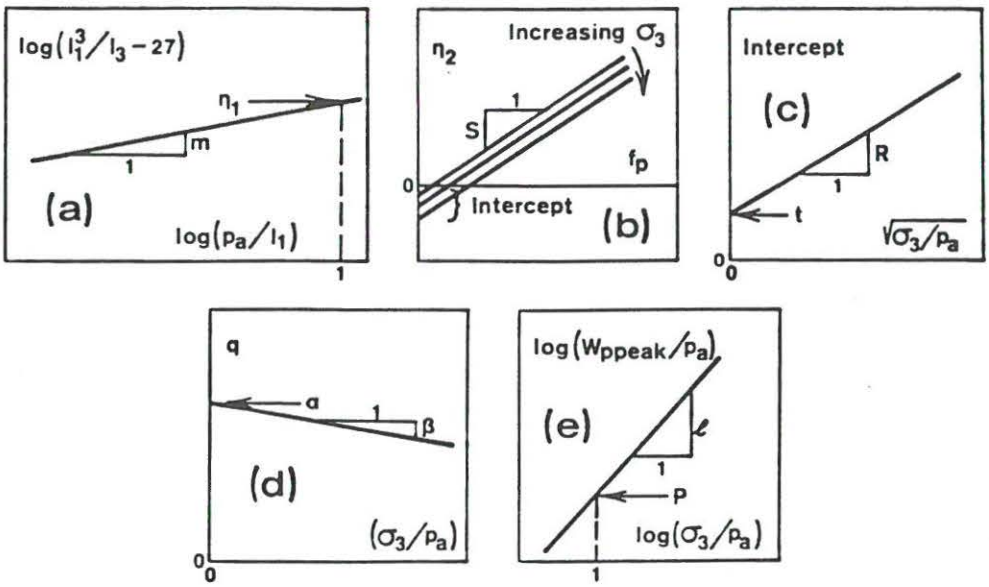

Figure 3. Determination of Soil Parameters for Plastic Expansive Stress-Strain Relationship.

pression tests using the following expression:

$$\eta_2 = \frac{3\cdot(1+\nu^P)\cdot I_1^2 - 27\cdot\sigma_3\cdot(\sigma_1+\nu^P\cdot\sigma_3)}{\left(\frac{p_a}{I_1}\right)^m\cdot\left[\sigma_3\cdot(\sigma_1+\nu^P\cdot\sigma_3) - \frac{m\cdot(1+\nu^P)\cdot I_1^2}{f_p\cdot\left(\frac{p_a}{I_1}\right)^m + 27}\right]} \quad (14)$$

where ν^P is a function of the plastic strain increments:

$$\nu^P = -\frac{\Delta\varepsilon_3^P}{\Delta\varepsilon_1^P} \quad (15)$$

The variation of η_2 with f_p and σ_3 is shown schematically in Figs. 3b and 3c. This variation can be expressed by a simple equation:

$$\eta_2 = S\cdot f_p + R\cdot\sqrt{\frac{\sigma_3}{p_a}} + t \quad (16)$$

The plastic expansive work is calculated from

$$W_p = \int \sigma_{ij}\cdot d\varepsilon_{ij}^P \quad (17)$$

and the variation of W_p with f_p (calculated from Equation 11a) can be approximated by exponential functions for which the following expression is used:

$$f_p = a\cdot e^{-b\cdot W_p}\cdot\left(\frac{W_p}{p_a}\right)^{1/q}, \quad q > 0 \quad (18)$$

where the parameters a, b, and q are constants for a given value of σ_3. The parameter q can be determined for a constant value of the confining pressure according to:

$$q = \frac{\log\left(\frac{W_{ppeak}}{W_{p60}}\right) - \left(1 - \frac{W_{p60}}{W_{ppeak}}\right)\cdot\log e}{\log\left(\frac{\eta_1}{f_{p60}}\right)} \quad (19)$$

where e is the base for natural logarithms, and (W_{ppeak} , η_1) and (W_{p60} , f_{p60}) are two sets of corresponding values from the relation between work input and stress level f_p. These two points correspond to the peak point and the point at 60% of η_1 on the work-hardening part of the W_p-f_p relation. The variation of q with confining pressure σ_3 can best be modeled by the following simple expression:

$$q = \alpha + \beta \cdot \frac{\sigma_3}{p_a} \qquad (20)$$

where the values of α and β represent the intercept and the slope of the straight line shown in Fig. 3d.

The parameters a and b in Eq. 18 are calculated from:

$$a = \eta_1 \cdot \left(\frac{e \cdot p_a}{W_{ppeak}}\right)^{1/q} \qquad (21)$$

and

$$b = \frac{1}{q \cdot W_{ppeak}} \qquad (22)$$

where q is determined from Eq. 20 and e is the base for natural logarithms. The variation of W_{ppeak} with the confining pressure σ_3 can be approximated by the following expression:

$$W_{ppeak} = P \cdot p_a \cdot \left(\frac{\sigma_3}{p_a}\right)^{\ell} \qquad (23)$$

where P and ℓ are constants to be determined as shown schematically on Fig. 3e. On this diagram P is the intercept with $(\sigma_3/p_a) = 1$ and ℓ is the slope of the straight line.

The form of the stress-strain relationships which account for the plastic expansive behavior of the cohesionless soil can be expressed as:

$$\Delta\varepsilon_{ij}^{p} = \Delta\lambda_p \cdot \frac{\delta g_p}{\delta \sigma_{ij}} \qquad (24)$$

The derivatives of g_p with regard to the normal stresses become:

$$\frac{\delta g_p}{\delta \sigma_x} = 3 \cdot I_1^2 - \left(27 + \eta_2 \cdot \left(\frac{p_a}{I_1}\right)^m\right) \cdot (\sigma_y \cdot \sigma_z - \tau_{yz}^2) + \frac{I_3}{I_1} \cdot m \cdot \eta_2 \cdot \left(\frac{p_a}{I_1}\right)^m \qquad (25a)$$

and similar expressions are obtained for the other normal stresses by interchanging the indices on the stresses. The derivatives of g_p with respect to the shear stresses become:

$$\frac{\delta g_p}{\delta \tau_{yz}} = \left(27 + \eta_2 \cdot \left(\frac{p_a}{I_1}\right)^m\right) \cdot (\sigma_x \cdot \tau_{yz} - \tau_{xy} \cdot \tau_{zx}) \qquad (25b)$$

and similar expressions can be obtained for the other shear stresses by interchanging the indices on the stresses.

The value of the proportionality constant $\Delta\lambda_p$ in Eq. 24 can be written as

$$\Delta\lambda_p = \frac{dW_p}{3 \cdot g_p + m \cdot \eta_2 \cdot \left(\frac{p_a}{I_1}\right)^m \cdot I_3} \qquad (26)$$

where g_p is the plastic potential function and dW_p is the increment in plastic work due to an increase in the stress level df_c:

$$dW_p = \frac{df_p}{f_p} \cdot \frac{1}{\left(\frac{1}{q \cdot W_p} - b\right)} \qquad (27)$$

where f_p is the current value of the stress level.

Fourteen soil parameters are incorporated in the stress-strain theory for cohesionless soil. The determination of thirteen of these parameters is illustrated in Figs. 2 and 3, and Poisson's ratio is 0.2. The governing equations are stated above, but without derivations and discussions. The development and the capabilities of this theory are discussed in detail elsewhere (8,9). The necessary modifications and the application of this theory to normally consolidated cohesive soil under three-dimensional loading conditions are considered in detail below.

3 DETERMINATION OF SOIL PARAMETERS FOR GRUNDITE CLAY

Cubical triaxial tests have been performed to investigate the influence of the intermediate principal stress on the stress-strain, pore pressure, and strength characteristics of normally consolidated, remolded Grundite Clay under undrained conditions. The results of these tests have been analyzed and presented (12,13), and they form the basis for the developments presented below. The modifications to the stress-strain theory are discussed, procedures are developed to determine the necessary soil parameters from undrained tests on clay, and the soil parameter values which characterize the behavior of normally consolidated, remolded Grundite Clay are determined using effective stresses.

3.1 Elastic Strains

The elastic strains are calculated from Hooke's law which requires values of the

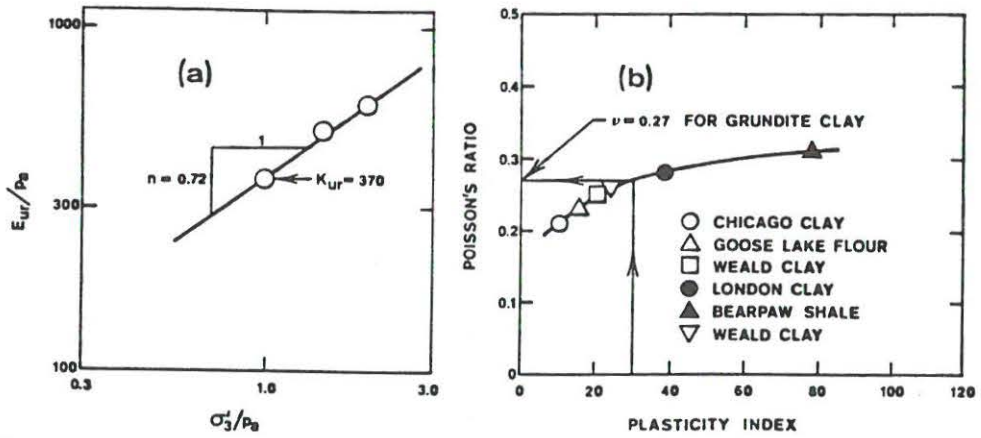

Figure 4. Determination of (a) Parameters for Elastic Modulus Variation, and (b) Poisson's Ratio for Grundite Clay.

modulus and Poisson's ratio for the clay.

Elastic Modulus. - The variation of the elastic modulus with effective confining pressure is given in Eq. 1. Since the strains observed in unloading-reloading cycles in triaxial compression tests on clay are excessively influenced by creep effects, the elastic moduli were calculated from the initial slopes of the primary loading stress-strain curves. These moduli were plotted versus the average effective confining pressure acting on the clay over the increment from which the moduli were determined. Fig. 4a shows the relation between the elastic modulus and the effective confining pressure. The values of the modulus number, K_{ur}, and the exponent, n, for use in Eq. 1 are 370 and 0.72, respectively.

Poisson's Ratio. - Poisson's ratio was determined on the basis of the plasticity index for Grundite Clay. A relation between Poisson's ratio and plasticity index was established from the results of one-dimensional consolidation tests performed by Brooker and Ireland (3) and Henkel and Sowa (5). Both vertical and horizontal effective stresses were measured, and both loading and unloading branches were established in these tests. Values of the coefficient of earth pressure at rest, K_o, can be calculated from these tests. A relation between Poisson's ratio and K_o exists for an elastic material such that:

$$\nu = \frac{K_o}{1 + K_o} \qquad (28)$$

where K_o may be defined in terms of effective stress increments:

$$K_o = \left(\frac{\Delta\sigma_h'}{\Delta\sigma_v'}\right)_{\epsilon_h=0} \qquad (29)$$

Values of K_o were determined from the initial parts of the unloading branches, because only elastic strains occur for these parts of the curves. Poisson's ratio was then calculated from Eq. 28 and plotted versus plasticity index as shown in Fig. 4b. According to this figure, Poisson's ratio increases from about 0.2 for clays with low plasticity to values slightly higher than 0.3 for highly plastic clays. Grundite Clay has a plasticity index of 30 corresponding to a Poisson's ratio of 0.27 as shown on Fig. 4b.

3.2 Plastic Collapse Strains

The plastic collapse strains for normally consolidated clay are calculated from the same stress-strain relations as those used for sand. However, the empirical work-hardening law, which is determined from the results of isotropic consolidation tests, takes another form for clay than for sand. This is because the compression curve obtained from normally consolidated clay has quite different characteristics than that obtained from sand. Fig. 5a shows a comparison of results from isotropic compression tests on normally consolidated, remolded Grundite Clay and on normally consolidated loose Sacramento River Sand (from (14)). The diagram in Fig. 5a is a conven-

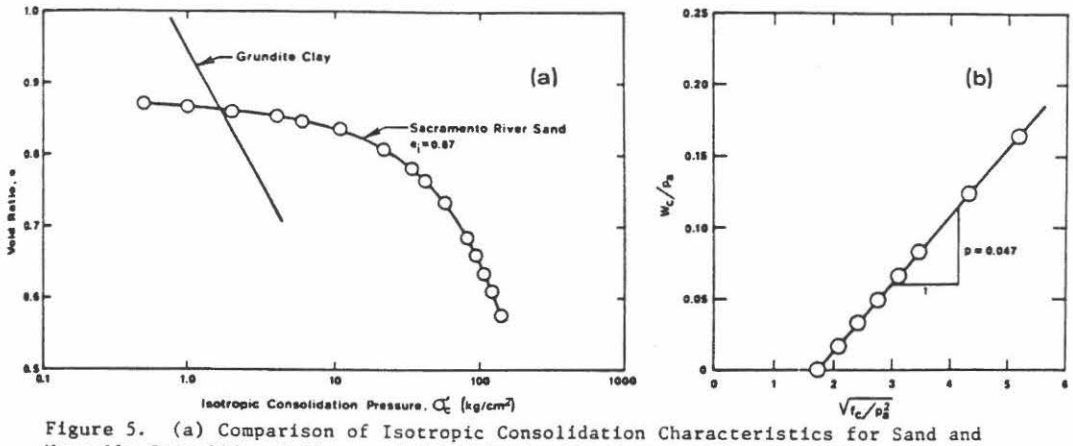

Figure 5. (a) Comparison of Isotropic Consolidation Characteristics for Sand and Normally Consolidated Clay, and (b) Relationship Between Plastic Collapse Work, W_c, and the Value of f_c for Grundite Clay.

tional e-log p' diagram with the isotropic consolidation pressure on the horizontal scale. It may be seen that the patterns of consolidation for the two types of soil are different. The consolidation curve for the normally consolidated sand never reaches a constant slope on this diagram. The work-hardening law for the plastic collapse strains in the clay therefore must take a form different from that used for sand.

The straight line shown in Fig. 5a for remolded Grundite Clay was obtained from the isotropic consolidation of the cubical triaxial specimens. The elastic compression was subtracted from the volumetric strain increments using Hooke's law and the plastic collapse work, W_c, was calculated from Eq. 7. The corresponding values of f_c were calculated from Eq. 8. Fig. 5b shows a diagram of the relationship between W_c and f_c plotted in dimensionless form on arithmetic scales for Grundite Clay. This relationship can be modeled by a straight line with the following expression:

$$\frac{W_c}{p_a} = C + p \cdot \sqrt{\frac{f_c}{p_a^2}} \qquad (30)$$

where C is the intercept with the horizontal axis and p is the slope of the line. The increment in plastic collapse work per unit volume then becomes:

$$dW_c = \frac{p}{2} \cdot p_a \cdot \left(\frac{f_c}{p_a^2}\right)^{-1/2} \cdot d\,(f_c/p_a^2) \qquad (31)$$

Note that only one parameter, the slope p of the straight line in Fig. 5b, is required to characterize the plastic collapse behavior of normally consolidated clay. It is therefore not necessary to determine the value of the intercept C. The expression in Eq. 31 is used with the stress-strain relations given in Eqs. 5a-f to determine the plastic collapse strains.

3.3 Plastic Expansive Strains

The plastic expansive strains for normally consolidated clays are calculated from the same stress-strain relations as those used for sand. However, because normally consolidated clay exhibits a relatively more simple behavior pattern than that for sand, some of the soil parameters which characterize the plastic expansive behavior of normally consolidated clay become zero or unity.

Failure Criterion. - The soil parameters required in the failure criterion given by Eq. 11 were determined as shown in Fig. 6. The straight line on this diagram corresponds to $n_1 = 22$ and $m = 0.40$. Note that only the data from triaxial compression tests on cubical specimens were used for the determination of these parameters.

The results of triaxial compression tests performed on short cylindrical specimens and the results of the cubical triaxial tests are shown on Fig. 6 for comparison. It may be seen that some scatter of the data around the solid line does exist, but the failure criterion selected on the basis of the triaxial compression tests on cubical specimens appears to represent the data

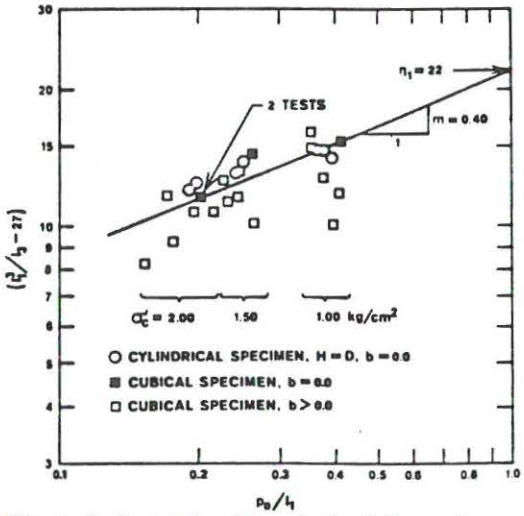

Figure 6. Determination of the Values of η_1 and m Involved in Failure Criterion for Grundite Clay.

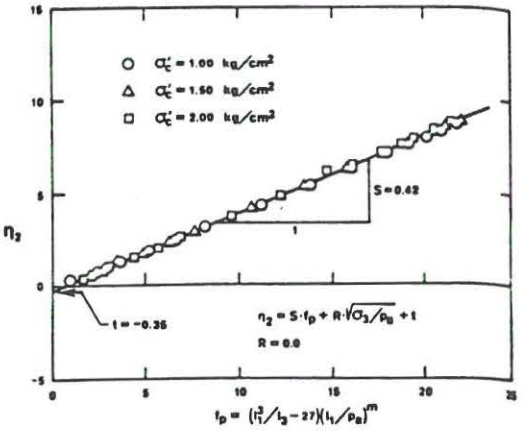

Figure 7. Variation of η_2 with f_p for Grundite Clay.

quite well.

The failure surface defined by Eq. 11 with the values of η_1 and m from Fig. 6 has been compared to the actual test data by Lade and Musante (13).

Plastic Potential Function. - The plastic potential function given in Eq. 13 requires determination of η_2. Values of η_2 were determined using Eq. 14 and the results of the triaxial compression tests on cubical specimens. These values were plotted versus the corresponding values of f_p given by Eq. 11a, and the diagram in Fig. 7 shows the relation between η_2 and f_p.

It may be seen from Fig. 7 that all points for practical purposes fall on one straight line in this diagram. This reflects the fact that essentially one type of stress-strain behavior is observed for a given normally consolidated clay. This behavior is not influenced much by the magnitude of the consolidation pressure. In comparison, the stress-strain behavior of sand at a given void ratio changes from that of a dense sand to that of a loose sand with increasing consolidation pressure. This change in stress-strain behavior with effective confining pressure is reflected in the critical void ratio-critical confining pressure concept (14,21). A similar concept is not relevant to normally consolidated clay, because the stress-strain behavior does not change much with consolidation pressure. The success of the concept of normalized behavior for normally consolidated clay (see (7)) is based on this fact. The concept of normalized behavior is not applicable to sand.

The effective friction angle for Grundite Clay decreases with increasing consolidation pressure (12,13) and the failure surface is therefore curved in the triaxial plane. The curvature of the failure surface is measured by the value of m in Eq. 11. Calculation of the values of η_2 from Eq. 14 includes the effect of the curved failure surface, and only one straight line is therefore obtained on the diagram in Fig. 7. The variation of η_2 with f_p can be expressed by Eq. 16, but since η_2 does not depend on the effective confining pressure, the value of R is zero for normally consolidated clay. The values of the other two soil parameters, S and t, necessary to characterize the variation of η_2 are 0.42 and -0.35, respectively.

Work-Hardening Law. - The plastic expansive work was calculated from the triaxial compression tests on cubical specimens using the expression in Eq. 17. The elastic and plastic collapse strains were subtracted from the total strains measured in the triaxial compression tests before the plastic expansive work was calculated. Taking advantage of the concept of normalized behavior for normally consolidated clay, each increment in plastic expansive work was normalized by dividing it by the current value of the effective confining pressure, σ_3'. Thus, the relations between normalized plastic expansive work, W_p/σ_3', and the value of f_p calculated from Eq. 11a for the three triaxial compression tests become the same, as shown on Fig. 8. This implies that the amount of work necessary to deform normally consolidated clay at a given stress level,

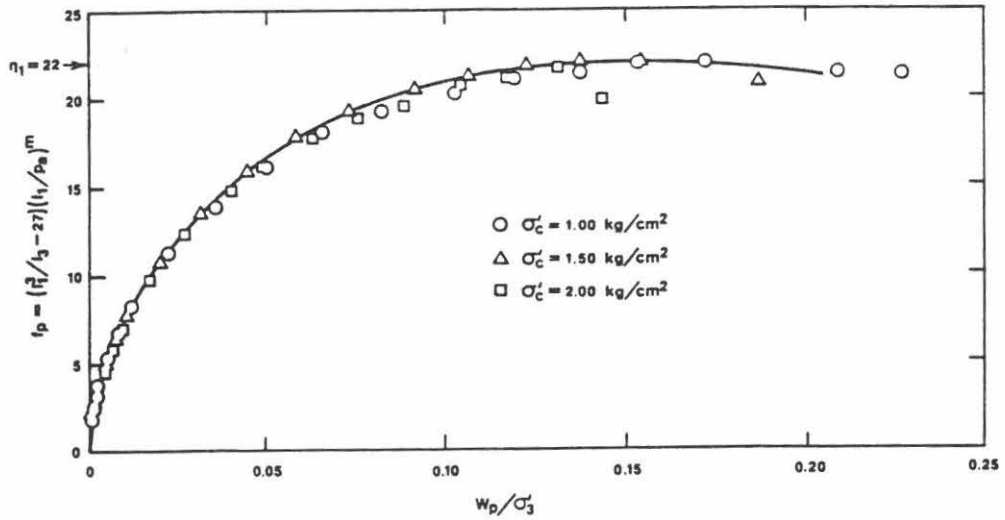

Figure 8. Variation of Normalized Plastic Expansive Work with f_p for Grundite Clay.

f_p, is directly proportional to the current effective confining pressure.

Due to the simple pattern of behavior indicated in Fig. 8, modeling of the work-hardening relationship for normally consolidated clay becomes relatively easy, because diagrams like those in Figs. 3d and 3e need not be drawn. Eq. 18 gives the basic expression for the work-hardening law. The value of q in this expression is calculated from Eq. 19, and only one value is obtained for all values of σ_3'. Thus, Eq. 20 which models the variation of q with σ_3' becomes simple, such that $q = \alpha = 1.58$ and $\beta = 0.0$ for Grundite Clay. The variation of W_{ppeak} is given by Eq. 23, and since W_p is directly proportional to σ_3', the value of ℓ is equal to unity, and the value of P is determined from the peak point on the curve shown in Fig. 8. For Grundite Clay, P is equal to 0.15. The expression for W_{ppeak} in Eq. 23 is then substituted in Eqs. 21 and 22 for determination of the parameters a and b, and these parameters are used in Eq. 18 for the relation between f_p and W_p.

4 SUMMARY OF PARAMETER VALUES OF GRUNDITE CLAY

The values of the parameters for Grundite Clay have been determined from isotropically consolidated, undrained triaxial compression tests only. In order to emphasize the similarity between the elasto-plastic stress-strain theories for sand and normally consolidated clay, the parameters for Grundite Clay are listed in Table 1, which has the same set-up as used for sand. Note that only 10 parameter values need be determined for normally consolidated clay. The remaining soil parameters are zero or unity or not used as indicated in Table 1. None

Table 1. Summary of Parameter Values for Grundite Clay.

Parameter	Value	Strain Component
Modulus No., K_{ur}	370	
Exponent, n	0.72	Elastic
Poisson's Ratio, ν	0.27	
[1]Collapse Modulus, C	--	Plastic
Collapse Const., p	0.047	Collapse
Yield Const., η_1	22	
Yield Exponent, m	0.40	
[2]Pl. Potent.Const., R	0.0	
Pl. Potent.Const., S	0.42	Plastic
Pl. Potent.Const., t	-0.35	Expansive
Work-Hard.Const., α	1.58	
[2]Work-Hard.Const., β	0.0	
Work-Hard.Const., P	0.15	
[2]Work-Hard.Exponent, ℓ	1.00	

[1]C is not used, see Equation (31).

[2]For normally consolidated clay, this parameter value is as indicated, and need not be determined (see explanation in text).

of the parameters have dimensions. All dimensions are controlled, where appropriate, by the dimension of the atmospheric pressure, p_a, as e.g. in Eq. 23. The parameters in Table 1 may be used to calculate strains in Grundite Clay for any combination of effective stresses during primary loading, neutral loading, unloading and reloading.

5 PREDICTION OF BEHAVIOR OF NORMALLY CONSOLIDATED CLAY

To test the abilities of the elasto-plastic stress-strain theory presented in the previous sections, predictions of this theory were compared to the behavior of Grundite Clay under conditions of undrained triaxial compression, undrained tests with three unequal principal stresses, and conventional K_o-consolidation.

Appropriate computer programs were developed to perform the necessary calculations involved in using the elasto-plastic stress-strain theory for prediction of the various loading conditions. Only the soil parameters derived from undrained triaxial compression tests on Grundite Clay and listed in Table 1 were used for all predictions.

5.1 Pore Pressure Prediction

The prediction of pore pressures and soil behavior under undrained conditions is based on the condition that no volume change occurs in the soil for any load increment. This condition can be formulated as follows:

$$\Delta\varepsilon_v^e + \Delta\varepsilon_v^c + \Delta\varepsilon_v^p = 0 \qquad (32)$$

where $\Delta\varepsilon_v^e$, $\Delta\varepsilon_v^c$, and $\Delta\varepsilon_v^p$ are the volumetric strain components corresponding to the three types of strain occurring in the soil. The calculation of pore pressures was performed by specifying the chamber pressure, the value of $b = (\sigma_2-\sigma_3)/(\sigma_1-\sigma_3)$, and discrete values of effective stress ratio σ_1'/σ_3', or stress difference, $(\sigma_1-\sigma_3)$. The effective confining pressure producing volumetric strains which would satisfy Eq. 32 within specified limits was found by iteration. The limits used for the total volumetric strain (not the volumetric strain increment for each load step) was ±0.020%, but narrower limits could have been used. However, a few calculations with different limits showed that the predicted pore pressures and soil behavior were not significantly affected by these limits as long as they were reasonably narrow. After having satisfied Eq. 32, the pore pressure was calculated as the difference between the total confining pressure and the effective confining pressure found by iteration. It should be noted that this approach to pore pressure prediction is based on the fact that a balance can be found between the compressive and the expansive volumetric strains such that their sum is zero for each value of σ_1'/σ_3' or $(\sigma_1-\sigma_3)$.

Because stress-path dependent behavior can be calculated by the elasto-plastic theory (11), the stress-strain relations for the undrained tests can be determined from the effective stress-path calculated as explained above.

5.2 Undrained Cubical Triaxial Tests

The results of the undrained cubical triaxial tests on normally consolidated, remolded Grundite Clay previously presented (13) are shown in Fig. 9 together with the predictions of the elasto-plastic stress-strain theory. The normalized stress difference, $(\sigma_1-\sigma_3)/\sigma_c'$, the effective stress ratio, σ_1'/σ_3', and the normalized pore pressure, $\Delta u/\sigma_c'$, are plotted against the major principal strain, ε_1. The points in this figure represent the measured soil and pore pressure behavior and the solid lines represent the predictions of the elasto-plastic theory.

The comparisons shown in Fig. 9a for the triaxial compression tests indicate that the soil and pore pressure behavior is calculated with good accuracy from the theory. The decrease in strength with increasing consolidation pressure (curved failure surface) is correctly reflected by the theory, and the variation in moduli also compares well with the calculations. Because the parameter values were initially derived from the results of these tests, the good agreement was to be expected.

The results of the cubical triaxial tests with three unequal principal stresses are compared with the predictions on Figs. 9b-f. The magnitude of the intermediate principal stress is indicated by the value of $b = (\sigma_2-\sigma_3)/(\sigma_1-\sigma_3)$: b is zero for triaxial compression in which $\sigma_2 = \sigma_3$, and it is unity for triaxial extension in which $\sigma_2 = \sigma_1$; for intermediate values of σ_2 the value of b is between zero and unity. The predicted response agrees well with the measured behavior for all the cubical tests. The influence of the intermediate principal stress on the soil and pore pressure behavior and on the variation in strength is correctly reflected by the theory. The

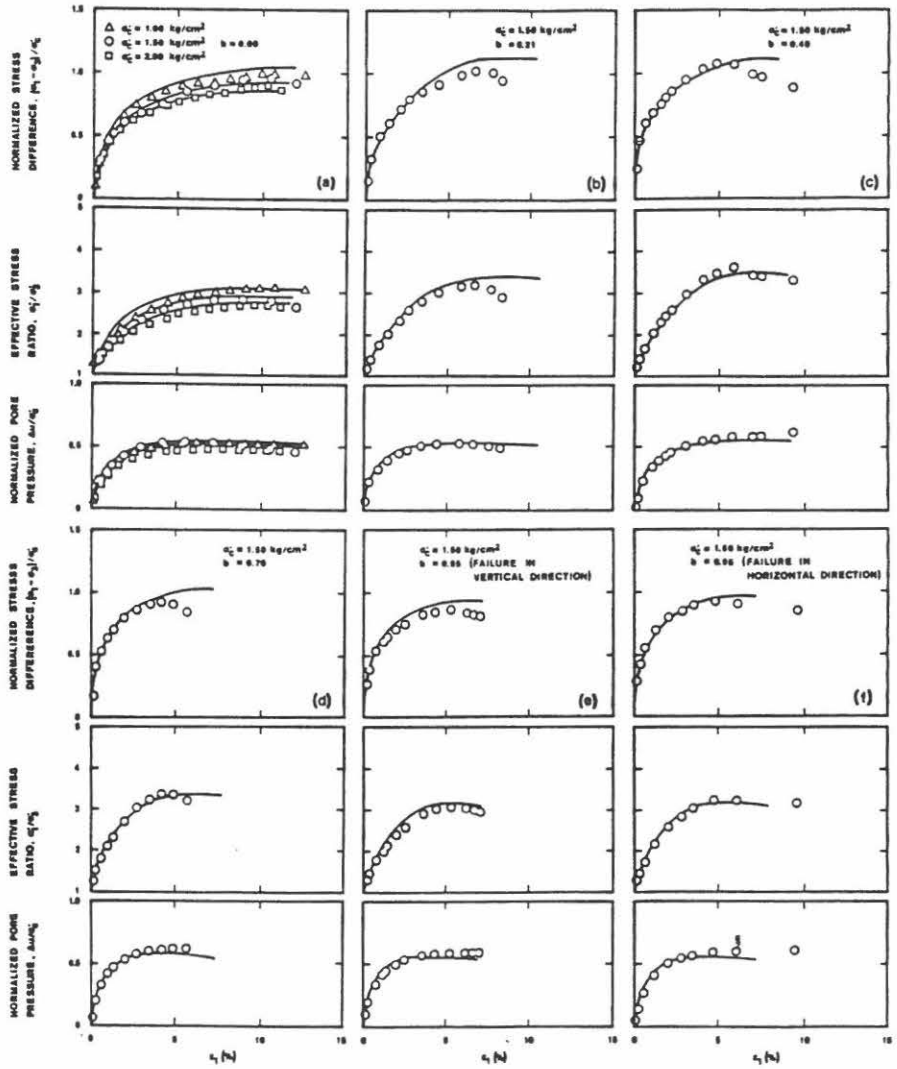

Figure 9. Comparison of Measured and Predicted Stress-Strain and Pore Pressure Characteristics for Cubical Triaxial Tests on Grundite Clay.

deviation in strength for the test with b = 0.21 shown in Fig. 9b was expected, because the measured effective friction angle was lower than that assumed in the theory (see (13)). Note also that the overestimate of the maximum deviator stress in the test with b = 0.70 (Fig. 9d) corresponds to the slightly lower predicted than measured values of pore pressure at large strains. However, the overall comparison of the calculated and measured behavior indicates that the theory is capable of predicting soil and pore pressure behavior under three-dimensional stress conditions with reasonable accuracy.

5.3 Conventional K_o-Consolidation

A conventional uniaxial consolidation test was performed on remolded Grundite Clay. The e-log p' curve for this test was predicted using the parameters in Table 1.

Both plastic and elastic strains occur

in a K_o-consolidation test with increasing stresses. The plastic and elastic horizontal strains cancel each other out such that the total horizontal strain is zero. This condition is expressed as follows:

$$\Delta\varepsilon_h^e + \Delta\varepsilon_h^c + \Delta\varepsilon_h^p = 0 \qquad (33)$$

where $\Delta\varepsilon_h^e$, $\Delta\varepsilon_h^c$, and $\Delta\varepsilon_h^p$ are the horizontal strain components corresponding to the three types of strain occurring in the soil. The calculations of the K_o-consolidation test was performed by specifying values of the stress difference, $(\sigma_1-\sigma_3)$, and finding the value of the horizontal stress, σ_3, by iteration that would result in horizontal strains fulfilling Eq. 33 within specified limits. The sum of the total horizontal strain was required to be within ±0.010%, but employment of narrower limits would not have resulted in different predictions.

The diagram in Fig. 10 shows the result of the consolidation test on remolded Grundite Clay. The void ratio is plotted versus the logarithm of the vertical effective stress, p', in this diagram. Since the soil parameters correspond to normally consolidated Grundite Clay, only the virgin compression curve can be predicted, and Fig. 10 shows that this curve is predicted accurately by the theory.

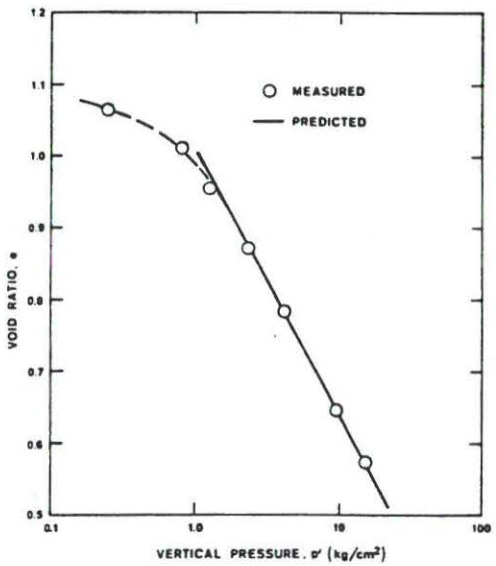

Figure 10. Measured and Predicted Relation Between Void Ratio and Vertical Consolidation Pressure in K_o- Test on Remolded Grundite Clay..

6 CONCLUSION

A recently developed elasto-plastic stress-strain theory for cohesionless soil with curved yield surfaces was employed for prediction of the behavior of normally consolidated, remolded Grundite Clay under three-dimensional loading conditions. One minor modification was required in the theoretical framework to accommodate the difference in behavior between normally consolidated sand and normally consolidated clay. Only ten soil parameters need be determined for normally consolidated clay (relative to fourteen soil parameters for sand), and procedures were developed so that the values of these parameters can be derived entirely from the results of isotropically consolidated, undrained triaxial compression tests.

The accuracy of the elasto-plastic stress-strain theory for normally consolidated cohesive soil was evaluated by comparing predicted and measured stress-strain, pore pressure, and strength behavior for remolded Grundite Clay under three-dimensional undrained loading conditions. All aspects of the behavior of this clay were predicted with reasonable accuracy for all magnitudes of the intermediate principal stress. The virgin compression curve from a conventional K_o-consolidation test on remolded Grundite Clay was also correctly predicted by the elasto-plastic theory. Thus, it seems likely that this theory will be useful for analyzing the behavior of normally consolidated clay under a wide variety of loading conditions.

7 ACKNOWLEDGMENT

The research presented here was supported by the National Science Foundation under Engineering Research Initiation Grant No. 37445.

8 REFERENCES

(1) Bishop, A.W. 1966, The Strength of Soils as Engineering Materials, Geotechnique 16: 91-130.
(2) Bishop, A.W. 1971, Shear Strength Parameters for Undisturbed and Remoulded Soil Specimens, Proc. Stress-Strain Behavior of Soils (Edited by R.H.G. Parry), Cambridge University, 3-58.
(3) Brooker, E.W. & H.O. Ireland 1965, Earth Pressures at Rest Related to Stress History, Can.Geotech.J. 2: 1-15.
(4) Duncan, J.M. & C.-Y. Chang 1970, Nonlinear Analysis of Stress and Strain in

Soils, ASCE: J.Soil Mech.Found.Div., 96: 1629-1653.
(5) Henkel, D.J. & V.A. Sowa 1963, The Influence of Stress History on Stress Paths in Undrained Triaxial Tests on Clay, ASTM STP 361: 280-291.
(6) Janbu, N. 1963, Soil Compressibility as Determined by Oedometer and Triaxial Tests, Proc. European Conf.Soil Mech. Found.Engr., Wiesbaden, 1: 19-25.
(7) Ladd, C.C. & R. Foott 1974, New Design Procedure for Stability of Soft Clays, ASCE: J.Geotech.Engr.Div. 100: 763-786.
(8) Lade, P.V. 1977, Elasto-Plastic Stress-Strain Theory for Cohesionless Soil with Curved Yield Surfaces, Int.J.Solids Structures, 13: 1019-1035.
(9) Lade, P.V. 1978, Prediction of Undrained Behavior of Sand, ASCE: J.Geotech. Engr.Div., 104: 721-735.
(10) Lade, P.V. & J.M. Duncan 1973, Cubical Triaxial Tests on Cohesionless Soil, ASCE: J.Soil Mech.Found.Div., 99: 793-812.
(11) Lade, P.V. & J.M. Duncan 1976, Stress-Path Dependent Behavior of Cohesionless Soil, ASCE: J.Geotech.Engr.Div., 102: 51-68.
(12) Lade, P.V. & H.M. Musante 1977, Failure Conditions in Sand and Remolded Clay, Proc.9th Int.Conf.Soil Mech.Found.Engr., Tokyo, I: 181-186.
(13) Lade, P.V. & H.M. Musante 1978, Three-Dimensional Behavior of Remolded Clay, ASCE: J.Geotech.Engr.Div., 104: 193-209.
(14) Lee, K.L. & H.B. Seed 1967, Drained Strength Characteristics of Sands, ASCE: J.Soil Mech.Found.Div., 93: 117-141.
(15) Olson, R.E. 1974, Shearing Strength of Kaolinite, Illite, and Montmorillonite, ASCE: J.Geotech.Engr.Div., 100: 1215-1229.
(16) Prevost, J.-H. & K. Hoeg 1975, Effective Stress-Strain Strength Model for Soils, ASCE: J.Geotech.Engr.Div., 101: 259-278.
(17) Prevost, J.-H. & K. Hoeg 1975, Soil Mechanics and Plasticity Analysis of Strain Softening, Geotechnique, 25: 279-297.
(18) Roscoe, K.H. & J.B. Burland 1968, On the Generalized Stress-Strain Behavior of 'Wet' Clay, Engineering Plasticity (Edited by J. Heyman & F.A. Leckie) Cambridge Univ., 535-609.
(19) Roscoe, K.H., A.N. Schofield & A. Thurairajah 1963, Yielding of Clays in States Wetter Than Critical, Geotechnique, 13: 211-240.
(20) Roscoe, K.H., A.N. Schofield & C.P. Wroth 1958, On the Yielding of Soils, Geotechnique, 8: 22-52.
(21) Seed, H.B. & K.L. Lee 1967, Undrained Strength Characteristics of Cohesionless Soil, ASCE: J.Soil Mech.Found.Div., 93: 333-360.
(22) Yong, R.N., E. McKeyes & V. Silvestri 1972, Yield and Failure of Clays, Arch. Mech., 24: 511-528.

Single Hardening Model and Its Capabilities

Computers and Geotechnics **5** (1988) 307–324

SINGLE HARDENING CONSTITUTIVE MODEL FOR FRICTIONAL MATERIALS

I. PLASTIC POTENTIAL FUNCTION

M.K. Kim
Department of Civil Engineering
Yonsei University
Seoul 120, Korea

and

P.V. Lade
Department of Civil Engineering
University of California
Los Angeles, California 90024, U.S.A.

ABSTRACT

Based on review and evaluation of a large number of test data, a general three-dimensional plastic potential function expressed in terms of stress invariants is proposed. Three parameter values are required in this function, but one is redundant with one of the failure surface parameters. The plastic potential surface resembles an asymmetric cigar in the principal stress space. It includes tensile behavior of materials with effective cohesion. Its capabilities are examined by comparisons with experimental data from two- and three-dimensional tests on different frictional materials.

INTRODUCTION

One of the most important components of an elasto-plastic work-hardening constitutive model is the plastic potential function. This is the basis for derivation of the plastic flow rule which establishes the relationship between stresses and plastic strain increments for the material under consideration.

Based on experimental evidence, St. Venant [1] proposed that the principal stress axes coincide with the corresponding principal axes of incremental plastic strain (not with those of total plastic strains) during rotation of stresses. This observation led to the suggestion that the plastic strain increments could be determined from a plastic potential function, g_p [2]:

$$d\underset{\sim}{\varepsilon}^p_{ij} = d\lambda_p \frac{\partial g_p}{\partial \underset{\sim}{\sigma}_{ij}} \tag{1}$$

In this plastic flow rule, $d\lambda_p$ is a positive constant of proportionality. The value of $d\lambda_p$ therefore determines the magnitude of the incremental plastic strain vector.

Computers and Geotechnics 0266-352X/88/$03·50

The plastic potential function is expressed in terms of stresses, and it describes a surface in stress space to which the plastic strain increment vectors are perpendicular, as expressed in Eq. (1). It is usually assumed in classical plasticity theory that the plastic potential function takes the same form as the yield function, i.e. associated flow is employed. However, this assumption is not necessary, and there is clear evidence that the yield surface and the plastic potential surface are not identical for frictional materials, i.e. nonassociated flow is obtained [3-6]. The plastic potential function can be determined independently of any other consideration relating to the constitutive model. A very important premise for Eq. (1) is that the plastic strain increments can in fact be determined from a potential function. This requires that the plastic strain increment vectors are uniquely determined from the state of stress, and is independent of the stress-path leading to this state of stress. This has been demonstrated to be the case by Poorooshasb et al. [3] and by Lade and Duncan [5].

Presented here is a study of the geometrical shape of the plastic potential surface for frictional materials in stress space. The data from many experimental studies of frictional materials have been examined, and the resulting pattern of behavior is presented and discussed with illustrations to support the findings. This study forms the basis for a proposed function to describe a single, isotropic, plastic potential surface and its variation with stress state. The function is expressed in terms of stress invariants, and it is sufficiently flexible to encompass a variety of observed behavior patterns, yet sufficiently structured to allow parameter determination from simple tests.

OBSERVED BEHAVIOR IN THE TRIAXIAL PLANE

To study the plastic potential surface, the plastic strain increments observed in experiments are plotted and superimposed on the stress space. The triaxial plane and the octahedral plane, both from the principal stress space, are used to visualize the directions of the incremental plastic strain vectors.

A strain increment vector that is oriented perpendicular to the hydrostatic axis corresponds to the condition of zero volumetric strain. This is indicated on the insert in Fig. 1. If the volume increases, corresponding to dilation, then the strain increment vector will point towards the origin. On the other hand, if the volume decreases due to compression, then the vector will point in the outward direction of the hydrostatic axis.

Fig. 1(a) shows the directions of plastic strain increment vectors $d\underline{\varepsilon}^p$ along stress paths from triaxial compression tests performed on Fine Silica Sand. Idealized directions of $d\underline{\varepsilon}^p$ during isotropic compression are drawn along the hydrostatic axis corresponding to isotropic behavior. Fig. 1(b) shows the results of proportional loading tests on sand as reported by Poorooshasb et al. [3]. From Fig. 1 it can be observed that the plastic volume change is highly compressive at stress states close to the hydrostatic axis, and the rate of change decreases as the stress level, i.e. the proximity to failure, is increased. At high stress levels near failure, the plastic volume change becomes dilative.

Similar observations can be made for materials with effective cohesion. Fig. 2(a) shows results of uniaxial compression ($\sigma_1 > \sigma_2 = \sigma_3 = 0$), biaxial compression ($\sigma_1 = 0$, $\sigma_2 = \sigma_3 > 0$), triaxial compression ($\sigma_1 > \sigma_2 = \sigma_3$, $\sigma_1 + \sigma_2 + \sigma_3 = \text{constant}$), and triaxial extension ($\sigma_1 < \sigma_2 = \sigma_3$, $\sigma_1 + \sigma_2 + \sigma_3 = \text{constant}$) tests on plain concrete reported by Schickert and Winkler [7]. The decreasing rate of compressive volume change with increasing stress level is similar to that of cohesionless soil. It should be noted that the results of triaxial compression and extension tests are not complete, because these tests were reported up to stress states

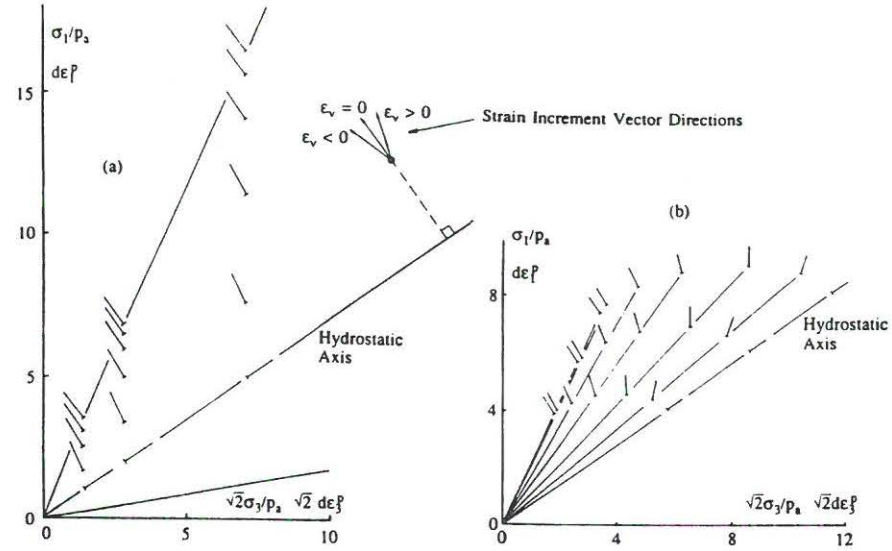

Fig. 1. Directions of Incremental Plastic Strain Vectors in Triaxial Plane for (a) Triaxial Compression Tests on Fine Silica Sand, and (b) Proportional Loading Tests on Sand [3].

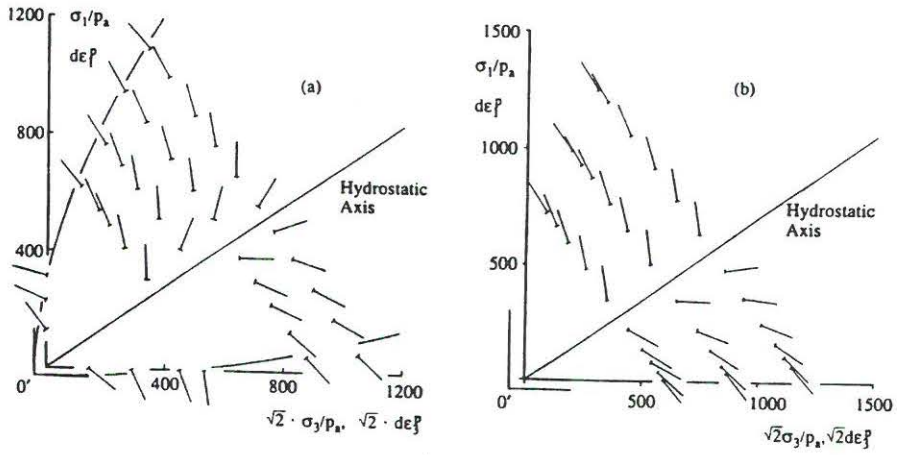

Fig. 2. Directions of Incremental Plastic Strain Vectors in Triaxial Plane for (a) Plain Concrete [7], and (b) Steel Fiber Reinforced Concrete [8].

corresponding to minimum volumes of the specimens. However, if continuous behavior of the material beyond the minimum volume state is assumed, then similar behavior as for sand (i.e. dilation) is expected as indicated on the diagram by the uniaxial and biaxial compression tests. Fig. 2(b) shows the results of triaxial compression and extension tests on steel fibre reinforced concrete performed by Egging and Ko [8]. This set of data is also available up to the minimum volume state, and the type of behavior observed for the plain concrete is repeated for steel fibre reinforced concrete.

The plastic potential surfaces, which are sought in this study, are perpendicular to the plastic strain increment vectors as indicated by the short line at the base of each vector. Based on these short lines and the observations made above, a family of curves may be drawn through the base points in the directions of the short lines. The resulting family of plastic potential surfaces would be shaped as distorted ellipses in the triaxial plane. Whereas the exact shapes of these surfaces seem to depend on the material, they do appear to be of similar type.

OBSERVED BEHAVIOR IN THE OCTAHEDRAL PLANE

Fig. 3 shows the directions of the incremental plastic strain vectors projected on an octahedral plane for the results of cubical triaxial compression tests on Fuji River Sand presented by Yamada and Ishihara [9]. The stress paths for these tests all lie in the same octahedral plane. The specimens were prepared with anisotropic fabric, and the anisotropic deformation of the specimens appears to be dominant at low stress levels (close to the hydrostatic axis). At higher stress levels near failure the effects of the initial anisotropic fabric are small. Similar observations were made by Ochiai and Lade [10] for anisotropically prepared Cambria Sand. They reported that the directions of $d\underline{\varepsilon}^p$ at failure resemble those of isotropically prepared specimens. In Fig. 3 some nonsymmetry in the directions of $d\underline{\varepsilon}^p$ may be noted at low stress levels. This may be due partly to inherent anisotropy and partly to inaccurate elastic parameters used for calculation and subtraction of elastic strain increments.

These observations may be supplemented by those made by Yong and McKeys [11]. They observed that the incremental strain vectors for Kaolinite Clay were almost normal to von Mises circles up to about half of the shear strength on the octahedral plane.

The following conclusions can be drawn regarding the shape of the plastic potential surface on the octahedral plane: (1) At low stress levels, the cross-sections have almost circular shapes, and (2) as the stress level increases towards failure, the plastic potential surfaces gradually change shapes from circular to rounded triangular.

Further inspection reveals that the angularity of the rounded triangle near failure is less pronounced than that of the failure envelope. In order to clarify this point, the Lode angles for stress vectors and for incremental plastic strain vectors are calculated and compared. As indicated on Fig. 4(a), the direction of the stress vector projected on the octahedral plane is measured from the σ_1-axis and indicated by ω_σ. Similarly, ω_ε indicates the angle between the $d\varepsilon_1^p$-axis and the direction of the incremental plastic strain vector projected on the octahedral plane. These angles can be calculated from:

$$\tan\omega_\sigma = \frac{\sqrt{3}(\sigma_2 - \sigma_3)}{2\sigma_1 - \sigma_2 - \sigma_3} \qquad (2)$$

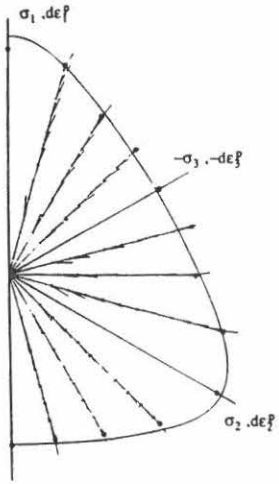

Fig. 3. Directions of Incremental Plastic Strain Vectors Projected on Octahedral Plane for Fuji River Sand [9].

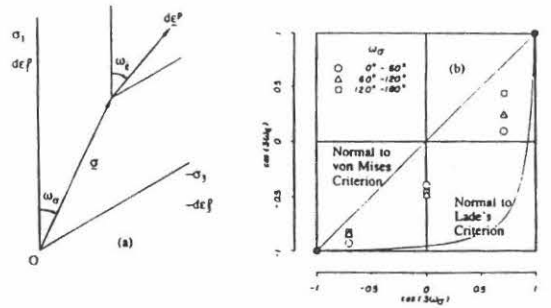

Fig. 4. (a) Definition of Lode Angles for Directions of Stress Vector and Incremental Plastic Strain Vector Projected on Octahedral Plane, and (b) Comparison of Lode Angles at Failure for Fuji River Sand [9] with Normals to Von Mises and Lade's Failure Surfaces.

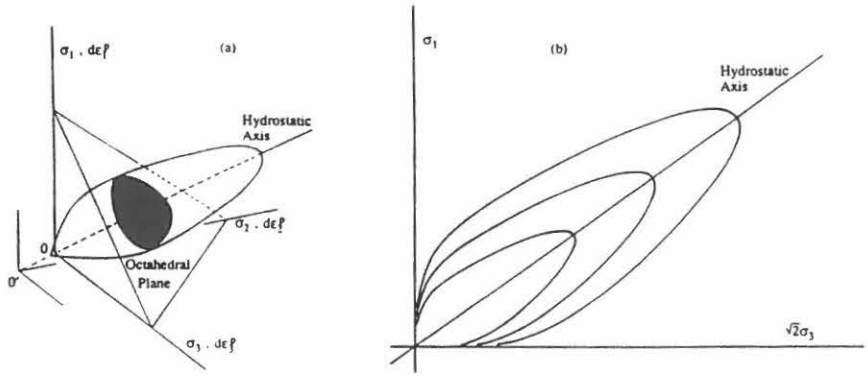

Fig. 5. (a) Schematic Illustration of the Proposed Plastic Potential Surface in Principal Stress Space, and (b) Contours in Triaxial Plane.

$$\tan\omega_{\dot{\varepsilon}} = \frac{\sqrt{3}(d\varepsilon_2^p - d\varepsilon_3^p)}{2d\varepsilon_1^p - d\varepsilon_2^p - d\varepsilon_3^p} \tag{3}$$

Comparison of ω_σ and $\omega_{\dot{\varepsilon}}$ is enhanced when plotted on a cos $(3\omega_\sigma)$-cos $(3\omega_{\dot{\varepsilon}})$ diagram. Fig. 4(b) shows such a diagram for failure conditions for Fuji River Sand. The triaxial compression condition ($\omega_\sigma = \omega_{\dot{\varepsilon}} = 0°$) is located at the bottom left corner, and the triaxial extension condition ($\omega_\sigma = \omega_{\dot{\varepsilon}} = 60°$) corresponds to the top right corner in the figure. Together with the data points, the analytical curves predicted by the normal directions to the von Mises circle and the normal directions to the failure envelope given by Lade [12] are drawn. the experimental data points are located between the analytical curves of these two criteria. Similar results have been obtained for other frictional materials. The plastic potential surface is therefore smoothly rounded but less angular than the failure surface.

PROPOSED PLASTIC POTENTIAL FUNCTION

Based on the observations presented in the previous sections, a plastic potential may be expressed in the following form:

$$g_p = \left[\psi_1 \cdot \frac{I_1^3}{I_3} - \frac{I_1^2}{I_2} + \psi_2\right] \cdot \left[\frac{I_1}{p_a}\right]^\mu \tag{4}$$

in which the three stress invariants are give by

$$I_1 = \sigma_1 + \sigma_2 + \sigma_3 = \sigma_x + \sigma_y + \sigma_z \tag{5a-b}$$

$$I_2 = -(\sigma_1 \cdot \sigma_2 + \sigma_2 \cdot \sigma_3 + \sigma_3 \cdot \sigma_1) \tag{6a}$$

$$= \tau_{xy} \cdot \tau_{yx} + \tau_{yz} \cdot \tau_{zy} + \tau_{zx} \cdot \tau_{xz} - (\sigma_x \cdot \sigma_y + \sigma_y \cdot \sigma_z + \sigma_z \cdot \sigma_x) \tag{6b}$$

$$I_3 = \sigma_1 \cdot \sigma_2 \cdot \sigma_3 \tag{7a}$$

$$= \sigma_x \cdot \sigma_y \cdot \sigma_z + \tau_{xy} \cdot \tau_{yz} \cdot \tau_{zx} + \tau_{yx} \cdot \tau_{zy} \cdot \tau_{xz} - (\sigma_x \cdot \tau_{yz} \cdot \tau_{zy} + \sigma_y \cdot \tau_{zx} \cdot \tau_{xz} + \sigma_z \cdot \tau_{xy} \cdot \tau_{yx}) \tag{7b}$$

The parameter ψ_1 in Eq. (4) acts as a weighting factor between the triangular shape (from the I_3 term) and the circular shape (from the I_2 term), the parameter ψ_2 controls the intersection with the hydrostatic axis, and the exponent μ determines the curvature of meridians.

The corresponding plastic potential surface is shaped as an asymmetric cigar with a smoothly rounded triangular cross-section, as shown in Fig. 5(a). The shape of the meridians are shown in the triaxial plane in Fig. 5(b) for Fine Silica Sand. This shape accounts for the rather abrupt change in volume change behavior near the hydrostatic axis observed in experiments and discussed further below. The plastic potential surface is continuous throughout stress space except at the intersection with the hydrostatic axis behind the origin of the space.

Substituting Eq. (4) into the flow equation (1), the components of the palstic strain increments are calculated as:

$$\begin{Bmatrix} d\varepsilon_x^p \\ d\varepsilon_y^p \\ d\varepsilon_z^p \\ d\gamma_{yz}^p \\ d\gamma_{zx}^p \\ d\gamma_{xy}^p \end{Bmatrix} = d\lambda_p \cdot \left[\frac{I_1}{p_a}\right]^\mu \begin{Bmatrix} G - (\sigma_y + \sigma_z) \cdot \frac{I_1^2}{I_2^2} - \psi_1 \cdot (\sigma_y \cdot \sigma_z - \tau_{yz}^2) \cdot \frac{I_1^3}{I_3^2} \\ G - (\sigma_z + \sigma_x) \cdot \frac{I_1^2}{I_2^2} - \psi_1 \cdot (\sigma_z \cdot \sigma_x - \tau_{zx}^2) \cdot \frac{I_1^3}{I_3^2} \\ G - (\sigma_x + \sigma_y) \cdot \frac{I_1^2}{I_2^2} - \psi_1 \cdot (\sigma_x \cdot \sigma_y - \tau_{xy}^2) \cdot \frac{I_1^3}{I_3^2} \\ 2 \cdot \frac{I_1^2}{I_2^2} \cdot \tau_{yz} - 2 \cdot \psi_1 \cdot (\tau_{xy} \cdot \tau_{zx} - \sigma_x \cdot \tau_{yz}) \cdot \frac{I_1^3}{I_3^2} \\ 2 \cdot \frac{I_1^2}{I_2^2} \cdot \tau_{zx} - 2 \cdot \psi_1 \cdot (\tau_{xy} \cdot \tau_{yz} - \sigma_y \cdot \tau_{zx}) \cdot \frac{I_1^3}{I_3^2} \\ 2 \cdot \frac{I_1^2}{I_2^2} \cdot \tau_{xy} - 2 \cdot \psi_1 \cdot (\tau_{yz} \cdot \tau_{zx} - \sigma_z \cdot \tau_{xy}) \cdot \frac{I_1^3}{I_3^2} \end{Bmatrix} \tag{8a-f}$$

in which

$$G = \psi_1 (\mu + 3) \frac{I_1^2}{I_3} - (\mu + 2) \frac{I_1}{I_2} + \psi_2 \cdot \mu \cdot \frac{1}{I_1} \tag{9}$$

If only principal stresses are applied to an element, then the plastic strain increment vector is given by:

$$\begin{Bmatrix} d\varepsilon_1^p \\ d\varepsilon_2^p \\ d\varepsilon_3^p \end{Bmatrix} = d\lambda_p \cdot \left[\frac{I_1}{p_a}\right]^\mu \begin{Bmatrix} G - \frac{I_1^2}{I_2^2}(\sigma_2 + \sigma_3) - \psi_1 \cdot \frac{I_1^3}{I_3^2}\sigma_2\sigma_3 \\ G - \frac{I_1^2}{I_2^2}(\sigma_3 + \sigma_1) - \psi_1 \cdot \frac{I_1^3}{I_3^2}\sigma_3\sigma_1 \\ G - \frac{I_1^2}{I_2^2}(\sigma_1 + \sigma_2) - \psi_1 \cdot \frac{I_1^3}{I_3^2}\sigma_1\sigma_2 \end{Bmatrix} \tag{10a-c}$$

MATERIALS WITH EFFECTIVE COHESION

The pointed apex of the plastic potential surface shown in Fig. 5 is located behind the origin of stress for materials without cohesion. Based on observations for concrete, as exemplified in Fig. 2, it appears that the plastic potential should have its apex at a translated stress origin O′ further behind the real stress origin. If the apex remains at the location for cohesionless soils, then the directions of incremental plastic strain vectors for uniaxial and biaxial compression cannot be derived from the proposed plastic potential. However, the function in Eq. (4) can be extended to materials with effective cohesion by a translation of the principal stress space along the hydrostatic axis from O to O′ in Fig. 5. Thus, a constant stress $a \cdot p_a$ is added to the normal stresses before substitution in Eqs. (5), (6) and (7):

$$\bar{\sigma}_{ij} = \sigma_{ij} + \delta_{ij} \cdot a \cdot p_a \tag{11}$$

in which δ_{ij} is Kronecker's delta ($\delta_{ij} = 1$ for $i = j$, and $\delta_{ij} = 0$ for $i \neq j$). The parameter 'a' is dimensionless and p_a is atmospheric pressure in the same units as σ_{ij}. The value of $a \cdot p_a$ reflects the effect of the tensile strength of the material, and it is determined as shown by Lade [13,14] and by Kim and Lade [15].

The flow rule in Eq. (1) still governs the incremental plastic strains, but the derivatives should be expressed in terms of the translated stresses to maintain mathematical consistency corresponding to a potential function formed in the translated space. The transformed stresses should also be used in the constitutive Eqs. (8), (9) and (10). This is consistent with the notion of cohesion explained in [13-15]. The plastic potential surface in this case has a shape similar to that for cohesionless soil shown in Fig. 5. However, the pointed apex lies at the origin O′ of the translated stress space.

CONDITION OF IRREVERSIBILITY

The condition of irreversibility requires that the plastic work is positive (or zero) whenever a change in plastic strain occurs [16]:

$$dW_p = \sigma_{ij} \cdot d\varepsilon^p_{ij} \geq 0 \tag{12}$$

This requires that the plastic potential surface is convex with regard to the stress origin. This condition may be satisfied when proper parameter values are employed. Since the plastic potential in Eq. 4 is a homogeneous function of the μth degree, Eq. 12 leads to

$$dW_p = \mu \cdot g_p \cdot d\lambda_p \tag{13}$$

Since $d\lambda_p > 0$, the condition of irreversibility requires that

$$\mu \cdot g_p \geq 0 \tag{14}$$

Fig. 6 shows the possible combinations of μ and g_p and the normal directions to the plastic potential. Fig. 6(b) indicates that a negative g_p is not suitable for a plastic potential function. Thus, the only possible combination that satisfies Eq. (14) is that of positive μ and positive g_p.

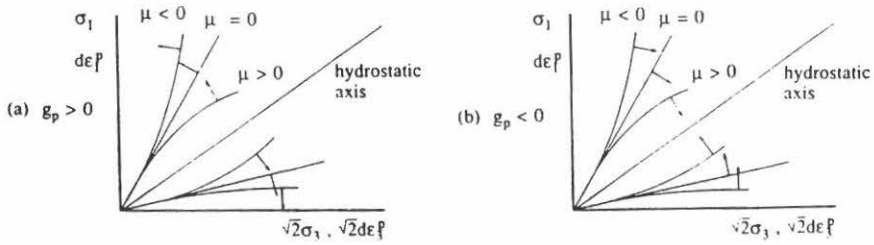

Fig. 6. Combinations of Plastic Potential g_p and Parameter μ in Triaxial Plane. (a) Case of Positive g_p, and (b) Case of Negative g_p.

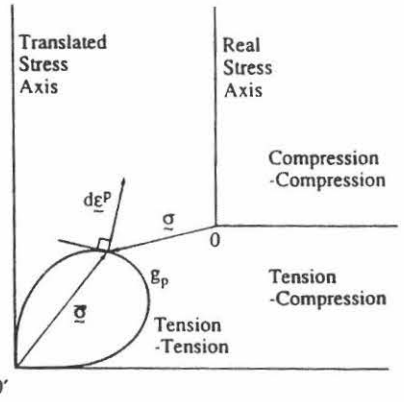

Fig. 7. Relation Between Stress and Incremental Plastic Strain Vectors in Tension-Tension Loading.

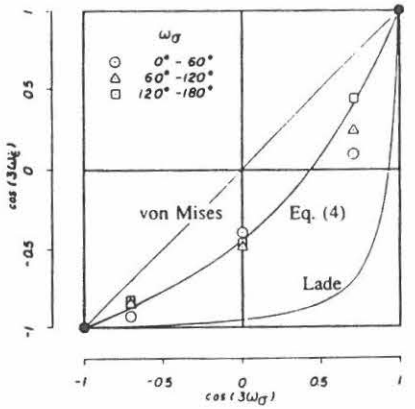

Fig. 8. Comparison of Calculated and Measured Lode Angles for Fuji River Sand (Data from [9]).

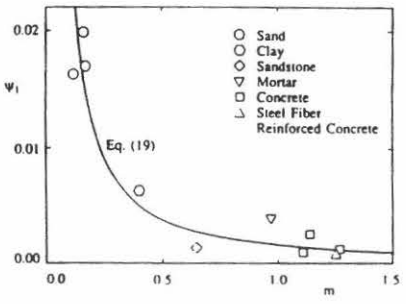

Fig. 9. Relation Between Material Parameters ψ_1 and m for Various Frictional Materials.

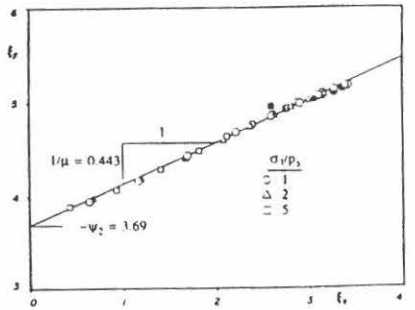

Fig. 10. Determination of Plastic Potential Parameters for Fine Silica Sand.

Since $(I_1^3/I_3) \geq 27$ and $(-I_1^2/I_2) \geq 3$ (where the equal signs hold on the hydrostatic axis) and (I_1/p_a) is always positive, the condition of irreversibility leads to the following requirements:

$$\mu > 0 \tag{15}$$

$$\psi_2 > -(27 \cdot \psi_1 + 3) \tag{16}$$

For materials with effective cohesion, the above conditions hold for the incremental plastic work done by the translated stresses. The real plastic work increment encountered in the tensile zone may be negative as indicated in Fig. 7. The incremental plastic strain vector forms an obtuse angle with the real stress vector thus resulting in a negative plastic work increment, while it forms an acute angle with the translated stress vector. However, this form of the plastic potential in the tensile stress zone never occurs if translation is retained throughout the theory. As will be explained in a companion paper, the stress state in Fig. 7 is treated as unloading and only elastic strains are produced. Thus, the condition of irreversibility is retained for cohesive materials.

PARAMETER DETERMINATION

Parameter ψ_1

As mentioned above, the parameter ψ_1 governs the shape of the plastic potential in octahedral planes. If $\psi_1 = 0$, then g describes a family of circles on the octahedral plane. If ψ_1 approaches infinity, the effect of I_2 vanishes and g_p describes a family of curves like the failure surfaces [12-15].

The incremental plastic strain angle $\omega_{\dot{\varepsilon}}$ can be derived by substitution of Eqs. (10) into Eq. (3):

$$\omega_{\dot{\varepsilon}} = \arctan \frac{\sqrt{3}\left\{\frac{I_1^2}{I_2^2}(\sigma_2 - \sigma_3) + \psi_1 \frac{I_1^3}{I_2^2}(\sigma_1\sigma_2 - \sigma_3\sigma_1)\right\}}{\frac{I_1^2}{I_2^2}(2\sigma_1 - \sigma_2 - \sigma_3) + \psi_1 \frac{I_1^3}{I_3^2}(\sigma_3\sigma_1 + \sigma_1\sigma_2 + \sigma_2\sigma_3)} \tag{17}$$

Note that the parameters μ and ψ_2 are completely eliminated. Solving Eq. (17) for ψ_1 produces:

$$\psi_1 = -\frac{I_3^2}{I_1 I_2^2} \frac{\sqrt{3}(\sigma_2 - \sigma_3) - (2\sigma_1 - \sigma_2 - \sigma_3)\tan\omega_{\dot{\varepsilon}}}{\sqrt{3}(\sigma_1\sigma_2 - \sigma_3\sigma_1) - (\sigma_3\sigma_1 + \sigma_1\sigma_2 - 2\sigma_2\sigma_3)\tan\omega_{\dot{\varepsilon}}} \tag{18}$$

Table 1 shows calculated values of ψ_1 at failure for Fuji River Sand [9]. The ψ_1-values listed in the right hand column indicate a fair amount of scatter. However, a small variation in $\omega_{\dot{\varepsilon}}$ results in a large change in ψ_1. Conversely, a change in ψ_1 does not affect the magnitude of $\omega_{\dot{\varepsilon}}$ very much. When the average value of $\psi_1 = 0.00472$ is used, the calculated values of $\omega_{\dot{\varepsilon}}$ are not much different from the measured values, as shown in Table 1. This comparison is also

Table 1. Determination of the Parameter ψ_1 for Fuji River Sand (Data from [9]).

Stress angle ω_σ (degrees)	Incremental Plastic Strain angle $\omega_{\dot{\varepsilon}}$ (degrees)		ψ_1
	Test data	Calculated Value	
15	28.1	24.1	0.00834
30	37.7	37.9	0.00451
45	52.7	49.8	0.00109
75	49.4	51.3	0.00269
90	39.6	37.9	0.00636
105	25.3	24.1	0.00561
135	21.2	22.9	0.00326
150	39.1	37.9	0.00583
165	48.8	48.7	0.00480

average $\psi_1 = 0.00472$

Table 2. Values of Parameters m and ψ_1 for Various Frictional Materials.

Material	m	ψ_1	Reference
Monterey No. 0 Sand			[17]
$D_r = 27\%$	0.12	0.01632	
$D_r = 98\%$	0.16	0.01984	
Cambria Sand	0.017	0.01697	[10]
Grundite Clay	0.4	0.00628	[18]
Mortar	0.969	0.00388	[7]
Sandstone	0.647	0.00130	[19]
Concrete	1.263	0.00122	[7]
Concrete	1.105	0.00078	[20]
Concrete	1.133	0.00250	[21]
Steel Fiber Reinforced Concrete	1.251	0.00067	[8]

shown graphically in Fig. 8. The proposed plastic potential function is seen to be consistent with the observed trend of experimental data.

Similar calculations of ψ_1 were made for various frictional materials for which three-dimensional test results were available. For materials with effective cohesion, calculation of ψ_1 proceed after stress translation according to Eq. (11). Table 2 shows that ψ_1 decreases as the rigidity of the materials increase, and the cross-section of the plastic potential surface changes from a triangular to a rounded shape. The effect of material rigidity was also observed in the characteristics of the failure surfaces. Thus, the curvature of failure surface meridians increases with increasing rigidity. This curvature is modeled by the parameter m in the failure criterion [12-15]. The values of m are listed for the various materials in Table 2, and a diagram of ψ_1 versus m is shown in Fig. 9. The relation between ψ_1 and m can be expressed as a power function:

$$\psi_1 = 0.00155 \cdot m^{-1.27} \tag{19}$$

The solid line in Fig. 9 represents the relation in Eq. (19). Recalling that the incremental plastic strain angle ω_ε is relatively insensitive to the value of ψ_1, Eq. (19) provides a reasonable approximation for the value of ψ_1. It is therefore not necessary to require results of three-dimensional tests to determine the value of ψ_1.

Parameters ψ_2 and μ

Once the parameter ψ_1 is evaluated, the other parameters, ψ_2 and μ, can be determined using triaxial compression test data. This is done by expressing the incremental plastic strain ratio defined as

$$\nu_p = -\frac{d\varepsilon_3^p}{d\varepsilon_1^p} \tag{20}$$

Substitution of Eqs. (10) for the plastic strain increments under triaxial compression conditions ($\sigma_2 = \sigma_3$) produces the following equation:

$$\xi_y = \frac{1}{\mu}\xi_x - \psi_2 \tag{21}$$

where

$$\xi_x = \frac{1}{1+\nu_p}\left\{\frac{I_1^3}{I_2^2}(\sigma_1+\sigma_3+2\nu_p\sigma_3) + \psi_1 \cdot \frac{I_1^4}{I_3^2}(\sigma_1\sigma_3+\nu_p\sigma_3^2)\right\} - 3\psi_1 \cdot \frac{I_1^3}{I_3} + 2\frac{I_1^2}{I_2} \tag{22}$$

and

$$\xi_y = \psi_1 \cdot \frac{I_1^3}{I_3} - \frac{I_1^2}{I_2} \tag{23}$$

Thus, $1/\mu$ and $-\psi_2$ can be determined by linear regression between ξ_x and ξ_y determined from several data points. Fig. 10 is a plot of ξ_x and ξ_y for the triaxial compression tests on Fine Silica Sand. All data points are consistent with Eq. (21). The value of $-\psi_2$ is the intercept value of ξ_y at $\xi_x = 0$, and the value of $1/\mu$ is the slope of the best fitting straight line.

Table 3 lists the parameter values for plastic potential functions for various materials. Only results of triaxial compression tests (including uniaxial compression tests for materials with effective cohesion) were employed in determination of parameters.

EVALUATION OF PROPOSED PLASTIC POTENTIAL FUNCTION

After the parameters are determined, the incremental plastic strains can be calculated from Eqs. (8), or from Eqs. (10) in the absence of shear stresses. In order to evaluate the plastic potential, the directions of incremental plastic strain vectors have been calculated at the measured stress points for various sets of test data. These calculated directions are compared with the measured directions on the triaxial planes, and the Lode angles on the octahedral plane are compared for three-dimensional test data.

Fig. 11(a) shows that the predicted directions of the vectors are almost identical to the measured directions for Fine Silica Sand. A rather abrupt change in volumetric strain rate near the hydrostatic axis is also predicted by the proposed cigar-shaped plastic potential function shown in Fig. 5.

Fig. 11(b) shows comparisons for uniaxial compression, biaxial compression, triaxial extension, and triaxial compression of concrete [7]. Considering that the parameters were derived from triaxial compression data, the good agreement between predicted and measured directions could be expected for these tests. In biaxial compression tests the measured vectors indicate a rather dilative behavior, and the potential is slow in capturing this pattern. However, the prediction is considered to be within reasonable range of the experimental data in view of the fact that Schickert and Winkler employed different specimen preparation methods and different testing schemes for triaxial and biaxial tests. The observed pattern of vectors correlates well with the potential function for the extension tests shown in Fig. 11(b).

Another comparison is shown for steel fiber reinforced concrete [8] in Fig. 11(c). Here the deviation between measured and predicted directions are significant in the initial loading range of some of the extension tests. It should be noted that the directions of strain increment vectors in this range is governed mainly by the elastic behavior. The elastic modulus for this material, determined from the initial slopes of the stress-strain curves, seems to be too high for this case. However, the influence of plastic strains on the stress-strain behavior in this initial loading region is negligible. Reasonable predictions within the scatter of the experimental data were obtained at higher stress levels.

In order to evaluate the plastic potential under three-dimensional loading conditions, the Lode angles at failure are compared for loose and dense Monterey No. O Sand in Fig. 12. Although the values of the parameter ψ_1 are based on the empirical Eq. (19), the predicted curves simulate the location of the experimental data very well. The density dependent variation of the angles are captured, such that the cross-sections of the plastic potential surfaces for dense sand are more triangular than those for loose sand.

Table 3. Plastic Potential Parameters ψ_1, ψ_2, and μ for Various Frictional Materials.

Material	D_r (%)	ψ_1	ψ_2	μ	Reference
Fine Silica Sand	30	0.0289	-3.69	2.26	
Sacramento River Sand	100	0.0100	-3.09	2.00	[22]
	38	0.0317	-3.72	2.36	[22]
Painted Rock Material	100	0.0113	-3.26	2.82	[23]
	70	0.0159	-3.39	2.72	[23]
Crushed Napa Basalt	100	0.0046	-2.97	2.80	[24]
	70	0.0072	-2.90	2.55	[24]
Monterey No. 0 Sand	98	0.0160	-3.38	2.30	[17]
	27	0.0229	-3.60	2.50	[17]
Edgar Kaolinite Clay		0.0034	-3.02	2.24	
Plain Concrete		0.00115	-2.77	2.51	[7]
		0.00135	-2.92	5.06	[21]
		0.00209	-3.02	4.88	[25]
		0.00119	-2.93	3.45	[20]
Steel Fiber Reinforced Concrete		0.00117	-2.58	2.63	[8]

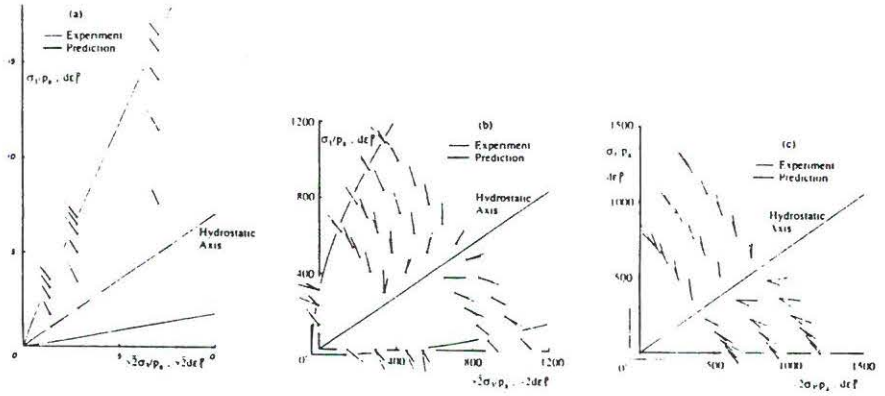

Fig. 11. Comparisons of Predicted and Observed Directions of Incremental Plastic Strain Vectors in Triaxial Plane for (a) Fine Silica Sand, (b) Plain Concrete (Data from [7]), and (c) Steel Fiber Reinforced Concrete (Data from [8]).

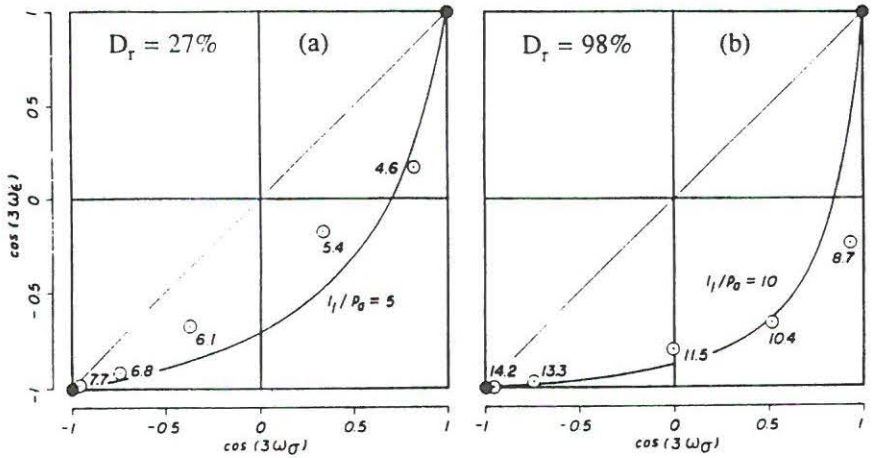

Fig. 12. Comparison of Predicted and Observed Lode Angles for (a) Loose, and (b) Dense Monterey No. 0 Sand (Data from [17]).

CONCLUSION

Based on classical concepts of incremental plasticity and careful review and evaluation of available test data, a general three-dimensional plastic potential function expressed in terms of stress invariants has been proposed. With three parameters (one of which is redundant with one of the failure surface parameters) to be determined, this cigar-shaped plastic potential is unique and continuous in stress space. This makes it applicable as an ingredient of a plasticity model without difficulty. In addition, it includes tensile behavior of cohesive materials without discontinuity or vertices except at the translated stress origin. Applied to general loading in three dimensions, it has the capability of predicting the behavior with good accuracy throughout the loading paths for many different types of frictional materials.

ACKNOWLEDGMENT

The basic developmental work presented here was supported by the National Science Foundation under Grant No. CEE 8211159. Additional developments and computational refinements were supported by Exxon Production Research Company, Houston, Texas, and by California Research and Technology, Chatsworth, California. Grateful appreciation is expressed for their support of this research.

REFERENCES

1. Saint-Venant, B.de,
Memoire sur l'etablissement des equations differentielles des mouvement interieurs operes dans les corps solides ductiles au dela des limites ou l'estasticite pourrait les ramener a leur premier etat.
Comptes Rendus Acad. Sci., Paris, 70 (1870) 473-480.

2. Melan, E.,
Plastizitaet des Raumlichen Kontinuums
Ingr.-Arch., 9 (1938) 116-126.

3. Poorooshasb, H.B., Holubec, I., and Sherbourne, A.N.,
Yielding and Flow of Sand in Triaxial Compression: Part I.
Can. Geot. J., 3 (1966) 179-190.

4. Ko, H.-Y. and Scott, R.F.,
Deformation of Sand in Shear.
J. Soil Mech. Found. Div., ASCE, 93, SM5 (1967) 283-310.

5. Lade, P.V. and Duncan, J.M.,
Stress-Path Dependent Behavior of Cohesionless Soil.
J. Geotech. Eng. Div., ASCE, 102 (1976) 51-68.

6. Lade, P.V., Nelson, R.B. and Ito, Y.M.,
Nonassociated Flow and Stability of Granular Materials.
J. Engr. Mech., ASCE, 113 (1987) 1302-1318.

7. Schickert, G. and Winkler, H.,
Results of Tests Concerning Strength and Strain of Concrete Subjected to Multiaxial Compressive Stresses.
Deutscher Ausschus fur Stahlbeton, 277 Berlin (1977).

8. Egging, D.E. and Ko, H.-Y.,
Constitutive Relations of Randomly Oriented Steel Fiber Reinforced Concrete Under Multiaxial Compressive Loadings.
University of Colorado, Boulder (1981).

9. Yamada, Y. and Ishihara, K.,
Anisotropic Deformation Characteristics of Sand Under Three-Dimensional Stress Conditions.
Soil and Foundations, JSSMFE, 19 (1979) 79-94.

10. Ochiai, H. and Lade, P.V.,
Three-Dimensional Behavior of Sand with Anisotropic Fabric.
J. Geotech. Eng. Div., ASCE, 109 (1983) 1313-1328.

11. Yong, R.N. and McKeys, E.
Yield and Failure of a Clay Under Triaxial Stresses.
J. Soil Mech. Found. Div., ASCE, 97 (1971) 159-176.

12. Lade, P.V.,
Elasto-Plastic Stress-Strain Theory for Cohesionless Soil with Curved Yield Surfaces.
Int. J. Solids Structures, Pergamon Press, 13 (1977) 1019-1035.

13. Lade, P.V.,
Three-Parameter Failure Criterion for Concrete.
J. Engr. Mech. Div., ASCE, 108 (1982) 850-863.

14. Lade, P.V.,
Failure Criterion for Frictional Materials.
Chapt. 20 in Mechanics of Engineering Materials, Ed. by C.S. Desai and R.H. Gallagher, Wiley (1984) 385-402.

15. Kim, M.K., and Lade, P.V.,
Modelling Rock Strength in Three Dimensions.
Int. J. Rock Mech. Min. Sci. & Geomech. Abstr., 21 (1984) 21-33.

16. Prager, W.,
Recent Developments in the Mathematical Theory of Plasticity.
J. Appl. Phys., 20 (1949) 235-241.

17. Lade, P.V.,
The Stress-Strain and Strength Characteristics of Cohesionless Soils.
Ph.D. Dissertation, University of California, Berkeley (1972).

18. Lade, P.V. and Musante, H.M.,
Three-Dimensional Behavior of Remolded Clay.
J. Geotech. Engr. Div., ASCE, 104 (1978) 193-209.

19. Maso, J. and Lerau, J.,
Mechanical Behavior of Darney Sandstone in Biaxial Compression.
Int. J. Rock Mech. Min. Sci. & Geomech. Abstr., 17 (1980) 109-115.

20. Aschl, H., Linse, D. and Stoeckl, S.,
Strength and Stress Strain Behavior of Concrete Under Multiaxial Compression and Tension.
Proc. 2nd Int. Conf. Mechanical Behavior of Materials, Boston Mass. (1976) 102-117.

21. Kupfer, H., Hilsdorf, H.K. and Rusch, H.,
Behavior of Concrete Under Biaxial Stresses.
J. Am. Concr. Inst., 66 (1969) 656-666.

22. Lee, K.L. and Seed, H.B.,
Drained Strength Characteristics of Sands.
J. Soil Mech. Found. Div., ASCE, 93 SM6 (1967) 117-141.

23. Al-Hussaini, M.M.,
Plane Strain and Triaxial Compression Tests on Painted Rock Dam Material.
Tech. Rep. S-71-2, No. 3, USAE, WES, Vicksburg, Miss. (1972).

24. Al-Hussaini, M.M.,
Drained Plane Strain and Triaxial Compression Tests on Crushed Napa Basalt.
Tech. Rep. S-71-2, No. 2, USAE, WES, Vicksburg, Miss. (1971).

25. Tasuji, M.E., Slate, F.O. and Nilson, A.H.,
Stress-Strain and Fracture of Concrete in Biaxial Loading.
J. Am. Concr.Inst., 75 (1978) 306-312.

Received 10 June 1988; revised version received and accepted 2 August 1988

Computers and Geotechnics 6 (1988) 13–29

SINGLE HARDENING CONSTITUTIVE MODEL FOR FRICTIONAL MATERIALS

II. YIELD CRITERION AND PLASTIC WORK CONTOURS

P.V. Lade
Department of Civil Engineering
University of California
Los Angeles, California 90024, U.S.A.

and

M.K. Kim
Department of Civil Engineering
Yonsei University
Seoul 120, Korea

ABSTRACT

A review of numerous experimental data sets for frictional materials has led to a reformulation of the condition for plastic yielding in such materials. A yield function is proposed such that yield surfaces are equivalent to plastic work contours. Two parameters are required in this function. The yield surface resembles an asymmetric tear drop in the principal stress space. It includes tensile behavior of materials with effective cohesion. Work hardening and softening behavior can be simulated through the formulation of plasticity proposed herein. The capabilities of this mathematically consistent formulation are examined by comparisons with experimental data from two- and three-dimensional tests on different frictional materials.

INTRODUCTION

The development of elasto-plastic stress-strain theories for engineering materials requires a criterion to describe the conditions for which plastic yielding occurs. Various criteria expressing combinations of multiaxial stresses that will cause yielding have been proposed in the literature, e.g. [1-12]. These criteria have most often been based on experimental observations, sometimes in combination with assumptions about the type of plastic behavior exhibited by the material (associated or nonassociated flow). Identification of yield points from measured stress-strain curves and combination of these points to form yield surfaces are not always simple. There are two reasons why it may be difficult to identify suitable yield surfaces: (1) Since yielding is a continuous process for frictional materials, there may not be a distinct yield point on a stress-strain curve. (2) In the plasticity theory, yield surfaces must be associated with hardening (and softening) parameters such that the combination uniquely defines the magnitude of incremental plastic strains.

Computers and Geotechnics 0266-352X/88/$03·50

Two methods of identification of yield points and yield surfaces in stress space are reviewed. Plastic yield points for primary loading are then compared to a yield criterion developed to describe contours of plastic work as determined from results of triaxial tests.

OBSERVED YIELD BEHAVIOR FOR SOILS

The existence and shapes of yield surfaces in stress space have been studied often since plasticity theory has been found effective in modeling deformation of frictional materials. Two important studies of yield behavior of soils are reviewed below.

Tatsuoka and Ishihara [13] presented results and analyses of triaxial compression tests on Fuji River Sand at three densities. The different types of stress paths used in their study are summarized in Fig. 1(d). A specimen was first triaxially compressed up to a certain stress level, unloaded at constant confining pressure, then loaded again at a different confining pressure. On a diagram of deviator stress ($\sigma_1-\sigma_3$) versus shear strain ($\varepsilon_1-\varepsilon_3$) obtained for reloading, two approximately linear portions were extended near the sudden increase in strains, and a yield point was located at the intersection. Connecting this yield point with the previous maximum stress point, a portion of a yield surface was established. They analyzed an extensive set of test data and found a series of curved yield surfaces as shown in the nondimensional p′–q diagrams in Fig. 1 for (a) loose, (b) medium dense, and (c) dense Fuji River Sand. In these diagrams, p_a is atmospheric pressure in the same units as p′ and q. Note that the yield surfaces exhibit varying curvature with stress level, and they do not coincide with the failure envelope. Instead they deviate from and cross the failure envelope, and they are more curved than the failure envelope.

Parry and Nadarajah [14] performed a series of tests on lightly overconsolidated specimens of kaolin. Each specimen was subjected to a different stress path. In a diagram of stress versus volumetric strains, a yield point was located in the same manner as done by Tatsuoka and Ishihara [13]. The resulting yield points were connected to form a cap shaped volumetric yield surface in a triaxial plane as shown in Fig. 2. This cap shaped yield surface is more curved than those shown in Fig. 1, and it cuts across the hydrostatic axis. However, it should be noted that plastic shear strains are not accounted for in this yield locus. Roscoe and Burland [2] performed similar tests examining the plastic shear strains. Their results indicated that significant plastic shear deformation could occur inside the volumetric yield locus.

PLASTIC WORK CONTOURS

As noted in the previous section, a yield criterion in an elasto-plastic model should not only simulate yield surfaces derived under various types of assumptions, but it should also be uniquely related to the hardening and softening characteristics of the materials. An obstacle in achieving these dual goals is that it is not a simple task to investigate yield behavior of the material under various reloading conditions including three-dimensional loading conditions.

An alternative is to examine the contours of the hardening parameters and to compare them with experimental data for yield surfaces. Huang [15] described a study of this type involving contours. In the study presented here the plastic work is used as the hardening parameter.

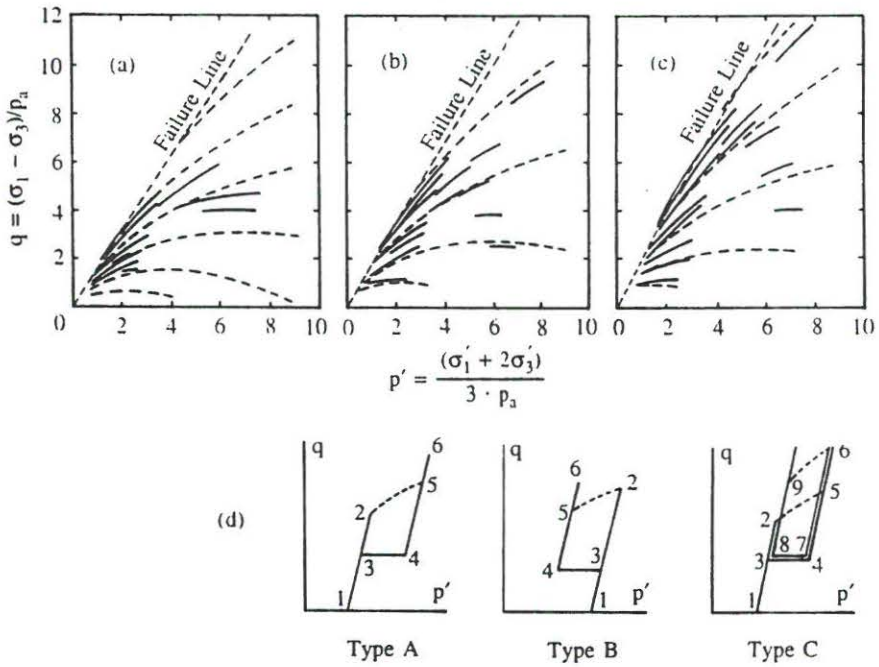

Fig. 1. Observed Yield Loci in p-q Diagram for (a) Loose, (b) Medium Dense, and (c) Dense Fuji River Sand, and (d) Stress-Paths used in Triaxial Tests [13].

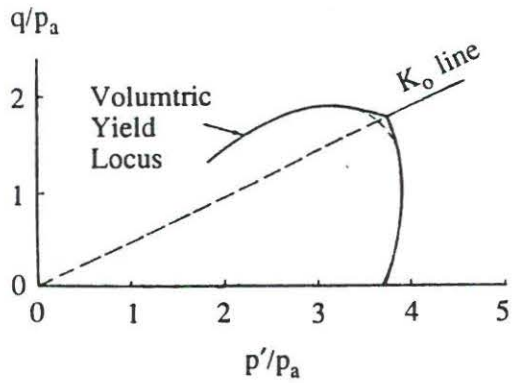

Fig. 2. Observed Volumetric Yield Surface in p-q Diagram for Lightly Overconsolidated Kaolin [14].

Using plastic work contours in the study of yield behavior of a material has several advantages. It does not involve tests with complicated stress-paths and it also avoids difficulties in determination of yield points on stress-strain curves. In comparison, computation of plastic work is straight forward, and the plastic work contours appear to capture yielding in terms of shear strains as well as volumetric strains.

Before further discussion of plastic work contours, it may be advantageous to study the plastic work during isotropic compression tests. An isotropic compression test involves a simple stress path in which the normal stresses are equal in all directions, and the data from this test may serve as a guide in plotting the plastic work contours. Isotropic compression of soil produces partly elastic and partly plastic deformations. The plastic work done by the isotropic pressure increases monotonically as the pressure increases. This plastic work may be modeled by a power function of pressure [4]:

$$W_p = C \cdot p_a \cdot \left(\frac{I_1}{p_a}\right)^p \qquad (1)$$

where I_1 is the first invariant of stresses which is three times the isotropic pressure, p_a is atmospheric pressure expressed in the same unit as W_p and I_1, and C and p are dimensionless parameters to be determined. The parameters C and p can be determined by plotting the variation of W_p/p_a and I_1/p_a in a log - log diagram and fitting a straight line, as shown in Fig. 3. The magnitude of C is the value of W_p/p_a at $I_1/p_a = 1$ and the value of p is the slope of the fitted line. Fig. 4 shows the variation of plastic work during an isotropic compression test on Fine Silica Sand (e=0.76) together with the modeling curve from Eq. (1). It can be seen that Eq. (1) models the work-hardening behavior in isotropic compression reasonably well. Eq. (1) is used in the following to determine values of W_p/p_a whenever the isotropic compression condition occurs.

Fig. 5 shows the data for plastic work obtained from three triaxial compression tests on Fine Silica Sand with confining pressures of 1, 2, and 5 kg/cm^2, respectively. For stress states near isotropic compression, i.e. at low stress levels, the plastic work increases slowly with increasing shear stress. As the shear stress increases further, however, the rate of plastic work increases rapidly until it reaches the failure state denoted by shaded circles in the figure. A family of contours can be drawn to connect stress points with the same values of W_p/p_a. It should be noted that the failure surface is not one of these contours. The value of W_p/p_a at failure increases as the confining pressure increases. Consequently, each plastic work contour crosses the failure envelope at a very shallow angle and gradually deviates from it as I_1/p_a increases.

The results of four undrained tests on normally consolidated, remolded Edgar Kaolinite Clay are shown in Fig. 6. A pattern similar to that observed for sand is seen in this figure. However, the plastic work contours enclose areas which are shorter and more rounded. This could be expected, because volume changes and therefore plastic work under isotropic compression are relatively larger for clay than for sand.

Fig. 7 shows the variation of plastic work on an octahedral plane for cubical triaxial tests on Fuji River Sand performed by Yamada and Ishihara [16]. These tests were all performed in the same octahedral plane, i.e. with constant mean normal stress. The specimens were prepared anisotropically, hence, a slight anisotropy can be seen in the figure. The underlying isotropic behavior was discussed by Lewin et al. [17]. However, the data reported by Yamada and Ishihara [16] are adopted without any correction, because only the behavior pattern is of concern at this stage. Qualitatively, the contours have circular shapes at low stress levels and they gradually change into rounded triangular shapes as the stress level increases up to failure. At the

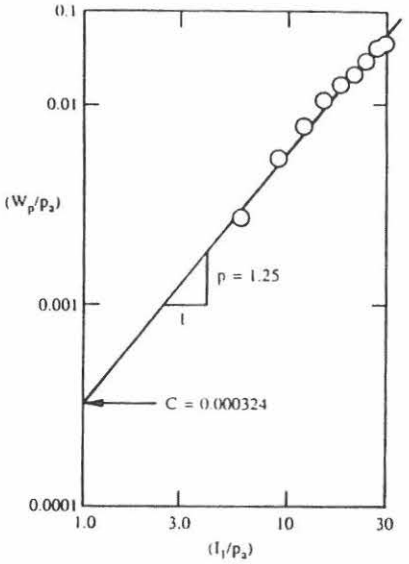

Fig. 3. Determination of Parameters C and p in Hardening Law for Fine Silica Sand.

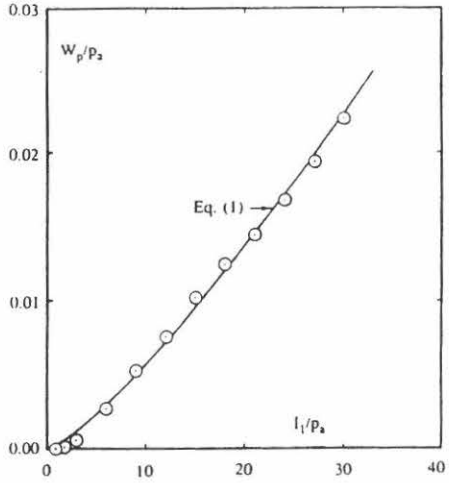

Fig. 4. Comparison of Predicted and Observed Variation of Plastic Work in Isotropic Compression Test on Fine Silica Sand.

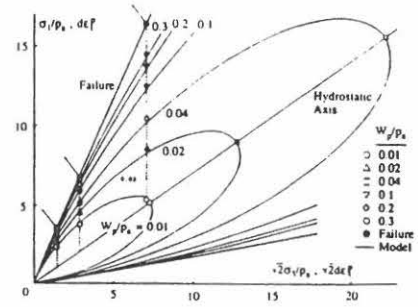

Fig. 5. Experimental Data Points and Contours of Constant Plastic Work Shown on Triaxial Plane for Fine Silica Sand.

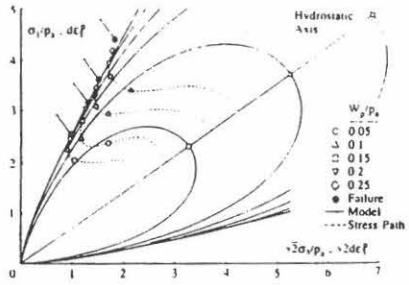

Fig. 6. Experimental Data Points and Contours of Constant Plastic Work Shown on Triaxial Plane for Undrained Tests on Edgar Kaolinite Clay.

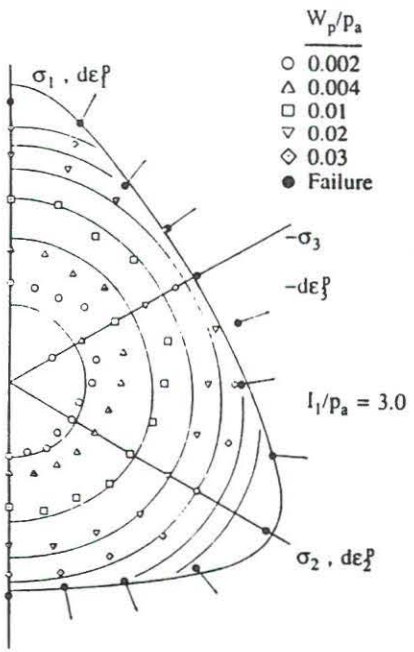

Fig. 7. Experimental Data Points and Contours of Constant Plastic Work Shown on Octahedral Plane for Fuji River Sand (Data from[16]).

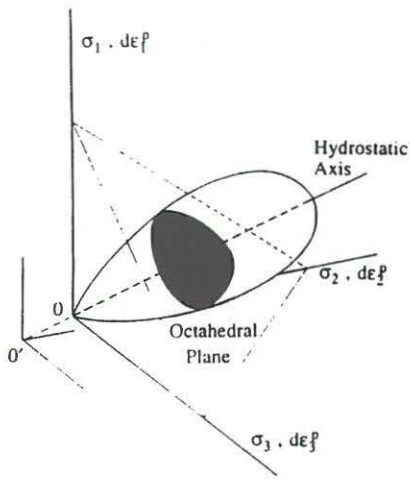

Fig. 8. Schematic Illustration of the Proposed Yield Surface in Principal Stress Space.

Table 1. Calculation of Yield Parameter h for Fine Silica Sand.

Triaxial Compression (B)			Isotropic Compression (A)	h
W_p/p_a	σ_3/p_a	σ_1/p_a	I_1/p_a	
0.313	1.00	3.55	244.2	0.348
0.739	2.00	6.81	485.6	0.341
0.582	2.00	6.74	401.2	0.356
1.401	5.00	16.42	810.3	0.373

Average h = 0.355

failure states, the values of W_p/p_a differ from each other on the same octahedral plane. The plastic work contours have more rounded shapes than the failure envelope.

The shapes of the plastic work contours generally agree with the shapes of the yield surfaces observed in unloading - reloading tests as reviewed in the previous section. The plastic work contours also resemble the material-dependent shapes of the yield surfaces: Contours for clay are shorter and more curved than those for sand.

It is interesting to check the normality of incremental plastic strain vectors to the yield surfaces, or equivalently, to the plastic work contours. The directions of the incremental plastic strain vectors at failure are drawn in Figs. 5 through 7. In Fig. 7 the directions of these vectors appear to coincide with the normal directions to the plastic work contours. However, on the triaxial planes shown in Figs. 5 and 6, the vectors are not normal to the plastic work contours. The directions normal to the yield surfaces at failure correspond to more dilation of the material than measured in experiments. This observation makes it necessary to employ a nonassociated flow rule.

PROPOSED YIELD CRITERION AND HARDENING LAW

Fig. 7 shows that the plastic work contours near failure have more rounded shapes than the failure surface, and that the directions of incremental plastic strain vectors are normal to the plastic work contours. Thus, a possible function to describe the plastic work contours, or a yield function in terms of stress is:

$$f_p' = \left(\psi_1 \cdot \frac{I_1^3}{I_3} - \frac{I_1^2}{I_2}\right) \cdot \left(\frac{I_1}{p_a}\right)^h \cdot e^q \qquad (2)$$

in which ψ_1 was determined in a companion paper dealing with a plastic potential function for frictional material [18]. This parameter controls the relative influence of the two terms within the parentheses, and it is used to model the normality condition on the octahedral plane. The second and third terms are introduced to model the meridional curvature of the yield surface. The value of h is constant and q is variable.

The yield surface is shaped as an asymmetric tear drop with a smoothly rounded triangular cross-section as shown in Fig. 8. The yield surface is continuous throughout stress space except at the origin ($\sigma_1 = \sigma_2 = \sigma_3 = 0$).

A family of yield surfaces described by Eq. (2) is drawn in Fig. 7 for a value of $\psi_1 = 0.00472$ for Fuji River Sand. The contours shown as yield surfaces were drawn for several constant values of f_p' in Eq. (2) and they are not directly related to the values of plastic work. However, the yield function describes the pattern of the plastic work contours reasonably well. The experimental points on Fig. 7 indicate anisotropic behavior as mentioned above, whereas Eq. (2) describes isotropically expanding yield surfaces. This yield function is suitable for an isotropic work-hardening stress-strain model.

The parameter q in Eq. (2) is devised as a function of stress level such that

$q = 0$ during isotropic compression
$0 < q < 1$ during hardening
$q = 1$ at failure stresses

The variation of q in the hardening regime will be investigated later. Once q = 1, a switch to a softening relation is effectuated. This is also discussed later.

For an isotropic compression state the value of f_p' in Eq. (2) is

$$f_p' = (27 \cdot \psi_1 + 3) \cdot \left(\frac{I_1}{p_a}\right)^h \tag{3}$$

Using this expression, the plastic work equation for isotropic compression (Eq. (1)) can be generalized as:

$$W_p = D \cdot p_a \cdot f_p''^{\rho} \tag{4a}$$

or

$$f_p'' = \left(\frac{1}{D}\right)^{1/\rho} \cdot \left(\frac{W_p}{p_a}\right)^{1/\rho} \tag{4b}$$

in which

$$D = \frac{C}{(27\psi_1 + 3)^{\rho}} \tag{5}$$

and

$$\rho = p/h \tag{6}$$

Eq. (4) provides a unique relation between the yield criterion, f_p'', and the plastic work, W_p, and serves as a work-hardening relation for all stress states.

PARAMETER DETERMINATION FOR YIELD CRITERION

Of the parameters that enter into the yield criterion only the constant value of h and the variation of q remain to be determined.

Constant Parameter h

Consider two stress points A and B on the same plastic work contour. Since these points are also located on the same yield surface, then ($f_{pA}' = f_{pB}'$):

$$\left(\psi_1 \cdot \frac{I_{1A}^3}{I_{3A}} - \frac{I_{1A}^2}{I_{2A}}\right) \cdot \left(\frac{I_{1A}}{p_a}\right)^h \cdot e^{q_A} = \left(\psi_1 \cdot \frac{I_{1B}^3}{I_{3B}} - \frac{I_{1B}^2}{I_{2B}}\right) \cdot \left(\frac{I_{1B}}{p_a}\right)^h \cdot e^{q_B} \tag{7}$$

where subscripts A and B denote the stresses at points A and B, respectively. If point A on the hydrostatic axis (where q = 0) and B on the failure envelope (where q = 1) are two points on the same plastic work contour, then

$$(27\psi_1+3) \left(\frac{I_{1A}}{p_a}\right)^h = \left(\psi_1 \cdot \frac{I_{1B}^3}{I_{3B}} - \frac{I_{1B}^2}{I_{2B}}\right) \left(\frac{I_{1B}}{p_a}\right)^h \cdot e \tag{8}$$

and therefore,

$$h = \log \frac{\left(\psi_1 \cdot \frac{I_{1B}^3}{I_{3B}} - \frac{I_{1B}^2}{I_{2B}}\right) \cdot e}{27\psi_1 + 3} \Big/ \log \frac{I_{1A}}{I_{1B}} \tag{9}$$

in which e is the base of natural logarithms. Table 1 shows the calculation of h for Fine Silica Sand based on four sets of failure stresses (point B) and four corresponding points on the hydrostatic axis (point A). The stresses at the latter points are determined from Eq. (1) based on constant amounts of plastic work along each contour. Thus, the total plastic work at failure (listed in column 1) from a triaxial compression test is used in Eq. (1) to determine the corresponding isotropic state of stress. Table 1 shows that an average value of h = 0.355 is reasonably representative of the individual values determined from Eq. (9).

Variation of q

The value of q varies with stress level S defined as:

$$S = f_n/\eta_1 = \frac{1}{\eta_1} \cdot (I_1^3/I_3 - 27) \left(\frac{I_1}{p_a}\right)^m \tag{10}$$

in which f_n is the function used to express failure for frictional materials [4, 19-21] and η_1 is the value of f_n at failure. The stress level S varies from zero at the hydrostatic axis to unity at the failure surface.

The value of q can now be determined from the test data using Eqs. (2) and (4):

$$q = ln \frac{\left(\frac{W_p}{D \cdot p_a}\right)^{1/\rho}}{\left(\psi_1 \cdot \frac{I_1^3}{I_3} - \frac{I_1^2}{I_2}\right)\left(\frac{I_1}{p_a}\right)^h} \tag{11}$$

Fig. 9 shows the variation of q with stress level S for Fine Silica Sand. Only the portion in the range $0 \le q \le 1$ is of importance, since a different relation between yielding and plastic work is employed in the softening range (discussed blow). In the hardening region the variation may be described by a hyperbolic expression:

$$S = \frac{q}{\alpha + \beta \cdot q} \tag{12}$$

Since the curve passes through (1,1), the value of $\beta = 1 - \alpha$. The best determination of α is

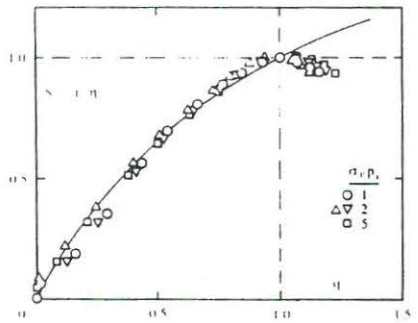

Fig. 9. Observed and Modeled Relation between S and q for Fine Silica Sand.

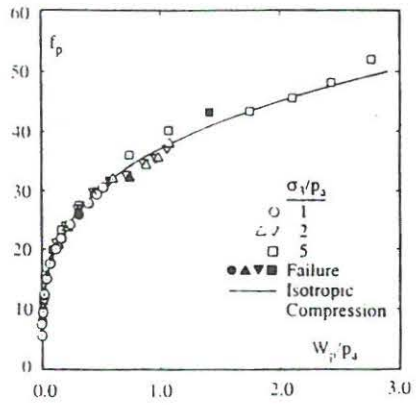

Fig. 10. Comparison of Analytical Hardening Curve Determined from Isotropic Compression Test and Experimental Data from Triaxial Compression Tests on Fine Silica Sand.

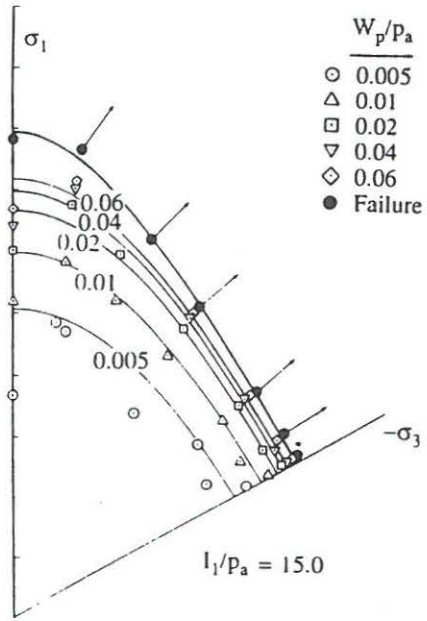

Fig. 11. Comparison of Analytical Contours of Plastic Work with Experimental Data Projected on Octahedral Plane for Dense Monterey No. 0 Sand (Data from [22]).

obtained at a stress level S = 0.80. Substitution in Eq. (12) produces

$$\alpha = \frac{1-S}{S} \cdot \frac{q_s}{1-q_s} = \frac{1}{4} \cdot \frac{q_{80}}{1-q_{80}} \tag{13}$$

For Fine Silica Sand $q_{80} = 0.67$ producing $\alpha = 0.515$. Finally, q is expressed as:

$$q = \frac{\alpha \cdot S}{1-(1-\alpha)\cdot S} \tag{14}$$

With determination of the parameters h and q, the yield function in Eq. (2) is defined and the plastic work during the yielding process can be determined from Eq. (4).

EVALUATION OF PROPOSED YIELD FUNCTION

Four parameters are required to determine the yield-plastic work relation: h and α to define the yield function, and C and p to define the plastic work equation for isotropic compression. The validity and flexibility of the proposed yield function and the plastic work relation can be examined in several independent ways as follows.

The plastic work contours described through the yield function in Eq. (2) have been compared with the experimental points on the triaxial planes in Figs. 5 and 6. The important aspects of the behavior of frictional materials in terms of the plastic work are well captured by the model, including the plastic work during isotropic compression, the slow increase in plastic work at low shear stress levels, and the pressure-dependent amount of plastic work at the peak stress state.

In the development of this model, the basic assumption is that, if yield surfaces are defined properly, the amount of plastic work during yielding may be defined uniquely. This assumption is examined quantitatively in Fig. 10 where the values of f_p' and W_p/p_a calculated from triaxial compression data are compared with those modeled through an isotropic compression test. It is seen that a unique, monotonic relation exists between yield and plastic work, and this relation is modeled through Eq. (4) with f_p' and W_p defined by Eqs. (2) and (1), respectively.

Plastic work under three-dimensional stress states is simulated through the parameter ψ_1 which depends on the rigidity of the material. The three-dimensional behavior is examined in Fig. 11 where experimental and predicted values of plastic work for the tests on Dense Monterey No. 0 Sand (D_r = 98%) [22] are compared on the octahedral plane. Because the stress points do not lie on the same octahedral plane, the data points are projected onto a common octahedral plane (I_1/p_a = 15) following the meridians of the proposed yield function (intersection of a yield surface and a constant $b = (\sigma_2-\sigma_3)/(\sigma_1-\sigma_3)$ plane). That is, a projected stress point possesses the same value of f_p' as the original data point. A pattern similar to that in Fig. 7 for Fuji River Sand can be seen. Although relatively higher test values of plastic work appear under triaxial compression conditions, the observed and modeled values of plastic work correspond to each other within a reasonable range. It is worth mentioning that the experimental stress points lie on the octahedral planes whose I_1/p_a values vary from 1.8 to 13.3. Thus, discrepancies between observed and modeled values appear larger on the plane of I_1/p_a = 15 than the real discrepancies.

In order to check if the plastic work contours are equivalent to yield surfaces, an independent test was performed on Fine Silica Sand. A specimen was isotropically consolidated up to 10 kg/cm^2 and unloaded isotropically to 1 kg/cm^2. That is, the specimen was prepared with an overconsolidation ratio of 10. Then, triaxial compressive loading was applied up to failure while maintaining the cell pressure at 1 kg/cm^2. The resulting stress-strain curve is compared with that from a normally consolidated specimen in Fig. 12(a). The overconsolidated specimen exhibits a stress range of small deformation which may be considered to be mainly elastic. A yield stress of σ_y = 2.5 kg/cm^2 can be located using a technique similar to that reviewed in the beginning of this paper. This stress state is shown on the triaxial plane in Fig. 12(b) together with the yield surface or plastic work contour corresponding to the initial preconsolidation of 10 kg/cm^2 and described by Eq. (2). The yield stress σ_y lies exactly on the predicted yield surface.

Finally, the yield surfaces reported by Tatsuoka and Ishihara [13] have been simulated using the proposed yield function. The experimental yield surfaces for loose Fuji River Sand are replotted as broken curves in Fig. 13 while the family of curves described by Eq. (2) are plotted as continuous curves. Some disagreement can be observed between experimental and analytical surfaces close to the hydrostatic axis. However, the stress paths adopted by Tatsuoka and Ishihara [13] in this region are sensitive to volumetric strains while more emphasis was placed on the shear strains in their investigation. If yield points were located according to volumetric strains, the yield surfaces would have more curvature and be more perpendicular to the hydrostatic axis. This argument agrees with the observation of Tatsuoka and Ishihara [13] who noted that their yield surfaces are correct as long as yielding is defined in terms of shear deformation. Except for the stress region near the hydrostatic axis, the proposed yield surfaces agree with their observed yield surfaces. Using the plastic work contours as yield surfaces takes into account effects of shear as well as volumetric strains.

SOFTENING BEHAVIOR

The evaluation of the yield criterion was performed in the hardening regime where the soil behavior has been studied experimentally and is reasonably well-known. Much less is known about the soil behavior in the softening regime. However, soils are known to exhibit peak failure and reduction in strength while deforming uniformly under certain conditions including triaxial compression stress states. The actual movement and shape of the yield surface after peak failure have not been studied experimentally in the past.

The simplest possible behavior may be described as isotropic softening following the pattern indicated on Fig. 14. Softening may begin anywhere along the monotonically increasing hardening curve and is initiated when q = 1, which in turn occurs when the stress level reaches unity (S=1) at the failure surface. The softening curve is described by an exponential decay function

$$f_p'' = A \cdot e^{-B\cdot(W_p/p_a)} \qquad (15)$$

in which A and B are positive constants. These are devised such that no additional material parameters are required. This seems reasonable in view of the limited knowledge about the actual softening behavior. However, to capture the experimentally observed pattern of greater relative strength decay at lower confining pressures, the slope of the softening curve is set equal to the negative slope of the hardening curve at the point of failure. Since the softening curve also intersects the hardening curve at the peak point, the following expressions for A and B can be derived:

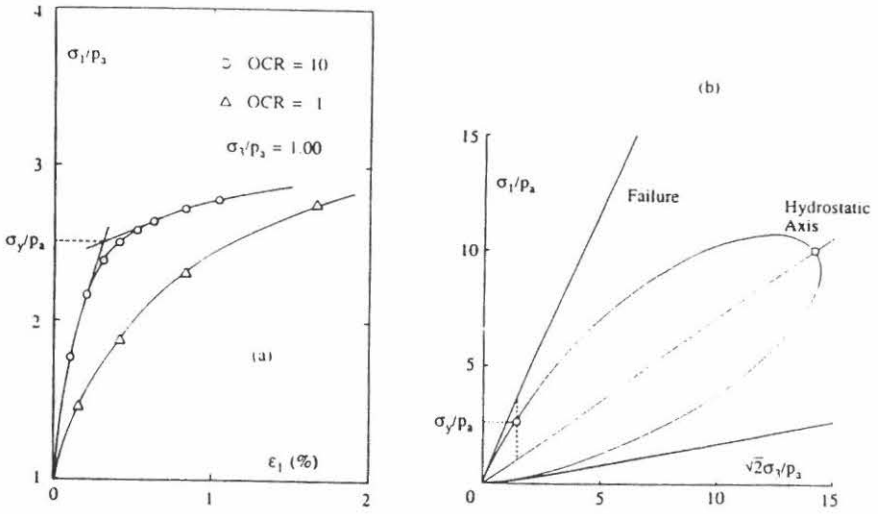

Fig. 12. (a) Stress-Strain Curves from Triaxial Compression Tests on Normally Consolidated and Overconsolidated (OCR = 10) Specimens of Fine Silica Sand, and (b) Comparison of Yield Stress (σ_y/p_a) with Yield Surface Produced by Overconsolidation (OCR = 10) of Fine Silica Sand.

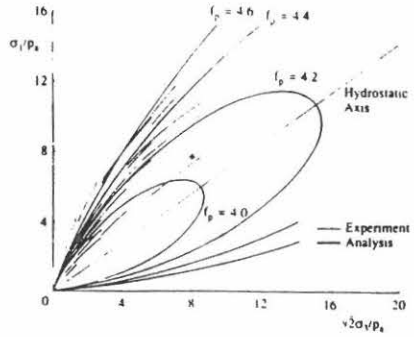

Fig. 13. Comparison of Analytical and Observed Yield Surfaces for Loose Fuji River Sand (Data from [13]).

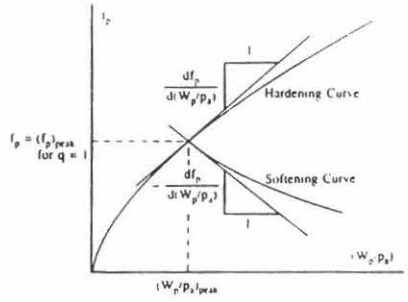

Fig. 14. Modeling of Work-Hardening and -Softening.

$$A = (f'_p)_{peak} \cdot e^{B\cdot(W_p/p_a)_{peak}} \tag{16}$$

$$B = \left[\frac{df''_p}{d(W_p/p_a)}\right]_{hard,peak} \cdot \frac{1}{(f'_p)_{peak}} \tag{17}$$

The transition from hardening to softening occurs abruptly at the peak failure point. Thus, there are no points with zero slope at the transition anywhere along the hardening curve. The absence of points with zero slope allows greater computational efficiency near peak failure, while the pointed peak is hardly noticeable in actual comparisons with experimental data.

MATERIALS WITH EFFECTIVE COHESION

The proposed yield function and hardening equation may also be employed for materials with effective cohesion. This requires a translation of the principal stress space as demonstrated for the failure criterion [19-21] and for the plastic potential function [18].

If the yield and plastic potential surfaces are treated in the same way as the failure surface, then inconsistencies in the condition of irreversibility may arise. This was discussed in detail in the companion paper [18]. Further inconsistencies in the plastic behavior of materials with effective cohesion are overcome by assuming that there exists an initial yield surface which goes through the origin of the real stress space as shown in Fig. 15. This implies that only elastic strains occur during major portions of tension type tests in which the main parts of the stress-paths are located inside the yield surface. Fig. 16 shows the stress-strain curves obtained from three types of biaxial tension tests on concrete by Kupfer et al. [23]. The strains observed in these tests are almost linear elastic. Small deviations from linear elastic behavior occur prior to the abrupt tensile failure experienced in these tests. Thus, the stresses applied along the stress-paths indicated in Fig. 15 do not produce plastic strains until they are close to failure. The existence of an initial yield surface therefore appears to simulate experimental observations of the type shown in Fig. 16 with good accuracy.

It is therefore assumed that the translated stresses represent the stress components in the development of the constitutive model for frictional materials with effective cohesion. Then, the translated plastic work may be defined as the work done by the translated stresses through the process of plastic deformation:

$$\overline{W}_p = \int \bar{\sigma}_{ij} d\varepsilon^p_{ij} \tag{18}$$

and substitution of the translated stresses produces

$$d\overline{W}_p = (\sigma_{ij} + a\cdot p_a\cdot\delta_{ij})\, d\varepsilon^p_{ij} = dW_p + a\cdot p_a\cdot d\varepsilon^p_v \tag{19}$$

Physically, it has not been shown that such work exists, but this approach provides a convenient tool for mathematical treatment of cohesive materials. Eq. (19) implies that work is done by an imaginary preload '$a\cdot p_a$' through the loading process. Since the plastic work is defined in terms of translated stresses, the yield function and the hardening equation can be generalized by substituting the translated stresses in place of the real stresses. For cohesionless materials for which 'a' vanish, all terms of the theory return to hold conventional physical meaning.

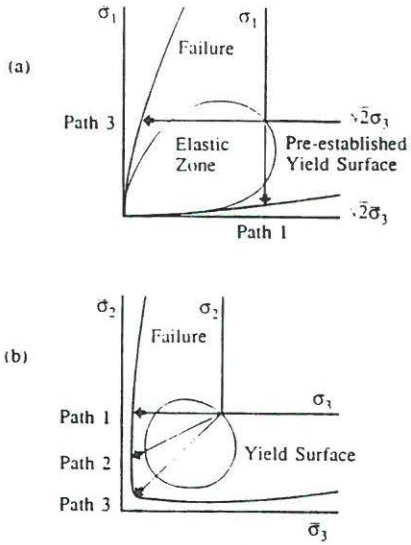

Fig. 15. Biaxial Stress Paths for Concrete Employed by Kupfer et al. [23] and Assumed Initial Yield Surface in (a) Triaxial Plane, and (b) Biaxial Plane.

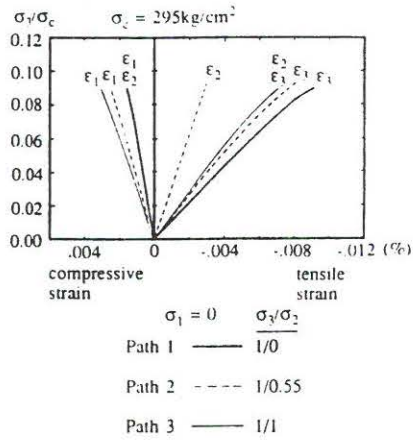

Fig. 16. Stress-Strain Relations Obtained from Biaxial Tension Tests on Concrete by Kupfer et al. [23].

CONCLUSION

The yield behavior of frictional materials has been examined phenomenologically as well as mathematically. A yield function is proposed as a result of the consideration that yield surfaces are equivalent to plastic work contours. Work hardening and softening behavior can be simulated through the formulation of plasticity proposed herein. Various independent checks are made to examine the validity of the formulation. The formulation is also extended to cohesive materials using translation of stresses. Consistency with mathematical work-hardening plasticity is retained.

ACKNOWLEDGMENT

The basic developmental work presented here was supported by the National Science Foundation under Grant No. CEE 8211159. Additional developments and computational refinements were supported by Exxon Production Research Company, Houston, Texas, and by California Research and Technology, Chatsworth, California. Grateful appreciation is expressed for their support of this research.

REFERENCES

1. Drucker, D.C., Gibson, R.E. and Henkel, D.J.,
Soil Mechanics and Work-Hardening Theories of Plasticity.
ASCE Transactions, 122 (1957) 338-346.

2. Roscoe, K.H. and Burland, J.B.,
On the Generalized Stress-Strain Behaviour of 'Wet' Clay.
In: Engineering Plasticity, Ed. by J. Heymann and F.A. Leckie, Cambridge University Press, Cambridge (1968) 535-609.

3. DiMaggio, F.L. and Sandler, I.S.,
Material Model for Granular Soils.
J. Engr. Mech. Div., ASCE, 97 (1971) 935-950.

4. Lade, P.V.,
Elasto-Plastic Stress-Strain Theory for Cohesionless Soil with Curved Yield Surfaces.
Int. J. Solids Struct., 13 (1977) 1019-1035.

5. Zienkiewicz, O.C. and Pande, G.N.,
Some Useful Forms of Isotropic Yield Surfaces for Soil and Rock Mechanics.
In: Finite Elements in Geomechanics, Ed. by G. Gudehus, Wiley, New York (1977) 179-190.

6. Prevost, J.-H.,
Plasticity Theory for Soil Stress-Strain Behavior.
J. Engr. Mech. Div., ASCE, 104 (1978) 1177-1194.

7. Dafalias, Y.F. and Herrmann, L.R.,
A Bounding Surface Soil Plasticity Model.
Proc. Int. Symp. Soils under Cyclic and Transient Loading,
Balkema, Rotterdam (1980) 335-345.

8. Mroz, Z., Norris, V.A. and Zienkiewicz, O.C.,
An Anisotropic, Critical State Model for Soils Subject to Cyclic Loading.
Geotechnique, 31 (1981) 451-469.

9. Ghaboussi, J. and Momen, H.,
Modelling and Analysis of Cyclic Behavior of Sands.
In: Soil Mechanics – Transient and Cyclic Loads, Ed. by G.N. Pande and O.C. Zienkiewicz, Wiley, London (1982) 313-342.

10. Pande, G.N. and Pietruszak, S.,
Reflecting Surface Model for Soils.
Proc. Int. Symp. Numerical Models in Geomechanics, Balkema, Rotterdam (1982) 50-64.

11. Poorooshasb, H.B. and Pietruszak, S.
On Yielding and Flow of Sand; A Generalized Two-Surface Model.
Computers and Geotechnics, 1 (1985) 33-58.

12. Frantziskonis, G., Desai, C.S. and Somasundaram, S.,
Constitutive Model for Nonassociate Behavior.
J. Engr. Mech., ASCE, 112 (1986) 932-946.

13. Tatsuoka, F. and Ishihara, K.,
Yielding of Sand in Triaxial Compression.
Soils and Foundations, JSSMFE, 14 (1974) 63-76.

14. Parry, R.H.G. and Nadarajah, V.,
A Volumetric Yield Locus for Lightly Overconsolidated Clay.
Geotechnique, 23 (1973) 450-453.

15. Huang, W.,
Effect of Work Hardening Rules on the Elasto-Plastic Matrix.
Proc. Int. Symp. on Soils under Cyclic and Transient Loading, Balkema, Rotterdam (1980) 277-282.

16. Yamada, Y. and Ishihara, K.,
Anisotropic Deformation Characteristics of Sand under Three Dimensional Stress Conditions.
Soils and Foundations, JSSMFE, 19 (1979) 79-94.

17. Lewin, P.I., Yamada, Y. and Ishihara, K.
Correlating Drained and Undrained 3D Tests on Loose Sand.
IUTAM Conf. on Deformation and Failure of Granular Materials, Delft (1982) 419-429.

18. Kim, M.K. and Lade, P.V.,
Single Hardening Constitutive Model for Frictional Materials, I. Plastic Potential Function.
Computers and Geotechnics

19. Lade, P.V.,
Three-Parameter Failure Criterion for Concrete.
J. Engr. Mech. Div., ASCE, 108 (1982) 850-863.

20. Lade, P.V.,
Fiailure Criterion for Frictional Materials.
Chapt. 20 in Mechanics of Engineering Material, Ed. by C.S. Desai and R.H. Gallagher, Wiley (1984) 385-402.

21. Kim, M.K. and Lade, P.V.,
Modelling Rock Strength in Three Dimensions.
Int. J. Rock Mech. Min. Sci. & Geomech. Abstr., 21 (1984) 21-33.

22. Lade, P.V.,
The Stress-Strain and Strength Characteristics of Cohesionless Soils.
Ph.D. Dissertation, University of California, Berkeley (1972).

23. Kupfer, H., Hilsdorf, H.K. and Rusch, H.,
Behavior of Concrete Under Biaxial Stresses.
J. Am. Concr. Inst., 66 (1969) 656-666.

Received 10 June 1988, revised version received and accepted 2 August 1988

Computers and Geotechnics 6 (1988) 31–47

SINGLE HARDENING CONSTITUTIVE MODEL FOR FRICTIONAL MATERIALS

III. COMPARISONS WITH EXPERIMENTAL DATA

P.V. Lade
Department of Civil Engineering
University of California
Los Angeles, California 90024,U.S.A.

and

M.K. Kim
Department of Civil Engineering
Yonsei University
Seoul 120, Korea

ABSTRACT

A unified constitutive model for the behavior of frictional materials is described. The model is based on concepts from elasticity and plasticity theories. In addition to Hooke's law for the elastic behavior, the framework for the plastic behavior consists of a failure criterion, a nonassociated flow rule, a yield criterion that describes contours of equal plastic work, and a work-hardening/softening law. The functions that describe these components are all expressed in terms of stress invariants. The model incorporates twelve parameters which can all be determined from simple experiments such as isotropic compression and conventional triaxial compression tests. Validation of the model is achieved by comparison of predicted and measured stress-strain curves for various two- and three-dimensional stress-paths obtained for different types of frictional materials.

INTRODUCTION

Development of constitutive models for the time-independent behavior of frictional materials has most often been based on experimental observations of material behavior and on a framework of elasticity and plasticity theories. The combination of experiment and theory has been employed with varying emphasis depending on access to experimental results, interpretation of physical concepts, and inclination towards mathematical developments. A number of models have therefore resulted with various capabilities relative to observed material behavior. The models contained in references [1-11] are representative of the types and capabilities presented in the literature.

Computers and Geotechnics 0266-352X/88/$03·50

The constitutive model presented here has been developed on the basis of a thorough review and evaluation of data from experiments on frictional materials such as sand, clay, concrete and rock. The framework for the evaluation and subsequent development consists of concepts contained in elasticity and work-hardening plasticity theories.

An important feature of the new model is the application of a single isotopic, yield surface shaped as an asymmetric tear-drop with the pointed apex at the origin of the principal stress space. This yield surface, expressed in terms of stress invariants, describes the locus at which the total plastic work is constant. The total plastic work (due to shear strains as well as volumetric strains) serves as the hardening parameter, and it is used to define the location and shape of the yield surfaces. This concept results in mathematical consistency in the model, and application of a single yield surface produces computational efficiency when used in large computer programs. The nonassociated flow rule is derived from a potential function which describes a three-dimensional surface shaped as a cigar with an asymmetric cross-section.

The model is devised such that the transition from hardening to softening occurs abruptly at the peak failure point. Thus, the transition does not involve any points at which the hardening modulus is zero. The absence of points with zero slope allows greater computational efficiency near peak failure, while the pointed peak is hardly noticeable in actual comparisons with experimental data.

Each component of the model has already been developed, presented, and discussed in the literature [12-19]. Only the main principles and the governing equations for each component will be given here. Values of material parameters are given for different frictional materials, and the stress-strain behavior of various types of laboratory tests is predicted by the constitutive model.

COMPONENTS OF CONSTITUTIVE MODEL

The total strain increments observed in a material when loaded are divided into elastic and plastic components such that

$$d\varepsilon_{ij} = d\varepsilon_{ij}^{e} + d\varepsilon_{ij}^{p} \tag{1}$$

These strains are then calculated separately, the elastic strains by Hooke's law, and the plastic strains by a plastic stress-strain law. Both are expressed in terms of effective stresses.

Below is a brief review of the framework and the components of the constitutive model. In order that the presentation follows a logic developmental sequence, the components are presented in the following order: Elastic behavior, failure criterion, flow rule, yield criterion and work-hardening/softening law.

Elastic Behavior

The elastic strain increments, which are recoverable upon unloading, are calculated from Hooke's law, using a model for the unloading-reloading modulus defined as [12]:

$$E_{ur} = K_{ur} \cdot p_a \cdot \left(\frac{\sigma_3}{p_a}\right)^m \tag{2}$$

The dimensionless, constant values of the modulus number, K_{ur}, and the exponent, n, are determined from triaxial compression tests performed with various values of the confining pressure, σ_3. In Eq. (2) p_a is atmospheric pressure expressed in the same units as E_{ur} and σ_3.

The value of Poisson's ratio has often been found to be close to 0.2 for the elastic parts of unloading-reloading stress-paths. This value is therefore used in the following calculations.

More recently a model for the nonlinear variation of Young's modulus with stress state has been developed [13, 14]. In this model, the value of Poisson's ratio, being limited between zero and one half for most materials, was assumed to be constant. The expression for Young's modulus was then derived from theoretical considerations based on the principle of conservation of energy. According to this derivation, Young's modulus can be expressed in terms of a power function involving nondimensional material constants and stress invariants. Although this more recent model could just as well have been used here, the parameters determined for the plasticity functions presented below were derived on the basis of the elastic strains being calculated using Eq. (2) for the elastic modulus.

Failure Criterion

A general, three-dimensional failure criterion has been developed for soils, concrete, and rock [4, 15-17]. The criterion is expressed in terms of the first and the third stress invariants of the stress tensor as follows:

$$\left(\frac{I_1^3}{I_3} - 27\right)\left(\frac{I_1}{p_a}\right)^m = \eta_1 \tag{3}$$

in which

$$I_1 = \sigma_x + \sigma_y + \sigma_z \tag{4}$$

and

$$I_3 = \sigma_x \cdot \sigma_y \cdot \sigma_z + \tau_{xy} \cdot \tau_{yz} \cdot \tau_{zx} + \tau_{yx} \cdot \tau_{zy} \cdot \tau_{xz} - (\sigma_x \cdot \tau_{yz} \cdot \tau_{zy} + \sigma_y \cdot \tau_{zx} \cdot \tau_{xz} + \sigma_z \cdot \tau_{xy} \cdot \tau_{yx}) \tag{5}$$

The parameters η_1 and m are constant dimensionless numbers.

In principal stress space, the failure surface is shaped like an asymmetric bullet with the pointed apex at the origin of the stress axes, as shown in Fig. 1. The apex angle increases with the value of η_1. The failure surface is always concave towards the hydrostatic axis, and its curvature increases with the value of m. For $m = 0$ the failure surface is straight, and if $m > 1.979$ the failure surface becomes convex towards the hydrostatic axis [17]. Analysis of numerous sets of data for concrete and rock indicates that m-values rarely exceed 1.5 [16]. For constant value of m and increasing η_1-values, the cross-sectional shape in the octahedral plane changes from circular to triangular with smoothly rounded edges in a fashion that conforms to experimental evidence. The shape of these cross-sections do not change with the value of I_1 when $m = 0$. for $m > 0$, the cross-sectional shape of the failure surface changes from triangular to become more circular with increasing value of I_1. Similar changes in cross-sectional shape are observed from experimental studies on soil, concrete, and rock.

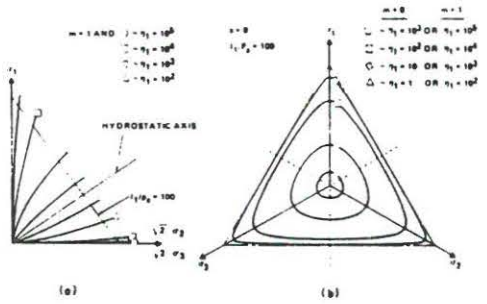

Fig. 1. Characteristics of Failure Surfaces Shown in Principal Stress Space. Traces of Failure Surfaces Shown in (a) Triaxial Plane, and (b) Octahedral Plane.

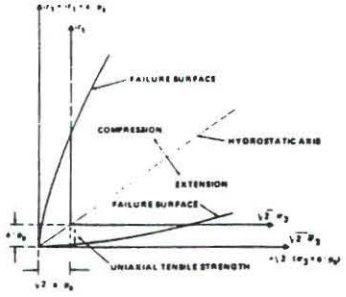

Fig. 2. Translation of Principal Stress Space along Hydrostatic Axis to Include Effect of Tensile Strength in Failure Criterion.

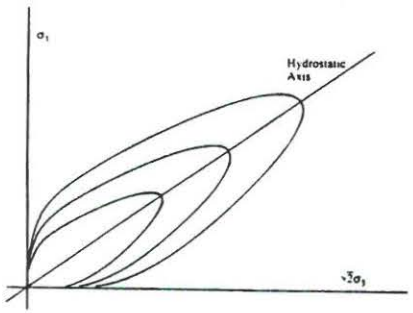

Fig. 3. Plastic Potential Surfaces Shown in Triaxial Plane.

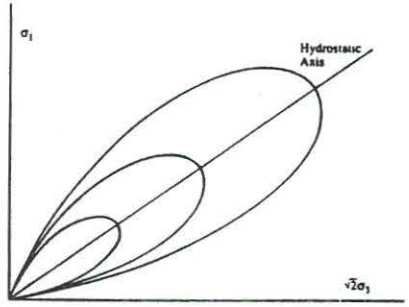

Fig. 4. Yield Surfaces Shown in Triaxial Plane.

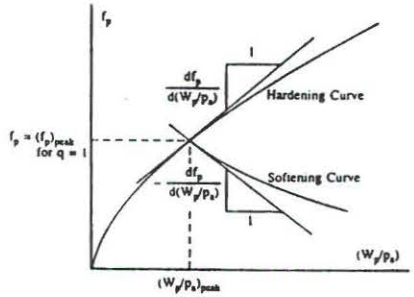

Fig. 5. Modeling of Work-Hardening and Softening.

In order to include the effective cohesion and the tension which can be sustained by concrete and rock, a translation of the principal stress space along the hydrostatic axis is performed as shown in Fig. 2. Thus, a constant stress, $a \cdot p_a$, is added to the normal stresses before substitution in Eq. (3):

$$\bar{\sigma}_{ij} = \sigma_{ij} + \delta_{ij} \cdot a \cdot p_a \tag{6}$$

in which 'a' is a dimensionless parameter, and δ_{ij} is Kronecker's delta (= 1 for i=j, and = 0 for $i \neq j$). The value of $a \cdot p_a$ reflects the effect of the tensile strength of the material. Although the three material parameters describe separate characteristics of the failure surface, they do interact in calculation of, e.g., the uniaxial compressive strength. Thus, an infinite number of combinations of η_1, m, and 'a' could results in the same value of the uniaxial compressive strength.

The three material parameters may be determined from results of simple tests such as triaxial compression tests. Further details on development, description and parameter evaluation for the failure criterion for frictional materials are given in [4,15-17].

Flow Rule

The plastic strain increments are calculated from the flow rule:

$$d\varepsilon_{ij}^{p} = d\lambda_p \cdot \frac{\partial g_p}{\partial \sigma_{ij}} \tag{7}$$

in which g_p is a plastic potential function and $d\lambda_p$ is a proportionality constant. A suitable plastic potential function for frictional materials was developed in a companion paper [18]. This function is different from the yield function and nonassociated flow is consequently obtained. The plastic potential function is written in terms of the three stress invariants of the stress tensor:

$$g_p = \left(\psi_1 \cdot \frac{I_1^3}{I_3} - \frac{I_1^2}{I_2} + \psi_2 \right) \cdot \left(\frac{I_1}{p_a} \right)^{\mu} \tag{8}$$

in which I_1 and I_3 are given by Eqs. (4) and (5) and the second stress invariant is defined as:

$$I_2 = \tau_{xy} \cdot \tau_{yx} + \tau_{yz} \cdot \tau_{zy} + \tau_{zx} \cdot \tau_{xz} - (\sigma_x \cdot \sigma_y + \sigma_y \cdot \sigma_z + \sigma_z \cdot \sigma_x) \tag{9}$$

The material parameters ψ_2 and μ are dimensionless constants that may be determined from triaxial compression tests. The parameter ψ_1 is related to the curvature parameter m for the failure criterion as indicated in [18], and it acts as a weighting factor between the triangular shape (from the I_3 term) and the circular shape (from the I_2 term). The parameter ψ_2 controls the intersection with the hydrostatic axis, and the exponent μ determines the curvature of meridians. The corresponding plastic potential surfaces are shown in Fig. 3. They are shaped as asymmetric cigars with smoothly rounded triangular cross-sections similar but not identical to those for the failure surfaces shown in Fig. 1.

The derivatives of g_p with regard to the stresses are

$$\frac{\partial g_p}{\partial \sigma_{ij}} = \left[\frac{I_1}{p_a}\right]^{\mu} \left\{ \begin{array}{l} G - (\sigma_y + \sigma_z) \cdot \dfrac{I_1^2}{I_2^2} - \psi_1 \cdot (\sigma_y \cdot \sigma_z - \tau_{yz}^2) \cdot \dfrac{I_1^3}{I_3^2} \\ G - (\sigma_z + \sigma_x) \cdot \dfrac{I_1^2}{I_2^2} - \psi_1 \cdot (\sigma_z \cdot \sigma_x - \tau_{zx}^2) \cdot \dfrac{I_1^3}{I_3^2} \\ G - (\sigma_x + \sigma_y) \cdot \dfrac{I_1^2}{I_2^2} - \psi_1 \cdot (\sigma_x \cdot \sigma_y - \tau_{xy}^2) \cdot \dfrac{I_1^3}{I_3^2} \\ 2 \cdot \dfrac{I_1^2}{I_2^2} \cdot \tau_{yz} - 2 \cdot \psi_1 \cdot (\tau_{xy} \cdot \tau_{zx} - \sigma_x \cdot \tau_{yz}) \cdot \dfrac{I_1^3}{I_3^2} \\ 2 \cdot \dfrac{I_1^2}{I_2^2} \cdot \tau_{zx} - 2 \cdot \psi_1 \cdot (\tau_{xy} \cdot \tau_{yz} - \sigma_y \cdot \tau_{zx}) \cdot \dfrac{I_1^3}{I_3^2} \\ 2 \cdot \dfrac{I_1^2}{I_2^2} \cdot \tau_{xy} - 2 \cdot \psi_1 \cdot (\tau_{yz} \cdot \tau_{zx} - \sigma_z \cdot \tau_{xy}) \cdot \dfrac{I_1^3}{I_3^2} \end{array} \right\} \qquad (10a\text{-}f)$$

where

$$G = \psi_1 \, (\mu+3) \, \frac{I_1^2}{I_3} - (\mu+2) \, \frac{I_1}{I_2} + \frac{\mu}{I_1} \, \psi_2 \qquad (11)$$

These derivatives are used to obtain the plastic strain increments from equation (7).

Yield Criterion and Work Hardening/Softening Law

The yield surfaces are intimately associated with and derived from surfaces of constant plastic work, as explained in a companion paper [19]. The isotropic yield function is expressed as follows:

$$f_p = f_p' \, (\sigma) - f_p'' \, (W_p) = 0 \qquad (12)$$

in which

$$f_p' = \left[\psi_1 \cdot \frac{I_1^3}{I_3} - \frac{I_1^2}{I_2}\right] \cdot \left[\frac{I_1}{p_a}\right]^h \cdot e^q \qquad (13)$$

and for *hardening*:

$$f_p'' = \left[\frac{1}{D}\right]^{1/\rho} \cdot \left[\frac{W_p}{p_a}\right]^{1/\rho} \qquad (14)$$

The expressions for I_1, I_2, and I_3 are given in Eqs. (4), (9), and (5), respectively. The parameter ψ_1 acts as a weighting factor between the triangular shape (from the I_3 term) and the circular shape (from the I_2 term), as in the expression for the plastic potential (Eq. (8)). The parameter h is constant for a given material and is determined on the basis that the plastic work is constant along a yield surface. The parameter q varies with stress level S from zero at the hydrostatic axis to unity at the failure surface according to the following expression:

$$q = \frac{\alpha \cdot S}{1 - (1-\alpha) \cdot S} \qquad (15)$$

Determination of the constant parameters h and α is explained in the companion paper [19].

In Eq. (14) the values of D and ρ are constants for a given material. Thus, f_p'' varies with the plastic work only. The value of α depends on p and h, and D is a function of C, ψ_1, and ρ, as explained in [19].

The yield surfaces are shaped as asymmetric tear drops with smoothly rounded triangular cross-sections and traces in the triaxial plane as shown in Fig. 4. As the plastic work increases, the isotropic yield surface inflates until the current stress point reaches the failure surface. The relation between f_p'' and W_p is described by a monotonically increasing function whose slope decreases with increasing plastic work, as shown in Fig. 5.

For *softening* the yield surface deflates isotropically according to an exponential decay function:

$$f_p'' = A \cdot e^{-B \cdot (W_p/p_a)} \qquad (16)$$

in which A and B are positive constants to be determined on the basis of the slope of the hardening curve at the point of peak failure, as indicated in Fig. 5 and explained in the companion paper [19].

Using the expression for the plastic potential in Eq. (8), the relation between plastic work increment and the proportionality constant $d\lambda_p$ in Eq. (7) may be expressed as [18]:

$$d\lambda_p = \frac{dW_p}{\mu \cdot g_p} \qquad (17)$$

in which the increment of plastic work can be determined by differentiation of the hardening and softening equations. For *hardening*, Eq. (14) yields:

$$dW_p = D \cdot p_a \cdot \rho \cdot f_p^{\rho-1} \cdot df_p \tag{18}$$

and for *softening* Eq. (16) produces:

$$dW_p = -\left(\frac{1}{B}\right) \cdot p_a \cdot f_p^{-1} \cdot df_p \tag{19}$$

in which df_p is negative during softening.

Combining Eqs. (18) and (19) with Eq. (17) and substituting this and Eqs. (10a-f) into Eq. (7) produces the expression for the incremental plastic strain increments.

MATERIALS WITH EFFECTIVE COHESION

As explained in connection with the failure criterion, it is possible to include the effective cohesion and the tension which can be sustained by concrete and rock. This is done by translating the principal stress space along the hydrostatic axis, as shown in Fig. 2, i.e. by adding a constant stress to the normal stresses, as in Eq. (6), before substitution into the failure criterion in Eq. (3).

A similar technique has been shown to work for the elastic modulus variation [13], the plastic potential [18], the yield criterion and the work-hardening/softening law [19]. The model presented here is therefore fully applicable to materials with effective cohesion such as concrete and rock.

PARAMETER VALUES FOR FRICTIONAL MATERIALS

The required number of parameters to be determined for a given material is twelve:

Elastic Moduli	ν, K_{ur}, n
Failure Criterion	η_1, m, a
Plastic Potential	ψ_2, μ
Yield Criterion	h, α
Hardening Function	C, p

For cohesionless materials the value of a = 0. All other parameters have values different from zero for most frictional materials. Table 1 summarizes the parameter values determined for various types of sand, clay, and concrete. These parameters were employed in the predictions presented below.

PREDICTIONS FOR SOILS AND CONCRETE

In the process of developing the model, individual components of the observed behavior of some frictional materials were compared to the model behavior, and it was shown that the components of the model were able to capture the observed behavior with good accuracy. Here the stress-strain behavior observed in various types of laboratory tests on frictional materials will be predicted. Thus, all model components must work in concert to produce reasonable predictions.

Table 1. Material Parameters for Various Frictional Materials

Material	D_r (%)	Failure Criterion			Elastic Behavior			Plastic Potential		Hardening Fucntion		Yield Function		Reference
		a	m	η_1	K_{ur}	n	ν	ψ_2	μ	C	p	h	α	
Fine Silica Sand	30		0.1	24.7	1170	0.53	0.2	-3.69	2.26	0.324E-03	1.25	0.355	0.515	
Sacramento River Sand	100		0.23	80.	1460	0.47	0.2	-3.09	2.00	0.396E-04	1.82	0.765	0.229	[20]
	38		0.093	28.	890	0.34	0.2	-3.72	2.36	0.127E-03	1.65	0.534	0.794	[20]
Painted Rock Material	100		0.21	101.	891	0.51	0.2	-3.26	2.82	0.351E-03	1.25	0.500	0.313	[21]
	70		0.16	67.	314	0.75	0.2	-3.39	2.72	0.460E-04	1.78	0.698	0.386	[21]
Crushed Napa Basalt	100		0.423	280.	470	0.58	0.2	-2.97	2.80	0.814E-04	1.61	0.546	0.727	[22]
	70		0.3	130.	481	0.36	0.2	-2.90	2.55	0.457E-03	1.39	0.542	0.851	[22]
Monterey No.0 Sand	98		0.16	104.	2300	0.80	0.2	-3.38	2.30	0.269E-04	1.44	0.490	0.896	[23]
	27		0.12	36.	1600	0.86	0.2	-3.60	2.50	0.214E-03	1.26	0.430	0.577	[23]
Edgar Kaolinite Clay			0.54	48.	110	1.23	0.25	-3.02	2.24	0.283E-02	1.48	0.886	0.594	
Plain Concrete		28.1	1.263	367200.	166000	0.	0.20	-2.77	2.51	0.350E-11	3.61	2.150	7.50	[24]
		28.5	1.113	159800.	361800	0.	0.18	-2.92	5.06	0.712E-12	3.80	1.990	0.75	[25]
		29.7	0.79	17370.	230100	0.	0.19	-3.02	4.88	0.934E-12	3.93	3.300	10.0	[26]
		28.2	1.231	336200.	321900	0.	0.14	-2.93	3.45	0.475E-09	2.93	1.666	1.65	[27]
Steel Fiber Reinforced Concrete		45.7	1.251	430100.	188000	0.	0.20	-2.58	2.63	0.252E-08	2.67	2.82	2.50	[28]

Isotropic Compression

Fig. 6 shows predictions of isotropic compression tests on sand and concrete. Loading and unloading is calculated for Fine Silica Sand in Fig. 6(a). Only elastic behavior is predicted for unloading. Both loading and unloading behavior (solid lines) is consistent with the observed behavior for this sand.

The isotropic compression behavior for plane concrete tested by Aschl et al. [27] is shown in Fig. 6(b). Insufficient data was available for this material to determine the elastic modulus variation. A constant elastic modulus was therefore used for prediction of the loading curve. The nonlinear behavior is caused by the plastic compression.

K_o-Compression

An example of sand behavior during K_o-compression is given in Fig. 7. In this test, the lateral strains are zero ($\varepsilon_2 = \varepsilon_3 = 0$) while the axial stress is increased or decreased. Only results for increasing stresses were available for dense Crushed Napa Basalt tested by Al-Hussaini [22]. The predicted behavior (solid lines) is seen to correspond very well with the measured behavior (points) for increasing stresses. The value of K_o increases with increasing stresses and this aspect of the soil behavior is accurately predicted by the model. Tests results were not available for decreasing stresses, but tests by others [29-31] indicate that they follow a pattern shown by the lines denoted "Decreasing Stresses". The directions of stress-path and stress-strain curve indicated by these lines are actually predicted by the model.

Triaxial Compression

Predictions for conventional drained triaxial compression tests on Fine silica Sand were calculated from the model and compared with experimental results in Fig. 8. In these tests, the confining pressure was held constant while the major principal stress was increased to peak failure and beyond. The model predictions capture the observed stress-strain relations accurately. The effects of confining pressure on the axial and the volumetric strains are also captured by the model. The breaks on the stress-strain curves at the peak are relatively shallow and hardly noticeable within the range of scatter of experimental results. Allowing for this shallow break enhances the computational efficiency of the model near failure.

Cubical Triaxial Tests

Particular attention has been paid to the three-dimensional characteristics of the stress-strain relationships. The proposed model can be examined through the predictions of cubical triaxial tests in which the three principal stresses are different form each other. The relative magnitude of the intermediate principal stress is characterized by the value of $b = (\sigma_2 - \sigma_3)/(\sigma_1 - \sigma_3)$, which is zero for triaxial compression and unity for triaxial extension.

The results of cubical triaxial tests on dense Monterey No. 0 Sand are shown in Fig. 9 together with model predictions. All model parameters were determined from triaxial compression tests as well as from an isotropic compression test. The pattern of increasing slope, decreasing strain to failure, and increasing rate of dilation with increasing b-value is captured well by the model. The strength first increases up to b = 0.50 and then decreases to b = 1.00 in both experiments and model predictions.

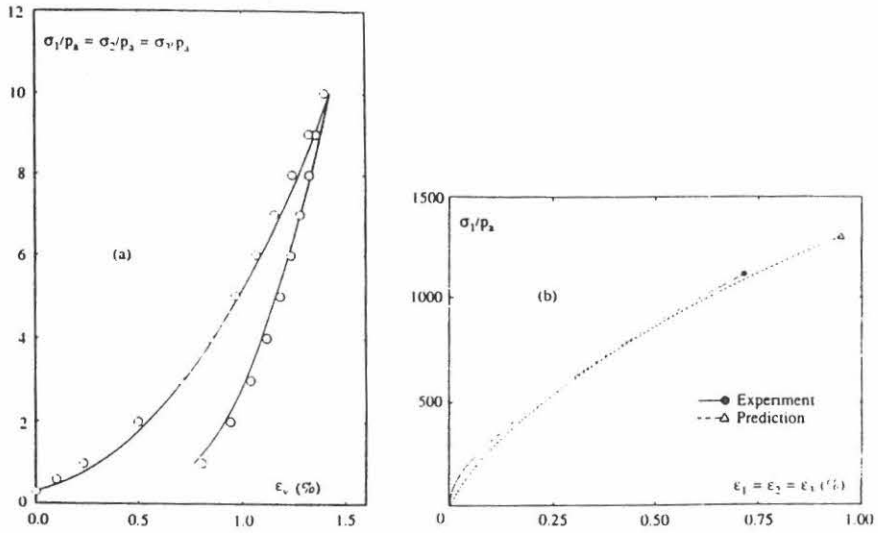

Fig. 6. Comparison of Predicted and Observed Stress-Strain Curves for Isotropic Compression Tests on (a) Fine Silica Sand, and (b) Plain Concrete (Data from [27]).

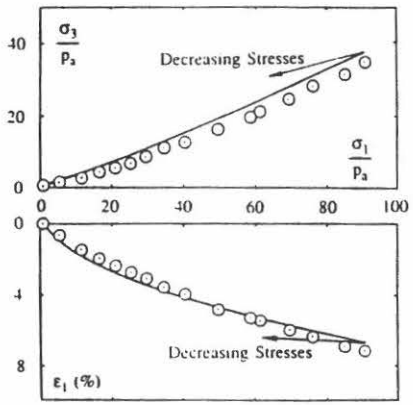

Fig. 7. Comparison of Predicted and Observed Behavior of Dense Crushed Napa Basalt in K_o-Test (Data from [22]).

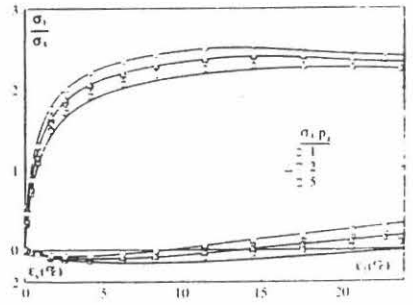

Fig. 8. Comparison of Predicted and Observed Behavior of Fine Silica Sand in Triaxial Compression Tests.

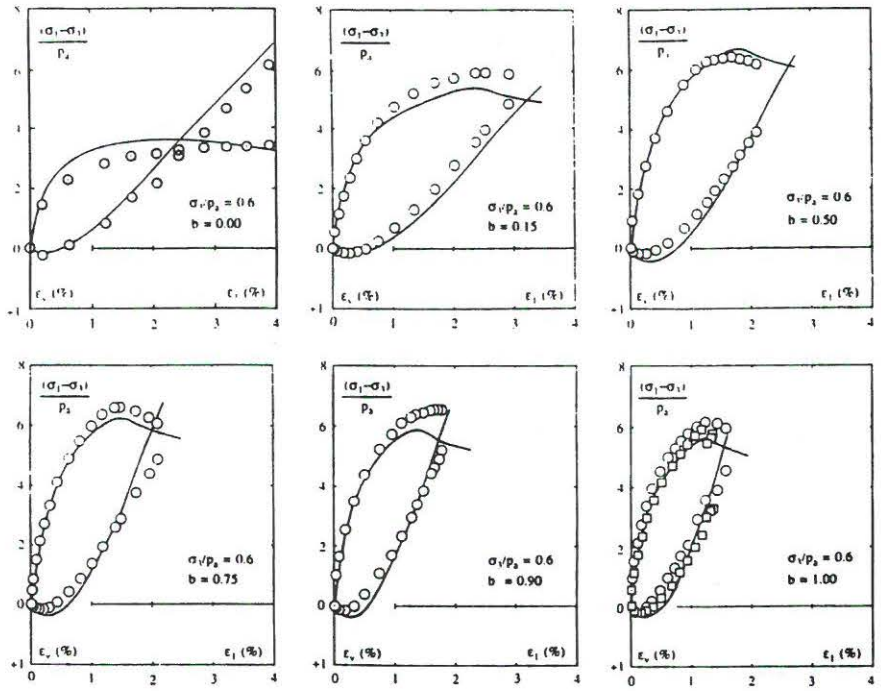

Fig. 9. Comparison of Predicted and Observed Stress-Strain and Volume Change Behavior of Dense Monterey No. 0 Sand in Cubical Triaxial Tests (Data from [23]).

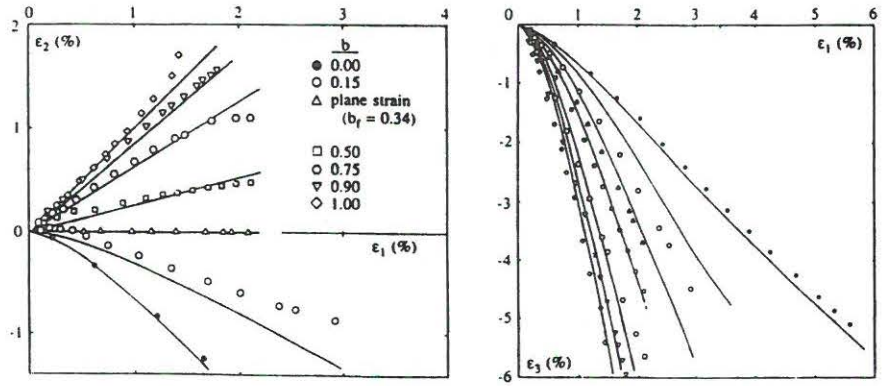

Fig. 10. Comparison of Predicted and Observed Strains in Dense Monterey No. 0 Sand in Cubical Triaxial Tests (Data from [23]).

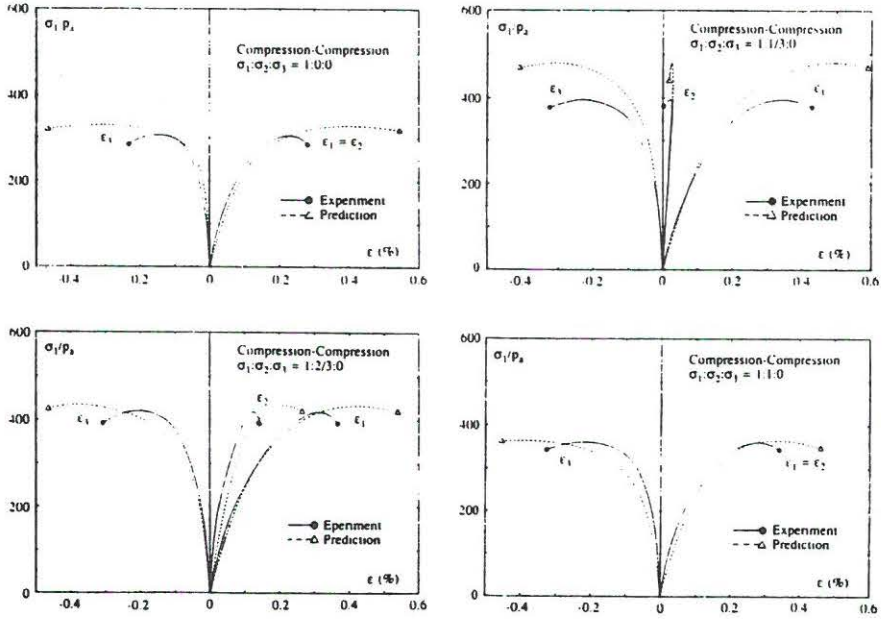

Fig. 11. Comparison of Predicted and Observed Stress-Strain Behavior of Plain Concrete in Biaxial Tests (Data from [27]).

Fig. 10 shows detailed comparisons of the principal strains. the predicted relations between the strains correspond well with the values measured in all the experiments.

Biaxial Tests

The model was also employed to predict the stress-strain behavior of concrete subjected to multiaxial loading. As explained above, for materials with effective cohesion the stress components in all stress functions correspond to translated stresses. The stresses are translated before any calculations are conducted, and the reverse translation is performed before the stresses are obtained for plotting.

The experimental results are compared with predictions for four biaxial tests on plane concrete in Fig. 11. The effect of the intermediate principal stress on the stress-strain curves are captured well in the model predictions. It may be noted that some disagreement appears after the peak stress conditions have been reached. However, measurement of stresses and strains in this stress range is less reliable than in the hardening range, because localized crushing or cracking of the concrete specimen may prevent accurate measurements. Thus, the model may represent the behavior of concrete quite well.

CONCLUSIONS

The behavior of frictional materials is such that a unified approach is possible in describing their failure surfaces as well as their stress-strain relations. A combination of elasticity theory and plasticity theory may provide a reasonable and consistent description of this behavior when appropriate mathematical functions are used in the framework provided by these theories. In addition to Hooke's law, the components in this framework are the failure criterion, the flow rule, the yield criterion and the work-hardening/softening law. Analyses of experimental data indicate that the shapes of the failure, yield, and plastic potential surfaces obtained from different types of frictional materials each have similar characteristics and may be modeled by similar mathematical functions. These functions are all expressible in terms of the three invariants of the stress tensor.

The nonassociated flow rule is derived from a plastic potential whose shape in the principal stress space resembles a cigar with an asymmetric cross-section. Yielding occurs along a single, isotropic yield surface shaped as an asymmetric tear drop. This yield surface describes a contour of constant plastic work. Because plastic yielding is related directly to plastic work contours, the description of the work-hardening/softening law is straight forward. The transition from hardening to softening occurs abruptly at the peak failure point. Thus, no points with a hardening modulus of zero are encountered, and this allows greater computational efficiency near peak failure.

The constitutive model combines all the governing functions studied individually in a mathematically consistent entity. The model requires twelve parameters which can be determined from simple laboratory tests such as isotropic compression and conventional triaxial compression tests.

Validation of the model was achieved by comparison of predicted and experimental stress-strain curves for various two- and three-dimensional stress-paths obtained for different types of frictional materials. Overall acceptable and accurate predictions were produced for soils as well as concrete for which experimental data were available.

ACKNOWLEDGMENT

The basic developmental work presented here was supported by the National Science Foundation under Grant No. CEE 8211159. Additional developments and computational refinements were supported by Exxon Production Research Company, Houston, Texas, and by California Research and Technology, Chatsworth, California. Grateful appreciation is expressed for their support of this research.

REFERENCES

1. Drucker, D.C., Gibson, R.E. and Henkel, D.J.,
Soil Mechanics and Work-Hardening Theories of Plasticity.
ASCE Transactions, 122 (1957) 338-346.

2. Roscoe, K.H. and Burland, J.B.,
On the Generalized Stress-Strain Behaviour of 'Wet' Clay.
In: Engineering Plasticity, Ed. by J. Heymann and F.A. Leckie, Cambridge University Press, Cambridge (1968) 535-609.

3. DiMaggio, F.L. and Sandler, I.S.,
Material Model for Granular Soils.
J.Engr. Mech. Div., ASCE, 97 (1971) 935-950.

4. Lade, P.V.,
Elasto-Plastic Stress-Strain Theory for Cohesionless Soil with Curved Yield Surfaces.
Int. J. Solids Struct., 13 (1977) 1019-1035.

5. Prevost, J.-H.,
Plasticity Theory for Soil Stress-Strain Behavior.
J. Engr. Mech. Div. ASCE, 104 (1978) 1177-1194.

6. Dafalias, Y.F. and Herrmann, L.R.,
A Bounding Surface Soil Plasticity Model.
Proc. Int. Symp. Soils under Cyclic and Transient Loading,
Balkema, Rotterdam (1980) 335-345.

7. Mroz, Z., Norris, V.A. and Zienkiewicz, O.C.,
An Anisotropic, Critical State Model for Soils Subject to Cyclic Loading.
Geotechnique, 31 (1981) 451-469.

8. Ghaboussi, J. and Momen, H.,
Modelling and Analysis of Cyclic Behavior of Sands.
In: Soil Mechanics–Transient and Cyclic Loads, Ed. by G.N. Pande and O.C. Zienkiewicz, Wiley, London (1982) 313-342.

9. Pande, G.N. and Pietruszak, S.,
Reflecting Surface Model for Soils.
Proc. Int. Symp. Numerical Models in Geomechanics,
Balkema, Rotterdam (1982) 50-64.

10. Poorooshasb, H.B. and Pietruszak, S.,
On Yielding and Flow of Sand; A Generalized Two-Surface Model.
Computers and Geotechnics, 1 (1985) 33-58.

11. Frantziskonis, G., Desai, C.S. and Somasundaram, S.,
Constitutive Model for Nonassociative Behavior.
J. Engr. Mech., ASCE, 112 (1986) 932-946.

12. Duncan, J.M. and Chang, C.-Y.,
Nonlinear Analysis of Stress and Strain in Soils.
J. Soil Mech. Found. Div., ASCE, 96 (1970) 1629-1653.

13. Lade, P.V. and Nelson, R.B.,
Modelling the Elastic Behaviour of Granular Materials.
Int. J. Num. Anal. Meth. Geomech., 11 (1987) 521-542.

14. Lade, P.V.,
Model and Parameters for the Elastic Behavior of Soils.
Proc. 6th Int. Conf. Num. Meth. Geomech.,
Balkema, Rotterdam (1988) 359-364.

15. Lade, P.V.,
Three-Parameter Failure Criterion for Concrete.
J. Engr. Mech. Div., ASCE, 108 (1982) 850-863.

16. Lade, P.V.,
Failure Criterion for Frictional Materials.
Chapt. 20 in Mechanics of Engineering Materials, Ed. by C.S. Desai and R.H. Gallagher, Wiley (1984) 385-402.

17. Kim, M.K. and Lade, P.V.,
Modelling Rock Strength in Three Dimensions.
Int. J. Rock Mech. Min. Sci. & Geomech. Abstr., 21 (1984) 21-33.

18. Kim, M.K. and Lade, P.V.,
Single Hardening Constitutive Model for Frictional Materials, I. Plastic Potential Function.
Computers and Geotechnics

19. Lade, P.V. and Kim, M.K.,
Single Hardening Constitutive Model for Frictional Materials, II. Yield Criterion and Plastic Work Contours.
Computers and Geotechnics

20. Lee, K.L. and Seed, H.B.,
Drained Strength Characteristics of Sands.
J. Soil Mech. Found. Div., ASCE, 93, SM6 (1967) 117-141.

21. Al-Hussaini, M.M.,
Plane Strain and Triaxial Compression Tests on Painted Rock Dam Material.
Tech. Rep. S-71-2, No. 3, USAE, WES, Vicksburg, Miss. (1972).

22. Al-Hussaini, M.M.,
Drained Plane Strain and Triaxial Compression Tests on Crushed Napa Basalt.
Tech. Rep. S-71-2, No. 2, USAE, WES, Vicksburg, Miss. (1971).

23. Lade, P.V.,
The Stress-Strain and Strength Characteristics of Cohesionless Soils.
Ph.D. Dissertation, University of California, Berkeley (1972).

24. Schickert, G. and Winkler, H.,
Results of Tests Concerning Strength and Strain of Concrete Subjected to Multiaxial Compressive Stresses.
Deutscher Ausschus für Stahlbeton, 277, Berlin (1977).

25. Kupfer, H., Hilsdorf, H.K. and Rusch, H.,
Behavior of Concrete Under Biaxial Stresses.
J. Am. Concr. Inst., 66 (1969) 656-666.

26. Tasuji, M.E., Slate, F.O. and Nilson, A.H.,
Stress-Strain and Fracture of Concrete in Biaxial Loading.
J. Am. Concr. Inst., 75 (1978) 306-312.

27. Aschl, H., Linse, D. and Stoeckl, S.,
Strength and Stress Strain Behavior of Concrete Under Multiaxial Compression and Tension.
Proc. 2nd Int. Conf. Mechanical Behavior of Materials,
Boston, Mass. (1976) 102-117.

28. Egging, D.E., and Ko, H.-Y.,
Constitutive Relations of Randomly Oriented Steel Fiber Reinforced Concrete Under Multiaxial Compressive Loadings.
University of Colorado, Boulder (1981).

29. Bishop, A.W. and Henkel, D.J.,
The Measurement of Soil Properties in the Triaxial Test,
St. Martin's Press, New York (1962).

30. Hendron, A.J.,
The Behavior of Sand in One-Dimensional Compression.
Ph.D. Dissertation, University of Illinois, Urbana (1963).

31. Brooker, E.W. and Ireland, H.O.,
Earth Pressures at Rest Related to Stress History.
Can. Geotech. J., 2 (1965) 1-15.

Received 10 June 1988; revised version received and accepted 2 August 1988

Single-Hardening Model with Application to NC Clay

By Poul V. Lade,[1] Member, ASCE

Abstract: A constitutive model with a single yield surface has been developed for the behavior of frictional materials, such as clay, sand, concrete, and rock. The model is based on concepts from elasticity and plasticity theories. In addition to Hooke's law for the elastic behavior, the framework for the plastic behavior consists of a failure criterion, a nonassociated flow rule, a yield criterion that describes contours of equal plastic work, and a work-hardening/softening law. The functions that describe these components are all expressed in terms of stress invariants. The model incorporates eleven parameters for normally consolidated clay that can be determined from simple experiments, such as isotropic compression and consolidated-undrained triaxial compression tests. A study of the three-dimensional behavior of remolded, normally consolidated clay has served as a basis for evaluating the capabilities of the model. Overall acceptable predictions are produced for the normally consolidated clay.

Introduction

Most constitutive models for the time-independent behavior of frictional materials have been based on experimental observations of material behavior and on a framework of elasticity and plasticity theories. The varying emphasis on experiment and theory has resulted in a number of models with different capabilities relative to material behavior. The models presented by Drucker et al. (1957), Roscoe and Burland (1968), DiMaggio and Sandler (1971), Lade (1977), Prevost (1978), Dafalias and Herrmann (1980), Mroz et al. (1981), Ghaboussi and Momen (1982), Pande and Pietruszak (1982), Desai and Faruque (1984), Poorooshasb and Pietruszak (1985), and Frantziskonis et al. (1986) are representative of the types of capabilities available in the literature.

A constitutive model has been developed on the basis of thorough review and evaluation of data from experiments on frictional materials, such as sand, clay, concrete, and rock (Kim and Lade 1988; Lade and Kim 1988a, 1988b). The framework for the evaluation and subsequent development consisted of concepts contained in elasticity and work-hardening plasticity theories.

The new model employs a single, isotropic yield surface shaped as an asymmetric teardrop with the pointed apex at the origin of the principal stress space. This yield surface, expressed in terms of stress invariants, describes the locus at which the total plastic work is constant. The total plastic work (due to shear strains as well as volumetric strains) serves as the hardening parameter and is used to define the location and shape of the yield surfaces. The use of contours of constant plastic work (or any other measure of hardening) as yield surfaces results in mathematical consistency in the model, because the measure of yielding and the measure of hardening are uniquely related through one monotonic function. In addition, application of a single-

[1]Prof., Dept. of Civ. Engrg., Univ. of California, Los Angeles, CA 90024.

Note. Discussion open until August 1, 1990. To extend the closing date one month, a written request must be filed with the ASCE Manager of Journals. The manuscript for this paper was submitted for review and possible publication on March 15, 1989. This paper is part of the ***Journal of Geotechnical Engineering***, Vol. 116, No. 3, March, 1990. ©ASCE, ISSN 0733-9410/90/0003-0394/$1.00 + $.15 per page. Paper No. 24404.

yield surface produces computational efficiency when used in large computer programs. The nonassociated flow rule is derived from a potential function that describes a three-dimensional surface shaped like a cigar with an asymmetric cross section.

The model is devised so that transition from hardening to softening occurs abruptly at peak failure point. Thus, transition does not involve any points at which the hardening modulus is zero, but the pointed peak is hardly noticeable in actual comparisons with experimental data.

The main principles of the model and the governing equations for each component are reviewed. Values of material parameters are then determined from tests on normally consolidated Edgar Plastic Kaolinite, and predictions of three-dimensional behavior are compared with experimental data for this clay.

Single-Hardening Stress-Strain Model

The total strain increments observed in material when loaded are divided into elastic and plastic components so that

$$d\epsilon_{ij} = d\epsilon^e_{ij} + d\epsilon^p_{ij} \quad \ldots\ldots (1)$$

These strains are then calculated separately, the elastic strains by Hooke's law, and the plastic strains by a plastic stress-strain law. Both are expressed in terms of effective stresses.

The framework and components of the constitutive model are described. In order that the presentation follow a logic developmental sequence, the components are presented in the order: Elastic behavior, failure criterion, flow rule, yield criterion, and work-hardening/softening law.

Elastic Behavior

The elastic strain increments, recoverable upon unloading, are calculated from Hooke's law, using a recently developed model for the nonlinear variation of Young's modulus with stress state (Lade and Nelson 1987; Lade 1988). The value of Poisson's ratio, limited between zero and one-half for most materials, is assumed to be constant. The expression for Young's modulus was derived from theoretical considerations based on the principle of conservation of energy. According to this derivation, Young's modulus E can be expressed in terms of a power law involving nondimensional material constants and stress functions as follows:

$$E = Mp_a\left[\left(\frac{I_1}{p_a}\right)^2 + R\frac{J_2'}{p_a^2}\right]^{\lambda} \quad \ldots\ldots (2)$$

in which

$$R = 6\cdot\frac{1+\nu}{1-2\nu} \quad \ldots\ldots (3)$$

I_1 = the first invariant of the stress tensor; and J_2' = the second invariant of the deviatoric stress tensor, given as follows:

$$I_1 = \sigma_x + \sigma_y + \sigma_z \quad \ldots\ldots (4)$$

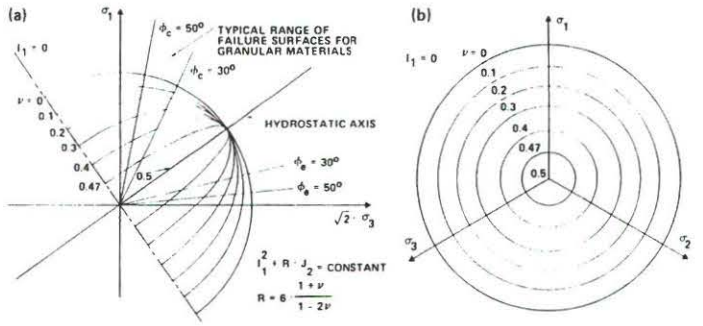

FIG. 1. Contours of Constant Young's Modulus Shown in (*a*) Triaxial Plane; and (*b*) Octahedral Plane

$$J_2' = \frac{1}{6}[(\sigma_x - \sigma_y)^2 + (\sigma_y - \sigma_z)^2 + (\sigma_z - \sigma_x)^2] + \tau_{xy}^2 + \tau_{yz}^2 + \tau_{zx}^2 \quad \ldots\ldots (5)$$

in which p_a = atmospheric pressure expressed in the same units as E, I_1, and $\sqrt{J_2'}$; and the modulus number M and λ = constant dimensionless numbers.

Eq. 2 and Fig. 1 indicate that Young's modulus is constant along rotationally symmetric ellipsoidal surfaces whose long axis coincides with the hydrostatic axis and whose center is located at the origin of the principal stress space. The magnitude of Poisson's ratio determines the shape of the ellipsoidal surface. For $\nu = 0$, $R = 6$, and the surface becomes spherical, whereas for $\nu = 0.5$, $R = \infty$, and the surface degenerates into a line coinciding with the hydrostatic axis.

The three material parameters v, M, and λ may be obtained from simple tests, such as triaxial compression tests, and the model can be used for materials with effective cohesion.

Failure Criterion

A general, three-dimensional failure criterion has been developed for soils, concrete, and rock (Lade 1977, 1982, 1984; Kim and Lade 1984). The criterion is expressed in terms of the first and third stress invariants of the stress tensor:

$$\left(\frac{I_1^3}{I_3} - 27\right)\left(\frac{I_1}{p_a}\right)^m = \eta_1 \quad \ldots\ldots (6)$$

in which I_1 is given by Eq. 4 and

$$I_3 = \sigma_x\sigma_y\sigma_z + \tau_{xy}\tau_{yz}\tau_{zx} + \tau_{yx}\tau_{zy}\tau_{xz} - (\sigma_x\tau_{yz}\tau_{zy} + \sigma_y\tau_{zx}\tau_{xz} + \sigma_z\tau_{xy}\tau_{yx}) \quad \ldots\ldots (7)$$

In Eq. 6, η_1 and m = constant dimensionless numbers, which may be determined from results of simple tests, such as triaxial compression tests.

In principal stress space, the failure surface is shaped like an asymmetric bullet with the pointed apex at the origin of the stress axes, as shown in Fig. 2. The apex angle increases with the value of η_1. The failure surface

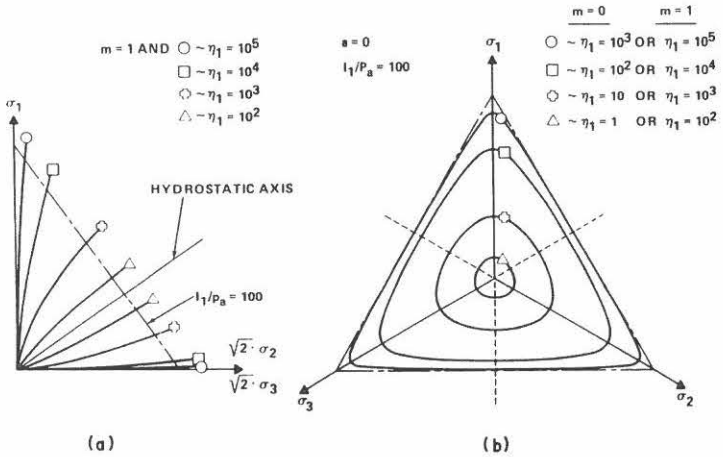

FIG. 2. Characteristics of Failure Surfaces Shown in Principal Stress Space: Traces of Failure Surfaces Shown in (*a*) Triaxial Plane; and (*b*) Octahedral Plane

is always concave towards the hydrostatic axis, and its curvature increases with the value of m. For $m = 0$ the failure surface is straight, and if $m > 1.979$ the failure surface becomes convex towards the hydrostatic axis (Kim and Lade 1984). Analysis of numerous sets of data for concrete and rock indicates that m values rarely exceed 1.5 (Lade 1984). For constant value of m and increasing η_1 values, the cross-sectional shape in the octahedral plane changes from circular to triangular with smoothly rounded edges in a fashion that conforms to experimental evidence. The shape of these cross sections does not change with the value of I_1 when $m = 0$. For $m > 0$, the cross-sectional shape of the failure surface changes from triangular to become more circular with increasing value of I_1. Similar changes in cross-sectional shape are observed from experimental studies on soil, concrete, and rock.

Flow Rule

The plastic strain increments are calculated from the flow rule:

$$d\epsilon_{ij}^p = d\lambda_p \cdot \frac{\partial g_p}{\partial \sigma_{ij}} \quad \ldots\ldots (8)$$

in which g_p = a plastic potential function; and $d\lambda_p$ = a scalar factor of proportionality. A suitable plastic potential function for frictional materials was developed and presented by Kim and Lade (1988). This function is different from the yield function and nonassociated flow is consequently obtained. The plastic potential function is written in terms of the three invariants of the stress tensor:

$$g_p = \left(\Psi_1 \cdot \frac{I_1^3}{I_3} - \frac{I_1^2}{I_2} + \Psi_2\right) \cdot \left(\frac{I_1}{p_a}\right)^{\mu} \quad \ldots\ldots (9)$$

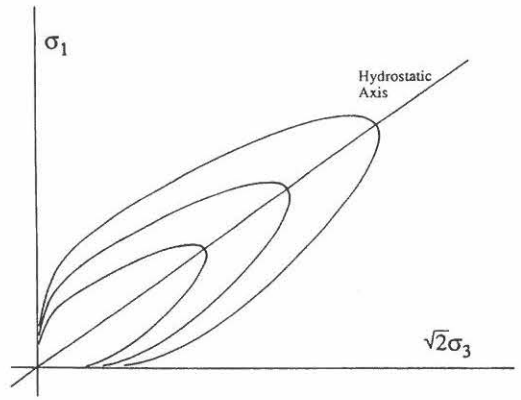

FIG. 3. Plastic Potential Surfaces Shown in Triaxial Plane

in which I_1 and I_3 are given by Eqs. 4 and 7; and the second stress invariant is defined as

$$I_2 = \tau_{xy}\cdot\tau_{yx} + \tau_{yz}\cdot\tau_{zy} + \tau_{zx}\cdot\tau_{xz} - (\sigma_x\cdot\sigma_y + \sigma_y\cdot\sigma_z + \sigma_z\cdot\sigma_x) \quad \ldots\ldots (10)$$

in which Ψ_2 and μ = dimensionless constants that may be determined from triaxial compression tests. The parameter Ψ_1 is related to the curvature parameter m of the failure criterion as follows:

$$\Psi_1 = 0.00155 \cdot m^{-1.27} \quad \ldots\ldots (11)$$

The parameter Ψ_1 acts as a weighting factor between the triangular shape (from the I_3 term) and the circular shape (from the I_2 term). The parameter Ψ_2 controls the intersection with the hydrostatic axis, and μ determines the curvature of meridians. The corresponding plastic potential surfaces are shown in Fig. 3. They are shaped as asymmetric cigars with smoothly rounded triangular cross sections similar but not identical to those for the failure surfaces shown in Fig. 2.

The derivatives of g_p with regard to the stresses are

$$\frac{\partial g_p}{\partial \sigma_{ij}} = \left(\frac{I_1}{p_a}\right)^{\mu} \begin{Bmatrix} G - (\sigma_y + \sigma_z)\cdot(I_1^2/I_2^2) - \Psi_1\cdot(\sigma_y\cdot\sigma_z - \tau_{yz}^2)\cdot(I_1^3/I_3^2) \\ G - (\sigma_z + \sigma_x)\cdot(I_1^2/I_2^2) - \Psi_1\cdot(\sigma_z\cdot\sigma_x - \tau_{zx}^2)\cdot(I_1^3/I_3^2) \\ G - (\sigma_x + \sigma_y)\cdot(I_1^2/I_2^2) - \Psi_1\cdot(\sigma_x\cdot\sigma_y - \tau_{xy}^2)\cdot(I_1^3/I_3^2) \\ 2\cdot(I_1^2/I_2^2)\cdot\tau_{yz} - 2\cdot\Psi_1\cdot(\tau_{xy}\cdot\tau_{zx} - \sigma_x\cdot\tau_{yz})\cdot(I_1^3/I_3^2) \\ 2\cdot(I_1^2/I_2^2)\cdot\tau_{zx} - 2\cdot\Psi_1\cdot(\tau_{xy}\cdot\tau_{yz} - \sigma_y\cdot\tau_{zx})\cdot(I_1^3/I_3^2) \\ 2\cdot(I_1^2/I_2^2)\cdot\tau_{xy} - 2\cdot\Psi_1\cdot(\tau_{yz}\cdot\tau_{zx} - \sigma_z\cdot\tau_{xy})\cdot(I_1^3/I_3^2) \end{Bmatrix} \quad \ldots\ldots (12)$$

$$G = \Psi_1(\mu + 3)\frac{I_1^2}{I_3} - (\mu + 2)\frac{I_1}{I_2} + \frac{\mu}{I_1}\Psi_2 \quad \ldots\ldots (13)$$

These derivatives are used to obtain the plastic strain increment from Eq. 8.

Once the parameter Ψ_1 is evaluated, the other parameters, Ψ_2 and μ, can

be determined using triaxial compression test data. To do this, the incremental plastic strain ratio is first defined as

$$\nu_p = -\frac{d\epsilon_3^p}{d\epsilon_1^p} \quad (14)$$

Substitution of Eqs. 8 and 12 for the plastic strain increments under triaxial compression conditions, $\sigma_2 = \sigma_3$, into Eq. 14 produces the following equation:

$$\xi_v = \frac{1}{\mu}\xi_x - \Psi_2 \quad (15)$$

where

$$\xi_x = \frac{1}{1+\nu_p}\left[\frac{I_1^3}{I_2^2}(\sigma_1+\sigma_3+2\nu_p\sigma_3) + \Psi_1 \cdot \frac{I_1^4}{I_3^2}(\sigma_1\sigma_3+\nu_p\sigma_3^2)\right]$$

$$- 3\Psi_1 \cdot \frac{I_1^3}{I_3} + 2\frac{I_1^2}{I_2} \quad (16)$$

and

$$\xi_v = \Psi_1 \cdot \frac{I_1^3}{I_3} - \frac{I_1^2}{I_2} \quad (17)$$

Thus, $1/\mu$ and $-\Psi_2$ in Eq. 15 can be determined by linear regression between ξ_x and ξ_v determined from several data points.

Yield Criterion and Work-Hardening/Softening Law

The yield surfaces are intimately associated with and derived from surfaces of constant plastic work, as explained by Lade and Kim (1988a). The isotropic yield function is expressed as follows:

$$f_p = f_p'(\sigma) - f_p''(W_p) = 0 \quad (18)$$

in which

$$f_p' = \left(\Psi_1 \cdot \frac{I_1^3}{I_3} - \frac{I_1^2}{I_2}\right) \cdot \left(\frac{I_1}{p_a}\right)^h \cdot e^q \quad (19)$$

in which h is constant, and q varies from zero at the hydrostatic axis to unity at the failure surface.

For hardening:

$$f_p'' = \left(\frac{1}{D}\right)^{1/\rho} \cdot \left(\frac{W_p}{p_a}\right)^{1/\rho} \quad (20)$$

The expressions for I_1, I_2, and I_3 in Eq. 19 are given in Eqs. 4, 10, and 7, respectively. The parameter Ψ_1 acts as a weighting factor between the triangular shape (from the I_3 term) and the circular shape (from the I_2 term), as in the expression for the plastic potential (Eq. 9). The constant parameter h is determined on the basis that the plastic work is constant along a yield surface. Thus, for two stress points, A on the hydrostatic axis and B on the failure surface, the following expression is obtained for h:

$$h = \frac{\ln \dfrac{\left(\Psi_1 \cdot \dfrac{I_{1B}^3}{I_{3B}} - \dfrac{I_{1B}}{I_{2B}}\right) \cdot e}{27\Psi_1 + 3}}{\ln \dfrac{I_{1A}}{I_{1B}}} \quad (21)$$

in which e = the base of natural logarithms.

The value of q varies with stress level S defined as

$$S = \frac{f_n}{\eta_1} = \frac{1}{\eta_1} \cdot \left(\frac{I_1^3}{I_3} - 27\right)\left(\frac{I_1}{p_a}\right)^m \quad (22)$$

in which f_n = the left-hand side of Eq. 6; and η_1 = the value of f_n at failure. The stress level S varies from zero at the hydrostatic axis to unity at the failure surface.

The value of q can now be determined from the test data according to

$$q = \ln \frac{\left(\dfrac{W_p}{D \cdot p_a}\right)^{1/\rho}}{\left(\Psi_1 \cdot \dfrac{I_1^3}{I_3} - \dfrac{I_1^2}{I_2}\right)\left(\dfrac{I_1}{p_a}\right)^h} \quad (23)$$

and the variation of q with S is expressed as

$$q = \frac{\alpha \cdot S}{1 - (1-\alpha) \cdot S} \quad (24)$$

in which α is constant.

In Eq. 20 the values of ρ and D are constants for a given material. Thus, f_p'' varies with the plastic work only. The values of ρ and D are given by

$$\rho = \frac{p}{h} \quad (25)$$

and

$$D = \frac{C}{(27\Psi_1 + 3)^\rho} \quad (26)$$

in which C and p are used to model the plastic work during isotropic compression:

$$W_p = C \cdot p_a \left(\frac{I_1}{p_a}\right)^p \quad (27)$$

The yield surfaces are shaped as asymmetric teardrops with smoothly rounded triangular cross sections and traces in the triaxial plane, as shown in Fig. 4. As the plastic work increases, the isotropic yield surface inflates until the current stress point reaches the failure surface. The relation between f_p and W_p is described by a monotonically increasing function whose slope decreases with increasing plastic work, as shown in Fig. 5.

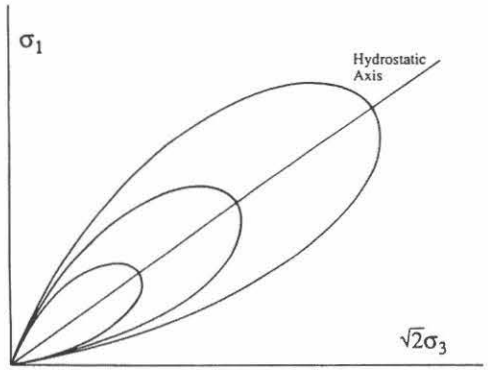

FIG. 4. Yield Surfaces Shown in Triaxial Plane

For softening the yield surface deflates isotropically according to an exponential decay function:

$$f_p'' = A \cdot e^{-B \cdot (W_p/p_a)} \quad \ldots\ldots (28)$$

in which A and B are positive constants to be determined on the basis of the slope of the hardening curve at the point of peak failure, as indicated in Fig. 5.

Using the expression for the plastic potential in Eq. 9, the relation between plastic work increment and the scalar factor of proportionality $d\lambda_p$ in Eq. 8 may be expressed as:

$$d\lambda_p = \frac{dW_p}{\mu \cdot g_p} \quad \ldots\ldots (29)$$

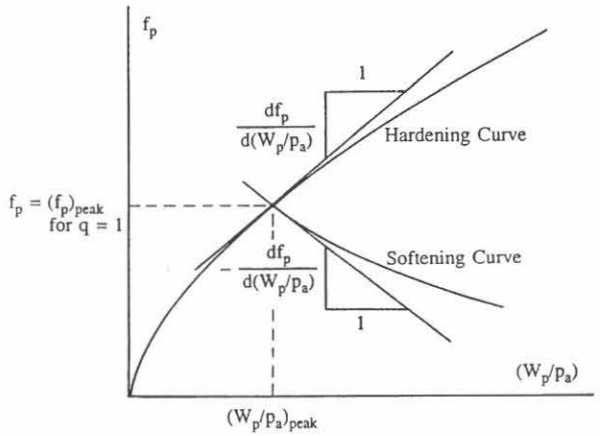

FIG. 5. Modeling of Work Hardening and Softening

in which the increment of plastic work can be determined by differentiation of the hardening and softening equations. For hardening, Eq. 20 yields:

$$dW_p = D \cdot p_a \cdot \rho \cdot f_p^{-1} \cdot df_p \quad \ldots\ldots (30)$$

and for softening Eq. 28 produces:

$$dW_p = -\left(\frac{1}{B}\right) \cdot p_a \cdot f_p^{-1} \cdot df_p \quad \ldots\ldots (31)$$

in which df_p is negative during softening.

Combining Eqs. 30 and 31 with Eq. 29 and substituting this and Eqs. 12*a–f* into Eq. 8 produces the expression for the incremental plastic strain increments.

3-D Experiments on Edgar Plastic Kaolinite

The single-hardening model has been employed for prediction of the three-dimensional behavior of normally consolidated, undrained clay. The experimental program is briefly reviewed.

Clay Tested

All tests reported here were performed on Edgar Plastic Kaolinite (EPK) clay whose specific gravity was 2.62. The particle size distribution indicated that the clay consisted of 50% silt and 50% clay size particles. Atterberg limits tests produced liquid limit (LL) = 58 and plastic limit (PL) = 37. The activity was 0.42. Note that this batch of EPK clay was different from those tested by Hicher and Lade (1987) and by Hong and Lade (1989). This may be seen from comparison of the Atterberg limits as well as the effective strength envelopes for the different batches.

Specimen Preparation

A slurry of EPK clay was mixed at a water content of twice the liquid limit and K_0-consolidated in a large double-draining consolidometer. Effective vertical consolidation pressures were chosen to be 0.2–0.5 kg/cm^2 (20–50 kPa) smaller than the final isotropic consolidation pressures to be used in the cubical triaxial tests. The consolidated clay cake was cut into pieces with volumes that were larger than those of the specimens to be tested. After thoroughly remolding the clay, cubical specimens were trimmed, installed in a cubical triaxial apparatus (Lade 1978), and consolidated isotropically at pressures near 2.5 kg/cm^2 (245 kPa). A few cubical specimens were prepared with other consolidation pressures to establish the basic behavior of the clay in triaxial compression.

A nominal back pressure of 1.50 kg/cm^2 (147 kPa) was applied in all tests to ensure full saturation of the specimens. The B values measured after the consolidation stage indicated that the specimens were fully saturated.

Cubical Triaxial Tests

In addition to isotropic consolidation and consolidated-undrained and drained triaxial compression tests, a series of consolidated-undrained cubical triaxial tests with different but constant values of $b = (\sigma_2 - \sigma_3)/(\sigma_1 - \sigma_3)$ was performed using a vertical strain rate of 0.04 %/min. The testing procedure

was described in detail by Lade and Musante (1978) and Lade (1978). The measured stress-strain relations and pore pressure responses are presented in the following along with predictions from the single-hardening model.

Parameter Determination for EPK Clay

Characterization of a soil, such as normally consolidated clay, involves 11 constant parameter values. These parameter values are determined from results of isotropic compression (including unloading-reloading) and consolidated-undrained triaxial compression tests, as shown. The results of these tests are shown in Figs. 6 and 7.

Elastic Behavior

Based on the plasticity index for EPK clay (PI = 21), the value of Poisson's ratio is determined to be $\nu = 0.25$ from the empirical relation given by Lade (1979).

The variation of Young's modulus in Eq. 2 is shown in Fig. 8 for EPK clay. The individual values were determined from the unloading-reloading branch of the isotropic compression test as well as from the initial slopes of the triaxial compression stress-strain curves. The best description of the elastic behavior is obtained with values of $M = 30$ and $\lambda = 0.68$.

Failure Criterion

The soil parameters required in the failure criterion given by Eq. 6 were determined from the log-log diagram in Fig. 9. The straight line on this diagram corresponds to $\eta_1 = 48$ and $m = 0.54$. Only the data from the triaxial compression tests were used for the determination of these parameters.

The results of the cubical triaxial tests are shown in Fig. 9 for comparison. Some scatter of the data around the solid line is present, but the failure criterion selected on the basis of the triaxial compression tests appears to represent the data quite well.

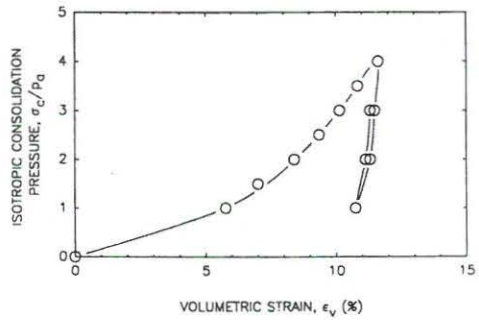

FIG. 6. Results of Isotropic Consolidation Test on Remolded, Normally Consolidated Edgar Plastic Kaolinite

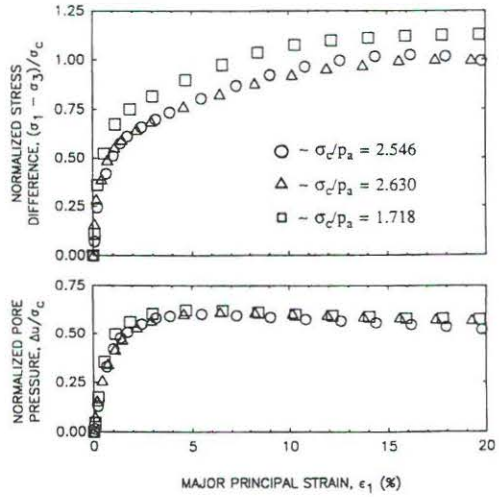

FIG. 7. Results of Three Consolidated-Undrained Triaxial Compression Tests on Remolded, Normally Consolidated Edgar Plastic Kaolinite

Plastic Potential Function

The plastic potential function given in Eq. 9 requires determination of Ψ_2 and μ from the experimental data. These parameters were determined using Eq. 15 and the results of some of the consolidated-undrained triaxial compression tests. Fig. 10 shows that all points for practical purposes fall on one straight line in this diagram. This demonstrates that essentially one

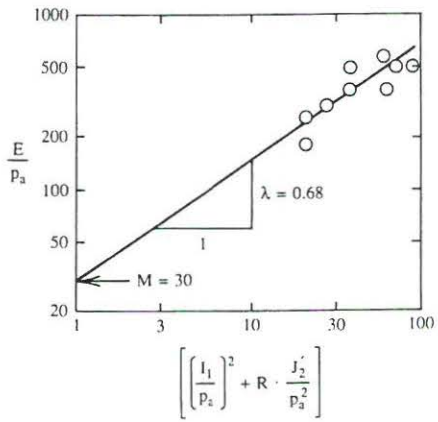

FIG. 8. Determination of M and λ for Young's Modulus for Edgar Plastic Kaolinite

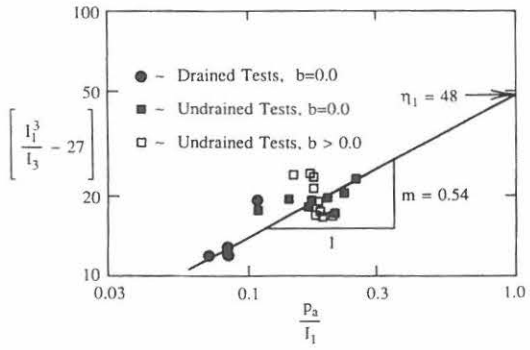

FIG. 9. Determination of η_1 and m for Failure Criterion for Edgar Plastic Kaolinite

type of stress-strain behavior is observed for a given normally consolidated clay independently of the magnitude of the consolidation pressure. The parameter values determined from this diagram are $\Psi_2 = -3.08$ and $\mu = 2.38$.

Yield Criterion and Work-Hardening/Softening Law

The work-hardening relation along the hydrostatic axis, expressed in Eq. 27, is determined first, since the parameter values of C and p are required in determination of q in the yield criterion.

Fig. 11 shows the plastic work obtained from an isotropic consolidation test plotted versus the value of the first stress invariant on dimensionless form. This relationship is modeled by Eq. 27 in which C is the intercept at $I_1/p_a = 1$, and p is the slope of the straight line. For EPK clay the best-fitting values are $C = 0.0030$ and $p = 1.48$.

The yield criterion in Eq. 19 requires two parameter values. The value of h is determined as the average obtained from Eq. 21, using data from three triaxial compression tests. For EPK clay, values of 0.785, 0.843, and 0.804

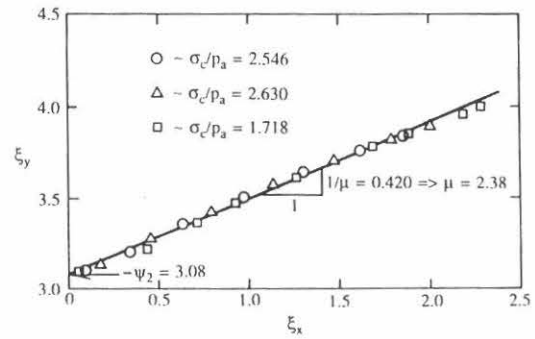

FIG. 10. Determination of ψ_2 and μ for Plastic Potential Function for Edgar Plastic Kaolinite

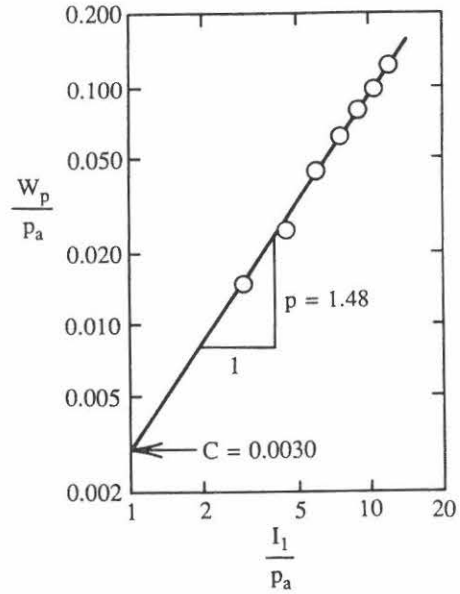

FIG. 11. Determination of C and p for Work-Hardening Relation for Edgar Plastic Kaolinite

were obtained from tests with increasingly high consolidation pressures, which produce an average value of $h = 0.81$.

To determine the variation of the exponent q in Eq. 19 with the stress level S, values of q are calculated from Eq. 23 and S values are obtained

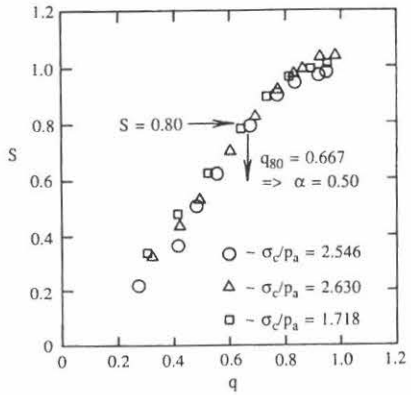

FIG. 12. Determination of α for Yield Criterion for Edgar Plastic Kaolinite

TABLE 1. Summary of Parameter Values for Edgar Plastic Kaolinite

Model component (1)	Parameter (2)	Value (3)
Elastic behavior	Modulus number M	30
	Exponent λ	0.68
	Poisson's ratio ν	0.25
Failure criterion	Intercept η_1	48
	Exponent m	0.54
Plastic potential	Intercept Ψ_2	−3.08
	Exponent μ	2.38
Yield criterion	Exponent h	0.81
	Constant α	0.50
Hardening function	Intercept C	0.0030
	Exponent p	1.48

from Eq. 22 and plotted as shown in Fig. 12. The variation of q with S is then described by Eq. 24 in which α is constant. The best-fitting value of α is determined from Eq. 24 using simultaneous values of q and S at S = 0.80. As indicated in Fig. 10, the value of α = 0.50 is determined for EPK clay.

Summary of Parameter Values for EPK Clay

The values of the parameters for Edgar Plastic Kaolinite have been determined from an isotropic compression test and consolidated-undrained triaxial compression tests. The 11 parameter values required for normally consolidated clay are listed in Table 1. None of the parameters have dimensions. All dimensions are controlled, where appropriate, by the dimension of the atmospheric pressure, p_a, as in Eq. 2. The parameters in Table 1 may be used to calculate strains in EPK clay for any combination of effective stresses during primary loading, neutral loading, unloading, and reloading.

Prediction of Behavior of Normally Consolidated EPK Clay

The model presented here is generally applicable to frictional materials, such as clay, sand, concrete, and rock. In the process of developing the model, individual components of observed behavior of some frictional materials were compared with the model behavior. Here the stress-strain behavior observed in consolidated-undrained cubical triaxial tests on remolded, normally consolidated Edgar Plastic Kaolinite will be predicted. Thus, all model components must work in concert to produce reasonable predictions.

A computer program was developed to perform the necessary calculations involved in using the single-hardening constitutive model for prediction of undrained tests. The prediction of pore pressures and soil behavior under undrained conditions is based on the conditions that no volume change occurs in the soil for any load increment, i.e.:

$$\Delta\epsilon_v^e + \Delta\epsilon_v^p = 0 \quad \ldots\ldots (32)$$

in which $\Delta\epsilon_v^e$ = elastic volumetric strain increment; and $\Delta\epsilon_v^p$ = plastic volumetric strain increment for a given load increment. Calculation of pore pressures was performed by specifying the cell pressure, the value of $b = (\sigma_2 - \sigma_3)/(\sigma_1 - \sigma_3)$, and discrete values of the stress difference $(\sigma_1 - \sigma_3)$. The effective confining pressure producing volumetric strains that would satisfy Eq. 32 within specified limits was found by iteration. The limits used for the total volumetric strain (not the volumetric strain increment for each load step) was ±0.010%, but narrower limits could have been used. However, the predicted pore pressures and soil behavior were not significantly affected by these limits as long as they were reasonably narrow. After having satisfied Eq. 32, the pore pressure was calculated as the difference between the total confining pressure and the effective confining pressure found by iteration.

Stress-Strain and Pore Pressure Behavior

The results of the cubical triaxial tests are shown in Fig. 13, together with the predictions of the single-hardening model. The normalized stress difference $(\sigma_1 - \sigma_3)/\sigma_c$, the effective stress ratio σ_1'/σ_3', and the normalized pore pressure $\Delta u/\sigma_c$ are plotted against the major principal strain ϵ_1. The isotropic consolidation pressure σ_c was near 2.5 kg/cm^2 (245 kPa) for all cases shown in Fig. 13. The points in this figure represent the measured soil and pore pressure behavior, and the solid lines represent the model predictions.

The comparisons shown in Fig. 13(*a*) for the triaxial compression test indicate that the soil and pore pressure behavior is calculated with good accuracy by the model. Because the parameter values were initially derived from the results of this and similar tests with other consolidation pressures, good agreement could be expected.

The results of the cubical triaxial tests with three unequal principal stresses are compared with the predictions in Fig. 13(*b–f*). The predicted response agrees well with the measured behavior for all cubical tests. The influence of the intermediate principal stress on the soil and pore pressure behavior and on the variation in strength is correctly reflected by the single-hardening model.

Relation Between Principal Strains

An important aspect of a constitutive model is its ability to capture correctly the relations between strains under three-dimensional stress conditions. Fig. 14 shows comparisons of measured and predicted relations between principal strains. The measured intermediate principal strains ϵ_2 are expansive for b values smaller than 0.40–0.45 and compressive for higher values of b. Predictions indicate that plane-strain conditions, $\epsilon_2 = 0$, occur near b = 0.46, but otherwise generally agree with the measured behavior. Small errors in strain measurements may be present, as indicated near triaxial extension b = 1.00, where the two principal strains are expected to be equal, $\epsilon_1 = \epsilon_2$, for an isotropic material. The model predicts this behavior correctly, while the measurements show small deviations from this ideal.

The minor principal strains ϵ_3 are expansive in all cases and decrease with increasing b value as indicated in Fig. 14(*b*) for both measurements and model predictions.

The points corresponding to failure according to the maximum effective stress ratio are indicated on each curve in Fig. 14. The major principal strain-to-failure decreases with increasing b value. The predicted behavior indicates

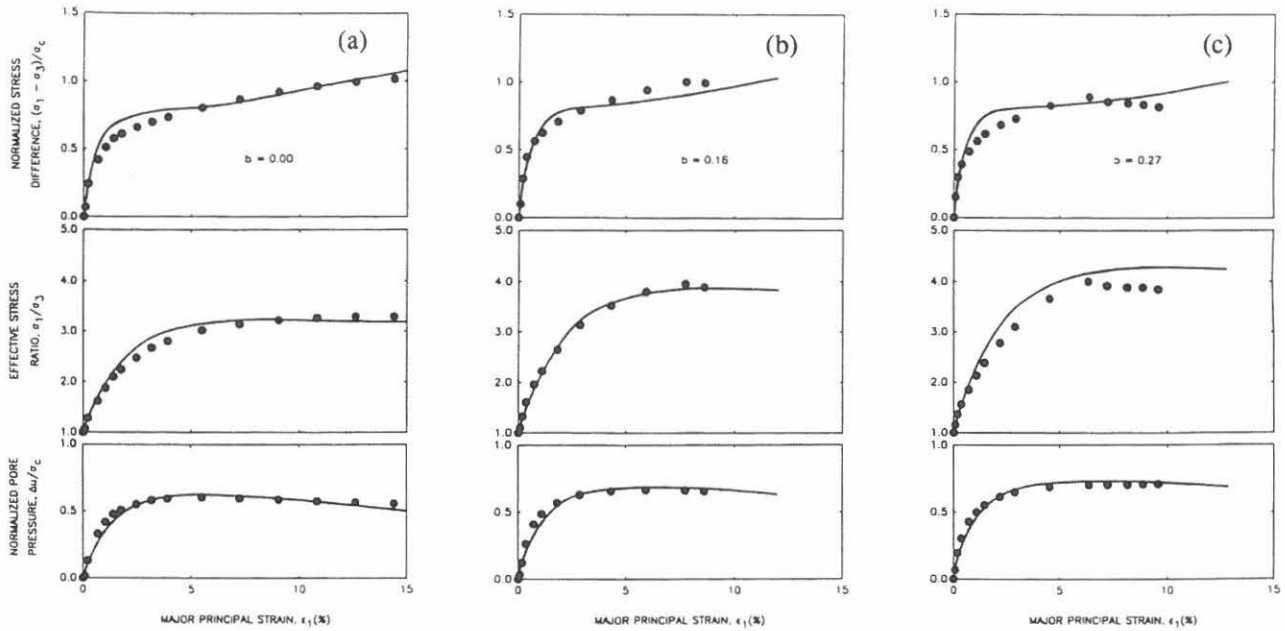

FIG. 13. Comparison of Measured and Predicted Stress-Strain and Pore Pressure Characteristics for Cubical Triaxial Tests on Edgar Plastic Kaolinite

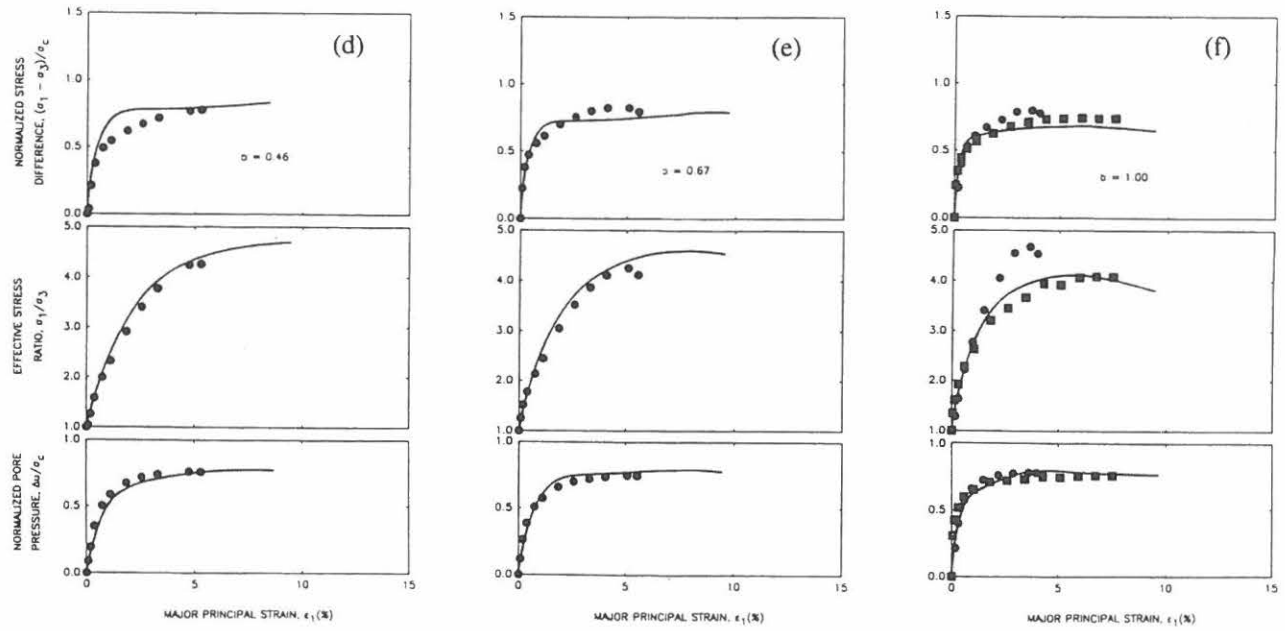

FIG. 13. (*Continued*)

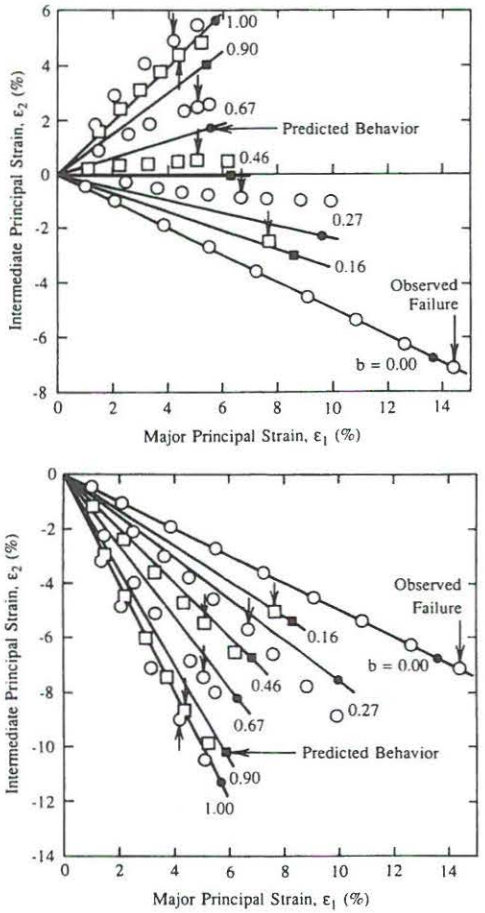

FIG. 14. Comparison of Measured and Predicted Relations Between Principal Strains for Cubical Triaxial Tests on Edgar Plastic Kaolinite

that the maximum effective stress ratio occurs at 1.5–5% larger strains. However, the predicted effective stress ratio curves in Fig. 13 exhibit very little variation near their maximum values, and this discrepancy in strain-to-failure may therefore not be significant.

Undrained Shear Strength

Of greater interest is the variation of the normalized undrained shear strength s_u/σ_c under three-dimensional conditions. A constant value of this ratio implies that Tresca's failure criterion applies to the soil under undrained conditions. Fig. 15 shows the variation of s_u/σ_c with b. Clearly, the experimental results for the remolded, normally consolidated EPK clay show that

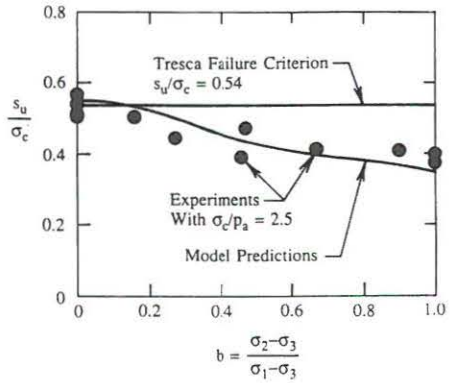

FIG. 15. Comparison of Measured and Predicted Normalized Undrained Shear Strength for Cubical Triaxial Tests on Edgar Plastic Kaolinite

Tresca failure criterion is not applicable and that, in fact, s_u/σ_c is not constant but decreases with increasing b value. The decrease in this ratio from $s_u/\sigma_c = 0.54$ in triaxial compression, $b = 0$, to $s_u/\sigma_c = 0.38$ in triaxial extension, $b = 1$, corresponds to a change of 30%. This substantial drop in normalized undrained shear strength is not accounted for by the Tresca failure criterion, which is most often assumed to hold for total stress stability analyses of soil structures. The decrease in s_u/σ_c from triaxial compression to plane strain conditions, $b = 0.40$–0.45, for which most analyses procedures have been developed, is in the order of 20% for the remolded EPK clay.

The predictions of maximum shear strengths from the single-hardening model are also shown in Fig. 15. The model predictions generally follow the experimental observations. For triaxial compression, the value of $s_u/\sigma_c = 0.55$, and for triaxial extension $s_u/\sigma_c = 0.34$, which corresponds to a 38% decrease. This decrease is a little larger than observed, but the predictions for plane-strain conditions correspond very well with the experimental observations. The overall comparison of predicted and measured normalized undrained shear strength indicates that the single-hardening constitutive model is capable of predicting the behavior under three-dimensional conditions with good accuracy.

The variation in undrained shear strength with b has often been attributed to effects of anisotropy (see e.g., Ladd and Foott 1974). However, the experiments performed for this study were carried out on laboratory-prepared, remolded, isotropically consolidated EPK clay, and the predictions of undrained behavior were made by an isotropic model. The differences in undrained shear strength observed and predicted for different test conditions could therefore not be due to anisotropy. These differences are accounted for by the presence of the third stress invariant I_3 in the model. Natural clay deposits exhibits cross-anisotropic behavior, and it is possible that the undrained shear strengths of such deposits exhibit further effects of cross-anisotropy.

Conclusions

The behavior of frictional materials allows for a unified approach in describing their failure surfaces as well as their stress-strain relations. A combination of elasticity theory and plasticity theory may provide a reasonable and consistent description of this behavior when appropriate mathematical functions are used in the framework provided by these theories. In addition to Hooke's law, the components in this framework are the failure criterion, the flow rule, the yield criterion, and the work-hardening/softening law. Analyses of experimental data indicate that the shapes of the failure, yield, and plastic potential surfaces obtained from different types of frictional materials each have similar characteristics and may be modeled by similar mathematical functions. These functions are all expressible in terms of the three invariants of the stress tensor.

The nonassociated flow rule is derived from a plastic potential whose shape in the principal stress space resembles a cigar with an asymmetric cross section. Yielding occurs along a single, isotropic yield surface shaped as an asymmetric teardrop. This yield surface describes a contour of constant plastic work. Because plastic yielding is related directly to plastic work contours, the description of the work-hardening/softening law is straightforward. The transition from hardening to softening occurs abruptly at the peak failure point. Thus, no points with a hardening modulus of zero are encountered, but the pointed peak is hardly noticeable in actual comparisons with experimental data.

The constitutive model combines all the governing functions studied individually in a mathematically consistent entity. The model requires 11 parameters for normally consolidated clay. These parameters can be determined from simple laboratory tests, such as isotropic compression and conventional consolidated-undrained triaxial compression tests.

The results of a study of the three-dimensional behavior of remolded, normally consolidated Edgar Plastic Kaolinite served as a basis for evaluating the capabilities of the model. In particular, the variations of stress-strain and pore pressure behavior, relation between principal strains, and normalized undrained shear strength with the relative magnitude of the intermediate principal stress were studied. Overall acceptable and accurate predictions were produced for the normally consolidated clay. The presence of the third stress invariant in the model accounts for the variation in undrained shear strength observed in three-dimensional tests on isotropic, normally consolidated clay.

Acknowledgment

This study was supported by the National Science Foundation under Grant No. CEE 8211159. Grateful appreciation is expressed for this support.

Appendix. References

Dafalias, Y. F., and Herrmann, L. R. (1980). "A bounding surface soil plasticity model." *Proc. Int. Symp. Soils under Cyclic and Transient Loading*, 335–345, Balkema, Rotterdam, Netherlands.

Desai, C. S., and Faruque, M. O. (1984). "Constitutive model for (geological) materials." *J. Engrg. Mech.*, ASCE, 110(9), 1391–1408.

DiMaggio, F. L., and Sandler, I. S. (1971). "Material model for granular soils." *J. Engrg. Mech. Div.*, ASCE, 97(3), 935–950.

Drucker, D. C., Gibson, R. E., and Henkel, D. J. (1957). "Soil mechanics and work-hardening theories of plasticity." *Trans.*, ASCE, 122, 338–346.

Frantziskonis, G., Desai, C. S., and Somasundaram, S. (1986). "Constitutive model for nonassociative behavior." *J. Engrg. Mech.*, ASCE, 112(9), 932–946.

Ghaboussi, J., and Momen, H. (1982). "Modelling and analysis of cyclic behavior of sands." *Soil mechanics-transient and cyclic loads*, G. N. Pande and O. C. Zienkiewicz, eds., John Wiley and Sons, Inc., London, England, 313–342.

Hicher, P.-Y., and Lade, P. V. (1987). "Rotation of principal directions in K_o-consolidated Clay." *J. Geotech. Engrg.*, ASCE, 113(7), 774–788.

Hong, W. P., and Lade, P. V. (1989). "Strain increment and stress directions in torsion shear tests." *J. Geotech. Engrg.*, ASCE, 115(10), 1388–1401.

Kim, M. K., and Lade, P. V. (1984). "Modelling rock strength in three dimensions." *Int. J. Rock Mech. Min. Sci. Geomech. Abstr.*, 21(1), 21–33.

Kim, M. K., and Lade, P. V. (1988). "Single hardening constitutive model for frictional materials, I. Plastic potential function." *Computers and Geotechnics*, 5(4), 307–324.

Ladd, C. C., and Foott, R. (1974). "New design procedure for stability of soft clays." *J. Geotech. Engrg. Div.*, ASCE, 100(7), 763–786.

Lade, P. V. (1977). "Elasto-plastic stress-strain theory for cohesionless soil with curved yield surfaces." *Int. J. Solids Struct.*, 13, 1019–1035.

Lade, P. V. (1978). "Cubical triaxial apparatus for soil testing." *Geotech. Test. J.*, 1(2), 93–101.

Lade, P. V. (1979). "Stress-strain theory for normally consolidated clay." *Proc. 3rd Int. Conf. Numerical Methods Geomechanics*, 1325–1337, Aachen, West Germany.

Lade, P. V. (1982). "Three-parameter failure criterion for concrete." *J. Engrg. Mech. Div.*, ASCE, 108(5), 850–863.

Lade, P. V. (1984). "Failure criterion for frictional materials." *Mechanics of engineering materials*, C. S. Desai and R. H. Gallagher, eds., John Wiley and Sons, Inc., New York, N.Y., 385–402.

Lade, P. V. (1988). "Model and parameters for the elastic behavior of soils." *Proc. 6th Int. Conf. Numerical Methods Geomechanics*, 359–364, Innsbruck, Austria.

Lade, P. V., and Kim, M. K. (1988a). "Single hardening constitutive model for frictional materials, II. Yield criterion and plastic work contours." *Computers and Geotechnics*, 6(1), 13–29.

Lade, P. V., and Kim, M. K. (1988b). "Single hardening constitutive model for frictional materials, III. Comparisons with experimental data." *Computers and Geotechnics*, 6(1), 30–47.

Lade, P. V., and Musante, H. M. (1978). "Three-dimensional behavior of remolded clay." *J. Geotech. Engrg. Div.*, ASCE, 104(2), 193–209.

Lade, P. V., and Nelson, R. B. (1987). "Modelling the elastic behaviour of granular materials." *Int. J. Numer. Anal. Methods Geomech.*, 11, 521–542.

Mroz, Z., Norris, V. A., and Zienkiewicz, O. C. (1981). "An anisotropic, critical state model for soils subjects to cyclic loading." *Geotechnique*, London, England, 31(4), 451–469.

Pande, G. N., and Pietruszak, S. (1982). "Reflecting surface model for soils." *Proc. Int. Symp. Numerical Models in Geomechanics*, 50–64, Balkema, Rotterdam, Netherlands.

Poorooshasb, H. B., and Pietruszak, S. (1985). "On yielding and flow of sand; a generalized two-surface model." *Computers and Geotechnics*, 1(1), 33–58.

Prevost, J.-H. (1978). "Plasticity theory for soil stress-strain behavior." *J. Engrg. Mech. Div.*, ASCE, 104(5), 1177–1194.

Roscoe, K. H., and Burland, J. B. (1968). "On the generalized stress-strain behaviour of 'wet' clay." *Engineering Plasticity*, J. Heymann and F. A. Leckie, eds., Cambridge University Press, Cambridge, England, 535–609.

Comparison of Double and Single Hardening Models

Numerical Models in Geomechanics, NUMOG III, Edited by S. Pietruszczak and G.N. Pande, Elsevier Applied Science, London, 1989

COMPARISON OF SINGLE AND DOUBLE HARDENING CONSTITUTIVE MODELS FOR FRICTIONAL MATERIALS

Poul V. Lade and Daniel Pradel
Department of Civil Engineering
University of California
Los Angeles, California 90024-1593, USA

ABSTRACT

Two constitutive models for frictional materials, one with a single yield surface and the other with two intersecting yield surfaces, are compared in terms of their capabilities to accurately capture the observed behavior of soils for various stress-paths and in terms of the ease with which they can be employed in large computer programs. Both models have been shown to capture the behavior of soils for a variety of stress-paths. The double hardening model may model the observed soil behavior with slightly better accuracy near the hydrostatic axis, but the single hardening model may be used with greater ease and economy in large scale computations.

INTRODUCTION

The primary concern in development of constitutive models is their capabilities in modeling the material behavior under all stress and strain conditions. It is therefore of interest to compare the capabilities and limitations of a newly developed model which employs a single yield surface and nonassociated flow and a previous model which uses two intersecting yield surfaces, one with associated flow and the other with nonassociated flow. Specifically, the definitions of yielding in the two models are different, and this results in different effective shapes of the yield surfaces. The combined plastic potential at the intersection of the two yield surfaces in the double hardening model is discussed in view of its dependence on the stress-path direction.

Another important consideration in choosing a constitutive model for practical use relates to the ease and efficiency with which it can be employed in large computer programs. Thus, the double hardening model involves four different combinations of active and inactive yield surfaces, whereas the single hardening model only incorporates two possibilities (loading and unloading). This results in different amounts of calculations and checking within the computer programs and the resulting differences in efficiency and economy may be decisive in the choice of constitutive model.

SINGLE AND DOUBLE HARDENING MODELS

The two elasto-plastic constitutive models have the elastic formulation and the failure criterion in common. The newly developed model [1,2,3] employs a single isotropic yield surface that is expressed as a contour of constant plastic work. The resulting yield surfaces are shaped as asymmetric tear drops with smoothly rounded triangular cross-sections in octahedral planes and traces in the triaxial plane as shown in Fig. 1. As the plastic work increases, the isotropic yield surface inflates until the current stress point reaches the failure surface. The relation between the yield criterion and the plastic work is described by a monotonically increasing function whose slope decreases with increasing plastic work as shown in Fig. 2. Beyond failure the yield surface contracts isotropically with increasing amount of plastic work [2]. A nonassociated flow rule is employed with the single yield surface. This flow rule is derived from a plastic potential whose shape in the principal stress space resembles an asymmetric cigar with smoothly rounded triangular cross-sections as shown in Fig. 3(a). The shape of the meridians are shown in the triaxial plane in Fig. 3(b). This shape accounts for the rather abrupt change in volume change behavior near the hydrostatic axis observed in experiments [1].

The double hardening model [4] involves two mechanisms which may or may not interact to produce the total plastic strain increment. The conical yield surface shown in Fig. 4(a) is shaped as an asymmetric bullet with its pointed apex at the origin of the stress space and with a smoothly rounded triangular cross-section in octahedral planes. Plastic expansive strain increments produced at this yield surface are calculated from a nonassociated flow rule as indicated in Fig. 4(a). The yield surface corresponding to the plastic collapse strains forms a cap on the open end of the conical yield surface as shown in Fig. 4(b). The collapse yield surface is shaped as a sphere with center in the origin of the principal stress space. The plastic collapse strains are calculated from an associated flow rule.

The result of a change in stress is shown in the triaxial plane in Fig. 4(b). Both plastic collapse and plastic expansive strains are caused by the change in stress from point A to point B, because both yield surfaces are pushed out. The magnitudes of the strain increments are indicated by the lengths of the vectors, and the total plastic strain increment is calculated as the vector sum of the two components. The elastic strain components are further added (not shown in Fig. 4) to obtain the total strain increment for the stress change from A to B.

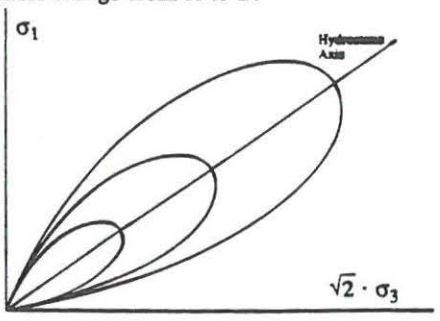

Figure 1. Yield Surfaces for Single Hardening Model Shown in Triaxial Plane.

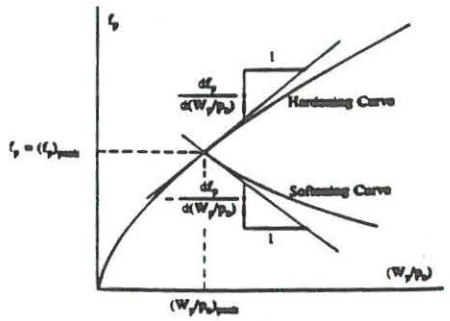

Figure 2. Modeling of Work-Hardening and Softening in Single Hardening Model.

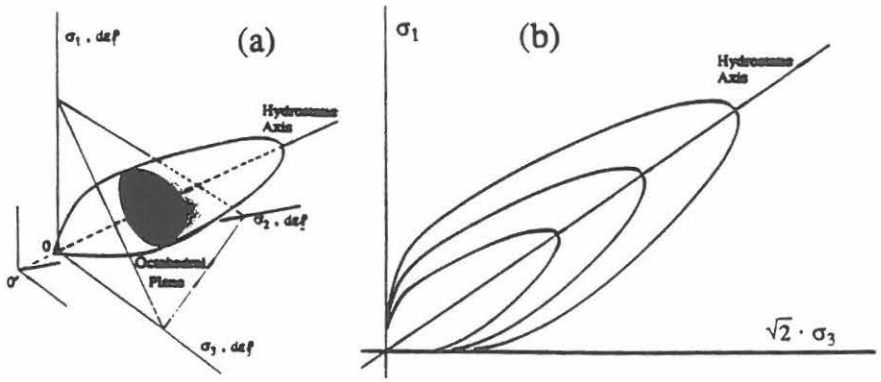

Figure 3. Plastic Potential Surfaces Employed in Single Hardening Model and Shown in (a) Principal Stress Space, and in (b) Triaxial Plane.

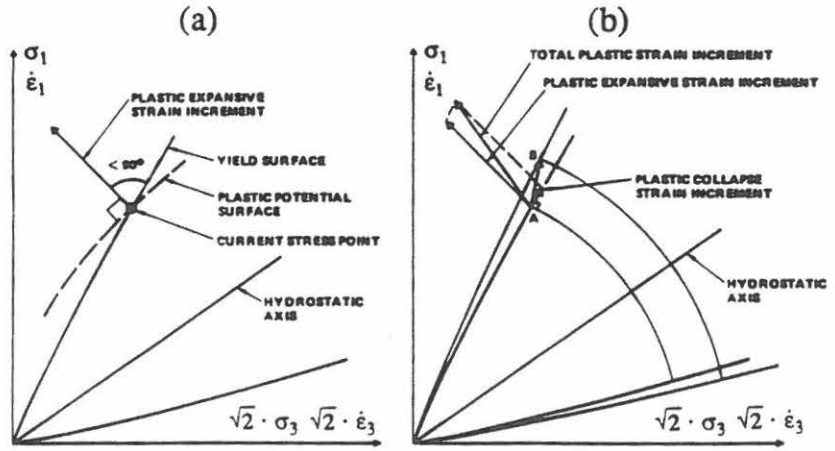

Figure 4. Schematic Diagrams of (a) Yield and Plastic Potential Surfaces for Plastic Expansive Strains, and of (b) Yielding Process with Both Yield Surfaces Activated and Combination of Plastic Strain Increments for Double Hardening Model.

EFFECT OF STRESS-PATH DIRECTION ON STRAINS

The magnitude of plastic strain produced for a given location of the yield surface is proportional to the movement of the yield surface expressed as Δf. For a given magnitude of stress increment (expressed as the length of the stress increment vector), the value of Δf depends on the direction of the stress increment, as illustrated in Fig. 5(a). The largest value of Δf is obtained when the stress increment direction is perpendicular to the yield surface.

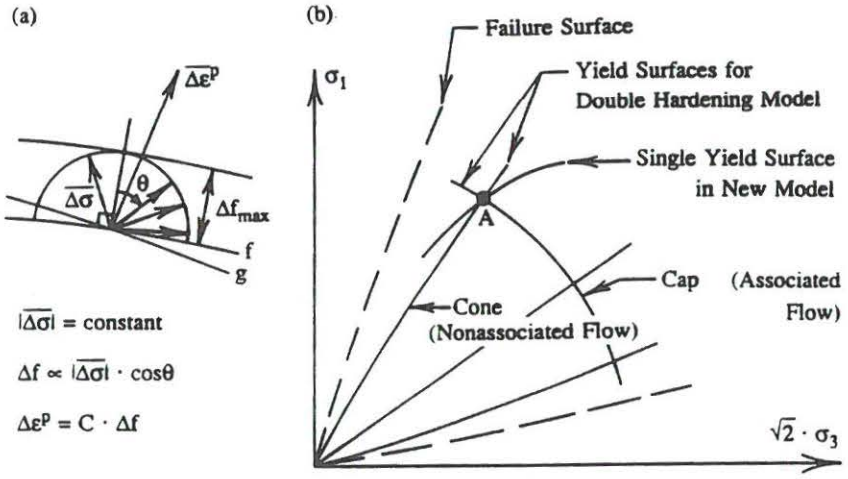

Figure 5. (a) Effect of Stress Path Direction on Resulting Magnitude and Direction of Plastic Strain Increment at Single Yield Surface, and (b) Yield Surfaces in Double Hardening and Single Hardening Models.

The direction of the plastic strain increment is by definition perpendicular to the plastic potential surface independently of the direction of the stress increment. This is illustrated for a nonassociated plastic potential surface in Fig. 5(a).

The yield surfaces used in the double hardening model as well as the yield surface used in the single hardening model are shown in Fig. 5(b). The effect of adding a stress increment of a given length at point A on the resulting plastic strain increment is demonstrated for both models in Fig. 6. Four directions of the stress increment vector are considered. In case (a) the stress increment vector is causing the conical yield surface to move out, while the cap remains stationary. The resulting plastic strain increment $\overline{\Delta\varepsilon^p}$ produced from the nonassociated plastic potential is shown in Fig. 6(a). The effect of the same stress increment in the single hardening model is shown in Fig. 6(e). The strain increments from the two models may be slightly different in direction and in magnitude, as shown in Fig. 6.

In case (b) the stress increment vector has the same length, but it is directed almost tangential to the spherical cap yield surface and therefore almost perpendicular to the conical yield surface. The plastic strain increment vector from the cap is small, whereas the conical yield surface produces a very large plastic strain increment vector. The resulting vector, $\overline{\Delta\varepsilon^{pc}}$, is longer, and it is pointed in a slightly different direction than that obtained from case (a). In comparison, the single yield surface model, shown in Fig. 6(f), produces a plastic strain increment vector which is pointed in the same direction as that indicated in Fig. 6(e). Its length is indicated to be much larger.

In case (c), the stress increment vector is pointing outwards from the origin and slightly upward from the conical yield surface. This results in a relatively large incremental movement of the cap yield surface with a correspondingly large plastic strain increment as indicated in Fig. 6(c). The conical yield surface moves comparatively very little and the corresponding plastic strain increment is small, as also indicated in Fig. 6(c). The

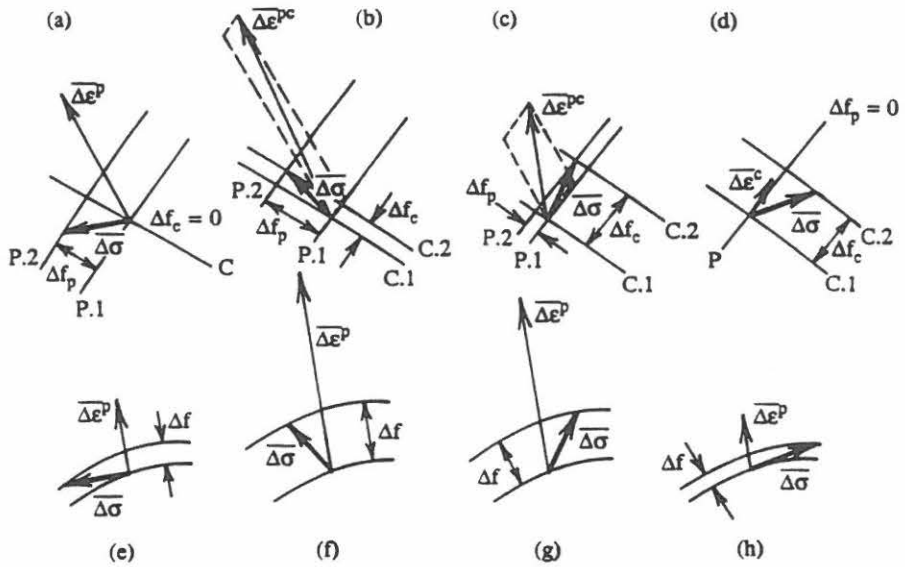

Figure 6. Schematic Illustrations of Effects of Stress-Path Direction in (a)-(d) Double Hardening Model, and in (e)-(h) Single Hardening Model.

combined plastic strain increment, $\overline{\Delta\varepsilon^{pc}}$, is obtained by adding the two vectors. Fig. 6(g) shows the result of the same stress increment for the single hardening model. The magnitudes of the two resulting plastic strain increment vectors are slightly different, but their directions are the same for this case.

The cap is the only active yield surface in case (d). Thus, a small plastic strain increment, $\overline{\Delta\varepsilon^c}$, perpendicular to the cap is produced for this case where the stress increment is directed outwards and towards the hydrostatic axis. The effect of the same stress increment in the single hardening model is shown in Fig. 6(h). Although similar in magnitude, the two strain increment vectors have different directions.

Thus, in principle the two models respond differently to the same increment in stress. However, the diagrams in Fig. 6 have been drawn to illustrate the difference between the two models in a schematic fashion. In reality, the strains produced by the cap are much smaller than those obtained from the conical yield surface. The contributions from the cap to the total plastic strain increments are therefore unimportant, except in the vicinity of the hydrostatic axis or for a stress-path directed outwards and towards the hydrostatic axis for which they are the only plastic strains to be produced.

Experimental evidence indicates that the stress-path dependent response obtained from the double hardening model is also observed for real soils. Fig. 7 shows the results of an investigation of stress-path dependency in sand performed by Tatsuoka and Ishihara [5]. The stress-paths and the corresponding strain increments from the experiments are replotted on the triaxial plane for direct comparison with the diagrams in Figs. 5 and 6. Point X in Fig. 7 is located relatively close to the hydrostatic axis (X corresponds to $\sigma_1/\sigma_3 = 1.75$ and the failure line has $\sigma_1/\sigma_3 = 4.33$) where the plastic strains are not very pronounced.

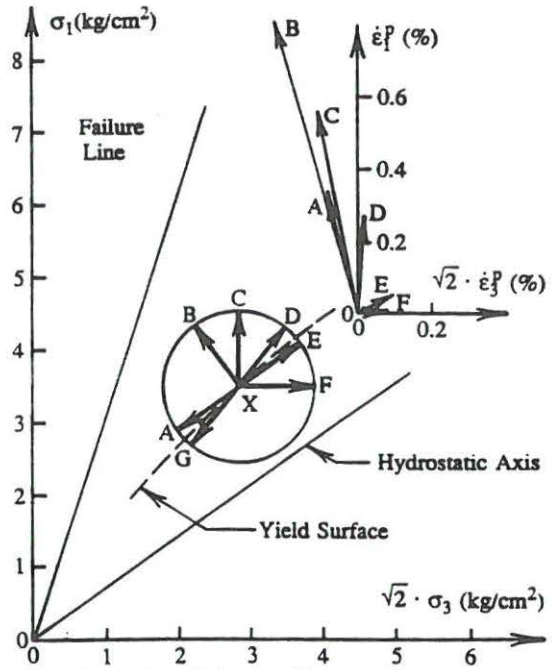

Figure 7. Stress-Path Dependent Behavior Observed in Fuji River Sand and Replotted in Triaxial Plane (after Tatsuoka and Ishihara [5]).

The stress probes, which have the same lengths, start at point X and have directions similar to those considered in Fig. 6. The resulting plastic strain increments shown on the insert in Fig. 7 are in most cases very similar to those constructed for the double hardening model in Fig. 6, i.e., compare case (a) with XA, case (b) with XB, case (c) with XD, and case (d) with XE and XF. Thus, the double hardening model is quite sensitive and can to some extent predict the effect of stress-path direction on the resulting plastic strains.

At higher stress levels closer to failure where the plastic strains are much larger, experiments by Poorooshasb et al. [6] show that the effect of the stress-path on the direction of the plastic strain increment vector is negligible. Thus, it is only near the hydrostatic axis where the plastic strains are small that stress-path dependent behavior is observed.

Both the single hardening and the double hardening models capture the experimentally observed behavior at the higher stress levels with good accuracy. The single hardening model is not sensitive to stress-path directions, and Fig. 6 shows that the same direction of the plastic strain increment vector is predicted for all cases. The predicted direction is that in which the plastic strains are largest, i.e., the general strain direction indicated by points A,B, and C in Fig. 7. Thus, a small volumetric component in the outward direction of the hydrostatic axis is missing in the single hardening model when exercised near, but off the hydrostatic axis. On the hydrostatic axis, the two models produce the same results.

However, more importantly, the single hardening model was devised to capture yielding using only one surface. This surface describes a contour of constant plastic work as measured from the origin. The resulting tear-drop shaped yield surface combined with the nonassociated, cigar-shaped plastic potential surface produced shear and volumetric plastic strains in agreement with experimental results for the majority of cases where plastic strains are observed. The tear-drop shaped yield surface is more curved than the conical surface used in the double hardening model, also near failure where it crosses the failure surface. This shape is in better agreement with experimental observations, e.g. [5]. Furthermore, the direct association between yielding and plastic work results in a unique hardening curve, as shown in Fig. 2, and it produces a model that is mathematically consistent.

EASE OF COMPUTATION

Whereas both models have been shown to capture the behavior of soils with good accuracy, the two models are not equally easy to use for computations in large computer programs. Fig. 8 illustrates the considerations involved. If the current state of stress for a material element is given at point A, then the double hardening model presents four options in terms of the activities of the yield surface: (1) none of the yield surfaces are active (elastic unloading or reloading), (2) the cap yield is active, (3) the conical yield surface is active, or (4) both the cap and the conical yield surfaces are active. Each of the four options leads to a new material stiffness matrix as discussed in [7]. Since the stress-paths for each element in a large structure is generally not known (except in some relatively simple cases), the number of combinations of computations and iterations could become rather large.

In comparison, the single hardening model presents only two choices of material stiffness matrix for each element, shown in Fig. 8(b): (1) the yield surface is not active (elastic unloading or reloading), or (2) the yield surface is active. Because there are only two options for each element stiffness matrix, the number of computations is substantially smaller than that required for the double hardening model.

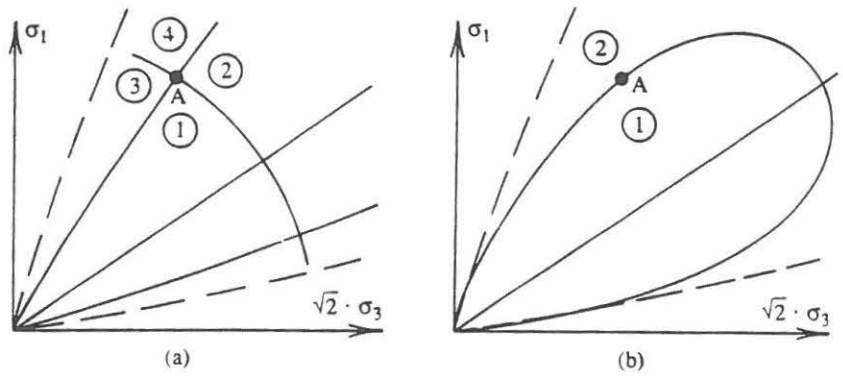

Figure 8. (a) Four Possibilities of Activities of Two Yield Surfaces, and (b) Two Possibilities for One Yield Surface.

Another feature of the single hardening model is that the transition from hardening to softening occurs abruptly at the peak failure point. Thus, there are no points with zero slope at the transition anywhere along the hardening curve. The absence of points with zero slope allows greater computational efficiency near peak failure, while the pointed peak is hardly noticeable in actual comparison with experimental data.

CONCLUSION

The consequences of employing single and double hardening constitutive models for the behavior of frictional materials have been presented in view of their abilities to model observed behavior and with regard to their application in large computer programs. In particular, the sensitivity of the models to predict the behavior along various stress-paths and their ability to capture the conditions for yielding correctly were reviewed. The ease with which computations may be made by each of the two models were also discussed. It was shown that except for some rather small contributions to the plastic strains near the hydrostatic axis, the single hardening model exhibited better capabilities than the double hardening model. Since only one yield surface is employed, the single hardening model is also more efficient for applications involving large computations.

REFERENCES

1. Kim, M.K. and Lade, P.V., Single Hardening Constitutive Model for Frictional Materials, I. Plastic Potential Function, Computers and Geotechnics, 5, 1988, 307-324.

2. Lade, P.V. and Kim, M.K., Single Hardening Constitutive Model for Frictional Materials, II. Yield Criterion and Plastic Work Contours, Computers and Geotechnics.

3. Lade, P.V. and Kim, M.K., Single Hardening Constitutive Model for Frictional Materials, III. Comparison with Experimental Data, Computers and Geotechnics.

4. Lade, P.V., Elasto-Plastic Stress-Strain Theory for Cohesionless Soil with Curved Yield Surfaces, Int. J. Solids Struct., 13, 1977, 1019-1035.

5. Tatsuoka, F. and Ishihara, K., Yielding of Sand in Triaxial Compression, Soils and Foundations, JSSMFE, 14, 1974, 63-76.

6. Poorooshasb, H.B., Holubec, I., and Sherbourne, A.N., Yielding and Flow of Sand in Triaxial Compression: Part I, Can. Geotech. J., 3, 1966, 179-190.

7. Lade, P.V. and Nelson, R.B., Incrementalization Procedure for Elasto-Plastic Constitutive Model with Multiple, Intersecting Yield Surfaces, Int. J. Num. Anal. Meth. Geomech., 8, 1984, 311-323.

Incrementalization Procedure

INTERNATIONAL JOURNAL FOR NUMERICAL AND ANALYTICAL METHODS IN GEOMECHANICS, VOL. 8, 311–323 (1984)

INCREMENTALIZATION PROCEDURE FOR ELASTO-PLASTIC CONSTITUTIVE MODEL WITH MULTIPLE, INTERSECTING YIELD SURFACES

POUL V. LADE AND RICHARD B. NELSON*

Mechanics and Structures Department, School of Engineering and Applied Science, University of California, Los Angeles, California 90024, U.S.A.

SUMMARY

Constitutive models for description of the non-linear stress–strain behaviour of engineering materials are often developed and presented in forms which cannot be employed directly in non-linear matrix computer analysis codes. Presented herein is a procedure for developing the incremental stiffness matrix for an elasto-plastic material model with multiple, intersecting yield surfaces. Associated or non-associated flow may occur on the individual yield surfaces. The material stiffness matrix is non-symmetric if non-associated flow occurs on any one of the yield surfaces. In order to illustrate the matrix forms which are generated, the case of a recently developed model with two yield surfaces is presented in detail. This model involves associated flow on one and non-associated flow on the other yield surface.

INTRODUCTION

The development of large, efficient computer codes capable of analysing static and dynamic response of geological media has rekindled interest in the basic mechanics of elasto-plastic materials. In fact, one of the weakest links in the analytical representations used in these analyses is the model of the material behaviour. This is especially true of the mathematical models which have been used to represent geological materials and concrete. However, based on relatively recent research (see, e.g., References 1–10), it is clear that geological media can be accurately modelled using concepts within the framework of the mathematical theories of elasticity and plasticity.

In such models, the strain increments are assumed to be separable into elastic and plastic parts with the elastic part linearly related to stress increments. The plastic strain increment is established by means of a plastic potential function and a yield function. The yield function defines the stress levels at which plastic strain increments will occur, and the plastic potential function defines the distribution (but not the magnitude) of the plastic strain increments during plastic flow. The actual magnitude of plastic deformation is determined from a work-hardening relationship. The plastic potential and the yield functions have often been assumed to be identical, in which case the plastic flow is termed associated. Pseudo thermo-dynamical arguments due to Drucker[11,12] have been used to justify this associated flow theory, and it should be noted that associated flow accurately represents the plastic behaviour of metals. In a series of careful experiments, Lade and others[13–15] have shown that geological media, in particular cohesionless soils, do not exhibit associated flow plasticity behaviour, but rather non-associated flow (resulting in separate yield and potential functions).

* Professors.

0363–9061/84/040311–13$01.30

Received 13 December 1982
Revised 28 January 1983

It has been proposed[16] that a number of yield surfaces may be employed to describe the boundaries of an elastic domain in stress space within which no yielding occurs. Plastic yielding occurs when at least one of the yield surfaces is activated. However, more than one surface may be active at the intersection of two or more yield surfaces. The phenomenological behaviour of geological materials can be modelled successfully by theories involving multiple, intersecting yield surfaces (e.g., see References 4 and 8). Each of these yield surfaces may have corresponding associated or non-associated plastic potential surfaces, which should be smooth and continuously differentiable[16] and convex with respect to the origin of the stress space.[17] Work-hardening or work-softening effects may be incorporated in yielding on each surface in order to model the various aspects of stress–strain behaviour observed for geological materials.

Models such as those proposed in References 7 and 18 employ several yield surfaces in descriptions involving kinematic hardening in order to predict anisotropic behaviour and hysteresis loops observed during large stress reversals. However, these yield surfaces do not intersect, and, in principle, only one yield surface is active at a time. These models therefore represent a restricted case of the types being considered here.

In this paper, a general mathematical procedure is presented for generating incremental elasto-plastic constitutive relations for materials modelled by multiple, intersecting yield surfaces. The development leads to a relatively simple, straightforward procedure for determining the incremental stress–strain relationship (stiffness matrix) required for use in a non-linear matrix computer analysis code. If the flow is non-associated on any one of the yield surfaces, the incremental stiffness matrix is non-symmetric.

Finally, the mathematical procedure is illustrated by the development of an elasto-plastic incremental stiffness matrix for Lade's non-associated, two yield surface model for soils.

ANALYTICAL DEVELOPMENT

Basic concepts from classical plasticity theory are employed in the derivation of the incremental elasto-plastic stress–strain relationship.[19–26]

An elasto-plastic constitutive model with multiple, intersecting yield surfaces is employed to capture the various aspects of non-linear stress–strain behaviour of soils. Each of these n yield surfaces is assumed to produce plastic strain increments whose sum, together with the elastic strain increments, makes up the total strain increments, $\{d\varepsilon\}$:

$$\{d\varepsilon\} = \{d\varepsilon^e\} + \{d\varepsilon^{p1}\} + \{d\varepsilon^{p2}\} + \ldots + \{d\varepsilon^{pk}\} + \ldots + \{d\varepsilon^{pn}\} \tag{1}$$

where $\{d\varepsilon^e\}$ are the elastic strain increments and $\{d\varepsilon^{pk}\}$ are the plastic strain increments associated with the kth surface ($1 \leq k \leq n$). Since $\{d\varepsilon\}$ is a 6×1 vector, the maximum possible number of independent strain increments is six. Since one strain increment is elastic, the maximum number of independent plastic strain increments is five, i.e. $1 \leq n \leq 5$. It should be noted that in expressing the strain increments in vector form,

$$\{d\varepsilon\}^T = \langle d\varepsilon_x, d\varepsilon_y, d\varepsilon_z, 2d\varepsilon_{yz}, 2d\varepsilon_{zx}, 2d\varepsilon_{xy}\rangle \tag{2}$$

The plastic strain increments for each yield surface $k (1 \leq k \leq n)$, $\{d\varepsilon^{pk}\}$, are assumed to be calculated from a work-hardening plasticity model, in which the plastic strain increments are expressed as functions of the total stress and the plastic work.

In order to incorporate such a constitutive model with n yield surfaces in a finite element or finite difference model, it is necessary to develop an incremental stress–incremental strain relationship of the form:

$$\{d\sigma\} = [C^{ep}]\{d\varepsilon\} \tag{3}$$

In this equation

$$\{d\sigma\}^T = \langle d\sigma_x, d\sigma_y, d\sigma_z, d\tau_{yz}, d\tau_{zx}, d\tau_{xy}\rangle \tag{4}$$

and $[C^{ep}]$ is an elasto-plastic material stiffness matrix.

In the following, a general procedure is presented for determining $[C^{ep}]$ for n $(1 \leq n \leq 5)$ simultaneous yield surfaces, each of which has either an associated or a non-associated flow rule. Finally, as a special case, the material stiffness is determined for a model with two yield surfaces, one with associated flow and the other with non-associated flow.

BASIC EQUATIONS

The total strain increments which occur during an increment in stress are assumed to be divisible into elastic components, $\{d\varepsilon^e\}$, and plastic components, $\{d\varepsilon^{pk}\}$, as expressed in equation (1).

Elastic strain increments

The stress increments and the elastic strain increments are assumed to be related by means of a symmetrical elasticity matrix, $[C^e]$:

$$\{d\sigma\} = [C^e]\{d\varepsilon^e\} \tag{5}$$

For an isotropic material:

$$[C^e] = \frac{E}{(1+\nu)(1-2\nu)} \cdot \begin{bmatrix} 1-\nu & \nu & \nu & 0 & 0 & 0 \\ & 1-\nu & \nu & 0 & 0 & 0 \\ & & 1-\nu & 0 & 0 & 0 \\ & & & \frac{1-2\nu}{2} & 0 & 0 \\ & \text{symmetric} & & & \frac{1-2\nu}{2} & 0 \\ & & & & & \frac{1-2\nu}{2} \end{bmatrix} \tag{6}$$

where E is Young's modulus and ν is Poisson's ratio.

Plastic strain increments

The plastic strain increments produced on the kth yield surface, where $1 \leq k \leq n \leq 5$, are assumed to be defined by means of a work-hardening plasticity theory which involves:

1. A yield criterion, which is used to distinguish between primary loading, neutral loading, unloading, and reloading. For a work-hardening material, the yield function may be written as:

$$f_k(\{\sigma\}, \{\varepsilon^{pk}\}) = 0 \tag{7}$$

2. A flow rule which relates the relative magnitudes of the plastic strain increments to the stresses:

$$\{d\varepsilon^{pk}\} = \lambda_k \cdot \left\{\frac{\partial g_k}{\partial \sigma}\right\} \tag{8}$$

where

$$g_k = g_k(\{\sigma\}) \tag{9}$$

is a plastic potential function which is a function of stress only. Again, if this function is the same as the yield function, f_k, then associated flow results; otherwise the flow is non-associated. The vector of derivatives of the kth plastic potential is

$$\left\{\frac{\partial g_k}{\partial \sigma}\right\}^T = \left\langle \frac{\partial g_k}{\partial \sigma_x}, \frac{\partial g_k}{\partial \sigma_y}, \frac{\partial g_k}{\partial \sigma_z}, 2\cdot\frac{\partial g_k}{\partial \tau_{yz}}, 2\cdot\frac{\partial g_k}{\partial \tau_{zx}}, 2\cdot\frac{\partial g_k}{\partial \tau_{xy}} \right\rangle \tag{10}$$

Using these basic equations, the incremental elasto-plastic stress–strain relationship may be derived as shown below.

INCREMENTALIZATION PROCEDURE

The basic concept in the incrementalization procedure is that all f_k (in equation (7)) which are zero, i.e. which indicate yielding, remain equal to zero during any increments in stress or strain. Thus, for each $f_k = 0$:

$$\left\{\frac{\partial f_k}{\partial \sigma}\right\}^T \{d\sigma\} + \left\{\frac{\partial f_k}{\partial \varepsilon^{pk}}\right\}^T \{d\varepsilon^{pk}\} = 0 \tag{11}$$

In equation (11)

$$\left\{\frac{\partial f_k}{\partial \sigma}\right\}^T = \left\langle \frac{\partial f_k}{\partial \sigma_x}, \frac{\partial f_k}{\partial \sigma_y}, \frac{\partial f_k}{\partial \sigma_z}, 2\cdot\frac{\partial f_k}{\partial \tau_{yz}}, 2\cdot\frac{\partial f_k}{\partial \tau_{zx}}, 2\cdot\frac{\partial f_k}{\partial \tau_{xy}} \right\rangle \tag{12}$$

$$\left\{\frac{\partial f_k}{\partial \varepsilon^{pk}}\right\}^T = \left\langle \frac{\partial f_k}{\partial \varepsilon_x^{pk}}, \frac{\partial f_k}{\partial \varepsilon_y^{pk}}, \frac{\partial f_k}{\partial \varepsilon_z^{pk}}, \frac{\partial f_k}{\partial \varepsilon_{yz}^{pk}}, \frac{\partial f_k}{\partial \varepsilon_{zx}^{pk}}, \frac{\partial f_k}{\partial \varepsilon_{xy}^{pk}} \right\rangle \tag{13}$$

Substituting the expression for $\{d\sigma\}$ in equation (5) into equation (11) gives:

$$\left\{\frac{\partial f_k}{\partial \sigma}\right\}^T [C^e]\{d\varepsilon^e\} + \left\{\frac{\partial f_k}{\partial \varepsilon^{pk}}\right\}^T \{d\varepsilon^{pk}\} = 0 \tag{14}$$

Substituting the expression for $\{d\varepsilon^e\}$ obtained from equation (1) into equation (14) gives:

$$\left\{\frac{\partial f_k}{\partial \sigma}\right\}^T [C^e]\left(\{d\varepsilon\} - \{d\varepsilon^{p1}\} - \ldots - \{d\varepsilon^{pk}\} - \ldots - \{d\varepsilon^{pn}\}\right) + \left\{\frac{\partial f_k}{\partial \varepsilon^{pk}}\right\}^T \{d\varepsilon^{pk}\} = 0 \quad k = 1, \ldots, n \tag{15}$$

Again, this result is based on the requirement that during flow, each of the n yield functions must remain zero so that $df_k = 0$.

At this point, the flow rule connected with f_k, equation (8), is substituted into equation (15), giving:

$$\left\{\frac{\partial f_k}{\partial \sigma}\right\}^T [C^e]\left(\{d\varepsilon\} - \lambda_1 \cdot \left\{\frac{\partial g_1}{\partial \sigma}\right\} - \ldots - \lambda_k \cdot \left\{\frac{\partial g_k}{\partial \sigma}\right\} - \ldots - \lambda_n \cdot \left\{\frac{\partial g_n}{\partial \sigma}\right\}\right)$$
$$+ \lambda_k \cdot \left\{\frac{\partial f_k}{\partial \varepsilon^{pk}}\right\}^T \left\{\frac{\partial g_k}{\partial \sigma}\right\} = 0 \quad k = 1, \ldots, n \tag{16}$$

These n equations must be solved to obtain the n unknowns, λ_k, $k = 1, \ldots, n$. Equation (16) may be written in the matrix form

$$\left[\frac{\partial f}{\partial \sigma}\right]^T [C^e]\left(\{d\varepsilon\} - \left[\frac{\partial g}{\partial \sigma}\right]\{\lambda\}\right) + [D]\{\lambda\} = \{0\} \tag{17}$$

where $[\partial f/\partial\sigma]$ is a $6\times n$ matrix, the kth column of which is $\{\partial f_k/\partial\sigma\}$; $[\partial g/\partial\sigma]$ is a $6\times n$ matrix, the kth column of which is $\{\partial g_k/\partial\sigma\}$; $[D]$ is a diagonal $n\times n$ matrix with the diagonal element $\{\partial f_k/\partial\varepsilon^{pk}\}^T\{\partial g_k/\partial\sigma\}$; and $\{\lambda\}$ is the $n\times 1$ vector of unknowns. This equation may be written as:

$$\left(\left[\frac{\partial f}{\partial\sigma}\right]^T[C^e]\left[\frac{\partial g}{\partial\sigma}\right]-[D]\right)\{\lambda\}=\left[\frac{\partial f}{\partial\sigma}\right]^T[C^e]\{d\varepsilon\} \tag{18}$$

Denoting

$$[L]=\left(\left[\frac{\partial f}{\partial\sigma}\right]^T[C^e]\left[\frac{\partial g}{\partial\sigma}\right]-[D]\right) \tag{19}$$

and its inverse as $[L]^{-1}$, then

$$\{\lambda\}=[L]^{-1}\left[\frac{\partial f}{\partial\sigma}\right]^T[C^e]\{d\varepsilon\} \tag{20}$$

Then from equations (5) and (1):

$$\{d\sigma\}=[C^e]\left(\{d\varepsilon\}-\{d\varepsilon^{p1}\}-\ldots-\{d\varepsilon^{pk}\}-\ldots-\{d\varepsilon^{pn}\}\right) \tag{21}$$

$$\{d\sigma\}=[C^e]\left(\{d\varepsilon\}-\left[\frac{\partial g}{\partial\sigma}\right]\{\lambda\}\right) \tag{22}$$

Using equation (20), equation (22) becomes

$$\{d\sigma\}=\left([C^e]-[C^e]\left[\frac{\partial g}{\partial\sigma}\right][L]^{-1}\left[\frac{\partial f}{\partial\sigma}\right]^T[C^e]\right)\{d\varepsilon\} \tag{23}$$

Thus

$$[C^{ep}]=[C^e]-[C^e]\left[\frac{\partial g}{\partial\sigma}\right][L]^{-1}\left[\frac{\partial f}{\partial\sigma}\right]^T[C^e] \tag{24}$$

which is the desired elasto-plastic stiffness matrix. Note that this matrix will by symmetric only if $[\partial f/\partial\sigma]=[\partial g/\partial\sigma]$, i.e. only if associated flow occurs on all active yield surfaces. In this case, $[L]$ is symmetric as is its inverse, so that $[C^{ep}]$ is symmetric.

It should also be recognized that if $[D]$ is zero, i.e. no work-hardening action is present, the elasto-plastic stiffness matrix is singular. This is easiest to demonstrate by noting that the strain increments

$$\{d\bar{\varepsilon}\}=\left[\frac{\partial g}{\partial\sigma}\right]\{\bar{\lambda}\} \tag{25}$$

where $\{\bar{\lambda}\}$ is *arbitrary* gives

$$\begin{aligned}\{d\sigma\}&=[C^{ep}]\{d\bar{\varepsilon}\}-[C^{ep}]\left[\frac{\partial g}{\partial\sigma}\right][L]^{-1}\left[\frac{\partial f}{\partial\sigma}\right]^T[C^e]\left[\frac{\partial g}{\partial\sigma}\right]\{\bar{\lambda}\}\\&=[C^{ep}]\{d\bar{\varepsilon}\}-[C^{ep}]\left[\frac{\partial g}{\partial\sigma}\right][L]^{-1}[L]\{\bar{\lambda}\}\\&=[C^{ep}]\{d\bar{\varepsilon}\}-[C^{ep}]\{d\bar{\varepsilon}\}\equiv 0\end{aligned} \tag{26}$$

Thus, the equations are singular. Physically, equation (25) indicates that the total strain increments, which are linear combinations of the n plastic strain increments, may occur without any change in the state of stress, i.e. flow will occur at a constant stress level.

Finally, it is noted that in equation (24), n independent yield conditions are all assumed to be active so that all the λ_k are positive. If the number of active yield surfaces changes, then the tangent stiffness matrix will be significantly altered, as the dimensions of $[L]$, $[\partial g/\partial\sigma]$ and $[\partial f/\partial\sigma]$ are changed.

ISOTROPIC HARDENING CASE

As a special, restricted case, the yield function is expressed as:

$$f_k(\{\sigma\}, \{\varepsilon^{pk}\}) \equiv f_k'(\{\sigma\}) - f_k''(W_{pk}) = 0 \tag{27}$$

where f_k' depends on stress only, and f_k'' contains the effect of work-hardening. Thus, the form or the shape of the kth yield surface is specified to within a single parameter f_k''. This is the case of isotropic hardening. Recognizing that

$$f_k''(W_{pk}) = f_k''\left(\int \{\sigma\}^T\{d\varepsilon^{pk}\}\right) \tag{28}$$

Then

$$\left\{\frac{\partial f_k}{\partial \varepsilon^{pk}}\right\} = -\left\{\frac{\partial f_k''}{\partial \varepsilon^{pk}}\right\} = -\frac{\partial f_k''}{\partial W_{pk}}\{\sigma\} \tag{29}$$

where $\partial f_k''/\partial W_{pk}$ is the slope of the kth work-hardening relation.

Assuming that all n yield surfaces are of the isotropic type, then D_{kk} in equation (18) takes the form

$$D_{kk} = -\frac{\partial f_k''}{\partial W_{pk}}\{\sigma\}^T\left\{\frac{\partial g_k}{\partial \sigma}\right\} \tag{30}$$

Finally, if $g_k\{\sigma\}$ is homogeneous to the degree α, then

$$D_{kk} = -\frac{\partial f_k''}{\partial W_{pk}} \cdot \alpha \cdot g_k \tag{31}$$

Again, it should be noted that the matrix $[C^{ep}]$ is not symmetrical if the yield functions and the plastic potential functions are not identical.

CONSTITUTIVE LAW FOR SAND WITH CURVED YIELD SURFACES

In order to illustrate the incrementalization procedure developed above, an incremental constitutive law with two yield surfaces is presented below.

The constitutive law described by Lade[4] employs two yield surfaces which may be activated simultaneously, one at a time, or not at all. The basic principles of this model are outlined below, and the incremental form of the model is then developed.

For the purpose of modelling the stress–strain behaviour of soils by an elasto-plastic theory, the total strain increments, $\{d\varepsilon\}$, are divided into an elastic component, $\{d\varepsilon^e\}$, a plastic collapse component, $\{d\varepsilon^c\}$, and a plastic expansive component, $\{d\varepsilon^p\}$, such that:

$$\{d\varepsilon\} = \{d\varepsilon^e\} + \{d\varepsilon^c\} + \{d\varepsilon^p\} \tag{32}$$

These strain components are calculated separately, the elastic strains by Hooke's law, and the plastic collapse strains and the plastic expansive strains by plastic stress–strain theories that involve, respectively, a cap-type yield surface and a conical yield surface with apex at the origin of the stress space.

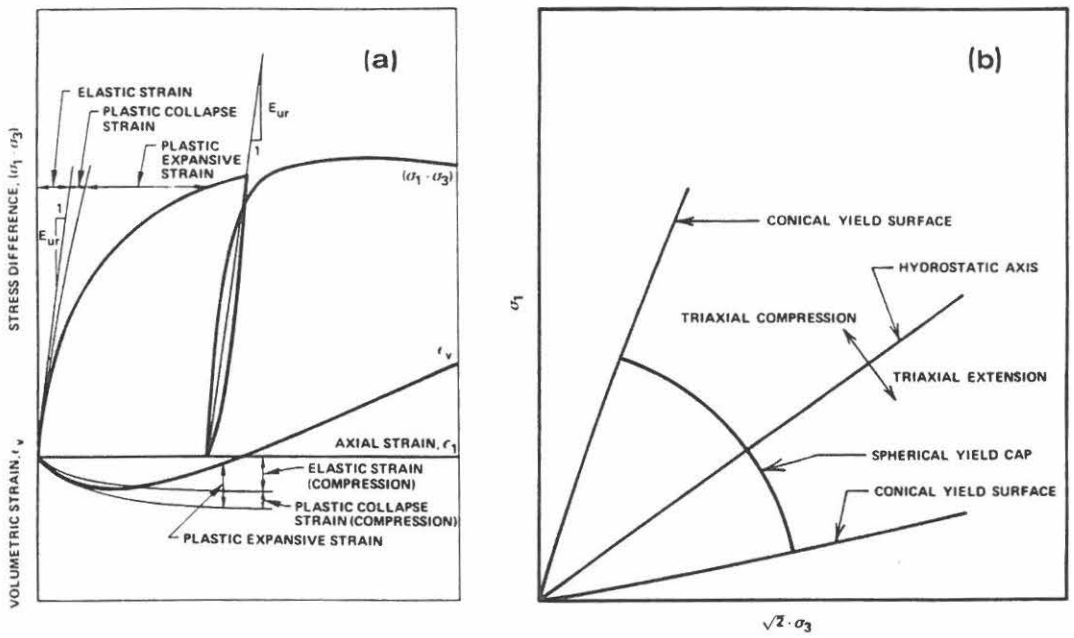

Figure 1. Schematic illustrations of (a) elastic, plastic collapse, and plastic expansive strain components in drained triaxial compression test, and of (b) conical and spherical cap yield surfaces in triaxial plane

Figure 1(a) shows the parts of the total strain that are considered to be elastic, plastic collapse, and plastic expansive components of strain in a drained triaxial compression test. Typical observed variations of stress difference, $(\sigma_1 - \sigma_3)$, and volumetric strain, ε_v, with axial strain, ε_1, are shown in this figure for a test performed with constant value of confining pressure, σ_3. Both elastic (recoverable) and plastic (irrecoverable) deformations occur from the initiation of loading in cohesionless soils. This behaviour is highly non-linear, and a decrease in strength may follow peak failure. The volumetric strain is initially compressive and this behaviour may be followed by expansion (as shown in Figure 1(a)) or by continued compression. The plastic strains are initially smaller than the elastic strains, but at high values of stress difference the plastic strains dominate the deformation.

Plastic expansive strains

The yield surfaces for the plastic strain components are indicated on the triaxial plane in Figure 1(b). The conical yield surface, which is curved in this plane, is described in terms of

the first and the third stress invariants, I_1 and I_3:

$$f'_p = (I_1^3/I_3 - 27)(I_1/p_a)^m \tag{33a}$$

$$f'_p = \eta_1 \quad \text{at failure} \tag{33b}$$

where

$$I_1 = \sigma_x + \sigma_y + \sigma_z \tag{34}$$

and

$$I_3 = \sigma_x \cdot \sigma_y \cdot \sigma_z + \tau_{xy} \cdot \tau_{yz} \cdot \tau_{zx} + \tau_{yx} \cdot \tau_{zy} \cdot \tau_{xz} - (\sigma_x \cdot \tau_{yz} \cdot \tau_{zy} + \sigma_y \cdot \tau_{zx} \cdot \tau_{xz} + \sigma_z \cdot \tau_{xy} \cdot \tau_{yx}) \tag{35}$$

The parameters η_1 and m in equation (33) are constants to be determined for specific soils at the desired density, and p_a is atmospheric pressure expressed in the same units as the stresses used in this equation. In principal stress space the yield and failure surfaces defined by equation (33) are shaped like asymmetric conoids with their pointed apices at the origin of the stress space as shown in Figure 2(a). For failure conditions the apex angle increases with the value of η_1, and the curvature of the failure surface increases with the value of m. For $m = 0$ the failure surface is straight and the expression becomes identical to that used in a previous theory.[3] Figure 2(b) shows typical cross-sections for given values of I_1^3/I_3 and a constant value of I_1. These cross-sections are exactly the same as those for the previous theory, and it has been shown that they model the experimentally determined three-dimensional strengths of sands and normally consolidated clay with good accuracy.[3,4,27]

The plastic potential function is modelled on the yield function as follows:

$$g_p = I_1^3 - (27 + \eta_2 \cdot (p_a/I_1)^m) \cdot I_3 \tag{36}$$

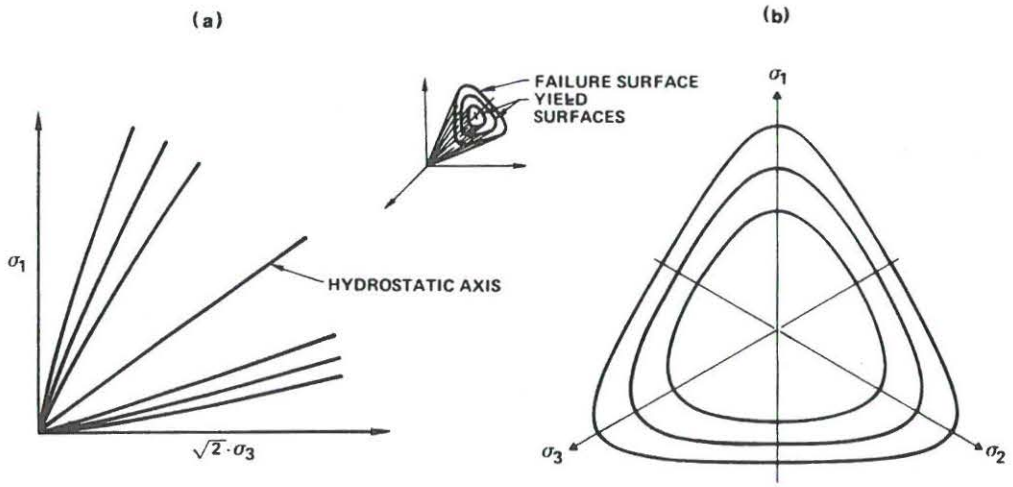

Figure 2. Characteristics of failure and yield surfaces shown in principal stress space. Traces of failure and yield surfaces in (a) triaxial plane, and in (b) octahedral plane

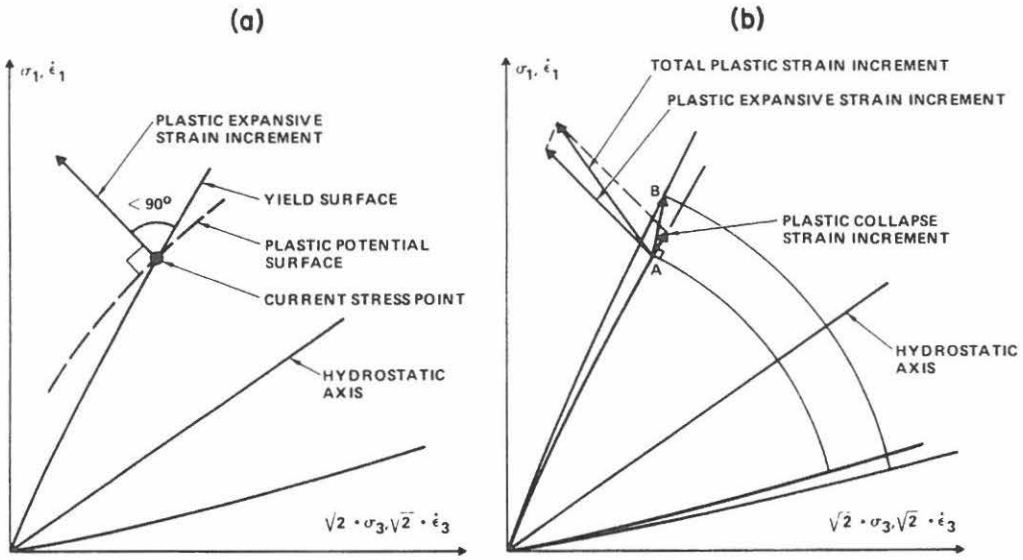

Figure 3. Schematic diagrams of (a) yield and plastic potential surfaces for plastic expansive strains, and of (b) yielding process with both yield surfaces activated and combination of plastic strain increments

where η_2 is constant for given values of f'_p and the confining pressure. Thus, the corresponding flow rule is non-associated, i.e. the plastic expansive strain increment vectors superimposed on the stress space form angles with the conical yield surfaces different from 90°, as indicated in Figure 3(a).

The work-hardening (and work-softening) law employed with the conical yield surface is expressed as

$$f''_p = a \cdot e^{-b \cdot W_p} \cdot (W_p / p_a)^{1/q}, \qquad q > 0 \tag{37}$$

where a, b, and q are constants for a given value of the confining pressure.

Plastic collapse strains

The yield surface corresponding to the plastic collapse strains forms a cap on the open end of the conical yield surface, as shown in Figure 1(b). The collapse yield surface is shaped as a sphere with centre at the origin of the principal stress space. This yield surface is described in terms of the first and the second stress invariants, I_1 and I_2:

$$f'_c = I_1^2 + 2 \cdot I_2 \tag{38}$$

where I_1 is given by equation (34) and

$$I_2 = \tau_{xy} \cdot \tau_{yx} + \tau_{yz} \cdot \tau_{zy} + \tau_{zx} \cdot \tau_{xz} - (\sigma_x \cdot \sigma_y + \sigma_y \cdot \sigma_z + \sigma_z \cdot \sigma_x) \tag{39}$$

It should be noted that yielding resulting from outward movement of the cap does not result in eventual failure. Failure is controlled entirely by the conical yield surface.

The plastic potential function is identical to the yield function:

$$g_c = I_1^2 + 2 \cdot I_2 \tag{40}$$

Thus, the normality condition used for this surface implies an associated flow rule, and the plastic collapse strain increment vectors are perpendicular to the spherical yield surface, as shown in Figure 3(b).

The work-hardening law used with the spherical yield surface is expressed as:

$$f_c'' = p_a^2 \cdot \left(\frac{1}{C}\right)^{1/p} \cdot \left(\frac{W_c}{p_a}\right)^{1/p} \tag{41}$$

where C and p are constants.

Combination of plastic strain increments

The result of a change in stress which involves both yield surfaces is shown in the triaxial plane in figure 3(b). The plastic strain increment vectors are superimposed on the stress space in this diagram. Both plastic collapse and plastic expansive strains are caused by the change in stress from point A to point B, because both yield surfaces are active. The magnitudes of the strain increments are indicated by the lengths of the vectors, and the total plastic strain increment is calculated according to equation (32) as the vector sum of the two components. The elastic strain components are further added (not shown in Figure 3(b)) to obtain the total strain increment for the stress change from A to B. It follows from the consistency condition from plasticity[28] that elasto-plastic constitutive models with one or several intersecting yield surfaces are continuous, independently of the type of flow rule employed (associated or non-associated).[29,30] Therefore, a continuous response is obtained when the stress increment vector AB is moved around the corner at point A in Figure 3(b).

The capabilities of the elasto-plastic constitutive model employed here have been described elsewhere.[4,5,27]

INCREMENTAL FORM OF CONSTITUTIVE LAW

To obtain the incremental form of the constitutive law with two yield surfaces, two linear equations of the type in equation (18) (with D_{kk} given in equation (30)) are solved to find λ_c and λ_p:

$$\begin{aligned} \lambda_c \cdot L_{11} + \lambda_p \cdot L_{12} &= T_1 \\ \lambda_c \cdot L_{21} + \lambda_p \cdot L_{22} &= T_2 \end{aligned} \tag{42}$$

from which

$$\lambda_c = \frac{L_{22} \cdot T_1 - L_{12} \cdot T_2}{L_{11} \cdot L_{22} - L_{12} \cdot L_{21}} \tag{43}$$

$$\lambda_p = \frac{L_{11} \cdot T_2 - L_{21} \cdot T_1}{L_{11} \cdot L_{22} - L_{12} \cdot L_{21}} \tag{44}$$

where

$$L_{11} = \left\{\frac{\partial f_c'}{\partial \sigma}\right\}^T [C^e] \left\{\frac{\partial g_c}{\partial \sigma}\right\} + \frac{\partial f_c''}{\partial W_c} \cdot \{\sigma\}^T \left\{\frac{\partial g_c}{\partial \sigma}\right\} \tag{45}$$

$$L_{22} = \left\{\frac{\partial f_p'}{\partial \sigma}\right\}^T [C^e] \left\{\frac{\partial g_p}{\partial \sigma}\right\} + \frac{\partial f_p''}{\partial W_p} \cdot \{\sigma\}^T \left\{\frac{\partial g_p}{\partial \sigma}\right\} \tag{46}$$

$$L_{12} = \left\{\frac{\partial f_c'}{\partial \sigma}\right\}^T [C^e] \left\{\frac{\partial g_p}{\partial \sigma}\right\} \tag{47}$$

$$L_{21}=\left\{\frac{\partial f'_{\mathrm{p}}}{\partial\sigma}\right\}^{\mathrm{T}}[C^{\mathrm{e}}]\left\{\frac{\partial g_{\mathrm{p}}}{\partial\sigma}\right\} \tag{48}$$

$$T_1=\left\{\frac{\partial f'}{\partial\sigma}\right\}^{\mathrm{T}}[C^{\mathrm{e}}]\{\mathrm{d}\varepsilon\} \tag{49}$$

$$T_2=\left\{\frac{\partial f'_{\mathrm{p}}}{\partial\sigma}\right\}^{\mathrm{T}}[C^{\mathrm{e}}]\{\mathrm{d}\varepsilon\} \tag{50}$$

In addition to the elasticity matrix in equation (6), the individual components involved in equations (45)–(50) are given below:

$$\left\{\frac{\partial f'_{\mathrm{c}}}{\partial\sigma}\right\}=\left\{\frac{\partial g_{\mathrm{c}}}{\partial\sigma}\right\}=2\cdot\begin{Bmatrix}\sigma_x\\ \sigma_y\\ \sigma_z\\ 2\cdot\tau_{yz}\\ 2\cdot\tau_{zx}\\ 2\cdot\tau_{xy}\end{Bmatrix} \tag{51}$$

$$\frac{\partial f''_{\mathrm{c}}}{\partial W_{\mathrm{c}}}=\frac{p_{\mathrm{a}}}{C\cdot p}\cdot\left(\frac{f'_{\mathrm{c}}}{p_{\mathrm{a}}^2}\right)^{1-p} \tag{52}$$

where f'_{c} is given by equation (38).

$$\{\sigma\}^{\mathrm{T}}\left\{\frac{\partial g_{\mathrm{c}}}{\partial\sigma}\right\}=2\cdot I_1^2+4\cdot I_2=2\cdot g_{\mathrm{c}} \tag{53}$$

where g_{c} is given by equation (40).

$$\left\{\frac{\partial f'_{\mathrm{p}}}{\partial\sigma}\right\}=\frac{I_1^2}{I_3^2}\cdot\left(\frac{I_1}{p_{\mathrm{a}}}\right)^m\cdot\begin{Bmatrix}3\cdot I_3-(\sigma_y\cdot\sigma_z-\tau_{yz}^2)\cdot I_1\\ 3\cdot I_3-(\sigma_z\cdot\sigma_x-\tau_{zx}^2)\cdot I_1\\ 3\cdot I_3-(\sigma_x\cdot\sigma_y-\tau_{xy}^2)\cdot I_1\\ 2\cdot(\sigma_x\cdot\tau_{yz}-\tau_{xy}\cdot\tau_{zx})\cdot I_1\\ 2\cdot(\sigma_y\cdot\tau_{zx}-\tau_{yz}\cdot\tau_{xy})\cdot I_1\\ 2\cdot(\sigma_z\cdot\tau_{xy}-\tau_{zx}\cdot\tau_{yz})\cdot I_1\end{Bmatrix}+\left(\frac{I_1^3}{I_3}-27\right)\cdot\frac{m}{p_{\mathrm{a}}}\left(\frac{I_1}{p_{\mathrm{a}}}\right)^{m-1}\cdot\begin{Bmatrix}1\\1\\1\\0\\0\\0\end{Bmatrix} \tag{54}$$

$$\left\{\frac{\partial g_{\mathrm{p}}}{\partial\sigma}\right\}=-\left(27+\eta_2\cdot\left(\frac{p_{\mathrm{a}}}{I_1}\right)^m\right)\cdot\begin{Bmatrix}\sigma_y\cdot\sigma_z-\tau_{yz}^2\\ \sigma_z\cdot\sigma_x-\tau_{zx}^2\\ \sigma_x\cdot\sigma_y-\tau_{xy}^2\\ -2\cdot(\sigma_x\cdot\tau_{yz}-\tau_{xy}\cdot\tau_{zx})\\ -2\cdot(\sigma_y\cdot\tau_{zx}-\tau_{yz}\cdot\tau_{xy})\\ -2\cdot(\sigma_z\cdot\tau_{xy}-\tau_{zx}\cdot\tau_{yz})\end{Bmatrix}+\left(3\cdot I_1^2+\frac{I_3}{I_1}\cdot m\cdot\eta_2\cdot\left(\frac{p_{\mathrm{a}}}{I_1}\right)^m\right)\cdot\begin{Bmatrix}1\\1\\1\\0\\0\\0\end{Bmatrix} \tag{55}$$

$$\frac{\partial f''_{\mathrm{p}}}{\partial W_{\mathrm{p}}}=\frac{f'_{\mathrm{p}}}{p_{\mathrm{a}}}\cdot\left[\frac{p_{\mathrm{a}}}{q\cdot W_{\mathrm{p}}}-b\cdot p_{\mathrm{a}}\right] \tag{56}$$

where f'_p is given by equation (33a).

$$\{\sigma\}^T \cdot \left\{\frac{\partial g_p}{\partial \sigma}\right\} = 3 \cdot g_p + m \cdot \eta_2 \cdot \left(\frac{p_a}{I_1}\right)^m \cdot I_3 \tag{57}$$

The incremental material stiffness matrix $[C^{ep}]$ for the constitutive law with two yield surfaces is then given by:

$$[C^{ep}] = [C^e] - \frac{[C^e]}{A} \cdot \left(\left\{\frac{\partial g_c}{\partial \sigma}\right\} \cdot \{b_c\}^T + \left\{\frac{\partial g_p}{\partial \sigma}\right\} \cdot \{b_p\}^T\right)[C^e] \tag{58}$$

where

$$A = L_{11} \cdot L_{22} - L_{12} \cdot L_{21} \tag{59}$$

$$\{b_c\} = L_{22} \cdot \left\{\frac{\partial f'_c}{\partial \sigma}\right\} - L_{12} \cdot \left\{\frac{\partial f'_p}{\partial \sigma}\right\} \tag{60}$$

$$\{b_p\} = L_{11} \cdot \left\{\frac{\partial f'_p}{\partial \sigma}\right\} - L_{21} \cdot \left\{\frac{\partial f'_c}{\partial \sigma}\right\} \tag{61}$$

Thus, the applicability of this general incrementalization procedure has been illustrated for a material model with two simultaneous yield surfaces.

CONCLUSION

A general procedure for developing the incremental stiffness matrix for an elasto-plastic material model with multiple, intersecting yield surfaces has been presented. Each yield surface has its own associated or non-associated flow rule and is assumed to depend on work-hardening or work-softening effects. Models with up to five independent, simultaneously activated yield surfaces may be incrementalized according to the procedure presented here. A recently developed model with two yield surfaces, one with associated and the other with non-associated flow, was used to illustrate the matrix forms which are generated. The material stiffness matrix, which is non-symmetric for non-associated flow on any one of the yield surfaces, may be used in non-linear elasto-plastic finite element or finite difference computer codes.

REFERENCES

1. D. C. Drucker, R. E. Gibson and D. J. Henkel, 'Soil mechanics and work-hardening theories of plasticity', *Transactions*, ASCE, **122**, 338–346 (1957).
2. K. H. Roscoe and J. B. Burland, 'On the generalized stress–strain behaviour of "wet" clay', *Engineering Plasticity* (J. Heyman and F. A. Leckie, Eds.), Cambridge University Press, Cambridge, England, 1968, pp. 535–609.
3. P. V. Lade and J. M. Duncan, 'Elastoplastic stress–strain theory for cohesionless soil', *J. Geot. Eng. Div.*, ASCE, **101**, GT10, 1037–1053 (1975).
4. P. V. Lade, 'Elasto-plastic stress–strain theory for cohesionless soil with curved yield surfaces', *Int. J. Solids Structures*, **13**, 1019–1035 (1977).
5. P. V. Lade, 'Prediction of undrained behavior of sand', *J. Geot. Eng. Div.*, ASCE, **104**, GT6, 721–735 (1978).
6. I. S. Sandler, F. L. DiMaggio and G. Y. Baladi, 'Generalized models for geological materials', *J. Geot. Eng. Div.*, ASCE, **102**, GT7, 683–699 (1976).
7. J-H. Prevost, 'Plasticity theory for soil stress–strain behavior', *J. Eng. Mech. Div.*, ASCE, **104**, EM5, 1177–1194 (1978).
8. P. A. Vermeer, 'A double hardening model for sand', *Geotechnique*, **28**, 413–433 (1978).
9. Y. F. Dafalias and L. R. Herrmann, 'A bounding surface soil plasticity model', *Soils under Cyclic and Transient Loading*, Balkema, Rotterdam, 1980, pp. 335–345.
10. Z. Mroz, V. A. Norris and O. C. Zienkiewicz, 'An anisotropic, critical state model for soils subject to cyclic loading', *Geotechnique*, **31**, 451–469 (1981).

11. D. C. Drucker, 'Stress–strain relations in the plastic range of metals—experiments and basic concepts', *Rheology, Theory and Applications*, I (F. R. Eirich, ed.), 1956, pp. 97–119.
12. D. C. Drucker, 'On stress–strain relations for soils and load carrying capacity', *Proc. 1st Int. Conf. Mech. Soil–Vehicle Systems*, Torino, Italy, 15–23 (1961).
13. P. V. Lade and J. M. Duncan, 'Cubical triaxial tests on cohesionless soil', *J. Soil Mech. Found. Div.*, ASCE, **99**, SM10, 793–812 (1973).
14. P. V. Lade and J. M. Duncan, 'Stress-path dependent behavior of cohesionless soil', *J. Geot. Eng. Div.*, ASCE, **102**, GT1, 51–68 (1976).
15. H. B. Poorooshasb, I. Holubec and A. N. Sherbourne, 'Yielding and flow of sand in triaxial compression: Part I', *Can. Geot. J.*, **3**, 179–190 (1966).
16. W. T. Koiter, 'Stress–strain relations, uniqueness and variational theorems for elastic–plastic materials with a singular yield surface', *Quart. Appl. Math.*, **11**, 350–354 (1953).
17. Z. Mroz, 'Non-associated flow laws in plasticity', *J. Mecanique*, **11**, 21–42 (1963).
18. Z. Mroz, 'On the description of anisotropic workhardening', *J. Mech. Phys. Solids*, **15**, 163–175 (1967).
19. R. Hill, *The Mathematical Theory of Plasticity*, Oxford University Press, London, 1950.
20. A. Mendelson, *Plasticity: Theory and Practice*, MacMillan, New York, 1968.
21. P. M. Naghdi, 'Stress–strain relations in plasticity and thermoplasticity', *Plasticity*, Proc. 2nd Symp. Naval Struct. Mech. (E. H. Lee and P. S. Symonds, eds.), 1960, pp. 121–169.
22. Y. Yamada, N. Yoshimura and T. Sakurai, 'Plastic stress–strain matrix and its application for the solution of elastic–plastic problems by the finite element method', *Int. J. Mech. Sci.*, **10**, 343–354 (1968).
23. O. C. Zienkiewicz, S. Valliappan and I. P. King, 'Elastic plastic solutions of engineering problems, initial stress, finite element approach', *Int. j. numer. methods Eng.*, **1**, 75–100 (1969).
24. O. C. Zienkiewicz, *The Finite Element Method*, 3rd edn, McGraw-Hill, New York, 1977.
25. K-J. Bathe, E. L. Wilson and R. H. Iding, 'NONSAP—a structural analysis program for static and dynamic response of nonlinear systems', *Report No. UC SESM 74-3*, Structural Engineering Laboratory, University of California, Berkeley (1974).
26. K-J. Bathe, H. Ozdemir and E. L. Wilson, 'Static and dynamic geometric and material nonlinear analysis', *Report No. UC SESM 74-4*, Structural Engineering Laboratory, University of California, Berkeley (1974).
27. P. V. Lade, 'Stress–strain theory for normally consolidated clay', *Proc. 3rd Int. Conf. Num. Methods Geomech.*, Aachen, West Germany, IV, 1325–1337 (1979).
28. W. Prager, 'Recent developments in the mathematical theory of plasticity', *J. Appl. Phys.*, **20**, 235–241 (1949).
29. Z. Mroz, 'On forms of constitutive laws for elastic–plastic solids', *Arch. Mech.*, **1**, 18, 3–35 (1966).
30. G. Gudehus, 'A comparison of some constitutive laws for soils under radially symmetric loading and unloading', *Proc. 3rd Int. Conf. Num. Methods Geomech.*, Aachen, West Germany, IV, 1309–1323 (1979).

INCREMENTAL FORM OF CONSTITUTIVE MODEL

Introduction

In order to use the constitutive model in nonlinear matrix computer codes employing finite element or finite difference techniques, it is necessary to obtain an incremental form of the constitutive model. Thus, it is necessary to obtain constitutive relations in which the stress increments are expressed in terms of strain increments or vice versa, i.e.

$$\{d\sigma\} = [C^{ep}]\{d\varepsilon\} \tag{9.1}$$

in which the subscripts have been omitted for simplicity. In this equation the stress increments are:

$$\{d\sigma\}^T = \left\langle d\sigma_x,\ d\sigma_y,\ d\sigma_z,\ d\tau_{yz},\ d\tau_{zx},\ d\tau_{xy} \right\rangle \tag{9.2}$$

and the increments of total strains are

$$\{d\varepsilon\}^T = \left\langle d\varepsilon_x,\ d\varepsilon_y,\ d\varepsilon_z,\ d\gamma_{yz},\ d\gamma_{zx},\ d\gamma_{xy} \right\rangle \qquad (9.3)$$

and $[C^{ep}]$ is an elasto-plastic material stiffness matrix.

Basic Equations

The stress increments and the elastic strain increments are assumed to be related according to Hooke's law:

$$\{d\sigma\} = [C^e]\ \{d\varepsilon\} \qquad (9.4)$$

where

$$[C^e] = \frac{E}{(1+\nu)(1-2\nu)} \begin{bmatrix} 1-\nu & \nu & \nu & 0 & 0 & 0 \\ & 1-\nu & \nu & 0 & 0 & 0 \\ & & 1-\nu & 0 & 0 & 0 \\ & & & \frac{1-2\nu}{2} & 0 & 0 \\ & \text{Symmetric} & & & \frac{1-2\nu}{2} & 0 \\ & & & & & \frac{1-2\nu}{2} \end{bmatrix} \qquad (9.5)$$

The plastic strain increments are defined by means of the work-hardening plasticity theory which involves a yield function and a flow rule. The yield function is given by

$$f_p\ (\{\sigma\}, \{\varepsilon^p\}) = 0 \qquad (9.6)$$

For an isotropic work-hardening material equation (9.6) may be expressed as:

$$f_p'(\{\sigma\}) - f''(W_p) = 0 \tag{9.7}$$

in which

$$f_p'(\{\sigma\}) = (\psi_1 \cdot \frac{I_1^3}{I_3} - \frac{I_1^2}{I_2})(\frac{I_1}{p_a})^h \cdot e^q \tag{9.8}$$

The parameters ψ_1 and h are constant for a given material. The parameter q varies with the stress level f_n/η_1 from zero at the hydrostatic axis to unity at the failure surface according to the following expression:

$$q = \frac{\alpha(f_n/\eta_1)}{1 - (1 - \alpha)(f_n/\eta_1)} \tag{9.9}$$

in which α is a constant and

$$f_n = (I_1^3/I_3 - 27)(I_1/p_a)^m \tag{9.10}$$

During strain hardening the yield surface becomes larger due to increasing plastic work through the relation

$$f_p'' = \left[\frac{1}{D}\right]^{\frac{1}{\rho}} \cdot \left[\frac{W_p}{p_a}\right]^{\frac{1}{\rho}} \tag{9.11}$$

where D and ρ are material constants. At the point of material failure this relationship is changed to one producing strain-softening, i.e., a decreasing yield surface,

$$f_p'' = A \cdot e^{-B\left[\frac{W_p}{p_a}\right]} \tag{9.12}$$

In Eq(9.12), A and B are positive constants set so Eq.(9.11) and(9.12) agree at the point of failure. with equal but opposite derivatives with respect to plastic work.

The flow rule is expressed as:

$$d\varepsilon^p = d\lambda_p \cdot \{\frac{\partial g_p}{\partial \sigma}\} \tag{9.13}$$

in which g_p is the plastic potential function:

$$g_p = g_p(\{\sigma\}) = (\psi_1 \cdot \frac{I_1^3}{I_3} - \frac{I_1^2}{I_2} + \psi_2)(\frac{I_1}{p_a})^{\mu} \tag{9.14}$$

and

$$\{\frac{\partial g_p}{\partial \sigma}\}^T = \langle \frac{\partial g_p}{\partial \sigma_x}, \frac{\partial g_p}{\partial \sigma_y}, \frac{\partial g_p}{\partial \sigma_z}, 2 \cdot \frac{\partial g_p}{\partial \tau_{yz}}, 2 \cdot \frac{\partial g_p}{\partial \tau_{zx}}, 2 \cdot \frac{\partial g_p}{\partial \tau_{xy}} \rangle \tag{9.15}$$

Using these basic equations, the incremental elasto-plastic stress-strain relationship may be obtained as given below.

Incremental Relations

A procedure for developing the incremental stiffness matrix for an elasto-plastic material with multiple, intersecting yield surfaces was presented by Lade and Nelson (1984). using this procedure for the present constitutive model, which has only a single yield surface, the following expression for the stiffness matrix is obtained (see detailed derivation on pages 9-13):

$$[C^{ep}]=[C^{e}]-\frac{[C^{e}]\{\frac{\partial g_p}{\partial \sigma}\}\{\frac{\partial f'_p}{\partial \sigma}\}^{T}[C^{e}]}{\{\frac{\partial f'_p}{\partial \sigma}\}^{T}[C^{e}]\{\frac{\partial g_p}{\partial \sigma}\}-\{\frac{\partial f''}{\partial \varepsilon^{p}}\}^{T}\{\frac{\partial g_p}{\partial \sigma}\}} \qquad (9.16)$$

In addition to the elasticity matrix in equation (9.5), the individual components involved in equation (9.16) are given below in a format which can readily be employed in a computer program.

Using the chain rule, the derivatives of the plastic potential function can be written as:

$$\{\frac{\partial g_p}{\partial \sigma}\} = \frac{\partial g_p}{\partial I_1}\cdot\{\frac{\partial I_1}{\partial \sigma}\} + \frac{\partial g_p}{\partial I_2}\cdot\{\frac{\partial I_2}{\partial \sigma}\} + \frac{\partial g_p}{\partial I_3}\cdot\{\frac{\partial I_3}{\partial \sigma}\} \qquad (9.17)$$

in which

$$\frac{\partial g_p}{\partial I_1} = \left[\psi_1\cdot(\mu+3)\cdot\frac{I_1^3}{I_3} - (\mu+2)\cdot\frac{I_1^2}{I_2} + \mu\cdot\psi_2\right]\cdot\frac{1}{I_1}\cdot\left(\frac{I_1}{p_a}\right)^{\mu} \qquad (9.18)$$

$$\frac{\partial g_p}{\partial I_2} = \frac{I_1^2}{I_2^2}\cdot\left(\frac{I_1}{p_a}\right)^{\mu} \qquad (9.19)$$

$$\frac{\partial g_p}{\partial I_3} = -\psi_1\cdot\frac{I_1^3}{I_3^2}\cdot\left(\frac{I_1}{p_a}\right)^{\mu} \qquad (9.20)$$

and the derivatives of the stress invariants with regard to the stresses are:

$$\{\frac{\partial I_1}{\partial \sigma}\} = \begin{Bmatrix} 1 \\ 1 \\ 1 \\ 0 \\ 0 \\ 0 \end{Bmatrix} \qquad (9.21)$$

$$\{\frac{\partial I_2}{\partial \sigma}\} = \begin{Bmatrix} -(\sigma_y+\sigma_z) \\ -(\sigma_z+\sigma_x) \\ -(\sigma_x+\sigma_y) \\ 2\cdot\tau_{yz} \\ 2\cdot\tau_{zx} \\ 2\cdot\tau_{xy} \end{Bmatrix} \qquad (9.22)$$

$$\{\frac{\partial I_3}{\partial \sigma}\} = \begin{Bmatrix} \sigma_y \cdot \sigma_z - \tau_{yz}^2 \\ \sigma_z \cdot \sigma_x - \tau_{zx}^2 \\ \sigma_x \cdot \sigma_y - \tau_{xy}^2 \\ 2 \cdot (\tau_{xy} \cdot \tau_{zx} - \sigma_x \cdot \tau_{yz}) \\ 2 \cdot (\tau_{yz} \cdot \tau_{xy} - \sigma_y \cdot \tau_{zx}) \\ 2 \cdot (\tau_{zx} \cdot \tau_{yz} - \sigma_z \cdot \tau_{xy}) \end{Bmatrix} \tag{9.23}$$

Using the chain rule, the derivatives of the yield function f' can be written as:

$$\{\frac{\partial f_p'}{\partial \sigma}\} = \frac{\partial f_p'}{\partial I_1} \cdot \{\frac{\partial I_1}{\partial \sigma}\} + \frac{\partial f_p'}{\partial I_2} \cdot \{\frac{\partial I_2}{\partial \sigma}\} + \frac{\partial f_p'}{\partial I_3} \cdot \{\frac{\partial I_3}{\partial \sigma}\} \tag{9.24}$$

in which the derivatives of the stress invariants are given by equations (9.21), (9.22) and (9.23), and the derivatives of f_p' with regard to the stress invariants are:

$$\frac{\partial f_p'}{\partial I_1} = (\frac{3+h}{I_1} + \frac{\partial q}{\partial I_1}) \cdot f_p' + \frac{I_1}{I_2} \cdot (\frac{I_1}{p_a})^h \cdot e^q \tag{9.25}$$

$$\frac{\partial f_p'}{\partial I_2} = \frac{I_1^2}{I_2^2} \cdot (\frac{I_1}{p_a})^h \cdot e^q \tag{9.26}$$

$$\frac{\partial f_p'}{\partial I_3} = f_p' \cdot \frac{\partial q}{\partial I_3} - \psi_1 \cdot \frac{I_1^3}{I_3^2} \cdot (\frac{I_1}{p_a})^h \cdot e^q \tag{9.27}$$

in which the derivatives of q with respect to the stress invariants are:

$$\frac{\partial q}{\partial I_1} = \frac{\alpha/\eta_1}{[1-(1-\alpha)f\eta/\eta_1]^2} \left[\frac{m}{I_1} f_n + \frac{3I_1^2}{I_3}\left[\frac{I_1}{p_a}\right]^m\right] \qquad (9.28)$$

$$\frac{\partial q}{\partial I_3} = \frac{-\alpha/\eta_1}{[1-(1-\alpha)f_n/\eta_1]^2} \cdot \frac{I_1^3}{I_3^2} \cdot \left[\frac{I_1}{p_a}\right]^m \qquad (9.29)$$

Finally, the last term in the denominator of equation (9.16) may be written as (Lade and Nelson, 1984):

$$\{\frac{\partial f_p''}{\partial \varepsilon^p}\}\{\frac{\partial g_p}{\partial \sigma}\} = -\frac{\partial f_p''}{\partial W_p} \cdot \mu \cdot g_p \qquad (9.30)$$

in which

$$\frac{\partial f''}{\partial W_p} = \frac{1}{\rho(D \cdot p_a)^{1/\rho}} \cdot W_p^{(1/\rho - 1)} \quad \text{for hardening} \qquad (9.31)$$

$$\frac{\partial f_p''}{\partial W_p} = -\frac{A \cdot B}{p_a} e^{-B\left[\frac{W_p}{p_a}\right]} \quad \text{for softening} \qquad (9.32)$$

It should be noted that the matrix $[C^{ep}]$ is not symmetrical, because the yield function and the plastic potential function are not identical.

D

General Incremental Elasto-Plastic Stress-Strain Relationship for Work-Hardening Materials

The following concepts and assumptions from classical plasticity theory provide a basis for derivation of incremental elasto-plastic stress-strain relationships:

(1) Yield Function. The yield function, f, for any work-hardening material may be expresses as:

$$f(\{\sigma_{ij}\}, \{\varepsilon^p_{ij}\}) = 0 \qquad (5.1)$$

(2) Plastic Potential Function. The plastic potential function may be expressed as a function of the stresses

$$g = g(\{\sigma_{ij}\}) \qquad (5.2)$$

(3) Flow Rule. The "normality rule" of plastic strain increment directions states that the plastic strain increments may be expressed as

$$\{d\varepsilon^p_{ij}\} = \lambda \cdot \left\{\frac{\partial g}{\partial \sigma_{ij}}\right\} \qquad (5.3)$$

in which λ is an arbitrary constant, g is the plastic potential function, and $\{\partial g/\partial \sigma_{ij}\}$ defines the outward normal to the plastic potential surface.

(4) Incremental Elastic and Plastic Strain. During an infinitesimal change in stress, the total strain increments, $\{d\varepsilon_{ij}\}$, are assumed to be divisible into elastic components, $\{d\varepsilon^e_{ij}\}$, and plastic components, $\{d\varepsilon^p_{ij}\}$. That is,

$$\{d\varepsilon_{ij}\} = \{d\varepsilon^e_{ij}\} + \{d\varepsilon^p_{ij}\} \qquad (5.4)$$

(5) Relationship Between Stress Increments and Elastic Strain Increments. The increments of stress are assumed to be related to the increments of elastic strain by means of a symmetrical elasticity matrix, $[C^e]$

$$\{d\sigma_{ij}\} = [C^e]\{d\varepsilon^e_{ij}\} \qquad (5.5)$$

Using these five equations, the elasto-plastic stress-strain relationship for work-hardening materials may be derived. The basic concept is that f must remain equal to zero during any increments of stress and strain, i.e.

$$\left\{\frac{\partial f}{\partial \sigma_{ij}}\right\}^T \{d\sigma_{ij}\} + \left\{\frac{\partial f}{\partial \varepsilon^p_{ij}}\right\}^T \{d\varepsilon^p_{ij}\} = 0 \qquad (5.6)$$

Substituting Eq. 5.5 into Eq. 5.6

$$\left\{\frac{\partial f}{\partial \sigma_{ij}}\right\}^T [C^e]\{d\varepsilon^e_{ij}\} + \left\{\frac{\partial f}{\partial \varepsilon^p_{ij}}\right\}^T \{d\varepsilon^p_{ij}\} = 0 \qquad (5.7)$$

Using Eq. 5.4, Eq. 5.7 may be rewritten as

$$\left\{\frac{\partial f}{\partial \sigma_{ij}}\right\}^T [C^e]\left(\{d\varepsilon_{ij}\} - \{d\varepsilon^p_{ij}\}\right) + \left\{\frac{\partial f}{\partial \varepsilon^p_{ij}}\right\}^T \{d\varepsilon^p_{ij}\} = 0 \qquad (5.8)$$

$$\left\{\frac{\partial f}{\partial \sigma_{ij}}\right\}^T [C^e]\{d\varepsilon_{ij}\} - \left(\left\{\frac{\partial f}{\partial \sigma_{ij}}\right\}^T [C^e] - \left\{\frac{\partial f}{\partial \varepsilon^p_{ij}}\right\}^T\right)\{d\varepsilon^p_{ij}\} = 0 \qquad (5.9)$$

Substitution of Eq. 5.3 into Eq. 5.9 gives

$$\left\{\frac{\partial f}{\partial \sigma_{ij}}\right\}^T [C^e]\{d\varepsilon_{ij}\} - \left(\left\{\frac{\partial f}{\partial \sigma_{ij}}\right\}^T [C^e] - \left\{\frac{\partial f}{\partial \varepsilon^p_{ij}}\right\}^T\right)\lambda \cdot \left\{\frac{\partial g}{\partial \sigma_{ij}}\right\} = 0 \qquad (5.10)$$

Solving for λ,

$$\lambda = \frac{\left\{\frac{\partial f}{\partial \sigma_{ij}}\right\}^T [C^e]\{d\varepsilon_{ij}\}}{\left\{\frac{\partial f}{\partial \sigma_{ij}}\right\}^T [C^e]\left\{\frac{\partial g}{\partial \sigma_{ij}}\right\} - \left\{\frac{\partial f}{\partial \varepsilon^p_{ij}}\right\}^T \left\{\frac{\partial g}{\partial \sigma_{ij}}\right\}} \tag{5.11}$$

Substituting this expression for λ into Eq. 5.3,

$$\{d\varepsilon^p_{ij}\} = \frac{\left\{\frac{\partial g}{\partial \sigma_{ij}}\right\}\left\{\frac{\partial f}{\partial \sigma_{ij}}\right\}^T [C^e]\{d\varepsilon_{ij}\}}{\left\{\frac{\partial f}{\partial \sigma_{ij}}\right\}^T [C^e]\left\{\frac{\partial g}{\partial \sigma_{ij}}\right\} - \left\{\frac{\partial f}{\partial \varepsilon^p_{ij}}\right\}^T \left\{\frac{\partial g}{\partial \sigma_{ij}}\right\}} \tag{5.12}$$

Finally, the incremental stress-strain relationship may be obtained using Eqs. 5.4, 5.5 and 5.12. That is,

$$\{d\sigma_{ij}\} = [C^e]\{d\varepsilon^e_{ij}\} \tag{5.13}$$

$$\{d\sigma_{ij}\} = [C^e](\{d\varepsilon_{ij}\} - \{d\varepsilon^p_{ij}\}) \tag{5.14}$$

$$\{d\sigma_{ij}\} = \left[[C^e] - \frac{[C^e]\left\{\frac{\partial g}{\partial \sigma_{ij}}\right\}\left\{\frac{\partial f}{\partial \sigma_{ij}}\right\}^T [C^e]}{\left\{\frac{\partial f}{\partial \sigma_{ij}}\right\}^T [C^e]\left\{\frac{\partial g}{\partial \sigma_{ij}}\right\} - \left\{\frac{\partial f}{\partial \varepsilon^p_{ij}}\right\}^T \left\{\frac{\partial g}{\partial \sigma_{ij}}\right\}}\right] \{d\varepsilon_{ij}\} \tag{5.15}$$

This equation may also be written as

$$\{d\sigma_{ij}\} = [C^{ep}]\{d\varepsilon_{ij}\} \tag{5.16}$$

in which $[C^{ep}]$ is the elasto-plastic stress-strain matrix and given as

$$[C^{ep}] = [C^e] - \frac{[C^e]\left\{\frac{\partial g}{\partial \sigma_{ij}}\right\}\left\{\frac{\partial f}{\partial \sigma_{ij}}\right\}^T [C^e]}{\left\{\frac{\partial f}{\partial \sigma_{ij}}\right\}^T [C^e]\left\{\frac{\partial g}{\partial \sigma_{ij}}\right\} - \left\{\frac{\partial f}{\partial \varepsilon^p_{ij}}\right\}^T \left\{\frac{\partial g}{\partial \sigma_{ij}}\right\}} \tag{5.17}$$

"

The matrix $[C^{ep}]$ may be used in performing incremental elasto-plastic finite element analyses, in the same way as the Generalized Hooke's Law is used in performing incremental elastic finite element analyses.

This elasto-plastic stress-strain relationship has the following characteristics:

1. The matrix $[C^{ep}]$ is not necessarily symmetrical if the yield function, f, and the plastic potential function, g, are not identical.
2. Since the matrix $[C^{ep}]$ depends on the current state of stress, the strains calculated in elasto-plastic finite element analyses are dependent on the current state of stress as well as the magnitude of changes in stress.
3. For some yield functions, f, and plastic potential functions, g, the inverse of the matrix $[C^{ep}]$ contains terms relating normal strain increments to shear stress increments. The relationship is thus capable of representing dilatant soil behavior.

Elasto-Plastic Stress-Strain Relationship for Isotropic Hardening Materials

It is assumed for isotropic hardening that as the yield surface expands, it retains the same shape as it had before, and hence that no functional anisotropy is introduced during plastic deformations. The yield function for this case may be expressed as

$$f(\{\sigma_{ij}\},\{\varepsilon^p_{ij}\}) = f^*(\{\sigma_{ij}\}) - f^{**}(\{\varepsilon^p_{ij}\}) \qquad (5.18)$$

in which f* depends only on the stress and f** depends only on the plastic strain history. The function f** may be expressed in terms of the plastic work, W^p:

$$f^{**} = F(\int dW^p) \qquad (5.19)$$

in which

$$dW^p = \{\sigma_{ij}\}^T\{d\varepsilon^p_{ij}\} \qquad (5.20)$$

Using Eqs. 5.18, 5.19 and 5.20, the following expression can be obtained:

$$\left\{\frac{\partial f}{\partial \varepsilon^p_{ij}}\right\} = -\frac{\partial F}{\partial W^p}\{\sigma_{ij}\}^T \qquad (5.21)$$

Substituting Eq. 5.21 into Eq. 5.17

$$[C^{ep}] = [C^e] - \frac{[C^e]\left\{\frac{\partial g}{\partial \sigma_{ij}}\right\}\left\{\frac{\partial f}{\partial \sigma_{ij}}\right\}^T[C^e]}{\left\{\frac{\partial f}{\partial \sigma_{ij}}\right\}^T[C^e]\left\{\frac{\partial g}{\partial \sigma_{ij}}\right\} + \left(\frac{\partial F}{\partial W^p}\right)\{\sigma_{ij}\}^T\left\{\frac{\partial g}{\partial \sigma_{ij}}\right\}} \qquad (5.22)$$

This form of the elasto-plastic stress-strain relationship is applicable to any isotropic hardening material.